DISSERTATION

submitted to the

Combined Faculty of Mathematics, Engineering and Natural Sciences

of

Heidelberg University, Germany

for the degree of

Doctor of Natural Sciences

put forward by

Christian Zimmer

born in Stuttgart

Oral examination:
15th December 2021

Experimental and Numerical Studies of Positronium Laser Cooling in a Magnetic Field

Referees:

Priv.-Doz. Dr. Alban Kellerbauer
Apl. Prof. Dr. Andreas Wolf

Zusammenfassung

Die vorliegende Dissertation behandelt die Anwendung von im Bereich der Quantenoptik entwick-elten Techniken auf das exotische Atom Positronium (Ps), zum Zweck der Bereitstellung kalter Ensembles von Ps Atomen in einem Magnetfeld.

Das Positronium-Atom, welches den gebundenen Zustand zwischen einem Elektron und seinem eigenen Antiteilchen, dem Positron, beschreibt, weist zahlreiche Besonderheiten auf, durch die es sich von allen anderen Atomen unterscheidet, die bislang lasergekühlt wurden. Insbesondere sein Antimaterie-Charakter sowie die außergewöhnlich kleine Masse gehen mit einigen ungewöhnlichen Phänomenen einher und haben, zusammen mit magnetfeldinduzierten Effekten, ein hochkomplexes Laserkühlungsschema zur Folge. Kalte und dichte Wolken von Ps-Atomen stellen, dank der exotischen Eigenschaften, kombiniert mit einer rein leptonischen Zusammensetzung, eine ideale Basis zur Überprüfung einiger fundamentaler Theorien dar und ebnen den Weg zu vielen weiteren faszinierenden Anwendungen, wie beispielsweise einer Positronium-Bose-Einstein-Kondensation.

Die durchgeführten numerischen Simulationen, die die gesamte Komplexität des Schemas berücksichtigen, ergeben, dass in schwachen ($|\boldsymbol{B}| \lesssim 50\,\text{mT}$) und starken Feldern ($|\boldsymbol{B}| \gtrsim 0.7\,\text{T}$) eine hohe Kühleffizienz für viele realistische experimentelle Konfigurationen erreicht werden kann. Auf der Grundlage dieser Ergebnisse wurde die Ps-Laserkühlung experimentell im Rahmen des AEḡIS-Experiments am CERN realisiert. Die Messungen zeigen deutlich, dass erfolgreich eine symmetrische optische Kraft auf das Ps-Ensemble in einem Feld von $|\boldsymbol{B}| = 180\,\text{G}$ aus-geübt wurde, und zwar in Form einer signifikanten Populationsanreicherung im Zentrum der Geschwindigkeitsverteilung, welches ein Hauptmerkmal für Laserkühlung darstellt, da es ein ein-deutiger Beweis für laserinduzierte Rückstoßeffekte ist.

Summary

The present thesis deals with the application of techniques developed in the field of quantum optics to the exotic atom positronium (Ps), for the purpose of the preparation of cold ensembles of Ps atoms in a magnetic field.

The positronium atom, which describes the bound state between an electron and its own antiparticle, the positron, shows numerous peculiarities setting it apart from all other atoms which have been subject to laser cooling so far. In particular, its antimatter character as well as the extraordinarily small mass are accompanied by several unusual phenomena and, together with magnetic-field-induced effects, entail a highly complex laser cooling scheme. Due to the exotic properties, combined with the purely leptonic composition, cold and dense clouds of Ps atoms would represent an ideal testing ground for several fundamental theories and pave the way for many further fascinating applications, such as positronium Bose-Einstein condensation.

The conducted numerical simulations, which consider the full complexity of the scheme, reveal that a high cooling efficiency can be achieved with appropriate laser radiation in weak ($|\boldsymbol{B}| \lesssim 50\,\text{mT}$) and strong fields ($|\boldsymbol{B}| \gtrsim 0.7\,\text{T}$) for many realistic experimental configurations. Based on these results, Ps laser cooling has been realised experimentally within the AEḡIS experiment at CERN. The measurements clearly demonstrate successful exertion of a symmetric optical force on the Ps ensemble in a field of $|\boldsymbol{B}| = 180\,\text{G}$, namely in the form of a significant population enhancement in the centre of the velocity distribution, which represents a key feature of laser cooling as it is unambiguous evidence for laser-induced recoil effects.

Beim Menschen ist es wie beim Velo.
Nur wenn er faehrt, kann er bequem die Balance halten.

– Albert Einstein,
5th February 1930, in a letter to his son Eduard [1].

Contents

Chapter 1

Introduction

Without a doubt, it is not easy to identify any equally intriguing physical phenomenon as the use of photons – the massless quanta of light – for the deceleration of massive particles, but the world of antimatter is certainly one of them. The combination of both within the same system can therefore justifiably be claimed to mark the dawn of a new era, opening up exciting new opportunities. With the establishment of laser cooling as a workhorse in many experiments in the fields of atomic physics and quantum optics, and the remarkable advances made recently in the production efficiency of antimatter particles, the time has finally come to enter this era.

Due to the property of antimatter particles to immediately annihilate when coming into contact with ordinary matter particles, they are intrinsically challenging to produce and trap. Even though a number of attempts have been made in recent years in this regard and some of them have even been crowned with success [2–4], a stable supply of pure antimatter atoms is still far out of reach. This is one reason for the growing interest in another very exotic atom, the positronium (Ps) atom[1], an antimatter system which is interesting to study also for many more reasons.

Positronium properties

Being the bound state of an electron (e^-) and its antimatter counterpart, the positron (e^+), the Ps atom exhibits both matter and antimatter character and is considerably easier to produce than any other antimatter atom. Its simple composition makes it very similar to hydrogen which does not only allow to apply well-established theories for describing Ps properties, but also to test and verify those theories on an atomic system with antimatter character.

However, being solely composed of two fundamental leptonic particles without further substructure, in particular being free of quarks, the positronium also exhibits very unique properties. In contrast to the hydrogen atom, where the proton has a quite significant impact on the energy states, the Ps level structure shows for example a degree of purity which can hardly be found elsewhere. High-precision spectroscopy on the Ps atom might thus make it possible to measure the Rydberg constant with unprecedented accuracy and shed a new light on a mystery surrounding the hydrogen atom which is still awaiting to be solved, namely the so-called proton radius puzzle [5–7] which relates to still contradicting measured values of the proton radius. The combination of its purely leptonic character and its composition of point-like particles furthermore ensures that the Ps atom is well described solely by the theory of electrodynamics, making it an ideal testing ground for (bound-state) quantum electrodynamics (QED) [7, 8].

As if these properties were not exceptional enough, the positronium atom is – with a mass of only twice the electron mass m_e – the lightest atom that can be produced artificially. Compared to the hydrogen system it will thus show huge recoil effects and – despite the lack of a real nucleus – so-called "hyperfine" splittings that are highly suppressed in ordinary atoms. The smaller the mass the more will spin-spin interactions eventually become apparent. In this context, it is noteworthy that the equality of electron and positron mass additionally implies that their associated magnetic momenta are as well of equal magnitude, albeit opposite value, which finally leads to interesting effects with regard to the energy level structure.

Much more intriguing, though, is the fact that its extraordinarily small mass makes the positronium atom a unique candidate for the investigation of relativistic quantum effects. Furthermore, the possibility to perform precise laser spectroscopy on the discrete internal energy states of Ps sets it clearly apart from other systems suitable for the investigation of relativistic effects, such

---

[1] While positronium is not an ordinary atomic system with a nucleus consisting of protons and neutrons, it exhibits very similar properties to the hydrogen atom.

as the electron. This distinctive feature opens up completely new opportunities, for example the exploration of relativistic quantum motion [9].

Physics enigma tested with positronium
In summary, its antimatter character, combined with the simple composition and pure level structure, makes the Ps atom an ideal candidate system for the investigation of antimatter properties in general. In particular, positronium can contribute to solving one of the most intriguing puzzles of our times, the baryon asymmetry problem, which describes the apparent excess of matter over antimatter in our universe. As the standard model of particle physics is entirely symmetric regarding matter and antimatter, it does not provide any convincing explanation for this observed imbalance and matter dominance [7]. Among the many approaches to resolve the riddle is the hypothesis of *baryogenesis*, which claims that certain processes during the development phase of the universe favoured the production of baryons over antibaryons [10]. This explanation necessarily requires the satisfaction of a number of conditions, formulated first by Andrei Sakharov in 1967 and therefore referred to as the *Sakharov conditions* [11]. One of them relates to the violation of fundamental symmetries of the standard model of particle physics, namely CP- and thus also T-violation. Another important Sakharov condition is the requirement that the universe should have experienced a period of thermal non-equilibrium.

Positronium, composed of a particle-antiparticle pair of opposite charge, is an ideal testing ground with regard to an investigation of this hypothesis as it opens up several possible approaches for the examination of CP-invariance especially. One of these approaches, for example, relies on the investigation of the Ps decay behaviour which is connected to CP-invariance in a very simple way: Due to the antimatter character, the positronium level structure is pervaded by numerous annihilation decay channels. Its charge neutrality, on the other hand, entails that it does not have any additive quantum numbers (more details will follow in Sec. 2.1.2) and is therefore an eigenstate of the charge conjugation operator C and CP. Consequently, an examination of its decay properties represents an efficient tool for testing CP-invariance since the observation of unexpected behaviour would be a direct indication of fundamental symmetry breaking [7, 12].

Apart from fundamental symmetries there is yet another elementary physical concept for which the positronium atom represents a unique testing ground, namely the equivalence principle of gravitational and inertial mass, the foundation of the theory of general relativity. One approach to verify this postulate consists in a measurement of the gravitational force experienced by the antimatter system. This can be achieved by means of free-fall or interferometry experiments, for example [9], for which positronium is considered a promising candidate system [13–15] among others, such as antihydrogen [16–18] or muonium [19], the exotic bound state between an electron and an antimuon. For such gravitational measurements it is crucial to use neutral antimatter systems, so that phase shifts of interest, resulting from inertial forces, for instance [9] cannot be masked by any Coulomb interaction. Here again, fundamental symmetry breaking would directly manifest itself in the observation of unexpected effects.

A need for cold positronium
In view of the many peculiarities, there is obviously good reason for the growing interest in the positronium atom over the past few decades. The story of the Ps atom initially started not even a hundred years ago, in 1934, with the first prediction of the existence of a bound state between the electron the positron, by Stjepan Mohorovičić [20] followed by the first experimental verification by Martin Deutsch in 1951 [21]. Triggered by these landmark events, the Ps business soon developed rapidly so that reliable and efficient positronium production has meanwhile become a well established practice. Thanks to extensive studies, its internal level structure is also well-known already [22]. With these advances, Ps experiments have meanwhile reached a state where measurements become limited by the thermal motion of the atom and would therefore highly benefit from the preparation of cold atomic ensembles, that means with reduced energetic spread of the particle clouds. It is not only the precision of interferometry measurements with positronium, for gravity experiments for example, which could be enhanced considerably by using monochromatic

particle beams, but also spectroscopic measurements would benefit a lot from the availability of intense cold beams with highly suppressed Doppler broadening. Beyond that, it would pave the way to many more exciting applications such as the creation of a positronium Bose-Einstein condensate (BEC) [23–26]. The use of fully spin-polarised Ps atoms in the 2^3S_1 state, for example, has recently been shown to be suitable for this purpose [27].

Even though the thermal energy of the atoms depends primarily on certain properties of the generation process, taking place in so-called converter targets for instance [28], it is technically very difficult to minimise the energy spread of the positronium atoms through the optimisation of the formation procedure. Instead, it is much more worthwhile to exploit the property of atoms to interact resonantly with electromagnetic fields and to resort to quantum-optical techniques for thermal energy reduction, subsequently to the formation process. An important experimental tool in this regard is the Doppler laser cooling technique, which has become an established procedure in many experiments in the field of atomic physics and quantum optics for cooling of different kinds of neutral atoms [29–32]. In principle, this technique is only limited by the energy of the recoil experienced by the atom during single photon transfer events (more details in following chapters). In the positronium case, this amounts to roughly $v_{rec} = 1.5\,\mathrm{km/s}$ in terms of Ps velocity or $T_{rec} = 74\,\mathrm{mK}$ in terms of the equivalent temperature. Although the cooling limit for the Ps atom is, due to its tiny mass, considerably higher than the typical Doppler temperature limits of the order of few hundred micro-Kelvin for alkali atoms for instance, it is still much lower than what can be achieved by any other means.

The general feasibility of positronium laser cooling, including Bose-Einstein condensation, has already been examined and demonstrated by several numerical proof-of-concept studies in the past [24, 33–36]. In fact, first experimental trials of Ps laser cooling have as well already been performed by the groups around K. Wada, M. Kajita and coworkers in the years between 2000 and 2002 [37–41]. In spite of the high cooling efficiency predicted by the simulation studies [42–44], none of the experimental attempts has so far been crowned with substantial success, primarily due to insufficient laser performance.

Much more important however is the fact that all numerical and analytical studies performed so far have been performed in field-free environments. Usually, experimental positronium production takes place in magnetic field environments which are required either for efficient positron transport to the converter target [7] or for the respective Ps experiments such as generation of antihydrogen atoms [45, 46].

A theoretical investigation and experimental implementation of Ps laser cooling in magnetic field environments are therefore essential steps on the way towards high-precision tests of bound-state QED or fundamental symmetries and the realisation of the many further intriguing applications, apart from the fact that Ps laser cooling is already a worthwhile goal in itself.

The objective of this thesis was to carry out thorough numerical as well as experimental studies of Ps laser cooling in magnetic fields. For this purpose, first numerical calculations on Ps laser cooling in a static and homogeneous magnetic field were conducted. This included studies of the general one-dimensional cooling scheme and the dependence of the cooling efficiency on the most relevant laser parameters, as well as on the magnetic field strength. Subsequently, realistic two- and three-dimensional cooling schemes in selected experimental configurations, such as the use of laser cooling as a tool for Ps beam collimation by reduction of the angular spread or 3D moving molasses cooling, were investigated. It is important to mention that parts of the results presented here have been published in Phys. Rev. A as an article [47].

The numerical results have then been verified in a dedicated experimental campaign within the "**A**ntimatter **E**xperiment: **g**ravity, **I**nterferometry, **S**pectroscopy" (AEḡIS experiment) at CERN. The results are substantiated by means of dedicated numerical simulations performed with the aim of reproducing the experimental measurements.

Chapter 2

Concepts for Ps laser cooling in a magnetic field

2.1 The positronium atom

First predicted by Stjepan Mohorovičić in 1934 [20] and experimentally discovered by Martin Deutsch at MIT in 1951 [21] the positronium atom still represents one of the most fascinating atomic systems in both theoretical as well as experimental respects. This is due to its numerous exceptional properties, as mentioned in the Introduction.

Especially the tiny mass of the Ps atom entails a few unusual effects which are not known from other atomic species. The most prominent example in this respect, and also the most relevant one regarding the subject of this thesis, is the relatively broad velocity distribution of Ps clouds and the accordingly large Doppler broadening of transition lines.

The impact of the Doppler effect on the transition plays an important role in Ps laser cooling. In practical terms, this is due to the fact that it imposes strong requirements with respect to appropriate cooling laser systems since they need to cover an appreciable part of the velocity distribution in order to ensure efficient cooling. On the other hand, it also reduces the pressure on the laser system used for probing the atomic cloud. The broader the distribution, the less narrow the probe bandwidth has to be in order to achieve the same resolution in scanning the Doppler distribution. In other words, in case the probe bandwidth cannot (easily) be reduced any further, broader distributions will be of benefit to the accuracy of velocity-resolved measurements. Still, the broad distribution also requires both laser systems to offer wavelength tunable over the whole Ps velocity range.

Apart from these practical considerations, the Doppler effect has a significant impact on the theoretical treatment of the atom-light interaction. Since it strongly affects the transition lines, it is described in detail (and quantitatively) in the context of transition linewidths in Section C.7.3.

2.1.1 Positronium formation

Even though the focus of this thesis lies on processes related to the internal level structure of the atom, its interaction with static magnetic fields and manipulation by laser radiation, the formation process naturally still represents an essential part, not to say condition *sine qua non* for any experiment involving positronium. The experimental setup, in which the measurements for this thesis have been performed, is described later in detail. Nevertheless, the basic mechanisms of Ps formation shall, for better understanding of the content of following chapters, be described here already.

In general, numerous methods exist to facilitate the formation of the bound state between an electron and a positron. Experimentally, though, only few methods have established to this end. An overview of these techniques can for example be found in [48] or [28]. The description here will concentrate on the most relevant technique with regard to this thesis, which is based on bombarding special nanostructured targets with positrons. Even though positronium can in principle be formed by shooting positrons on any material, there exist only few materials in which it can be produced efficiently with temperatures of $\simeq 300\,\mathrm{K}$ or less. One of the most important examples are converter targets consisting of silicon dioxide (SiO_2).

In the AE$\bar{\mathrm{g}}$IS experiment, these targets are etched with so called nano-channels to facilitate the formation even further. Since these nano-channels typically do not traverse the target completely from one side to the other, such converter targets are called reflection targets. That means the positronium atoms are emitted from the same side as the positrons enter.

If a beam of positrons[2] is pointed at such a target, the particles will enter the nano-channels with high energies ($\approx 5\,\mathrm{keV}$ in the AE$\bar{\mathrm{g}}$IS experiment) where they penetrate deeply into the nearest wall. Due to inelastic collisions with the grid atoms of the bulk material (which in the present case is the silicon which encloses the nano-channels that are covered by only few nanometre-thick layers of SiO_2, much thinner than the positron penetration depth), the positrons thermalise quickly (within a few picoseconds) with the material. As soon as a thermal positron comes into contact with a channel wall again, it eventually combines with an electron from the (SiO_2) surface to form a Ps atom with an energy of a few electronvolts, equivalent to the binding energy of the respective positron-electron pair[3]. In case the positron has not yet been able to fully thermalise with the bulk material, when arriving at a channel wall, it might also first knock out an electron from the SiO_2 surface to combine with and finally form the bound state.

In the process of finding its way out of the respective channel, the Ps atom will once again repeatedly collide with the surface inside the channel and thereby lose further energy. It is important to note that the Ps atoms do not necessarily thermalise completely with the target, though. Each Ps atom will rather undergo an individual number of collisions depending on its penetration depth into the respective channel (with $\approx 10^4$ collisions per μm, which leads to roughly 100 to 1000 collisions for Ps formed close to the surface). Consequently, the kinetic energy of each atom will differ from atom to atom, depending on the amount of energy lost during the collisions.

The resulting velocity distribution can be modelled by means of a 3D isotropic Maxwell-Boltzmann distribution

$$f(v) = \left(\frac{m_{\mathrm{Ps}}}{2\pi k_{\mathrm{B}} T}\right)^{3/2} 4\pi v^2 \exp\left(-\frac{m_{\mathrm{Ps}} v^2}{2 k_{\mathrm{B}} T}\right), \tag{2.1}$$

which can be assigned a characteristic temperature T, defined in terms of the most probable velocity v_{p} (solving $\mathrm{d}/\mathrm{d}v f(v) = 0$) according to

$$k_{\mathrm{B}} T = \frac{m_{\mathrm{Ps}}}{2} v_{\mathrm{p}}^2 , \tag{2.2}$$

where k_{B} indicates the Boltzmann constant and m_{Ps} the mass of the Ps atom. In three dimensions, the relation of v_{p} to the root-mean-square (rms) speed $v_{\mathrm{rms}} = \sqrt{\langle v^2 \rangle}$ is thereby given by $v_{\mathrm{p}} = \sqrt{2/3}\, v_{\mathrm{rms}}$.

Thus, during the time interval $\mathrm{d}t$, the number of Ps atoms ejected from the target under an angle θ with respect to the normal of the target, that is, in the conical solid angle $\mathrm{d}\Omega = \sin(\theta)\,\mathrm{d}\theta\mathrm{d}\phi$ (in spherical coordinates) and with a velocity $\|\boldsymbol{v}\|$ between v and $v + \mathrm{d}v$, is proportional to $f(v) v \cos(\theta) \mathrm{d}t \mathrm{d}\Omega \mathrm{d}v$. Numerically, the distribution of such an effusive beam can be created by means of inverse transform sampling, also known as Smirnov inverse probability integral transform [49].

The resulting temperature value is a unique characteristic of each single target (depending on various parameters as described in [28]) which, in the AE$\bar{\mathrm{g}}$IS experiment and for the target used for the measurements presented in this thesis, amounts to roughly $280\,\mathrm{K}$ to $300\,\mathrm{K}$ [50].

It should be noted that even in case of arbitrary, non-Maxwell-Boltzmann distributions it is still possible to define an effective temperature parameter T which is directly related to the rms speed v_{rms}. This is especially useful for the description and analysis of the velocity distribution of the atomic cloud after manipulation of the atoms for example by means of laser interaction, which affects only certain velocity ranges of the distribution. This temperature definition is also chosen and described in more detail in Section 3.1.2 for analysing the numerically acquired data.

---

[2] More details on the generation of such a positron beam can be found in Sec. 4.2.2. Further information on the sophisticated sequence of steps necessary to produce such a beam, including a characterisation of the assembly in the AE$\bar{\mathrm{g}}$IS experiment, can be found in [28].

[3] Of course Ps formation does not only take place inside the nano-channels but potentially also on the target surface. The fraction of Ps produced there is however negligible compared to the amount of atoms produced inside the channels. This is due to the fact that less than 0.1% of the positrons impinging the target already stop at the surface. Furthermore, the surface itself can, metaphorically speaking, in fact be described as a crater landscape riddled with nano-channels.

The definition of an effective temperature parameter based on the particle momenta $m_{\mathrm{Ps}}v$ allows for assigning the ejected cloud, consisting of N Ps atoms in a volume V, a thermal de Broglie wavelength λ_{dB} according to

$$\lambda_{\mathrm{dB}} = \sqrt{\frac{2\pi\hbar^2}{m_{\mathrm{Ps}}k_{\mathrm{B}}T}} \; . \tag{2.3}$$

The thermal de Broglie wavelength usually serves for quantifying the coherence length of the (ideal) gas that determines its quantum nature. In case λ_{dB} exceeds the inter-particle distance, given by $(V/N)^{1/3}$, quantum effects can potentially become evident and the distribution of Ps atoms will obey the Bose-Einstein statistics. In the opposite case, i.e. $(V/N)^{1/3} \gg \lambda_{\mathrm{dB}}$, a quantum description is not necessary and the gas can be described by the Maxwell-Boltzmann statistics, for example [48].

For a cloud of positronium atoms at an effective temperature[4] of $300\,\mathrm{K}$ the de Broglie wavelength becomes $\lambda_{\mathrm{dB,Ps}} \approx 3\,\mathrm{nm}$ which is obviously much smaller than the typical inter-particle distance of the order of $10^{-4}\,\mathrm{m}$ to $10^{-5}\,\mathrm{m}$ for densities of $N/V \approx 10^4$ to $10^5\,\mathrm{atoms/mm^3}$ as found in the AE$\bar{\mathrm{g}}$IS experiment. A quantum description of the Ps cloud is thus clearly dispensable.

Finally, it should be mentioned that in the AE$\bar{\mathrm{g}}$IS experiment, the active area of the target, which is the area in which Ps are produced most efficiently, has a diameter of $10\,\mathrm{mm}$ and the atoms can be assumed to leave the target isotropically distributed over all possible directions of the half space in front of the target. Typically, each Ps pulse contains about 10^6 atoms for the targets used in the scope of this thesis.

Naturally, the Ps atoms are not emitted simultaneously by the target but within a short period of time which typically amounts to few nanoseconds. In a simplified description, this time spread can adequately be mimicked by simultaneously creating all atoms at the same point of time, within a spatial slab of few tens of millimetres, corresponding to roughly the distance travelled by a Ps atom within the mentioned time spread of production or, respectively, corresponding to the lead of the fastest with respect to the slowest atoms. In this model the Ps cloud is thus created within a volume of the area of the active area times the thickness of the spatial slab. A more detailed description of the complete Ps formation procedure including the mechanism and assembly necessary for initial generation of the positron beam are given in [28] and references therein.

2.1.2 Antimatter nature and annihilation

The second peculiar feature of the positronium atom, besides its exceptionally small mass, is of course the fact that it consists of a particle and its own antiparticle. Since positronium represents the antimatter particle which is easiest to produce, it provides a unique testing ground for the verification of various theoretical predictions and hypotheses, as announced in the introduction. First and foremost to be mentioned in this regard is CP-violation which, according to the hypothesis of baryogenesis and the corresponding Sakharov conditions, is required to explain the matter-antimatter asymmetry in the universe [51]. Another prominent example is the precise confirmation of quantum electrodynamics (QED), as reported for instance in [52], which could be achieved by measuring the annihilation lifetime of the Ps atom. Equally important as the lifetime, with respect to precision tests, is however also the measurement of the Ps energy levels [22].

Apart from these fundamental investigations, the comparatively easy production and relatively long annihilation times of ortho-Ps (the triplet state of the atom) of the order of a few hundred nanoseconds (including also the excited states) offer the possibility to carry out sophisticated laser manipulation and spectroscopy experiments on a particle with antimatter character. This connection between quantum optics, and particle and antimatter physics represents a completely novel field of study.

---

[4] It is important to point out that this effective temperature of the Ps atoms must not be confused with the temperature of the experimental environment as it does not describe an absolute temperature but rather the energy spread of the Ps cloud *relative* to the environmental temperature.

The positronium atom is composed of two spin-$1/2$ leptons and is thus of purely leptonic nature. In combination, the two spins can produce a singlet or triplet state which are referred to as *para*- and *ortho*-positronium, or in short, p-Ps and o-Ps, respectively. In the first case, where the spins have antiparallel orientation with respect to each other, the total spin of the atom becomes $S = 0$, whereas in the latter case with parallel alignment of the individual spins s_{e^-} and s_{e^+} of the electron and positron, respectively, it is $S = 1$.

In general, the term "annihilation" refers to the collision between a particle and its antiparticle with concomitant formation of new particles (or light quanta) and complete disappearance of the original particle-antiparticle pair. In the Ps case annihilation is thus the mutual destruction of the electron-positron pair under transformation into gamma radiation.

In an illustrative manner the annihilation process can be described in the following way: According to the Dirac pair theory, the total rest mass $2m_e c^2$ which becomes available in the annihilation process (where m_e is the electron mass), is entirely converted into photons. The number of decay products, i.e. gamma quanta, is determined by the initial spin state of the atom and is governed by the fundamental laws of conservation of translational and angular momentum.

The probability for the annihilation of any Ps state, which is the rate at which it occurs, is determined by the overlap of the wave functions of electron and positron. The larger this overlap, the higher the probability for the collapse of the total wave function and destruction of the bound state. This implies that there must be a clear deviation in annihilation times between ground and excited states since the distance between e^- and e^+ increases for higher excitation states, which in turn reduces the overlap of their wave functions [53]. In this context, it is worth mentioning already that obviously the lifetime of a Ps atom can, to a certain extent, be artificially enhanced by exciting it, for instance by laser radiation, from the ground state to longer-lived excited states.

While this overlap argument only explains the relative difference in annihilation probability for the different states belonging to the same spin state, the mismatch in lifetimes of singlet and triplet states directly originates from the principle of conservation of momentum and the probability for the production of the resulting product particles.

In compliance with these conservation laws the annihilation of the para-Ps (singlet) ground state[5] 1^1S_0 is accompanied by the emission of (at least) two gamma quanta of opposite translational and angular momentum. On average, this process is observed to occur at a rate of $\Gamma^{(\mathrm{ann})}(1^1S_0) \approx 8\,\mathrm{ns}^{-1}$ which is equivalent to a lifetime of $\tau^{(\mathrm{ann})}(1^1S_0) = 125\,\mathrm{ps}$ [53].

In contrast, to comply with the conservation of angular momentum, the annihilation of the triplet ground state would only need to be accompanied by the emission of a single photon, which, however, conflicts with the conservation of linear momentum. For this reason it results in the emission of (at least) three gamma rays. Since this is a process of higher order, though, it is much less likely to occur compared to singlet annihilation. Triplet lifetimes are therefore in general significantly longer than their singlet counterparts, usually by a few orders of magnitude. The triplet ground state 1^3S_1, for example, decays at a rate of only $\Gamma^{(\mathrm{ann})}(1^3S_1) \approx 7\,\mu\mathrm{s}^{-1}$, which results in a lifetime of $\tau^{(\mathrm{ann})}(1^3S_1) = 142\,\mathrm{ns}$ [53], considerably longer than for the singlet ground state.

In order to address the question why the decay products are specifically photons and to understand how many of them are emitted as a result of the annihilation of excited states, the process needs to be treated on a deeper level. For this purpose, it is necessary to introduce the transformation of *charge conjugation* and the corresponding operator C. C reverses all quantum charges of the system to which it is applied, that means, in particular, also the sign of all electric charges (but also any other charges such as flavour charges, lepton numbers, etc.). It does, however, neither affect the mass of the particle nor its linear momentum or spin. Since particle-antiparticle pairs only differ in charge-related properties, C is the operator which converts particles into their antiparticles.

The eigenvalue λ_C of the charge conjugation operator C describes how the state or wave function of the system (i.e. particle) changes as a result of the reversal of charges and is called *C-parity*.

---

[5] A detailed description of these term symbols will be given later, for readers not familiar with them.

With regard to the Ps atom, the C-parity thus describes how charge conjugation of both the e^- and e^+ changes the total wave function of the atom. In this context it is worth to note that the Ps atom is its own antiparticle, with its wave function only changing its sign under the application of charge conjugation. In general, twofold application of C on a given particle must leave its wave function unchanged; the resulting particle must be absolutely identical to the original one. The eigenvalues of λ_C are thus given by ± 1.

According to the Standard Model of particle physics, both the strong and the electromagnetic interaction obey charge conjugation symmetry. This means that the eigenvalue of the charge conjugation operation, C-parity, is a quantum number which is conserved in all particle reactions that are mediated by either of the two interactions. Thereby, the term "particle reaction" refers to the conversion of particles as a result of any interaction in the system.

In contrast to the individual charges of the system (in case of Ps, the electric charges of e^- and e^+), C-parity is a *multiplicative quantum number*, that means, the product of the C-parities of the interacting particles is conserved (i.e. $\lambda_C^{(e^-)} \times \lambda_C^{(e^+)}$). The charges themselves, on the other hand, are *additive quantum numbers* since it is their sum which is preserved in the course of the reaction. Other examples for additive quantum numbers, besides charge Q, are the lepton number, the baryon number and strangeness, charm, bottomness and topness. It is furthermore important to mention, that for each additive quantum number A of a matter particle, the corresponding antiparticle has quantum number $-A$ [54].

The following conclusions can now be drawn with regard to the process of annihilation of a positronium atom: Obviously, the process of annihilation of the Ps atom is a particle reaction that is mediated by the electromagnetic interaction and thus results in the emission of exchange particles of the electromagnetic force, namely photons, the quanta of the electromagnetic field[6]. Consequently, C-parity must be conserved during annihilation.

Furthermore, due to the fact that positronium is a bound state consisting of a particle and its own antiparticle, it is clearly an eigenstate of the charge conjugation operator C. As its wave function changes sign under the operation of charge conjugation, it is the eigenstate with eigenvalue -1. Interestingly, the positronium atom is thus its own antiparticle, as mentioned above.

The number N_γ of photons emitted during Ps annihilation then directly results from the comparison of the C-parities, $\lambda_C^{(Ps)}$ of the initial (Ps atom) and $\lambda_C^{(\gamma)}$ of the final state (N_γ photons), in combination with the conservation laws. In order to derive the expressions for $\lambda_C^{(Ps)}$ and $\lambda_C^{(\gamma)}$, it is important to mention that the application of the C operator is equivalent to the simultaneous operation of both parity and spin exchange [55].

Consequently, the eigenvalue $\lambda_C^{(Ps)}$ of the initial state, the Ps atom, results from a combination of three operations, namely spin and parity exchange as well as exchange of particle and antiparticle, where the individual contributions are given by $(-1)^{S+1}$, $(-1)^l$ (with l denoting the orbital angular momentum quantum number which characterises the parity state) [48] and finally, according to Dirac theory, an additional factor of (-1) from the antimatter exchange [56]. Hence, $\lambda_C^{(Ps)} = (-1)^{l+S}$.

The eigenvalue of the charge conjugation operator for photons on the other hand is given by $(-1)^{N_\gamma}$ which follows from the following two arguments: Firstly, the photon is its own antiparticle and thus an eigenstate of C. This restricts the possible values of the C-parity of a single photon to (± 1). Secondly, charge conjugation leads to the inversion of the electromagnetic field, which finally fixes the eigenvalue to an odd value, thus (-1) for one photon and $\lambda_C^{(\gamma)} = (-1)^{N_\gamma}$ for N_γ photons.

Ultimately, charge conjugation invariance requires that the annihilation process must necessarily obey the selection rule

$$(-1)^{l+S} = (-1)^{N_\gamma} \, , \tag{2.4}$$

which implies the emission of an even (odd) number of photons during annihilation of singlet (triplet) states [48].

---

[6] If electrons and positrons were more massive, the Ps annihilation could actually also result in the creation of massive particles.

Since additionally radiation-less and single-photon decay is forbidden by the laws of conservation of momenta, the decay of both singlet and triplet Ps states has to take place by emission of at least two or three photons, depending on the orbital angular momentum quantum number of the respective state. This finally gives the explanation for the type and number of decay products produced as a result of the collapse of the e^--e^+ bound state.

As mentioned above, the positronium atom provides a unique testing ground for the examination of various theories and hypotheses such as the fundamental symmetries. Especially the observation of the annihilation process, including, *inter alia*, corresponding lifetimes and decay products, represents an important tool to this end, since violations of the predictions would manifest themselves in the occurrence of forbidden decay modes. Having no additive quantum numbers, the Ps atom can, in principle, couple as well to various other exotic systems providing a mechanism for invisible decay, such as Dark Matter [7, 57–59]. Since this topic, however, greatly exceeds the scope of the present introduction, it shall not be explored any further here. The main message of all experiments performed to the present day is that no anomalous behaviour or violation of any theory could be observed so far [7].

In particle physics, charge conjugation symmetry represents only one of the most fundamental symmetries that govern particle reactions. Other examples for symmetries existing in the framework of the Standard Model are the P- and T-symmetries responsible for parity and time reversal properties, respectively. Apart from these three standalone symmetries, the Standard Model of particle physics is based on the necessary condition that the combination of all three, known as CPT-symmetry, must be a symmetry as well. The combination of charge conjugation C and parity inversion P, though, is no fundamental symmetry as it was observed to be violated in some physical systems (CP-violation) [60–65]. In general, CP-violation also entails T-violation (provided that CPT-symmetry is conserved).

The impact of annihilation on Ps laser experiments is primarily limited to the disappearance of atoms. In this respect annihilation thus represents an impediment to measurements since it might finally impair their accuracy. On the other hand, though, annihilation can also be exploited for detection and diagnostics in such measurements. The most important technique to be mentioned here is single-shot positron annihilation lifetime spectroscopy (SSPALS), which has also been used in the context of this thesis to acquire the data presented. More information on this technique will be given there (see Sec. 4.1.1). It should already be mentioned here, though, that this detection tool relies on time-resolved recording of decay products within a certain spatial area.

Due to their general importance of annihilation with regard to laser cooling experiments (and simulations), it is finally worth to briefly introduce the analytical expressions which can be used to evaluate the annihilation rate $\Gamma^{(\text{ann})}$ and, respectively, the lifetime $\tau^{(\text{ann})} = 1/\Gamma^{(\text{ann})}$. Elaborate calculations have been performed to this end, most notably by Alekseev in the late 1950's [66, 67]. The analytical results for all states with orbital angular momentum quantum number $l = 0$ and 1 (S- and P-state respectively) are presented in the overview in Eq. (2.5) (primarily taken from [66, 67] with additions from [68] and [7]). The respective state is denoted by means of its term symbol in the beginning of each line in brackets following $\Gamma^{(\text{ann})}$. The information in brackets at the end additionally indicates the (predominant) decay products of the respective state. All rates are given only to the lowest order in α since higher-order corrections, such as the two-loop corrections calculated by Adkins in 2002 and 2003 [69, 70], can be considered irrelevant for the discussions in this thesis.

The annihilation rates of all states with orbital quantum numbers $l > 1$ can in general be neglected due to increasingly reduced overlap of electron and positron wave functions and accordingly small annihilation probability [47]. For these states radiative decay (more details will follow in Sec. 2.2.2) is much more likely than annihilation decay.

para-Positronium:

$$\Gamma^{(\mathrm{ann})}(n^1\mathrm{S}_0) \qquad = \alpha^5 \, \frac{m_\mathrm{e}c^2}{2\hbar} \, n^{-3} \qquad\qquad \approx \frac{n^{-3}}{125.1\,\mathrm{ps}} \qquad (2\gamma\text{-decay})$$

$$\Gamma^{(\mathrm{ann})}(n^1\mathrm{P}_1) \qquad = \alpha^8 \, \frac{m_\mathrm{e}c^2}{\hbar} \, \frac{n^2-1}{9\pi n^5} \ln\left(\frac{8n^2}{\alpha^2}\right) \qquad\qquad (3\gamma\text{-decay})$$

ortho-Positronium: $\qquad\qquad\qquad\qquad\qquad\qquad\qquad\qquad\qquad\qquad\qquad$ (2.5)

$$\Gamma^{(\mathrm{ann})}(n^3\mathrm{S}_1) \qquad = \alpha^6 \, \frac{m_\mathrm{e}c^2}{2\hbar} \, n^{-3} \, \frac{4(\pi^2-9)}{9\pi} \qquad \approx \frac{n^{-3}}{142.0\,\mathrm{ns}} \qquad (3\gamma\text{-decay})$$

$$\Gamma^{(\mathrm{ann})}(n^3\mathrm{P}_0) \qquad = \alpha^7 \, \frac{m_\mathrm{e}c^2}{\hbar} \, \frac{n^2-1}{8n^5} \qquad\qquad (2\gamma\text{-decay})$$

$$\Gamma^{(\mathrm{ann})}(n^3\mathrm{P}_1) \qquad = 0 \qquad\qquad\qquad\qquad\qquad (\text{No } 2\gamma\text{- or } 3\gamma\text{- decay.})$$

$$\Gamma^{(\mathrm{ann})}(n^3\mathrm{P}_2) \qquad = \alpha^7 \, \frac{m_\mathrm{e}c^2}{\hbar} \, \frac{n^2-1}{30n^5} \qquad\qquad (2\gamma\text{-decay})$$

Obviously, all expressions have a factor $m_\mathrm{e}c^2/\hbar$ in common, which is the quantised Ps rest mass in terms of $\hbar$, the fundamental unit of energy. Furthermore, they all show a similar dependence on the principal quantum number n. Only the rates of the P-states deviate slightly from the general n^{-3} scaling for low n-states. On the other hand, though, the rates clearly differ in their dependence on the fine structure constant α, which in fact reflects the mismatch in annihilation probabilities based on the overlap of the wave functions. While the decay of longer-lived states, i.e., those decaying by 3γ-emission as well as the (excited) P-states, show a proportionality of α^6 (for the triplet S-state) or even α^7 (all P-states); the rates of the fastest decaying singlet S-states only scale with α^5.

Interestingly enough, the triplet $n^3\mathrm{P}_1$ states do not even show any 2γ- or 3γ-annihilation decay at all, which implies that these states can be considered stable bound states to this order of decay[7]. Due to a non-zero, albeit negligibly small, probability for higher-order decay they still do not have infinite annihilation lifetimes. It can nevertheless be assumed that atoms populating one of the $n^3\mathrm{P}_1$ states will more likely decay radiatively to the next lower $(n-1)^3\mathrm{S}_1$ state, i.e. by emission of an ultraviolet photon, than be completely destroyed via annihilation. This annihilation behaviour can, illustratively, again be explained by means of the overlap of the corresponding wave functions. For the $n^3\mathrm{P}_1$ states with $l=1$ and $J=1$, the vectors of the total angular momentum[8] $\boldsymbol{l}$ (which is the sum of the individual orbital momenta of e^- and e^+) and the total spin $\boldsymbol{S}$ (sum of the individual spins) are oriented orthogonally to each other. In this configuration, at least four gamma quanta are required as particle reaction products to conserve the quantum numbers S and J of $\boldsymbol{S}$ and $\boldsymbol{J} = \boldsymbol{l} + \boldsymbol{S}$, respectively, during an annihilation.

2.2 Positronium level structure

2.2.1 Quantum numbers and eigenfunctions

Quantum numbers

Before jumping into the discussion of the positronium level scheme in the absence of fields, it is necessary to briefly introduce some terminology used throughout this thesis: As done in the context of the annihilation rates above, each energy levels is generally specified by its spectroscopic term symbol $\left(n^{2S+1}l_J\right)$ which is composed of all quantum numbers required to describe a certain level.

---

[7]   It should be noted, though, that this description is only valid in the absence of external fields. Due to the interaction with such fields, different internal states can couple to each other, leading to often unpredictable changes in lifetimes.

[8]   More details on the terminology and angular momentum coupling will be given in Sec. 2.2.

As usual, n denotes the *principal quantum number* of the "shell" (known from the Bohr model), l is the quantum number associated with the total *orbital angular momentum* $\boldsymbol{l}$, S, which determines the spin multiplicity $(2S+1)$, is the quantum number of the total spin $\boldsymbol{S}$ and J the one belonging to the *total angular momentum* $\boldsymbol{J} = \boldsymbol{l} + \boldsymbol{S}$. J can take integer values in the range $|l - S| \leq J \leq l + S$.

It is further recalled that all angular momenta $\boldsymbol{l}, \boldsymbol{S}$ and $\boldsymbol{J}$ are connected to their quantum numbers according to the corresponding eigenvalue equation, which for $\boldsymbol{J}$, for example, reads $\hat{\boldsymbol{J}}^2 |\Psi\rangle = J(J+1)\hbar^2 |\Psi\rangle$, where $|\Psi\rangle$ denotes the state of the atom and quantities with hats indicate operators.

Generally, the term *level* refers to the set of $2J + 1$ states with specific numbers l, S and J, but different orientation in space. *States* in turn are always described by a full set of quantum numbers (n,l,S,J,m) where m is the quantum number assigned to the projection J_p of $\boldsymbol{J}$ onto the quantisation axis of the system which is defined for example by an external magnetic field, as is the case here for laser cooling positronium atoms in magnetic fields. The corresponding eigenvalue equation is given by $\hat{J}_p^2 |\Psi\rangle = m\hbar |\Psi\rangle$. The values of m can thus take $(2J + 1)$ integer values ranging from $-J$ to $+J$. Similarly, the magnetic quantum numbers m_s and m_l describe the magnitude (in units of $\hbar$) of the projections $\boldsymbol{S}$ and $\boldsymbol{l}$, respectively.

Angular momentum coupling

Several coupling schemes exist to obtain the total angular momentum from the separate angular momenta of the system, whose suitability is determined by the respective circumstances of the interaction. The most important type in atomic physics is spin-orbit coupling mediated by weak magnetic fields, induced by the motion of the particles with respect to each other. In atoms with small mass, the separate momenta couple according to the so-called *LS-* or *Russell-Saunders coupling scheme* where first all individual spins $\boldsymbol{s}_i$ and orbital momenta $\boldsymbol{l}_i$ of the system combine separately to a total spin $\boldsymbol{S} = \sum_i \boldsymbol{s}_i$ and $\boldsymbol{l} = \sum_i \boldsymbol{l}_i$ respectively before subsequently $\boldsymbol{S}$ and $\boldsymbol{l}$ are coupled to form the total angular momentum $\boldsymbol{J} = \boldsymbol{l} + \boldsymbol{S}$. In heavy atoms (that means higher nuclear charges) in turn, it is more adequate to describe the process by means of the so called jj-coupling, where all individual spins $\boldsymbol{s}_i$ combine first with their according orbital momenta $\boldsymbol{l}_i$ to individual total angular momenta $\boldsymbol{j}_i$ which then add up to the total angular momentum $\boldsymbol{J} = \sum_i \boldsymbol{j}_i = \sum_i (\boldsymbol{l}_i + \boldsymbol{s}_i)$ of the atom.

Since Ps is the lightest atomic system, it is in general the LS-coupling scheme which is adopted in this thesis, if not explicitly specified otherwise.

Finally, it should be pointed out that the quantum number J is only a good quantum number, or rather defined at all, if the coupling between the angular momenta $\boldsymbol{l}$ and $\boldsymbol{S}$ is the dominant interaction. This is especially only the case, if there are no external perturbations, such as electromagnetic fields, which are sufficiently strong to break this coupling and become themselves the dominant interaction partner for the separate momenta. In this case it is no longer valid to apply the LS-coupling scheme.

Eigenfunctions

In general, the eigenstate $|\Psi_i\rangle$ of an operator, such as position, angular momentum or energy (given by the Hamiltonian) is a vector in Hilbert space which solves the corresponding eigenvalue equation of the operator. Each eigenstate is thus assigned a unique eigenvalue. The eigenstates can either be expressed as linear combinations of a certain set of basis states or can themselves constitute such a basis, that means a complete and enumerable set of usually orthonormal vectors. In this context, the term "complete" means that the set of basis states spans the whole Hilbert space, so that any state can be expanded as a linear combination in terms of these basis states.

Thus, the eigenstates of a quantum system such as the positronium atom can in principle be chosen arbitrarily, however it is common to express them, similarly to the case of hydrogen, each in terms of their corresponding quantum numbers (n,l,s,j,m), i.e., as elements of the (n,l,s,j,m)-basis which, in bra-ket notation, are written as $|nlsjm\rangle$. Alternatively, each eigenstate can also be expanded in terms of the factorised kets $|nlm_l\rangle |Sm_s\rangle$ which are the natural basis states of the spin

and orbital wave functions, used in absence of spin-orbit coupling. The corresponding expansion coefficients are then given by the *Clebsch-Gordan coefficients* C_{lm_l,Sm_s}^{Jm} defined as

$$C_{lm_l,Sm_s}^{Jm} = \langle nlm_l | \langle Sm_s | \cdot | nlSJm \rangle . \tag{2.6}$$

The series expansion of $|nlSJm\rangle$ then becomes [71, 72]

$$|nlSJm\rangle = \sum_{m_l=-l}^{l} \sum_{m_s=-S}^{S} \delta_{m,m_l+m_s}\, C_{lm_l,Sm_s}^{Jm}\, |nlm_l\rangle\, |Sm_s\rangle . \tag{2.7}$$

In spherical coordinates, the wave functions Ψ_{n,l,m_l} of the eigenstates $|nlm_l\rangle$ of hydrogen-like atoms can be separated into radial and angular parts as

$$\Psi_{n,l,m_l}(r,\theta,\phi) = R_{n,l}(r) \cdot Y_{lm_l}(\theta,\phi) , \tag{2.8}$$

where the eigenfunctions of the angular part are given by the complete set of (in the relativistic case complex) orthonormal spherical harmonics $Y_{lm_l}(\theta, \phi)$ and the radial part $R_{n,l}(r)$ can be described by the orthogonal, so called *associated Laguerre polynomials* $L_n^{\alpha}(x)$. The explicit (and lengthy) expressions of $R_{n,l}(r)$ and $Y_{lm_l}(\theta, \phi)$ will not be given here and interested readers are instead referred to the literature [73, 74]. Including also the spin parts $|Sm_s\rangle$ the eigenfunctions $|nlSJm\rangle$ are given by the so called *generalised spherical harmonics* $\mathcal{Y}_{Jlm}(\theta,\phi)$ which are in turn functions of $Y_{lm_l}(\theta, \phi)$.

2.2.2 Ps energy levels and lifetimes in the absence of external fields

Relativistic Hamiltonian of positronium in the absence of fields

In the absence of fields, the positronium atom is very accurately described by quantum electrodynamics (QED). Up to the present date, QED corrections to Ps energy levels are exactly known up to the order $m\alpha^6$ (cf. e.g. Refs. [75–77]), some more are known for higher order terms as well. On the non-relativistic level, the Ps energy scheme is qualitatively very similar to the one of the hydrogenic system. Quantitatively, the states differ slightly in energy due to the different masses of the constituent particles. This difference can easily be incorporated by scaling all Ps-related properties such as the eigen-energies or the Bohr radius by the reduced mass

$$\mu = (m_{e^-}^{-1} + m_{e^+}^{-1})^{-1} = \frac{m_{e^-} m_{e^+}}{m_{e^-} + m_{e^+}} , \tag{2.9}$$

which for the positronium with $m_{e^-} = m_{e^+} = m_e$ simply becomes $\mu_{Ps} = m_e/2$, compared to $\mu_H = 0.9995 \times m_e$ for the hydrogen atom. Consequently, the positronium Bohr radius a_{Ps} becomes approximately twice the hydrogen Bohr radius a_0. A similar adaptation yields the non-relativistic Hamiltonian of the Ps system which, in position space and spherical coordinates, thus reads

$$\hat{H}_0 = \frac{\hat{p}^2}{2\mu} - \frac{e^2}{4\pi\epsilon_0}\frac{1}{r} . \tag{2.10}$$

The energy eigenvalues of the corresponding Schrödinger equation are given by the well-known μ_{Ps}-corrected Bohr energy levels with respect to the continuum. In terms of the Hartree energy $E_h = m_e c^2 \alpha^2 = 13.6\,\text{eV}$, the classical non-relativistic Ps energy levels are given by [7, 53]

$$E_0^{(n)} = -\frac{E_h}{2n^2} = -\frac{6.803\,\text{eV}}{n^2} . \tag{2.11}$$

Naturally, the binding energy of 6.803 eV of the electron-positron pair, which is given by the energy of the lowest bound state relative to the continuum, is as well half its hydrogen counterpart.

It should be noted that this non-relativistic treatment entirely ignores the spin character of the electron and positron. Since the Hamiltonian $\hat{H}_0$ does not involve any spin operator, the

Schrödinger equation is solved completely by eigenfunctions which can be expressed exclusively in terms of the quantum numbers n, l and m_l (cf. Eq. (2.8)).

As mentioned above, a much more accurate description is obtained in the framework of quantum electrodynamics based on the Dirac theory, i.e., by introducing relativistic corrections to $\hat{H}_0$ and solving the corresponding relativistic wave equation. This Dirac equation is valid for all massive spin-1/2 particles with parity symmetry. It involves electromagnetic effects and is consistent with both quantum mechanics and special relativity. In the broader context of positronium, it is interesting to mention that the Dirac equation was in fact the first equation to predict the existence of antimatter, including the processes of creation and annihilation of particles, even though antiparticles were interpreted slightly wrong as "positively charged holes" in an otherwise completely negative sea of energies, instead of defining them as new, independent particles.

For the purpose of the studies for this thesis it is sufficient to consider only energy corrections up to and including the order of α^4. Small corrections of the order of α^2 or higher can be treated by first order perturbation theory by using the Breit equation, which is the relativistic wave equation derived from the more general Dirac equation and describes electromagnetically interacting particles up to the first order of perturbation. Additionally, in the context of the Ps atom the treatment can be further simplified by applying the Pauli approximation, which is valid for spin-1/2 particles in reasonably weak potentials with stationary states for which the average velocity $\bar{v}$ becomes non-relativistic and the total energy E hardly differs from the rest mass energy E_0 [53].

On this level of corrections (up to and including α^4) the atomic level structure of positronium diverges substantially with respect to hydrogen. This is mostly due to spin-spin interactions between the electron and positron and (for triplet states) due to virtual annihilation contributions (i.e., the loops in the corresponding Feynman diagrams) which add up to the common shifts also found in hydrogen and summed up as "fine structure". The deviations manifest, for example, in a considerably larger ground state singlet-triplet splitting of $203\,\mathrm{GHz}$ in Ps compared to $\approx 1.4\,\mathrm{GHz}$ in hydrogen [7].

In order to quantify the relativistic QED corrections, still ignoring external fields for the moment, five additional terms have to be introduced so that the total Hamiltonian can formally be written as

$$\hat{H}_{\mathrm{QED}} = \hat{H}_0 + \hat{H}_1 + \hat{H}_2 + \hat{H}_3 + \hat{H}_4 + \hat{H}_5 . \tag{2.12}$$

For the following discussion it is useful to transform the coordinates to the centre-of-mass frame[9] in which the corresponding wave functions only depend on the relative displacement $r = |\boldsymbol{r}_{\mathrm{e}^-} - \boldsymbol{r}_{\mathrm{e}^+}|$ of the electron and the positron. Furthermore, all quantities and terms are given in SI-units.

Following Refs. [53] and [78] the individual contributions in position space read as follows. The first term

$$\hat{H}_1 = -\frac{1}{4m_{\mathrm{e}}^3 c^2} \cdot \hat{\boldsymbol{p}}^4$$

is the correction due to relativistic kinetic energy. Next,

$$\hat{H}_2 = -\frac{e^2}{4\pi\epsilon_0} \frac{1}{2m_{\mathrm{e}}^2 c^2} \cdot \frac{1}{r} \cdot \left[\hat{\boldsymbol{p}}^2 + \frac{1}{r^2}(\boldsymbol{r} \cdot (\boldsymbol{r} \cdot \hat{\boldsymbol{p}}) \cdot \hat{\boldsymbol{p}}) \right]$$

represents a classical relativistic correction arising from the interaction between the orbital magnetic dipole moments of the moving electron and positron and is sometimes also referred to as orbit-orbit coupling. It takes into account the retardation of the electromagnetic field produced by a particle with charge e. The third term

$$\hat{H}_3 = 3\frac{e^2}{4\pi\epsilon_0} \frac{\hbar}{2m_{\mathrm{e}}^2 c^2} \cdot \frac{1}{r^3} \cdot \hat{\boldsymbol{l}} \cdot \hat{\boldsymbol{S}}$$

is the well-known spin-orbit coupling (for the case where the Coulomb potential is the central potential between the particles), i.e., the interaction between the magnetic moment associated to

---

[9] The centre-of-mass (CM) frame is a special case of the centre-of-momentum frame. In this inertial frame both the centre of mass coincides with the origin and the total momentum vanishes, i.e., in the Ps case, $\boldsymbol{p}_{\mathrm{e}^-} + \boldsymbol{p}_{\mathrm{e}^+} = 0$, where $\boldsymbol{p} = m\boldsymbol{v}$ is the momentum of the particle.

the total spin $\boldsymbol{S}$ and the one belonging to the orbital angular momentum $\boldsymbol{l}$. The factor of three accounts both for the separate interaction between the spin and orbital momentum of each particle and for the interaction between the total momenta of the combined electron-positron pair. The next contribution

$$\hat{H}_4 = 4\pi \frac{e^2}{4\pi\epsilon_0} \frac{\hbar}{m_{\rm e}^2 c^2} \cdot \delta^3(\boldsymbol{r})$$

is a non-classical term that arises from the treatment in the framework of the Dirac theory and is also known as the *Darwin term*. Illustratively, it is sometimes associated with a "Zitterbewegung" of the particles and explained by means of quantum fluctuations. Even though this phenomenon is no exclusive feature of the Ps atom, but also occurs in the hydrogen Hamiltonian, it is by a factor of two stronger in the Ps case due to contributions of both the electron and the positron. Finally, the Hamiltonian

$$\hat{H}_5 = -\frac{e^2}{4\pi\epsilon_0} \frac{\hbar^2}{m_{\rm e}^2 c^2} \left[-\frac{8\pi}{3} (\hat{\boldsymbol{s}}_{\rm e^-} \cdot \hat{\boldsymbol{s}}_{\rm e^+}) \, \delta^3(\boldsymbol{r}) + \frac{1}{r^3} \left(\hat{\boldsymbol{s}}_{\rm e^-} \cdot \hat{\boldsymbol{s}}_{\rm e^+} - \frac{3}{r^2} (\hat{\boldsymbol{s}}_{\rm e^-} \cdot \boldsymbol{r}) \cdot (\hat{\boldsymbol{s}}_{\rm e^+} \cdot \boldsymbol{r}) \right) \right]$$

$$= -\frac{e^2}{4\pi\epsilon_0} \frac{\hbar^2}{m_{\rm e}^2 c^2} \left[-\frac{8\pi}{3} (\hat{\boldsymbol{s}}_{\rm e^-} \cdot \hat{\boldsymbol{s}}_{\rm e^+}) \, \delta^3(\boldsymbol{r}) - \frac{1}{(2l+3)(2l-1)} \frac{1}{r^3} \times \right.$$

$$\left. \left(\left(2\hat{\boldsymbol{s}}_{\rm e^-} \cdot \hat{\boldsymbol{s}}_{\rm e^+} + \frac{3}{2} \right) l^2 - \frac{3}{2} (\hat{\boldsymbol{S}} \cdot \hat{\boldsymbol{l}}) - \frac{3}{2} (\hat{\boldsymbol{S}} \cdot \hat{\boldsymbol{l}})^2 \right) \right]$$

purely arises from the presence of the spin and describes the interaction between the individual electron and positron spin magnetic dipole moments. The first term represents the so-called contact interaction which contributes only in the case where the electron and positron are located at the same position, whereas the second term simply originates from the classical dipole-dipole interaction.

Since $\hat{H}_3$ and $\hat{H}_5$ describe interactions involving the spin operator, they require relativistic treatment just like the purely relativistic $\hat{H}_1$. $\hat{H}_2$ and $\hat{H}_4$ in turn can, in principle, be evaluated by means of only the principal and orbital quantum numbers n and l.

Even though all effects presented above appear in both the Ps and the hydrogen atom, some of them vary considerably between the two systems, especially the interaction between the individual spins. Since in hydrogen this contribution (i.e., the electron-proton spin interaction) is highly suppressed and thus much weaker than all fine structure terms, it is generally classified as hyperfine interaction there. The analogous electron-positron spin interaction as well as Ps-inherent corrections due to annihilation are in turn of the same order as fine structure contributions so that Ps in fact does not show any hyperfine structure in the proper meaning of the name. Nevertheless and mainly for historical reasons, the ground state singlet-triplet energy splitting and other equivalent effects are still often (misleadingly) referred to as hyperfine structure. This is, however, only a semantic difference which does of course not have any effect on the actual physics [7].

Finally, it should be noted that in general l and S are not good quantum numbers of the relativistic Hamiltonian since mixing can occur between wave functions with different l and S [53]. Since this effect is very tiny though, it is justified to neglect the corresponding off-diagonal relativistic matrix elements. Only then is it adequate to consider $\boldsymbol{l}^2$ and $\boldsymbol{S}^2$ as conserved, making their eigenvalues l and S good quantum numbers, which is also a requirement for using the angular momentum coupling scheme. In this context, it should also be mentioned that the approximation of LS-coupling is only allowed in the case where the electron and positron basically behave non-relativistically, i.e., states with different L and S do not lie too close together in energy [53], a condition which is well satisfied by Ps.

Energy levels and level scheme

Perturbation theory-based calculations of the positronium energy corrections (with respect to the Bohr levels (2.11)) up to and including the order of α^4 for any level with quantum numbers n, l, S and J, were first conducted 1944 by Pirenne in [79] and [80] and Berestetskii [81] (with corrections

FIGURE 2.1: *Positronium level structure in the absence of fields.*

The diagram shows the fine structure energy levels of the positronium atom resulting from the calculation including QED-corrections in the absence of fields for the ground and first excited states with $n = 2$. The energy values are given with respect to the continuum.

The frequency values additionally specify the respective energy differences $\Delta E^{(\mathrm{QED})}$ of each QED-corrected energy from the classical Bohr levels given by Eq. (2.11) and indicated by the dashed lines.

The figure indicates energies E (in eV), frequencies $\nu = E/h$ (in MHz) and wavelengths $\lambda = hc/E$ (in nm). Figure taken from [83].
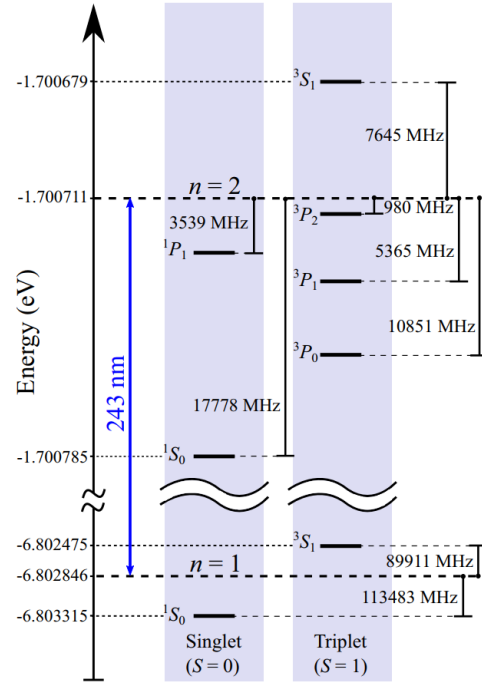
from Ferrell [82]), and yield energy levels [7]

$$E^{(nlSJ)} = E_0^{(n)} + \Delta E^{(nlSJ)} \ , \tag{2.13}$$

in which the QED energy corrections are given by

$$\Delta E^{(nlSJ)} = \frac{E_\mathrm{h}}{4n^3} \alpha^2 \left[\frac{11}{32n} - \frac{1}{2l+1} - \delta_{S1} \epsilon_{l,J} \right] \tag{2.14}$$

with

$$\epsilon_{l,J} = -\frac{7}{6}\delta_{l0} + \frac{1 - \delta_{l0}}{2(2l+1)} \begin{pmatrix} \dfrac{-(3l+4)}{(l+1)(2l+3)} & \text{if } J = l+1 \\[2mm] \dfrac{1}{l(l+1)} & \text{if } J = l \\[2mm] \dfrac{3l-1}{l(2l-1)} & \text{if } J = l-1 \end{pmatrix} \tag{2.15}$$

and where δ_{ij} denotes the Kronecker delta function of the variables i and j.

Figure 2.1 depicts the zero-field Ps level structure described by Eq. (2.13) for all states with principal quantum numbers $n = 1$ and 2.

In anticipation of the main topic, laser cooling on the 1S $\leftrightarrow$ 2P transition, this level scheme shows very illustratively the significant energy difference of the ground spin states, i.e., between the singlet 1^1S_0 and the triplet 1^3S_1. Due to this large splitting of more than 200 GHz, the singlet ground state is, under typical conditions, generally far off-resonance for a laser tuned to any 1^3S_1 $\leftrightarrow 2^3P_J$ transition. In most practical cases, singlet ground states are therefore not involved in the excitation process (but in decay processes!) so that transitions *from* this state will not be discussed or taken into account in this thesis.

Fluorescence lifetimes

The lifetimes of states play an important role with respect to atom-photon interactions since they can be considered as a measure for the strength of a transition. Hence, they represent a major parameter which determines the potential efficiency of laser cooling and are therefore, among others, an evaluation criterion for choosing the central cooling transition.

In general, the total lifetime, which is the inverse of the corresponding rate Γ, of each (excited) state is composed of both the intrinsic annihilation rate $\Gamma^{(\text{ann})} = 1/\tau^{(\text{ann})}$ and the fluorescence decay time $\Gamma^{(\text{fl})} = 1/\tau^{(\text{fl})}$ and simply given by the sum of both:

$$\Gamma^{(\text{tot})} = \Gamma^{(\text{ann})} + \Gamma^{(\text{fl})} \ . \tag{2.16}$$

Ground states can of course only decay by annihilation, and, as seen above, certain excited states do not show any annihilation.

On the most fundamental level, the fluorescence decay lifetime $\tau_{n,l}^{(\text{fl})}$ of a pure l-state can be calculated by summing over all allowed decay channels to lower-lying states $|n'l'\rangle$ pursuant to

$$\tau_{n,l}^{(\text{fl})} = \left[\sum_{|n'l'\rangle} A_{n'l',nl} \right]^{-1} , \tag{2.17}$$

where A denotes the Einstein A-coefficient which characterises the rate for spontaneous emission to $|n'l'\rangle$ and is given by

$$A_{n'l',nl} = \frac{2e^2\omega_0^3}{3\pi\epsilon_0\hbar c^3} \ \frac{l_{\max}}{2l+1} \ |\langle n'l'|r|nl\rangle|^2 , \tag{2.18}$$

where $\omega_0 = 2\pi\nu_0$ is the angular resonance frequency corresponding to the energy difference of the transition between $|n'l'\rangle$ and $|nl\rangle$ and $l_{\max} = \max(l,l')$ [7]. The Einstein coefficient directly follows from the theory of radiative transitions in atoms which is described more comprehensively and systematically in Appendix C, with a special focus on the Einstein A-coefficient in subsection C.4.1.

The lifetimes of Ps in particular, though, can be deduced much more straightforward from the results known from the hydrogen atom: In accordance with the omnipresent scaling by the reduced mass, positronium fluorescence lifetimes are roughly twice as long as the ones of corresponding hydrogen levels [7, 84]. For example, the lifetime of the 2^3P_J state thus amounts to 3.19 ns instead of the 1.6 ns for H. This value represents the shortest fluorescence decay time of all 2S-states. This makes the $1^3\text{S}_1 \leftrightarrow 2^3\text{P}_J$ transition the most promising candidate for laser cooling experiments as far as the cycling rate is concerned, which is determined by the transition lifetime. Annihilation as well as fluorescence lifetime values of further states of relevance to the present thesis are listed in Tab. A.1 in Appendix A, ordered by the respective state energy and illustrated in Fig. A.1. Additionally, the energy corrections $\Delta E^{(\text{QED})}$ of each state with respect to the according Bohr level energy are specified.

The most important result is that all excited states decay rather quickly, with lifetimes of the order of nanoseconds, except for the 2S-states with a significantly longer annihilation lifetime of $\tau^{(\text{ann})} = 1.11\,\mu\text{s}$ and, more importantly, a fluorescence time of the order of hundreds of milliseconds. These excited states are thus more likely to annihilate than to decay by fluorescence, which is very unsual. This phenomenon is known as metastability and originates from the fact that excited S-states primarily decay by double-photon emission, a process which is much less probable to occur compared to the usual one-step process under single-photon emission as it is the case for all other states [85].

2.2.3 The positronium atom in magnetic fields

In the presence of a magnetic field $\boldsymbol{B}$ the positronium atom shows a number of characteristic effects that can have significant impact on the level structure. This not only manifests itself in a modification of the energy level of the states, but also in the form of coupling and mixing of

eigenstates. The most important magnetic field induced effects to be mentioned are the Zeeman and an additional motional Stark effect in case the atoms are not at rest. Even though the latter can also be observed in hydrogen, it is much more pronounced in Ps due to the tiny mass and thus extraordinarily large thermal velocities. The derivation of all effects from the most fundamental interaction Hamiltonian is in fact not trivial. However, since a thorough theoretical derivation is only of limited relevance for the main topic of this thesis, namely studies of Ps laser cooling in magnetic fields, it has been moved to Appendix B. Only the most important results shall be summarised in the following. It is nevertheless instructive to have a closer look at the step-by-step analysis in the appendix as it gives some further insights in the interaction process and the actual origin of certain phenomena, which are not visible at first glance.

1. The Hamiltonian of the Ps atom in a magnetic field can be written as

$$\hat{H} = \hat{H}_{\mathrm{QED}} + \hat{H}_{\mathrm{S}} + \hat{H}_{\mathrm{z}} + \hat{H}_{\mathrm{dia}} \tag{2.19}$$

and consists of mainly four terms, namely the field-free QED-corrected Hamiltonian $\hat{H}_{\mathrm{QED}}$ (2.12), the motional Stark term $\hat{H}_{\mathrm{S}}$ which originates from the interaction of the atomic dipole with the self-induced motional Stark field $\boldsymbol{E}_{\mathrm{MS}} = (\boldsymbol{v} \times \boldsymbol{B})$, the term $\hat{H}_{\mathrm{z}}$ describing the linear Zeeman effect, and the quadratic Zeeman effect, also called the diamagnetic term $\hat{H}_{\mathrm{dia}}$. The individual contributions are given by

$$\hat{H}_{\mathrm{z}} = -\left(\hat{\boldsymbol{\mu}}_s^{(\mathrm{e}^-)} + \hat{\boldsymbol{\mu}}_s^{(\mathrm{e}^+)}\right) \cdot \boldsymbol{B} \tag{2.20}$$

$$\hat{H}_{\mathrm{dia}} = \frac{e^2}{16m_{\mathrm{e}}} \left(\boldsymbol{B} \times \boldsymbol{r}\right)^2 \tag{2.21}$$

$$\hat{H}_{\mathrm{S}} = e\boldsymbol{r} \cdot \left(\boldsymbol{v} \times \boldsymbol{B}\right) , \tag{2.22}$$

where $\boldsymbol{v}$ is the velocity of the neutral atom in the centre-of-mass frame and $\hat{\boldsymbol{\mu}}_s = g_s q/(2m)\hat{\boldsymbol{s}}$ the spin magnetic dipole moment with g_s denoting the spin g-factor. It is equal for the electron and positron and denoted by $g_e = g_{\mathrm{e}^-} = g_{\mathrm{e}^+}$. Due to QED corrections g_e is not exactly 2 as predicted by the Dirac theory but $g_e \approx -2.002319$ [7].

2. Similar to most other atomic systems, the positronium shows a typical Zeeman effect which, in moderate fields, is linear in the field strength B. The term "moderate" thereby strongly depends on the principle quantum number n. While for $n = 1$ fields with strengths up to $B = 5\,\mathrm{T}$, for example, are still part of the linear regime, the $n = 2$ states already make the transition to the contiguous strong field regime at $B = 1\,\mathrm{T}$.

In the most instructive spin representation with basis states $|S, m_s\rangle$ containing the total spin quantum number S (with $S = 0$ comprising singlet and $S = 1$ triplet states, respectively) and the corresponding magnetic quantum numbers m_s, the effect of the linear Zeeman Hamiltonian $\hat{H}_{\mathrm{z}}$ is given by

$$\hat{H}_{\mathrm{z}}\,|S, m_s\rangle = g_e\mu_{\mathrm{B}}B\,\delta_{0m_s}\,|1 - S, 0\rangle \tag{2.23}$$

with the Bohr magneton $\mu_{\mathrm{B}} = e\hbar/(2m_{\mathrm{e}})$.

This compact notation clearly shows that, for $m_s = 0$, the interaction with the magnetic field in the linear regime does not only produce an energy shift but also induces the coupling of different eigenstates. In fact, the matrix elements $\langle S'm_s'|\hat{H}_{\mathrm{z}}|Sm_s\rangle$ are non-zero only if $S \neq S'$ and $m_s = m_s' = 0$, $n = n'$ and $l = l'$ [47], which shows that the Zeeman interaction couples states from the singlet manifold with compatible ones from the triplet manifold and vice versa. All triplet states with $m_s = \pm 1$ are completely unaffected.

The so-called Zeeman map in Fig. 2.2 visualises the effect of the Zeeman effect on the level scheme for the most relevant states for Ps laser cooling.
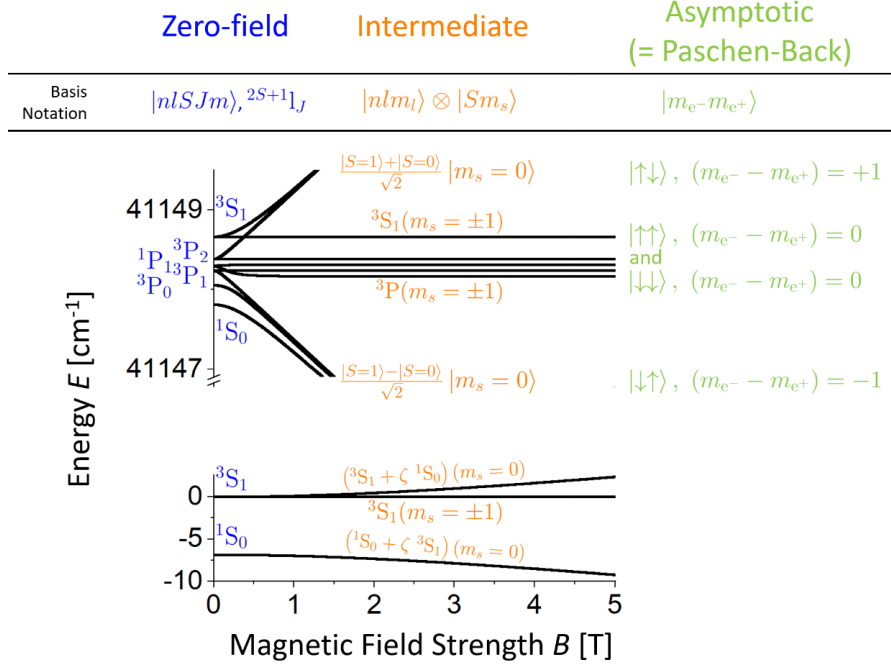
FIGURE 2.2: *Pure Zeeman effect from $B = 0\,\mathrm{T}$ to $B = 5\,\mathrm{T}$ for the $n = 1$ and $n = 2$ manifolds.* *The levels are labelled in the $|nlsjm\rangle$ basis for zero field, in the $|nlm_l, Sm_s\rangle$ basis for intermediate fields and in the $|nlm_l, s_{e^-}m_{e^-}s_{e^+}m_{e^+}\rangle$ basis for high fields using arrows for spin states with $\uparrow = \frac{1}{2}$ and $\downarrow = -\frac{1}{2}$. The states are denoted by their term symbols $^{2S+1}l_j$ and given as wave numbers (in cm^{-1}).*
For $n = 2$, the upper and lower branches are, for $B \gtrsim 1\,\mathrm{T}$, in the Paschen-Back regime where the electron and positron spins are decoupled completely. Except for the flat branches, consisting only of pure triplet states, the perturbation creates superpositions of singlet and triplet levels. For $n = 1$, the field is not yet strong enough to force the states into the decoupling regime. Apart from the pure and flat triplet branch (with $m_s = \pm 1$), the $m_s = 0$ singlet and triplet states show increasing coupling, quantified by the coupling parameter $\epsilon(B)$.

3. The coupling of eigenstates, induced by the magnetic field perturbation, has a large impact also on the annihilation lifetime of the states. Due to distinctly different annihilation rates of singlet and triplet states (cf. App. A) the mixing of eigenstates in magnetic fields can lead to significant changes in the annihilation lifetimes. This phenomenon is generally referred to as *magnetic quenching*. To convey an impression of the strength of this effect, it is worth noting that the annihilation lifetime of the unperturbed triplet ground state $1^3\mathrm{S}(m_s = 0)$, for example, is reduced from $142\,\mathrm{ns}$ in zero field to only $3\,\mathrm{ns}$ in $B = 1\,\mathrm{T}$. Fig. B.1 illustrates the evolution of this dramatic reduction with increasing magnetic field strength B up to $B = 2.5\,\mathrm{T}$. It is important to note that the phenomenon of magnetic quenching is not restricted to the ground states, but is rather completely independent of n. In excited states, though, quenching might have a less severe impact on atom numbers due to the possibility for radiative decay. Because of magnetic quenching it is essential to avoid the population of mixed states for efficient Ps laser cooling with as little loss in atom numbers as possible.

4. As soon as the magnetic magnetic interaction energy $\mu_{\mathrm{B}}B$ exceeds spin-orbit coupling, the electron and positron spins are decoupled, creating a superposition of singlet and triplet levels except for the flat branches where only pure triplet states exist, as shown in Fig. 2.2. This strong field region is also known as the Paschen-Back regime. The magnetic field values needed to reach the Paschen-Back regime are very different for the different n manifolds. While obviously, for $n = 1$, fields of $5\,\mathrm{T}$ are not yet strong enough to break spin-orbit coupling,

the $n = 2$ states already enter this regime for fields above $1\,\mathrm{T}$. With regard to Ps laser cooling in magnetic fields it is important to mention that the cooling efficiency might indeed benefit from the interaction with strong fields. This will be treated in further detail in Sec. 3.2.1.

5. The Ps atom also shows a Zeeman effect which is quadratic in B and known as the diamagnetic effect. However, since it becomes apparent only for extreme field strength $B \approx 100\,\mathrm{T}$ or, in weaker fields, solely in states with high principle quantum numbers, which are irrelevant for Ps laser cooling, the diamagnetic contribution is neglected in this thesis.

6. Additional complexity of the interaction with the magnetic field arises from the fact that the Ps atoms experience a self-induced electric field, the so-called motional Stark field $\boldsymbol{E}_{\mathrm{MS}} = \boldsymbol{v} \times \boldsymbol{B}$, solely due to their motion in the magnetic field. This implies that the atoms are subject to a motional Stark effect, described by $\hat{H}_{\mathrm{S}} = e\boldsymbol{r} \cdot (\boldsymbol{v} \times \boldsymbol{B})$ which, for positronium, is particularly pronounced due to the tiny mass and therefore usually very high velocities. The motional Stark field only depends on the transverse velocity component $v_{\perp}$ and is orthogonal to the quantisation axis, defined by the magnetic field $\boldsymbol{B}$. It can be shown (cf. App. B) that $\hat{H}_{\mathrm{S}}$ couples $m_l = 0$ and $m_l = \pm 1$ states and therefore becomes apparent only in manifolds with $n > 1$, in $n = 2$ for example in the form of mixing of corresponding S- and P-states.

An important consequence of the motional Stark effect with regard to Ps cooling is the fact that some of the pure flat triplet states $2^3\mathrm{P}(m_s = \pm 1)$ are coupled to the metastable $2^3\mathrm{S}$ states in magnetic fields. The new eigenstates, when fully mixed in high fields, have a spontaneous emission lifetime of $6.4\,\mathrm{ns}$ which reduces the number of potentially scattered photons by a factor of two.

2.3 Interaction between positronium and light fields

In view of Ps laser cooling, even more important than the interaction with external magnetic fields is the interaction with electromagnetic radiation, particularly in the form of laser beams, to induce transitions between the internal atomic energy levels. Again, the theoretical framework and derivation of relevant equations shall not be discussed here, but can be found in App. C, for the atom-field interaction and transitions in general, and App. D for the dynamics of the interaction. Literature references are given there. In the following, a brief overview of the most important aspects with regard to Ps laser cooling are presented.

Fundamental processes and transition rates

The full Hamiltonian $\hat{H} = \hat{H}_{\mathrm{A}} + \hat{H}_{\mathrm{int}} + \hat{H}_{\mathrm{F}}$ of the Ps atom in an electromagnetic field that is characterised by the vector potential $\hat{\boldsymbol{A}}(\boldsymbol{r})$ consists of mainly three components where $\hat{H}_{\mathrm{A}}$ describes the atomic part, given by Eq. (2.12), $\hat{H}_{\mathrm{F}}$ the field contribution and $\hat{H}_{\mathrm{int}}$ the interaction between both.

In terms of the quantum mechanical creation and annihilation operators, $\hat{b}_{\lambda}^{\dagger}$ and $\hat{b}_{\lambda}$, respectively (with commutation relations $[\hat{b}_{\lambda}, \hat{b}_{\lambda'}^{\dagger}] = \delta_{\lambda,\lambda'}$ where λ denotes the light mode), the field and interaction components can be expressed as

$$\hat{H}_{\mathrm{F}} = \sum_{\lambda} \frac{\hbar\omega_{\lambda}}{2} \left(\hat{b}_{\lambda}^{\dagger}\hat{b}_{\lambda} + \hat{b}_{\lambda}\hat{b}_{\lambda}^{\dagger} \right) = \sum_{\lambda} \hbar\omega_{\lambda} \left(\hat{b}_{\lambda}^{\dagger}\hat{b}_{\lambda} + \frac{1}{2} \right) \tag{2.24}$$

$$\hat{H}_{\mathrm{int}} = -\frac{1}{\sqrt{2\epsilon_0 V}} \sum_{i=\{\mathrm{e}^-,\mathrm{e}^+\}} \frac{q_i}{\mu} \sum_{\lambda} \sqrt{\frac{\hbar}{\omega_{\lambda}}} \, \hat{\boldsymbol{p}}_i \cdot \left[\boldsymbol{\epsilon}_{\lambda}\hat{b}_{\lambda} - \boldsymbol{\epsilon}_{\lambda}^{*}\hat{b}_{\lambda}^{\dagger} \right], \tag{2.25}$$

where ω indicates the frequency of mode λ with wave vector $\boldsymbol{k}_{\lambda}$, ϵ its polarisation, $\hat{\boldsymbol{p}}$ the atomic momentum operator, μ the reduced mass and q the charge of each particle (e^- and e^+). The treatment of the interaction between Ps atoms and light fields is carried out in Coulomb gauge. It should furthermore be noted, that it is restricted to interactions induced by the electric dipole under

application of the dipole approximation. Interactions of higher order, such as due to quadrupole or octupole moments, the second- and third-order terms of the expansion of the matrix element that mediates the interaction, are not considered due to their negligible contribution. For the same reason, interactions induced by magnetic moments remain unconsidered as well.

The most important effect of the interaction with the electromagnetic wave is the stimulation of a transition between the internal states of the atom under absorption or emission of photons, the quanta of the light field. After photon absorption and excitation to an internal state with higher n, the atom can either decay back naturally via spontaneous emission of a photon after the characteristic fluorescence lifetime of the corresponding excited state (cf. Tab. A.1) or due to stimulation by the laser, known as stimulated emission. In all cases photon exchange events are accompanied by momentum transfer in multiples of the photon momentum $\hbar\boldsymbol{k}$. However, while the photons transmitted during absorption and stimulated emission have well-defined orientation, determined by the wave vector $\boldsymbol{k}$, spontaneous emission events generate photons with arbitrary spatial orientation, distributed isotropically over the full solid angle. This is the crucial effect exploited for laser cooling, as will be explained in the following section.

The transition rates of the three fundamental types of transition with photon exchange can be determined conveniently in the framework of perturbation theory. Step-by-step derivations are given in App. C on the basis of Fermi's Golden Rule. Finally, the corresponding probabilities for a transition between a pair of ground and excited states, $|\chi_\mathrm{g}\rangle$ and $|\chi_\mathrm{e}\rangle$, induced by the interaction with light in mode λ, can be expressed in terms of the Einstein A- and B-coefficients as listed below.

Spontaneous emission: $\quad |\chi_\mathrm{g}\rangle \longleftarrow |\chi_\mathrm{e}\rangle \quad \mathcal{P}_{\mathrm{g}\leftarrow\mathrm{e}}^{\mathrm{(spont)}} = \dfrac{1}{3\pi\epsilon_0}\dfrac{\omega_\lambda^3}{\hbar c^3}\,|\boldsymbol{d}_\mathrm{ge}|^2 \qquad\quad = A_\mathrm{ge}$

Stimulated emission: $\quad |\chi_\mathrm{g}\rangle \longleftarrow |\chi_\mathrm{e}\rangle \quad \mathcal{P}_{\mathrm{g}\leftarrow\mathrm{e}}^{\mathrm{(stim)}} = \dfrac{\pi}{3\epsilon_0\hbar^2 c}\,|\boldsymbol{d}_\mathrm{ge}|^2\,I_\omega(\omega_\lambda) = B_\mathrm{ge}\dfrac{I_\omega(\omega_\lambda)}{c}$

Absorption: $\quad |\chi_\mathrm{g}\rangle \longrightarrow |\chi_\mathrm{e}\rangle \quad \mathcal{P}_{\mathrm{g}\rightarrow\mathrm{e}}^{\mathrm{(abs)}} = \dfrac{\pi}{3\epsilon_0\hbar^2 c}\,|\boldsymbol{d}_\mathrm{eg}|^2\,I_\omega(\omega_\lambda) = B_\mathrm{eg}\dfrac{I_\omega(\omega_\lambda)}{c}\;.$

The Einstein A- and B-coefficients are related to each other according to

$$B_\mathrm{ge} = \frac{\pi}{3\epsilon_0\hbar^2}\,|\boldsymbol{d}_\mathrm{ge}|^2 = A_\mathrm{ge}\frac{\pi^2 c^3}{\hbar\omega_\lambda^3}\;. \tag{2.26}$$

The transition probabilities clearly reveal a similarity and interdependence of the three fundamental processes. They have an inverse relation to the (fluorescence) lifetime of the according transition. For a single-channel decay from excited state $|e\rangle$ to ground state $|g\rangle$ the spontaneous rate is, for example, given by $\Gamma_\mathrm{ge} = 1/\tau^{\mathrm{(fl)}}$ (with the subscripts indicating the initial and final states, in this case $|e\rangle$ and $|g\rangle$).

A special type of photon absorption process is photoionisation, which is the excitation of the atom to the energy continuum above the ionisation threshold. The probability for photoionisation is usually evaluated from the according photoionisation cross section

$$\sigma^{\mathrm{(phion)}}(E) = \frac{\pi\omega_\lambda}{\epsilon_0 c}\,|\boldsymbol{\epsilon}_\lambda \cdot \boldsymbol{d}_\mathrm{fi}|^2\;, \tag{2.27}$$

where $\boldsymbol{d}_\mathrm{fi} = \langle\chi_\mathrm{f}|\hat{\boldsymbol{d}}|\chi_\mathrm{i}\rangle = \langle\chi_\mathrm{f}|\sum_j q_j\boldsymbol{r}_j|\chi_\mathrm{i}\rangle$ denotes the so-called transition dipole moment which is given by the matrix elements of the electric dipole moment operator $\hat{\boldsymbol{d}}$ acting on the initial and final atomic states $|\chi_\mathrm{i}\rangle$ and $|\chi_\mathrm{f}\rangle$, respectively.

Due to the fact that the transition dipole moments are zero for specific configurations, transitions can only take place under well-defined conditions which are described by so-called selection rules in terms of the involved quantum numbers. Transitions which obey these rules are referred to as *allowed*. The selection rule for the angular momentum l in electric dipole transitions is given by

$$\Delta l = l_\mathrm{f} - l_\mathrm{i} = \pm 1 \qquad \text{and} \qquad \Delta m_l = m_\mathrm{f} - m_\mathrm{i} = 0, \pm 1\;, \tag{2.28}$$

where m denotes the magnetic quantum number assigned to the orbital angular momentum $\boldsymbol{l}$ that specifies the magnitude of the projection of $\boldsymbol{l}$ onto the quantisation axis of the system. Further restriction is imposed by the selection rules for the total angular momentum $\boldsymbol{J}$ as well as the total spin quantum number S given by

$$\Delta J = J_\mathrm{f} - J_\mathrm{i} = 0, \pm 1 \qquad \text{and} \qquad \Delta m = m_\mathrm{f} - m_\mathrm{i} = 0, \pm 1 \tag{2.29}$$

$$\Delta S = 0 \qquad \text{and} \qquad \Delta m_s = 0 \;, \tag{2.30}$$

where this time m relates to the projection of $\boldsymbol{J}$. The spin selection rule clearly shows that pure electric dipole transitions can, under no circumstances, induce spin flips. The full derivation of the selection rules is given in App. C.

The existence of selection rules furthermore gives rise to a polarisation dependence of the transitions. Transitions with a quantum number change of $\Delta m = \pm 1$ can, for example, only be induced by light with right-/left-handed circular polarisation, indicated by $\sigma^{(\pm)}$, respectively, whereas light with linear polarisation, parallel to the quantisation axis, can only stimulate so-called π-transitions accompanied by $\Delta m = 0$. By controlling the polarisation it is thus possible to drive certain transitions exclusively, avoiding for example the involvement of short-lived or magnetically quenched states. The most important polarisation scheme to be mentioned is optical pumping, in which the atom is excited on a pure transition (including only pure triplet states that are insensitive to the magnetic perturbation and are thus not coupled to any state from the singlet manifold) by means of circularly polarised light. Optical pumping also represents a crucial tool with regard to laser cooling. Its mechanism is schematically illustrated in Fig. C.5 on the basis of a reduced level scheme.

Naturally, in the frequency domain, the transition probability is not restricted to single frequencies ω_λ. Transition rates are rather described by distribution functions that depend both on the line shape of the atomic transition and the laser spectrum which is mainly characterised by the bandwidth and the detuning. The line shapes can thereby be subject to different types of line broadening. First of all, due to the Heisenberg uncertainty relation each transition line shows a natural line with Γ_ge, described by a Lorentzian line shape function $g(\omega)$. The width is equal to the inverse spontaneous emission lifetime $\Gamma_\mathrm{ge} = \tau^{-1} = A_\mathrm{ge}$ of the corresponding transition from excited state $|e\rangle$ to ground state $|g\rangle$. Further relevant line broadening mechanisms are (inhomogeneous) Doppler broadening due to the distribution of Ps velocities and laser-induced broadening originating either from broadband intensity spectra with bandwidth Γ_L or high intensities leading to power broadening. In laser cooling experiments typically a combination of both can be found.

The frequency dependence of the excitation rate $\gamma_\mathrm{i \to f}(\omega)$ for absorption or stimulated emission between the final and initial states $|f\rangle$ and $|i\rangle$, respectively, is given by the convolution of the transition line shape function and the laser spectrum in terms of the local spectral irradiance function $I_\omega(\omega)$. In case the laser spectrum can be modelled by a Lorentzian function and in the absence of power broadening, the excitation rates $\gamma_\mathrm{i \to f}(\omega)$ can be evaluated analytically and written in a closed-form expression as

$$\gamma_\mathrm{i \to f}(\omega) = \frac{1}{3\epsilon_0 \hbar^2 c} \left| \boldsymbol{d}_\mathrm{fi} \right|^2 I \, \frac{(\Gamma_\mathrm{fi} + \Gamma_\mathrm{L})/2}{(\omega + \boldsymbol{k}\boldsymbol{v} - \omega_0)^2 + ((\Gamma_\mathrm{fi} + \Gamma_\mathrm{L})/2)^2} \;, \tag{2.31}$$

where the Doppler effect directly manifests itself in the form of the additional term $\boldsymbol{k}\boldsymbol{v}$ in the detuning $\delta = \omega + \boldsymbol{k}\boldsymbol{v} - \omega_0$. As expected from the convolution of two Lorentzian functions, the total width of the transition rate function is equal to the sum of the linewidth Γ_fi and the laser bandwidth Γ_L. In case of (more realistic) Gaussian laser spectra (or any other arbitrary spectral distribution functions) $\gamma_\mathrm{i \to f}(\omega)$ can in general no longer be written as a closed expression. However, for Gaussian spectra it can very well be approximated by a Voigt profile, as described in details in App. C.

If the laser intensity exceeds a certain threshold the transition rate (and all other functions that are derived from the line shape function or, equivalently, the cross section) is additionally subject to power broadening. This threshold intensity is characteristic for each transition and primarily depends on the spontaneous emission rate Γ_ge and the wavelength λ. Saturation and

power broadening can, however, only be treated appropriately after introducing the interaction dynamics and relevant quantities and concepts such as decoherence of the interaction process and the resultant steady state.

Dynamics of atom-light interaction

Even though this aspect has not become apparent so far, atom-light interaction and, in particular, transition events and photon exchange are intrinsically coherent processes. For this reason, it is essential to base a theoretical treatment on the concept of coherence in the framework of the density matrix formalism which, next to the (incoherent) state populations, also accounts for the phase relation between the states. The equations for the coherent dynamics during light-matter interaction can then be obtained by solving the fundamental time-dependent Schrödinger equation of the system, given by

$$i\hbar\frac{\partial\Psi}{\partial t} = \hat{H}\Psi ,$$

where the Hamiltonian $\hat{H} = \hat{H}_0 + \hat{H}_{\mathrm{int}}(t)$ is composed of the unperturbed Hamiltonian $\hat{H}_0$ and the generally time-dependent interaction part $\hat{H}_{\mathrm{int}}(t)$. The unperturbed system is described by $\hat{H}_0$ with energies E_n belonging to the corresponding wave functions $\Psi(\boldsymbol{r},t) = c_n(t)\phi_n(\boldsymbol{r})\exp(-iE_nt/\hbar)$ that result from $\hat{H}_0\psi_n(\boldsymbol{r}) = E_n\psi_n(\boldsymbol{r})$. In a semi-classical treatment and applying the rotating-wave approximation, the set of differential equations that results from the Schrödinger equation leads to the general optical Bloch equations which are the most fundamental set of equations for describing the interaction dynamics (cf. Sec. D.4.2).

A crucial aspect of this formalism, apart from the inclusion of coherence, is the consideration of damping of the coherent dynamics. The process is quantified in terms of a damping rate Γ and can be induced by different kinds of mechanisms which all lead to a decoherence of the phase relations between the states involved. One usually differentiates between two characteristic types of damping, first those mechanisms which affect only the off-diagonal density matrix elements, the coherence, and, on the other hand, those which are responsible for changes in the diagonal elements that describe the state populations. While the first are specified in terms of the so-called transverse relaxation rate $\Gamma_{\perp}$, the latter are summarised in the longitudinal rate $\Gamma_{\parallel}$. Spontaneous decay is, for example, a process which enters both, $\Gamma_{\perp}$ as well as $\Gamma_{\parallel}$. With regard to atom-light interaction, the most important source of (transverse) phase damping is the excitation by broadband laser radiation which introduces random phase fluctuations in the otherwise coherent level dynamics.

In case of strong transverse relaxation, the coherent relations between the states phase out quickly, which implies that the dynamics enters into a quasi-steady state in which coherences have vanished completely, but the populations have not necessarily reached a steady state yet. In this quasi-steady state the description of the level dynamics can be simplified significantly as it does not require to treat the state evolution in the framework of the complex Bloch equations but allows to replace the latter by a set of incoherent rate equations that only describe the state populations P. Mathematically, the condition for the validity of the rate equation approach can be expressed in terms of the simple inequality condition $\Gamma_{\perp} \gg \Omega$ or, equivalently, $\Gamma_{\perp} \gg \gamma$, where γ is the excitation rate. The Rabi frequency Ω, which appears in the first condition, plays an important role throughout the entire description and is defined as the frequency that corresponds to the coupling energy of the transition dipole moment $\boldsymbol{d}$ and the electric field amplitude $\boldsymbol{E}_0$. It is thus given by $\Omega = 1/\hbar \langle \mathrm{e}|\boldsymbol{dE}_0|\mathrm{g}\rangle$. Since the use of the Rabi frequency shall here be restricted to the treatment of transitions between bound states, Ω can be treated as a real instead of a complex quantity, i.e., $\Omega_{\mathrm{ge}} = \Omega_{\mathrm{eg}} = \Omega$.

For a pair of ground and excited states, $|\mathrm{g}\rangle$ and $|\mathrm{e}\rangle$ with $E_{\mathrm{e}} > E_{\mathrm{g}}$, the set of rate equations for the populations P_{g} and P_{e} can be written in a very symmetric structure as

$$\frac{\mathrm{d}}{\mathrm{d}t}P_{\mathrm{e}} = \sum_{|\mathrm{g}\rangle} \gamma_{\mathrm{eg}}P_{\mathrm{g}} - (\Gamma_{\mathrm{ge}} + \gamma_{\mathrm{ge}})P_{\mathrm{e}}$$

$$\frac{\mathrm{d}}{\mathrm{d}t}P_{\mathrm{g}} = \sum_{|\mathrm{e}\rangle} (\Gamma_{\mathrm{ge}} + \gamma_{\mathrm{ge}})P_{\mathrm{e}} - \gamma_{\mathrm{eg}}P_{\mathrm{g}}$$

(2.32)

using the compact notation $\gamma_{eg} = \gamma_{e \to g}$ (and $\gamma_{ge} = \gamma_{g \to e}$, respectively) for the transition with dipole moment $\boldsymbol{d}_{eg} = \langle \chi_e | \hat{\boldsymbol{d}} | \chi_g \rangle$ (or $\boldsymbol{d}_{ge} = \langle \chi_g | \hat{\boldsymbol{d}} | \chi_e \rangle$). For all configurations presented in this thesis $\gamma_{eg} = \gamma_{ge}$.

Finally, on time scales much longer than the inverse longitudinal relaxation rate, which, in the present case, is primarily governed by the spontaneous emission rate Γ_{ge}, the populations converge towards a constant value and the whole system assumes a steady state. The excited state population obeys the Lorentzian function

$$\rho_{ee} = \frac{\Omega_{ge}^2/4}{\delta^2 + \Omega_{ge}^2/2 + \Gamma_{ge}^2/4} \tag{2.33}$$

where ρ_{ee} denotes the diagonal density matrix element for the excited state. This equation represents a very important relation as it expresses the population exclusively in terms of the key parameters for characterising the interaction, which are the Rabi frequency Ω_{ge}, the detuning δ and the spontaneous decay rate Γ_{ge}.

It is important to point out that Eq. (2.33) does not account for annihilation. Nevertheless, the atoms are of course constantly subject to annihilation decay, which implies that, strictly speaking, no real steady state exists. In the present context, the use of the term "steady" rather refers to the coherent interaction process between the atoms and the light field.

Saturation of the transition and power broadening

As Eq. (2.33) shows, in the steady state it is by no means possible to realise complete population inversion, not even by means of excessive laser radiation. Rather, an equilibrium is established with the populations depending on the values of the three decisive parameters δ, Ω and Γ_{ge}. While the detuning and the linewidth can only cause a reduction in excited state population, the light intensity (in terms of the coupling strength Ω) can, however, still be employed as a tool for population enhancement, albeit only up to a limit value of $1/2$. This simply originates from the simultaneous stimulation of absorption and emission due to laser interaction, which compete with each other with equal probability of occurrence. The regime in which the excited state population cannot be increased any further is generally referred to as saturation. The intensity required to reach this state is given by $I_s(\omega) = 1/2 \ \hbar\omega A_{eg}/\sigma(\omega)$ where σ denotes the cross section of the respective transition. The term saturation intensity is used for the minimum value of I_s which is reached on resonance and amounts to

$$I_{sat} = I_s(\omega_0) = \frac{\pi}{3} \frac{hc}{\lambda_0^3 \tau} \ . \tag{2.34}$$

A quantity often used in the context of saturation is the saturation parameter s which quantifies the laser intensity relative to the saturation intensity and is defined as

$$s = \frac{2\Omega^2}{4\delta^2 + \Gamma_{ge}^2} \ . \tag{2.35}$$

The parameter s can, for example, be used to instructively reformulate expressions such as the excited state population $\rho_{ee} = s/(2(1+s))$. On resonance s simplifies to $s_0 = 2\Omega^2/\Gamma_{ge}^2 = I/I_{sat}$.

It is important to note that saturation does not imply that the surplus energy of the light field is lost. Rather, it leads to an accumulation of atoms in adjoining frequency regions which is reflected in a broadening of the transition line that is commonly referred to as power broadening. This effect can be illustrated by means of the Lorentzian function of the excited state population (Eq. (2.33)) by defining an effective linewidth $\Gamma_{eff} = \Gamma_{ge}\sqrt{1+s_0}$, in terms of which ρ_{ee} simplifies to

$$\rho_{ee} = \frac{\Omega^2}{4\delta^2 + \Gamma_{eff}^2} \ . \tag{2.36}$$

Power broadening is a phenomenon that manifests itself in a comparable way as excitation by means of broadband radiation. In case of a combination of both, i.e., if the transition is excited by

(incoherent) broadband radiation with intensities above the saturation threshold, the expression of Γ_{eff} has to be modified to ensure further applicability of expressions such as Eq. (2.33). This is achieved by incorporating the bandwidth Γ_{L} which yields[10] $\Gamma_{\text{eff,L}} = (\Gamma_{\text{ge}} + \Gamma_{\text{L}})\sqrt{1 + s_{0,\text{L}}}$ with $s_{0,\text{L}} = I/I_{\text{sat,L}}$ and $I_{\text{sat,L}} = I_{\text{sat}}(1 + \Gamma_{\text{L}}/\Gamma_{\text{ge}})$. More details can again be found in App. D. This includes in particular also a table (cf. Tab. D.1) that lists the values of the most relevant quantities with regard to Ps laser cooling (Ω, γ, I_{sat} and Γ_{eff} or $I_{\text{sat,L}}$ and $\Gamma_{\text{eff,L}}$, respectively, for the more important case of incoherent broadband radiation) for different realistic laser parameter combinations and both monochromatic and incoherent broadband radiation.

2.4 Doppler laser cooling of positronium

The technique of laser cooling is based on a process which has been neglected almost completely so far, namely the fact that each photon absorption and emission event is connected to a transfer of momentum equal to the momentum carried by one photon. Briefly, the concept of laser cooling relies on exploiting the net loss of momentum resulting from a sequence of excitation and subsequent spontaneous emission events for the purpose of slowing down the atom.

2.4.1 General concept of Doppler laser cooling

Due to the principle of conservation of momentum and due to the fact that each photon carries a distinct momentum $\hbar \boldsymbol{k}$ every photon absorption event is accompanied by a transfer of momentum, effectively creating a force which the light field exerts on the atom during the interaction process. While the orientation of the absorbed momentum is clearly defined by the propagation direction of the incident photon, the one of the spontaneously emitted photon has no preferred direction and is thus isotropically distributed over all spatial directions. The recoil experienced by the atom is oriented in the opposite direction of the momentum which is transferred to the emitted photon. The sequence of absorption and emission events thus results in a net force on the atom which is directed parallel to the incoming light.

This effect can experimentally be exploited for the purpose of laser cooling by directing an intense collimated laser beam onto the cloud of atoms in such a way that it is resonant with those atoms that are moving towards the laser source. Subsequent resonant interaction will then effectively slow down the irradiated fraction of atoms until their velocity has been reduced to such an extent that the Doppler-shifted laser detuning is no longer resonant with the transition. Since the velocity range of the addressed atoms is controlled by means of the Doppler shift, namely by choosing the laser detuning δ such that it fulfils the resonance condition $\delta = \omega - \omega_0 + \boldsymbol{k}\boldsymbol{v}$, this technique is referred to as *Doppler laser cooling*.

This procedure can of course only result in a reduction in temperature if the atom is not only addressed from one direction but, in a 1D configuration, also by a counter-propagating beam which allows to reduce the overall velocity spread of the atoms in the cloud. In this configuration each atom perceives the frequency of the counter-propagating laser beam (counter-propagating with respect to its own velocity) closer to resonance than the frequency of the co-propagating beam. This ensures that the radiation force is always directed opposite to the velocity of each atom, creating a kind of friction force which damps the motion of the atoms and thus cools them down. In 3D the cloud should ideally be addressed by three pairs of counter-propagating laser beams along all spatial directions. This configuration is also referred to as *optical molasses cooling*.

Considering this scheme it eventually becomes clear why, for the purpose of laser cooling, it is advisable to excite the atom on the transition with the highest possible decay rate. The faster the atom decays, the more photons it can scatter and the more absorption and emission cycles it can go through in a given time. Choosing the fastest transition thus allows to minimise the time required to slow down the atom.

---

[10] It should once more be emphasised that these simple equations are only valid if the laser spectrum is described by a Lorentzian function. Gaussian spectra do not allow for equally instructive expressions.

Radiation forces

In the dipole approximation, where the electric field varies only slowly on the atomic length scale, the force exerted on the atom during its interaction with the resonant light field can be derived classically way[11]. As usual, the force arises from the gradient of the interaction potential U which, in case of Ps-light interaction, is given by $U = e/2 \, \boldsymbol{r} \cdot \boldsymbol{E}$, where $\boldsymbol{E}$ denotes the electric field vector of the radiation and $\boldsymbol{r}$ the displacement vector between the electron and the positron.

The time average of the resulting force over many oscillation periods is composed of two terms, a component which is in phase with the electric dipole $e\boldsymbol{r}$, producing the so-called *dipole force*, proportional to the gradient of the intensity I, and an out-of-phase component proportional to I/c and pointing along the propagation direction of the photon, given by the wavevector $\boldsymbol{k}$. The second component, which is also referred to as scattering or radiation-pressure force, is the one which is relevant for laser cooling. This is due to the fact that this is the term which is responsible for exerting a dissipative force on the atom that can be exploited for deceleration. This directly results from the quantum mechanical derivation which reveals that the scattering force originates from cycles of absorption and spontaneous emission while the dipole force results from the combination of absorption and stimulated emission. The latter force can thus not be used for momentum transfer by means of a laser beam where all photons have equal momentum and therefore induce opposite recoils in each cycle of absorption and stimulated emission. The dipole force is thus a conservative force that cannot be exploited for slowing down the atom, but instead for creating a so-called dipole trap where the atom can be confined in a region of maximum intensity (cf. for example [86]).

Furthermore, only the scattering force is proportional to the light intensity and can thus be scaled up considerably. Since the scattering and dipole force show completely different frequency dependence, with maximum dissipation on resonance, where the dipole force is zero, the latter does not play a role in the dynamics of the laser cooling process[12]. Furthermore, the dipole force is generally much too weak to influence the motion under the conditions relevant for laser cooling.

Scattering force

The scattering force can be regarded as the rate of change of momentum and is thus equal to the rate of energy transfer divided by the speed of light which can be expressed in terms of the single-particle absorption cross section $\sigma_1^{\text{(abs)}}$ (cf. Eq. (D.33) with[13] $g(\omega; \Gamma \approx \Gamma_{\text{ge}} + \Gamma_{\text{L}})$) by $F = \sigma_1^{\text{(abs)}} I/c$. The force is proportional to the rate of photons which are scattered by the atom and can therefore alternatively be expressed as the product of photon momentum $\hbar\boldsymbol{k}$ and scattering rate R_{scatt}.

Since absorption and stimulated emission balance out due to their equal probabilities, the scattering rate R_{scatt} is completely determined by the spontaneous decay rate Γ_{ge} multiplied by the population ρ_{ee} in the excited state. Using the steady state solution (D.38) for $\rho_{\text{ee}}(\delta)$ (with the power-broadened width $\Gamma_{\text{eff,L}}$ for excitation by high-intense broadband radiation) and writing $\hbar\boldsymbol{k}$

---

[11] The transition from a quantum mechanical to the classical treatment of the force is ensured by the fact that, in the dipole approximation, the classical equations of motion correspond to the equations of the quantum operators. This is one application of the Ehrenfest theorem. It should be noted that the classical model, however, does not account for saturation [86]. A rigorous quantum mechanical derivation can, for example, be found in [87].

[12] In this context it is worth noting that the dipole force is also closely related to the light shift which describes the offset of the energy levels induced by the exposure of the atom with the radiation, as briefly introduced in Sec. D.5.3. In fact, the dipole force is the gradient of the light shift, given by the interaction potential [88]. The dipole force is thus still present in the present scheme, albeit only indirectly and without observable effect.

[13] In this context, it should be recalled that it is generally not possible to give a closed-form expression for the line shape function $g(\omega)$ for photon absorption without making any assumptions about the spectral shape of the laser. Only in case of Lorentzian laser spectra it is given by a Lorentzian function with a width of $\Gamma = \Gamma_{\text{ge}} + \Gamma_{\text{L}}$ (cf. Sec. C.7 for more details). It is furthermore important to note that the transition line might additionally be power-broadened, in which case the linewidth is given by $\Gamma_{\text{eff,L}}$ (cf. Sec. D.5).

for the photon momentum, the detuning-dependent scattering force becomes

$$
\begin{aligned}
\boldsymbol{F}_{\mathrm{scatt}}(\delta) &= \hbar \boldsymbol{k}\, \frac{\Gamma_{\mathrm{ge}}}{2}\, \frac{\Omega^2/2}{\delta^2 + \frac{\Omega^2}{2}\frac{\Gamma_{\mathrm{ge}}+\Gamma_{\mathrm{L}}}{\Gamma_{\mathrm{ge}}} + \frac{(\Gamma_{\mathrm{ge}}+\Gamma_{\mathrm{L}})^2}{4}} \\
&= \hbar \boldsymbol{k}\, \frac{\Gamma_{\mathrm{ge}}^2}{2(\Gamma_{\mathrm{ge}}+\Gamma_{\mathrm{L}})}\, \frac{I/I_{\mathrm{sat,L}}}{1 + I/I_{\mathrm{sat,L}} + 4\delta^2/(\Gamma_{\mathrm{ge}}+\Gamma_{\mathrm{L}})^2} \;,
\end{aligned}
\tag{2.37}
$$

with the detuning δ as defined in Sec. 2.3 [86, 89].

In a configuration of counter-propagating laser beams, the corresponding friction force is simply given by the sum of the individual radiation forces from each beam. In the limit of small velocities $v \ll \max(\delta, \Omega, \Gamma)$ this force can be approximated by its first expansion term linear in the velocity which, along one direction, yields

$$
F_{\mathrm{fric}} = -\alpha_{\mathrm{fric}} v \;,
\tag{2.38}
$$

where α is called the *friction coefficient* and is given by

$$
\alpha_{\mathrm{fric}} = -\hbar k^2\, \frac{s}{(1+s)^2}\, \frac{\delta\,\Gamma}{\delta^2 + \Gamma^2/4} \;,
\tag{2.39}
$$

as derived, for example, by Cohen-Tannoudji in [90]. s denotes the saturation parameter defined in Eq. (D.36) and Γ the (effective) transition linewidth.

2.4.2 Characteristic parameters

Recoil velocity

Due to its direct proportionality to the excited state population ρ_{ee} the scattering force likewise converges to a maximum value with increasing intensity I. It saturates at a value of

$$
\boldsymbol{F}_{\mathrm{max}} = \frac{\hbar \boldsymbol{k}}{2}\, \frac{\Gamma_{\mathrm{ge}}^2}{\Gamma_{\mathrm{ge}}+\Gamma_{\mathrm{L}}} \;,
$$

which results in a maximum acceleration of $v_{\mathrm{rec}}/(2\tau)$ of the atom, where

$$
v_{\mathrm{rec}} = \frac{\hbar|\boldsymbol{k}|}{m_{\mathrm{Ps}}} = \frac{h}{\lambda m_{\mathrm{Ps}}}
$$

denotes the change in velocity associated with the recoil which the atom experiences as a result of a single photon emission or absorption event. For positronium this velocity amounts to $v_{\mathrm{rec,Ps}} \approx 1.5\,\mathrm{km/s}$ for the transition from $1^3\mathrm{S}$ to $2^3\mathrm{P}$.

In order to compare the associated recoil energy

$$
E_{\mathrm{rec}} = \hbar\omega_{\mathrm{rec}} = \frac{(\hbar \boldsymbol{k})^2}{2m_{\mathrm{Ps}}}
$$

to any other spectral width, rate or damping constant, the size of the recoil is usually specified in terms of the corresponding angular frequency ω_{rec}, which for the given example amounts to $\omega_{\mathrm{rec}} = 19.3\,\mathrm{ns}^{-1} = 2\pi(3.1\,\mathrm{GHz})$. The comparison to the spontaneous emission rate $\Gamma_{\mathrm{ge}} = 1/\omega_{\mathrm{rec}} = 0.313\,\mathrm{ns}^{-1}$ which is almost two orders of magnitude smaller than ω_{rec}, demonstrates the extraordinarily recoil in the case of positronium.

This in turn implies that it might happen that the internal motion of the atom has not yet reached a steady state before the atom experiences the next recoil that changes the variables of external motion. In this case, it might become problematic to express the scattering force in terms of the steady solution of the Bloch equations as presented above. This is discussed and analysed in more detail in App. E. It is explained there that it possible to differentiate between two models for the theoretical description of laser cooling, depending on the size of the involved recoils. The

final sections of this chapter will expand further on the specialities in the Ps case which, inter alia, originate from the tiny mass and therefore huge recoils.

As the numbers in Tab. D.1 (see page 199) show, it is, however, possible to significantly enhance the decay rate by exciting the atom by means of highly energetic incoherent broadband laser pulses, which, under realistic experimental conditions, allows to recover a situation where the decay rate exceeds the recoil frequency.

Choice of laser parameters

Both the recoil velocity v_{rec} and the saturation intensity I_{sat} are useful quantities to assess the laser parameters suitable for laser cooling of a cloud of positronium atoms. In the first instance the velocity distribution of the atomic cloud can be approximated[14] by a Maxwell-Boltzmann distribution with a probability density function

$$f(v) = \left(\frac{m_{\mathrm{Ps}}}{2\pi k_{\mathrm{B}}T} \right)^{3/2} 4\pi v^2 \exp\left(-\frac{m_{\mathrm{Ps}}v^2}{2k_{\mathrm{B}}T} \right) \ . \tag{2.40}$$

The Doppler broadening along each axis is usually quantified in terms of the standard deviation $\sigma_{\mathcal{G}}$ of the velocity vector component in this direction. It is completely defined by the temperature T and, in terms of the velocity, given by $\sigma_v = \sqrt{k_{\mathrm{B}}T/m_{\mathrm{Ps}}}$. This width is (in the non-relativistic approximation) equivalent to an (angular) frequency of $\sigma_\omega \approx (\sigma_v/c)\,\omega_0$.

For typical temperatures of $T = 300\,\mathrm{K}$ the Doppler broadening of Ps clouds amounts to roughly $\sigma_v = 5 \times 10^4\,\mathrm{m/s}$ or $\sigma_\omega = 1230\,\mathrm{ns}^{-1} = 2\pi(196\,\mathrm{GHz})$ respectively. After conversion to FWHM-quantities, labelled by Γ (where the standard conversion factor $\Gamma/\sigma = 2\sqrt{2\ln 2} \approx 2.35$ applies), these numbers are useful for a comparison to laser widths and decay rates that means the width of the (Lorentzian) line shape function. The Doppler broadening at $300\,\mathrm{K}$ thus amounts to $\Gamma_{\mathrm{Doppler}} = 2\pi(462\,\mathrm{GHz})$ FWHM, as also specified in Tab. D.1.

Generally speaking, as far as the laser detuning δ_{L} is concerned, a good estimation for first numerical or experimental laser cooling trials is given by $\delta_{\mathrm{L}} \approx \sigma_\omega$ or smaller. This defines the central value of the velocity range of addressed atoms, i.e., the ones which interact with the laser and thus feel the radiation force. In frequency space the width of this velocity range conforms with the laser bandwidth Γ_{L}. In case of intense broadband laser radiation[15] the resonance condition is fulfilled only by atoms with velocities in the interval $v \pm \Delta v/2$ that corresponds to the spectral range $\delta_{\mathrm{L}} \pm \Gamma_{\mathrm{eff,L}}/2$ with $\Gamma_{\mathrm{eff,L}} = (\Gamma_{\mathrm{ge}} + \Gamma_{\mathrm{L}})\sqrt{1 + I/I_{\mathrm{sat,L}}} = (\Gamma_{\mathrm{ge}} + \Gamma_{\mathrm{L}})\sqrt{1 + 2\Omega^2/(\Gamma_{\mathrm{ge}}(\Gamma_{\mathrm{ge}} + \Gamma_{\mathrm{L}}))}$ in the approximation of Lorentzian laser spectra.

Obviously, by means of excessive laser intensities it is thus possible to "artificially" broaden the line to such an extent that, at $T = 300\,\mathrm{K}$, atoms from all classes of the Doppler-broadened velocity distribution can potentially interact with the radiation. As shown in Table D.1 (page 199), $75\,\mathrm{GHz}$ broad lasers with a quite realistic power of $P = 10\,\mathrm{kW}$ already cover a frequency range equivalent to the Doppler-broadened width. One should consider, however, that excitation probabilities are highly suppressed far off-resonance even for extreme intensities.

This clearly demonstrates that power broadening distorts the scales on the basis of which a meaningful assessment for appropriate laser bandwidths can be made. For a much more useful and reliable estimation of the desired capture range it is therefore advisable to fall back on the unaltered width $(\Gamma_{\mathrm{eg}} + \Gamma_{\mathrm{L}})$ (or even simply Γ_{L}) instead of the full width $\Gamma_{\mathrm{eff,L}}$.

---

[14] As described in the introductory section on Ps formation (cf. Sec. 2.1.1), the velocity distribution can, in reality, not be described by any trivial standard distribution function since it depends on several formation-related parameters that complicate the description. For this reason, the velocities of the atoms, strictly speaking, do not obey a Maxwell-Boltzmann distribution. Since a Maxwell-Boltzmann approximation differs only marginally from the real distribution, it nevertheless represents an adequate approach that allows for convenient initialisation of Ps velocities in numerical calculations.

[15] In fact $\Gamma_{\mathrm{eff,L}}$ is just the most general expression for the linewidth and is valid also for any other laser configuration. That means, it especially covers as well the cases of monochromatic or low-intensity radiation. Such laser properties are taken into account by simply setting $\Gamma_{\mathrm{L}} = 0$ or, respectively, adjusting I accordingly.

It should additionally be noted that, especially in the positronium case, the tool of power broadening should always be used with caution and only after careful consideration. Even though it might intuitively be reasonable to bombard the atoms with the highest possible intensities in order to address as many atoms as possible, this strategy might in fact have severe implications on the cooling performance which might be affected in quite an undesirable way: Due to the motional Stark effect the internal level structure of atoms from different velocity classes is shifted and mixed in different ways. It might therefore happen that in certain velocity ranges the internal states involved in the cooling transitions are coupled to states with significantly less suitable annihilation and decay properties with respect to laser cooling, i.e., in particular, faster annihilation or enhanced spontaneous emission lifetimes. Since this might have a negative impact on the cooling performance it would not be beneficial to include these atoms in the cooling scheme.

Another quite obvious disadvantage of higher laser power is the enhancement of the probability for 2-photon transitions which implies higher risks for photoionisation of the bound state. In order to preserve a maximum number of atoms it is therefore advisable to keep the laser intensity on a reasonable level. This can be assessed by means of the photoionisation cross section $\sigma^{\mathrm{(phion)}}$ quantifying the probability for such events. A laser with a power of $10\,\mathrm{kW}$ on a $1\,\mathrm{cm}^2$ uniform spot size and $200\,\mathrm{ns}$ pulse duration for example photoionises about 0.4% of those atoms which populate the excited state of the transition, the 2P state [47].

Finally, disregarding of power broadening, the capture range as defined by the velocity spread Δv can simply be estimated as $\Delta v \approx (\Gamma_{\mathrm{ge}} + \Gamma_{\mathrm{L}})c/\omega_0 = (\Gamma_{\mathrm{ge}} + \Gamma_{\mathrm{L}})\lambda_0/2\pi$ where $\omega_0 = 2\pi c/\lambda_0$ denotes the resonance frequency and λ_0 the resonance wavelength. A laser width of $75\,\mathrm{GHz}$ thus covers a velocity range of about $18\,\mathrm{km/s}$ on the Ps cooling transition $1^3\mathrm{S}\leftrightarrow2^3\mathrm{P}$ which is roughly equivalent to twelve times the recoil velocity, $\Delta v_{75\,\mathrm{GHz}} \approx 12 v_{\mathrm{rec}}$. With regard to laser cooling this means that, as a rough estimate, twelve photons can be scattered on each atom by means of a laser with such parameters (and fixed detuning), or in other words, the atom can undergo up to twelve absorption-emission cycles before it is kicked out of the capture range by a random recoil. As soon as this happens the velocity of the atom has changed by such an amount that the detuning seen by the atom no longer fulfils the resonance condition and it becomes "invisible" to the laser light. In order to keep addressing a maximum fraction of atoms it might therefore be wise, if experimentally feasible, to consider a continuous adjustment of the laser parameters during the cooling procedure.

For this purpose Liang and Dermer proposed a "snowplough" scheme [91] for instance, which means to rapidly sweep the laser frequency from the outermost edges of the Doppler velocity distribution towards its center. This, however, requires tuning the laser frequency by a rate faster than $10^9\,\mathrm{GHz/s}$ (equivalent to one recoil per spontaneous decay, i.e., $\approx \omega_{\mathrm{rec}}/\tau$) which might hardly be realisable. Instead, a more feasible (but still challenging) approach is the use of a very broadband laser with fixed negative detuning which covers all atoms moving towards the laser source.

Temperature limits

In most atomic species laser cooling is performed on a transition that satisfies the broad-line condition[16], allowing to treat them in the Brownian motion formalism. By deriving the diffusion constant of such a system it can be shown that the Doppler cooling limit, in terms of the lowest temperature $T_{\mathrm{min}}^{\mathrm{(broad)}}$ attainable on a broad line, depends exclusively on the natural linewidth Γ_{ge} and is given by

$$k_{\mathrm{B}}T_{\mathrm{min}}^{\mathrm{(broad)}} = E_{\mathrm{Doppler}} = \frac{\hbar\Gamma_{\mathrm{ge}}}{2} \; . \tag{2.41}$$

This energy is typically referred to as the *Doppler energy* E_{Doppler} (and $T_{\mathrm{min}}^{\mathrm{(broad)}}$ as the *Doppler temperature* T_{Doppler}) since it represents the standard Doppler laser cooling configuration. The derivation of the Doppler cooling limit is not elaborated in detail here since it does not yield any further insights.

---

[16] More details on the differentiation between broad- and narrow-line transitions can be found in App. E where the importance of the classification is explained on the basis of the effects on fundamental interaction parameters, such as the excitation rate, as well as from the perspective of characteristic time scales.

As soon as ω_{rec} becomes comparable in size to the linewidth Γ, the momentum fluctuations at the cooling limit can no longer treated by means of a diffusion model. In this case the derivation of the cooling limit in the narrow-line configuration becomes a bit more complex. As shown in [92], the minimum temperature is then limited by the size of the recoils and given by

$$k_{\mathrm{B}} T_{\min}^{(\mathrm{narrow})} = E_{\mathrm{rec}} = \frac{\hbar^2 k^2}{2m} \; . \tag{2.42}$$

$T_{\min}^{(\mathrm{narrow})}$ is also known as the *recoil temperature* T_{rec}, which is the temperature that corresponds to the transfer of a single photon recoil.

As a general rule it can be noted, that the cooling limit is in both cases governed by the dominant characteristic energy, either $\hbar\Gamma_{\mathrm{ge}}$ or $\hbar\omega_{\mathrm{rec}}$. A comprehensive treatment and discussion of the temperature limit for laser cooling, covering both broad-line and narrow-line configurations is given by Castin, Wallis and Dalibard in [93].

Temperature evolution during laser cooling

The differentiation between narrow- and broad-line configurations does not only manifest in different approaches for treating the cooling limit. In fact, the velocity distributions, defined by the variance $\langle v^2 \rangle$ which enters the statistical definition of the kinetic energy, evolves as well in very different characteristic ways. While in case of broad-line cooling the velocity distribution shows an exponential evolution, it exhibits a smoother development, proportional to $|v|^{-2|\delta|/\omega_{\mathrm{rec}}}$, in the narrow-line case [92].

A comprehensive theoretical derivation and discussion of the dynamics of the atom in the light field including also laser cooling and the evolution of the temperature is presented by Cohen-Tannoudji in [90] and Dalibard in [94]. It is also shown there that in the limit of a **broad-line** transition a simple differential equation can be found for describing the temperature evolution during Doppler laser cooling. If the atomic motion in the steady state is considered as a random walk in momentum space with step size $\hbar k$ at a rate of $\approx 2\Gamma s_0$, where Γ is the (potentially broadened) transition linewidth and s_0 the saturation parameter (cf. Eq. (D.36) with Γ_{ge} replaced by Γ) in resonance, the randomness of the momentum carried away by the spontaneously emitted photons gives rise to a diffusion of the momentum. The corresponding momentum diffusion coefficient can then be written as

$$D = \hbar^2 k^2 \Gamma s_0 \; . \tag{2.43}$$

Based on the steady state relation

$$\frac{\langle p^2 \rangle}{2m_{\mathrm{Ps}}} = \frac{1}{2} k_{\mathrm{B}} T \tag{2.44}$$

between the temperature T of the ensemble of atoms and the variance $\langle p^2 \rangle$ of the momentum p, the further derivation finally yields the differential equation

$$\frac{\mathrm{d}}{\mathrm{d}t}(k_{\mathrm{B}} T) \;=\; -\frac{2\alpha}{m_{\mathrm{Ps}}}(k_{\mathrm{B}} T) + \frac{2D}{m_{\mathrm{Ps}}} \tag{2.45}$$

for the temperature T, where α denotes the friction coefficient already introduced above as the proportionality factor between friction force and velocity v. The model is based on a 1D cooling configuration consisting of two similar counter-propagating laser beams.

The plot on the right of Fig. 2.3 shows the temperature evolution of a cloud of atoms with Ps parameters and an initial temperature of $T = 300\,\mathrm{K}$ over a typical laser cooling time of $200\,\mathrm{ns}$ as resulting from Eq. (2.45). The data for the plot was calculated for a fixed laser detuning of $\delta = 2\pi(75\,\mathrm{GHz})$ and the laser bandwidths Γ_{L} was varied between $2\pi(25\,\mathrm{GHz})$ and $2\pi(200\,\mathrm{GHz})$. Furthermore, the laser was assumed to have a power of $P = 2\,\mathrm{kW}$ (which is equivalent to a typical energy of $400\,\mu\mathrm{J}$ for pulses of $200\,\mathrm{ns}$ length) and a Gaussian beam waist of $w_{\mathrm{L}} = 5\,\mathrm{mm}$. Since these parameters yield an intensity in the high saturation regime, the linewidth Γ in the model is given by the power-broadened linewidth $\Gamma_{\mathrm{eff,L}}$ valid for excitation by broadband radiation.
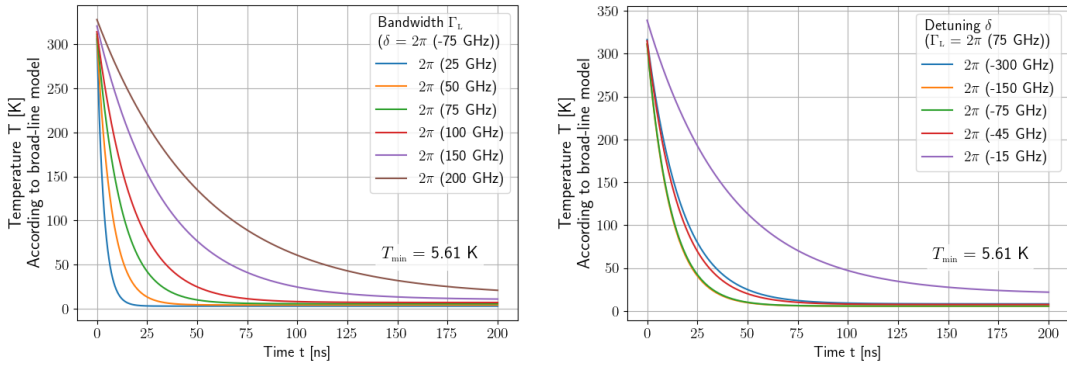
FIGURE 2.3: *Temperature evolution for Ps laser cooling based on the model of broad-line transitions.*

The plot on the left shows the evolution of the temperature during laser cooling for an interaction time of $200\,\text{ns}$ and varied bandwidth Γ_L (with values indicated in the legend) and fixed red detuning $\delta = 2\pi(-75\,\text{GHz})$. The right hand plot shows the same but for different detuning values (cf. legend) at fixed bandwidth $\Gamma_\text{L} = 2\pi(75\,\text{GHz})$. Apart from these laser parameters the beams are assumed to have a power of $P = 2\,\text{kW}$ each and a Gaussian waist of $w_\text{L} = 5\,\text{mm}$.

The temperature value in each plot indicates the minimally attainable temperature after $200\,\text{ns}$ in the most efficient configuration which on the left is reached for either $\Gamma_\text{L} = 2\pi(25, 50 \text{ or } 75\,\text{GHz})$ and on the right for all values except for $\delta = 2\pi(-15\,\text{GHz})$.

The curves are evaluated according to Eq. (2.45) and show the temperature evolution of 1D-cooling with a pair of similarly configured counter-propagating beams. It must be emphasised that the model has very restricted validity. It is applicable only for cooling on broad-line transitions in the small velocity limit $k|v| \ll \delta$. It does furthermore not include any magnetic field effects such as Zeeman or Stark coupling.

The plot on the left of Fig. 2.3 shows the temperature evolution for exactly the same laser cooling configuration, but this time with fixed bandwidth $\Gamma_\text{L} = 2\pi(75\,\text{GHz})$ and for different values of the (red) detuning δ ranging from $2\pi(-300\,\text{GHz})$ up to $2\pi(-25\,\text{GHz})$ (or, equivalently, $-10.0\,\text{cm}^{-1}$ to $-0.5\,\text{cm}^{-1}$ in units of wavenumber $\tilde{\nu} = 1/\lambda$ as commonly used in spectroscopy). The most prominent observation from both plots is the fact that for all laser parameter configurations it is possible to significantly reduce the initial temperature of $300\,\text{K}$ by means of exerting the scattering force for an interaction time of $200\,\text{ns}$. In almost all cases the minimally attainable temperature is of the order of only a few kelvin.

While, except for extreme values, the evolution apparently does not react very sensitively to changes in the detuning the bandwidth, on the other hand, seems to have a much higher impact. Surprisingly and contrary to intuitive expectations, the efficiency of laser cooling, in terms of the rate of decrease in temperature, can apparently be enhanced by reducing the bandwidth. This finding can be explained by the fact that the model is valid only with great restrictions, and has therefore only limited applicability to Ps laser cooling. Most importantly, the model itself is based on a scattering force linear in velocity v which is only valid in the limit of small velocities. Consequently, the model provides an accurate description of the cooling process only if the condition $kv \ll \delta$ is fulfilled, i.e., for configurations with Doppler shifts kv much smaller than the spectral position of the laser in terms of the detuning δ [94].

However, huge Doppler broadening as can be found for clouds of Ps atoms at room temperature fails to satisfy prerequisite, which a priori limits the suitability of the model for the Ps case quite significantly. Furthermore, this rather simple description of laser cooling completely ignores external fields. Especially the Zeeman and motional Stark effects make Ps laser cooling a very unique case. For this reason the temperature evolution given above can merely be useful for zero-field configurations. Another important prerequisite for this model is of course the broad-line condition

$\hbar\Gamma \gg \hbar\omega_{\mathrm{rec}}$ [90, 94]. Applied to the Ps case this can however again not be guaranteed for all laser parameters. In fact, with decreasing laser bandwidth the broad-line condition can be satisfied only with increasing uncertainty.

It thus becomes clear that the diffusion-based temperature evolution can be applied to Ps laser cooling only under very limited conditions such as in the case that an already quite cold cloud (with small Doppler broadening) is cooled by means of an intense and broadband laser source in a magnetic field-free environment. In spite of its very restricted validity, this simple model is still useful for assessing the mere feasibility of Ps laser cooling and for making rough estimations and giving a first impression of expectable temperature evolutions and the cooling limit. Taking into account these limitations, analytical predictions of the model seem to be quite promising with respect to Ps laser cooling.

For a more extensive and in-depth derivation and discussion of laser cooling, as well including narrow-line configurations and how they differ from the standard broad-line case, interested readers (with sufficient knowledge in French) are advised to study Dalibard's lecture notes [92]. The exposition there also covers the case of cooling on power- or bandwidth-broadened transition lines which can be found only rarely in the literature.

A fully quantum mechanical treatment of broadband cooling on narrow-line transitions can furthermore be found in [95]. Even though the discussion has a strong focus on V-shaped transition schemes, the authors come as well to the conclusion that narrow-line cooling is limited by the recoil energy and that the minimum kinetic energy converges to the broad-line limit with increasing linewidth. Interestingly, they state that "The application of broadband laser light appears to be the only feasible way to cool an atomic ensemble with a Doppler width much larger than the recoil width using a narrow transition." which supports the Ps laser cooling strategy pursued for this thesis.

2.4.3 Specialities of Ps laser cooling

Considering the various effects presented above, it is easy to see that the positronium atom represents a very special case in many respects. Interestingly, though, upon closer examination one realises that almost all peculiarities of the Ps atom can be attributed to mainly two properties, namely the antimatter character and the unusual mass-related properties.

Mass-related phenomena

One of the most important consequences of the extraordinarily small mass is certainly the fact that Ps atoms tend to move at much higher translational speed than other atomic species. The high velocities in turn have a number of further implications:

1. **Huge Doppler broadening**
   First and foremost to be mentioned is certainly the huge Doppler broadening of Ps clouds, which exceeds the single-atom transition linewidth by several orders of magnitude. The Doppler broadening represents the first obstacle to be overcome in an experimental realisation as it poses considerable requirements to the laser source, which needs to provide intense radiation over broad frequency bands in order to ensure optimum capture ranges.

2. **Huge recoil energies**
   Next, the tiny mass also implies that momentum transfer during photon exchange processes has huge impact on the atomic motion which manifests itself in unusually high recoil energies E_{rec}, equivalent to a recoil temperature of $1/2 \; m_{\mathrm{Ps}} v_{\mathrm{rec}}^2 / k_{\mathrm{B}} = 0.15\,\mathrm{K}$ and resulting in velocity kicks of $v_{\mathrm{rec}} = 1.5\,\mathrm{km/s}$. At first glance this may in fact appear to be very beneficial to the cooling efficiency as such big recoils facilitate fast removal of momentum from the atoms. After all, already a few successive absorption and emission cycles might potentially be sufficient to dissipate a great amount of kinetic energy.

   On the other hand, though, recoil frequencies which considerably exceed the linewidth also put a higher limit to the minimally achievable temperature. Furthermore, large recoils, of the

order of the transition linewidth or more, directly thwart any attempt to model the cooling scheme by means of the well established "standard" theory for broad-line configurations.

3. **Broad- or narrow-line cooling?**
   The origin of the uncertainty about the categorisation into narrow- or broad-lines can in fact as well be attributed to the small size of the Ps mass, which leads to huge recoils, by far exceeding the natural linewidth. As seen, an analytical assessment of the feasibility and the expectable cooling efficiency is therefore not as straightforward as for any standard cooling scheme. Calculations based on a steady state of the internal dynamics and based on the Brownian motion approach for the cooling limit can, for example, only be applied under certain circumstances and after close scrutiny.

   As the numbers in Tab. D.1 suggest, the positronium atom represents a truly limiting case as far as the ratio of the rate Γ and the recoil frequency ω_{rec} is concerned. The cooling scheme can therefore, in general, not be clearly assigned to either the narrow- or broad-line case. Rather, the applicability of the corresponding models strongly depends on the laser parameters used: In the absence of any line broadening Ps laser cooling can be clearly classified as cooling on narrow-line transitions with $\Gamma = \Gamma_{\mathrm{ge}} \ll \omega_{\mathrm{rec}}$. However, as soon as the laser parameters are modified, either by enlarging the bandwidth, by increasing the laser power or even both, the width Γ of the absorption and stimulated emission profile becomes subject to considerable power and bandwidth broadening and can in this way be brought to a comparable or even higher level than the recoil frequency Γ_{rec}. It is then possible to recover the broad-line condition $\Gamma = \Gamma_{\mathrm{eff,L}} \gg \omega_{\mathrm{rec}}$, which in turn would allow for the use of standard laser cooling models to find appropriate laser parameters for an experimental realisation.

   In view of this modelling difficulty it is, however, advisable to avoid the use of such models and instead base calculations on more fundamental equations, as commonly done in numerical simulations. A corresponding approach is also taken here: In the simulations preformed for this thesis the dynamics is completely based on the concept of rate equations whose solution is subsequently used to evaluate parameters such as an effective temperature from the resulting momentum spread obtained from the final velocity distribution after laser cooling.

4. **Vanishing atomic orbital magnetic momentum**
   Of rather secondary importance, but still related to the Ps mass properties, is the absence of the total orbital magnetic dipole moment $\boldsymbol{\mu}_l = \boldsymbol{\mu}_l^{(e^+)} + \boldsymbol{\mu}_l^{(e^-)}$ in the centre of momentum, which finally accounts for the deviation of the Ps level scheme with respect to the hydrogenic one.

5. **Motional Stark effect**
   Besides a huge Doppler broadening and recoil sizes, the last very important consequence of the unusually high Ps velocities to be mentioned is certainly the Stark effect. Even though the occurrence of this dynamic effect is of course not restricted only to the Ps atom, it is significantly more pronounced in Ps than in other atom, such as hydrogen, which is again due to the high Ps velocities and thus strong motional fields E_{MS}. Due to its great importance for Ps laser cooling and the multitude of partly subtle interference with the cooling scheme, the role of the motional Stark effect on Ps laser cooling will be considered separately in Section 2.4.3.

Implications of annihilation on the cooling scheme

The ubiquitous effect of annihilation that results from the antimatter character of the Ps atom has mainly two important consequences for any Ps cooling scheme:

1. **Cooling time limitation**
   The limited lifetime of $142\,\mathrm{ns}$ for ortho-positronium and $125\,\mathrm{ps}$ for para-positronium in the ground state imposes a clear restriction on the time available to cool down the atoms. In order to maximise the measurement accuracy experiments must generally be performed on a

maximum number of atoms and should thus be completed on time scales of less than about 200 ns. Since laser cooling is often also envisaged as an intermediate step to subsequent experimental measurements performed on the cooled cloud, excessive loss of atoms must absolutely be avoided since it could a priori jeopardise any subsequent experiment. It thus follows, that much faster and and more efficient cooling schemes are required for Ps than in the "standard" realisation of Doppler cooling, using alkali atoms for instance, which is usually designed to take place on millisecond time scales.

A second crucial benchmark for evaluating the suitability of cooling schemes, of equal importance as the minimum attainable temperature, is thus the "speed" at which cooling is conducted, that means the rate at which momentum can be removed from the atomic motion. In fact there is even a trade-off between the two goals: In case the cooling process stretches over too long periods of time the achievable measurement accuracy becomes severely impaired by the reduction in the number of available atoms. On the other hand, longer cooling times generally allow for lower final temperatures. One of the most crucial tasks of the numerical investigations was thus to identify the best set of parameters to achieve the lowest possible temperatures within the least amount of time. The compromise between final temperature and particle number thereby of course depends on the specific purpose of the experiment, that means whether cooling is performed for its own sake or rather as a preparatory step to further experiments.

2. **Pure state cycling**
In the context of the previous discussion of the cooling time limitation it was implicitly assumed that cooling is exclusively performed on ortho-positronium whose lifetime is three orders of magnitude higher than for para-Ps. This would imply that transition schemes are entirely restricted to triplet states which keep purely triplet character also in magnetic fields. In consideration of the Zeeman and motional Stark effects resulting from the interaction of the atom with magnetic fields it becomes directly clear that this is indeed a very strong and restrictive requirement which in reality can only be fulfilled with difficulty.

In fact there are only very few states which do not become subject to mixing in the presence of magnetic fields. One example for states which are insusceptible to magnetic fields are those with lowest or, respectively, highest m-quantum number of a given J-manifold. Due to their outermost position in Zeeman maps, which schematically illustrate the splitting of the respective level in magnetic fields, those states are commonly referred to as *stretched states*.

An often-used technique in which the atom is exclusively cycled on pure transitions connecting purely triplet states and in which laser interaction is restricted to stretched states, is optical pumping, which is introduced and described in Section C.6.

In experiments it is in general highly challenging to stay on states which, for all magnetic field configurations, are neither directly nor indirectly (via secondary processes such as coupling of other ground states which the atom might decay to) coupled to singlet states, resulting in a significant lifetime reduction (as explained in Section B.5.2 on magnetic quenching and illustrated by Fig. B.1) and thus accelerated loss of atoms. This is due to the fact that compliance with a purely triplet transition scheme requires precise control of both the laser wavelength and polarisation state.

How the process of annihilation is finally technically integrated into the calculation is described separately in Sec. 3.1.1, in the context of the explanation of the model used for the numerical simulations.

Implications of magnetic field-induced effects on Ps laser cooling

The interaction with an external magnetic field certainly adds the highest complexity to the cooling considerations. As discussed in detail in App. B, interleaving Zeeman and motional Stark

effects induce various modes of coupling between the states, resulting in energy shifts and, more importantly, state mixing which, in its entirety, is difficult to predict analytically. This is especially the case for an atomic cloud consisting of several thousands of thermal particles with velocities $\boldsymbol{v}$ distributed isotropically in space where the internal states of each atom are coupled in their very own way. Needless to say that the result of laser interaction with such a cloud, taking into account the sum of the individual contributions of all atoms, are only assessable numerically.

Zeeman effect
The situation is considerably simplified if the atoms are either completely at rest or are only moving at velocities $\boldsymbol{v} \parallel \boldsymbol{B}$ parallel to the magnetic field direction. In this case no motional Stark effect arises and the internal level structure of the atom can only be affected by a Zeeman effect. The impact of the magnetic field on the internal level structure of the $n = 1$ and $n = 2$ manifolds as a result of the Zeeman effect has already been visualised in Fig. 2.2 as a function of the magnetic field strength B for values ranging from $1\,\text{T}$ to $5\,\text{T}$. This Zeeman map helps to understand in which way the effect differs for the two manifolds and allows to classify the field strength into certain regions with different characteristic behaviour of the atomic levels.

Obviously, the states from the $n = 2$ manifold are much more susceptible to the perturbation than those belonging to the $n = 1$ level. While in the latter case the field is, over the whole range up to $5\,\text{T}$, not strong enough to break the LS-coupling scheme, this is clearly the case for the $n = 2$ states, which even reach the Paschen-Back regime already for $B \gtrsim 1\,\text{T}$. Since in this regime the states are coupled to each other, superpositions of singlet and triplet states are formed and it is no longer appropriate to express the states in terms of the pure $|nlsjm\rangle$ basis states. For intermediate field strengths the states are instead more properly described by means of the product states $|nlm_l\rangle \otimes |Sm_s\rangle$. In case the field is strong enough to decouple the electron and positron spins $\boldsymbol{s}_{\text{e}-}$ and $\boldsymbol{s}_{\text{e}+}$ completely, the states should, however, be described by their individual magnetic quantum numbers $m_{\text{e}-}$ and $m_{\text{e}-}$ respectively, labelled by $|m_{\text{e}-} m_{\text{e}+}\rangle$.

Such strong decoupling of the magnetic moments can indeed be beneficial for laser cooling as it allows for cycling on pure triplet states. How this manifests itself in the cooling efficiency will be described below (cf. Section 3.1.2).

Motional Stark effect
Needless to say that configurations with velocities fully aligned along the magnetic field axis are in general fairly unrealistic, especially for thermal clouds in three dimensions. Hence, under realistic conditions, the level structure is usually far more complex. The motional Stark effect does not only add complexity due to the fact that it opens additional coupling channels but, much more importantly, by introducing an additional velocity dependence to the description.

The combined influence of Zeeman and motional Stark effects on the internal level structure, the subsequent "playground" for laser cooling, makes it of course even more difficult to make predictions on the annihilation behaviour and internal level dynamics, and thus also the external motion, during laser interaction. Nevertheless, there are a few general conclusions which can be drawn for such configurations.

1. **Consequences of the velocity dependence of the Stark effect**
   One important consequence of the motional Stark effect is the fact that the atoms in the thermal cloud no longer show the same response to magnetic field perturbations. Since the Stark effect originates from the motion-induced electric Stark field $\boldsymbol{E}_{\text{MS}}$ (see Sections B.3 and B.6) and thus depends on the velocity of the atom, particles from different classes of the velocity distribution are affected in different ways. While fast atoms show the strongest interaction, the effect completely disappears for atoms with zero velocity $v_{\perp} = 0$ in the plane perpendicular to $\boldsymbol{B}$. It is important to keep this aspect in mind when considering to change the laser parameters and to address another range from the velocity distribution.

2. **Importance of the orientation between laser and magnetic field**
   Since the purpose of laser cooling is to slow the atoms down by modifying their velocities

via continuous internal state cycling, laser interaction will of course also lead to changing motional Stark effects in the course of the cooling process. However, since the Stark field $\boldsymbol{E}_{\mathrm{MS}} \propto \boldsymbol{v} \times \boldsymbol{B}$ does not only depend on $\boldsymbol{v}$ but also on its orientation to the magnetic field $\boldsymbol{B}$, the Stark effect will only be affected by laser interaction under certain conditions:

Over the whole cooling time, i.e., the average over many absorption-emission-cycles the atoms will experience a net transfer of momentum primarily pointing along the laser axis $\boldsymbol{k}$ since spontaneous emission recoils balance out over time. Thus, in case of a longitudinal orientation of magnetic field and laser axis, the interaction with the radiation will lead to changes of the velocity component $v_{\parallel}$ parallel to the magnetic field and the vector product $\boldsymbol{v} \times \boldsymbol{B}$, which gives rise to the motional Stark field $\boldsymbol{E}_{\mathrm{MS}}$, will stay unaffected. However, as soon as $\boldsymbol{k}$ has a non-zero component in the plane perpendicular to $\boldsymbol{B}$ and the laser interaction also modifies $v_{\perp}$, the Stark field will of course be affected as well.

Both the non-uniformity of the Stark effect throughout the atomic cloud and the possibility of altering Stark effects in the course of laser cooling are important aspects to keep in mind for analysing the results of the numerical simulation, as the Stark effect is closely related to certain properties of the atom. Hence, altering Stark fields, either between individual particles at a certain point in time or in a certain atom at different points in time during cooling, can also have implications on those properties. This can be exemplified on the basis of the annihilation lifetime (see below).

3. **Impact on lifetime and implications for cooling**
   The recoil experienced by the atom as a result of photon absorption or emission has a direct impact on the properties of the atom itself. Most importantly, changes in the velocity lead to modifications of the Stark effect, which in turn affects the lifetimes via changing mixing behaviours. Since this phenomenon originates from singlet-triplet coupling, it does not result only from Stark but in fact also Zeeman effects.

It is important to mention that in this context the term "lifetime" refers to both the contribution from fluorescence and from annihilation. While the Zeeman effect primarily causes coupling between the different spin states and thus mostly affects annihilation, the Stark effect creates mixing between different l-states. This does not mean, though, that Stark coupling can only affect the spontaneous decay properties of the excited states. Rather, there is also an indirect link to annihilation, since Stark mixing of excited states might, for example, open a quenching channel which in zero-field does not exist, as explained by means of Fig. B.2 in Section B.5.2. This is of course completely irrelevant in absence of laser interaction, but can become effective as soon as radiation stimulates transitions in the atom, in which case a link is established between laser interaction and observable lifetimes.

Since each state possesses characteristic annihilation and spontaneous decay rates (cf. Table A.1), the mixing ratios directly translate to modified rates in magnetic fields. As long as the atom does not populate the states which are affected by the motional Stark effect, the altered rates do not have any impact on the effective lifetimes of the atom, i.e., the ones which can be observed in experiments. However, as soon as the laser creates a population of these mixed states, the potentially modified lifetimes in magnetic fields can have an impact on the cooling efficiency, due to different annihilation and/or spontaneous decay behaviour. Even though this already affects ground states (magnetic quenching of the $m = 0$ ground state), it will have much more severe implications for excited states which are the product of different Stark-coupled initial states.

First of all, there is of course a general increase in effective annihilation lifetimes if an atom interacts with a laser field, which occurs in all cases, i.e., also in the absence of an external magnetic field or for stationary atoms in magnetic field environments. This is simply due to the fact that excited states typically show much lower annihilation rates than the ground state. The reduced dwell time in shorter-lived ground states thus directly translates to longer effective annihilation times. This can be estimated from the sum of the involved lifetimes weighted by the dwell time in the respective states.

The annihilation (as well as the spontaneous decay) rate can however be further modified through the impact of the interaction with magnetic fields, namely in two ways: First of all, as mentioned before, excitation to a state which is the result of either Stark- or Zeeman-induced coupling it will lead to different decay properties compared to the zero-field case. There is, however, also a secondary effect, namely the fact that the mixed state might in turn decay to other ground states with substantially different annihilation behaviour (e.g., quenching) than the original one. Magnetic perturbation-induced opening of additional decay channels, both spontaneous and annihilation, might thus result in a considerably modified level dynamics compared to the zero-field case. Due to the coexistence of life-prolonging and -shortening effects, it is almost impossible to predict in which way this will modify the lifetime. One can nevertheless again draw the conclusions that the population of (either ground or excited) states which are subject to magnetic quenching should be avoided as far as possible.

A noteworthy example for lifetime extension is the excitation to a Stark-mixed state with partially metastable character with almost negligible spontaneous decay rates. At first glance one might be led to the premature conclusion that this can in fact only be beneficial since it entails significantly enhanced lifetimes, which in turn would allow for much longer laser cooling times. This argument, however, completely ignores the fact, that excitation to metastable states not only implies shorter annihilation rates but also significantly reduced spontaneous emission rates, which means that the atom will effectively be lost for laser cooling as it can no longer be excited and cooled down further.

This can be exemplified very well by means of the cooling transition $1^3\mathrm{S} \leftrightarrow 2^3\mathrm{P}$: In the presence of static external magnetic fields, the motional Stark effect leads to coupling of the excited $2^3\mathrm{P}$ to the state $2^3\mathrm{S}$ where the coupling strength depends on the value of E_{MS} and thus on the magnetic field strength B and the velocity component $v_\perp$. The $2^3\mathrm{S}$ state in turn is a metastable state since the selection rules prohibit single-photon decay to any ground state with same orbital angular moment quantum number l. Decay to the ground state can therefore only take place via second-order processes and two-photon emission, which however is far less probable and takes place at a much smaller rate than decay mediated by single-photon emission.

As specified in Tab. A.1 the $2^3\mathrm{S}$ state has a fluorescence lifetime of about $243\,\mathrm{ms}$, which even by far exceeds its annihilation lifetime of $1.11\,\mu\mathrm{s}$. Once the atom populates this state, it is thus more likely for it to annihilate than to decay back to the ground state. Casually speaking, once the atom ends up in the $2^3\mathrm{S}$ state it will probably be parked there until it dies[17]. Obviously, the atom will then no longer take part in the laser cooling process.

This influence of the motional Stark effect on the lifetime of states from the $n = 2$ manifold has already been illustrated in Fig. B.3 which shows the B-dependence of the combined lifetime for two example values of $v_\perp$. The figure clearly confirms that the considerable modification of lifetimes in moderate fields ($B \lesssim 1\,\mathrm{T}$) compared to the zero- or low-field case. A comparison of the two subplots additionally demonstrates that the lifetimes of these states not only change with the magnetic field strength but, of course, also with the velocity $v_\perp$ due to the fact that the Stark effect originates from the motional Stark field $E_{\mathrm{MS}} = \boldsymbol{v} \times \boldsymbol{B}$. The figure shows a lifetime increase by a factor of three as the velocity increases from $34\,\mathrm{km/s}$ to $107\,\mathrm{km/s}$.

Additional complexity arises from the fact (as discussed above) that the impact of the motional Stark effect depends on the Doppler-velocity class addressed by the laser. As explained, the velocity-dependent Stark mixing directly translates to individually different

---

[17] This interesting feature can and is in fact experimentally exploited for various purposes, see for instance [96, 97]. Its metastable property makes the $2^3\mathrm{S}_1$ state furthermore amenable to precision experiments, since the extraordinarily long fluorescence lifetime entails an extremely narrow linewidth $\Gamma = \tau^{-1}$. Since fluorescence decay is however not the only decay channel in Ps atoms but always accompanied by the immanent annihilation decay, the linewidth is not entirely determined by the two-photon emission rate but subject to significant annihilation-induced broadening which manifests itself in a linewidth $\Gamma = \Gamma^{(\mathrm{ann})} + \Gamma^{(\mathrm{fl})}$ or lifetime $\tau = \left[(\tau^{(\mathrm{ann})})^{-1} + (\tau^{(\mathrm{fl})})^{-1}\right]^{-1}$ respectively.

decay properties of each atom in the cloud, especially if laser interaction causes the atoms to populate a variety of states. This effective velocity-dependence of the decay behaviour of the atom in turn implies that the cooling efficiency will depend on which velocity range is ultimately addressed (determined by the laser detuning). Based on the previous example, it might therefore happen that atoms from a one velocity range are excited to mixed states with partially metastable character while those from neighbouring classes do not show any coupling at all.

This phenomenon becomes especially important if laser parameters are adjusted in the course of the cooling process in order to constantly optimise the number of addressed atoms. If the frequency is swept over a velocity interval with unfavourable mixing behaviour the adjustment of laser parameters might therefore, under certain circumstances, be detrimental to the cooling efficiency. It should, however, be noted that the benefit of laser parameter adjustments for the purpose of a maximum number of interacting atoms in general by far outweighs the minor negative disadvantaged caused by mixing induced by magnetic perturbation. Needless to say that the Stark effect and thus a potential modification of lifetimes of laser-interacting atoms again changes in the course of the cooling process due to the velocity changes caused by the recoils which accompany photon absorption and emission.

The described interference of magnetic perturbation with the dynamics during laser cooling is of vital importance with respect to the simulations performed for this thesis as it reveals the novelty of these studies, which is the inclusion of magnetic fields as well as the extension of the scheme to three dimensions.

Chapter 3

Numerical studies of Ps laser cooling in a magnetic field

Ps-laser interaction on level schemes which are highly affected by Zeeman and Stark effects and furthermore consist of states with very different annihilation properties is very complex. It is therefore indispensable that envisaged experiments are conceived with special care. Ideally, this should first of all also include thorough studies of the very feasibility of the scheme. In case of positronium, well-established theoretical models can, however, either not be applied at all or only under excessive restrictions. Therefore, it is almost impossible to make reliable predictions on the basis of analytical calculations and investigations have to be performed numerically, based on the most fundamental concepts of light-matter interaction under consideration of magnetic field perturbation.

In fact, a number of numerical investigations have already been performed on laser cooling of clouds of positronium atoms. In 1988, for example Liang and Dermer carried out feasibility studies of Ps laser cooling with the goal of Bose-Einstein condensation (BEC) [91]. They based their simulations on the $1^3S_1 \leftrightarrow 2^3P_2$ transition and subsequently employed the commonly used rate equation approach to describe the level or rather population dynamics. Their results suggest that Ps laser cooling (in zero field) is indeed feasible and that the critical temperature for BEC formation is as well reachable, even within the ortho-Ps lifetime.

Further numerical investigations using laser radiation at 243 nm to drive the $1^3S_1 \leftrightarrow 2^3P_2$ transition with a power of a few kW (corresponding to ≈ 1 mJ for ≈ 100 ns long pulses) and focussed onto a spot of a few millimetres in size (equivalent to the distance travelled by the Ps atoms during the interaction time), come to equally promising conclusions [98–100]. These studies were based on laser bandwidths in the range of ≈ 100 GHz and (red) detuning of roughly similar size in order to ensure simultaneous excitation of all $2^3P_{J=0,1,2}$ states under consideration of the huge Doppler broadening of positronium clouds.

The weakness of these studies is, however, the fact that they were all performed in a field-free environment. Since positronium is usually generated in magnetic field environments though, it is indispensable to take external field-induced effects into account in the cooling calculations. In view of the discussions in the previous chapter, the presence of magnetic fields adds considerable complexity to the scheme. Nevertheless, the results of the previous theoretical and numerical studies of Ps laser cooling are encouraging and give good reason to assume that experimental Ps laser cooling will be successful in magnetic fields as well upon compliance with a number of recommendations such as the implementation of pure state cycling schemes. The verification of these predictions is the reason and motivation for the extensive numerical investigations carried out in the scope of this thesis which were also published in a peer-reviewed scientific article [47]. Next to the exploration of the general feasibility of Ps laser cooling in magnetic fields, their purpose was to examine possible implementation schemes and to identify experimental limitations with regard to a realisation of Ps laser cooling within the AE$\bar{g}$IS experiment.

3.1 General considerations

3.1.1 Conceptual framework for simulation of Ps laser cooling

Numerically, it is not practically feasible to base calculations on the full optical Bloch equations since this would make excessive demands on computing resources. As derived in Section D.4.4

and discussed in Section D.6, this is, however, anyway only necessary under certain conditions. In all other cases the description of the level dynamics during laser cooling can be simplified considerably by using a set of incoherent rate equations, which requires much lower computational efforts by making less demands on available capacities. The crucial prerequisite for the validity of this approximation is to ensure that the evolution dephases much faster (as characterised by the transverse relaxation rate $\Gamma_\perp$) than it is coherently excited (as characterised by the Rabi frequency Ω). In other words, on the time scale of interest for laser cooling, coherences must be damped strongly enough to allow the system to reach a quasi-steady state in which it is adequate to only consider the state populations and neglect coherences. This requirement is well satisfied by using incoherent broadband laser radiation as is the case here. For this reason the numerical model is based on rate equations.

Implementation of annihilation and photoionisation

Annihilation, the second major peculiarity of the Ps atom besides the tiny mass, makes it however impossible to fall back on the simple system of rate equations given by Eq. (2.32). For the various reasons introduced in Sec. 2.4.3, it is rather indispensable to incorporate this phenomenon in the equations describing the state populations. Effectively, the cooling process is then described on the basis of an open instead of the simple closed two-level system with constant total number of atoms N.

A similar issue arises from the effect of light-induced photoionisation. Even though photoionisation is, in contrast to annihilation, no ubiquitous effect but only occurs in the presence of (sufficiently intense) light fields, both phenomena affect the populations in a similar way. Both produce a continuous loss of atoms which implies that the total number of atoms decreases exponentially over time.

Due to the simplicity of the impact on the overall process, it is straightforward to include both effects in the rate equation formalism: Since rate equations are by construction based on the populations of the individual states, any permanent loss of atoms can be taken into account by interpreting the respective process as a concurrent decay channel which can easily be integrated by defining additional, artificial levels to which the particles can decay. In case of photoionisation, these auxiliary levels can be considered as discrete representatives of the energy continuum even though in reality of course no bound state exists in this energy range. In case of annihilation the additional "dead" levels are even more artificial since the final state after annihilation does not even consist of massive particles anymore.

The rates $\Gamma^{(\mathrm{ann})}$ for annihilation[18] can directly be obtained from the formulas given in Eq. (2.5), whereas those for photoionisation can be calculated from the cross section $\sigma^{(\mathrm{phion})}$ (cf. Eq. (C.49)) according to

$$\Gamma^{(\mathrm{phion})} = \sum_{\mathrm{L}} \frac{I_{\mathrm{L}}}{\hbar\omega_{\mathrm{L}}} \sigma^{(\mathrm{phion})} \ . \tag{3.1}$$

The sum over all lasers takes into account irradiation by several independent laser beams which incoherently superpose each other, in line with the approach taken in the numerical studies [47]. The one-way property can furthermore be implemented by defining infinite decay lifetimes for the level(s) which represent the energy continuum (photoionisation) and zero absorption rates for the "dead" levels used for annihilation. In this way re-excitation of annihilated atoms and decay of photoionised ones can be prohibited. Upon integration of the corresponding rates laser cooling then effectively takes place on an open instead of closed 2-level system. More details on the actual technical realisation for numerical simulations can be found in the appendix of [47].

---

[18] As the time scale of annihilation of atoms in excited states (of the order of micro- up to few milliseconds; cf. Tab. A.1) exceeds typical durations of laser interaction by far, it would in principle be sufficient to only account for annihilation of the ground states in the rate equation model.

Extension from the single atom to the atomic cloud

Naturally, it is an oversimplification to restrict the treatment of laser cooling to laser interaction on a single transition. In most cases the use of broadband lasers can of course also provoke excitation of other transitions in the respective atom. Excitation of secondary transitions next to the main cooling transition might however also occur as the result of interaction with external static fields, such as the Zeeman effect, which might shift previously off-resonant energy levels into resonance, or the Stark effect which primarily manifests itself in state coupling and mixing instead of shifting.

Additional states are, however, not only involved in excitation but also in de-excitation processes since, in reality, the atom will not necessarily decay back to the original ground state but potentially also to different ones, in full compliance with the selection rules. Thus, any attempt to model the real process necessarily needs to account for the possibility of such multiple excitation and the coexistence of different decay channels. Technically, this is realised in the rate equation formalism by simply introducing an individual two-level systems for each transition in the atom. Those systems are then "coupled" to each other via sums over all allowed excitation and decay channels where the interrelations (i.e., transition strengths, branching ratios, etc.) are governed by the corresponding transition rates. In case of a forbidden transition the corresponding rate is simply zero.

In specific terms this means that for each atomic state, the model allows for, first, excitation from all states lying lower in energy, second, excitation to all states higher in energy and finally for stimulated and spontaneous decay to all lower-lying states, including annihilation and photoionisation via the additional "dead" and "continuum" states. In other words, population inflow can originate from excitation from all possible lower states and fluorescence decay of all possible excited atoms while outflow simply occurs via all allowed decay channels either in the form of photon emission, excitation, annihilation or photoionisation.

Finally, these considerations yield a set of rate equations:

$$\frac{\mathrm{d}}{\mathrm{d}t}\rho_{\mathrm{ee}} = -(\Gamma_{\mathrm{e}}^{(\mathrm{ann})} + \Gamma_{\mathrm{e}}^{(\mathrm{phion})})\rho_{\mathrm{ee}} + \sum_{|\mathrm{g}\rangle}\gamma_{\mathrm{eg}}\rho_{\mathrm{gg}} - (\Gamma_{\mathrm{ge}} + \gamma_{\mathrm{ge}})\rho_{\mathrm{ee}}$$

$$\frac{\mathrm{d}}{\mathrm{d}t}\rho_{\mathrm{gg}} = -(\Gamma_{\mathrm{g}}^{(\mathrm{ann})} + \Gamma_{\mathrm{g}}^{(\mathrm{phion})})\rho_{\mathrm{gg}} + \sum_{|\mathrm{e}\rangle}(\Gamma_{\mathrm{ge}} + \gamma_{\mathrm{ge}})\rho_{\mathrm{ee}} - \gamma_{\mathrm{eg}}\rho_{\mathrm{gg}}$$

(3.2)

for each pair $(|\mathrm{g}\rangle, |\mathrm{e}\rangle)$ of atomic states from the level scheme (depicted in Fig. A.1) with $E_{\mathrm{e}} > E_{\mathrm{g}}$ and $\gamma_{\mathrm{ge}} = \gamma_{\mathrm{g}\leftarrow\mathrm{e}}$ as usual. Again, ρ denotes the diagonal elements of the density matrix which are equivalent to the populations, i.e., $\rho_{\mathrm{gg}} = P_{\mathrm{g}}$ and $\rho_{\mathrm{ee}} = P_{\mathrm{e}}$, respectively (cf. Sec. D.1.3). Rates indicated by capital Greek letters denote either spontaneous, annihilation or photoionisation rates and those in lower-case Greek letters indicate the ones for the standard laser-interaction processes, i.e., absorption or stimulated emission[19]. One directly recognises the symmetry in the structure of Eq. (3.2). This reflects the fact that they effectively represent balance equations since inflow into one state must at all times equal outflow from other states and vice versa.

By denoting the population of states belonging to the ground manifold by the matrix P_{g} and by P_{e} for the excited state manifold, Eq. (3.2) can be transformed to the matrix structure

$$\frac{\mathrm{d}}{\mathrm{d}t}\begin{pmatrix} P_{\mathrm{e}} \\ P_{\mathrm{g}} \end{pmatrix} = \begin{pmatrix} -\Gamma_{\mathrm{e}}^{(\mathrm{loss})} & \gamma^{\dagger} \\ \gamma + \Gamma & -\Gamma_{\mathrm{g}}^{(\mathrm{loss})} \end{pmatrix} \begin{pmatrix} P_{\mathrm{e}} \\ P_{\mathrm{g}} \end{pmatrix} ,$$

where the diagonal decay matrices $\Gamma_{\mathrm{e}}^{(\mathrm{loss})} = \Gamma_{\mathrm{e}}^{(\mathrm{ann})} + \Gamma_{\mathrm{e}}^{(\mathrm{phion})} + \Gamma_{\mathrm{e}} + \gamma_{\mathrm{e}}$ and $\Gamma_{\mathrm{g}}^{(\mathrm{loss})} = \Gamma_{\mathrm{g}}^{(\mathrm{ann})} + \Gamma_{\mathrm{g}}^{(\mathrm{phion})} + \gamma_{\mathrm{g}}$ each consist of annihilation ($\Gamma^{(\mathrm{ann})}$), photoionisation ($\Gamma^{(\mathrm{phion})}$), spontaneous decay ($\Gamma$) and stimulated emission rates (γ), respectively. The jth matrix element of Γ_{e} is, for example, given by $\Gamma_{\mathrm{e};j} = \sum_i \Gamma_{i\leftarrow j}$ and the ith matrix element of γ_{g} by $\gamma_{\mathrm{g};i} = \sum_j \gamma_{ij}$.

---

[19] Calculated pursuant to Eq. (C.69) for absorption and stimulated emission, Eq. (C.41) for spontaneous emission, Eq. (3.1) for photoionisation and Eq. (2.5) for annihilation, based on the relevant laser parameters, namely propagation direction $\boldsymbol{k}$, the polarization $\boldsymbol{\epsilon}$ and the spectral irradiance distribution $I_\omega(\omega)$ (defined by detuning, bandwidth and electric field amplitude or laser power, respectively).

Finally, the calculation is extended to the whole cloud of atoms by solving the set of rate equations (3.2) separately for all transitions in each individual particle. The separate treatment is only possible due to the fact that the atoms do not interact with each other so that their individual contributions add up linearly. Particle densities in the cloud are typically sufficiently small to neglect collisions between atoms.

As far as the solution of the rate equations is concerned, one can distinguish between two cases:

1. If the interaction, time between atom(s) and laser(s) T_{int} takes place on time scales much shorter than the annihilation time scale $\tau^{(\mathrm{ann})}$, it is legitimate to neglect annihilation and assume a constant number of atoms. In doing so one immediately recovers the standard closed two-level system, which means that on such short time scales the well-known steady state equations (D.22) apply, including all expressions derived thereof.

2. In the usual case of interaction time scales of the order of the annihilation lifetime or longer, though, there does not exist any real steady state since the population of each individual state $|i\rangle$ is subject to permanent loss of atoms. This complicates the description considerably, in particular if a large number of states with individually different annihilation lifetimes is involved, as in the present case. Only in a simplified two-level system is it still possible to define a quasi-steady state on the characteristic time scale of laser interaction (given by the inverse spontaneous emission rate $\Gamma_{\mathrm{ge}}^{-1}$), in which the equations known from the closed system can be recovered by introducing an additional factor $[1 - \exp(-\Gamma^{(\mathrm{ann})}\rho_{\mathrm{ii}}t)]$ [101].

When establishing the rate equation framework for simulating Ps laser cooling, it should finally be mentioned that, even in the validity range of rate equations, situations might occur in which they produce results that are physically wrong. Of particular relevance in this respect is the case in which eigenstates can be coherent superposition states of degenerate energy states. The problem then emerges due to the fact that rate equations, by definition, treat the state dynamics in an incoherent way, that means in this case do not account for the phase relations between the incoherent states. The situation gains even more complexity if the calculation procedure includes a diagonalisation of the full interaction Hamiltonian. Since this issue can be expected to only marginally affect the results presented in the following and since it is closely related to the technical implementation of the calculation, it will not be discussed any further here, but rather in the context of the descriptions of the simulation tool in the appendix (cf. Sec. F.3.3). The discussion also includes the presentation of mitigation measures implemented in the code.

3.1.2   Cooling efficiency and suitable cooling schemes

This finally leads to the question about the most suitable scheme for the implementation of laser cooling on positronium. As the lifetimes in Table A.1 already suggest, the highest cycling rate can be achieved for the transition between the triplet $n = 1$ and $n = 2$ levels. Even though it might therefore seem obvious that the cooling scheme can be assessed solely based on the cycling rate which is limited by the spontaneous lifetime, it is in fact by no means only the spontaneous rate which influences the cooling efficiency. Instead it is crucial to also take annihilation into consideration as the continuous loss of atoms naturally counteracts the cooling process. Due to the additional influence of annihilation, it is thus not as straightforward to quantify the cooling efficiency as it might appear at first glance.

While in the general studies on Ps laser cooling in magnetic fields transitions will be restricted to the $n = 1$ and $n = 2$ manifolds, the subsequent investigations with focus on the measurements performed within the AE$\bar{\mathrm{g}}$IS environment will additionally include the $n = 3$ manifold. In an experimental scheme, the inclusion of an additional n-manifold becomes necessary for the purpose of probing the cloud independently of the cooling process, i.e., probing the cloud on transitions which ideally do not interfere with the cooling dynamics but only share the same ground states. To ensure highest accuracy, photoionisation and annihilation are taken into account separately for each individual atomic state in order to include all possible decay channels.

Cooling efficiency

Obviously, the most efficient laser cooling scheme is the one which maximises the amount of momentum removed from the atomic motion. In consideration of the discussion on broad- and narrow-line cooling in Chapter 2.4 it becomes clear that, in case of positronium, it is difficult to quantify this by means of the scattering force. Instead, a much more appropriate and universally applicable measure of the cooling efficiency is based on the number N_scat of photons scattered on the atom during laser interaction. The purpose of the following section is to find the optimum strategy for cooling in magnetic fields which maximises N_scat. This includes a discussion of the influence of Zeeman und motional Stark effects on the cooling efficiency in terms of N_scat.

It can be shown that for an infinite cooling time the number of scattered atoms is given by the trace of the spontaneous decay matrix consisting of the matrix Γ containing all excited state decay rates and the integral over the excited state population matrix P_e [47], according to

$$N_\text{scat} = \sum_j \Gamma_{\text{e};j} \int_0^\infty P_j = \text{Tr}\left[\Gamma \int_0^\infty P_\text{e}\right] . \tag{3.3}$$

Under typical conditions, the atoms are initially equally distributed over all possible ground states, i.e., the initial ground state population is given by a scalar matrix with $\text{Tr}[P_\text{g}(0)] = N$ and the initial population in excited state is zero, $\text{Tr}[P_\text{e}(0)] = 0$. Taking these initial conditions into account and assuming constant laser intensity throughout the whole interaction, the integral in Eq. (3.3) can be solved by means of Block matrix inversion [47], which results in

$$\int_0^\infty P_\text{e} = \left[\Gamma_\text{e}^\text{(loss)} - \gamma^\dagger \Gamma_\text{g}^{\text{(loss)}-1}(\gamma + \Gamma)\right]^{-1} \gamma^\dagger \Gamma_\text{g}^{\text{(loss)}-1} P_\text{g}(0) . \tag{3.4}$$

Obviously, the stimulated transition rate matrix γ is the only parameter which can be used experimentally to influence the number of scattered photons. In order to maximise the cooling efficiency it is thus necessary to find the matrix γ which maximises N_scat. Due to annihilation it is however not obvious which laser parameters have to be chosen to achieve this.

In order to tackle this question and gain insight into the influence of annihilation on the laser cooling process, it is worthwhile to first consider the simplest case which is the two-level system consisting of one ground and one excited state. Additionally, photoionisation is ignored for the moment (only for these introductory considerations) in order to separate the effects of photoionisation and annihilation and to focus on the latter. Due to very small photoionisation rates it is justified to ignore this process. Irradiation by means of a laser with a power of $10\,\text{kW}$, uniformly distributed over a spot of $1\,\text{cm}^2$, for a period of $200\,\text{ns}$, for example, leads to a photoionisation rate of only 0.4% of the (2P) atoms. For these parameters the photoionisation cross sections amount to $\sigma_{n=2,l=1}^{k=0.71,l'=2} + \sigma_{n=2,l=1}^{k=0.71,l'=0} = 1.5 \times 10^{-22}\,\text{m}^2$ [47].

In this simple model case, the number of scattered photons can be maximised simply by increasing the laser intensity as much as possible. With $\gamma = \infty$ Eq. (3.3) then considerably simplifies to

$$N_\text{scat} = \frac{\Gamma}{\Gamma_\text{e}^\text{(ann)} + \Gamma_\text{g}^\text{(ann)}} . \tag{3.5}$$

This result suggests that the number of scattered photons can be increased by exciting a level with slow annihilation $\Gamma_\text{e}^\text{(ann)}$ and fast spontaneous emission rates Γ which furthermore decays towards a state with long lifetime (small $\Gamma_\text{g}^\text{(ann)}$). This again highlights the fact that the singlet part of the ground state should not be populated during the cooling process, as already reasoned before by concluding with the recommendation for pure state cycling (cf. Sec. 2.4.3). This directly confirms the initial intuitive presumption that cooling is most efficient in case of cycling transitions to the $n = 2$ manifold as the 2P states have the smallest spontaneous emission lifetime among all Ps energy levels. Cooling on the transition from a triplet ground state to a 2P excited state with an annihilation lifetime of the order of $100\,\text{µs}$ or higher (cf. Tab. A.1), finally yields $N_\text{scat} = \frac{142\,\text{ns}}{3.2\,\text{ns}} \approx 45$ photons. In a rough estimation, the velocity can thus be modified by $70\,\text{km/s}$, with the recoil

velocity of $v_{\text{rec}} = \hbar k_{\text{B}}/m_{\text{Ps}} \approx 1.5\,\text{km/s}$.

Numerical studies of simple 3- and 4-level systems confirm the findings of the simple approach based on a two-level system: In all cases it is crucial to select an excited state for which the spontaneous emission rate $\Gamma_{i \leftarrow e}$ towards a state $|i\rangle$ is larger than the annihilation rate $\Gamma_i^{(\text{ann})}$ of this state $|i\rangle$. This becomes clearer by considering the following practical example: For $B = 1.5\,\text{T}$, the two $m = 0$ ground states are mixed, even though one is still mainly of triplet character (as illustrated in Fig. 2.2). These states are superposition states of $1^1\text{S}(m = 0)$ and $1^3\text{S}(m = 0)$. However, the annihilation lifetime of this state is drastically shortened (as shown in Fig. B.1) and almost equal to the spontaneous emission lifetime of the 2P state. This implies that only one or two photons could be scattered on the transition involving the $m = 0$ ground state before annihilation of the Ps occurs, precluding any cooling process. Therefore, for a magnetic field $B > 1.5\,\text{T}$, the laser pulse should be designed to avoid populating the $m = 0$ ground states even if one of them has still mainly triplet character.

Another interesting aspect is that it may be advisable to stimulate several transitions in parallel (provided that they have small annihilation rates) because this increases the dressed state system annihilation lifetime and the overall cycling time. In an extreme toy example, imagining that it would be possible to saturate all triplet transitions in zero-field, equalisation of the level populations of all three ground 1^3S and all nine excited $2^3\text{P}_{J=0,1,2}$ levels would lead to the scattering of $N_{\text{scat}} = \frac{9}{3}\frac{142\,\text{ns}}{3.2\,\text{ns}} \approx 133$ photons [47]. This would clearly allow more efficient cooling than cycling between only two levels.

Cooling efficiency in an external magnetic field

As the goal here is to study Ps laser cooling in magnetic fields, a field $\boldsymbol{B} = B\,\hat{\mathbf{e}}_z$ along the z-axis will be included into the considerations next. All expressions for the transition dipole moments, the Hamiltonian, as well as possible coupling channels caused by Stark and Zeeman effects, are derived and discussed in Appendices B, C and D. The main ingredients for the following discussion and reasoning leading to the choice of initial parameters for the numerical studies are the (singlet and triplet) character, the Zeeman and dynamical Stark coupling between these states as well as the energy broadening.

Influence of the Zeeman effect

The influence of the pure Zeeman effect (neglecting the Stark effect for the moment) is illustrated by Fig. 2.2. With regard to the cooling transition proposed above, it can be summarised that, in the $n = 1$ manifold, the two triplet $m = \pm 1$ levels are entirely unaffected by the Zeeman effect and maintain an annihilation lifetime of 142 ns independently of the strength of the magnetic field. The lifetime of the $m = 0$ o-Ps (triplet) state, on the other hand, is dramatically shortened in magnetic fields due to coupling to the p-Ps (singlet) $m = 0$ state.

As highlighted by Eq. (3.5), the ratio between the spontaneous emission and the annihilation lifetimes is the pertinent parameter which determines the cooling efficiency. To illustrate this, subplots (a) and (b) in Fig. 3.1 show two colour-coded Zeeman maps: While the first colour code highlights the annihilation lifetime of the $n = 1$ levels and therefore only applies to the lower part of each panel, a second one (for the upper part of each panel, above the horizontal line) gives a rough estimate of the number of scattered photons for each eigenstate j of the $n = 2$ manifold. It is defined as the sum over the individual ratios between the spontaneous emission lifetime and the annihilation lifetime for all ground states $|g_i\rangle$, given by

$$N_{\text{scat}} \approx \sum_i \frac{\Gamma_{ij}}{\Gamma_j^{(\text{ann})} + \Gamma_i^{(\text{ann})}} \ . \tag{3.6}$$

In $n = 2$, eight eigenstates with $m_s = \pm 1$, namely two in the ^{3}S- and six in the ^{3}P-manifold, are insensitive to the Zeeman effect because $m_{\text{e}^-} = m_{\text{e}^+} = \pm 1/2$ (cf. Eq. (B.30) and corresponding discussion in Section B.5). For this reason the ^{3}P($m_s = \pm 1$) excited states, which have no singlet
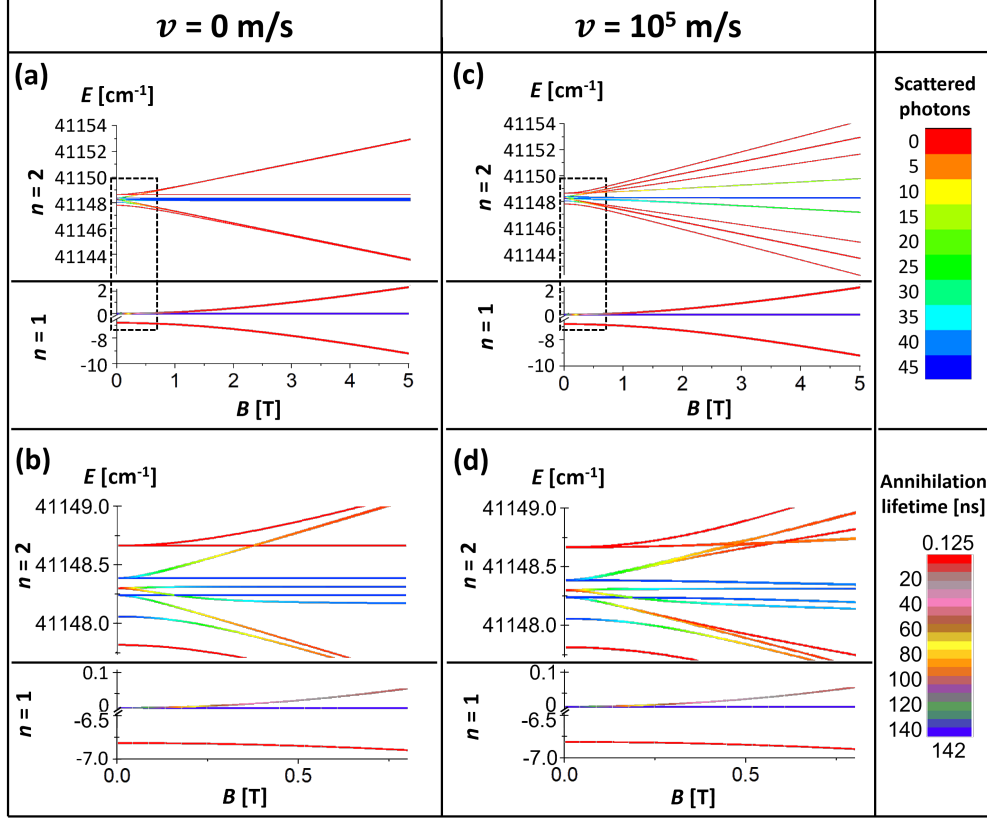
FIGURE 3.1: *Zeeman and dynamical Stark effect for Ps in a magnetic field B for values ranging from $0\,\mathrm{T}$ to $5\,\mathrm{T}$.*

Two extreme velocity cases (transverse to the magnetic field) are presented: $v_\perp = 0$ (a) (and a zoom into the region enclosed by the dashed frame in (b)) and $v_\perp = 1 \times 10^5\,\mathrm{m/s}$ (c) (and a zoom in (d)). For better separation of the curves the vertical scales (for the $n = 1$ manifold) have been adjusted accordingly. A first colour code specifies the annihilation lifetime for the ground ($n = 1$) states. A second colour code gives, for the excited ($n = 2$) states, a rough estimate of the number of photons that can be scattered according to Eq. (3.6).

component, are very good candidates for an efficient laser cooling scheme. The remaining eight m_s = 0 eigenstates have, in high magnetic fields, energies shifted by $\pm 2\mu_\mathrm{B}B$. Since these states have 50% singlet and 50% triplet character, an efficient laser cooling scheme should avoid excitation and to these states.

Unfortunately, there does not exist a one-size-fits-all approach, i.e., a single universally applicable method to achieve this state selection. Several methods with different suitability depending on the actual cooling configuration might be considered: To avoid certain states it is for example conceivable to "tailor" the transition scheme by controlling the laser polarisation in compliance with the selection rules (cf. Section C.5). This allows to minimise population of unfavourable states, i.e., with detrimental contribution to the cooling efficiency. This approach will, however, only work in 1D-cooling setups, since in 2D- or 3D-configurations where lasers from several spatial directions contribute to the scheme, the superimposed polarisations lead to an uncontrollable mixture of excitations. Alternatively, in high magnetic fields, belonging to the Paschen-Back regime where $\hat{\boldsymbol{L}}$ and $\hat{\boldsymbol{S}}$ are decoupled and states are sufficiently separated in energy, it is possible to avoid population of unfavourable certain states by accurately selecting the laser wavelength.

Influence of the motional Stark effect

As discussed in detail in Sections B.6 and 2.4.3, considerable additional complexity arises from

the high Ps velocities. It is worth to briefly recall the main results here: An atom moving in a pure magnetic field perceives an electric field which, in the non-relativistic limit, is given by $\boldsymbol{E}_{\mathrm{MS}} = \boldsymbol{v} \times \boldsymbol{B}$. This motional electric field is orthogonal to the quantisation axis defined by the magnetic field and only depends on $v_\perp$, the velocity component transverse to $\boldsymbol{B}$ (v_x or v_y for $\boldsymbol{B}$ along z). The atom is thus affected by a (motional) Stark effect $\hat{H}_\mathrm{s} = e\hat{\boldsymbol{r}}\boldsymbol{E}_{\mathrm{MS}}$ which couples only $m_l = 0$ and $m_l = \pm 1$ states belonging to the same spin multiplicity. Therefore, the influence of the motional Stark effect is restricted to the $n = 2$ manifold where it mixes S- and P-states.

In the $|n,l,m\rangle$ basis this coupling can be written as

$$\langle 2,0,0| \; \hat{x} \; |2,1,\pm 1\rangle \;\; = \;\; \mp i \, \langle 2,0,0| \; \hat{y} \; |2,1,\pm 1\rangle \;\; = \;\; \mp 3\sqrt{2}ea_{\mathrm{Ps}} \; ,$$

where e is the elementary charge and $a_{\mathrm{Ps}} = 1.05836 \times 10^{-10}\,\mathrm{m}$ is the positronium Bohr radius. This leads to a matrix element for the Stark effect of $5\,\mathrm{GHz}$ for $v_\perp = 1 \times 10^5\,\mathrm{m/s}$ and $B = 1\,\mathrm{T}$, as illustrated in the comparison of subplots (c) and (a) in the Zeeman-Stark map of Fig. 3.1. A net effect is that some of the pure "flat" triplet states ${}^3\mathrm{P}(m_s = \pm 1)$ in a pure magnetic field with zero transverse velocity considered (that can scatter 45 photons) are now (in the $v_\perp = 1 \times 10^5\,\mathrm{m/s}$ case) mixed with the metastable ${}^3\mathrm{S}$ level, as explained in detail in the last of Section 2.4.3. Consequently, the new eigenstates, when fully mixed in high fields, have a spontaneous emission lifetime of $6.4\,\mathrm{ns}$ which reduces the number of possibly scattered photons by a factor of two.

Figures of merit for a quantification of the cooling efficiency

The most expedient way to evaluate and quantify the cooling efficiency is to define an N-particle effective temperature parameter T_i along the i axis. For this calculation, only 50% of all atoms are taken into account, namely those from the second and third quartiles of the velocity distribution along i (i.e., those with smallest absolute velocities v_i), whereas the remaining 50% with extreme velocities are ignored. T_i is then defined by means of the variance of the distribution, quantified by the root-mean-square $v_{\mathrm{rms},i}$ around the mean value $\bar{v}_i$ of the velocity along axis i of all atoms considered, according to

$$\frac{1}{2}k_\mathrm{B}T_i \;\; = \;\; \frac{1}{\chi}\frac{1}{2}m_{\mathrm{Ps}}v_{\mathrm{rms},i}^2 \;\; = \;\; \frac{1}{\chi}\frac{1}{2}m_{\mathrm{Ps}}\frac{1}{N/2}\sum_{j \leq N/2}(\bar{v}_i - v_{i,j})^2 \; , \tag{3.7}$$

where $v_{i,j}$ denotes the velocity of particle j along axis i, m_{Ps} the mass of a Ps atom and

$$\bar{v}_i = \frac{1}{N/2}\sum_{j \leq N/2}v_{i,j}$$

is the mean velocity of all the $N/2$ particles with the slowest absolute velocity along axis i. The parameter χ, defined as

$$\chi \;\; = \;\; \frac{1}{\sqrt{2\pi}\sigma}\int_{v_i^{(25)}}^{v_i^{(75)}}\exp\left(-\frac{v_i^2}{2\sigma^2}\right)\left(\frac{\frac{1}{2}m_{\mathrm{Ps}}v_i^2}{\frac{1}{2}k_\mathrm{B}T}\right)\mathrm{d}v_i \;\; \approx \;\; 0.142652 \tag{3.8}$$

is a normalisation factor required to recover the usual temperature T of a Maxwellian velocity distribution. $v_i^{(25)}$ denotes the first (lower) quartile and $v_i^{(75)}$ the third (upper) quartile of the velocity distribution along axis i.

To complement T_i, a second figure of merit for the cooling efficiency is n_r, the number of Ps atoms with a velocity in the range of two times the recoil velocity, $|v_i| \leq 2v_\mathrm{r}$. For additional insight, n_r is evaluated both with and without the laser-cooling pulse (denoted by $n_\mathrm{r}^{(\mathrm{ON})}$ and $n_\mathrm{r}^{(\mathrm{OFF})}$, respectively). The comparison between $n_\mathrm{r}^{(\mathrm{ON})}$ and $n_\mathrm{r}^{(\mathrm{OFF})}$, expressed by the parameter

$$S = \frac{n_\mathrm{r}^{(\mathrm{ON})} - n_\mathrm{r}^{(\mathrm{OFF})}}{n_\mathrm{r}^{(\mathrm{OFF})}} \; , \tag{3.9}$$

highlights the effect of the laser pulse on n_r for a given parameter configuration.

3.2 Numerical studies of Ps laser cooling in magnetic fields

The basic approach of the employed algorithm is as follows: The numerical simulation of atom-light interaction is based on the concept of incoherent rate equations which are solved by means of a kinetic Monte Carlo algorithm. To accurately account for all magnetic field-induced interaction processes and allow for arbitrary field configurations, the eigenstates and -values are obtained from diagonalisation of the full Hamiltonian at each fundamental time step of the calculation. The code is highly versatile and reliably simulates (within the validity of the rate equation formalism) the evolution of the Ps cloud by deterministically solving the trajectories of the positronium atoms in laser and external fields, while stochastically accounting for the internal level dynamics. The initial population of Ps is in all cases initialised such that all three triplet ground states are populated equally. More details on the actual technical realisation of the simulation code, including implemented numerical methods, can be found in Appendix F.

3.2.1 1D cooling

All 1D-cooling simulations were carried out for a stationary cloud of 2000 Ps atoms which is expanding isotropically in 3D with thermal velocities corresponding to an experimentally typical temperature of $T = 300\,\mathrm{K}$ [7].

1D cooling dynamics

To limit the effects of the Zeeman mixing on laser cooling, the σ^+-σ^+-configuration can be used to cycle on the $1^3\mathrm{S}_1(m=1) \leftrightarrow 2^3\mathrm{P}_2(m=2)$ states that do not mix in a pure magnetic field (see Fig. 3.1 (a and b)). In this configuration, the two laser beams propagate along the z axis which is also the axis of magnetic field ($\boldsymbol{B} \parallel z$). The polarization of the lasers is in the $\sigma^{(+)}$-$\sigma^{(+)}$-configuration (one left- and one right-handed circular polarisation).

Fig. 3.2 presents the results of these simulations including the evolution over time of T_z, $n_\mathrm{r}^{(\mathrm{ON})}$, $n_\mathrm{r}^{(\mathrm{OFF})}$, S and the population in different states as well as histograms of the final distributions of the Ps velocity component along the laser direction. As mentioned in Sec. 3.1.2 photoionisation is very weak for the cooling transition from $1^3\mathrm{S}$ to $2^3\mathrm{P}$, which is confirmed by the simulations where only 1 Ps among the 2000 atoms is photoionised. This suggests that photoionisation can be neglected in this range of laser power. The first important result is that S constantly increases over the entire 200 ns window, demonstrating that the cooling laser allows to increase the number of cold atoms compared to a situation without laser excitation.

A second noticeable feature is the initial sudden rise of the excited states population (red dash-dotted curve) which reaches a peak within a few nanoseconds and then slowly drops. This is the expected behaviour for a saturated excitation: A large fraction of the atoms is excited within the first instants of the laser-Ps interaction. This, combined with the rapid annihilation of the singlet states, explains the initial sudden decrease in the population of the ground state (blue dashed curve), which however does not reach a linear regime until about 20 ns, much later than the time when the population in the excited states peaks. This excess of loss in the ground state can be linked to the reduced annihilation lifetime (6.7 ns for $B = 1\,\mathrm{T}$) of the $m = 0$ ortho-Ps mixed with para-Ps.

Another general observation linked to the previous one is that, after 200 ns, the fraction of annihilated Ps atoms in a 1 T field is nearly 85%. This is due to the presence of the magnetic field which leads to magnetic quenching and internal state mixing induced by the Zeeman effect.

In conclusion of this first study, cooling can occur mainly on transitions involving long-lived m states despite the Zeeman and motional Stark mixing, allowing long cooling interaction times with a relatively limited enhanced annihilation rate (after a first period of fast annihilation of the $m = 0$ initial states). If the phase loss issue resulting from the diagonalisation of the Hamiltonian (see Sections F.3.3 and F.5.6) has any effect on the results presented in this section, it is only to reduce the efficiency of the cooling process by artificially populating fast annihilating states that in reality are not populated when using this scheme.
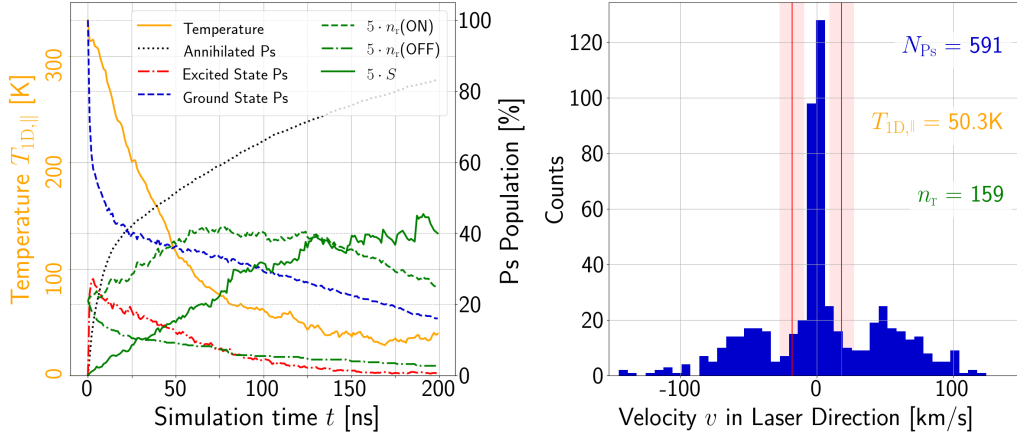
FIGURE 3.2: *1D laser cooling of a 3D expanding cloud of* $N = 2000$ *Ps atoms.*
The laser parameters were $\Gamma_{\mathrm{L}}/(2\pi) = 75\,\mathrm{GHz}$, $\delta = -2.5\,\mathrm{cm}^{-1}$ *and* $P = 2\,\mathrm{kW}$. *The magnetic field* $\boldsymbol{B}$ *and the lasers were oriented along* z. *Lasers were circularly polarised.*
Left: *Evolution of* T_{z} (*orange, solid line*)*, the percentage of annihilated Ps* (*black, dotted*) *and of the Ps population in ground* (*blue, dashed*) *and excited states* (*red, dash-dotted*)*. The green dashed line gives the percentage* $n_{\mathrm{r}}^{(\mathrm{ON})}/N$ *of Ps around* $v = 0$ *for the laser ON case, the dash-dotted one* $n_{\mathrm{r}}^{(\mathrm{OFF})}/N$ *for laser OFF and the solid one shows* $S = [n_{\mathrm{r}}^{(\mathrm{ON})} - n_{\mathrm{r}}^{(\mathrm{OFF})}]/n_{\mathrm{r}}^{(\mathrm{OFF})}$ *representing the percentage of gain of the laser ON case compared to laser OFF, all scaled by a factor of five for the sake of visibility.*
Right: *Histogram of the* v_{z} *distribution at* $t = 120\,\mathrm{ns}$. *For illustration purposes, the red lines show the spectral position of the laser light in terms of the detuning* δ *and the transparent areas indicate the laser bandwidth* Γ_{L} (*FWHM*)*. The blue number indicates the number of non-annihilated atoms, the orange one the corresponding final value of* T_{z} *and the green one gives* n_{r} *at* $t = 120\,\mathrm{ns}$.

Effect of laser interaction on the velocity distribution for 1D cooling

A more detailed quantitative analysis of the effect of the laser interaction on the velocity distribution can be carried out by considering the evolution of the first and third quartiles $v_{\mathrm{z}}^{(25)}$ and $v_{\mathrm{z}}^{(75)}$ of the distribution which form the basis for the calculation of T. Even though these parameters are less tangible than the derived temperature, they provide a more direct indicator of the cooling effect since, in contrast to T, they are not only a measure for the width of the distribution but can additionally reveal potential asymmetries of the influence of cooling.

In order to study the evolution of $v_{\mathrm{z}}^{(25)}$ and $v_{\mathrm{z}}^{(75)}$ in the course of the laser interaction, simulations with the same set of laser parameters as above were repeated for ten different values of the seed of the random number generator in zero-field as well as in a magnetic field environment of 1 T. A plot of the mean and the corresponding deviation, analogous to the studies of the statistical significance of the simulation results in Section F.5.7, enables a more refined examination than the results for only one RNG seed does. Fig. 3.3 visualises the results for both magnetic field cases, 0 T in the top and 1 T in the bottom row. While the first plot shows the evolution of the mean value and standard deviation of $v_{\mathrm{z}}^{(25)}$ and $v_{\mathrm{z}}^{(75)}$ separately, the second and third present their ratio and difference, respectively. For illustration purposes and direct comparison, each subplot additionally shows the evolution of the resulting temperature in orange.

The most prominent observation from the results is the fact that the evolutions of $v_{\mathrm{z}}^{(25)}$ and $v_{\mathrm{z}}^{(75)}$ differ considerably depending on the magnetic field value. While in zero-field the upper and lower quartiles are, in absolute numbers, reduced almost symmetrically, as shown by the almost constant (black) mean value of $v_{\mathrm{z}}^{(25)}$ and $v_{\mathrm{z}}^{(75)}$ in the first subplot and the only slightly increasing ratio $v_{\mathrm{z}}^{(25)}/v_{\mathrm{z}}^{(75)}$ in the second plot, the results for the 1 T-case reveal a clearly asymmetric effect of the cooling laser on the velocity distribution. While starting at the same initial values of about $\pm 32\,\mathrm{km/s}$, the mean value of $|v_{\mathrm{z}}^{(25)}|$ finally reaches a velocity of only $\approx 20\,\mathrm{km/s}$
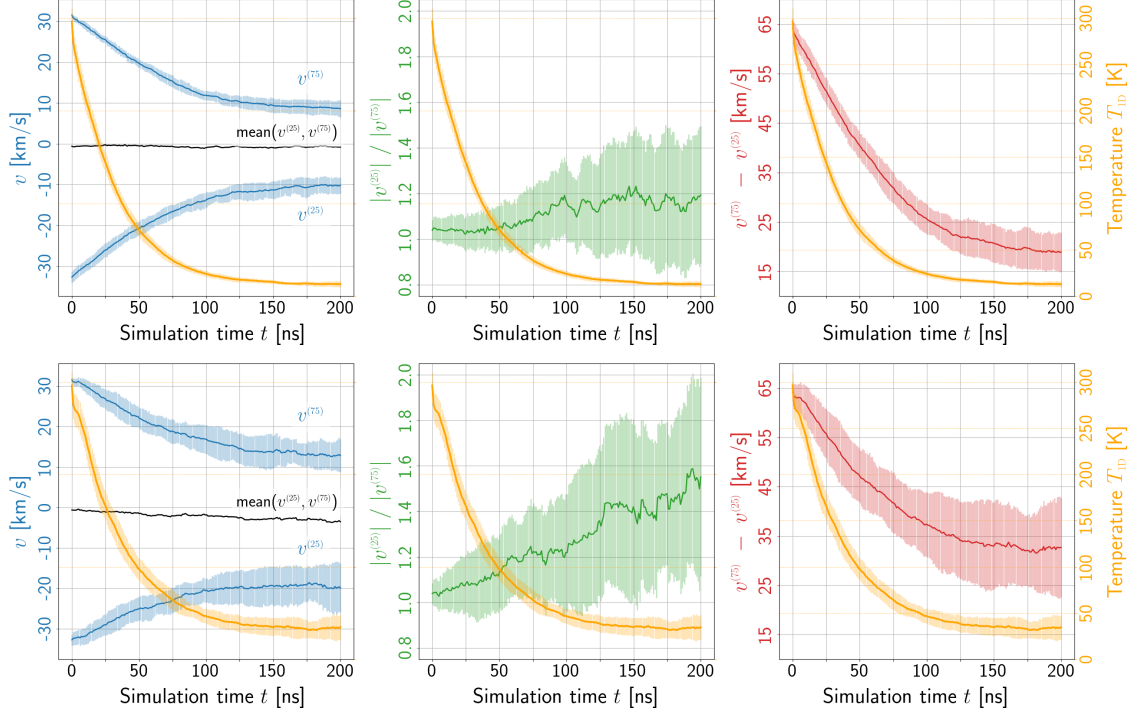
FIGURE 3.3: *Evolution of the first and third quartiles during 1D laser cooling of a cloud of 2000 particles with a temperature of* $300\,\mathrm{K}$ *in either zero- or* $1\,\mathrm{T}$*-field.*
The first plot shows the time evolution of the values of $v_{\mathrm{z}}^{(25)}$ *and* $v_{\mathrm{z}}^{(75)}$*, used for calculation of the temperature parameter* T_{z} *(cf. Eq. (3.7)), together with their mean values (black) as a function of the simulation time* t*. The second and third plots show the ratio and, respectively, the difference of the lower and upper quartiles.*
Laser interaction takes place over the whole duration of $200\,\mathrm{ns}$*. All curves are based on a dataset resulting from simulations with similar laser parameters as for Fig. 3.2 and show the mean as well as standard deviation for ten different values of the RNG seed. For illustration purposes and direct comparison each subplot additionally shows the evolution of the temperature (orange).*

(corresponding to a reduction of $\approx 40\%$) whereas $v_{\mathrm{z}}^{(75)}$ goes far below this level and is more than halved in the course of the simulation, reaching a value of $\approx 13\,\mathrm{km/s}$ (a reduction by $\approx 60\%$). Consequently, the mean of $v_{\mathrm{z}}^{(25)}$ and $v_{\mathrm{z}}^{(75)}$ at each point in time (black line) continuously decreases from around 0 to $-3.5\,\mathrm{km/s}$, indicating a shift of the centre of the distribution. The 50% rise of the ratio of $v_{\mathrm{z}}^{(25)}$ and $v_{\mathrm{z}}^{(75)}$, shown in the second plot in the bottom row, confirms that the two quartiles are affected differently by the cooling laser in $1\,\mathrm{T}$. A further interesting observation is the fact that the difference of the results is significantly larger in $1\,\mathrm{T}$ compared to the zero-field case.

The comparison between the two cases with different fields suggests that the asymmetry in the evolution of the quartiles must necessarily be caused by the presence of the magnetic field. This can be explained on the basis of the Zeeman effect. Due to the energy shift resulting from the Zeeman effect (cf. Fig. 3.1) transition energies in a magnetic field differ from their zero-field values. Consequently, the resonance is shifted to either smaller or larger values depending on the actual transition, i.e., depending on the behaviour of the two involved states in the magnetic field.

This shift of the absorption spectrum directly translates into an asymmetric effect on the velocity distribution if the laser frequency is not adjusted in the magnetic fields compared to the zero-field case. Fig. 3.3 confirms that the energy of the Ps cooling transition $1^3\mathrm{S}\leftrightarrow2^3\mathrm{P}$ is shifted such that, with a laser with fixed red-detuning from the $0\,\mathrm{T}$ resonance, transition rates are

enhanced for positive Ps velocities, while those moving towards the laser interact less strongly with the incoming photons, creating the observed asymmetry in the velocity distribution.

Since the quartiles only serve for setting the integration limits in the temperature calculation, such an asymmetric cooling result in the distribution does not manifest itself in the evolution of T. The comparison of the third plots in Fig. 3.3 suggests, however, that the shift of transition frequencies due to the magnetic field effects is accompanied by a reduction of the total excitation rate, if the laser parameters are not adjusted accordingly. This is due to the fact that the overlap between laser emission spectrum and velocity distribution (i.e., the overlap of the red area with the blue distribution in Fig. 3.2) is reduced if they no longer match perfectly, i.e., if the laser spectrum is no longer centred around the mean of the velocity distribution. Consequently, less atoms are excited and slowed down, resulting in a less pronounced modification of the velocity spectrum, indicated by the difference $v_z^{(75)} - v_z^{(25)}$, and thus a higher final temperature.

Hence, in order to maximise the cooling performance in magnetic fields it is advisable to adjust the laser parameters, in particular, the central frequency, according to the shift of the transition spectrum.

Finally, it is important to recall that the temperature parameter T, by definition, only accounts for 50% of the non-annihilated atoms, namely those with smallest velocities around the centre of the distribution. This means that changes of the interaction with the remaining faster atoms, located in the fringes of the distribution, do not affect the value of T. This, however, becomes important only for large laser detunings not studied here, so that the cooling performance can be evaluated based on the temperature evolution. In case of further detuned lasers it might, however, be preferable to either consider an additional figure of merit to account for the peripheral regions of the distribution or to redefine the temperature parameter.

Laser parameter scans for 1D cooling in $1\,\mathrm{T}$

To investigate the influence of the laser power, bandwidth and detuning on the cooling dynamics, these parameters are scanned separately in the $\sigma^{(+)}$-$\sigma^{(+)}$-configuration used before. Fig. 3.4 shows the evolution of the usual cooling parameters temperature, $n_r^{(ON)}$, the number of annihilated atoms and the populations in the ground and excited states. The resulting longitudinal velocity distributions at $t = 120\,\mathrm{ns}$ are presented in Fig. 3.5 as kind of a snapshot at $t = 120\,\mathrm{ns}$ of the evolutions in Fig. 3.4. When not scanned, the parameters are set to the following default parameters: the laser power $P = 2\,\mathrm{kW}$, the FWHM bandwidth corresponding to a standard deviation of about $\sigma/(2\pi) = 32\,\mathrm{GHz}$ for a Gaussian laser spectrum, $\Gamma_L/(2\pi) = 75\,\mathrm{GHz}$, detuning corresponding to $-75\,\mathrm{GHz}$, $\delta = -2.5\,\mathrm{cm}^{-1}$ and laser waist $w = 5\,\mathrm{mm}$. The cloud, which contains 2000 Ps atoms at $t = 0\,\mathrm{ns}$, is always initialised at a temperature of $300\,\mathrm{K}$ and such that the initial population is distributed equally over all three ground states.

From the results displayed in Fig. 3.5, apart from extreme values of the scanned parameters, efficient laser cooling is observed for all considered configurations: the number n_r of slow atoms within the $\pm 2 \times v_{rec}$ velocity range is always higher after $120\,\mathrm{ns}$ of laser-Ps interaction, compared to the situation with no laser and to its value at $t = 0\,\mathrm{ns}$. All velocity histograms shown in Fig. 3.5 present a strong peak centred at $v_z = 0$, surrounded by two depleted classes of velocity, the laser-cooled velocity ranges, selected by the laser detuning, bandwidth and power. This is the result of a momentum transfer towards lower velocities. The height and width of these peaks reflect the efficiency of laser cooling using different sets of laser parameters.

This is confirmed by the evolution presented in Fig. 3.4. Except for extreme values of the laser parameters, in all cases laser interaction produces the usual sudden rise in the number of atoms populating excited states with a corresponding evolution of the number of ground state atoms. The annihilation rate is almost identical for all configurations. Significant differences can only be observed in the number of slow atoms $n_r^{(ON)}$ and the evolution of the temperature parameter T_z.

One important parameter to maximise the cooling efficiency is the laser bandwidth, which should be large enough to cover most of the Doppler broadening of the Ps cloud, but not too wide in order to avoid exciting also the atoms in the zero-velocity class. This is shown in the first row of Fig. 3.5, which illustrates how the structure of the velocity distribution changes with the laser
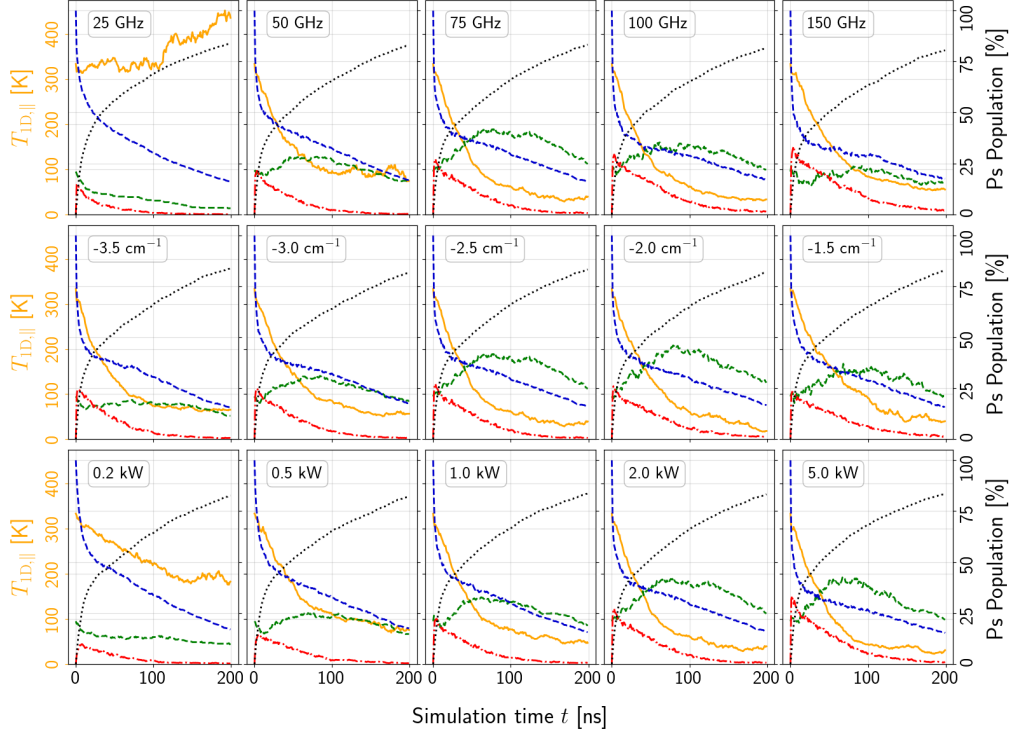
FIGURE 3.4: *Evolution of the cooling parameters for laser parameter scans in $B = 1\,\mathrm{T}$ **for 1D longitudinal cooling.** Evolution of T_z (orange, solid line), the percentage of annihilated Ps (black, dotted) and of the Ps population in ground (blue, dashed) and excited states (red, dash-dotted) as a function of the cooling time t for the three laser parameters bandwidth Γ_L (1st row), detuning δ (2nd row) and power P (3rd row). The dashed green line indicates the percentage $n_r^{(\mathrm{ON})}/N$ of Ps around $v = 0$ for the laser ON case, again scaled by a factor of five. If not scanned, the parameters are $\Gamma_L/(2\pi) = 75\,\mathrm{GHz}$, $\delta = -2.5\,\mathrm{cm}^{-1}$ and $P = 2\,\mathrm{kW}$. Plots are based on the similar dataset as for Fig. 3.5.*

bandwidth: when it is too narrow, the capture range is too small to cool a large part of the atoms. As a consequence, two central peaks build up symmetrically around $v_z = 0$ instead of accumulating atoms in the $v_z = 0$ range. This is because the middle-range velocity class is not addressed by the laser which is too far detuned and too narrow to excite and cool them down to the $v_z = 0$ range. On the other hand, when the laser is too broad, the depletion becomes less and less pronounced and the central peak is damped, as even the zero-velocity atoms can be in resonance with this broad laser and receive a momentum transfer to kick them out of the zero-velocity range.

Fig. 3.4 additionally shows that, even though very broad bandwidths lead to an enhanced excitation rate, the number of slow atoms $n_r^{(\mathrm{ON})}$ and the temperature evolution do not necessarily follow the same trend. This is due to the fact that the laser also addresses high velocity ranges for broad bandwidth values. Atoms located there can, however, not be pushed completely into the slow velocity range around the resonance so that the number n_r will not benefit from the enhanced excitation rate. For the same reason the temperature is optimised for intermediate bandwidth values. For too small bandwidths at fixed detuning (cf. first plot in the first row of Fig. 3.4), on the other hand, a too narrow velocity range is addressed as to increase the number of slow atoms n_r at all. The temperature evolution even suggests that laser-excited atoms are stimulated to annihilate faster due to excitation to states with singlet character, i.e., initially triplet states that are coupled to short-lived singlet states by Zeeman and Stark effects in the magnetic field.

The results of the detuning scan are plotted in the second row of Fig. 3.5. As expected, when the laser detuning approximately matches the Doppler width (between $\delta = -3.0\,\mathrm{cm}^{-1}$ and
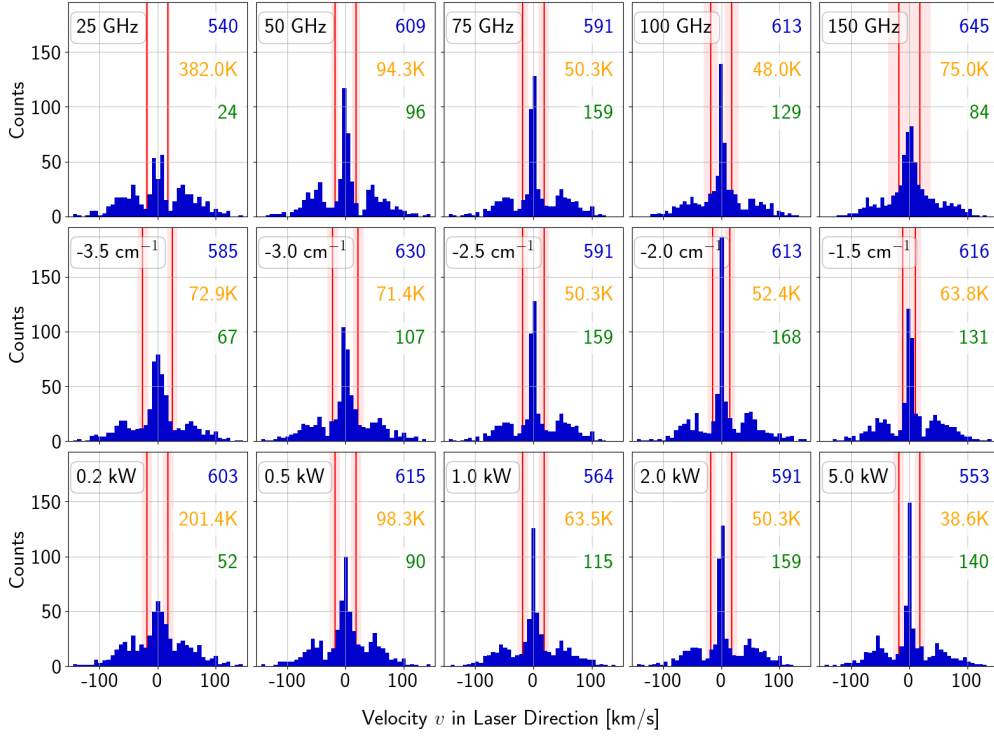
FIGURE 3.5: *Velocity distributions for laser parameter scans in* $B = 1\,\text{T}$ *for 1D longitudinal cooling.* *Histograms of the Ps velocity component along the laser direction z after $120\,\text{ns}$ for the three laser parameters bandwidth Γ_L (1st row), detuning δ (2nd row) and power P (3rd row). Notations are similar to Fig. 3.2 with all numbers referring to 2000 Ps atoms. If not scanned, the parameters are $\Gamma_\text{L}/(2\pi) = 75\,\text{GHz}$, $\delta = -2.5\,\text{cm}^{-1}$ and $P = 2\,\text{kW}$.*

$\delta = -2.0\,\text{cm}^{-1}$) and the laser bandwidth roughly takes the same value ($\Gamma_\text{L}/(2\pi) = 75\,\text{GHz}$), the cooling effect is strongest. This is again confirmed by the results visualised in Fig 3.4. Consequently, in the remainder of this section, the detuning is set at its $-2.5\,\text{cm}^{-1}$ optimum for a Ps cloud of 300 K initial temperature.

The last scan of this investigation aimed at optimising the laser power. As derived in App. D the saturation parameter s (for broadband lasers) and the saturation intensity I_sat are defined as

$$s = \frac{I_\text{L}}{I_\text{sat}} \frac{\Gamma_\text{ge}}{\Gamma_\text{ge} + \Gamma_\text{L}} \qquad \text{with} \qquad I_\text{sat} = \frac{1}{6}\hbar c \left(\frac{2\pi}{\lambda}\right)^3 \frac{\Gamma_\text{ge}}{2\pi}\,, \tag{3.10}$$

where Γ_L is the laser bandwidth, $\Gamma_\text{ge} = 1/3.2\,\text{ns}$ the spontaneous emission rate of the cooling transition, $\lambda = 243\,\text{nm}$ and $I_\text{L} = 2P/(\pi w^2)$ the laser intensity that corresponds to an excitation rate of $\gamma = 1/1.7\,\text{ns}$ (cf. Eq. (F.5)). The range of laser power explored in the simulation covers values from below saturation ($s < 1$) to well into the saturation regime ($P = 5\,\text{kW}$ corresponds to $s \approx 20$). The results presented in the third row of Fig. 3.5 suggest that a power of $2\,\text{kW}$, leading to a moderate saturation regime ($s \approx 8$), is a good compromise between a higher final number of atoms and reasonable laser power. Fig 3.4 reveals that the evolution of n_r is as well optimised at $P = 2\,\text{kW}$ even though higher powers might lead to higher excitation rates (but generally slightly higher temperatures).

From these scans, it can be concluded that there is a range of laser parameters that yield a similar laser cooling efficiency for which the initial temperature T_z is reduced by a factor of four at $t = 120\,\text{ns}$ and $n_\text{r} \approx 160$ which represents an increase of 100% compared to the initial value of
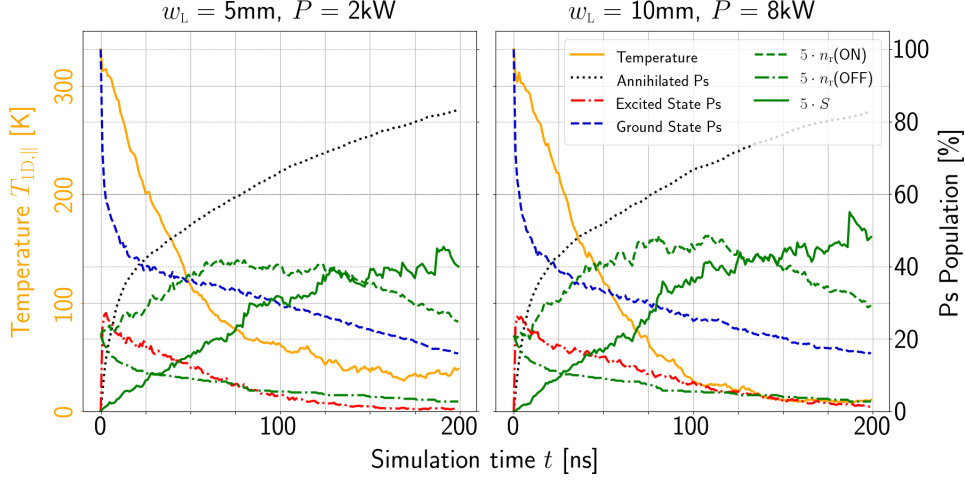
Figure 3.6: *Comparison of 1D longitudinal cooling performance in* $1\,\mathrm{T}$ *for waists* $w_{\mathrm{L}} = 5\,\mathrm{mm}$ (*left*) *and* $10\,\mathrm{mm}$ (*right*). *Plot of the time evolution of the 1D-temperature* T_{z} *and populations in the usual state categories for two different laser waists* $w_{\mathrm{L}} = 5\,\mathrm{mm}$ *and* $10\,\mathrm{mm}$. *The green lines indicate the time evolution of* $n_{\mathrm{r}}^{(\mathrm{ON})}/N$ (*dashed*), $n_{\mathrm{r}}^{(\mathrm{OFF})}/N$ (*dash-dotted*) *and* $S = [n_{\mathrm{r}}^{(\mathrm{ON})} - n_{\mathrm{r}}^{(\mathrm{OFF})}]/n_{\mathrm{r}}^{(\mathrm{OFF})}$ (*solid*), *all scaled by a factor five. Same colour code as in Figure 3.2.*
A cloud of $N = 2000$ *atoms and standard laser parameters were used. For the simulation with* $w_{\mathrm{L}} = 10\,\mathrm{mm}$ *the power was increased to* $P = 8\,\mathrm{kW}$ *to keep the power density constant.*

$n_{\mathrm{r}} \approx 80$. One important effect that limits the achieved temperature is the fact that Ps atoms move so fast that they can escape the Ps-laser interaction area during the cooling time. Consequently, cooling the majority of the Ps atoms requires a large enough beam waist to continue interacting with the moving Ps during the whole pulse duration. As a consequence, the ideal laser power required to spatially cover the Ps cloud during $\approx (100 - 200)\,\mathrm{ns}$ is relatively high. This is an experimental limitation to overcome. For the simulations presented here, it has been opted for a large $5\,\mathrm{mm}$ laser beam radius (waist), $2\,\mathrm{kW}$ power and $200\,\mathrm{ns}$ pulse duration, which is a realistic choice for future experiments.

However, as the comparison in Fig. 3.6 shows, the cooling performance can be enhanced by using laser beams with broader waists and the power adjusted to provide similar power densities. Doubling the waist to $10\,\mathrm{mm}$ and increasing the power to $8\,\mathrm{kW}$ typically leads to an increase in the population of excited states with a corresponding reduction of ground state atoms while annihilation stays almost unchanged. The enhanced excitation rate manifests itself in a $\approx 10\%$ increase in the number of slow Ps (n_{r}) after a $120\,\mathrm{ns}$ laser interaction time compared to a $5\,\mathrm{mm}$ interaction region, reaching 180 atoms instead of 160 atoms. The final temperature is reduced even more markedly by doubling the waist, namely from $50.3\,\mathrm{K}$ for $w_{\mathrm{L}} = 5\,\mathrm{mm}$ to $23.1\,\mathrm{K}$ for $w_{\mathrm{L}} = 10\,\mathrm{mm}$ after $120\,\mathrm{ns}$ or from $39.3\,\mathrm{K}$ to $10.7\,\mathrm{K}$ after $200\,\mathrm{ns}$, respectively.

As suggested by the presented studies, it is recommended to optimise the laser power when changing the geometry of the setup (Ps and laser initial waists). In the following, except if specified differently, the simulations are run with the following optimised values for a laser waist $w_{\mathrm{L}} = 5\,\mathrm{mm}$: $\Gamma_{\mathrm{L}}/(2\pi) = 75\,\mathrm{GHz}$, $\delta = -2.5\,\mathrm{cm}^{-1}$ and $P = 2\,\mathrm{kW}$.

Limitations due to ceasing laser interaction

The limiting effect of atoms leaving the interaction regions by escaping the laser beam also becomes apparent in the case that cooling is interrupted due to a sudden absence of the laser field, for example at the end of the laser pulse. In order to investigate how the ceasing laser interaction, either gradually due to atoms moving out of the beam or abruptly due to sudden absence of the
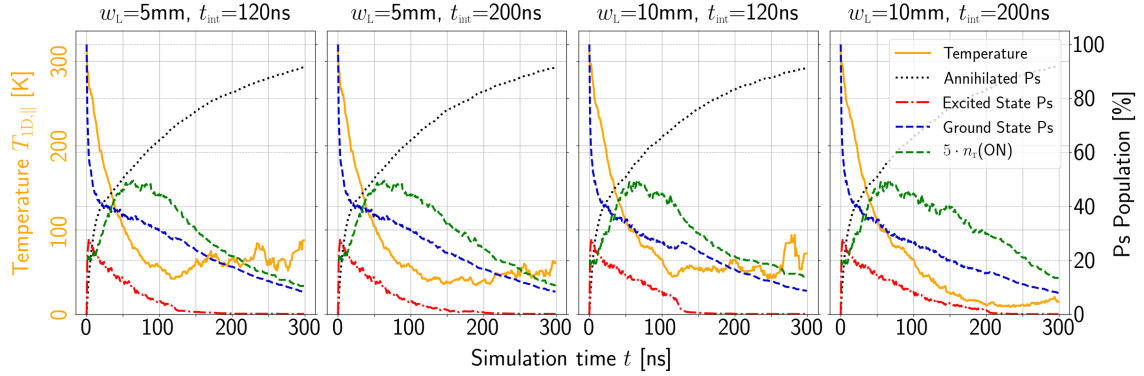
FIGURE 3.7: *Evolution of figures of merit of 1D longitudinal cooling in $B = 1\,\mathrm{T}$ for different configurations of ceasing laser interaction.*
Plot of the time evolution of the 1D-temperature T_{z} (orange), the number of slow atoms n_{r} (green) and the populations in the relevant state categories (with the usual colour code) for a simulation time of $300\,\mathrm{ns}$ for four different combinations of laser waist and pulse durations. The first two plots show the result for the standard set of laser parameters (i.e., especially with $w_{\mathrm{L}} = 5\,\mathrm{mm}$) where the laser stops after either $120\,\mathrm{ns}$ (first plot) or $200\,\mathrm{ns}$ (second case). The third and fourth subfigures contain the results for similar configurations ($120\,\mathrm{ns}$ in the third and $200\,\mathrm{ns}$ in the fourth plot) but a laser waist of $w_{\mathrm{L}} = 10\,\mathrm{mm}$.
A cloud of $N = 2000$ atoms and standard laser parameters have been used. For the simulation with $w_{\mathrm{L}} = 10\,\mathrm{mm}$ the power was increased to $P = 8\,\mathrm{kW}$.

laser field, affects the further development of the cooling parameters, the evolution of the cloud was simulated for a duration of $t = 300\,\mathrm{ns}$ and two different beam waists ($w_{\mathrm{L}} = 5\,\mathrm{mm}$ and $10\,\mathrm{mm}$ with $P = 2\,\mathrm{kW}$ and $8\,\mathrm{kW}$, respectively, to keep power densities constant) and with the laser stopping at either $120\,\mathrm{ns}$ or $200\,\mathrm{ns}$. The values of all remaining parameters are similar to the standard ones in the previous studies. Fig. 3.7 presents the numerical results for the four different configurations.

The results allow to draw a clear conclusion with respect to the effect of ceasing laser interaction. In all cases the temperature immediately stops declining further and in some configurations even starts rising again slightly. The way the remaining cooling parameters shown in Fig. 3.7 respond to the disappearance of laser interaction depends on whether it happens abruptly at the end of the pulse or rather gradually as is the case when the atoms move out of the beam. This is best reflected by the evolution of the population in excited states: As expected, the more abruptly the laser interaction stops, the more drastic are the changes in the number of excited atoms. This is illustrated in the third plot in Fig. 3.7 which shows the result of cooling using a laser beam with $w_{\mathrm{L}} = 10\,\mathrm{mm}$ and pulse durations of $120\,\mathrm{ns}$, is much shorter than the average time which the atoms spend within the interaction region. An atom with $\approx 50\,\mathrm{K}$, approximately the temperature after $120\,\mathrm{ns}$, has a thermal velocity of $v_{\mathrm{th}} = \sqrt{2k_{\mathrm{B}}T/(\pi m_{\mathrm{Ps}})} \approx 15.5\,\mathrm{km/s}$ and thus leaves the $10\,\mathrm{mm}$ broad beam, at the earliest, after more than $600\,\mathrm{ns}$. Even the fastest atoms do not leave the beam before the end of the pulse. In the configuration corresponding to the third plot cooling is thus completely limited by the laser pulse length. Consequently, the excited state population immediately drops to zero within few nanoseconds, the spontaneous decay time of the excited states. Similarly, but much less pronounced, this can be observed in the fourth case where the pulse lasts for $200\,\mathrm{ns}$. Here as well the excited state population, then already very low, falls to zero.

The situation is very different in the configurations with narrower laser beams (first and second plots). In these cases the excited state population shows three instead of only two regimes. In the first one, up to about $60\,\mathrm{ns}$, the cooling laser can still capture the whole cloud and the excited state population stays on a maximum level. At longer times, until the end of the pulse the fastest atoms start escaping from the interaction region, leading to an additional reduction in the number of excited atoms, in addition to the constant decrease due to annihilation. This can even be observed in the red curve, indicated by the very small drop at $\approx 60\,\mathrm{ns}$. Due to this gradual reduction in

laser-addressed atoms, the excited state population subsequently declines much faster than for broader beams and the effect of the ending laser pulse becomes hardly noticeable. For $w_\mathrm{L} = 5\,\mathrm{mm}$ cooling is thus completely limited by the restricted beam size and governed by gradual cessation of laser interaction instead of abrupt disappearance.

The changes in the number of excited atoms is in all cases accompanied and reflected by a corresponding change in the figures of merit for cooling: While the temperature stops declining further and even starts rising a bit again, once laser interaction stops, the evolution of the fraction n_r/N of cool atoms, additionally affected by annihilation, approaches the typical smooth exponential decrease. While this clearly sets in at the end of the laser pulse in the first and third configurations it becomes much less obvious for longer interaction times. An interesting observation is furthermore that the first three configurations result in equal final temperatures, within the statistical significance (cf. Sec. F.5.7 for a detailed analysis of the statistical significance of the simulation results). This demonstrates that longer interaction times do not bring any additional advantage if the beam is not broad enough to accommodate the whole cloud for the full pulse length. At the same time it suggests that the laser interaction can be stopped once the atoms start leaving the interaction area since then the figures of merit cannot be improved further.

In addition to revealing the limiting processes depending on the parameter configuration, Fig. 3.7 also presents the further evolution of the cloud, subsequent to laser interaction. In this regard the conclusion is clear as well: Depending on the respective purpose of cooling, that means either to reduce the overall temperature of the atomic cloud and/or to enhance the number of slow atoms, there exists a certain time after which the added value of cooling is lost. In general, cooling allows to increase n_r above the initial level for much longer than the actual cooling time, depending on the laser parameters. Subsequently, though, when it falls below this level, the effect of cooling is no longer reflected in n_r but only in the temperature. In case cooling represents a tool to create better experimental conditions for subsequent measurements where n_r plays a role, it is thus advisable to keep transfer times shorter than this threshold time.

Dependence of 1D cooling performance on the magnetic field strength

To study the influence of the magnetic field strength on the cooling performance, simulations were carried out where the B field value was scanned between 0 and 5 T. The laser parameters were not optimised anew for each B value. It was checked for a few of them, though, that if some precise numbers are affected, this did not change the overall outcome.

The results are shown in Fig. 3.8, which contains the 1D-temperature (T_z in orange) as well as the population in different state categories ($n = 1$ in dashed blue, $n = 2$ in dash-dotted red and the annihilation percentage in dotted black) and in the slow velocity range (n_r, in dashed green). The top part of Fig. 3.8 summarises the results at $t = 120\,\mathrm{ns}$ as a function of the magnetic field, scanned in steps of 0.03 T from 0 to 1 T and in steps of 0.1 T from 1 to 5 T. The bottom part of the figure features a zoom-in at three magnetic field values of interest: zero-field, low-field (0.3 T) and high field regions (1 T) corresponding to the Paschen-Back regime for $n = 2$.

The most interesting observation is the evolution of T_z at $t = 120\,\mathrm{ns}$ as a function of the magnetic field. Considering this figure of merit, cooling becomes completely futile for B between $\approx 0.1\,\mathrm{T}$ and $0.7\,\mathrm{T}$, where the final estimated temperature exceeds the initial 300 K. This rise results from the fast annihilation of laser-excited atoms that are mixed with short-lived states due to Zeeman and motional Stark mixing, so that only the non-excited faster atoms remain and contribute to the temperature calculation. However, it must be emphasised that the number of slow atoms (n_r) within the range of interest ($\pm\, 2v_\mathrm{rec}$) is even higher than for the no-laser case, even in the low-field region, thanks to the polarisation cycling with $\sigma^{(+)}$ polarisation, as discussed in Section 3.2.1.

In order to analyse the different results obtained here, the discussion shall first be focussed on the zero-field case for later comparison. For $B = 0\,\mathrm{T}$, it can be verified that a bit more than 25% of the atoms are excited to $n = 2$ in the first instants of interaction, which corresponds to
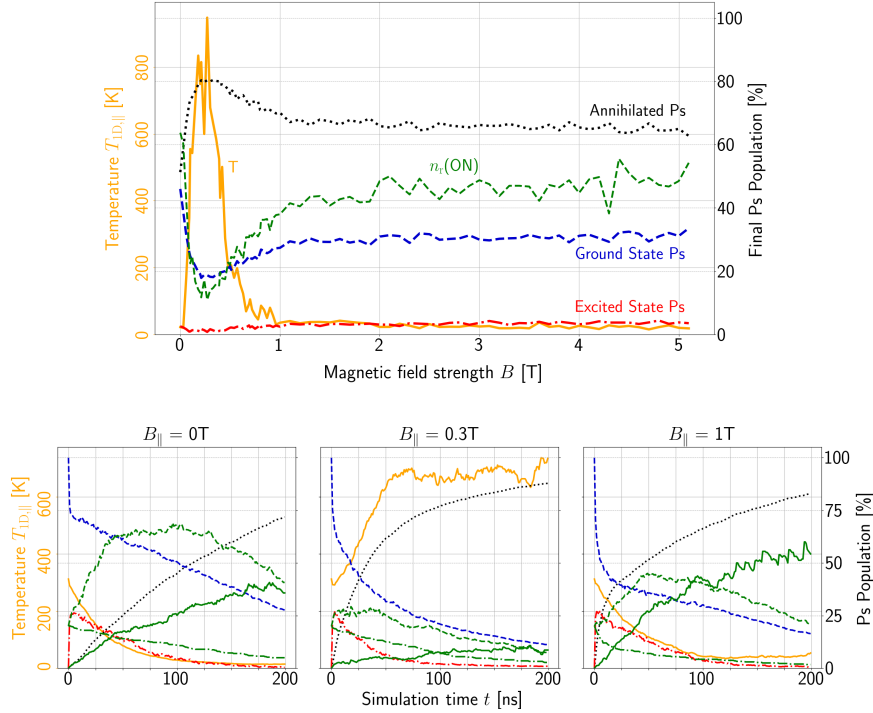
FIGURE 3.8: *Ps cooling efficiency versus magnetic field strength.*
Top: *Final 1D-temperature (left axis, T_z at $t = 120$ ns, orange) and final fraction of annihilated Ps (right axis, black, dotted) and the population in ground (blue, dashed) and excited (red, dash-dotted) states (right axis) at $t = 120$ ns. The green dashed line gives the value of n_r (scaled by a factor of five for visibility) at the end of the laser-Ps interaction.*
Bottom: *Time evolution of the 1D-temperature T_z and populations in the usual state categories for the three magnetic field strengths 0, 0.3 and 1 T. The green lines indicate the time evolution of $n_r^{(ON)}/N$ (dashed), $n_r^{(OFF)}/N$ (dash-dotted) and $S = [n_r^{(ON)} - n_r^{(OFF)}]/n_r^{(OFF)}$ (solid), all scaled by a factor of five. Same colour code as in Figure 3.2.*
A cloud of $N = 2000$ atoms and standard laser parameters were used.

the observed 25% drop in the ground state population. This drop is thus not due to any fast annihilation mechanism as in the non-zero magnetic field cases. Indeed, since the triplet and singlet states are not mixed by any external electromagnetic field, no enhancement of the annihilation takes place during the excitation process. At $t = 120$ ns, the 1D-temperature has dropped below 50 K, and the number of slow atoms has increased by more than a factor of three.

The situation is quite different for the low B-field regime. For $B = 0.3$ T, the annihilation is enhanced during the whole cooling interaction, consistent with the Zeeman effect mixing of short- and long-living states. A third of the initial population of the Ps cloud is initialised in the $m = 0$ ground state with mainly triplet character that is coupled to the (mainly singlet) $m = 0$ ground state with short lifetime. These atoms quickly annihilate and are responsible for the fast increase of the annihilation at the beginning of the simulation. As the strength of the magnetic field increases, the mixing between triplet and singlet $m = 0$ ground states becomes stronger, increasing the speed and the total amount of annihilation of Ps at the end of the laser interaction. As shown in the upper part of Fig. 3.8, once the Paschen-Back regime is reached for $n = 2$ ($B \gtrsim 1$ T), the total amount of annihilation at $t = 120$ ns does not vary with the magnetic field any longer.

Indeed, for $B = 1$ T and higher values of the magnetic field, a similar sudden initial annihilation jump is observed. In the same way as for lower values of B, this jump corresponds to the annihilation of the atoms initially in the $m = 0$ (mainly) triplet state, Zeeman-coupled to the $m = 0$ singlet state, and lasts until about $t = 10$ ns. At this point, all atoms initially in the $m = 0$ triplet state have been annihilated. As a result, the annihilation rate is much lower and comparable to what

is observed for $B = 0\,\mathrm{T}$. This is due to the decoupling between m_l and m_s states for the $n = 2$ levels. In this strong B-field regime, the laser interaction starting on $m = \pm 1$ ground states (which annihilate slowly) mainly keeps cycling on long-living states, decoupled from short-lived states.

As shown in Fig. 2.2, in the Paschen-Back regime, three state branches have developed in the $n = 2$ manifold due to the Zeeman effect. As suggested in Sec. B.5.3 with the appropriately detuned laser, cooling becomes much more efficient again. From these results it can be concluded that, even though the laser-Ps interaction increases the number of slow atoms (n_r) for all values of the magnetic field, laser cooling experiments should be carried out either in magnetic fields of $B \lesssim 0.05\,\mathrm{T}$ or environments of fairly high field strengths above $1\,\mathrm{T}$, if possible, in order to ensure laser interaction with high efficiency.

1D cooling performance for different spatial beam profiles

In order to examine how the cooling performance depends on the radial distribution of the energy density of the laser beam, the 1D longitudinal cooling scheme was simulated in the same standard laser parameter configuration for a tophat beam profile. An ideal tophat beam features a uniform energy density within its circular cross section. Compared to the common Gaussian beam profile it thus provides higher fluence in the fringes but reduced energy density in the central region.

Fig. 3.9 shows the simulation results for both beam shapes, for the Gaussian beam on the left and the tophat one on the right. The comparison of the two plots reveals that the difference in energy density directly manifests itself in the excited states population. Obviously, in case of the tophat profile, the reduction in the centre of the interaction region impairs the excitation process more than it is enhanced by increased laser power in the boundary zones. This can be explained by higher particle densities in the centre compared to regions further away. Especially at the beginning of the Ps-laser interaction, the cloud has not yet spread sufficiently far into the border areas of the interaction region as to profit from higher energy densities there. This has a lasting effect on the cooling parameters since it slows down the cooling process. The final temperature cannot be reduced to equally small values as for Gaussian beam profiles and the number of slow atoms n_r, and thus the signal S, generally does not reach equal values.

In order to ensure a maximum excitation rate right from the beginning, it is therefore preferable to use laser beams with spatial energy distributions equivalent to the particle densities. This implies that Gaussian beam profiles are advisable for initial times while it might be worth considering to switch to tophat profiles at later times, if technically feasible. The simulations presented in this thesis are all based on constant Gaussian beam shapes.

Dependence of cooling parameters on the initial temperature

Even though the Ps atoms are typically generated with a thermal energy around room temperature, it is of course possible for the cloud to show a lower temperature when the cooling process is initiated. For this reason, in the next step, cooling was studied for different initial temperatures. For this purpose the simulation was initialised in the usual configuration for 1D longitudinal cooling with standard parameters ($w_\mathrm{L} = 5\,\mathrm{mm}$, $\Gamma_\mathrm{L}/(2\pi) = 75\,\mathrm{GHz}$, $\delta = -2.5\,\mathrm{cm}^{-1}$, $P = 2\,\mathrm{kW}$ for 2000 atoms in a field of $1\,\mathrm{T}$) and run for different initial temperatures T_initial. The values were scanned in a descending way from the typical temperature of $300\,\mathrm{K}$ down to $10\,\mathrm{K}$ in steps of $25\,\mathrm{K}$ for higher initial temperatures and $5\,\mathrm{K}$ for smaller values.

The results of the scan are visualised in Fig. 3.10 for a cooling time of $120\,\mathrm{ns}$ (dashed curves) as well as $200\,\mathrm{ns}$ (solid curves). The plot on the left shows the final values for the 1D temperature and the populations in the usual colour code. The plot on the right contains the result for the fraction of slow atoms $n_\mathrm{r}^{(\mathrm{ON})}/N$ for the laser ON case as well as once more the temperature. With regard to the populations in the different state categories is concerned, it is observed that a change in the initial temperature does not significantly affect the results. As expected, the annihilations stay at a constant level within the statistical significance. The fraction of excited atoms, on the other hand, can be slightly enhanced if cooling is started at lower initial temperatures, albeit at the expense of the ground state population. This is simply due to the fact that with lower temperatures a higher
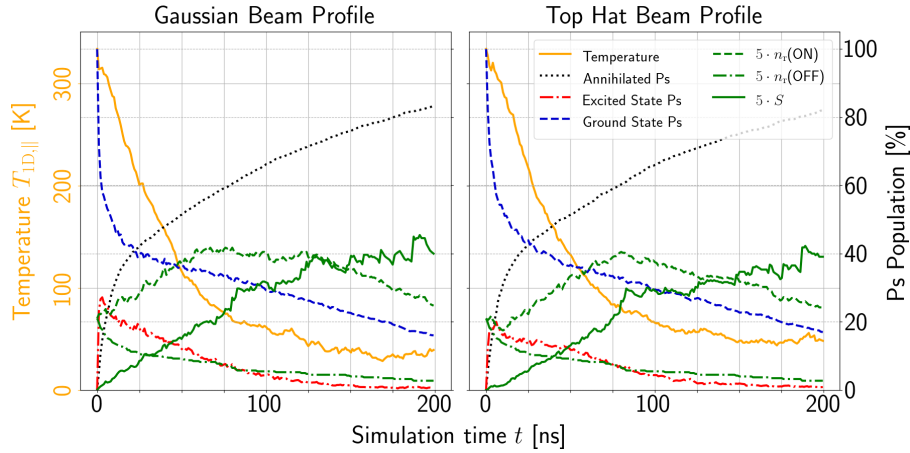
FIGURE 3.9: *Comparison of 1D longitudinal cooling in* $B = 1\,\mathrm{T}$ *with Gaussian beam profile to a tophat shape.* *Time evolution of the 1D-temperature* T_z *and populations in the usual state categories for a Gaussian beam profile (left) compared to tophat version on the right. The green lines indicate the time evolution of* $n_r^{(ON)}/N$ *(dashed),* $n_r^{(OFF)}/N$ *(dash-dotted) and* $S = [n_r^{(ON)} - n_r^{(OFF)}]/n_r^{(OFF)}$ *(solid), all scaled by a factor of five. Same colour code as in Figure 3.2. A cloud of* $N = 2000$ *atoms and standard laser parameters were used.*

fraction of atoms is initially located in the capture range of the laser (defined by the (constant) bandwidth and detuning) so that more atoms are excited. As expected, the ground and excited state populations are smaller the longer the cooling time (dashed curves compared to solid lines) due to continuous annihilation. The populations are reduced to a similar extent for all initial temperatures simulated.

As far as the two figures of merit for cooling, the final temperature (orange) and the number of slow atoms (green), are concerned, it can be noted that both parameters can be improved at lower initial temperatures. For the final temperature this reduction can of course partly be simply attributed to the fact that cooling has been launched at lower starting values. As the comparison to the dotted curve (bisector line of the coordinate system, showing the values of $T_{initial}$ on the T_{final}-axis) reveals, with the chosen laser parameters, cooling is in fact most efficient for moderate initial temperature values. In percentage terms the reduction in temperature by means of cooling is largest for $T_{initial}$ between $50\,\mathrm{K}$ and $100\,\mathrm{K}$. The results furthermore show that, over the whole range of initial temperatures, it is clearly not possible to cool the atoms down to the recoil limit, marked by the faint orange area in the left plot, with the standard laser parameters and within a cooling time of $200\,\mathrm{ns}$.

The most important result of this study, however, is, that the enhancement in the number of slow atoms $n_r^{(ON)}$ is mainly due to the fact that, at smaller temperatures, a larger fraction of atoms initially resides in the slow velocity range and that there exists a cooling-time-dependent threshold temperature (green numbers in the right plot) below which cooling does not enhance the fraction of slow atoms at all. To illustrate this, the right plot in Fig. 3.10 additionally presents the initial fraction of slow atoms (dotted green line) and, marked by coloured areas, the range of initial temperature values for which n_r can be increased by means of cooling. Obviously, the relative amount by which n_r can be increased is again highest for initial temperatures around $100\,\mathrm{K}$, for the used set of laser parameters. For values below $T_{initial} \approx 37\,\mathrm{K}$ ($\approx 16\,\mathrm{K}$), though, the final fraction of slow atoms after $200\,\mathrm{ns}$ ($120\,\mathrm{ns}$, respectively) of laser interaction no longer exceeds the initial fraction. Here the competing process of annihilation outweighs cooling, thus leading to a reduction in n_r. This implies that for such small initial values it is advisable to either skip cooling completely and directly proceed with the subsequent experiment step or to adjust the laser parameters. The latter might, however, become difficult to implement due to much lower required
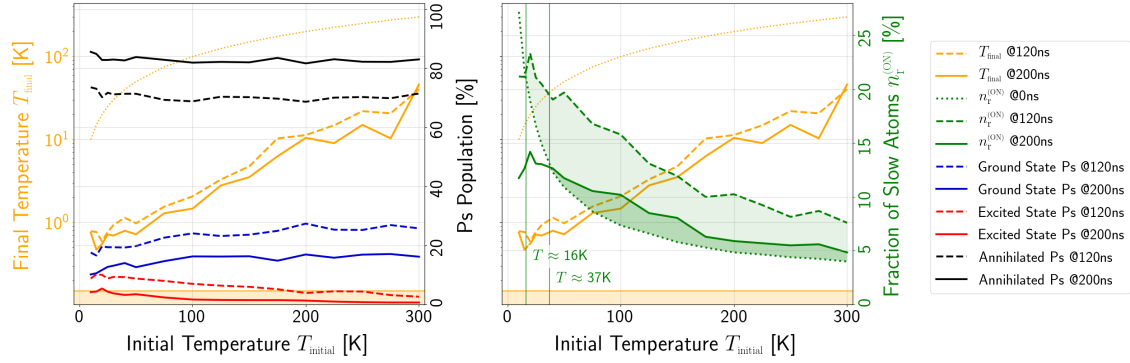
FIGURE 3.10: *Dependence of cooling parameters for 1D longitudinal cooling in* $B = 1\,\mathrm{T}$ *on the initial temperature* T_{initial}.
Final values of all relevant cooling parameters after $t = 120\,\mathrm{ns}$ *(all dashed lines) and* $t = 200\,\mathrm{ns}$ *cooling time (all solid lines) for different initial temperatures ranging from* $10\,\mathrm{K}$ *to the typical experimental Ps temperature of* $300\,\mathrm{K}$. T_{initial} *is scanned in steps of* $5\,\mathrm{K}$ *for small and* $25\,\mathrm{K}$ *for larger values, respectively. The curves are marked with the usual colour code.*
Left: *Final values for the 1D-temperature* T_{final} *(in orange on logarithmic scale; left axis), the number of annihilated atoms and the populations in ground as well as excited states (scaled by N; right axis). The faint orange area additionally indicates the sub-recoil temperature region (i.e., with* $T_{\mathrm{final}} < T_{\mathrm{rec}}$*) and the dotted line illustrates the values of* T_{initial} *plotted on the* T_{final}*-axis (i.e. the bisector line of the coordinate system), to evaluate the cooling effect.*
Right: *Evolution of the final fraction* $n_{\mathrm{r}}^{(\mathrm{ON})}/N$ *of slow atoms for the laser ON case (solid (after* $120\,\mathrm{ns}$ *cooling time) and dashed (after* $200\,\mathrm{ns}$*) green lines; right axis). The dotted green curve additionally specifies the initial values of* $n_{\mathrm{r}}^{(\mathrm{ON})}/N$*. The area coloured in faint green indicates the range of initial temperatures* T_{initial} *for which the the final fraction after* $120\,\mathrm{ns}$ *is larger than the initial one and the area coloured in dark green the same for the fraction after* $200\,\mathrm{ns}$ *of cooling time. The green vertical lines mark the threshold temperature (green values) below which the fraction* $n_{\mathrm{r}}^{(\mathrm{ON})}/N$ *is no longer increased by cooling.*
The plot again contains the evolution of T_{final} *and the region with* $T_{\mathrm{final}} < T_{\mathrm{rec}}$*, to be read on the left axis.*

bandwidths. At the same time this result suggests that 1D cooling can be stopped once these threshold temperatures are reached below which cooling will not enhance $n_{\mathrm{r}}^{(\mathrm{ON})}$ any further.

In order to investigate the effectiveness of cooling in this range of initial temperatures, simulations were performed for $T_{\mathrm{initial}} = 4\,\mathrm{K}, 6\,\mathrm{K}, 8\,\mathrm{K}$ and $10\,\mathrm{K}$ with adjusted laser parameters, namely a bandwidth of $\Gamma_{\mathrm{L}}/(2\pi) = 15\,\mathrm{GHz}$, a correspondingly reduced detuning of $\delta = -0.5\,\mathrm{cm}^{-1}$ but unchanged power $P = 2\,\mathrm{kW}$. The results reveal that this adjustment of laser parameters allows to further reduce the temperature, even close to the recoil limit for an initial temperature of $4\,\mathrm{K}$. It does still not yield an enhancement of the number of slow atoms $n_{\mathrm{r}}^{(\mathrm{ON})}$. Cooling in this range of initial temperatures is thus only worthwhile to reduce the temperature, but not to increase the number of cool atoms. In other words, in this scenario cooling goes at the expense of the number of atoms.

3.2.2 2D and 3D cases

In the next step 2D and 3D Ps laser cooling schemes were considered, starting with a 3D configuration with lasers irradiating a 3D isotropically expanding Ps cloud from all three spatial directions, for different magnetic field strengths. This allows to draw general conclusions on the feasibility of 3D laser cooling.

The 3D expanding cloud is in all cases initialised at a temperature of $300\,\mathrm{K}$ and the counter-propagating laser beams always have the standard left-/right-handed circular polarisation. Each beam has a power of $2\,\mathrm{kW}$. As the main figure of merit for 3D-cooling the effective 3D-temperature T_{3D} is used, which is the rms-value of the three individual 1D-temperatures T_{x}, T_{y} and T_{z}. For
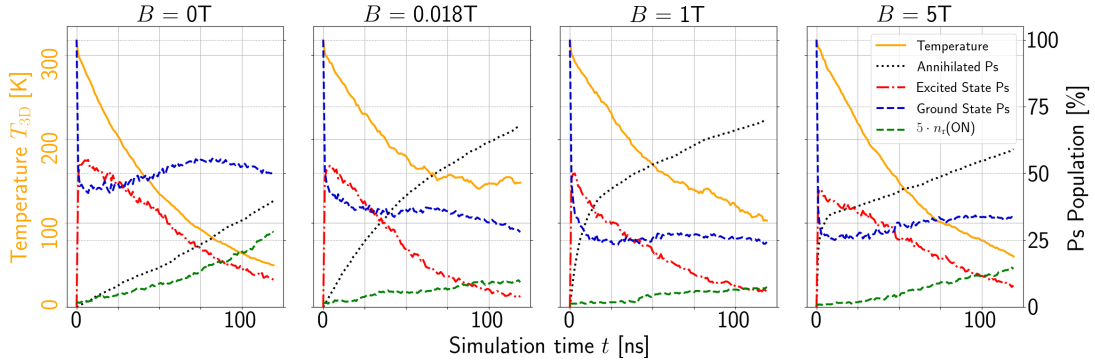
FIGURE 3.11: ***3D-cooling in different magnetic fields.***
Left axis: *Evolution of T_{3D} (orange, solid line).* ***Right axis:*** *Evolution of the fraction of annihilated Ps atoms (black, dotted), the fraction of Ps atoms in the $n = 1$ ground state (blue, dashed) and the $n = 2$ excited state (red, dash-dotted), normalised by N (the initial number of atoms) for four different magnetic field strengths 0, 0.018, 1 and 5 T. The green dashed line represents $n_{r,3D}^{(ON)}/N$, scaled by a factor of five.*
The plots are based on the results of simulations for a cloud of 2000 Ps atoms initialised at 300 K and isotropically expanding in all three spatial directions in a static magnetic field $\mathbf{B}$. The cloud is cooled by three pairs of left-/right-handed circularly polarised counter-propagating beams along x, y and z, each beam with a power of 2 kW, 75 GHz bandwidth and detuned by -2.5 cm^{-1}.

2D-cooling, the according 2D-temperature T_{2D} is used, which is the rms value of the two individual 1D-temperatures T_x and T_y. In analogy to $n_r^{(ON)}$ for 1D schemes, it is expedient to introduce $n_{r,3D}^{(ON)}$ for 3D-cooling, defined as the number of atoms with velocity

$$\sqrt{v_x^2 + v_y^2 + v_z^2} \leq 16 \times v_{rec}$$

and $n_{r,2D}^{(ON)}$ for 2D-cooling, defined as the number of atoms with velocity

$$\sqrt{v_x^2 + v_y^2} \leq 8 \times v_{rec} \ .$$

The coefficients 16 and 8 in the definition of $n_{r,3D}^{(ON)}$ and $n_{r,2D}^{(ON)}$ are arbitrary and were chosen to ensure that enough atoms contribute to the calculation of n_r in each case.

Laser cooling in 3D

To investigate the influence of the magnetic field on the 3D-cooling performance, laser cooling of the Ps cloud was simulated for four values of the B field (0 T, 0.018 T, 1 T and 5 T) in the previously identified favourable regions. Fig. 3.11 gives an overview of the corresponding results.

All laser beams have the same standard optimised set of parameters as for 1D-cooling. The population in the excited state quickly becomes nearly equal to or slightly higher than the population in the ground state for all values of the magnetic field, confirming that the saturation regime is reached. Furthermore, the same enhanced annihilation process is noticed for the non-zero magnetic field cases as in the previous 1D-studies. Indeed, shortly after $t \approx 1$ ns, half of the initial number of Ps atoms is in the excited state for $B = 0$ T and only a third of N is excited for $B = 5$ T. This is consistent with fast annihilation of the $m = 0$ triplet ground state in a strong magnetic field due to the Zeeman effect. In all cases, the population in the ground state stays almost constant over time. This means that spontaneous emission from the excited states tends to compensate the losses due to annihilation and re-excitation. As a result, the population in the excited states decreases at the same rate as annihilation in the ground state increases.

For $B = 0\,\text{T}$, the annihilation rate is lower during 3D-cooling compared to 1D-cooling, which is consistent with the idea that the average lifetime of Ps increases when more atoms are excited to $n = 2$ ("infinite" lifetime for the excited states compared to $n = 1$ levels), as explained before in Sec. 2.4.3. As mentioned in Section 3.1.2, this is valid only under the condition that the excitation does not populate mixed states that could decay towards the $n = 1$, $m = 0$ states with shorter lifetimes. In the zero-magnetic field case, this is ensured at all times because the laser interaction occurs only between triplet states. $B = 0.018\,\text{T}$ is an intermediate situation where the $m = 0$ triplet ground state does not annihilate instantaneously at $t = 0\,\text{ns}$ but still annihilates faster than the $m = \pm 1$ states which breaks the *stationary* regime observed for the other values of magnetic field presented in Fig. 3.11.

Conversely, and as seen also in the 1D case studies, in the high field regime, the decoupling of m_s and m_l allows to separate three branches of states (see Fig. 2.2). However, this regime is reached for a higher magnetic field in $n = 1$ compared to the excited level. Therefore, the ground $m = 0$ states (triplet-singlet superposition) are still mixed even for 5 T, and a fast initial annihilation of all the atoms in the $m = 0$ ground state is observed during the first few nanoseconds. After this initial (almost) instantaneous annihilation of the atoms in the $m = 0$ ground state, the annihilation rate becomes smaller again, consistent with the $B = 0\,\text{T}$ annihilation rate of the atoms in the $m = \pm 1$ ground states. It can furthermore be observed that the total amount of annihilated atoms is higher in the 0.018 T and 1 T cases compared to the 5 T one. By selecting the proper detuning of the laser, one can cycle only on long-lived states, avoiding the states mixed by the Zeeman effect that would decay towards the $m = 0$ ground states. The Zeeman effect at 1 T and higher is strong enough to reach the Paschen-Back regime for the $n = 2$ states, where three branches of states of different lifetimes are split in energy (see Fig. 2.2). The further separated these branches are in energy, the easier it is to tune the laser frequency such that the resonant transitions excite only long-lived states. Therefore, the 5 T case again seems to be more favourable than the other intermediate field strength configurations. Fig. 3.11 also shows that both T_{3D} and $n_{r,3D}^{(ON)}$ have better values for $B = 0\,\text{T}$ and 5 T than for the intermediate values of magnetic field.

For these two extreme cases, the final temperature of the cloud can reach below 100 K and the number of slow atoms ($n_{r,3D}^{(ON)}$) can increase by at least a factor of six in 0 T and by a factor of two in 5 T, for a 100 ns laser interaction time. In contrast, for the experimentally more typical magnetic field values of 0.018 T and for 1 T [96, 97, 102], the temperature can merely be reduced to 150 K.

Finally, a comparison between T_z for 1D longitudinal cooling and T_{3D} suggests that 3D-cooling is less efficient than 1D-cooling in both 0 T and 5 T. While temperatures of almost 40 K can be reached for 1D longitudinal cooling in 5 T, the minimal 3D-temperature merely drops below 100 K. This is simply due to the fact that in 3D three times more events are required to scatter the same amount of photons per axis than in 1D.

In magnetic fields a different evolution might also be due to the fact that cooling in 3D consists of a superposition of different 1D cooling configurations, comprising both longitudinal and transverse schemes. As described in detail in Sec. 2.4.3, in transverse schemes the cooling performance is modified in the course of the interaction due to the influence of the motional Stark effect. If the interaction with the laser beam and concomitant transfer of momentum moves the atom to another range of the velocity distribution, it experiences the Stark effect in a modified way. This can only be observed in 3D since 1D cooling schemes have been restricted to longitudinal configurations as the study of different rotations is prohibited due to the phase loss issue induced by the rate equations (cf. Sec. F.5.6). However, the motional Stark effect affects the cooling only marginally since the simulation results reveal that only a very small fraction of atoms is transferred to the metastable state 2^3S in the course of the interaction, which is a convenient criterion to assess the influence of the Stark effect (cf. Sections 2.4.3 and 3.1.2).

Varying the laser parameters in the 3D simulations for optimisation reveals that for best cooling results in terms of final 3D temperature, it is advisable to choose the same bandwidth and detuning values as in 1D. As far as the laser power is concerned, slightly higher values than in 1D are recommended. To summarise these studies, when choosing an external environment, it is preferable

to ensure performing 3D laser cooling either in a zero-magnetic field region, or in a high magnetic field region to reach the Paschen-Back regime for $n = 2$.

2D and 3D beam experiments

For 2D transverse cooling and transverse cooling of a moving molasses, the Ps ensemble is modelled as an effusive beam formed after positron implantation into a nano-channelled silicon Ps-reflection target [103]. Once thermalised inside the target, the Ps atoms have a 3D isotropic Maxwellian distribution

$$f(v) = \left(\frac{m_{\mathrm{Ps}}}{2\pi k_{\mathrm{B}}T} \right)^{3/2} 4\pi v^2 \, \exp\left(-\frac{m_{\mathrm{Ps}}v^2}{2k_{\mathrm{B}}T} \right) \; . \tag{3.11}$$

Thus, during the time interval $\mathrm{d}t$, the number of Ps atoms ejected from the target under an angle θ with respect to the normal of the target, i.e., in the conical solid angle $\mathrm{d}\Omega = \sin(\theta) \, \mathrm{d}\theta \, \mathrm{d}\phi$ (in spherical coordinates) and with a velocity $\|v\|$ between v and $v + \mathrm{d}v$, is proportional to $f(v) \, v \cos(\theta) \, \mathrm{d}t \, \mathrm{d}\Omega \, \mathrm{d}v$. Such a distribution is created by means of the inverse transform sampling (Smirnov inverse probability integral transform). In real experiments, the thermalisation and ejection processes produce a time spread of about ten nanoseconds. However, for simplicity, here the effusive beam is modelled as an area of $(0.1 \times 2 \times 2) \, \mathrm{mm}^3$ representing the typical $2 \, \mathrm{mm}$ spot from which Ps atoms are emitted. Thus, creating all Ps atoms at time $t = 0$, but in a spatial slab of $0.1 \, \mathrm{mm}$ parallel to the target mimics the proper time distribution.

The cooling process of a beam, which is intrinsically a phase space density enhancement, is quantified by means of a (4D) reduced beam brightness B_{r}, i.e., the total current I (here the number of Ps per second emitted by the target) divided by the beam area, by the solid angle divergence and by the beam kinetic energy $\frac{1}{2}mv_{\mathrm{z}}^2$. It is thus given by

$$B_{\mathrm{r}} = \frac{I}{8\pi^2 \sigma_{\mathrm{x}} \sigma_{\mathrm{y}} k_{\mathrm{B}} \sqrt{T_{\mathrm{x}}T_{\mathrm{y}}}} \; , \tag{3.12}$$

where σ_{x} and σ_{y} are the rms widths of the beam in the x and y direction, respectively [104]. B_{r} is an invariant along the beam path for any Hamiltonian force field and, thus, only true cooling (neither filtering nor slowing) can increase it [104–108]. Consistently with the definition of the temperature parameter, only the particles from the second and third quartiles of the distribution are taken into account to evaluate σ_{x} and σ_{y} in the calculation of B_{r}.

2D transverse cooling in 1 T

Next, 2D laser cooling of the effusive beam in a field of $1 \, \mathrm{T}$ aligned parallel to the Ps propagation direction z was investigated. The laser configuration consists of two pairs of counter-propagating beams in the transverse $(x\text{-}y)$-plane with standard circular polarisation. The main goal of such an experiment is to reduce the solid angle of the Ps beam by means of laser cooling. The simulation results show that cooling is optimised again for similar laser parameters as for 1D-cooling.

The sketch on the left in Fig. 3.12 illustrates the setup. The results of the simulation are plotted on the right part of the figure, featuring the evolution of the temperature parameter T_{2D} (the rms value of T_{x} and T_{y}) and the population in selected state categories.

Compared to 3D-cooling in $1 \, \mathrm{T}$, there are about 5% fewer atoms in excited states and the annihilation curves are almost identical, consistent with a negligible decrease of the average lifetime of the Ps atoms due to this 5% difference in excited state population. The results validate a successful collimation of the Ps beam thanks to 2D transverse laser cooling. T_{2D} can be reduced to $70 \, \mathrm{K}$ and $n_{\mathrm{r,2D}}^{(\mathrm{ON})}$ is multiplied by a factor of ten over the course of $120 \, \mathrm{ns}$. Finally, the brightness is increased by a factor of seven at $t = 120 \, \mathrm{ns}$.

3D moving molasses cooling

For the 3D-cooling of the effusive Ps beam, emitted by a reflective positron converter target, in a kind of moving molasses configuration as sketched in Fig. 3.13, the three components of the velocity
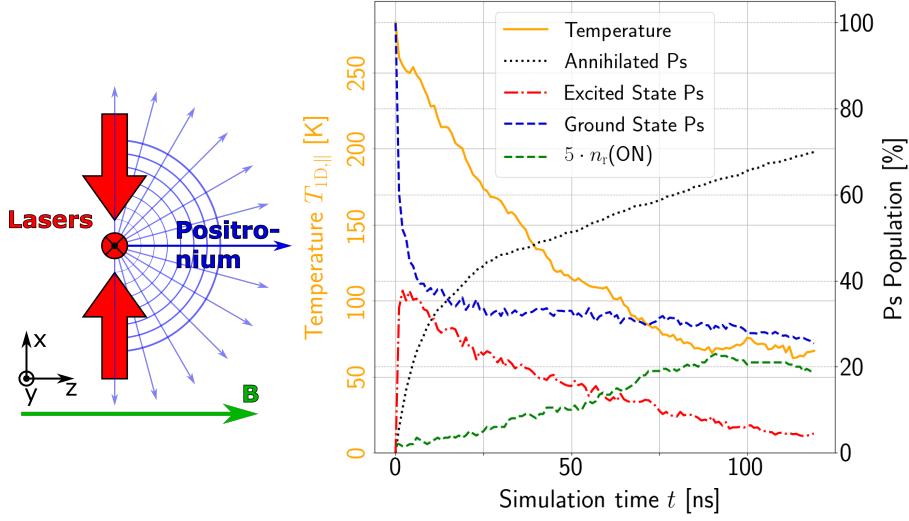
FIGURE 3.12: *2D transverse cooling in* 1 T.
*The sketch on the left illustrates the experimental setup including the magnetic field **B** (green arrow) along z, two pairs of counter-propagating laser beams along x and y (red arrows) and Ps emission (blue) as an effusive beam along z originating from a 2 mm spot.*
The plot on the right shows the time evolution of the populations, T_{2D} and $n_{r,2D}^{(ON)}/N$. Same colour code as in Fig. 3.2.

must be controlled to produce a monochromatic beam that can be sent to another experimental chamber for interferometric measurements, for instance. Therefore, these studies were carried out in an environment with very low (negligible, but non-zero to impose a quantisation axis) magnetic field. In real experiments, such small fields would result in a large positron implantation area, typically of the order of 2 mm. In addition to the reduction of the transverse angular spread, this scheme was aimed at focussing the distribution along the propagation direction z to a well-defined mean velocity v_{mean}.

In this setup, the lasers are not sent directly onto the target to prevent damage to it. Thus, in order to accommodate a target of 2 mm length, the target is offset by 8 mm along the z-axis (see Fig. 3.13) while keeping all laser beams aligned onto the origin. The previous configuration of two transverse pairs of counter-propagating laser beams is replaced by a set of three pairs of counter-propagating laser beams. One pair lies still purely in the transverse plane (pointing along y) while the other two form a cross in the (x-z)-plane, which also contains the Ps propagation direction. These two beams are tilted by 45° with respect to the Ps beam. A value of $v_{\mathrm{mean}} = 60$ km/s is chosen as the target mean velocity, which is well in the range of the thermal velocity distribution at 300 K. Thus, for each pair of counter-propagating beams in the (x-z)-plane the detuning values of the two counter-propagating beams have to differ by

$$\pm \frac{1}{\sqrt{2}} \frac{v_{\mathrm{mean}}}{c} E_0 \;=\; \pm 5.82\,\mathrm{cm}^{-1}$$

from resonance (E_0), in addition to the detuning δ required for 3D-cooling.

Fig. 3.13 shows the evolution of the distributions of velocity components both in transverse (middle) and axial direction (right) at four equidistant time steps. Since it takes almost 130 ns for the emitted Ps to reach the crossing point with the laser beams, the evolution of the cooling process is simulated for the time span of 330 ns during which the lasers are constantly on and shining light along the three spatial directions.

The process efficiency is highest for the same bandwidth of 75 GHz, coinciding with the width of the Doppler distribution. However, as far as the detuning and the power are concerned, the results differ from all previous settings. Instead of $\delta = -2.5\,\mathrm{cm}^{-1}$ and $P = 2$ kW, the atoms are
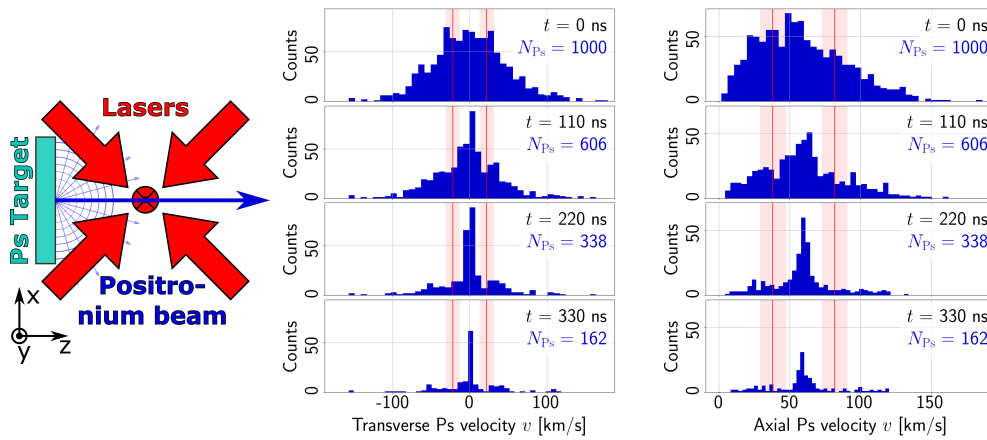
FIGURE 3.13: *3D moving molasses cooling in zero-field.*
As shown in the sketch on the left, six crossed laser beams from all spatial directions, with the ones in the (x-z)-plane tilted by 45°, address the effusive Ps beam, generated by a reflective Ps formation target and offset by 8 mm with respect to the laser crossing point. The evolution of the transverse (respectively axial) velocity component distribution is presented in the middle and right, respectively.

collimated best around the target mean velocity for the slightly higher values of $-3.0\,\mathrm{cm}^{-1}$ and $5\,\mathrm{kW}$.

The distributions of both the transverse and the axial velocity components confirm that the two goals of this application can be reached. The width of the initial distribution in the transverse direction and thus the velocity dispersion is clearly reduced during the $330\,\mathrm{ns}$ of laser-Ps interaction, implying an efficient collimation of the Ps cloud along the direction of propagation of interest (longitudinal axis). This is also reflected by the final transverse 2D-temperature (rms value of T_x and T_y) $T_\mathrm{2D} = 10.5\,\mathrm{K}$.

In the axial direction, the width of the distribution is narrowed and centred around the desired velocity of $60\,\mathrm{km/s}$. The rather high cooling efficiency compared to the previous application is, to a large extent, due to the fact that this 3D-cooling of the effusive beam in the moving molasses scheme is carried out in an almost zero-field environment. This implies that the level structure is influenced neither by Zeeman nor by motional Stark effects. Such a mono-energetic beam with well-defined axial mean velocity and better collimation due to reduced angular spread, could subsequently be subject to well-defined time-of-flight or optical grating experiments as well as interferometry. Finally, the formation of antihydrogen via charge exchange between Rydberg Ps and antiprotons would definitely benefit as well from such an improved velocity distribution.

Chapter 4

Experimental realisation of Ps laser cooling in a magnetic field

4.1 Concepts of an experimental implementation of Ps laser cooling

4.1.1 General considerations

The key difference between all numerical and experimental studies is the step of data acquisition. In simulations processes are computed based on given parameters, finally generating output data. In experiments, on the other hand, data acquisition includes a number of additional steps which require much more efforts than for numerical studies.

Hence, the most important aspect in designing an experimental measurement scheme is the question of the most appropriate observables, i.e., physical measurands, suitable for a given problem. From the previous chapter it becomes clear that, in case of positronium laser cooling, the key indicator that all analyses are based on is the momentary velocity distribution of non-annihilated Ps atoms at a given time. To obtain similar data in experiments one must therefore measure the number of non-annihilated atoms at a time t, resolved by their velocities in the direction of the cooling radiation.

Observable for Ps laser cooling

It goes without saying that, experimentally, this quantity is not as easy to access as numerically, but rather requires a sophisticated measurement scheme based on the most expedient observable from which the velocity spectrum can finally be deduced. In case of positronium, the easiest way to gain information on the number of non-annihilated atoms is to measure its counterpart, which is the number of annihilated atoms within a certain time interval. This is achieved by integrating the time-resolved signal of a detector which captures the gamma rays that originate from Ps annihilation, as will be explained in the following section.

However, since the initial number of Ps atoms emitted by the converter target (cf. Sec. 2.1.1) is unknown and furthermore differs from one experiment run to the other, it is impossible to deduce absolute Ps numbers from the detector signal. For this reason, it is finally the difference between numbers of annihilated atoms or, more specifically, the difference between the detector signals for different experimental configurations which allows to draw conclusions with regard to certain processes or the effect of parameter changes. This differential quantity is commonly referred to as *signal*, labelled by S and specified in percent.

Positronium detection method

The meaning of the S parameter and how it differs from the "detector signal" itself can best be explained on the basis of a typical plot of an arbitrary measurement run which is shown in Fig. 4.1. The plotted curves are based on data that stems from a $PbWO_4$ scintillation detector (cf. Sec. 4.2.2 for more technical details), which records the amount of incoming gamma rays resulting from annihilation decay of positrons over time. Naturally, the detector is also sensitive to the decay of positronium atoms, since Ps annihilation is nothing else than regular positron annihilation, with

FIGURE 4.1: *Exemple SSPALS spectra.*
The grey line represents a Ps-free background measurement, based only on e$^+$-decay. The black and red lines show the detector signal for experiments after Ps formation and with lasers turned on (red) or off (black). The dashed vertical line in red indicates the time at which the laser irradiates the Ps cloud in this example. The time axis has been shifted to the point of maximum annihilation.
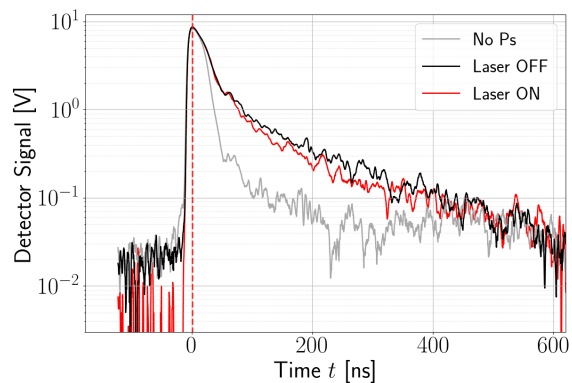
the only difference that it is the bound-state electron instead of a free e$^-$ which participates in the decay.

This technique of detecting e$^+$ decay is known as single-shot positron annihilation lifetime spectroscopy (SSPALS). It is a well-established tool that is employed in many experiments using positrons or positronium. The SSPALS scheme is a universal tool since it is capable of revealing the effect of the modification of any experimental parameter as long as it can be encoded in the positrons' annihilation behaviour (which, in fact, is sometimes not trivial). All details about this detection method can be found in Ref. [109] in which it is exhaustively described by its inventors.

In Fig. 4.1 SSPALS spectra (i.e., the "detector signals") for three different experimental configurations are shown. While the grey line shows a measurement run in which no Ps atoms were produced, the other two curves represent measurements in which Ps was formed in advance. The difference between the data for the black and red curves lies in the presence of laser light in the respective measurement. In the experiment represented by the red curve, the Ps atoms were irradiated by two lasers with 205 nm and 1064 nm (the reason for the choice of exactly these two wavelengths will become clear later and should be taken for granted for the time being), whereas for the measurement plotted in black the laser was turned off. All other parameters, besides the presence of laser light, were kept unchanged.

With this information, it is easy to understand the shape of the curves. In all three configurations positrons enter the chamber in which the detector is located a few nanoseconds prior to zero time, which was arbitrarily set to the time at which the signal reaches its maximum value. Three characteristic regions can be identified: In the first one, up to about $t \approx -10$ ns, the detector signal shows only noise since no particles are available yet to decay. The following prompt peak in the interval around $t = 0$ ns originates, in the absence of Ps formation, from annihilation of the positron bunch on the chamber walls and, in the other two cases, from the annihilation of para-Ps atoms. In the third regime, subsequent to this peak, the signal quickly drops to the noise level again if no Ps were formed initially. Otherwise it continues to show a slowly decreasing annihilation signal, which results solely from ortho-Ps atoms with a much longer lifetimes of 142 ns. The SSPALS detection method owes its name to the fact that the appearance of the spectra is a direct indication of the lifetime of the measured particles. The lifetime of the ortho-Ps can, for example, be directly extracted from the slope of the corresponding curves.

The meaning of the previously introduced signal S of a measurement (or, in short[20] , S%), can now easily be explained on the basis of this exemplary SSPALS signal: As mentioned, since the detection method is based on annihilation, the effect of parameter modifications on the Ps atoms can only be studied by designing the measurement scheme such that the parameter modification manifests itself in a changing annihilation behaviour. Since additionally, absolute Ps numbers cannot be measured, it is the difference between the detector signals which serves as final indicator.

---

[20] It is important to point out that S is only labelled in conjunction with a % symbol, i.e. as S%, if it relates to the signal value in percent or in free text or axes labels, if applicable. It is not used explicitly in equations where S does not represent a percentage value.
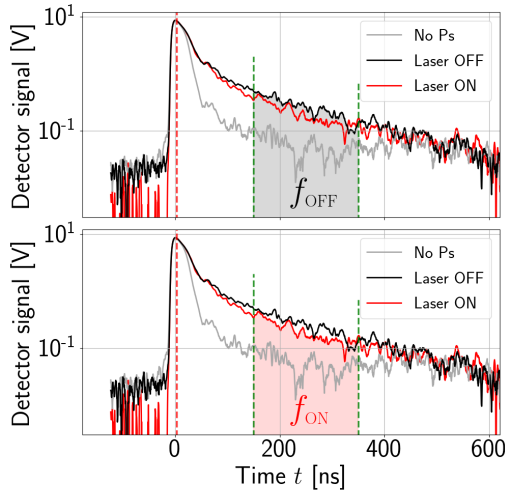
FIGURE 4.2: *Illustration of the calculation of $S\%$.*

Based on Fig. 4.1, the two plots visualise the areas f_{OFF} (black area in the upper plot) and f_{ON} (red area in the lower plot) under the SSPALS spectra of the laser off and on measurements, respectively, which are used for the evaluation of the signal S (cf. Eq. (4.1)). In this case, it is the interval between $150\,\mathrm{ns}$ and $350\,\mathrm{ns}$, with respect to the prompt annihilation peak, which was used.

In order to measure the effect of cooling on the velocity distribution via SSPALS, it is clear that in this case it is the presence of laser interaction at $243\,\mathrm{nm}$ which potentially creates this difference in the experiment configurations. In practice, this requires a comparison of the detector signals for the measurements with ("Laser ON" in the figure) and without ("Laser OFF") laser interaction.

In order to quantify these changes in the SSPALS signal, the experimental S parameter is defined as the absolute value of the reduction in detector signal due to the presence of laser interaction with respect to the laser OFF-signal. It is calculated according to

$$S = \frac{f_{\mathrm{OFF}} - f_{\mathrm{ON}}}{f_{\mathrm{OFF}}} \ , \tag{4.1}$$

where f denotes the area under the SSPALS spectrum within a defined time interval. The subscripts "ON/OFF" specify the state of the laser. Due to the fact that differences in the detector signal are generally not pronounced enough to stand out of the prompt peak, they become apparent only in the long tail beginning at $t \approx 50\,\mathrm{ns}$ after the peak. For this reason, f is usually calculated from the integration of the signal over a time interval of about $\Delta t = (150 - 200)\,\mathrm{ns}$ length in the long tail. In order to avoid the inclusion of secondary e^+ peaks in the area under the curve and to furthermore exclude annihilation events caused by Ps collisions with the chamber walls that begin to appear in the signal at later times, the interval is typically chosen from the time window between $150\,\mathrm{ns}$ to $600\,\mathrm{ns}$. To ensure an adequate signal-to-noise ratio, the interval should not reach too far towards the end of the long annihilation tail.

The method of the calculation of $S\%$ is illustrated in Fig. 4.2. Here, the interval for the calcuation of f is indicated by the two vertical dashed lines in green which delimit the arbitrarily chosen range from $150\,\mathrm{ns}$ to $350\,\mathrm{ns}$. The black area under the laser OFF curve (upper plot) then represents f_{OFF} whereas the red one in the lower plot represents f_{ON}. For the Ps laser cooling measurements the interval between $450\,\mathrm{ns}$ to $600\,\mathrm{ns}$ has proven to be the best choice, i.e., to yield maximum signals.

It is worth pointing out that the definition of S for the numerical studies (cf. Eq. (3.9)) shows an (intentional) similarity with the definition of the experimental $S\%$ parameter. However, while in the simulations S is calculated from the number of slow atoms in the centre of the distribution and thus quantifies the gain in cold atoms, in the experimental measurements it is, for reasons of detection, based on the inverse, i.e., the number of annihilated atoms and thus represents the laser-induced enhancement in Ps decay. It should, however, also be noted, that, in the numerical studies, S is a parameter introduced to quantitatively evaluate the efficiency of laser cooling and therefore only accounts for slow atoms, whereas in the experiment it is the key parameter for probing and evaluating the *entire* population distribution by detecting changes in the Ps annihilation behaviour.

In addition, there are still a few considerations that need to be addressed with regard to the measurement of laser cooling by means of SSPALS:

1. First of all, it is still not clear how the presence of laser interaction can be encoded in changes in the number of annihilated atoms and thus be made observable in the SSPALS signal or $S\%$, respectively. This question can only be answered in consideration of the experimental laser scheme and will therefore be explained in the following chapter.

2. Based on the answer to the first question it is, in the next step, necessary to find a way to resolve the different velocity classes of the distribution by reliably attributing the signal to the atoms belonging to individual velocity bands. Since it is of course not possible to prevent atoms from other velocity intervals from annihilating, this can only be realised by subjecting the atoms from the selected band to a special treatment. Since, in the present case of Ps laser cooling, the most expedient method to this end relies on a second laser-excitation scheme, the issue of velocity selection only becomes clear in the context of the laser scheme.

3. The last open question is how the velocity-dependent signal S can finally be used for the verification of laser cooling. This can, however, only be addressed after defining what laser cooling actually signifies in experimental terms.

Definition of *laser cooling* in experimental terms

As shown by the numerical studies, the effect of laser interaction generally manifests itself in a modification of the velocity distribution, where laser cooling in particular leads to a narrowing of the distribution. There are thus several figures of merit conceivable for an experimental verification of successful laser cooling. The most obvious one is of course to probe (i.e., measure) the whole Doppler profile, called "Doppler scan", via SSPALS in a velocity-selective way for the two cases with and without cooling laser. With regard to a cooling effect it is, however, not sufficient to only show a single collective recoil effect, i.e., an alteration of the distribution in only one velocity range. This is due to the fact that a modification in a single velocity range merely demonstrates the successful exertion of an optical force, but not necessarily a narrowing of the distribution. Narrowing can only be achieved by means of a pair of counter-propagating laser beams, whereas exertion of an optical force that leads to a single modification in the distribution can in fact already be produced by interaction with a single beam. Successful laser cooling can thus only be claimed in case of a symmetrical modification of the distribution. In other words, laser cooling can only be demonstrated by proving that the width of the distribution was reduced with a sufficient degree of statistical significance.

The results of the simulations also show that in case of laser cooling it is possible to take advantage of a second feature besides the mere narrowing of the distribution. Obviously, laser cooling always leads to an enhancement of the population in resonance (cf. Fig. 3.5 for instance). In line with the above conclusion, it must, however, be mentioned that the detection of only this feature is no sufficient proof of laser cooling as it could, in principle, result from an interaction with only a single laser beam. It can thus be concluded that, independent by of the finally pursued measurement strategy, all experimental schemes for demonstrating laser cooling must essentially be capable of resolving the velocity of the atoms in the cloud, specifically its component along the laser propagation direction, along which the atoms are cooled.

4.1.2 Laser scheme for Ps cooling

Possible Probing Schemes

To experimentally probe the velocity distribution of the Ps atoms in the cloud, it is necessary, contrary to the scheme used for the numerical studies, necessary to add a second laser system in addition to the cooling laser at 243 nm. In order to understand the reason for this, it is worth to briefly recall the basic idea behind probing. This will enable us to address the three questions

raised above how the presence of laser interaction can be made observable in the SSPALS signal and how it is furthermore possible to distinguish between the different velocity classes (and what determines the velocity resolution).

As concluded above, the aim of probing is to determine the number of survived atoms, classified by velocity ranges, once with and once without the cooling laser. It has also been explained that in the Ps case, atom numbers can most conveniently be measured in terms of a difference in the long tail of the SSPALS signal, quantified by $S\%$. Probing of the velocity distribution at a certain point in time thus means to experimentally create a signal S for each velocity class of the distribution separately, and to perform this measurement once with cooling and once without.

The first step in approaching this goal is to consider how it is experimentally possible to produce a change in the long tail of the SSPALS signal. There are effectively two processes which can be made use of to realise this. Besides the obvious possibility of a change in the number of annihilating atoms, it is also conceivable to induce signal changes by means of a modification of the lifetimes of the atoms, without artificially reducing the number of atoms. The latter is, for example, the case if the atoms are excited to higher states which in general have much smaller annihilation rates than the ground state (cf. Tab. A.1). The problem with this approach is the fact that it produces only a very small change in the SSPALS spectrum. The resulting signals S are by far not big enough to ensure statistical significance of the measurement within realistic acquisition times.

For this reason, a much more effective way to influence the SSPALS signal, and thus create a signal S, is to act on the number of available atoms instead of their lifetimes. This can for example be achieved by using a second laser beam which photoionises all atoms that populate the $n = 2$ states. With an appropriate laser pulse (in terms of power, frequency and bandwidth) it is in principle possible to deplete the whole excited state population and thus to instantaneously reduce the total number of atoms by up to 50% (in saturation a maximum of 50% of the atoms are excited to $n = 2$). This reduction in the number of available atoms directly implies less annihilation at later times, which manifests itself in a proportionally reduced detector signal. The problem with this approach is the fact that the 243 nm-pulse would not only have the task to cool the atoms, but would at the same time be involved in the probing scheme, making it difficult to independently measure the recoil effect in any range of the velocity distribution. In this scheme it is only possible to resolve the whole Doppler curve by scanning the detuning of the 243 nm-cooling laser which is not ideal. To reach a high resolving power it would additionally be necessary to choose sufficiently small bandwidths, which conflicts with the parameter recommendations for maximised cooling performance resulting from the numerical studies in Chap. 3.

This makes it clear that the only expedient strategy is to implement an additional independent probing scheme, even though this involves much larger experimental efforts. Only the separation of cooling and probing enables to choose optimum parameters for cooling (requiring fixed detuning and rather broad bandwidths to cover a high fraction of the velocity distribution) as well as for probing (rather small bandwidth and medium power to avoid power broadening and ensure maximum resolving power, with a sufficient degree of significance). The use of two separate laser systems furthermore allows to schedule probing completely independent of the cooling pulse and thus to arbitrarily vary the time delay between the end of cooling and probing.

Standard scheme

Therefore, to minimise the influence of the detection procedure on the cooling process, it is crucial that the two laser excitation schemes (for cooling or probing) are not only separated in time, but furthermore do not share any common laser transition. This means, in particular, that probing should not be performed via the $n = 2$ manifold since it would otherwise not be possible to attribute detected effects entirely to the cooling pulse.

Considering additionally the fact that a maximum signal S can conveniently be achieved by means of photoionisation, it can thus be concluded that probing consists in a velocity-selective photoionisation by means of a second laser scheme. Velocity resolution is achieved by photoionising only certain ranges of the distribution by appropriately choosing the laser detuning and small spectral bandwidths for the probing laser. Due to the unavailability of lasers which are capable of

FIGURE 4.3: *Schematic of the entire transition scheme used for cooling and probing.* Overview of all transitions and atomic states involved in both cooling and probing, based on the Ps level scheme. The blue arrows represent the two-photon ionisation procedure via the $3^3\mathrm{P}$ level as an intermediate excited state manifold. The red arrow indicates the cooling transition. The numbers next to the arrows specify the corresponding transition wavelengths. Similarly, the green arrows and numbers give the fluorescence lifetimes for the transition from the corresponding excited states to the triplet ground state $1^3\mathrm{S}$. The orange arrows and labels symbolise the different annihilation channels. While the $1^3\mathrm{S}$ state decays via regular annihilation with a lifetime of $142\,\mathrm{ns}$, the excited states annihilate primarily due to magnetic-field induced quenching with lifetimes depending on the field strength B. All transitions between bound states are indicated by double arrows whereas one-way processes (annihilation or photoionisation) are marked by single arrows.
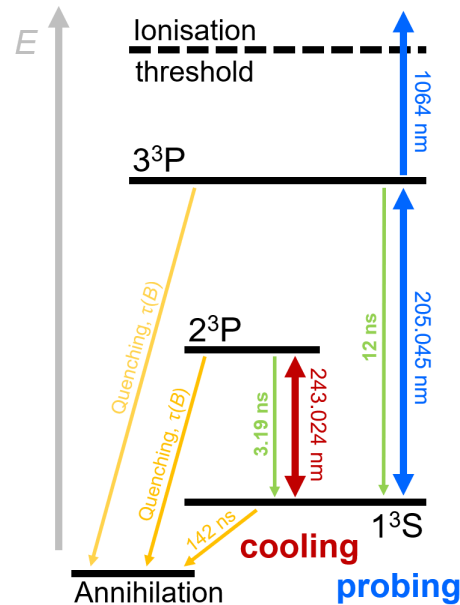
directly photoionising ground state atoms, probing cannot be realised by means of a single laser pulse. Instead, a two-photon transition scheme has to be implemented which uses any excited state other than $n = 2$ as intermediate state. An appropriate choice in this regard is the $n = 3$ manifold; excitation to this level is well known as it has been studied extensively in recent years [15, 72, 96, 110].

The transition scheme required for cooling and probing is shown schematically in Fig. 4.3, limited to the relevant part of the entire Ps level scheme. As known from previous chapters, the cooling laser cycles the atoms on the transition between the $1^3\mathrm{S}$ ground and $2^3\mathrm{P}$ excited states which on average decay back to the ground state within $3.19\,\mathrm{ns}$. The double-photon excitation printed in blue represents the probing scheme. In order to probe the remaining ground state population at any point in time and in a way which does not interfere with the cooling process, a dedicated UV pulse drives the transition between the $1^3\mathrm{S}$ and $3^3\mathrm{P}$ states. An additional IR pulse then serves to deplete the $n = 3$ level by photoionisation. Both pulses are sent simultaneously so that the atoms do not have the chance to decay from the intermediate state back to the ground state. Effectively, this probing scheme is thus a one-way process.

To ensure that only those atoms are addressed and ionised which populate the $3^3\mathrm{P}$ state, but explicitly not the ones excited to $2^3\mathrm{P}$ state, the IR pulse has to provide photon energies which are only powerful enough to overcome the ionisation threshold for the $3^3\mathrm{P}$ state while keeping the atoms in the $2^3\mathrm{P}$ state untouched. This is the case for all wavelength above $729\,\mathrm{nm}$ (cf. energies given in Tab. A.1 and Fig. A.1). Due to their easier availability it is most convenient to use powerful pulses at $1064\,\mathrm{nm}$ for depleting the $3^3\mathrm{P}$ population via photoionisation.

As usual and unavoidable in case of positronium, the whole procedure is accompanied by the competing effect of annihilation, leading to a steady loss of atoms. While, in zero-field, atoms populating the excited triplet states show negligible rates for direct annihilation, ground state atoms decay within $142\,\mathrm{ns}$ (giving rise to the requirement to complete the sequence of cooling and probing within a time span of this order of magnitude, in order not to impair the measurement accuracy too much). The situation is quite different, though, in the presence of magnetic fields since interaction with the field induces coupling of excited triplet and singlet states, thereby opening an additional fast annihilation decay channel, known as magnetic quenching. The rate at which the excited states annihilate depends on the magnetic field strength B. It is considerably higher, however, than for the direct annihilation of the triplet excited states. This shows that quenching plays an important role in a measurement of Ps laser cooling and will therefore be discussed in

more details in a dedicated section below (see Sec. 4.1.3). The great advantage of the scheme shown in Fig. 4.3 is obviously the separation of cooling and probing, as it completely decouples the parameters used for both steps. This especially allows to tune the cooling laser to study the effect of laser parameters on the cooling performance and to finally set it to the optimum value (if technically feasible), while leaving the probing scheme unchanged.

Which parameters to choose for probing?

As far as the parameters for probing are concerned, the primary objective is to ensure maximum resolving power. The key parameter to this end is the bandwidth of the first probing laser which excites the ground state atoms to the 3^3P level. The smaller the bandwidth, the smaller the velocity range of the distribution which is probed for a given detuning. The bandwidth should, however, not be reduced too much since the signal strength scales with the number of probed atoms, which in turn depends on the capture range of the laser. The bandwidth of the IR-pulse does not play a role as long as it depletes the whole excited state population. Since photoionisation pulses are typically extremely powerful, their bandwidth is strongly affected by power broadening anyway. Precise control of the detuning of the IR pulse is therefore not important either.

Power broadening is, however, not only important to consider in the context of the photoionisation pulse, but in fact also with regard to the UV-pulse. This is simply due to the fact that oversaturation is accompanied by an equivalently broader effective bandwidth (cf. explanation in Sec. D.5) which would be detrimental to the resolving power. It is therefore advisable to choose a power for the 205 nm-laser which does not exceed the saturation threshold, or to reduce the nominal bandwidth accordingly, if possible. Finally, the detuning of the UV-pulse is the parameter which sets the spectral position of the laser and thus the region of the Doppler velocity distribution that is in resonance and probed by the combination of 205 nm- and 1064 nm-pulses.

Laser timing schedule

Another parameter to consider, besides the laser parameters, is the timing of the pulses. In order to address a maximum amount of atoms, the cooling pulse should be scheduled to start at the same time as the first Ps atoms are ejected from the target into the experimental chamber. Needless to say that the pulse should last as long as experimentally possible. As previously mentioned, as far as the relative timing of the probing pulses is concerned, i.e., the delay between the excitation pulse at 205 nm and the photoionisation pulse at 1064 nm, both of them should coincide in order to probe the maximum number of atoms.

Concerning the relative delay with respect to the cooling pulse, probing can in principle be scheduled at any time, depending on the main objective of the measurement. However, to most efficiently detect the effect of cooling on the velocity distribution, the atoms should be probed subsequently to the end of cooling, i.e., after the cooling pulse has ended. To maximise the measurement accuracy, the delay between the falling edge of the 243 nm-cooling pulse and the rising edge of the probing pulses has to be chosen such that the maximum number of ground state atoms is photoionised. This might sound more trivial than it actually is. In fact, if the probing pulses are sent too early (less than a few nanoseconds delay with respect to the end of cooling) still too many atoms populate the $n = 2$ states where they cannot be addressed by the 205 nm-probing pulse. However, the later probing takes place, the more atoms can annihilate meanwhile and the smaller is the number of probed atoms. Thus, for the exact timing of probing a compromise has to be made between the two effects. This can be illustrated based on the evolution of the populations in the different state categories, as shown on the left of Fig. 4.4. The plot represents the result of a simulation for $N = 10^4$ atoms and laser parameters similar to the experiment, for the case where only the cooling laser is involved (left), as well as the case where both the cooling and probing lasers are turned on (right). Obviously, the most expedient time for probing is a delay of a few nanoseconds with respect to the end of cooling. This ensures that in the meantime a maximum of $n = 2$ excited state atoms (red) have decayed back to the ground state while the number of additionally annihilated ground state atoms is kept as small as possible. The effect of probing is
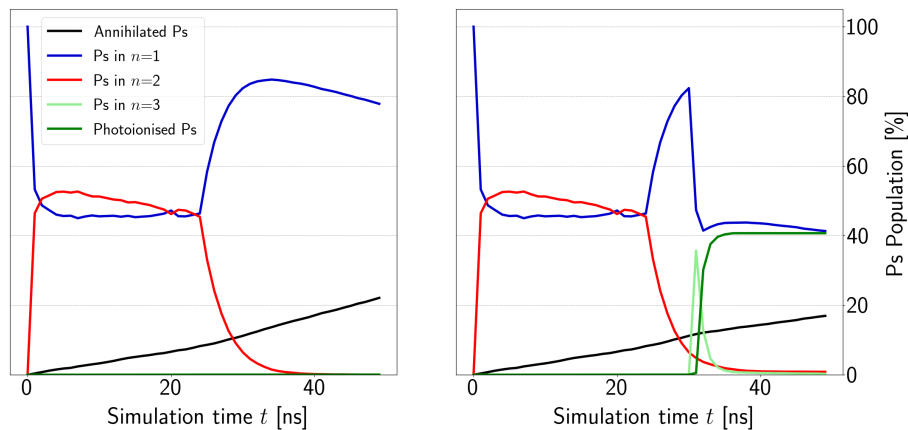
Figure 4.4: *Evolution of Ps populations in different state categories during laser cooling experiments.* *Both plots are based on simulations of the evolution of a cloud of $N = 10^4$ atoms for cooling with a pulse of about $25\,\text{ns}$ length in the absence (left) or presence (right) of probing. Laser parameters have been chosen similar to the experiment. The different state categories are colour-coded to distinguish between annihilated atoms (black), atoms in ground states ($n = 1$, blue), excited atoms in either $n = 2$ (red) or $n = 3$ (light-green) and, finally, Ps which has been photoionised from $n = 3$ (dark-green).*

visualised on the right of Fig. 4.4, revealing successful photoionisation (dark-green) of a significant fraction of ground state atoms (blue).

In the experiment, the timing of the probe laser was eventually optimised by performing SSPALS measurements while scanning the laser delay. The results will be shown in the context of the experimental realisation in Section 4.2.4.

4.1.3 The role of magnetic quenching

As indicated above, in magnetic fields quenching plays a non-negligible role in the whole scheme of cooling and probing. To completely understand the influence of quenching on the measurement signal, it is worth recalling its underlying principle: Due to the Zeeman effect, the triplet state with magnetic quantum number $m = 0$ is coupled to the appropriate singlet state from the same n-manifold. As explained in Sec. B.5.2, this opens up a fast decay channel which leads to a significant reduction in the effective annihilation lifetime of all atoms populating quenched triplet states. For typical experimental magnetic field strength of about $1\,\text{T}$ this results in lifetimes of the order of only a few nanoseconds instead of the $142\,\text{ns}$ in zero-field (cf. Fig. B.1). As shown in the numerical simulations, in case the initial population is equally distributed over all three triplet ground states (as it can be assumed in experiments) one third of them are directly lost within the first few nanoseconds after formation of the Ps cloud.

Since the loss in *ground state* atoms is completely independent of laser interaction and also occurs in the (laser OFF) background measurement, it can simply be subtracted from the laser ON case and thus has the "only" consequence of impairing the measurement accuracy without complicating the measurement method any further. However, the situation becomes a bit more complex in case the atoms interact with the cooling laser. As soon as the laser excites atoms to the $n = 2$ states, it is no longer only the ground states but also the excited states which are quenched in magnetic fields. Moreover, for $n > 1$ not only S-states are affected but in fact also the P-states. This entails a significant enhancement of excited state annihilation rates in the presence of the cooling laser, which leads to an additional loss of atoms during cooling. With regard to the SSPALS signal, the increase in excited state annihilation rate due to $n = 2$ quenching effectively manifests in a forward shift of the signal from the SSPALS tail towards earlier times. Even though the early increase in decay products is lost in the initial peak of the detector signal since para-Ps decay highly dominates in this time window, the corresponding reduction of the signal at later times is

well observable. The most important difference compared to ground state quenching is, however, the fact that $n = 2$ quenching is induced by laser excitation and therefore does not occur in the laser OFF background measurement. This type of quenching can thus not easily be eliminated by subtracting the background, but is rather a parasitic and unavoidable side effect of cooling in magnetic fields. It is furthermore independent of probing.

Consequently, the signal S observed in a combined cooling and probing measurement does not entirely result from photoionisation of the probed atoms, but in fact also contains a contribution from quenching of atoms in $n = 2$ states whose share cannot easily be identified. Elimination of this quenching contribution or at least separation from the photoionisation signal requires a more sophisticated analysis procedure than only subtraction of the laser OFF background. Before discussing this in detail, it should finally be pointed out that quenching can of course also occur for the $n = 3$ states in principle. Since the probing procedure is, however, designed such that the UV- and IR-pulse interact with the atoms simultaneously, the whole $n = 3$ excited state population will be depleted almost instantaneously by the photoionising beam so that quenching of $n = 3$ atoms can be safely ignored here. This annihilation channel has only been included in Fig. 4.3 in the form of the leftmost (faintly shaded) orange arrow for the sake of completeness due to its theoretical possibility.

4.1.4 Measurement methodology and corresponding terminology

At first glance one might wonder why the quenching signal must be eliminated at all. In order to understand that the quenching contribution cannot be made use of, but rather impairs the measurement, it is necessary to consider how it differs from the probing signal through photoionisation: While the probing signal results from a velocity-selective excitation, obtained by scanning the 205 nm-laser detuning over the whole Doppler distribution, the quenching signal arises from the excitation of a larger fraction of the distribution due to interaction with the cooling laser at fixed detuning. The crucial difference is thus that the probing signal contains information on the velocity distribution, and is therefore eligible as indicator for the cooling effect, whereas the quenching signal produces a constant offset to the signal without yielding any spectral information of the distribution. For this reason, the quenching contribution is not useful for the quantification of a recoil-induced cooling effect, which manifests itself in a local modification of the distribution. It should therefore be eliminated from the signal.

As mentioned above, the signal can, however, not be corrected for quenching simply by subtraction of the laser OFF background measurement as it is possible for any laser-unrelated effects. Instead, a dedicated second reference measurement is required with the configuration "cooling laser ON, probing lasers OFF" for which the detector signal solely contains the quenching contribution. The different laser configurations, i.e., combinations of lasers turned on or off, will in the following be abbreviated by a terminology naming all involved UV wavelengths. The configuration for the quenching reference measurement is thus simply denoted by "243". Subtraction of this quenching background from the measurement run with all lasers turned on ("cooling laser ON, probing lasers ON", abbreviated as "205+243") then allows to eliminate the quenching contribution or, in other words, extract the photoionisation contribution from the "205+243"-run. The resulting difference will in the following be abbreviated as "205+243_243" as it represents the comparison of the "205+243" to the "243" measurement.

This information is still not complete, though, as it so far only allows to reconstruct the quenching-corrected velocity distribution after exposure to the cooling laser. To enable a quantification of the 243 nm-recoil effect it is additionally necessary to subtract the velocity distribution of a similar measurement with deactivated 243 nm-laser from the "205+243_243" distribution. This "unmodified" spectrum (i.e., without cooling) is simply obtained from a comparison of the measurement with exactly the same parameter configuration as for "205+243", but with the cooling laser turned OFF (abbreviated as "205"), to the background where all lasers are turned OFF (referred to as "OFF"). The result of this comparison is in the following called "205_OFF". The actual information of interest, revealing the pure 243 nm-recoil effect on the distribution, is finally obtained from the difference of the "205+243_243" and the "205_OFF" measurement, i.e.,
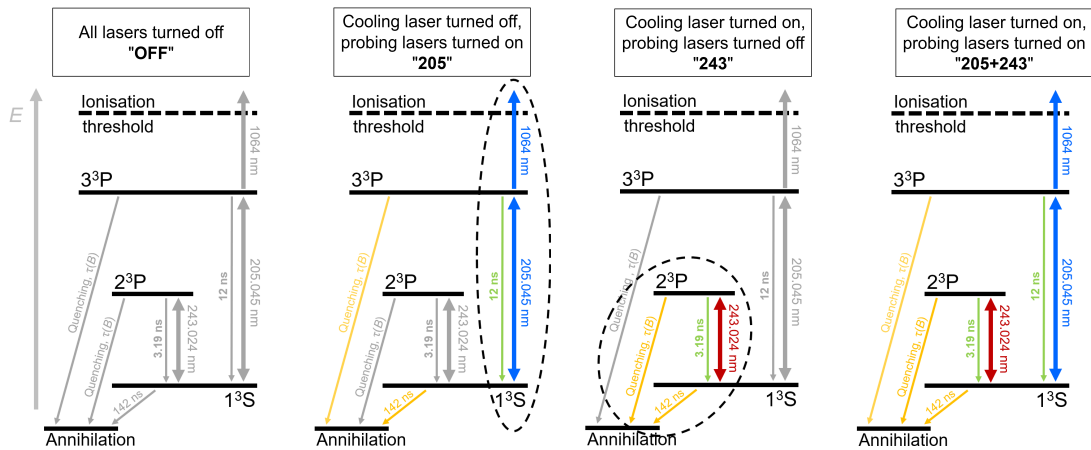
FIGURE 4.5: *Schematic of the fourfold measurement methodology for Ps laser cooling based on the reduced level scheme.*
Each scheme represents one of the four laser configurations required for a measurement of the effect of laser cooling on the velocity distribution of the Ps atoms (see explanations in the text). The overview is based on the level scheme presented in Fig. 4.3 with the difference that here only involved lasers and transitions are highlighted in colour while others are grayed out. The respective laser states are additionally specified in the descriptions in the title boxes which additionally contain the abbreviations according to the terminology introduced in the text.

"(205+243_243) – (205_OFF)". Due to the time-dependence of the Ps formation procedure, it is crucial that for these reference measurements, the probing pulses are sent at exactly the same time as in the "205+243" measurement, i.e., especially with same relative delay to Ps production. Otherwise, the probed distribution would differ from the one of a "205+243" measurement.

To avoid losing track of all mentioned laser combinations and comparisons, Fig. 4.5 schematically illustrates the different measurement configurations required for the measurement of the recoil effect, based on the transition scheme shown in Fig. 4.3. The timing of the lasers complies with the schedule described in Sec. 4.1.2 which means, in particular, that there is a relative delay of a few nanoseconds between probing and the end of cooling. The additional time dimension is not visualised in Fig. 4.5. It should once more be emphasised, though, that in the 2nd scheme the two probing pulses (blue) are fired at the same time as in the 4th.

To obtain the unmodified velocity distribution, in the absence of cooling, it is thus necessary

1. to execute two separate experiment runs in the configurations shown in the 1st and 2nd panels of Fig. 4.5, which only differ in the presence of the probing laser, and

2. to compare the signal acquired in the latter ("205") to the one obtained in the first measurement ("OFF").

The result of this comparison yields the "205_OFF" distribution.

On the other hand, to obtain the cooling-modified velocity distribution it is necessary

1. to execute two separate experiment runs in the configurations shown in the 3rd and 4th panels of Fig. 4.5, again differing only in the presence of the probing pulses but this time with the additional cooling pulse, and subsequently

2. to compare the signal acquired in the latter ("205+243") to the one obtained in the first measurement ("243") which contains the quenching signal.

The result of this comparison yields the "205+243_243" distribution, which contains both the contribution of interaction with the probing as well as with the cooling laser, but corrected for quenching. The recoil effect is finally obtained from the comparison of the modified velocity distribution ("205+243_243") to the unmodified one ("205_OFF"). To probe each velocity class of the distribution separately, it is necessary to pass through the illustrated fourfold scheme for all 205 nm-detunings.

As far as the order of the measurement of the fourfold scheme and the detuning scan is concerned, it is in principle not important whether each of the four configurations is first measured separately for all detunings or whether four configurations are measured collectively for a fixed detuning before moving on to the next detuning. To avoid any influence of potential Ps production instabilities on the comparisons described above, it might, however, be more appropriate to first scan the fourfold scheme (Fig. 4.5) before changing the 205 nm-detuning. Finally, to increase the statistical significance of the measurement the whole procedure should be repeated as often as possible and experimentally feasible under stable conditions. In this regard, it is advisable to nest the two sequences from above into the iteration for statistics. In this way, it is easier to eliminate long-term drifts of the experimental assembly (temperature-induced effects, Ps production stability, etc.) in the subsequent data analysis procedure.

In conclusion, the description of the methodological scheme given above clearly demonstrates that the measurement of laser cooling of Ps atoms implies quite significant experimental efforts, not to mention the sophisticated experimental setup, consisting of two separate pulsed laser systems at UV- and IR-wavelengths, in combination with the multistage setup for Ps generation in a vacuum environment and final synchronisation of all experiment steps. The implementation of the required hard- and software components within the AEgIS experiment for the Ps laser cooling measurements is the topic of the following chapter.

4.2 Experimental implementation of Ps laser cooling

4.2.1 AEḡIS experiment overview

As its name indicates, the main goal of the "Antihydrogen Experiment: Gravity, Interferometry, Spectroscopy" (AEḡIS) is a measurement of the gravitational constant of antimatter, especially antihydrogen, by means of interferometry, but also to perform spectroscopy experiments on all kinds of (anti)atoms which are either directly involved in antihydrogen production or can be produced within the AEḡIS setup. The positronium experiments, to which Ps laser cooling for this thesis belongs, is only one of the numerous steps on the way to the final gravity measurement. Since the experimental setup for laser cooling therefore does not make use of the whole AEḡIS assembly, those components of the main experiment which have not been used shall not be described in details here. Only a brief overview of the AEḡIS experiment will be given in order to show how the Ps cooling setup is accommodated in the main experiment and to visualise the overlap between the two. For more details on the remaining setup, especially the antiproton part, interested readers are referred to the literature (e.g., Ref. [111]) and theses such as Refs. [72, 99] and [28].

Fig. 4.6 shows a schematic of the core of the AEḡIS experiment, comprising the structure of the vacuum chambers as well as the cryogenic environment required to cool down the enclosed two-stage Penning trap system. The latter consists of a 5 T- and a 1 T-trap further downstream to catch and manipulate the antiprotons provided by the CERN antiproton decelerator (AD). They enter the experiment via the antiproton line on the left in the drawing. The second ingredient required for antihydrogen production, the positrons, are inserted in a pulsed way via the positron line that transfers them from the multi-stage positron production region (top left), located above the antiproton line, down into the main beam line. They are injected right in front of the entrance of the 5 T-trap. The positrons are converted to positronium by means of a reflection converter target located at the end of the beam line. Finally, subsequent to Rydberg-excitation of the produced positronium atoms, antihydrogen production takes place in the 1 T-trap via a charge-exchange
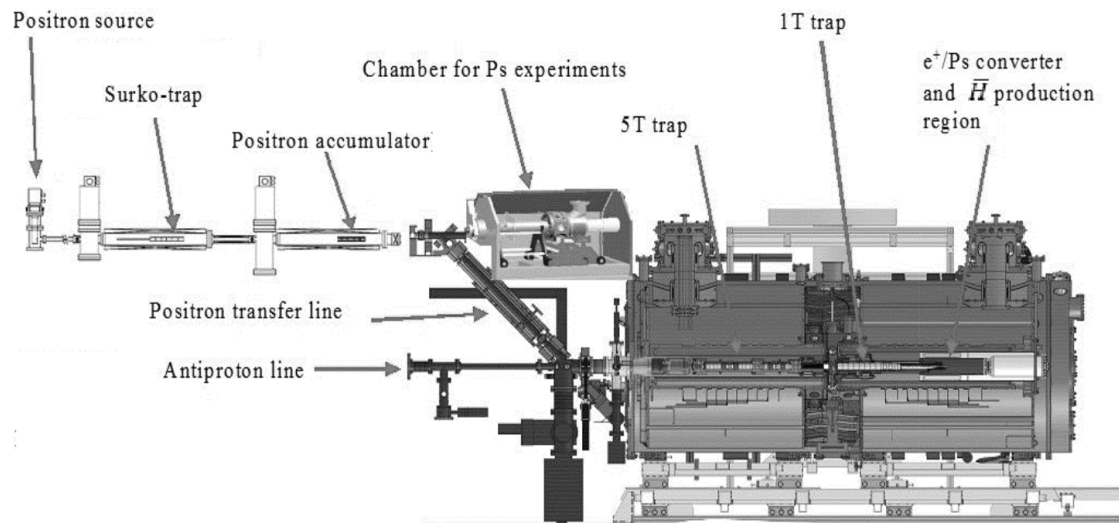
FIGURE 4.6: *Schematic of the AEḡIS experimental setup.* *A description of all parts shown in the sketch is given in the text. Figure taken from [112].*

reaction between the Rydberg positronium atoms and the captured antiprotons. More details on the antihydrogen production scheme can be found in [111] which reports on the successful generation of a pulsed antihydrogen beam within the AEḡIS experiment.

Besides the main experimental chamber, enclosed by the liquid helium-cooled superconducting magnets, the AEḡIS experiment comprises a second, much smaller experimental environment at room temperature (shown at the top centre of Fig. 4.6). It is designed for dedicated positronium experiments and colloquially referred to as *breadbox* chamber. It is connected to the positron beamline as a straight extension of the positron production stage and is therefore located above the positron transfer line which leads to the main experiment. The pulsed positron beam can be directed either straight into the breadbox chamber or deflected into the transfer line towards the main experiment.

The accessory parts of the experiment, such as electronics and other control systems, are not shown in Fig. 4.6. Also not included is the laser setup, primarily used and required for laser manipulation of positronium, both in the central traps and in the breadbox chamber.

4.2.2 Positron setup and breadbox environment

In order to focus on the part of the main experiment relevant for this thesis, Fig. 4.7 shows a technical overview drawing of the whole positron setup, located in the top left in the AEḡIS setup in Fig. 4.6. The figure shows a sketch of the experimental assembly required for the generation of pulsed positron beams. It can be divided into three basic parts, the source, the trap and the accumulator stage, all separated by valves. Again not shown are the accessory devices, i.e., control elements, gauges or power supplies. For details on the mechanisms of each stage as well as of the positron and positronium generation procedure please refer to Benjamin Rienäcker's PhD thesis [28]. The only important information with regard to the experiments presented here is that, with the current source intensity, the setup is capable of producing pulses that contain up to 10^5 positrons every 152 ms [28]. The generated pulses typically show a temporal spread of about 12 ns (FWHM). For the Ps laser cooling experiments, the produced positron beam is projected straight through a buncher for beam collimation into the breadbox environment (called "test chamber with target" in Fig. 4.7).

Figure 4.8 shows, on the left, a photograph of the interior of the breadbox from the top and, on the right, a sketch of the AEḡIS setup from the opposite side than shown in Fig. 4.6. As the drawing on the right illustrates, the central part of the breadbox chamber is a positronium
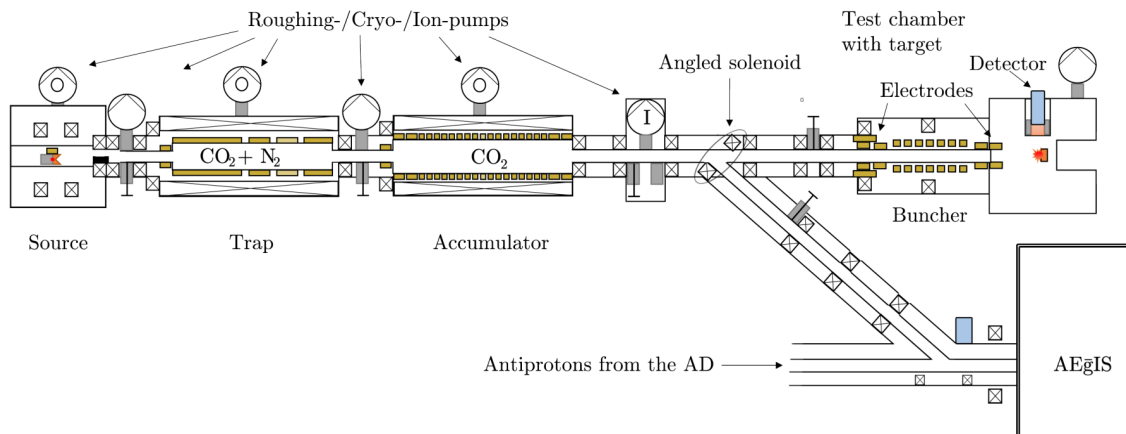
FIGURE 4.7: *Schematic of the positron setup of the AE$\bar{\mathrm{g}}$IS experiment.* Figure taken from [113].
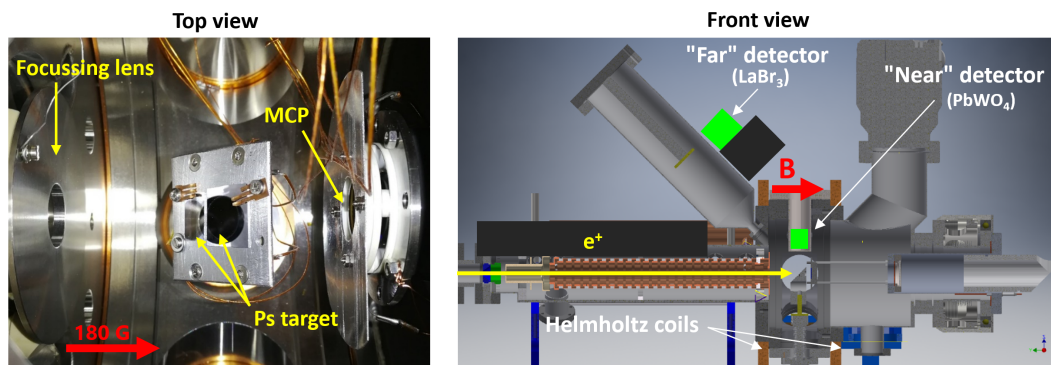

FIGURE 4.8: *Photograph and detailed sketch of the interior of the breadbox experiment chamber.* The photograph on the left shows the interior of the breadbox chamber as seen from the top in Figs. 4.7 and 4.6 while the sketch on the right additionally visualises surrounding parts, most importantly the connection to the positron beam line as well as the second transfer line above. More details are given in the text.

reflection converter target. Apart from the target, the second important element accommodated by the breadbox chamber is the scintillation detector right above the target. It contains a crystal made of lead tungstate ($PbWO_4$), a commonly used material for detection of particle decay. The crystal is mounted on a photo multiplier tube (PMT) to enhance the signal generated in the crystal. The PMT is connected to a fast 12-bit oscilloscope (*Teledyne-LeCroy HD4096*) for readout, monitoring and processing of the signal. This detector signal is the central signal for all Ps cooling measurements performed in the course of this thesis. It is also the one which has previously been referred to as "SSPALS signal". The $PbWO_4$ crystal is called "near" detector due to its close position to the target.

The target itself is angled by 45° to the top in order to direct the emitted pulse of Ps atoms towards a second transfer line, attached to the breadbox chamber above the positron beam line. It can be used to guide the positronium atoms towards a subsequent chamber for further measurements on a (potentially cooled) beam of Ps atoms produced in the breadbox chamber. A second "far" detector, consisting of a lanthanum(III) bromide ($LaBr_3$) crystal, is installed on top of the transfer line. Neither this second detector nor the transfer line were involved the measurements for the present thesis. The breadbox chamber furthermore houses a microchannel plate detector (MCP) opposite to the entrance aperture of the positrons. It serves as an alternative for particle detection and is capable of imaging the cloud. At the time of this thesis the MCP was still in development and

could therefore not be used for the measurements. In the future its use will allow to considerably enhance the data acquisiton rate and the detection scheme which so far is limited by the rather cumbersome SSPALS technique.

The breadbox chamber is enclosed by a magnetic coil setup in Helmholtz configuration for the generation of a homogeneous magnetic field inside the chamber. At the time of the Ps cooling measurements for this thesis it produced a field of 180 G pointing towards the target, i.e., parallel to the positron propagation direction. This is also the reason for having chosen this field strength in the numerical investigations of 2D- and 3D-laser cooling in the previous chapter (cf. Sec. 3.2.2). The magnetic field is required to facilitate transport of high numbers of positrons towards the target. Without magnetic field their spread becomes too large to ensure efficient Ps production.

4.2.3 Laser setup – Hardware

The laser setup of the AEḡIS experiment consists of two independent systems. The first one, the main AEḡIS experiment laser setup, is used to generate light at various wavelengths required for antihydrogen experiments. For the measurement of Ps laser cooling it was used and reconfigured for production of separate light pulses with wavelengths of 205 nm and 1064 nm, pointed along a common laser beam line. This laser system is in the following called "probe" or "probing laser". The light at 243 nm required for Ps laser cooling is generated by a second setup, accordingly called "cooling laser". The development, assembly and maintenance of this laser system was an essential part of this PhD thesis.

Cooling laser system

For a generation of light at a wavelength of 243 nm a sophisticated procedure was developed which comprises both non-linear optical conversion processes as well as an intermediate dye laser for wavelength conversion from 355 nm to 486 nm. The reason for choosing this input wavelength is the fact that 355 nm is the fourth harmonic of 1064 nm, a very common wavelength in laser experiments for which a wide range of laser sources is commercially available.

Figure 4.9 shows a schematic of the whole optical system required to produce the laser pulses for cooling. The first central element is a solid-state laser (*CNI LPS-L-532*) used for pumping the whole setup. It is equipped with a flash lamp consisting of Nd:YAG as lasing material which emits light at a wavelength of 1064 nm. The generation of laser pulses is realised by means of a so-called Q-switch, which is an optical switch that only opens after population inversion in the lasing material. It allows to produce light pulses with much higher instantaneous powers than would be possible in continuous wave mode. The resulting light pulses were measured to have lengths (FWHM) in the range of $(6 - 8)$ ns with a Gaussian profile and energies of up to 100 mJ, depending on the degree of flash lamp deterioration. The laser has a pulse repetition rate of 10 Hz.

The second crucial device is a dye laser (*Continuum ND6000*) which comprises two stages, namely an oscillator and an amplifier stage containing two different distinct dye solutions. As mentioned, the task of the dye laser is to provide light at a wavelength of 486 nm which is required to generate the final wavelength of 243 nm by means of the non-linear optical process of second harmonic generation (SHG). In the present setup, 486 nm-pulses are produced by guiding the incoming 355 nm-pulses that results from fourth harmonic generation of 1064 nm through an ethanol-dye solution containing a mixture of the two different dyes coumarin 480 (Cou480) and coumarin 500 (Cou500) (where the numbers specify the approximate fluorescence wavelengths of the dye molecules). For the measurements presented here, the oscillator was fed with a solution with a mixing ratio of 1:3 between Cou500 and Cou480, where the concentration of the first (2 g Cou500 in 1 l ethanol) was, however, twice as high as that of the latter (1 g Cou480 in 1 l ethanol). In order to flush the oscillator dye cell with a constant flow of dye solution, it was integrated in a dedicated pump circuit.

Subsequent to the first oscillator stage, the amplifier is used to enhance the energy of the 486 nm-pulses emitted by the oscillator. This is realised by sending the 486 nm pulses together with some input light of the dye laser at 355 nm through a second dye cell which is flushed by
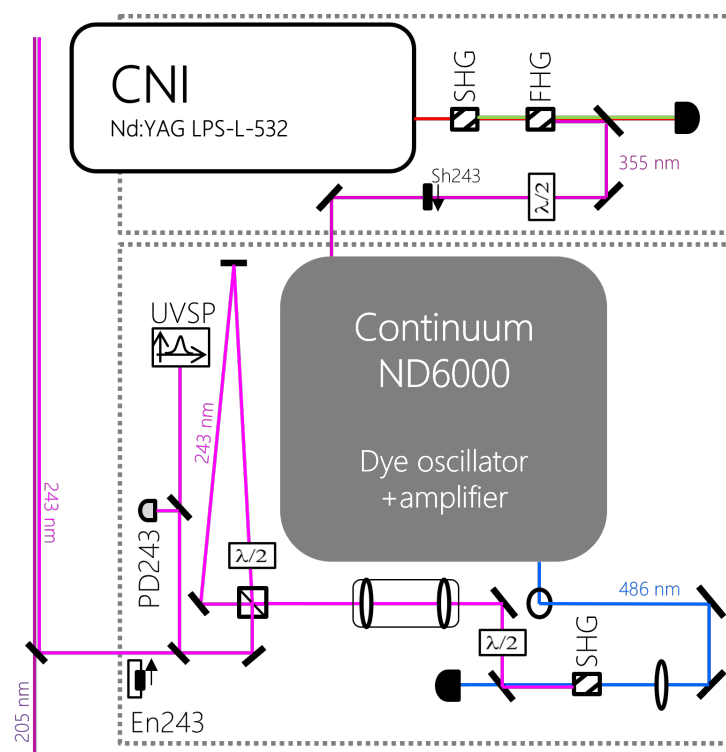
FIGURE 4.9: *Schematic of the laser setup used for the generation of* 243 nm-*light.*
*Besides the two central elements, the pump laser (top left) and the dye laser (centre), the
figure shows all additional optical elements required for the generation, manipulation and
monitoring of the pulses at a wavelength of 243 nm. The coloured lines depict the laser beam
path for the different wavelengths involved. The generation procedure is described in the text.
In addition to the optical setup required for 243 nm-light production, the figure also shows the
three devices used for the automatic monitoring of the pulses, which includes a photodiode
(PD243), a spectrometer (UVSP) and a power meter (En243).*
*On the far left, the 243 nm pulse is superimposed with the 205 nm-beam generated by the
probing laser.*

another dedicated pump circuit filled with a different dye solution. Even though the constituent
types of dyes, Cou500 and Cou480, are similar to the ones used for the oscillator, the amplifier dye
solution has a slightly different mixing ratio of 1:4 (including the same 2:1 concentration ratio).
The developed recipes for the preparation of the oscillator and amplifier solutions are summarised
in Table 4.1.

The reason for sticking to such a cumbersome two-step mixing procedure, i.e., preparation of the
final solution by means of two mother solutions of Cou480 and Cou500, instead of directly pouring
the according amount of dye powder into ethanol, is the fact that the developed procedure allows
for a much more precise preparation. Due to the rather low consumption of final dye solutions for
the continuous operation of the dye laser (few litres of final dye solution per year for each, the
oscillator and the amplifier) and due to gradual deterioration of the dissolved dye solution, it is
not advisable to prepare the solution in large amounts in advance, but rather to store the dyes
in powdered form. Since both solutions contain the same types of dyes, it is thus preferable to
choose the two-step procedure and prepare the final solutions from Cou480 and Cou500 mother
solutions. This helps to reduce the inaccuracy in weighing the correct amounts of dye powder and
to maximise the accuracy of the concentrations of the dyes in the solutions.

The interior setup of the dye laser comprises, inter alia, a combination of motorised mirror
and grating which allows to adjust the final 243 nm-wavelength over a large range of several

	Cou500-Ethanol Solution (2 g/l)		Cou480-Ethanol Solution (1 g/l)		Pure Ethanol
Oscillator	50 ml	+	150 ml	+	300 ml
Amplifier	20 ml	+	80 ml	+	450 ml

TABLE 4.1: *Recipe for preparation of the oscillator and amplifier solutions for the dye laser. The oscillator and amplifier solutions contain the same components (coumarin 480 and coumarin 500), but in different mixing ratios as specified in the uppermost line. All solutions are based on ethanol as solvent.*

nanometres with very high precision. The establishment of this automated, externally controllable wavelength-tuning was a major hardware upgrade of the 243 nm-laser system implemented in the course of this thesis. Its precision and accuracy are characterised in Sec. 4.2.4.

In addition to the two central elements, the pump and the intermediate dye laser, Fig. 4.9 also shows the optical elements required for three wavelength conversion steps based on different non-linear optical processes. In order to pump the dye laser with light pulses at 355 nm, a two-stage sequence was implemented. The 1064 nm-output of the pump laser was first converted to 532 nm by means of second-harmonic generation (SHG) and subsequently transformed to the required wavelength of 355 nm in a sum-frequency generation (SFG) process (shown in the top right corner in Fig. 4.9). The crystals used for second-harmonic as well as sum-frequency generation are made of lithium triborate (LBO). They are temperature-stabilised by means of Peltier elements and installed on kinematic mounts enabling optimised phase matching. After SFG, the residual 1064 nm-light is dumped on a metal beam block. The 355 nm-pulses are guided into the dye laser via a dichroic and two further mirrors. In total, a conversion rate of roughly 60% was achieved. More specifically, under optimal conditions, the dye laser was pumped with 355 ns-pulses with energies of up to 60 mJ. An additional shutter was installed between pump and dye laser in order to save the lifetime of the dyes in the periods of the measurement sequence during which no 243 nm-pulses are requested.

Having passed the dye laser, the beam is lifted by a periscope to the final height before being guided by two further kinematic steering mirrors towards the last frequency doubling stage. Here, a beta barium borate (BBO) crystal, cut at 55°, is used to double the frequency of the 486 nm-pulses by means of second-harmonic generation (SHG) to the final frequency required for cooling (equivalent to 243 nm). With maximum 486 nm-energies of about $(7-8)$ mJ, it was possible to produce 243 nm-pulses with energies up to almost 1 mJ under optimum conditions (i.e., in particular fresh dye solutions and optimised phase matching of the 243 nm-SHG stage).

The sequence of frequency modulation steps required for the generation of light at 243 nm is summarised in Table 4.2, where the subscripts specify the polarisation state of the laser beams involved in the corresponding non-linear optical process (as usual "o" denotes ordinarily and "e" extraordinarily polarised light).

$$(1064\,\text{nm})_{(o)} + (1064\,\text{nm})_{(o)} \longrightarrow (532\,\text{nm})_{(e)} \quad \text{by means of SHG (Type I)}$$
$$(1064\,\text{nm})_{(e)} + (532\,\text{nm})_{(o)} \longrightarrow (355\,\text{nm})_{(e)} \quad \text{by means of SFG (Type II)}$$
$$355\,\text{nm} \longrightarrow 486\,\text{nm} \quad \text{by Cou480+Cou500 oscillator solution}$$
$$486\,\text{nm} + 355\,\text{nm} \longrightarrow 486\,\text{nm} \quad \text{by Cou480+Cou500 amplifier solution}$$
$$(486\,\text{nm})_{(o)} + (486\,\text{nm})_{(o)} \longrightarrow (243\,\text{nm})_{(e)} \quad \text{by means of SHG (Type I)}$$

TABLE 4.2: *Frequency modulation steps required for the generation of light at* 243 nm. *Details are given in the text.*

It is worth mentioning that, in the course of this PhD thesis, the pump laser device showed very unstable performance and had to be sent for repair several times to the company in Paris and China. This caused considerable additional maintenance work and efforts, finally leading to a severe

reduction of measurement time. Measurements could only be carried out if stable 243 nm-energies of $(0.7 - 1)$ mJ were achieved. The energy of the 243 nm-pulses is read automatically ("En243" in Fig. 4.9) prior to superposition of the 243 nm-beam path with the probing beam line. This allows to constantly monitor the energy during measurements.

Up to this point the length of the laser pulses is still equal to the original value of $(6 - 8)$ ns. Considering the results of the numerical investigations, this is, however, not an appropriate pulse length for sufficient laser interaction and efficient cooling. For this reason, a so called stretching cavity was established to extend the length of the "short" 243 nm-pulses available so far. As shown in Fig. 4.9 (between monitoring beam branch and dye laser), this cavity basically consists of two distant mirrors, a $\lambda/2$-wave plate (HWP) and a polarising beam-splitting cube (PBS). The alignment of this cavity is a delicate task which consists of a combined optimisation of the HWP-setting and simultaneous fine-tuning of the overlap of the pulses to maximise the number of pulses circulating in the cavity while ensuring that the power is as constant as possible over the entire pulse length. The perfect setting is difficult to find since the manipulation of each of the numerous degrees of freedom has huge a impact on the others. Due to the large distance between the mirrors (nearly one metre) mechanical stability is thereby of crucial importance.

Finally, it was possible to generate three laser pulses in the cavity which allows to stretch the 243 nm-pulses to a length of up to 28 ns with satisfactory flatness of the power plateau, as shown in Fig. 4.10. The figure shows the plot of a typical 243 nm-pulse, recorded by means of the monitoring photodiode PD243 (cf. Fig. 4.9). Apart from the photodiode signal (blue), three Gaussian pulses (dashed orange) were fitted (manually) to the data and inserted into the figure to indicate the three constituent cavity laser pulses. Since the standard definition, based on a Gaussian shape, cannot be applied, the pulse length has been defined as the FWHM of the sum of the three cavity pulses (illustrated by the solid orange curve), yielding a value of 28 ns.

In this context it is important to mention that the pulse shown in Fig. 4.10 represents one of the better examples in terms of pulse length and temporal shape. Even in the course of a single Doppler scan (that means repetition of the fourfold measurement scheme explained in Sec. 4.1.4 while scanning the 205 nm-detuning), which typically lasts for several hours, the pulse was observed to change considerably, both in length as well as shape. These variations are primarily due to the jitter of the pump laser which has implications on the entire subsequent process of 243 nm-pulse generation. Another source of drifts causing slight misalignments, albeit on much longer time scales, is the thermal expansion of the optical setup. This concerns, in particular, the pulse stretching cavity, which, due to its length, is most sensitive to such expansions. Especially the change in temperature over the day-night cycle turned out to have quite a significant impact on the pulse length and shape. The same is the case for sudden drops or peaks in temperature on cold winter or hot summer days, respectively.[21]

For this reason, it is reasonable to assume that the 243 nm-pulses have a length of about 26 ns on average. With such a pulse length, it is possible to cycle the Ps atoms more than eight times on average on the cooling transition with an excited state lifetime of 3.2 ns.

By controlling the setting of the HWP in front of the stretching cavity it is possible to choose whether the beam is directed through the stretching cavity or not before joining the main laser beam line in the far left in Fig. 4.9.

The 243 nm-pulses have an average spectral bandwidth of 129.45 GHz FWHM. This value was measured by means of a spectrometer (*Avantes AvaSpec-3648-USB2*) which is connected by optical fibre to a sample of the final beam, as shown in Fig. 4.9 (with the spectrometer labelled with UVSP). (More details on the bandwidth determination based on the wavelength readout will be given in the context of laser operation and live-monitoring of laser parameters in Sec. 4.2.4). In connection with the bandwidth it is important to mention that no efforts have been made to modify the spectral width of the generated 243 nm-beam for the cooling measurements. Since the experiment presented here is, in the first instance, intended to serve for a principle feasibility

---

[21] It should be noted that the laser environment was not equipped with an air conditioning system at the time of the measurements.
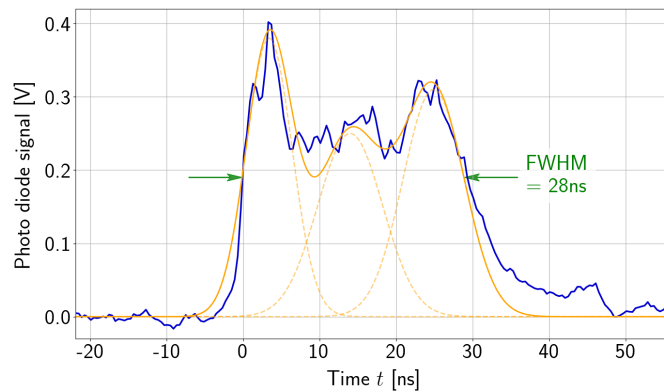
FIGURE 4.10: *Temporal shape of a typical* 243 nm-*pulse during measurements. The plot is based on the readout of photodiode* PD243 *(cf. Fig. 4.9), used for live monitoring of the timing and temporal pulse shape of the* 243 nm-*laser. In addition to the raw signal (blue), the dashed orange lines illustrate the three Gaussian beams that pass the stretching cavity and, in sum, extend the pulse to a FWHM of* 28 ns *in this example. The time axis has been shifted to the left margin of the FWHM.*

study of Ps laser cooling in a magnetic field, for the time being, no attempt has been made to modify the bandwidth. This decision was also taken in view of the fact that according modification measures involve significant efforts, requiring elaborate and time-consuming actions. Considering furthermore that the available bandwidth is already close to the optimum value suggested by the simulations, it is legitimate to expect that the existing setup is well capable of demonstrating significant cooling effects.

It is finally worth mentioning that the spatial spread of the 243 nm-beam was increased by means of a beam expander inserted in front of the stretching cavity to maximise the spatial overlap between the 205 nm- and 243 nm-spots in the breadbox chamber at the position of the Ps converter target.

Probing laser system

As detailed above, probing was carried out by means of the main AEḡIS laser system which, in the antihydrogen (H̄) formation scheme, is used for excitation of the Ps atoms to Rydberg states to increase the cross section of H̄ formation and thereby enhance the production efficiency [111]. The laser system was designed and developed by the group of Marco Giammarchi at the National Institute for Nuclear Physics in Milan and is described in detail in Ref. [114]. Since it was set up and characterised primarily by Ruggero Caravita in his master's and PhD studies (cf. Refs. [72] and [115], respectively), only the central steps for the generation of the probing pulses shall be described here.

Fig. 4.11 shows a schematic overview of the whole laser setup which can be divided into essentially three subsystems (indicated by the dashed boxes): The initial pumping stage (top) consists of a commercially available, Q-switched Nd:YAG laser source (*EKSPLA*) for generating short 1064 nm-pulses with 1.5 ns FWHM at a repetition rate of 10 Hz. It also directly provides pulses at the second and fourth harmonic wavelength 532 nm and 266 nm, respectively, via two additional separate output beam lines. The pumping stage is followed by two independent optical setups designed for conversion of the original pump beams to the ultraviolet light at 205.045 nm required for the excitation of Ps to the $n = 3$ states (subsystem on the right, labelled with "UV") or to infrared light at 1693 nm required for Rydberg excitation from $n = 3$ to $n = 17$ (subsystem on the left, labelled with "RY"). Both subsystems can be pumped in parallel. As indicated in the figure, only the UV-setup was used for the Ps laser cooling measurements. The RY-beam line was permanently blocked by means of a flip mirror ("ShIon"). Instead of entering the RY-stage, the 1064 nm-pulses are directly directed to the end of the setup via a dedicated transfer line between
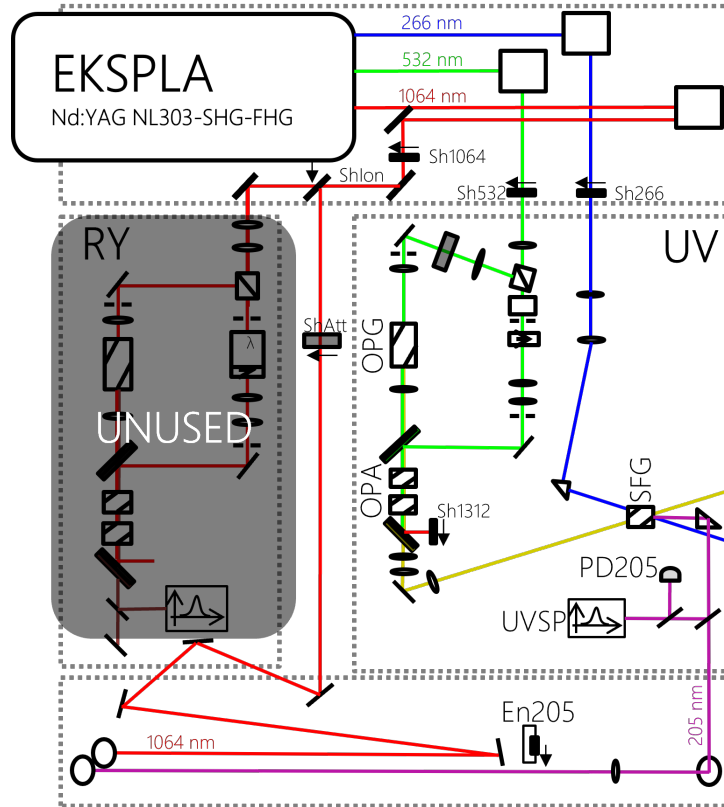
Figure 4.11: *Schematic of the main* AEḡIS *laser setup used for the generation of the laser pulses used for probing in the Ps laser cooling measurements.* The laser system consists of mainly three stages (indicated by the dashed boxes): the pumping stage (top), the Rydberg stage (RY) for the generation of laser pulses at around 1.7 μm (left) and the UV-stage (right). The RY is only required for experiments including Ps Rydberg excitation, and is therefore blocked here by means of the flip mirror ShIon, which instead directs the 1064 nm-pump beam directly to the end of the setup via the transfer line between the RY- and UV-stages, from where it is guided to the breadbox chamber to be used for photoionisation. The UV-probing pulses are the result of a sequence of non-linear optical processes which culminate in the final sum-frequency generation (SFG) stage that allows to tune the 205 nm-wavelength with very high precision over a scanning range of several nanometres. More details are given in the text. Similar to the 243 nm-setup, a small fraction of the final 205 nm-beam is sampled onto a photodiode (PD205) and spectrometer (UVSP) for monitoring purposes.

the RY and UV subsystems. There they are freely available for being used for photoionisation of the Ps atoms.

The UV-probing pulses are produced from the two pump wavelengths 266 nm and 532 nm in a sophisticated multi-stage procedure based on different non-linear optical processes. The central step is the sum-frequency generation of pulses at the final wavelength from input beams at 266 nm, coming directly from the pump, and 894 nm, resulting from a sequence of optical parametric generation (OPG) and optical parametric amplification (OPA), driven by the second harmonic beam line at 532 nm. The final SFG stage allows for externally controlled tuning of the 205 nm-wavelength by modification of the phase matching angle over a wide range of few nanoseconds with very high precision.

In short, the sequence of non-linear optical processes employed for generation of probing pulses can be summarised as shown in Tab. 4.3.

$$
\begin{aligned}
(532\,\text{nm})_{(\text{o})} &\longrightarrow (894\,\text{nm})_{(\text{o})} + (1314\,\text{nm})_{(\text{o})} && \text{by means of OPG (Type II)} \\
(532\,\text{nm})_{(\text{e})} &\longrightarrow (894\,\text{nm})_{(\text{o})} + (1314\,\text{nm})_{(\text{o})} && \text{by means of OPA (Type I)} \\
(894\,\text{nm})_{(\text{o})} + (266\,\text{nm})_{(\text{o})} &\longrightarrow (205\,\text{nm})_{(\text{e})} && \text{by means of SFG (Type II)}
\end{aligned}
$$

TABLE 4.3: *Frequency modulation steps required for the generation of light at 205 nm. Details are given in the text.*

Similarly to the cooling laser setup, small amounts of the probing UV light are sampled onto a dedicated beam branch for constantly feeding a photodiode and the previously mentioned fibre-coupled UV-spectrometer (UVSP) for monitoring purposes. A measurement of the spectral bandwidth of the final 205 nm-pulses yielded an average value of $\sigma_{205} = 111.4\,\text{GHz}$ (more details in Sec. 4.2.4). As far as the possibility for modification of the 205 nm-bandwidth is concerned, the same argument applies as for the 243 nm-laser system. Due to the considerable efforts required to allow for bandwidth tuning, no measures were taken to this end. Which implications this will have on the measurements, especially with regard to the resolving power, will be discussed later.

The final 205 nm-pulses have pulse lengths of about 2 ns with energies of around 130 μJ. The 1064 nm pulses, on the other hand, are typically a bit longer with lengths of about 5 ns. The energy provided for photoionisation amounts to more than 50 mJ. Similarly to the 243 nm-energy, the 205 nm-energy is also read out automatically by means of the power metre which, by being installed on a flip mount, allows for live monitoring during measurements and for subsequent processing and consideration of the energy parameter in the data analysis. As mentioned above, the laser system used for probing was already available, set up and configured at the time of the cooling measurements. Nevertheless, it experienced a number of hardware upgrades for the cooling measurements, including a new power supply, the refurbishment of the Nd:YAG oscillator, the replacement of the SFG-crystal and finally the installation of a temperature stabilisation for the OPA- and SFG-crystals.

Transfer line and breadbox alignment

The probing laser setup is installed on the same height as the main AE$\bar{\text{g}}$IS particle beam line, i.e., the symmetry axis of the central traps (cf. Fig. 4.6). It is located directly underneath the cooling laser setup which is on the same level as the breadbox chamber. The 243 nm-pulses can thus be guided towards the breadbox where the cooling measurements were performed, without further beam path elevation. For the two probing beams a periscope is necessary to direct them to the upper floor and bring the probing and cooling beam lines as close together as possible. It should be noted that, due to the necessity of the final 243 nm-mirror (cf. bottom left in Fig. 4.9), is is not possible to superimpose them completely.

Fig. 4.12 shows a sketch of the transfer line to the breadbox and the optical setup surrounding the experiment chamber. For the sake of clarity the chamber itself is not shown, its position is, however, indicated by the two viewports that enclose the chamber and the target in its centre. The three beam lines which enter the sketch in the bottom left hand corner are the continuation of
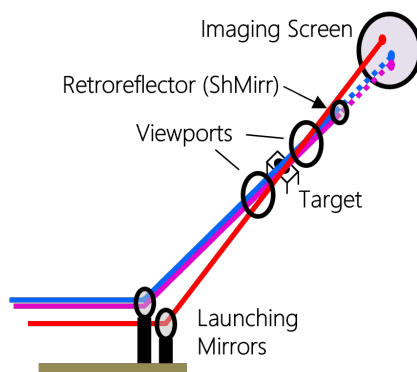
FIGURE 4.12: *Schematic of the transfer line to the breadbox. The sketch shows the main optical elements required to align the probing and cooling laser beams on the target in a grazing configuration, as described in the text. The viewports indicate the position and dimension of the breadbox chamber. The retroreflecting mirror serves to produce the counter-propagating pulses, required, in particular, for the cooling beam, along the same beam path as the incoming light. The IR-pulse is not reflected but ends on the imaging screen at the end of the beam line. The screen is made of paper so that the beams are visible from the back where they are recorded by a CCD camera (not shown). The retroreflector can be flipped out of the beam to allow for imaging the UV-beams as well. Typical images are presented in Fig. 4.13.*

the UV-beam lines which end in the top left hand corner of the drawing of the cooling laser setup (Fig 4.9). From there they pass on to a kinematic "launching" mirror, shown at the bottom of Fig. 4.12 with the 205 nm-beam coloured in blue and the 243 nm in violet. In order to maximise the geometric overlap between the lasers and the positronium cloud emitted from the target, the beams must be aligned parallel to the surface of the target, i.e., orthogonal to its normal. Furthermore, highest Ps-laser interaction efficiency is achieved if the beams graze the target in such a way that the centre of their radial intensity distribution (that means the region of maximum energy density) passes the target just above its surface, even though this implies that almost half of the beam is dumped laterally onto the target holder.

The following procedure was carried out to achieve this alignment for all three beams: First, the final UV-mirror along the 205 nm-beam path (which is the left "launching mirror" at the bottom of Fig. 4.12) was adjusted to ensure the grazing alignment for the 205 nm-beam. The alignment was monitored on the imaging screen at the very end of the setup by means of a camera which records the screen from the back (with the retroreflecting mirror not yet installed of course). This camera was also used during the measurements to verify the correct beam alignment. Since both UV-beams (205 nm and 243 nm) share the same optical path and since the cooling beam is required to irradiate the cloud in a counter-propagating configuration from both directions, it is inevitable that the superimposed 205 nm-beam is mirrored and sent back towards the target as well. Therefore, as a next alignment step the retroreflector (UV-coated mirror in a kinematic holder installed on a flip mount) was put in place and aligned such that the counter-propagating pulse had the same grazing alignment as the initial beam. This was achieved by inserting a pin hole, of the same size as the beam, into the beam path in front of the breadbox chamber and adjusting the mirror such that the back-reflected beam passed through the same hole as the initial beam.

To proceed with the alignment of the 243 nm-beam path, the last two mirrors of the 243 nm-setup (at the bottom left of Fig. 4.9) were used to bring the 243 nm-beam into the very same grazing alignment configuration for both the initial and the reflected beam, via the common final UV-"launching mirror" shown at the bottom left of Fig. 4.12). This was a remarkably delicate job, in particular considering the exceptionally inconvenient location of the mirrors (access only from the right hand side of the setup) and their extreme sensitivity to mechanical manipulations due to the great distance to the breadbox (several metres).
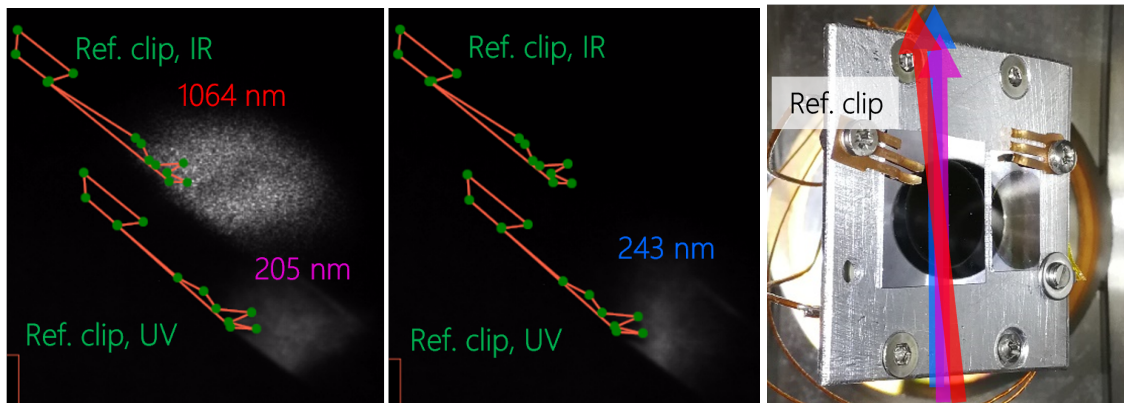
FIGURE 4.13: *Images of the cross sections of the cooling and probing beams.*
The image on the left shows a (back-to-front) picture of the cross section of the probing beams when dumped on the imaging screen, recorded by the camera from the back. The image in the middle shows the same for the 243 nm-cooling beam (faint spot at the bottom).
To facilitate identification and location of the elements shown in the images on the left, the photo on the right (taken from the top with the beams coming from the bottom) illustrates the position of the clip that holds the upper edge of the target (black round circle on the rectangular silicon chip) on the target holder (screwed metal plate). The additionally drawn outline of the reference clip in the two pictures on the left allows to allocate the beams in horizontal and vertical direction with respect to the tilted target surface.
The two probing beams do not overlap each other on the screen due to the small angle between them (cf. Fig. 4.12), resulting in the vertical offset on the screen. The same is true for the outlines of the reference clip as shadows of the corresponding beam.

Finally, a second IR-launching mirror was installed next to the UV-launching mirror to align the 1064 nm-photoionisation beam in a grazing configuration as well, albeit unavoidably under a slight angle with respect to the UV-beams. This angular deviation is due to the necessity of using another type of mirror for the IR-beam in order to prevent damage to the coating of the UV-mirrors. The IR-beam is dumped on the imaging screen since retroreflection is dispensable for the photoionisation beam.

Beam profiles and fine-tuning of the alignment

The images in Fig. 4.13 give an impression of the final beam shape in the area around the target. The image on the left shows the beam cross sections of the grazing probing beams. The shadow of the target is clearly visible as a dark area with the surface tilted upwards by 45°, in the bottom left of each beam. The vertical offset between the probing beams on the imaging screen is caused by the small angle between them due to the use of different launching mirrors as mentioned above. The two probing beams were overlapped by using the upper target holder clip as reference, whose position is outlined by the red lines in the image for both the UV (bottom) and the IR beam (top). The image on the right, taken from the top with the beams coming from the bottom (in this image), helps locate the reference clip with respect to the target (which is the black round circle on the rectangular silicon chip that is attached to the metal holder by means of the two clips of which the upper one is used as reference for laser alignment). It is worth noting that the images of the beams seen by the camera from the back of the imaging screen initially show inverted images. To reconstruct the scene as seen by the laser beams the images were flipped left-to-right in Fig. 4.13. Both probing beams are almost round and have waists of about 5 mm (even though this might look differently on the photo).

Finding the maximum overlap between the probing beams and the Ps cloud is a tedious process
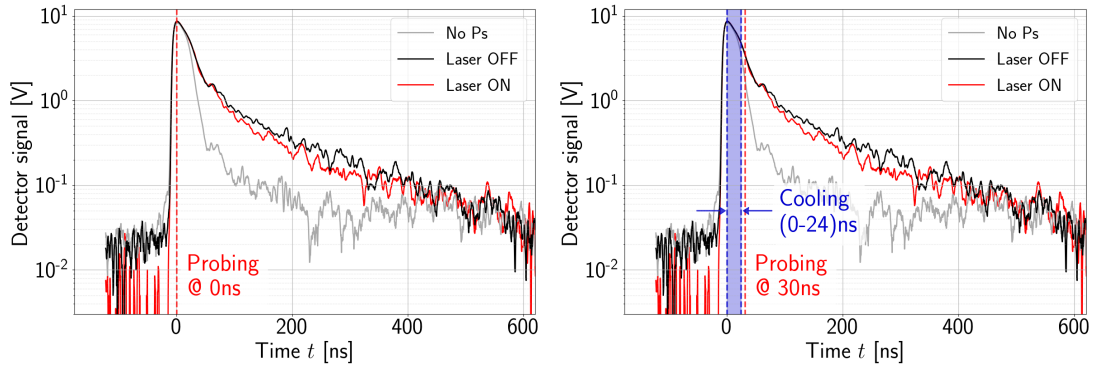
FIGURE 4.14: *Typical SSPALS spectra including laser timings.* *SSPALS signals for experiment runs with Ps formation and lasers turned on (red) and off (black). For reference, the grey line shows the detector signal without Ps formation, leading to the absence of the long tail that results from long-lived ortho-Ps atoms. The time axis is shifted to the time of maximum Ps ejection by the target that manifests itself in the peak in the annihilation spectrum. The dashed lines visualise the timings of the lasers. The setting on the left, which only includes the probing beams, is used for spatial alignment of the beams relative to the target and the one on the right represents the laser timing schedule used for the cooling measurements.*

which basically consists of maximising the signal S by stepwise moving both beams simultaneously along the target surface, with the 205 nm-pulses set to resonance. At each alignment, measured with respect to the reference clip, several tens of SSPALS signals are acquired to calculate an average $S\%$ value for this position. Finally, the beams are set to the position of maximum $S\%$ as this indicates maximum photoionisation and thus probing efficiency. In this optimum position (which is the one shown in the left image of Fig. 4.13) maximum signals of up to 18% could be achieved for zero time delay of probing relative to the maximum of Ps formation that manifests itself in the prompt para-Ps annihilation peak in the SSPALS spectrum. For a delay of 30 ns, the value which complies with the schedule for Ps laser cooling, the signal reaches a maximum level of about 12% in resonance. The difference of six percentage points is due to a combination of cloud expansion, leading to a reduced overlap between lasers and cloud, and annihilation of atoms during the 30 ns-waiting time. For better understanding, Fig. 4.14 illustrates the two timing configurations, based on a typical SSPALS signal, with the probing laser timing marked by the vertical red dashed lines. The left plot represents the setting used for beam alignment and the right one the timing for the cooling measurements, where the blue-coloured area additionally indicates the timing and duration of the cooling pulse.

Returning to Fig. 4.13, the (back-to-front) camera image in the middle shows the spatial profile of the cooling beam alone. As can be seen, the 243 nm-beam has, in contrast to the probing pulses, a clearly elliptical shape with elongation in vertical direction. It was not possible to eliminate this ellipticity by means of available standard optics. The vertical and horizontal waist of the beam was measured by means of the knife-edge technique, which consists of mounting a beam block with a sharp edge onto a translation stage and moving it step-by-step into the beam, perpendicularly to the optical axis. While thereby partially blocking the beam, the residual transmitted optical power was monitored by means of a hand-held power meter. An error function analysis of the measurement data yields FHWM-waists of 2.82 mm in horizontal and 6.51 mm in vertical direction. Plots of the results are shown in Fig. 4.15.

Finally, the 243 nm-beam must be spatially aligned to the position of maximum overlap with the 205 nm-beam (and thus also the IR-pulse). Similar to the grazing alignment described above, this fine-tuning was achieved iteratively by using the two final mirrors of the cooling laser setup for adjusting the 243 nm-beam while monitoring the overlap of both UV-beams (205 nm and 243 nm)
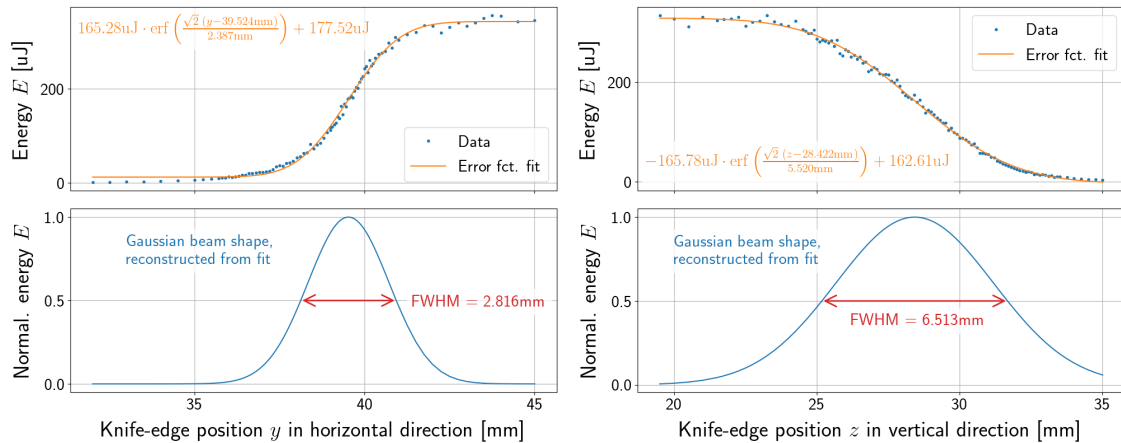
FIGURE 4.15: *Measurement of the* 243 ns-*beam waists. Results of beam waist measurements in both horizontal (left) and vertical direction (right). The subplots at the top contain the raw measurement data (blue dots) together with the error function fit (orange line), the ones at the bottom show Gaussian beam reconstructions, based on the resulting error fit parameters (blue curves), with the FWHM indicated by the red arrows. The measurement was carried out directly in front of the breadbox chamber.*

alternatingly on the imaging screen behind the breadbox chamber or the pin hole in front of the chamber.

4.2.4 Laser setup – Control and monitoring

Laser operation mode

In addition to the hardware improvements, for the measurements performed for this thesis both laser systems also experienced a number of upgrades related to the software and operation mode. The most important upgrade in this respect was the realisation of triggerable laser operation. The idea behind this is to change the standard continuous laser pulse generation of the pump, at a constant rate of 10 Hz, to an operation mode in which the pulses are only produced on request by the control program of the experiment. This laser operation mode is in the following called "burst" modality. Even though the primary goal of this single-shot lasing mode is to slow down the progressive deterioration of the flash lamp performance and to reduce the strain on the optical setup resulting from constant bombardment by high-energy pulses, it indirectly entails another significant improvement related to the determination of the wavelength by means of the spectrometer. This will be described in more details later. To illustrate the importance of the burst modality it is worth mentioning that a single experiment run, i.e., the sequence consisting of device initialisation, parameter configuration, Ps production, laser irradiation, SSPALS detection and data storage, typically takes about 100 s. Since in the course of this sequence in principle only a single laser shot is required, the switching from continuous to burst laser operation obviously allows to considerably reduce the laser duty cycle.

At first glance, the burst operation modality might seem to be straightforward to implement since, on the hardware level, it apparently "only" requires to trigger the pump laser externally instead of internally. However, this modification in fact represents a substantial intervention into the laser operating procedure. This is due to the fact that such pulsed laser sources are typically designed for continuous operation in which all parameters, such as the operation voltages, are optimised for a constant output of laser pulses. An important effect to be mentioned in this context is thermal lensing, which basically describes the temperature-dependency of the refractive index n of the laser material. If the active laser medium is no longer kept at a stable temperature, as would be the case for single pulse generation, the refractive index might change
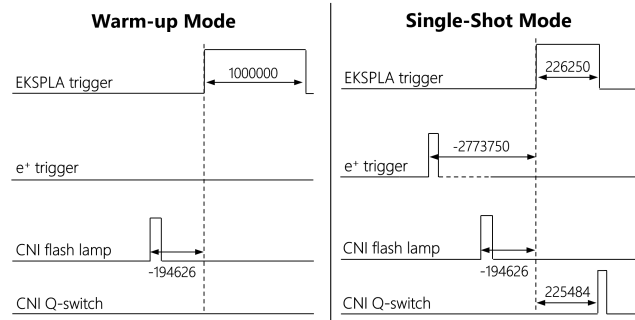
FIGURE 4.16: *Trigger schedule for burst mode laser operation.* *The scheme on the left shows the triggers sent to the EKSPLA (1st line) and CNI (flash lamp in the 3rd and Q-switch in the 4th line) in the warm-up period. The sequence on the right shows the trigger configuration when the lasers are requested to fire the final pulses for the cooling experiment. Only in this state is the e^+ setup (2nd line) involved as well and receives a trigger to ensure that Ps production takes place synchronously with the laser pulses.*

significantly compared to the continuous operation mode. This could potentially cause a severe impairment of the lasing performance or, in the worst case, even damage the laser head. It is therefore crucial to prevent thermal lensing effects. This requires a re-optimisation of operating voltages and flash lamp timings. As the far as the two employed pump lasers are concerned, it was measured that it takes about 15 ns (10 ns) in continuous operation at 10 Hz-pulse repetition rate for the *EKSPLA* (*CNI* respectively) to warm up and reach a stable value $n(T)$ to avoid thermal lensing.

Consequently, for the technical implementation of the externally triggered single-shot laser operation it is necessary to divide the experiment cycle into three laser modes. To understand the laser operation in these modes it is essential to know that the generation of pulsed laser beams comprises basically two stages, namely first the activation of the flash lamp which provides the actual energy and pumps the lasing process and, subsequently, triggering of the Q-switch as soon as a state of population inversion has been reached and the final pulse can be released.

During the (longest) period in which no laser radiation is required, neither the flash lamps nor the Q-switch are triggered and the laser remains completely idle. The next mode is the flash lamp warm-up period, during which the laser must be heated up before the final Q-switch trigger arrives. It is initiated roughly 15 ns (10 ns) before the *EKSPLA* (*CNI*) is requested to fire the crucial pulse for the cooling experiment. In this state both pump lasers are running in a kind of armed mode, that means with stable cavities and warmed-up laser medium for being prepared to send the final pulse. For hardware reasons the *EKSPLA* (probing laser) and *CNI* (cooling laser) have to be treated differently in this state as far as flash lamp and Q-switch operation is concerned. While the *CNI* is equipped with two independent trigger inputs for the flash lamp and Q-switch, the *EKSPLA* can only be controlled via a single input channel for both the flash lamp and the Q-switch. For this reason, the *EKSPLA* must already be operated in full mode (with activated flash lamp and Q-switch) in which laser pulses are constantly generated at 10 Hz, whereas the *CNI* can still be kept in a semi-idle mode in which only the flash lamps pulse at 10 Hz while the Q-switch is still deactivated and no laser pulses are produced yet. The pulse pattern on the left of Fig. 4.16 shows the resulting sequence of hardware triggers that have to be sent to the *EKSPLA* and *CNI* power supplies in order to achieve the described operation mode in the second state. The scheme clearly shows that only the *EKSPLA* laser and the *CNI* flash lamp stage receive TTL trigger pulses. The dashed line represents the common reference time used for calibration purposes. The third and final mode is the very short period of firing the single shot for the measurement. The corresponding trigger schedule is illustrated by the pattern on the right in Fig. 4.16.

To understand the scheme, it is important to know in which way the laser controllers receive the hardware timing trigger. Briefly, the whole experiment is managed by means of a central *LabVIEW* programme which ensures the correct initialisation and configuration of the whole AEḡIS

experiment and the execution of the measurement procedure according to the parameters defined by the user. It has control over all experimental parts of the AE$\bar{g}$IS setup (cf. Fig. 4.6) of which the lasers and e$^+$ setup are only two small puzzle stones. To achieve correct functioning it communicates with all devices, either directly or via intermediate devices. As far as the lasers are concerned, the timing sequence shown in Fig. 4.16 is finally transmitted via a field-programmable gate array (FPGA) which receives commands from the run manager and thereupon sends corresponding triggers to the laser power supplies. The reason for using an intermediate FPGA instead of the CPU is that FPGAs are much better suited and show superior performance for this task. They typically allow not only for much faster processing of signals but also for parallel execution of the internally programmed tasks with high temporal precision and minimised jitter with reference to their internal clock. They are furthermore very flexibly programmable allowing, for example, for easy reprogramming in case of modifications of the timing schedule.

In light of these advantages, synchronisation of experiment steps for which time plays a crucial role, such as for the timing of the laser pulses, both relative to each other as well as with respect to Ps formation, is best achieved by controlling all relevant devices by one and the same FPGA. This is why the FPGA not only triggers the lasers but also communicates with the e$^+$ system, as shown on the 2nd line in Fig. 4.16. As soon as Ps production is requested by the run manager, it instructs the FPGA to switch from the laser warm-up mode to the single-shot mode, which is the first (and only) time in the whole experiment cycle in which the e$^+$ system is triggered.

Scheduling of all devices in the run manager is of course only possible if the timings have previously been calibrated. As far as the laser timings are concerned, this means to precisely determine the time stamps of the events included in the FPGA schedules of Fig. 4.16. This calibration procedure was carried out by monitoring the laser beams on a common photodiode upstream of the breadbox chamber and programming the FPGA pulse pattern, strictly speaking the numbers with respect to the dashed line, such that the rising edges of the laser pulses coincide in the photodiode signal. The only constants in the sequence which must not be changed (for hardware reasons), are the length of the *EKSPLA*-TTL pulse and the relative delay of the two *CNI*-TTL pulses. While this fixes the relative timing of the laser pulses, the delay with respect to the positrons was calibrated by monitoring the mentioned laser photodiode on the same oscilloscope as that used for SSPALS detection. The e$^+$ trigger (2nd line in Fig. 4.16) was then adjusted such that the rising edge of the laser pulses coincides with the maximum of the prompt para-Ps annihilation peak (i.e., the zero position of the SSPALS spectra shown in Fig. 4.14).

This procedure finally led to the numbers specified in Fig. 4.16. As illustrated, if involved, the e$^+$ system receives the trigger almost 3 ms prior to laser operation. In the subsequent sequence of laser triggers it the *CNI* flash lamp is then triggered first, precisely 420.89 µs before the Q-switch is triggered. The *EKSPLA* receives the command for laser pulse generation in the form of a 226.25 µs long TTL-pulses between the two *CNI* events to ensure that the final probing pulses precede the cooling pulse by exactly 766 ns. The reason for the long duration of the TTL-pulses sent to the *EKSPLA* is that optimum pulse properties are obtained if the flash lamp (on the rising edge) is activated exactly 226.25 µs before the laser pulse release by the Q-switch (on the falling edge). This timing is related to the previously mentioned requirement of population inversion. The timings set in the run manager are then referenced to these calibrated numbers.

The values which result from this calibration procedure are, however, not necessarily the optimum timings with regard to the final experimental scheme, i.e., the ones which yield highest probing efficiency for example. For this reason, the relative timing between the lasers and their common timing with respect to the positronium formation were further optimised by means of dedicated SSPALS measurements during which the respective timing parameters were scanned in the run manager while keeping all remaining parameters fixed. The results of these scans will be presented in the final Section 4.4, in the context of the corresponding experimental results. It should finally be mentioned that the realisation of this burst lasing modality allowed to reduce the flash lamp duty cycle by a considerable factor of 20 and the usage of dyes even by a factor of 100.
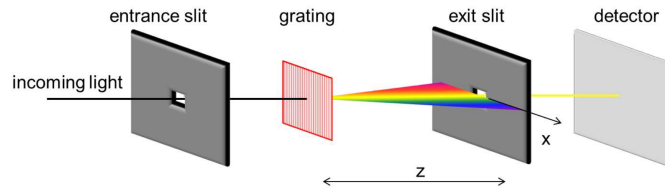
FIGURE 4.17: *Schematic of the basic operating principle of a standard spectrometer. The wavelength and light spectrum of the input beam are determined from the diffraction pattern of a grating which is detected on the CCD chip behind a narrow exit slit. Figure taken from [116].*

Wavelength readout and bandwidth characterisation

As briefly mentioned before, the implementation of the burst lasing modality not only allows to reduce the strain on all optical parts and devices but also entails a major improvement with regard to wavelength readout. This is due to the fact that the used UV spectrometer has been observed to saturate if it receives laser pulses at the usual continuous-mode repetition rate of 10 Hz. This saturation effect, which manifests itself in a broadening of the readout spectrum, could not be eliminated by simple attenuation of the beam intensity, for example by inserting neutral density filters. The change in laser operation, from continuously pulsed to burst mode, however, enabled to completely prevent the spectrometer from saturating. This constitutes a major upgrade of the wavelength determination as it yields a considerable enhancement in readout precision. Furthermore, the elimination of saturation-induced broadening effects allowed for the first time to evaluate the laser bandwidth directly from the detected spectrum instead of using much more cumbersome methods, such as Fabry-Pérot interferometry.

The UV spectrometer can easily be integrated into the measurement schedule as it is equipped with an external trigger input that allows to trigger it by means of the same FPGA as that used for controlling the laser timings. By adding it to the FPGA sequence shown in Fig. 4.16 it only reads the wavelength of the final pulse sent to the experiment. The wavelength can then be stored together with the remaining experiment parameters (timings, laser parameters, etc.) as metadata of the corresponding SSPALS spectrum, to be processed further in the subsequent step of data analysis.

The spectrometer is capable of reading simultaneously both UV-wavelengths involved in the experiment, i.e., the one of the 205 nm- as well as 243 nm-pulses. For this purpose, samples of both UV-beam lines are coupled into separate fibres (cf. UVSP-lines in Figs. 4.9 and 4.11) which are merged subsequently, in order to be connected to the spectrometer via a common optical fibre. Both incoming UV-wavelengths can then be read from a single spectrum. The operating principle of the spectrometer used for wavelength and spectrum read-out is based on the detection of the diffraction pattern of the input beam that is produced by a grating, as illustrated in Fig. 4.17. The device used here, is equipped with a grating with 3600 lines/mm behind a slit of 10 μm size, whose diffraction pattern is detected on a CCD chip with 3648 pixels. This assembly yields a maximum resolving power in wavelength determination of 6.55 pm at 205 nm and 5.44 pm at 243 nm, respectively. Fig. 4.18 shows plots of the results of dedicated bandwidth measurements for the 205 nm- as well as 243 nm-pulses.

Each data point in the plot represents the bandwidth value evaluated from a single spectrum measurement. To this end the intensity registered by the detector was first integrated in vertical direction separately along all pixel arrays, each responsible for detecting a different wavelength range. After mapping the pixel size to the corresponding wavelength range, the bandwidth can directly be extracted from the horizontal distribution of the integrated intensities. Subsequent to a few post-processing operations, such as masking of bad pixels, fitting of the spectra with Gaussian functions and deconvolution by the pixel variance, the resulting values of all individual measurements were finally plotted over the corresponding central wavelengths, which is shown in Fig. 4.18 for the 205 nm-bandwidth measurement on the left and for 243 nm in the middle. After
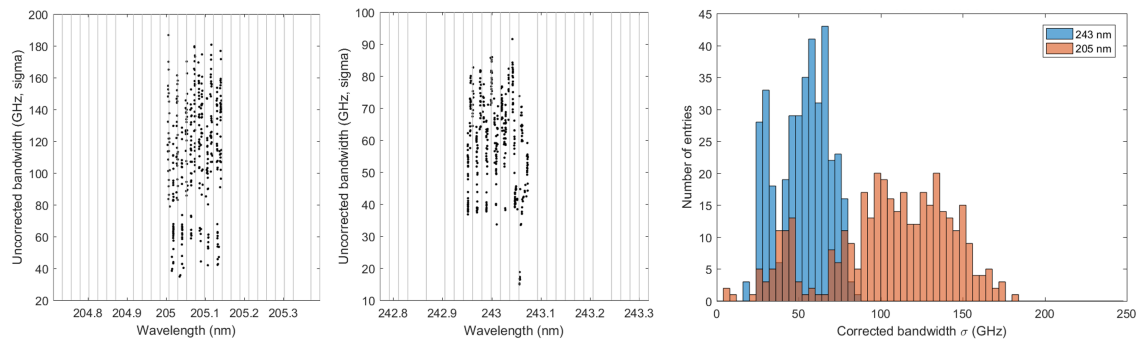
FIGURE 4.18: *Results of the measurement of the bandwidths of the* 205 nm-*and* 243 nm-*laser beams.* *The two left plots show the bandwidth values evaluated directly from the output of the CCD detector acquired in dedicated measurements of the* 205 nm- *(left) and* 243 nm-*bandwidth (middle). The histogram on the right contains the background-corrected measured values. The analysis yields bandwidths of* $\sigma_{205} = 111.4^{140.6}_{71.1}$ GHz *(red) and* $\sigma_{243} = 55.0^{68.0}_{37.7}$ GHz *(blue).*

correcting the obtained bandwidth values for the background signal, the measured values were converted to a histogram, shown on the right, which finally yields mean (sigma-) bandwidths of $\sigma_{205} = 111.4^{140.6}_{71.1}$ GHz for the 205 nm-pulses and $\sigma_{243} = 55.0^{68.0}_{37.7}$ GHz for 243 nm, respectively. The accumulation of entries around ≈ 30 GHz in the 243 nm- and ≈ 45 GHz in the 205 nm-measurement might be artefacts of the measurement method and result from the discretisation of the intensity distribution. This assumption could not be clarified conclusively, though.

Fig. 4.19 shows plots of the results of the wavelength readout during a real measurement in which the respective UV-wavelength was scanned in small steps over a range from -50 pm to $+50$ pm around resonance. The purpose of this wavelength recording was to verify that the laser pulses are generated with the correct wavelength, i.e., that the wavelength which is requested by the run manager (x-axis), agrees with the wavelength of the generated pulses which are finally sent to the experiment (y-axis). The plots nicely show that, especially for the 243 nm-pulses, the wavelength is set with very high precision. Only the evolution of the 205 nm-wavelength shows a slightly wavy behaviour. This is due to the different ways of wavelength tuning for the two wavelengths. While for the 205 nm-pulses this is done by modification of the phase matching conditions (primarily the crystal position) of the 205 nm-sum-frequency generation, for the 243 nm-beam it is realised by using different fractions of the diffraction pattern produced by the motorised grating stage inside the dye laser (cf. Sec. 4.2.3).

By recording and plotting the wavelength during the wavelength scans it is, moreover, possible to study the possibility for the occurrence of hysteresis induced by the wavelength tuning procedure and to which extent it affects the finally generated wavelength. To understand the possibility for this effect, it is important to mention that the wavelength scans are carried out by ramping the wavelength in a triangular zigzag scheme, scanning back and forth, instead of a sawtooth pattern where the values are scanned in only one direction. The first scheme was chosen in order to allow the system to settle to stable conditions after each wavelength change. This can only be ensured by keeping the requested wavelength changes as small as possible, thereby avoiding too large jumps in the tuning parameters which might require too much time for the system to adapt to the new conditions. After changing the scanning direction in the triangular scheme, it might, however, occur that the system does not return to the same state for similar setting parameters. This can cause a hysteresis which manifests itself in an offset of the values generated during the ascending wavelength ramps (red data in the plots in Fig. 4.19) with respect to the ones produced on the descending ramps (blue data points).

The plots in Fig. 4.19 reveal that both wavelength scans do not show any strong hysteresis behaviour. Only in the scan of the 243 nm-wavelength a very weakly pronounced offset between
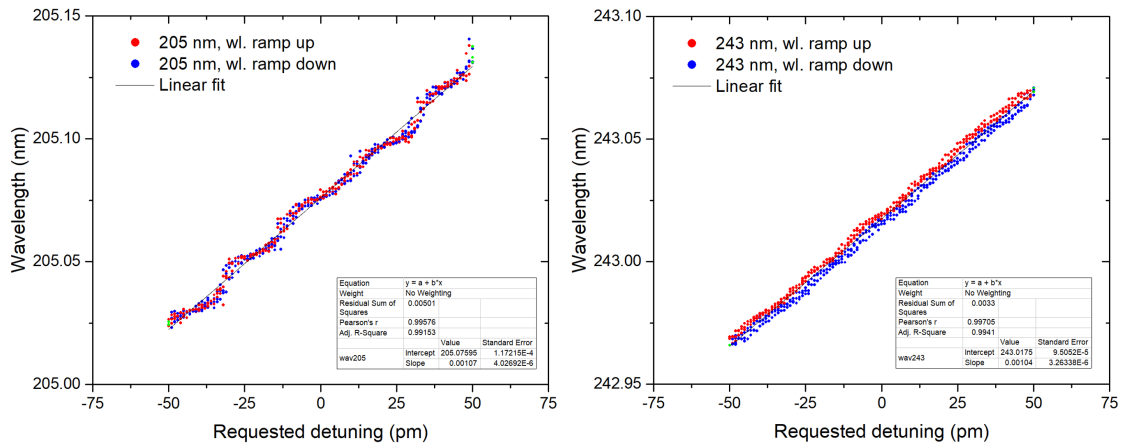
Left plot:

Wavelength (nm) — 205.15, 205.10, 205.05, 205.00
Requested detuning (pm) — -75, -50, -25, 0, 25, 50, 75

Legend:
- 205 nm, wl. ramp up
- 205 nm, wl. ramp down
- Linear fit

Equation	y = a + b*x	
Weight	No Weighting	
Residual Sum of Squares	0.00501	
Pearson's r	0.99576	
Adj. R-Square	0.99153	
	Value	Standard Error
wav205 Intercept	205.07595	1.17215E-4
Slope	0.00107	4.02692E-6

Right plot:

Wavelength (nm) — 243.10, 243.05, 243.00, 242.95
Requested detuning (pm) — -75, -50, -25, 0, 25, 50, 75

Legend:
- 243 nm, wl. ramp up
- 243 nm, wl. ramp down
- Linear fit

Equation	y = a + b*x	
Weight	No Weighting	
Residual Sum of Squares	0.0033	
Pearson's r	0.99705	
Adj. R-Square	0.9941	
	Value	Standard Error
wav243 Intercept	243.0175	9.5052E-5
Slope	0.00104	3.26338E-6

FIGURE 4.19: *Spectrometer wavelength readout during UV-wavelength scans. The plots show the readout of the spectrometer during measurements with UV-wavelength scans in the range from -50 pm to $+50$ pm around resonance, for the 205 nm-pulses on the left and for 243 nm on the right. The measured wavelength values are plotted as a function of the detuning values specified in and requested by the run manager. The red dots represent the data acquired during ascending wavelength ramps and the blue ones during descending ramps of the triangular scanning scheme, respectively.*

red and blue data can be observed, which can, however, safely be ignored as it is expected to affect the measurement only marginally, if at all.

Central control software

The operation of both laser systems can be monitored and controlled, either manually or automatically, via the run manager, by means of a number of *LabVIEW* programmes, called *virtual instruments* (VIs). The screenshot in Fig. 4.20 presents an overview of the graphical user interfaces of all laser control VIs. In the course of this thesis the whole control system experienced several major upgrades, finally allowing for live-monitoring of all relevant laser parameters, which enables easy diagnosis of the correct operation and analysis of potential failures. For example, the implementation of an automated logging of the energy of both UV-beams ("Energy Readout", bottom right) as well as their spectra, central wavelengths and wavelength evolution over time ("UV Spectrometer" in the centre) is worth mentioning. This data can be used to verify the correct execution of wavelength scans or to monitor the potential wavelength drift during a measurement. Storing this monitoring data as metadata of the corresponding measurement runs allows for further processing in later data analysis. Another VI ("EKSPLA PS") is available to remote control the *EKSPLA* power supply and output state as well as to monitor its operating temperature (top left). The VI named "205 nm Controller" (left) is responsible for tuning the 205 nm-wavelength, which is integrated in the automated procedure for setting the 205 nm-detuning via the run manager. However, it also allows for manual tuning of the wavelength and re-calibration of the detuning by modifying the calibration constants for the OPG and SFG stages. An autonomous monitoring procedure additionally indicates whether the detuning has been set correctly. The detuning of the 243 nm-laser system is controlled via the VI named "243 nm Controller"(bottom left). It performs several tasks, including controlling the motor responsible for wavelength tuning, the phase matching angle of the 243 nm-SHG-crystal, the state of the half-wave plates and finally calibrating the wavelength tuning procedure by means of all mentioned parameters. This VI is integrated in the central run control, but also allows for manual operation.

Finally, a dedicated VI is available for controlling the FPGA timings and laser operation modalities ("Timing FPGA", top right). It can, for example, be used to switch between the burst and continuous lasing modes for both laser systems separately, but also offers the possibility to
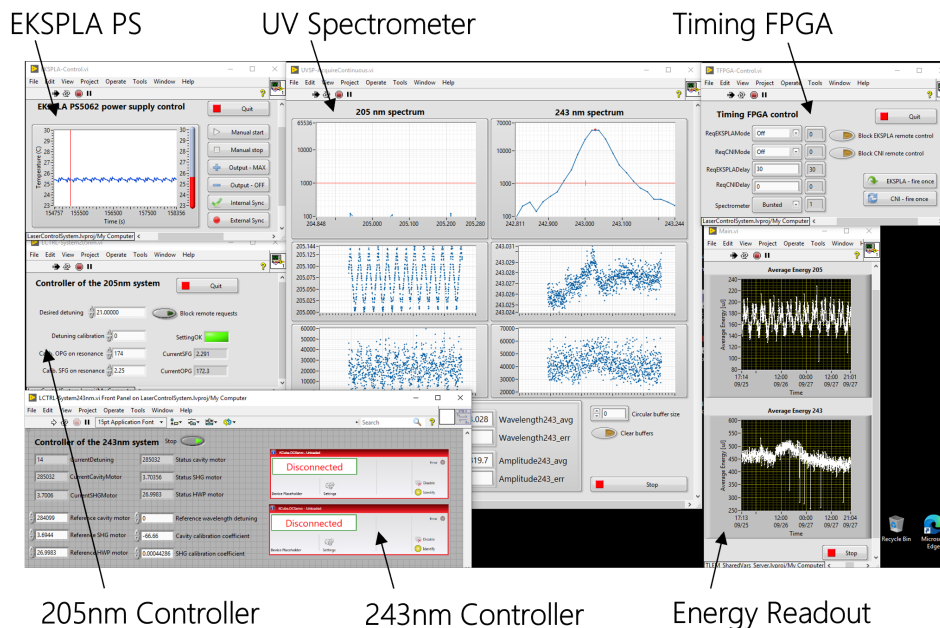
FIGURE 4.20: *Screenshot of the LabVIEW VIs used for controlling, monitoring and manually operating the laser system.* The screenshot includes the graphical user interfaces (GUIs) of all laser control VIs. Their functional scope is described in the text.

monitor the correct execution of wavelength requests submitted by the run manager to the FPGA. During laser development or maintenance work this VI can be used to manually adjust the laser timings. The VI used for the actual programming of the FPGA is, due to lack of space, not shown in the screenshot in Fig. 4.20. The development and interconnection of all these VIs finally allowed for the operation, re-calibration of the wavelength tuning procedure, failure analysis, debugging and troubleshooting in a completely autonomous and remote way which represented a major software improvement with regard to the laser operation.

4.3 Data analysis – The semi-detrending technique

The method used for analysing the measurement data of the Ps cooling experiment consists of a sophisticated procedure developed and optimised over many iterations in the course of a number of past experiments based on the SSPALS detection technique. Therefore it shall not be described in detail in the following. Only the central steps necessary for understanding the procedure will be outlined. In summary, the well-established AE$\overline{\text{g}}$IS *detrending* technique was adopted (described in detail in [96]), but significantly modified, switching from a full detrending to a *semi-detrending* technique.

As described in Section 4.1.4 the general measurement scheme for Ps laser cooling consists of the consecutive measurement of all four possible laser ON/OFF combinations, repeated for all different 205 nm-detunings (detuning scan). To achieve higher statistical significance these scans are again repeated several times. In total, the whole measurement thus consists of interleaved detuning scans. The nesting of the different repetitions is illustrated in the upper panel of Fig. 4.21 where each point represents a single measurement run for a distinct set of parameters. The probe detuning is shown as a function of the run number. The colour code indicates the corresponding measurement scheme, i.e., combination of involved lasers. All runs with only the cooling laser are, for example, coloured in green. The different scans are nested such that first the fourfold

FIGURE 4.21: *Schematic of the sequence and nesting of parameter scanning within a single measurement.*

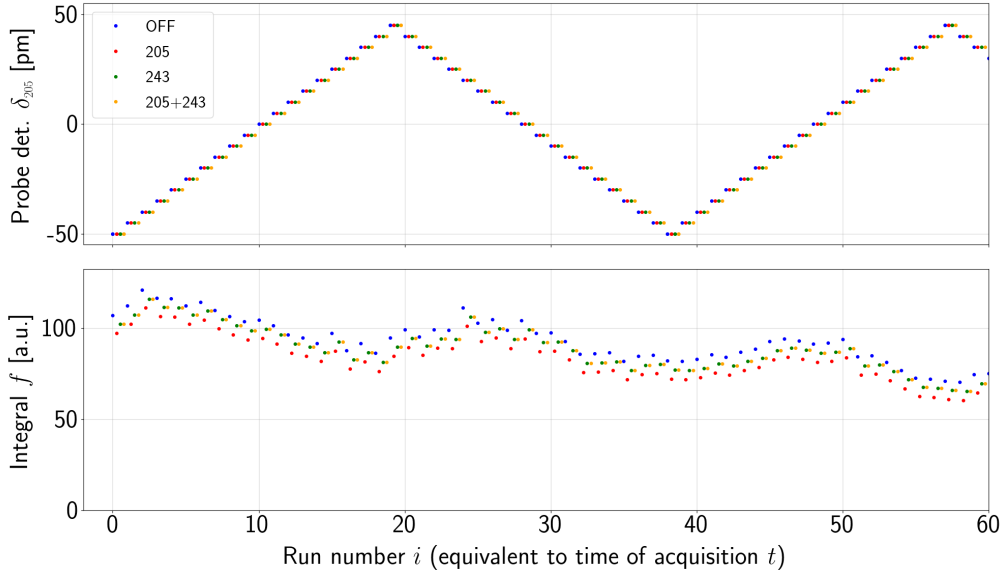*The upper panel shows the nesting of the different scans. While scanning the probe detuning δ_{205} (y-axis) from minimum to maximum, the fourfold measurement methodology (cf. Fig. 4.5) is repeated for each detuning value. The colour code given in the legend specifies the different laser configurations in terms of cooling/probing laser. Upon completion in one direction the detuning scan is continuously repeated in the reverse direction. The lower panel shows the drift in the course of a measurement manifesting itself in a reduction in SSPALS intensity and thus the integrals f (in arbitrary units) of the SSPALS signal over the time window used for the calculation of $S\%$. In general, all four configurations (different colours) are subject to individual drifts.*

measurement scheme is completed before the probe detuning is scanned in a triangular pattern. Finally, these scans are repeated to increase statistical significance.

In order to construct, in the next step, the different velocity distributions described in Section 4.1.4, such as "205+243_243", which compares the runs where both lasers are involved ("205+243"; cf. Fig. 4.5 for explanations of the terminology) to those where only the cooling laser is present ("243"), it is necessary to calculate the individual signals $S\%(\delta_{205})$ for each probe detuning δ_{205}. We briefly recall that the signal $S\%$ is always calculated from the integrals f under the SSPALS spectra of a set of corresponding ON and OFF measurement runs (cf. Sec. 4.1.1), where the terminology ON/OFF refers to the parameter in which the two runs differ, typically the laser state. To generalise this labelling, to be applicable for example to the "205+243_243" distribution where lasers are involved in both configurations, in "205+243" as well as "243" and to avoid confusion with the laser state for example, it is convenient to use an alternative terminology which splits the runs into positive and negative manifolds where the negative runs are those which serve as reference/background for the positive runs. In the previous example the "205+243"-runs belong to the positive and the "243" ones to the negative side. The ON/OFF-terminology based on the laser state is thus only a special case in which the positive manifold contains all laser ON runs. The corresponding background runs, with the laser turned OFF, are subsumed under "negative".

Regardless of the terminology, in each case the first step in calculating the signals $S\%(\delta_{205})$ is the integration of the SSPALS signal over the chosen time interval. Since in general more than one measurement exists for a particular set of laser combination and 205 nm-detuning δ_{205}, namely as many as repetitions of the detuning scan, more than one strategy is conceivable for calculating the signals $S\%(\delta_{205})$ in the next step:

1. At first glance, the most straightforward approach seems to be to cluster all measurements with similar parameters and to calculate the signals $S\%(\delta_{205})$ from the mean of these grouped integrals. For the "205+243_243" distribution, the signals $S\%(\delta_{205})$ would, for example, be calculated from the averaged integrals $\bar{f}^{(205+243)}(\delta_{205})$ and $\bar{f}^{(243)}(\delta_{205})$ of the individual values $f_i^{(205+243)}(\delta_{205})$ (all orange points, labelled "205+243") and $f_i^{(243)}(\delta_{205})$ (all green points, labelled "243"), respectively, that belong to the same 205 nm-detuning value δ_{205}. Finally, the signals $S\%(\delta_{205})$ were then given by $S(\delta_{205}) = 1 - \bar{f}^{(205+243)}(\delta_{205})/\bar{f}^{(243)}(\delta_{205})$, pursuant to Eq. (4.1).

   The central problem with this approach is, however, the fact that it implicitly assumes long-term stability of the experimental conditions, i.e., stable laser performance or constant SSPALS intensity over the entire measuring period. This is, however, an undue simplification since, in real experiments, the signals are subject to temporal drifts due to multiple causes and on different time scales. The most noteworthy factor in this regard is the ageing of the e^+ moderator, which results in a constant reduction in positron and thus Ps numbers over time. The fluctuations and long-term trends of the SSPALS intensity of course directly translate to equivalent variations of the integrals f, as shown in the lower panel of Fig. 4.21. In addition, the different measurement configurations are typically subject to individually different drifts, i.e., in the example, the green points follow another trend than the orange points. Even if these differences are in fact rather small, it is necessary to take them into account since the (possibly small) cooling-recoil effect can only be verified if the measurement and its analysis are performed at the highest possible level of precision.

   A second problem of this approach of averaging the clustered integrals for $S\%$-calculation is the fact that it overly reduces the data, in the sense that it smoothes out all subtleties and local features that possibly appear in the measurement. This also counteracts the target of achieving the highest possible precision.

2. To circumvent both problems and take into account both long-term trends and all local peculiarities, it seems much more appropriate to reverse the steps of clustering and $S\%$-calculation. Instead of calculating the signals $S\%(\delta_{205})$ from the mean of all integrals of the runs with similar parameters, in this approach the $S\%(\delta_{205})$ values are evaluated from individual signals $S_n\%(\delta)$ of each pair of runs belonging to the two measurement classes to be compared (i.e., one from "205+243" and the corresponding one from "243" in the above example). The individual integrals $f_i(\delta_{205})$ would thus be directly transformed to individual signals $S_n\%(\delta_{205})$ instead of first being averaged and subsequently processed into total signals $S\%(\delta_{205})$. To protect the calculation of the $S_n\%(\delta_{205})$ values from being affected by the trend of the data, it is important to use those two runs for calculation of each $S_n\%(\delta_{205})$ value which lie closest together in time. For this reason, this approach is also referred to as *closest-time analysis*.

   In more concrete terms, for the above example (the "205+243_243" distribution) the closest-time analysis consists of the following steps:
   (1) Building pairs n of single "205+243" and "243" runs (i.e., combining a green and corresponding orange dot in Fig. 4.21);
   (2) Calculating the individual signals $S_n\%(\delta_{205})$ from the corresponding integrals $f_i^{(205+243)}(\delta_{205})$ and $f_i^{(243)}(\delta_{205})$;
   (3) Clustering all $S_n\%(\delta_{205})$ that belong to the same probe detuning δ_{205}; and finally
   (4) Processing them into total signals $S\%(\delta_{205})$ which can eventually be used to build the Ps velocity distribution.
   It should in this context be noted that the conversion of the individual signals $S_n\%(\delta_{205})$ into a total signal $S\%(\delta_{205})$ does not necessarily have to be based on standard averaging. Any other averaging technique is possible as well, such as the use of rolling averages. However, in this case error bars should be understood as confidence bands rather than uncorrelated errors.

Even though the closest-time analysis solves the two shortcomings of the first approach, it is still not the best solution. This is primarily because, in a real measurement, it might happen from time to time that single runs have to be discarded ("bad run") due to any malfunction in the experiment, such as problems in the positron transport to the breadbox chamber or failure of laser shutters. Since the $S\%$-calculation always requires a pair of runs, the corresponding counterparts would then also be ignored, which implies that effectively two runs would be lost. Furthermore, there is the intrinsic shortcoming that closest time does actually not mean equal time. Considering the relatively long duration of a single run (almost 2 min), there is an inevitable but non-negligible temporal offset of up to a few minutes (in case of bad runs) between single runs. This asynchronicity additionally reveals that there exists an intrinsic ambiguity in choosing the closest neighbour: Is it the preceding or rather the subsequent run which a specific run should be paired with?

3. The analysis method which therefore proved most expedient and efficient for analysing SSPALS signals of interleaved parameter scans, such as the present one, is the so-called *semi-detrending* technique. After further development and refinement, it was therefore adopted for the analysis of the Ps laser cooling measurements. The semi-detrending technique is a kind of mixture of the two previous approaches, which however avoids all mentioned shortcomings. It takes into account the individuality of each signal $S_n\%(\delta_{205})$ while effectively compensating the main trends in the data caused, for example, by the ageing of the e^+ moderator.

In short, this is achieved by comparing each "positive" run ("205+243" in the above example) to a trend line of the corresponding "negative" one (i.e., reference "243" in the example) instead of comparing averaged values, as in the first approach, or two individual runs, as in the closest-time analysis. The semi-detrending approach thus reduces the data as little as possible to still conserve all subtleties, and as much as necessary to eliminate the temporal drift. This approach proved to be more accurate and suitable for detecting effects in the signal than the full detrending technique which is based on two trend lines, for the negative as well as positive shots.

It is important to point out that there is good reason for using the negatives to evaluate the trend line. This is not only because the features of the negative shots are in general much less diverse since generally less experimental steps are involved. More importantly, especially the features of the positive runs are of interest for the measurement and thus must be conserved. Furthermore, this strategy implicitly mitigates the influence of "bad runs". In case of a faulty positive run the consequence is just the loss of a single run and in case of a faulty negative one it is legitimate to assume that the trend line is only marginally affected.
Moreover, in case of a scan, the scanning parameter appears, by definition, either in both the positive and negative runs, or only in the positive runs. In the latter case it would thus not even make sense to build a trend line as it would partially erase the actual effect of the scan by smoothing the data; not to mention the difficulties in building a trend line at the crossover point to the subsequent scan. Finally, the semi-detrending technique also allows to perfectly satisfy the aspect of simultaneity in the comparison between positive and negative runs. This is due to the continuity of the trend line function, which provides countervalues at all times, in particular also at the time of each positive run.

Semi-detrending technique

The mentioned characteristics of the semi-detrending technique become clearer when the included steps are described in more detail. First of all, the whole data set that belongs to one measurement, consisting of a certain number of detuning scans, is separated into so-called families pursuant to the time of acquisition. In doing so it is not rare that one measurement is interrupted for some time, for the purpose of laser maintenance or recovery of the positron system, for instance. In case of gaps of more than 15 minutes the measurement is then separated into different families to account for the new experimental conditions, perhaps leading to a different negative trend line, for example.
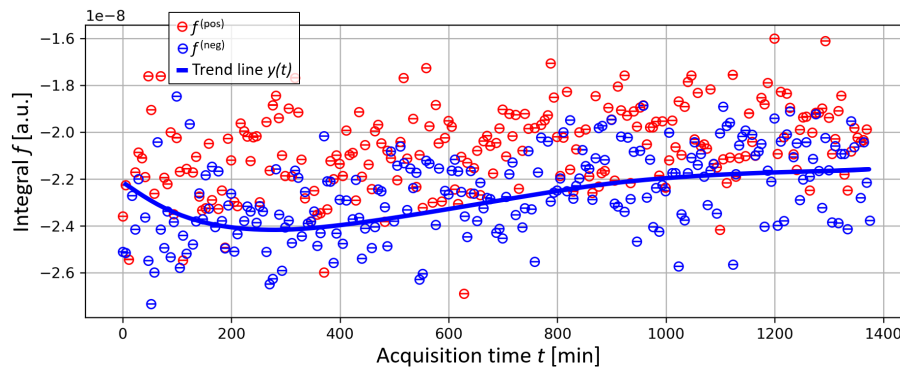
FIGURE 4.22: *Typical evolution of measured SSPALS integrals.* *The red (blue) points are the integrals $f_i^{(\mathrm{pos})}$ ($f_i^{(\mathrm{neg})}$) and the blue line the nth order polynomial trend line fit $y(t)$.*

Next, upon definition of the time window of interest for calculation of the area under the SSPALS signal, the integrals f_i are calculated for each run i. For each family, the individual measurements are then split into negatives and positives, with the negative runs serving as relative background of the positives. The corresponding integrals f_i are accordingly labelled $f_i^{(\mathrm{pos})}$ or $f_i^{(\mathrm{neg})}$ and associated with the time of acquisition $t_i^{(\mathrm{pos})}$ and $t_i^{(\mathrm{neg})}$, respectively. Next, to obtain the trend line in the form of a continuous function $y(t)$, the negative data set $\{t_i^{(\mathrm{neg})}, f_i^{(\mathrm{neg})}\}$ is fitted with an appropriate interpolation function. In general, this is a polynomial function with maximum order $\alpha = \sqrt{N}$, where N is the number of data points in the negative set. The integral of each positive run $f_i^{(\mathrm{pos})}$ is then paired with its corresponding background integral, given by the value of the negative interpolation function $y(t_i^{(\mathrm{pos})})$ at the acquisition time $t_i^{(\mathrm{pos})}$ of the positive run to satisfy the simultaneity condition. The signal $S_i\%$ that belongs to this positive run i is finally calculated according to Eq. (4.1) as

$$S_i = \frac{y(t_i^{(\mathrm{pos})}) - f_i^{(\mathrm{pos})}}{y(t_i^{(\mathrm{pos})})} = 1 - \frac{f_i^{(\mathrm{pos})}}{y(t_i^{(\mathrm{pos})})} \ , \qquad (4.2)$$

which is referred to as the actual semi-detrending operation. For illustration, Fig. 4.22 shows a typical evolution of the integrals f for a real measurement as well as the nth order polynomial trend line fit $y(t)$, represented by the solid blue line.

To offer the highest degree of flexibility in post-processing the data based on the list of individual signals $S_i\%$, each $S_i\%$ value is associated with the metadata information of the corresponding positive run. This includes, inter alia, the run number, the acquisition time and several kinds of time stamps, but also all recorded parameters of the positron and laser systems such as laser shutter states, energies and wavelengths. In this way, the data can subsequently be renormalised with respect to the pulse energies for instance, or for classification by scan parameters such as laser delay or detuning.

The latter is essential for the last step, in which the resulting dictionary of signals $S_i\%$ plus metadata is eventually used to construct the final histogram of interest. The velocity distribution is for example obtained by plotting the $S_i\%$ values versus the probe detuning δ_{205}. For timing scans (which are performed for fixed detuning, typically on resonance, $\delta_{205} = 0\,\mathrm{nm}$) the signals are plotted as a function of the according laser delays. Different methods are finally conceivable for plotting. Typically, the data sets are transformed to histograms using moving averages, or sometimes K-means clustering, to take into account the non-infinite resolving power of probing caused by the 205 nm-bandwidth. All plots of the measurement results presented in the following, are based on rolling averages with square windows of 20 pm width, equivalent to a resolution of few tens of GHz. All error bars represent 68% confidence bands rather than uncorrelated errors.

4.4 Experimental results of Ps laser cooling

The overall measurement campaign was launched by a set of preparatory measurements to create best conditions for the actual cooling measurements subsequently. The purpose of these measurements was to optimise all parameters, especially the laser timings. In addition, the value of the cooling pulse length measured with the photodiode was verified by means of the SSPALS technique in order to make sure that the entire pulse ultimately also reaches the atoms. Finally, a dedicated scan was performed to study the saturation of the cooling transition.

4.4.1 Preparatory measurements

Laser timing optimisation

As described in Sec. 4.2.4, the timing of the laser pulses was calibrated using their rising edges in the photodiode signal. However, this method does not give any feedback on whether the calibrated timings are also the optimum values with respect to Ps-laser interaction. For this reason, the timings determined in the calibration procedure were verified by means of SSPALS measurements, which give the most direct insight into the actual excitation efficiency. Of course, in principle, it would have been possible to calibrate the FPGA directly based on the laser interaction response. However, without any rough indication of the initial offset, calibration via SSPALS requires scanning the pulse timings over a very large range. Considering the excessively long duration of such a scan and the resulting blocking of the apparatus for other measurements, this is not the most appropriate approach. For this reason, the calibration was performed by means of the very fast photodiode, yielding useful results with regard to the Ps-laser interaction. For the fine-tuning via SSPALS, scanning of the respective timing parameters could then be restricted to a very small range near the calibrated values. It should be mentioned that in each scan the laser-ON-measurement was followed by a corresponding laser-OFF-measurement with similar parameters but without laser light, as required for the calculation of $S\%$.

Cooling pulse delay with respect to Ps formation

In the first step, the relative delay between the cooling pulse and positronium formation was optimised by scanning the timing Δt_{CNI} of the *CNI* laser over a range from $-8\,\mathrm{ns}$ to $22\,\mathrm{ns}$, in steps of $3\,\mathrm{ns}$, where a timing of $0\,\mathrm{ns}$ means coincidence of laser and Ps peak, as previously found in the calibration procedure. The detuning was set to zero to drive the cooling transition on resonance and maximise the excitation rate and thus also the signal $S\%$. The scan was repeated twelve times. During the whole measurement, the probe laser was turned off, which means that the detected $S\%$ signals are entirely based on the contribution of magnetic quenching of $n = 2$ states to the detector signal. It should be noted that quenching is the most suitable tool for this laser timing check as it is the best indicator for the $n = 2$ excitation efficiency.

For each of the 180 runs (12 repetitions $\times$ 15 delays) the resulting $S\%$ values were plotted as a function of the requested delay values (light green points in Fig. 4.23), with error bars that result from the fit of the trend line to the negative data. The dark green points represent the mean (with error bars) of all $S\%$ values belonging to the same delay. It can be observed that the calibrated *CNI* timing leads to a maximum $S\%$ signal and thus does not have to be modified further. For negative delay no excitation takes place, confirming that the coincidence of cooling pulse and Ps peak found in the oscilloscope signal agrees with real conditions. However, the plot also shows that for delays above $t \approx 0\,\mathrm{ns}$, the signal still remains on a relatively high level, suggesting that the $n = 2$ excitation efficiency is not very sensitive to the delay of the cooling pulse relative to the Ps emission time. This result is to be expected, considering that it is no longer crucial to control the delay of the laser pulse on a single nanosecond time scale if the transition is saturated for $26\,\mathrm{ns}$ ($=$ typical pulse length), provided that it interacts with the Ps cloud within the first $(10 - 20)\,\mathrm{ns}$ after formation where the number of annihilated atoms is still low and the Ps intensity high.
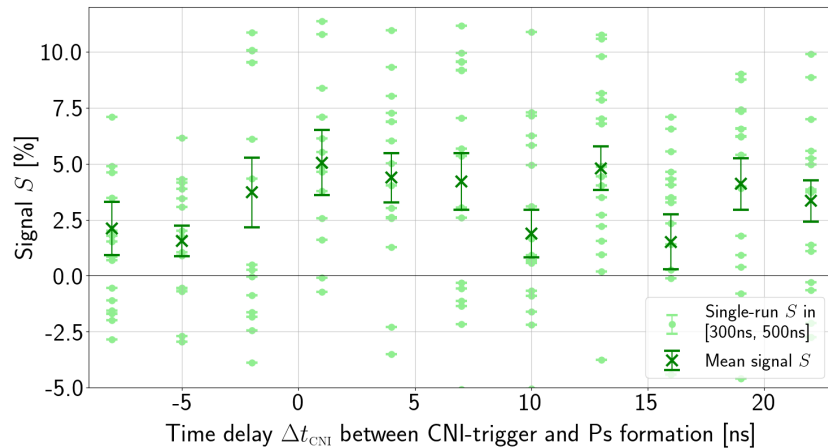
FIGURE 4.23: *Signal $S\%$ as a function of the delay Δt_{CNI} of the 243 nm-laser pulse with respect to Ps formation.* *Scan of the timing of the rising edge of the 243 nm-pulse relative to the calibrated time of the para-Ps annihilation peak in the SSPALS spectrum. To this end, the delay Δt_{CNI} of the trigger to the CNI laser for generation of the 243 nm-pulse was scanned 12 times over the range from -8 ns to 22 ns in steps of 3 ns. The light green points are the individual $S\%$ signals of each single run, referenced to the laser-OFF background and based on the areas under the SSPALS signal in the time window $[300\,\text{ns}, 500\,\text{ns}]$ after the initial prompt Ps annihilation peak. The error bars are the error of the trend line fit to the negative background data. Dark green crosses indicate the mean and standard deviation of all individual signals belonging to the same timing value Δt_{CNI}. The 243 nm-detuning was set to zero and the probing laser was blocked to detect the pure $n = 2$ quenching signal.*

Relative delay between cooling and probing

Next, the relative delay between the cooling and probing pulses, which was calibrated based on the coincidence of the rising edges of the UV-pulses in the photodiode signal had to be checked also via SSPALS and a similar timing scan. For this purpose, several approaches are conceivable. The most intuitive one is to optimise the delay based on the final sequence for Ps laser cooling (cf. Sec. 4.1.2). This method is, however, not the most expedient one for identifying the probe delay with sufficient accuracy, on the nanosecond time scale. This is due to the fluctuations in the cooling pulse length but also because the signal acquired in this way, i.e., based on probing the ground state population, does not change on the (sub-)nanosecond time scale considering that the annihilation-induced reduction in Ps numbers takes place on the 142 ns-time scale.

Therefore, another approach was taken which does not start from a ≈ 30 ns delay of probing with respect to cooling, as in the measurement schedule, but rather on the actual coincidence of the two laser pulses. The easiest way to realise this is to directly probe the total $n = 2$ excited state population instead of the ground state population subsequently to cooling. For this purpose, the probing scheme was slightly modified and the laser system reconfigured in the following reversible way. Instead of using the two probing pulses at 205 nm and 1064 nm to photoionise the ground state atoms via the $n = 3$ level, the UV-line was blocked and the IR-pulse frequency-doubled to 532 nm by inserting an appropriate SHG-crystal into the final 1064 nm-beam line to selectively photoionise only the $n = 2$-atoms excited by the cooling pulse. It is important to point out that this operation does not have any impact on the timing of the pulse or its length. The 532 nm will interact with the atoms at exactly the same time as the two pulses at 205 nm and 1064 nm since all are generated by the same pump laser[22].

In this configuration, the cooling pulse was set to the optimum timing relative to Ps formation

---

[22] For the same reason it is in fact not necessary to verify the relative timing between the two probing pulses at 205 nm and 1064 nm. Since they both originate from the same beam that pumps the entire setup, they will both enter the experiment at exactly the same time, unless one of them is delayed artificially by means of any additional optical elements, which is however not the case here.
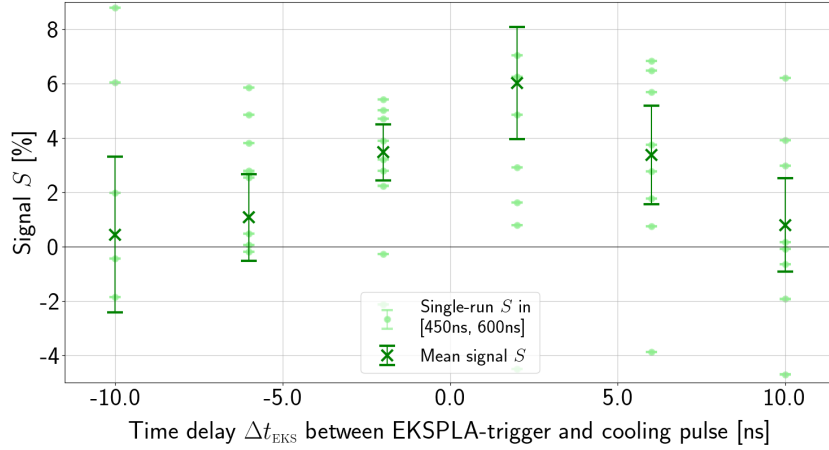
FIGURE 4.24: *Signal $S\%$ as a function of the delay Δt_{EKS} of the EKSPLA laser relative to the CNI laser.* *Scan of the relative timing between cooling and probing laser pulses with respect to the time of coincidence, calibrated by means of the photodiode signal. For this scan, the delay Δt_{EKS} of the trigger to the EKSPLA laser was scanned 10 times over the range from -10 ns to $+10$ ns in steps of 4 ns. The same colour code as in Fig. 4.23 was used. The 243 nm-pulses were configured as short pulses and their detuning set to zero. The 205 nm-beam line was blocked and the IR-pulse frequency-doubled to 532 nm to selectively photoionise the excited $n = 2$ population.*

and the timing Δt_{EKS} of the *EKSPLA*-trigger was scanned between -10 ns and $+10$ ns, in steps of 4 ns, with respect to the calibrated time of coincidence. The detuning of the 243 nm-pulse was set to zero. To facilitate the determination of the largest temporal overlap of the pulses, which is where the $S\%$ signal is maximised, the 243 nm-pulse length was set to the "short" configuration $(7 - 8$ ns in length) by modifying the angle of the half-wave plate in front of the beam expander (cf. Fig. 4.9) such that the pulses do not enter the stretching cavity.

The $S\%$ values resulting from ten scan cycles (using the "OFF" measurement as reference) are presented in Fig. 4.24, where the light green points again indicate the individual signals of each run and the dark green ones the mean value for each delay Δt_{EKS} between *EKSPLA*-and *CNI*-trigger. The plot clearly shows that the highest signal is obtained for a delay of about $+2$ ns. To take this slight temporal offset into account in the measurements, the FPGA was reprogrammed by postponing the *EKSPLA*-trigger by 2 ns. It should be noted that, due to the fact that the "OFF" configuration was selected as background for calculation of $S\%$, the signal will never completely drop to zero but rather converge to a constant level due to quenching. Since short pulses were used, this quenching background is, however, lower ($\approx 1\%$ in the experimental conditions at the time of this measurement) than for the long pulse (up to 5%).

Relative delay between lasers and Ps formation

To fine-tune the common delay of the laser pulses relative to Ps formation, the laser trigger timings Δt_{L} were scanned simultaneously (i.e., by delaying the triggers in lockstep, with fixed relative timing between all laser pulses) with 7.5 ns step size over the range from -50 ns to $+100$ ns with respect to the calibrated coincidence of the prompt Ps annihilation peak in the SSPALS spectra and the rising edge of the laser pulses. The 243 nm-pulse was again configured as a "short" pulse, the 205 nm-beam path blocked and the 1064 nm-pulse frequency-doubled to 532 nm. With zero relative delay between the two laser system, this excitation scheme probes the ground state population via selective photoionisation of the $n = 2$ level at each delay Δt_{L}. A maximum signal is therefore expected at the time when the lasers excite the earliest part of the long tail of ortho-positronium decay.

Fig. 4.25 shows the distribution of the $S\%$ values resulting from 15 iterations of this scan (in the
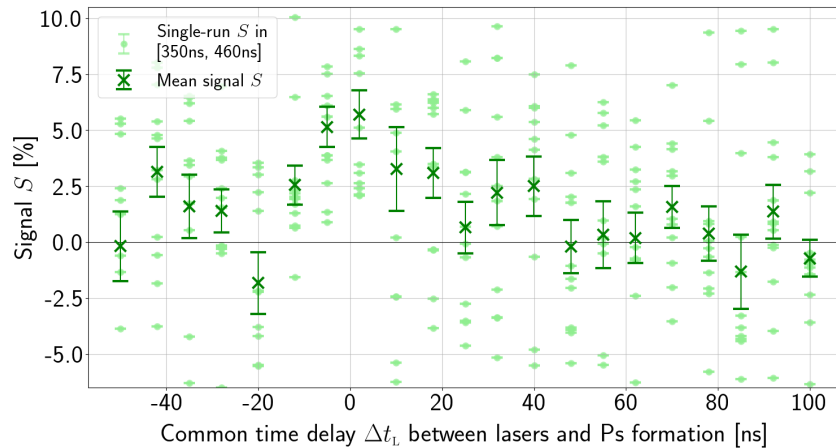
FIGURE 4.25: *Signal $S\%$ as a function of the delay Δt_{L} of the laser pulses with respect to Ps formation.* *Scan of the common delay Δt_{L} of the laser pulses with respect to the time of the Ps annihilation peak in the SSPALS spectrum. The delay Δt_{L} of the laser pulses was scanned* 15 *times between* $-50\,\mathrm{ns}$ *and* $+100\,\mathrm{ns}$ *in steps of* 7.5 ns. *The colour code is similar to Fig. 4.23. The time interval* $[350\,\mathrm{ns}, 460\,\mathrm{ns}]$ *was chosen for the calculation of* $S\%$. *The* 243 nm-*pulses were configured as short pulses and both the* 243 nm-*detuning and the relative delay between the laser pulses were set to zero. The* 205 nm-*beam line was blocked and the IR-pulse frequency-doubled to* 532 nm *to selectively photoionise the excited* $n = 2$ *population.*

usual colour code and laser ON runs again referenced to the corresponding "OFF" measurements for $S\%$ calculation). It is clearly visible that the calibrated FPGA schedule is confirmed by the SSPALS measurement. The maximum signal is obtained at zero delay Δt_{L}, i.e., for the calibrated coincidence of both laser triggers. This furthermore confirms the outcome of the first scan of only the timing of the cooling laser. It should be pointed out that the rather low overall signal strength observed in the present scan was due to a mispositioning of the Ps converter target at the time of this measurement. Realignment of the target with respect to the height of the positron beam and, subsequently, of the laser beams with respect to the target led to a recovery of the usual signal strength for the following measurements.

Cooling pulse length measurement via SSPALS

Similar to the laser timings, the cooling pulse length measured by means of the photodiode (see Fig. 4.10) was also checked by means of an SSPALS measurement. This was necessary because finally it is the period of Ps excitation instead of the pulse length detected by the photodiode which determines the effect of cooling. This measurement in fact not only verifies the pulse length but at the same time the temporal and geometric overlap between the laser beam and the Ps cloud. For this measurement, the 243 nm-laser was again set on resonance with zero delay relative to the Ps peak in order to maximise the excitation rate to $n = 2$. The HWP in front of the stretching cavity was set back to the setting for generation of long pulses. The probing setup was again configured such that only IR-pulses at 532 nm were directed to the experiment to selectively photoionise the atoms excited by the cooling laser. In this setting, the probing IR-pulse was scanned over the 243 nm-pulse in order to determine the time span of excitation of the cooling transition. The delay t_{phion} between the pulses was scanned from $-15\,\mathrm{ns}$ to $+45\,\mathrm{ns}$ in step sizes of 2 ns in the centre and 3 ns on the edges of the scanning range.

The result of this scan is presented in Fig. 4.26, where blue crosses represent the mean $S\%$ signal of 30 pairs of laser ON/OFF measurements acquired consecutively for each delay $\Delta t_{\mathrm{phion}}$. The error bars are the standard deviation of the corresponding 30 individual signals. Similarly to Fig. 4.10, the plot additionally contains three Gaussian pulses (dashed orange lines) as a guide to the eye, indicating the result of pulse extension due to the use of the stretching cavity. The
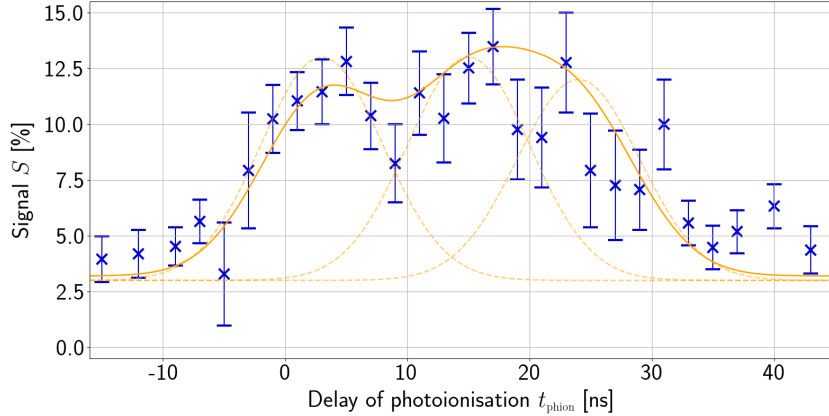
FIGURE 4.26: *Signal $S\%$ as a function of the $532\,\text{nm}$-laser delay over the temporal shape of the $243\,\text{nm}$-pulse.* *To determine the duration of Ps excitation to the $n = 2$ level via SSPALS, the $205\,\text{nm}$-beam path was blocked and the $1064\,\text{nm}$-pulses frequency-doubled to $532\,\text{nm}$ to selectively photoionise the population excited to the $n = 2$ level by the $243\,\text{nm}$-pulses fired at $t = 0\,\text{ns}$ with zero detuning. While scanning the relative delay Δt_{phion} between $532\,\text{ns}$- and $243\,\text{nm}$-pulses over the range from $-15\,\text{ns}$ to $+45\,\text{ns}$, in steps of $2\,\text{ns}$ in the centre and $3\,\text{ns}$ on the edges, 30 pairs of laser-ON/OFF data points were acquired for each delay Δt_{phion}. The blue crosses with error bars are the mean and standard deviation of the resulting 30 individual signals. As a guide to the eye the three dashed Gaussian curves in orange indicate the three pulses emitted from the stretching cavity, extending the overall pulse length to $26\,\text{ns}$ on average (represented by the solid orange line that sums up the three individual pulses).*

comparison of the measurement data to the sum of these three pulses (solid orange line) reveals that the SSPALS results agree well with the modelled pulses. This is clear evidence of proper temporal and geometric alignment, which is a key condition for converting the entire energy transferred by the $\approx 26\,\text{ns}$-long pulse into Ps-laser interaction.

It is worth noting that in this scan the signal on each side again does not approach zero but a constant level of about 4% due to the fact that the laser-OFF measurement was chosen as background, producing a constant quenching-induced offset of the whole measurement, independently of probing.

Saturation curve of the $1^3\text{S} \leftrightarrow 2^3\text{P}$ transition

As a final preparatory measurement, the SSPALS technique was used to study the saturation of the $1^3\text{S} \leftrightarrow 2^3\text{P}$ transition as a function of the energy of the $243\,\text{nm}$-pulses in the given experimental configuration. For this measurement, the cooling pulse was timed to coincide with beginning Ps formation, i.e., the time when the prompt annihilation peak in the SSPALS curves reaches its maximum, and set on resonance to maximise the signal-to-noise ratio. Experimentally, the saturation curve, or the excitation efficiency, respectively, can only be determined by probing the number of atoms excited to the $n = 2$ state. For this reason, the probing laser system was again configured such that it emitted only $532\,\text{nm}$-pulses to selectively photoionise the $n = 2$ population. The relative timing between excitation and probing was set to the optimum value found before.

As far as the adjustment of the energy of the $243\,\text{nm}$-pulses is concerned, which is required to explore the saturation curve, several methods are conceivable in the given laser setup. Examples are the insertion of reflective neutral density filters with different optical densities or modulation of the voltages of the *CNI*-power supply. However, to ensure unaltered laser pulse generation conditions throughout the whole measurement, none of the laser control settings were modified. Instead, the energy was tuned by means of the half-wave plate in front of the beam expander (cf. Fig. 4.9 on p. 79) while internally blocking the pulse stretching cavity. This allows to continuously
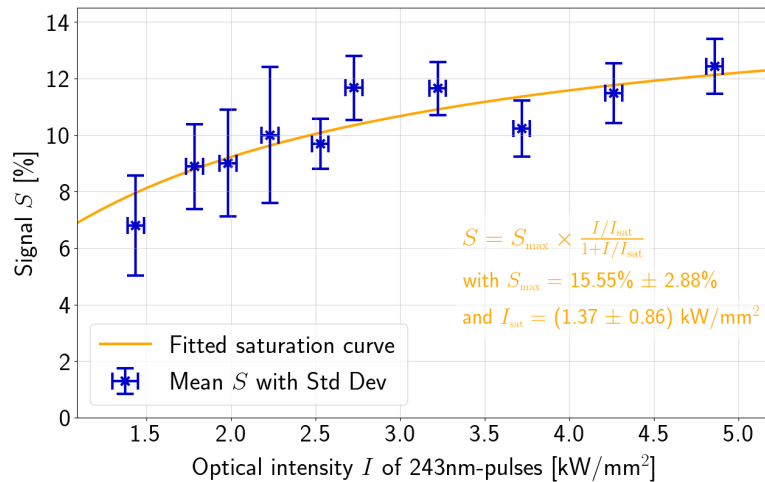
FIGURE 4.27: *Saturation curve of the $1^3S \leftrightarrow 2^3P$ transition in Ps by means of the SSPALS technique.* *The blue data points show the mean of* 40 *individual S% signals, each resulting from a pair of laser ON/OFF measurements via SSPALS (where laser ON represents photoionisation via the $n = 2$ level using coinciding laser pulses at* 243 nm- *and* 532 nm) *for ten different pulse energies between* $\approx 300\,\mu J$ *up to almost* 1 mJ. *For better comparability, the energies were converted to optical intensities based on the given laser beam parameters. The vertical error bars represent the standard deviations of the mean values and the horizontal ones the intensity range corresponding to the reading error of the power meter. The orange line is the weighted curve fit of the data with a saturation function in the form specified in the bottom right-hand corner, with the resulting fit parameters including fitting errors (one standard deviation).*

reduce the pulse energy by controlling the ratio of energy reflected by the PBS or dumped in the cavity. Another advantage of this method is that the HWP is motorised, which means that the adjustment can be carried out entirely remotely to avoid a potentially detrimental mechanical impact of manual interventions. Needless to say, the use of this technique for energy modulation implies that the 243 nm-pulses are directed to the experiment as short pulses.

With these settings, 40 alternating data pairs of laser ON/OFF configuration were acquired for ten different 243 nm-energies in the range from $\approx 300\,\mu J$ to almost 1 mJ. The means of the 40 resulting $S\%$ signals for each energy value are plotted as blue points in Fig. 4.27, together with their standard deviations, as a function of the optical intensity I. To this end, the pulse energies were converted to optical intensities I according to $I = 2P/A$ where $P = E/\tau_{\mathrm{pulse}}$ denotes the optical power of an equivalent cw-laser that provides similar optical intensities. $A = \pi ab$ is the cross-sectional area of the elliptical beam with half-axes a and b. The calculation is based on the characteristics of the beam used for this measurement, in particular $\tau_{\mathrm{pulse}} = 7$ ns, $a = 6.5$ mm and $b = 2.8$ mm (cf. Fig. 4.15). The horizontal error bars indicate the error of the values read on the power meter, which typically fluctuate by about $\pm 10\,\mu J$.

In this context, it is important to point out that the intensity values in the plot do not represent the amount of energy finally available for Ps excitation, since the energy was recorded by means of the automated power meter in the 243 nm-setup ("En243" in Fig. 4.9). It can be assumed that only a maximum fraction of about 75% of the energy finally reaches the target location due to transport losses and attenuation during viewport transmission. It is furthermore worth mentioning that the energy in the short pulse configuration is generally higher than in the corresponding temporally stretched state, even in case of similar properties of the initial beam in front of the PBS. This can be attributed to the losses that accrue while the beam passes the pulse stretching cavity.

The signals obtained in this way were fitted[23] with a saturation function (orange curve) of the

---

[23] In order to account for the non-uniformity of the standard deviations, the data was weighted for the fit, using the inverses of the corresponding variances as weights. In this way, more weight is given to more precise values.

form

$$S = S_{\text{max}} \times \frac{I/I_{\text{sat}}}{1 + I/I_{\text{sat}}}$$

based on the saturation model derived in Section D.5, according to which the excited state population shows this functional dependence on the saturation parameter $s = 2\Omega^2/\Gamma_{\text{ge}}^2 = I/I_{\text{sat}}$ for $\delta = 0$ (cf. Eq. (D.37)). Since in case of photoionisation of the $n = 2$ level, the signal S effectively quantifies the gain in excited state population in the laser ON case compared to that without lasers, S can be expected to show this dependence on the intensity I.

The most important result of this measurement is that the measured signals show a clear saturation behaviour. For intensities above $\approx 2.5\,\text{kW/mm}^2$ (as displayed on the power meter) the $S\%$ values, and thus the fraction of excited atoms, can no longer be increased significantly. According to the fit, they instead approach a maximum value of 15.6%. This maximum signal level depends on a number of factors, the most important of which are the different kinds of alignments involved. Besides the most obvious ones, such as the alignment of the target relative to the positron beam and the geometric and temporal overlaps between the laser beam and the Ps cloud, also the spectral coverage of the Doppler velocity distribution by the laser spectrum plays a crucial role. As far as the timing is concerned, a 7 ns-long laser pulse is, for example, not capable of catching all atoms leaving the target, considering the temporal spread of about 10 ns (FWHM) of the Ps formation process. The fastest atoms might furthermore escape from the laser interaction region (defined by the laser beam waist) even before the laser pulse ceases. This limits the interaction period and thus the average dwell time in excited states as well as the photoionisation efficiency for these atoms. With regard to the spatial overlap it must be assumed that the overlap of the crossed 243 nm- and IR-laser beams cannot cover the whole Ps cloud even in the optimum case. Finally, the maximum signal strength also depends on the employed laser system. With regard to the present experimental setup this means that the maximum signal depends on whether the atoms are photoionised via the $n = 2$ or $n = 3$ level, which is simply given by the different characteristics of the corresponding UV-laser beams.

In this context, it is worth noting that in the measurements performed in the course of this thesis, signals of maximally 18% have been observed, albeit only for optimum temporal overlap of the photoionisation pulse and the Ps cloud. For a delay of 30 ns, as it is the case in the cooling scheme, $S\%$ values did not reach more than about 15%.

The plot in Fig. 4.27 furthermore reveals a clear agreement of the measurement outcome with the theoretical model. Except for two data points the fitted curve passes very near the mean values or at least well through the error bars. This qualitative agreement can also be confirmed in quantitative terms. At first glance, the experimentally determined value of $I_{\text{sat}} = 1.37\,\text{kW/mm}^2$ might seem disproportionately high, considering the theoretically predicted effective saturation intensity of $I_{\text{sat,L}} = 11.79\,\text{W/mm}^2$ for a laser bandwidth of 129.45 GHz FWHM (cf. Eq. (D.42)). This mismatch by two orders of magnitude can, however, be entirely ascribed to an incompleteness of the theoretical model. The decisive weakness of the latter is the fact that it assumes excitation of stationary atoms and thus does not account for the huge Doppler broadening of the transition line.

Taking this effect into consideration, the expression for the saturation intensity must be slightly modified. As derived in Ref. [117], based on a rate equation approach for the incoherent excitation process, the saturation fluence F_{sat} for Ps atoms with Doppler-broadened transition lines in magnetic fields is instead given by

$$F_{\text{sat}} = \frac{c^2}{B} \sqrt{\frac{2\pi^3}{\ln 2}} \frac{(\Delta\lambda)_{\text{Doppler}}}{\lambda_0^2} \ , \tag{4.3}$$

where B denotes the Einstein B-coefficient, $(\Delta\lambda)_{\text{Doppler}}$ the FWHM of the Doppler linewidth and λ_0 the resonance wavelength. For a pulse length of 7 ns this finally yields a saturation intensity of $I_{\text{sat}} = 644.86\,\text{W/mm}^2$. Considering the mentioned alignment imperfections and the quite significant fitting error, the experimental value, obtained from the saturation curve fit, is thus well in line with the theoretical predictions.

In summary, the key message of this measurement is the fact that the available laser source easily achieves the saturation of the $1^3\mathrm{S} \leftrightarrow 2^3\mathrm{P}$ transition, providing typical pulse energies of more than $600\,\mu\mathrm{J}$ (equivalent to about $3\,\mathrm{kW/mm^2}$). This finding is of vital importance with regard to the laser cooling experiment, as saturation is a crucial prerequisite for efficient cooling.

Based on the results of the optimisation procedure described above, the experiment could finally be configured for the actual laser cooling measurements. For this purpose, the cooling laser system was first of all reset to long pulse generation. Furthermore, the probing laser system was reset to the configuration required for the cooling scheme, i.e., the $1064\,\mathrm{nm} \to 532\,\mathrm{nm}$ SHG crystal was removed and the $205\,\mathrm{nm}$-beam path unblocked. As far as the timings are concerned, the cooling laser was scheduled to coincide with the time of Ps generation and the probe laser such that it follows $30\,\mathrm{ns}$ later, i.e., a few nanoseconds after the $n = 2$-laser excitation has come to an end. In the course of the measurements, the energy of the $243\,\mathrm{nm}$-pulses was at all times kept above a minimum level of $600\,\mu\mathrm{J}$ to ensure saturation of the cooling transition.

4.4.2 Experimental results

Definition of objectives and parameter choice

To the best knowledge of the author, the measurements presented in the following represent the first attempt to demonstrate the effect of an optical force on a cloud of positronium atoms in a magnetic field. Since this force acts in a symmetrical way on the velocity distribution, the designed scheme is furthermore intended to demonstrate a cooling effect on the atoms, according to the definition formulated in Sec. 4.1.1. In light of this novel aspect it becomes clear that the primary objective of the experiment was in the first instance a proof of concept of Ps laser cooling in magnetic fields as well as the exploration of the capabilities of the designed experimental scheme.

As the numerical investigations in Chap. 3 revealed, apart from the timing aspects, especially the bandwidth and detuning of the cooling laser play a key role in successful Ps laser cooling. For this reason it is in general worth making every effort to establish optimum conditions with regard to these two laser parameters. In particular, Fig. 3.4 shows that the bandwidth of the cooling pulses provided by the laser system ($\approx 130\,\mathrm{GHz}$ FWHM) does not represent the optimum spectral width for most efficient cooling at Ps temperatures of $\approx 300\,\mathrm{K}$. However, the impact of this discrepancy on the success of cooling also depends on the chosen figure of merit. The numerical results clearly indicate that the temperature parameter T (dashed green vs. orange line in Fig. 3.4) can be reduced significantly in all cases (except for the extreme cases which are not relevant here), whereas the number $n_{\mathrm{r}}^{\mathrm{(ON)}}$ of slow atoms located in the centre of the distribution is slightly more sensitive to an increase in bandwidth above the optimum value. Considering the limited pulse length of $26\,\mathrm{ns}$, the laser interaction can be expected to produce a clear enhancement in $n_{\mathrm{r}}^{\mathrm{(ON)}}$, or at least keep it at a constant level which would not be possible without laser interaction. In this context, it must furthermore be considered that $n_{\mathrm{r}}^{\mathrm{(ON)}}$ represents the number of atoms with velocities smaller than twice the recoil velocity v_{rec}. Especially for large laser detuning it might in fact be more expedient to apply a slightly less restrictive criterion. As an example it is worth mentioning that, using the range $v < 5v_{\mathrm{rec}}$, the simulation predicts an increase of almost 50% in the number of slow atoms after a cooling time of $120\,\mathrm{ns}$ (from 159 for $v < 2v_{\mathrm{rec}}$ to 233 for $v < 5v_{\mathrm{rec}}$) for standard parameters $\delta = -2.5\,\mathrm{cm^{-1}}$, $\Gamma = 2\pi(75\,\mathrm{GHz})$ and $N = 2000$.

Based on these results and considering the proof of concept strategy of the measurements, it was, for the time being, deemed appropriate to refrain from any attempt to modify the bandwidth and instead initiate the measurements with the existing parameters. As mentioned in the context of the experimental setup, this decision was also taken in view of the fact that corresponding modification measures would involve significant efforts.

The cooling measurements were finally performed for three different detunings of the cooling laser, starting from $+12\,\mathrm{pm}$, equivalent to $-2.0\,\mathrm{cm^{-1}}$, following the suggestions of the numerical studies. It is important to point out that the numerical results can, however, not in all cases be transferred directly and one-to-one to the experimental configuration. This is due to the fact

that theoretical investigations can be based directly on the Ps velocity distribution itself which in experimental measurements can only be accessed and reproduced by means of an additional probe. In assessing an appropriate laser detuning for an experimental realisation the raw distribution can therefore not be viewed in isolation. Rather, it is indispensable to also account for other aspects, especially the resolving power of the probing scheme. In view of the properties of the available probing laser system, i.e., in particular, its bandwidth of $\sigma_{205} = 111\,\text{GHz}$, a 243 nm-detuning of $+12\,\text{pm}$ can therefore be considered almost the lowest reasonable value. With much lower values it becomes very difficult to resolve the effect of the laser interaction on the velocity distribution in detail.

The necessity of an additional probe furthermore implies that the distribution that can be constructed from the measured data is a convolution of the velocity distribution after cooling with the spectrum of the probe laser. In other words, a quantification of the isolated effect of the 243 nm-pulse always requires a deconvolution of the involved spectra.

Based on these considerations, two further detunings were chosen for laser cooling in addition to the value of $+12\,\text{pm}$, namely $+25\,\text{pm}$ and $+42\,\text{pm}$. The idea behind this choice is to facilitate the observation of the effect of laser interaction on the distribution by moving the counter-propagating cooling pulses further apart from each other in spectral terms. The larger the detuning, the more clearly visible the modifications become, albeit at the expense of a reduced cooling efficiency, which is, however, acceptable in view of the proof of concept strategy. In this configuration, the cooling effect is expected to become apparent in the form of a depletion in the velocity regions covered by the lasers and a corresponding enhancement in population in the adjoining regions closer to resonance, as suggested for example in Fig. 3.5.

Finally, the measurement was set up in the fourfold scheme described before and the probe detuning was scanned in steps of $3\,\text{pm}$ over the range of the whole Ps Doppler profile which, at $\approx 300\,\text{K}$ spans roughly $\pm 60\,\text{pm}$ around its central value (in wavelength units of the 205 nm-probe). The scan was typically repeated at least ten times in the described triangular scanning pattern (with alternating ramps in ascending and descending direction) to obtain results with sufficient statistical significance. The whole measurement campaign of Ps laser cooling comprised almost 20 of such measurement series (i.e., ten-fold repetition of 205 nm-detuning scans at fixed 243 nm-detuning). However, due to the complexity of the measurement scheme and the high demands on the setup, only a few of the measurement series were finally successful. This is due to the fact that, experimentally, it is highly challenging to operate a system that consists of several interacting subsystems without failures and to produce stable output over several hours of non-stop data acquisition time. Even the most sophisticated analysis techniques are sometimes insufficient to eliminate all sources of error or fluctuations caused by external influences, such as variations in temperature with several secondary effects. Especially the spatial laser alignment with respect to the target turned out to be one of the most crucial parameters for an efficient exertion and detection of the optical force of the cooling laser. Even slight misalignments on the millimetre-scale, which might occur even in the course of a single measurement series, can lead to significant impairment of the appearance of laser-induced features in the distribution, or even destroy them completely. For this reason, only the results of the best candidate of each of the three 243 nm-detuning categories are presented and discussed below.

Photoionisation scan in the absence of 243 nm-light

The identification of the effects induced by the 243 nm-laser was described in the context of the measurement methodology and the fourfold measurement scheme in Sec. 4.1.4. It requires first of all, to examine the original Ps velocity distribution provided by the employed Ps converter target, i.e., the distribution of Ps atoms without exposure to laser radiation. This distribution is obtained from an analysis of the respective data in the "205_OFF" configuration, where the $S\%$ signals result from the comparison of the "205" runs with respect to the laser OFF background (cf. Fig. 4.5). Due to the layout of the measurement scheme, the data required for this analysis is implicitly included in each measurement series.

Since the UV-probe laser pulses share the same beam path as the counter-propagating cooling pulses, the 205 nm-beam is inevitably arranged in double-pass configuration as well. For this reason, the "205_OFF" photoionisation scan, in which only the probing laser is present, effectively represents a two-photon absorption spectroscopy measurement of the Doppler-broadened $1^3S \leftrightarrow 3^3P$ line of positronium. This is in fact an interesting measurement in its own since, in case of saturation, a Lamb dip is expected to show up in the transition centre, potentially allowing for a Doppler-free study of the transition line. This dip emerges from the competition of the two counter-propagating beams for excitation of the same fraction of atoms. This can easily be understood by visualising the two extreme detuning cases in which the UV-laser is resonant either with the atoms in the centre or the ones on the flanks of the distribution. In the latter case the two laser beams address atoms from different velocity regions, whereas in the first case they compete for atoms from the same velocity class. Consequently, in saturation, the total number of excited (and, in the present detection scheme, photoionised) atoms is reduced for all detunings δ_{205} for which the laser spectra at least partially overlap, with maximum overlap for $\delta_{205} = 0$. As a result, the velocity spectrum exhibits a spectral hole in the centre, which is expected to be as broad as the laser bandwidth ($\sigma_{205} = (110 \pm 30)\,\text{GHz}$), but narrower than the Gaussian width of the Doppler distribution, $\sigma_{\text{Doppler}} \approx 200\,\text{GHz}$ in the present case. This dip is commonly referred to as *Lamb dip* of Doppler-free saturation spectroscopy (not to be confused with the Lamb shift).

Since the presence of the Lamb dip only plays a secondary role in the present measurements, it shall not be discussed and analysed in detail here. It is, however, important to be aware of this phenomenon, as it is expected to become apparent in all Doppler scans carried out in the present measurement scheme with a pair of counter-propagating probe beams. With regard to the cooling measurements, the presence of the dip might even be taken advantage of, as it facilitates the identification of cooling effects in the centre of the distribution. For a properly chosen 243 nm-detuning the Ps-laser interaction produces an enhancement of the population in the (Lamb-dip reduced) central region of the distribution, leading to an increase up to the level of the adjoining regions or even further. The observation of such a "filling" of the hole would already be sufficient proof of successful laser cooling.

An example of this "205_OFF" photoionisation scan is shown in Fig. 4.28. The plotted data results from one of the three "good" measurement series, namely the one in which the detuning of the cooling laser was set to the value $+25\,\text{pm}$. The velocity-resolved $S\%$ signals which make up this distribution, result from the semi-detrending analysis with the "205" runs as positive data and the "OFF" background as negatives used for trend line fitting. The plot was generated by using rolling averages with each of the blue $S\%(\delta_{205})$ values representing the mean of all individual signals $S_i\%$ in the 20 pm-wide wavelength range that symmetrically surrounds the respective probe wavelength value λ_{205}. This choice of bin width is based on the spectral width $\sigma_{205} = 111\,\text{GHz}$ of the probe laser which is comparable to 20 pm in the 205 nm-wavelength space. The step size in the binning procedure was chosen similar to the measurement, where the probe detuning was scanned in steps of 3 pm in the centre. This combination of bin width and step size implies that neighbouring bins partially overlap each other or, in other words, each binned $S\%(\delta_{205})$ value is partially based on the same individual signals $S_i\%(\delta_{205})$ as the three neighbouring values on each side. Error bars represent the standard deviation of the averaged signals.

The distribution shown in Fig. 4.28 represents the typical measurement of a Doppler-broadened velocity spectrum with Gaussian shape, probed by means of a laser with relatively broad bandwidth, saturating the transition and irradiating the atomic cloud in double-pass configuration. Since the distribution is the convolution of the initial Ps velocity spectrum with the spectrum of the probe laser, the width of the curve is approximately the sum of the width of the real distribution and the bandwidth σ_{205} of the 205 nm-probing laser. Based on the measured value $\sigma_{205} = 111\,\text{GHz}$ the curve in Fig. 4.28 allows for a rough estimation of the temperature of the Ps cloud of just below 300 K.

The most prominent feature of the Doppler curve is the characteristic Lamb dip in the centre, which clearly confirms the initial expectation for a saturated $1^3S \leftrightarrow 3^3P$ probing transition. The competition of the two beams for the excitation of the same fraction of atoms leads to considerable
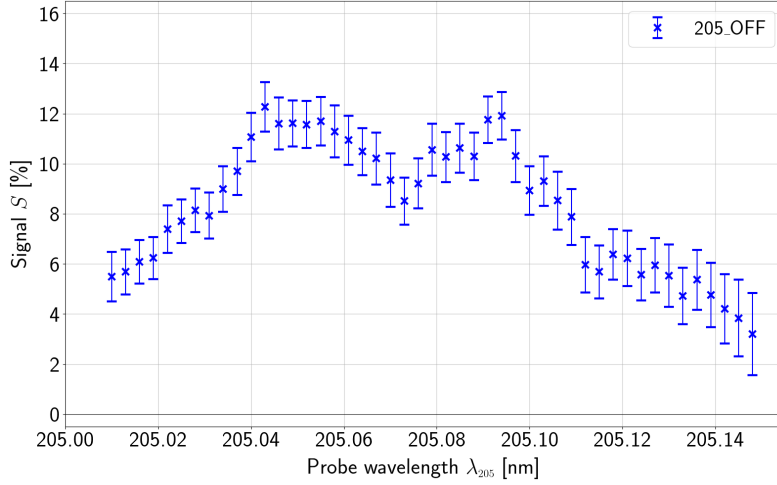
FIGURE 4.28: **Measurement result of a photoionisation scan in the absence of** 243 nm-**light.** *Plot of the binned S% signals with the individual values resulting from the semi-detrending analysis of the SSPALS data of the "205" photoionisation scan with laser OFF runs as background, called "205_OFF". Each of the 3 pm-spaced data points represents the rolling average of all individual signals S_i% within the surrounding wavelength window of width 20 pm. Error bars indicate the corresponding standard deviation. Velocity resolution is achieved by scanning the laser detuning over the whole Ps Doppler distribution and calculating all individual S_i% signals separately, prior to binning. The calculation of the S_i% values is based on integration of the SSPALS signals over the time window between 450 ns and 600 ns. The shown distribution is part of the measurement series with 243 nm-detuning of +25 pm.*

reduction of the signal in the centre, namely by more than a quarter. The appearance of the hole furthermore allows for a clear identification of the resonance wavelength of the transition line of exactly $\lambda = 205.073$ nm (based on the given spectrometer calibration). Apart from the Lamb dip the Doppler curve exhibits a second prominent feature on the falling edge in the wavelength region between 205.10 nm and 205.12 nm, where the curve is slightly attenuated compared to a perfect Gaussian. Further experimental investigations allowed to exclude any additional two-photon effects, as a consequence of unintentional reflections for example, as the cause of this local signal reduction. It was instead concluded that this feature must instead originate from an anisotropy in Ps production which finally leads to a slightly asymmetric distribution.

Results and analysis of the effects of interaction with 243 nm-light

To proceed with the analysis of the effect of the interaction between the Ps atoms and the 243 nm-laser on the unmodified velocity distribution, Fig. 4.29 shows an overview of the measured "205+243_243" distributions for the best result for each of the chosen cooling detunings $\delta_{243} = 12$ pm, 25 pm and 42 pm. Each subplot additionally contains the corresponding "205_OFF" spectrum. All curves included in the figure were generated in the same way as the photoionisation scan in Fig. 4.28, i.e., by applying the same analysis steps to the raw data. While for the "205_OFF" distribution (blue) the signals are based on the "205" runs corrected for the laser OFF background, the "205+243_243" (red) distributions consist of the binned signals of the comparison between each "205+243" run and its corresponding background, the "243" runs. Only this choice of background allows to uncover the pure recoil effect by eliminating the signal induced by the quenching of the $n = 2$ excited state atoms.

Qualitative analysis

By comparing the measurement with the cooling laser (red curves) to the corresponding photoion-isation scan without Ps-243 nm-light interaction (blue curves), it can clearly be observed that

the interaction with the cooling light produces the expected modifications of the initial velocity distribution. While the Ps population is reduced in the regions that are spectrally covered by the laser beams (namely on the flanks of the Doppler curves), the population is increased in those regions to which the atoms are pushed. Although these characteristic effects can be observed for all chosen cooling detunings, they are differently pronounced in each case. The effects become most apparent in the measurement with a detuning of $\delta_{243} = 25\,\text{pm}$. Here, the distribution is modified symmetrically in exactly the expected way with a depletion on the flanks due to a net transfer of momentum and a corresponding velocity change as a result of photon absorption and emission, accompanied by population enhancement in the central region.

For the other two cases the result is much less clear, however. In both measurements, both the red and the blue distributions show a distinct asymmetry. Especially in the $\delta_{243} = 12\,\text{pm}$-case the red curve seems to be shifted significantly to the left compared to the unmodified distribution. Furthermore, while the blue curve still shows a Lamb dip, albeit less pronounced as expected and as well with asymmetric shape, this effect does not appear at all in the red curve. On the other hand, after cooling a clear population depletion can be observed in the relatively broad wavelength region between 205.08 nm and 205.11 nm, while much more atoms can be found in the region between 205.04 nm and 205.075 nm. Both effects are statistically significant with respect to the "205_OFF" case, namely by more than one standard deviation, as for the rising edge in the $\delta_{243} = 25\,\text{pm}$-measurement. This distinctness must however partially be ascribed to the relative shift of the two curves. The more the red curve was shifted to the right, the weaker the depletion on the falling edge would be.

In the $\delta_{243} = 42\,\text{pm}$-case, in turn, the effects are least pronounced. Only a weak depletion is found in the more central region around 205.08 nm. The enhancement which has developed in the wavelength region just below 205.06 nm is also very weak. Additionally, both curves do not exhibit the expected pronounced Lamb dip in the centre of the distribution, at best the red curve gives a hint of the effect.

The observations made in the latter two detuning cases are an indication for a slight misalignment of the laser beam(s). In particular, the pronounced asymmetries in the curves of the $\delta_{243} = 12\,\text{pm}$-measurement might be caused by a situation where the two counter-propagating beams of similar wavelength are not perfectly parallel to each other, as illustrated on the left of Fig. 4.30. The fact that the red curve is shifted to the left is, for example, a hint for a configuration in which the first beam (which acts on the right side of the plotted distribution due to an inversion of wavelength and velocity axes), creates better interaction conditions than the back-reflected one. This is due to the fact that the better the alignment, the stronger the depletion in the spectral region covered by this beam. Therefore, a discrepancy in the alignment of the two cooling beams inevitably manifests itself in a shift of the red curve to smaller wavelength regions with respect to the unmodified distribution.

The asymmetry of the blue curve, as well, is most likely a consequence of slightly misaligned laser beams, in this case of course of the probing beams. Since the signals of the blue curve are produced by the interaction of three beams, it is, however, difficult to identify the exact type of misalignment. In contrast to the two 243 nm-beams, each of which is responsible for cooling a different spectral region of the distribution, it is much harder to distinguish between the individual contributions of each of the two probing UV-beams. Since the probe detuning is scanned over the whole Doppler curve, symmetrically around the centre, each wavelength range is probed twice, first by the red-detuned initial beam and then by the correspondingly blue-detuned back-reflected beam. The observation of higher signals at larger wavelengths is, however, a strong indication of a "walk-off" of the back-reflected beam relative to the (well aligned) first beam, potentially caused by a slightly rotated back-reflecting mirror, for example, as shown in the figure. The angle between the counter-propagating beams causes the back-reflected beam to exhibit a better alignment with the atoms that approach the second beam than with the ones moving away. The alignment with the central fraction is still good enough to produce a (weak) Lamb dip. This implies that the signal produced by the back-reflected beam is higher for red detuning (i.e., larger wavelengths) for which the beam is resonant (due to the Doppler effect) with the
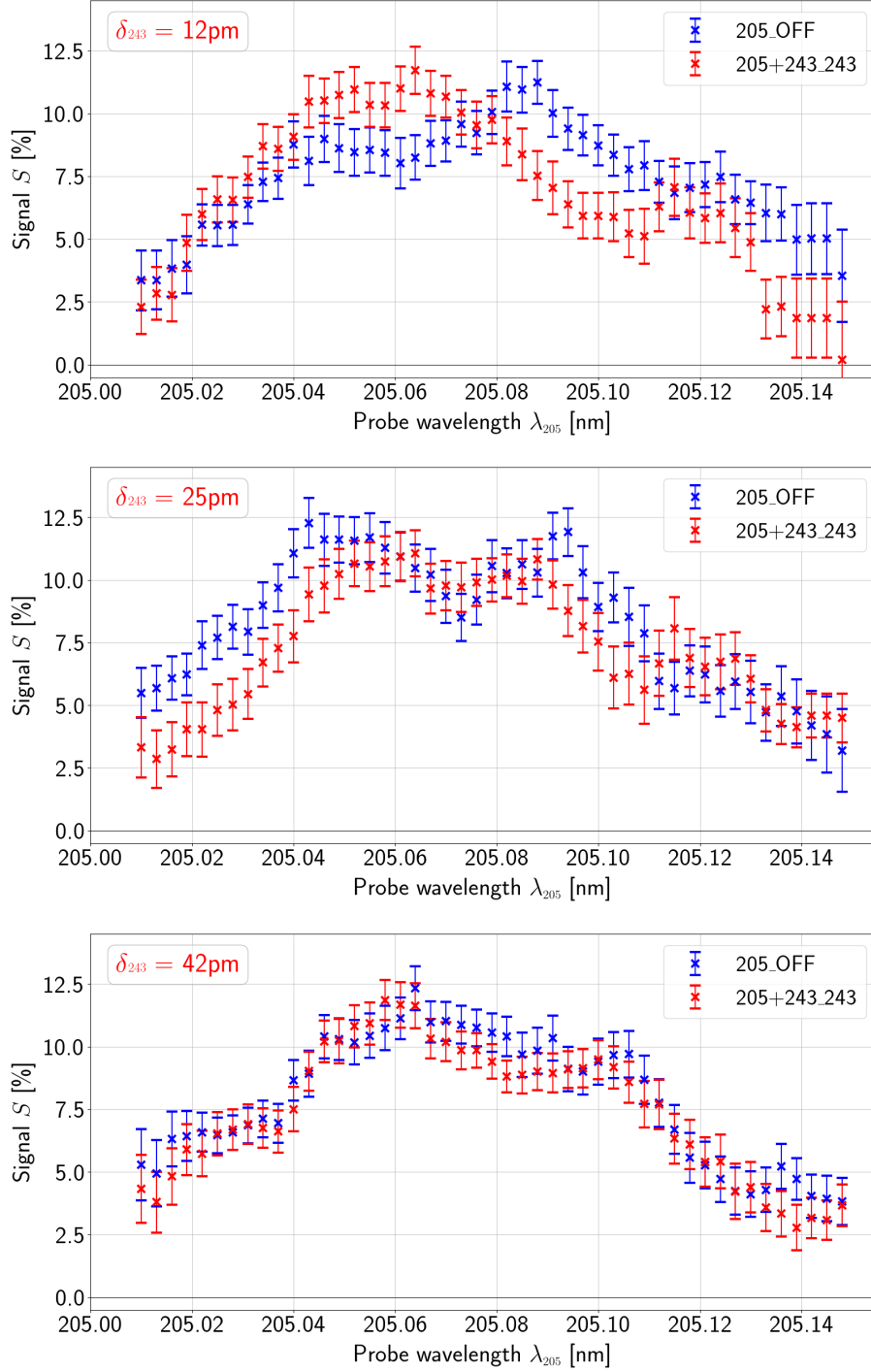
FIGURE 4.29: *Cooling measurement results for three different* 243 nm-*detunings.* *Probed Ps distributions after interaction with the counter-propagating pair of* 243 nm-*cooling beams with fixed detuning (*"205+243_243"*, red data points) and the corresponding reference measurement* "205_OFF" (*blue data points) from the same data set. In contrast to the* "205_OFF" *distribution, the* "205+243_243" *spectrum is based on the* "243"-*background to eliminate the quenching contribution to the S% signals. Results for three different cooling detunings are shown,* $\delta_{243} = 12$ pm *in the top,* $\delta_{243} = 25$ pm *in the middle and* $\delta_{243} = 42$ pm *in the bottom. All shown distributions are based on binned S% signals with individual values* S_i% *resulting from a similar acquisition, analysis and binning procedure as for the distribution shown in Fig. 4.28.*

FIGURE 4.30: *Potential misalignments of laser beams.*
Left: *Misalignment caused by a rotated back-reflecting mirror (exaggerated) which affects both cooling and probing beams (labelled as "Laser Beams").*
Right: *Misalignment caused by an angle between well aligned cooling, but rotated probing beams (exaggerated). More details in the text.*
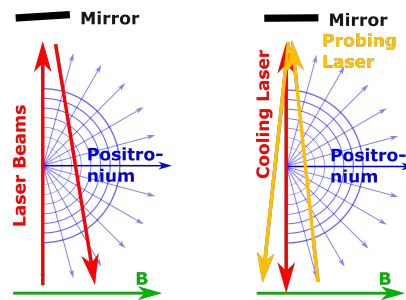
atoms moving towards the laser, than for blue detuning for which the overlap with the addressed fraction of atoms is worse. This explanation is in line with the observed shift of the red curve towards smaller wavelengths, which probably also results from a misaligned back-reflected beam, as described above. It is important to note that the "205+243_243" curve is then affected by both the misaligned probing and cooling beams, since both are involved in the corresponding laser scheme.

With regard to the $\delta_{243} = 42$ pm-case the conclusion is much less clear. The observation of the small region of population depletion at rather larger wavelengths might, for example, be interpreted as a shift of the curve towards lower wavelengths caused by a slightly better alignment of the first-pass cooling beam than of the back-reflected one. This could, however, not be caused by a rotated back-reflecting mirror since then the back-reflected probing pulse would also be misaligned, producing a similar pattern as in the $\delta_{243} = 12$ pm-case, which is obviously not the case. Instead, both curves show the same kind of pattern with generally higher signals at smaller wavelengths. This asymmetry that affects both curves in the same way might be due to a slight misalignment of the probing UV-beam pair caused, for example, by an angle between probing and cooling beams, as (exaggeratedly) illustrated on the right of Fig. 4.30. Even if the cooling pulses are well aligned and create a symmetric distribution after laser interaction, such a slight rotation of the probing UV-beams would also manifest itself in the "cooled" distribution ("205+243_243"), which is probed by exactly the same beam pair as the unmodified one ("205_OFF"). The observation of increased signals at lower wavelengths is an indication of larger overlap with the atoms which move away from the laser as it would be the case for the illustrated configuration. The almost complete absence of a Lamb dip in both curves would support this explanation.

In consideration of the large parameter space of this kind of measurement it is, however, important to avoid jumping to conclusions. There are, in fact, numerous other factors that influence the shape of the measured distribution and could potentially cause asymmetries. The observed imbalance in signals on the low- and high-wavelength side might, for example, also be due to anisotropies in the Ps production or a wavelength-dependence of certain laser parameters such as the energy. Nevertheless, it is difficult to explain shifts or inverse asymmetries between the curves by these factors as they are expected to affect all distributions in the same way. This shows that it is in general impossible to clearly identify the cause of certain imperfections. The spatial laser beam alignment definitely plays a crucial role, though. Even the smallest discrepancies can have serious negative consequences that only become visible in the final measurement result. Identification of the optimum alignment is therefore often the result of trial and error. Even though the $\delta_{243} = 12$ pm- and $\delta_{243} = 42$ pm-distributions qualitatively show clear cooling effects, further quantitative analyses are strongly impeded by the asymmetries observed in these cases. For this reason, the following treatment will be restricted to the measurement result for the 243 nm-detuning of $\delta_{243} = 25$ pm.

Quantitative analysis
As explained in the context of the measurement methodology in Sec. 4.1.4, the identification of the effect of interaction between atoms and 243 nm-pulses is based on a comparison of the distributions with and without cooling laser (i.e., "205+243_243" vs. "205_OFF"). For this
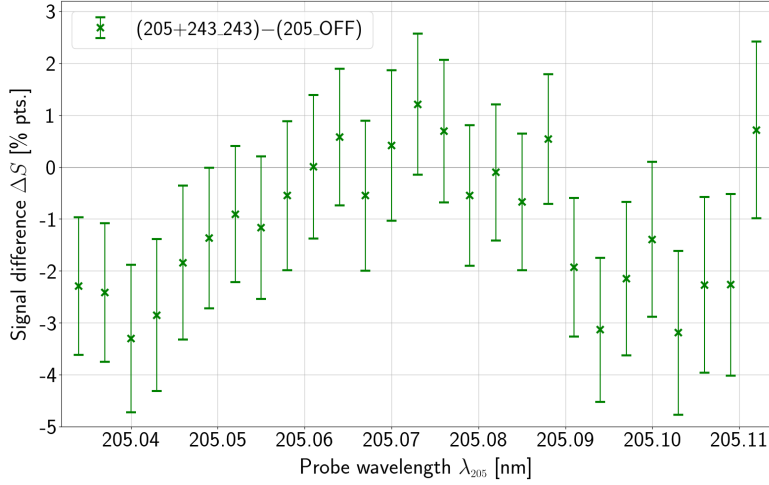
FIGURE 4.31: *Signal differences* $\Delta(S\%)$ *for cooling at* $\delta_{243} = 25\,\text{pm}$.
$\Delta S\%(\lambda_{205})$ specifies the difference between the $S\%$ signal of the "205+243_243" distribution from the cooling measurement at $\delta_{243} = +25\,\text{pm}$ (middle panel in Fig. 4.29) and its corresponding value from the "205_OFF" distribution for similar probe wavelength λ_{205}. Error bars are based on simple error propagation. The wavelength range is restricted to the region of interest around the centre of the $n = 3$ probe transition at $\lambda_0 = 205.073\,\text{nm}$ (deduced from the data set shown in the middle of Fig. 4.29) where the effects of atom pushing and laser cooling are expected to become apparent. Since ΔS represents differences in $S\%$, it is given in units of percentage points.

purpose, the signal values $S^{(205\_\text{OFF})}(\lambda_{205})$ of the unmodified distribution were subtracted from the ones which constitute the modified one $(S^{(205+243\_243)}(\lambda_{205}))$ and the resulting differences[24] $\Delta S(\lambda_{205}) = S^{(205+243\_243)}(\lambda_{205}) - S^{(205\_\text{OFF})}(\lambda_{205})$ were plotted as a function of the corresponding probe wavelengths λ_{205}. Fig. 4.31 shows a zoom into the (relevant) central wavelength range of this plot, i.e., the region where the cooling effect is expected to become apparent. The plot clearly confirms the symmetry of the raw distributions around the central wavelength which was already found in Fig. 4.29. This observation justifies the construction of a symmetrised plot, obtained by mirroring all values on the low-wavelength side to the opposite side, with respect to the resonance wavelength, and evaluating the mean value of each pair of signal differences belonging to the same absolute detuning value. Since each of the resulting values is then based on twice the amount of raw data, this transformation enhances the statistical significance by a factor of $\approx \sqrt{2}$. The plot of the symmetrised distribution of signal differences $\Delta(S\%)$ is presented in Fig. 4.32, now as a function of the absolute values $|\delta_{205}|$ of the probe detuning.

The plot exhibits two distinctive features, namely a clearly positive signal difference $\Delta S = (1.21 \pm 0.96)\,\text{p.p.}$ on resonance and a much broader region of negative values ranging from a detuning of $|\delta_{205}| = 15\,\text{pm}$ up to $42\,\text{pm}$. Beyond this detuning value the significance of $\Delta(S\%)$ is not high enough to allow for an unambiguous assessment. What adds to the large width is the fact that, with a minimum of $\Delta S = (-3.02 \pm 1.08)\,\text{p.p.}$, the depletion zone is more than twice as deep as the excess on resonance is high, with a statistical significance of 3σ according to the error bars. In general, the combination of surplus signals on resonance and reduced signals around the spectral position of the laser fully agrees with the initial expectations for laser cooling. Both features are an indication of a

---

[24] It is important to point out that ΔS describes a difference in percentage values and thus has units of percentage points (abbreviated as p.p. or % pts.). This will not be explicitly stated each time (except for the axis labels in plots) but should be kept in mind when analysing the evolution of ΔS as a function of the probe wavelength or detuning. Since the signals S are usually marked with "$S\%$", i.e., including units in the label (except for mathematical equations), the signal differences will as well be denoted by $\Delta(S\%)$ in the following (again except for equations). However, brackets are used in order to clarify that the "%" symbol in this case only refers to S, not to ΔS.
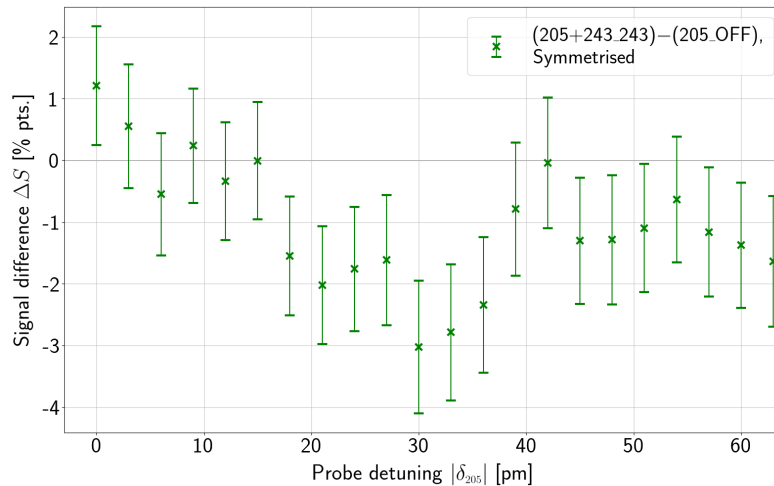
FIGURE 4.32: *Symmetrised signal differences* $\Delta(S\%)$ *for cooling at* $\delta_{243} = 25\,\mathrm{pm}$. *Each data points gives the mean of the pair of $S\%$ signals from the plot Fig. 4.31, which belong to the same absolute detuning values $|\delta_{205}|$. The curve effectively results from a mirroring of all data points from one side of the $n = 3$ probe transition centre at 205.073 nm to the opposite side, followed by an averaging of the data pairs for each detuning $|\delta_{205}|$. Error bars are obtained from error propagation. ΔS is specified in units of percentage points.*

successful net transfer of momentum during Ps-laser interaction, i.e., the recoil effect, which pushes the atoms towards resonance. At first glance the observation of a significant imbalance between the positive and negative signal differences contradicts the expectations, however, as it implies that the interaction with the cooling laser causes a net loss in atoms. The inequality between the excess and depletion areas seems to suggest that the "205+243_243" distribution contains less atoms than the reference distribution "205_OFF". Since, except for the presence of the cooling laser, all measurement conditions and parameters are the same for both distributions, this effect can only be explained by the interaction with the 243 nm-radiation.

Impact of quenching on $S\%$ signals and imperfection of the quenching correction
To resolve this apparent contradiction and to understand the reason for the observed imbalance it is worth recalling the exact procedure of the calculation of the plotted signal differences $\Delta(S\%)$ and breaking it down into single steps. Basically, each value $\Delta S(\delta_{205}) = S^{(205+243\_243)}(\delta_{205}) - S^{(205\_\mathrm{OFF})}(\delta_{205})$ describes the difference between the signal $S^{(205+243\_243)}(\delta_{205})$ of the "205+243_243" distribution at the probe detuning δ_{205} and the corresponding signal $S^{(205\_\mathrm{OFF})}(\delta_{205})$ of the "205_OFF" distribution and thus effectively quantifies the changes in the "205+243_243" with respect to the "205_OFF" spectrum. Each of the two distributions is, in turn, the result of the comparison of the areas f under the SSPALS spectra (cf. Sec. 4.3) of the "positive" runs with respect to the trend line of the "negative" reference data.

For the "205+243_243" distribution, the positive data is given by the "205+243" measurements, in which the atoms are irradiated by both lasers and the trend line is fitted to the "243" data. The reason for choosing the "243" instead of the "OFF" background, in which all lasers are turned off, is to separate between recoil and quenching contributions in the "205+243" runs and ideally to eliminate the latter. The signals $S^{(205+243\_243)}(\delta_{205})$ are thus given by

$$S^{(205+243\_243)}(\delta_{205}) = 1 - f^{(205+243)}(\delta_{205})/f^{(243)}(\delta_{205})\,,$$

where $f^{(243)}(\delta_{205})$ denotes the value of the trend line fitted to the "243"-data at the acquisition time of the corresponding "205+243" run. Similarly, the signals $S^{(205\_\mathrm{OFF})}(\delta_{205})$ are calculated according to

$$S^{(205\_\mathrm{OFF})}(\delta_{205}) = 1 - f^{(205)}(\delta_{205})/f^{(\mathrm{OFF})}(\delta_{205})\,,$$

Probing and **cooling** spectra **do not** overlap

Probing and **cooling** spectra **do** overlap
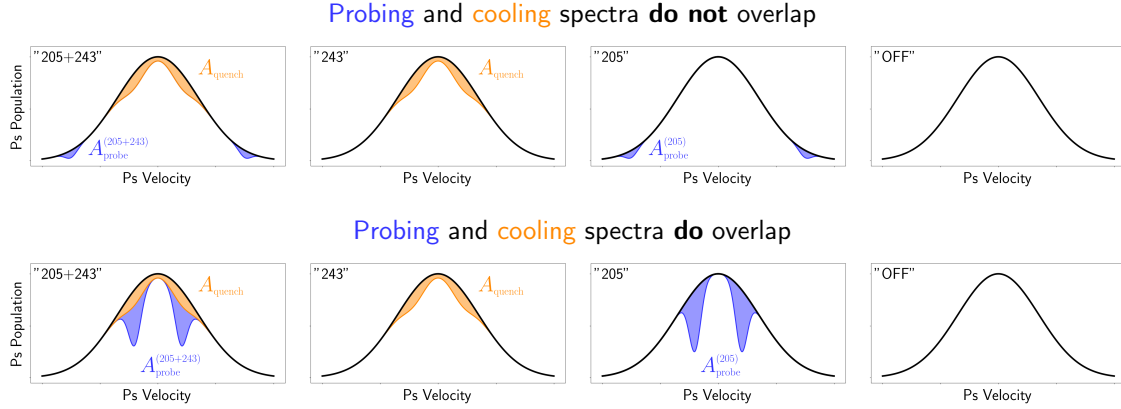
FIGURE 4.33: *Schematic of the imperfection of the quenching correction. Each subplot schematically shows the Ps population distribution at the time of probing for two different cases of probe detunings (top (bottom): 205 nm- and 243 nm-laser spectra do not (do) overlap) and all four laser schemes ("205+243", "243", "205" and "OFF" from left to right) of the fourfold measurement methodology. To enable an isolated study of the effect of quenching on the SSPALS, and finally on the S% signal, each graph shows the distribution for the imaginary scenario in which 243 nm-laser interaction is only accompanied by quenching, but not by additional transfer of momentum.*

where $f^{(\mathrm{OFF})}(\delta_{205})$ denotes the value of the trend line of the laser OFF background at the acquisition time of the corresponding "205" measurement.

Finally, the crucial question is what exactly is contained in the areas f, i.e., means which contributions exist in each of the four measurement configurations and how these depend on the probe detuning δ_{205}. Even though the SSPALS signal, and thus the integrals f, a priori, do not contain any information about the velocity distribution of the atoms that contribute to the signal, the observation of an imbalance in the $\Delta(S\%)$ values can only be understood by visualising this additional dimensionality, i.e. detuning dependency, of the detector signal. It is therefore necessary to focus on the effect of magnetic quenching of the atoms excited to $n = 2$ on the overall signal. For this purpose, it is expedient to neglect the recoil effect for the moment and to imagine a scenario in which the excitation by photon absorption only leads to magnetic quenching but is not additionally accompanied by transfer of momentum. This separation is justified because quenching and recoil effects are independent, uncoupled processes which add linearly to the SSPALS signal, allowing for an isolated inspection of their respective impacts[25]. For the sake of clarity, the permanently existing process of annihilation of Ps ground state atoms is also ignored in this consideration, as it is involved in all cases and therefore cancels out in the calculation of $S\%$ and does not contribute to $\Delta(S\%)$, the parameter of interest.

To facilitate the understanding of the impact of quenching on the measurement signal and the resulting signal differences $\Delta(S\%)$ in this recoil-free scenario, Fig. 4.33 shows a schematic overview of the Ps population distributions at the time of probing for two different detuning configurations and for each of the four involved cases, "205+243", "243", "205" and "OFF", from left to right. The plots in the upper row illustrate the probing configuration in which the spectra of the two UV-lasers do not overlap, whereas those in the lower row show the situation if their spectral positions coincide.

---

[25] It should be noted that, in the general case, it is not valid to perform this separation also for the $S\%$ signals. Even though quenching and recoil are indeed two independent effects, both of them can, in principle, affect the SSPALS spectra of both the positive and negative runs. Since the signals $S\%$ is, however, not linear in the integrals $f^{(\mathrm{neg})}$ and $f^{(\mathrm{pos})}$, a linearisation and isolated consideration of quenching- and recoil-$S\%$ components would ignore the impact of quenching on the recoil effect. For the present consideration, this second-order effect can, however, be neglected safely.

In each case, the black curve indicates the typical initial Doppler population distribution as a function of the velocities of the atoms.

Additionally, each figure contains coloured areas A which indicate the fraction of atoms whose decay properties are modified as a result of laser interaction, either by photoionisation via excitation to $n = 3$ by the probe laser (blue area A_{probe}) or by magnetic quenching upon excitation to $n = 2$ by the cooling laser (orange area A_{quench}). In the presence of laser interaction these atoms become subject to fast annihilation (or dissociation in case of photoionisation, respectively) and therefore contribute to the SSPALS signal at earlier times, leading to a reduction at later times, compared to the case without $n = 2$-excitation. Since the $S\%$ signals are calculated from areas f under the SSPALS spectra within a time window at later times (in the long annihilation tail) it is finally this reduction, quantified by the area A, which is responsible for the emergence of an $S\%$ signal. Mathematically, the areas A are, in good approximation, linked to the integrals f according to $f^{(\mathrm{pos})} = f^{(\mathrm{neg})} - \eta A$, where $f^{(\mathrm{pos})}$ denotes the integral under the SSPALS spectrum of a "positive" run (such as "205+243" in case of "205+243_243") and $f^{(\mathrm{neg})}$ the one of the corresponding background measurement. η is a scaling factor given by the ratio between the width of the f-integration window with respect to the entire width of the tail of the SSPALS spectrum.

Consequently, the larger the fraction A, the smaller the integral $f^{(\mathrm{ON})}$ and, therefore, the higher the $S\%$ signal. More specifically, in the case that A only affects the SSPALS signal of the positive runs, $S\%$ simplifies to

$$S = 1 - \frac{f^{(\mathrm{pos})}}{f^{(\mathrm{neg})}} = 1 - \frac{f^{(\mathrm{neg})} - \eta A}{f^{(\mathrm{neg})}} = \tilde{\eta} A \tag{4.4}$$

using Eq. (4.2) and the approximation $y(t^{(\mathrm{pos})}) \approx f^{(\mathrm{neg})}$. $\tilde{\eta}$ denotes the modified scaling factor $\eta / f^{(\mathrm{neg})}$. In the more complex case in which A_1 describes an effect that becomes apparent in the spectra of all runs, such as magnetic quenching, and A_2 a second effect which only appears in the measurement scheme of the positives, $S\%$ can be expressed as

$$S = 1 - \frac{f^{(\mathrm{pos})}}{f^{(\mathrm{neg})}} = 1 - \frac{f^{(\mathrm{OFF})} - \eta(A_1 + A_2)}{f^{(\mathrm{OFF})} - \eta A_1} \; , \tag{4.5}$$

which can be approximated by $S \approx \tilde{\eta}(A_1 + A_2) - \tilde{\eta} A_1$ in first order of $\tilde{\eta}$.

To return to the initial question, the areas A shown in Fig. 4.33 can now be used to illustrate the impact of quenching on the signal difference $\Delta(S\%)$. $(\Delta S)_{\mathrm{quench}} = \tilde{S}^{(205+243\_243)} - \tilde{S}^{(205\_\mathrm{OFF})}$ is obtained by subtracting the difference between the areas A appearing in the 3$^{\mathrm{rd}}$ and 4$^{\mathrm{th}}$ subplot from the difference between those of the 1$^{\mathrm{st}}$ and 2$^{\mathrm{nd}}$ one. Since the recoil effect was ignored for illustration purposes in the distributions of Fig. 4.33, the described difference, by construction, only describes the quenching contribution $(\Delta(S\%))_{\mathrm{quench}}$ of the total signal difference $\Delta(S\%) = (\Delta(S\%))_{\mathrm{quench}} + (\Delta(S\%))_{\mathrm{recoil}}$. Denoting, analogously, the recoil-free $S\%$ signal components as $\tilde{S}\%$, and using Eqs. (4.4) and (4.5) and the labelling from the figure, $(\Delta S)_{\mathrm{quench}}$ can be written as

$$\begin{aligned}
(\Delta S)_{\mathrm{quench}} &= [\tilde{S}^{(205+243\_243)}] - [\tilde{S}^{(205\_\mathrm{OFF})}] \\
&\propto [(A_{\mathrm{quench}} + A_{\mathrm{probe}}^{(205+243)}) - A_{\mathrm{quench}}] - [A_{\mathrm{probe}}^{(205)}] \; = \; A_{\mathrm{probe}}^{(205+243)} - A_{\mathrm{probe}}^{(205)} \; .
\end{aligned}$$

As described, the primary objective of calculating signal differences $\Delta(S\%)$ is to identify the pure recoil effect, while effectively compensating for the detrimental impact of quenching. For this reason, the "205+243" runs are corrected by the "243" runs (instead of "OFF") as background. In this imaginary scenario, ignoring all kinds of recoil effects, the result of this background correction is then supposed to reproduce exactly the same (recoil-free) $S\%$ value $\tilde{S}^{(205+243\_243)}$, as the "205_OFF"-operation resulting in $\tilde{S}^{(205\_\mathrm{OFF})}$. Consequently, $(\Delta S)_{\mathrm{quench}}$ should vanish so that $\Delta S = (\Delta S)_{\mathrm{quench}} + (\Delta S)_{\mathrm{recoil}}$ becomes a suitable parameter for identifying the pure recoil effect.

In reality this is, however, not the case for all detunings and $(\Delta S)_{\mathrm{quench}}$ has a subtle detuning-dependence. To understand this, it is necessary to distinguish between two configurations of the 205 nm- and 243 nm-laser spectra. For this purpose, the areas A were resolved by their spectral coverage in the illustration in Fig. 4.33, even though each subplot visualises only the processes

occurring only in a single measurement, i.e., for a single detuning value δ_{205}. In the first limiting case, in which both lasers are spectrally well separated (upper row), the 205 nm-laser probes a fraction of fast-moving atoms which, due to the Doppler effect, are dark for 243 nm-light with a given detuning. As a result, the area $A_{\mathrm{probe}}^{(205+243)}$ is completely unaffected by the population reduction due to the emergence of A_{quench}, which means that the probe photoionises exactly the same amount $A_{\mathrm{probe}}^{(205+243)}$ of atoms than if no cooling laser was present, i.e., $A_{\mathrm{probe}}^{(205+243)} = A_{\mathrm{probe}}^{(205)}$. In these cases $(\Delta S)_{\mathrm{quench}} = 0$, and "243" is obviously a good background for the "205+243" runs.

In the second limiting case, however, in which the laser spectra overlap (upper row), the 205 nm-laser probes a fraction of atoms which have interacted with the 243 nm-laser prior to probing, as usual accompanied by the quenching of a certain number of atoms. Due to the local population reduction the probe excites, and thus photoionises, a smaller number $A_{\mathrm{probe}}^{(205+243)}$ of atoms than it would without the cooling laser, so that $A_{\mathrm{probe}}^{(205+243)} = A_{\mathrm{probe}}^{(205)}$). In this case of spectral overlap, the "243"-distribution is thus **not** a good background for the "205+243_243" measurement as it does not fully compensate for the impact of quenching. Instead, it overestimates the quenching effect in these regions, which leads to non-vanishing signal differences $(\Delta S)_{\mathrm{quench}} < 0$, adding an offset to ΔS. This effect finally explains the imbalance observed in the experimental distribution $\Delta(S\%)(\delta_{205})$. For the given combination of 243 nm-detuning ($\delta_{243} = +25\,\mathrm{pm}$) and -bandwidth ($\Gamma_{243} = 2\pi(129\,\mathrm{GHz})$), this region is not restricted to two narrow velocity ranges around $+25\,\mathrm{pm}$, but rather stretches over the resonance. Finally, it is important to note that the described phenomenon is only a secondary effect of quenching resulting from the impact of the primary effect, the population reduction given by A_{quench}, on the probe signal produced by A_{probe}.

Hence, it can be concluded that the indirect impact of $n = 2$ magnetic quenching on the probed atoms produces a small artificial reduction of the recoil component $(\Delta S)_{\mathrm{recoil}}$ for certain spectral configurations, which is large enough to distort the observation of a symmetric recoil effect with equal excess and depletion areas in the symmetrised plot of $\Delta(S\%)$. The fact that the $S\%$ calculation procedure does not account for this subtle secondary effect of quenching on the probing signal shall in the following be called "imperfection of the quenching correction". The term "quenching correction" refers to the choice of "243" as background for the "205+243" data with the original goal to eliminate the quenching effect, which, however, only works reliably for the primary effect. One important consequence of this imperfection is the artificial reduction of the resonance signal in all "205+243_243" distributions by the data analysis. In reality, the signal on resonance (where the atom-pushing effect is expected to become most apparent) is more pronounced than the analysis results suggest. This, in turn, means that an observation of equal resonance signals in the constructed "205+243_243" and "205_OFF" distributions can, in fact, be interpreted as a population surplus and thus a successful pushing of atoms by an optical force. Due to the large parameter space of the cooling measurements, which rules out a precise determination of the described secondary quenching effect, it is impossible to quantify the real surplus and compensate for it by adding a certain offset to the signals for example.

As the imperfection of the quenching correction is obviously induced by the applied analysis procedure, one might wonder whether it might be possible to eliminate it by choosing another background for the "205+243" runs than "243". In the fourfold measurement scheme the only eligible candidate is the "OFF" configuration. The use of this laser OFF background is, however, not a good solution either. Instead, it is even less suitable for eliminating the quenching since the SSPALS spectra of the "OFF" runs do not even contain the primary quenching effect. Consequently, the resulting "205+243_OFF" distribution would show a global detuning-dependent quenching offset even in the regions of spectral overlap. One soon realises that the designed measurement scheme for Ps cooling does not in fact provide any more suitable means to eliminate the quenching effect from the "205-243" distribution than the subtraction of the "243" data. The imperfection of the quenching correction is inherent to the whole scheme and is certainly one of its main limitations. It is, however, important to point out that this defect could only be rectified by measuring the recoil and quenching effects in isolation. Since they are both inextricably linked to $n = 2$ excitation, however, it is simply impossible to design and construct an alternative measurement scheme for identifying the pure recoil effect. Finally, there is thus only one possibility to overcome this problem,

which is a complete removal of magnetic quenching by eliminating the magnetic field. This is, however, experimentally highly challenging and would require a lot of further development work with regard to efficient positronium production.

4.4.3 Numerical studies of Ps laser cooling in the AEḡIS experiment

To gain more insight into the impact of the previously explained imperfection of the quenching correction on the signal differences $\Delta(S\%)$, the measurement results were reproduced numerically by means of further customised simulations. This finally allows the verification of the successful exertion of an optical force in the measurement results. In contrast to the experimental measurements, these numerical investigations allow for a separation of the quenching and recoil effects and thus for an isolated study of each of their contributions to the overall signal.

The studies were carried out by means of the same simulation tool used for the general investigations presented in Chap. 3 (cf. App. F for the technical details about the simulation code itself). The employed rate equation approach and its limitations as well as the numerical methods used are described in detail in Sec. 3.1 and App. F. Due to its great versatility the code allows to simulate Ps laser cooling in a configuration which is as close to the given experimental realisation as numerically possible. This concerns, in particular, the implementation of laser pulses with precise timing sequences and the simultaneous interaction of the Ps cloud with several laser beams at different wavelengths.

Simulation parameters

Before discussing the numerical results, it is necessary to briefly describe the chosen simulation parameters in order to show that the resulting replicated cooling configuration differs from the real setup in a few subtle, but unavoidable details. One of the most pivotal parameters for reproducing the experimentally observed quenching effect is the homogeneous **magnetic field B**. The numerically simulated field has exactly the same parameters as the experimental configuration: B has a strength of $B = |B| = 180\,\text{G}$ and is oriented parallel to the positron propagation direction, i.e., under an angle of $45°$ to the target surface (or, equivalently, the target normal; cf. Fig. 4.8).

The whole **laser setup** in the simulation consists of the same three laser systems used in the experiment. Each of the two pairs of counter-propagating UV-beams was replicated by means of two separate beams from opposite directions. Laser powers, detunings, bandwidths and timings agree exactly with the values measured in the experimental setup. This mean, in particular, that the pulses that belong to the same beam pair also have different energies to account for the attenuation caused by multiple transmission through the viewports. To incorporate the **probing scheme**, all states belonging to the $n = 3$ manifold were added to the already existing set of ground, $n = 2$ excited and artificial dead and continuum states. It is worth recalling that the latter are required to treat the processes of annihilation and photoionisation similarly to photon absorption and emission, as regular transitions between two discrete energy levels induced by photon transfer. The most important characteristic parameters to be defined in this regard are the absolute energy values of each state as well as the strengths of the transition from and to these states.

Since it is difficult to simulate **laser spectra** other than standard distribution functions, all laser spectra were approximated by Gaussian functions. It can be assumed that this approach appropriately replicates the real spectrum of the probe laser while representing a simplification of the cooling laser spectrum. Due to the generation procedure of the spectrum of the 243 nm-pulses, they cannot be expected to show a perfect Gaussian shape. Instead, it can be assumed they the 243 nm-spectrum resembles a comb that consists of numerous individual lines with different peak intensities, spread over the whole laser bandwidth and located very close to each other. The exact position and width of the individual spikes is defined by the convolution of the fluorescence spectra of the dyes with the velocity distribution of the molecules in the solution. Needless to say, it is very difficult to measure this complex substructure, so that every numerical replication is again only an approximation. However, given that the 243 nm-spectrum fluctuates from pulse to pulse, it is

legitimate to assume that an exact reproduction is not required. In the present case, the Gaussian model can be viewed as a sufficiently adequate approach.

As far as their **temporal shape** is concerned, all laser pulses are modelled as rectangular signals with starting times given by the experimental sequence. Pulse lengths are equal to the properties of the real pulses. Just like the spectrum, this is again a slight simplification. In reality, the stretched cooling beams, consisting of the sum of three cavity pulses (cf. Fig. 4.10), resemble a rectangular function more than the shape of the 205 nm-pulses with a sharp rising but an elongated falling edge. In view of the fluctuations of the pulse lengths as well as of the timings in the experiment, temporally rectangular profiles can, however, again be considered appropriate. The **spatial alignment** of the laser beams is the same as in the experiment, except for the very small angle between the UV-beam path and the orientation of the IR-line, which should, however, not have any impact on the photoionisation rate.

An important aspect to be mentioned is the simulation of the **generation procedure** of the Ps cloud and the resulting geometric conditions for laser interaction, since this is the part that deviates most from the real case. In contrast to the experimental process that takes place in the converter target, where Ps emission extends over a period of about 10 ns, all Ps atoms are generated simultaneously in the simulation. The time-dimensionality of the experimental Ps production process is instead mimicked by elongating the area of the target surface into the third spatial dimension and randomly distributing the initial positions of the atoms over the resulting volume. The depth of this volume is chosen such that the time spread of the simulated cloud is equivalent to the experimental value.

While this approach seems appropriate for reproducing the temporal distribution, it causes a problem in other respects. As described in the context of the experimental setup, the laser beams hit the target laterally, thereby grazing it in such a way that the centre of the beam, which is the region of highest energy density, is located just above the target surface with maximum overlap with the Ps cloud. Consequently, a small part of the beam is cut off by the target holder. In the experiment, this alignment ensures that all atoms emitted by the target directly enter the region of maximum laser interaction. Because spatial beam-clipping is not implemented in the simulation, the generation of the atoms within a certain, albeit narrow, spatial volume makes it impossible to reproduce the same initial laser interaction conditions as in the experiment. Those atoms which are initialised in the region furthest from the target surface, representing those that are generated at later times in the experiment, will thus neither start to laser-interact with some time delay, nor in the region of highest energy density. Instead, all atoms start to interact with the laser right from the beginning and at the position where they are initiated numerically. On the other hand, this initialisation procedure correctly simulates the distribution of the times at which the atoms experience the highest beam intensities. Effectively, the only difference between the simulated and the real case is thus the premature laser interaction for some of the atoms, as the laser interaction starts before the atoms leave the target. It is important to point out that the described discrepancy should neither be compensated by simply offsetting the target or the lasers nor by adjusting the laser delay accordingly, since both approaches would produce interaction conditions which would be even less consistent with the experiment.

Finally, the **spatial expansion** of the Ps cloud after emission from the target is simulated by means of the effusive beam model described in Sec. 3.2.2. It produces an ensemble of atoms that propagate, with a Maxwellian velocity distribution, along a preferred direction which, in the present case, is the normal of the target. It must, however, be mentioned that the real Ps ensemble does not naturally obey an ideal Maxwell-Boltzmann distribution due to the complex formation process. Nevertheless, the effusive beam model has proven to provide a very accurate description of the real distribution. The use of the Maxwell-Boltzmann temperature as the characteristic parameter for the quantification of the width of the distribution is also only an approximation, albeit again a very accurate one. As soon as the distribution becomes modified as a result of laser cooling, the Maxwell-Boltzmann temperature must be replaced by an alternative parameter. The use of an effective temperature parameter based on the variance of the distribution, which was also employed for the numerical studies presented in Sec. 3.1, represents a very expedient approach for this purpose. Its precise definition can be found in Sec. 3.1.2.

The analysis of intermediate simulation results revealed that a statistical significance comparable to the experimental measurements can only be obtained by using clouds of at least $N = 10000$ atoms[26], which naturally entails an enormous additional burden with regard to the required **computation resources**, as discussed and quantified in Sec. F.5.2. It is worth noting that by use of the full range of numerical methods as for the simulations in Sec. 3.1, the simulation of the measurement results for all three 243 nm-detunings, with and without recoil effect, would take several months on a standard computer, even after parallelisation of the code. In this context, one should recall that the evaluation of a single $\Delta(S\%)(\delta_{205})$ value requires to carry out four individual 600 ns-long simulation runs[27], namely for each of the four laser combinations involved in the fourfold measurement scheme. Repetition of this procedure for 41 values of the 205 nm-detuning δ_{205}, for all three detunings δ_{243} as well as for the two cases with and without recoil effect (to allow for an isolated investigation of the recoil and quenching effect) yields a total of 504 simulations, each of which takes roughly twelve days of computation time. Obviously, this undertaking would not be feasible. For this reason, measures had to be taken to considerably reduce the computation time, either by simplifying the simulation scheme or by approximating certain processes, for example, without impairing the reliability of the results.

Mainly two approaches were pursued and realised to this end:

1. The relatively small field strength of $B = 180\,\mathrm{G}$ eliminates the need for **diagonalisation** of the Hamiltonian matrix (which, after integration of the $n = 3$, has a size of 72×72 instead of only 32×32) and allows to use the zero-field energy levels instead. This makes the execution of the code considerably faster while yielding almost identical results, as verified by means of dedicated simulations.

2. Further acceleration was achieved by reducing the simulation time from 600 ns to 50 ns, i.e., by stopping the calculation a few nanoseconds after the evolution has demonstrably reached a semi-steady state. Beyond this point in time the atoms no longer experience any laser interaction nor show fluorescence decay, but are only subject to annihilation decay that is governed by a simple exponential decay law. This obviously does not have to be simulated, but can be calculated analytically. Numerical calculations are only required to solve the complex laser interaction dynamics which, in the present laser cooling scheme, is however restricted to approximately the first 35 ns. To allow the remaining excited atoms to spontaneously decay back to the ground state, a few nanoseconds of temporal margin were included before the simulation is stopped at $t = 50\,\mathrm{ns}$. All atoms that still survived up to this point, i.e., that have neither annihilated nor been photoionised before, populate either the ground or the metastable 2^3S state. As shown by the lifetimes in Tab. A.1, the metastable state is much more likely to annihilate than to decay back to the 1^3S state via two-photon decay. The only source of error introduced by the premature termination of the simulation is thus the fact that it ignores this very low probability for spontaneous decay of the metastable state, which is far smaller though than the Poisson noise. Furthermore, this error is far outweighed by the achieved speed-up by a factor of 12, which finally makes the simulation and reproduction of the measurement results a realistic plan again. Nevertheless it took several weeks to acquire the whole data set.

Definition of the numerical $S\%$ signal

The preceding explanations in the context of the second method for code acceleration directly lead to the calculation of the $S\%$ signals from the numerically acquired data. This question arises in particular in case of a premature termination of the simulation and the resulting unavailability of complete SSPALS spectra so that especially the time window between 450 ns and 600 ns, used for integration, is missing. To develop the most accurate and faithful replication of the experimental

---

[26] In contrast to the experimental measurements, the error in the simulations is given by the Poisson noise in the number of atoms.

[27] The long duration of 600 ns is required to reproduce the entire SSPALS spectrum.

computation procedure based on the numerically available data, it is worth taking a closer look at the actual meaning of the areas f under the SSPALS curves that are used in the experimental analysis. Since the PbWO$_4$ detector monitors the number of incident gamma rays resulting from instantaneous positron annihilation, the integral f of the SSPALS spectrum between $t = 450\,\mathrm{ns}$ and $t = 600\,\mathrm{ns}$ is equivalent to the number of annihilated atoms in this time range. Furthermore, this number of atoms can only result from the decay of ground state atoms or those in the metastable state because these are the only states that are still populated by atoms at these late times. It is easy to see that this allows to reproduce the integrals f from an extrapolated signal based on the final simulated populations $\mathcal{P}$ in the ground and metastable states (i.e., those at $t = 50\,\mathrm{ns}$) and their individual annihilation lifetimes.

In analogy to definition (4.2) of the experimental $S\%$ signal, the numerical $S\%$ parameter is therefore calculated according to

$$S = 1 - \frac{N_{\mathrm{grd}}^{(\mathrm{pos})} + N_{\mathrm{meta}}^{(\mathrm{pos})}}{N_{\mathrm{grd}}^{(\mathrm{neg})} + N_{\mathrm{meta}}^{(\mathrm{neg})}} \tag{4.6}$$

$$\text{with} \quad N_{\mathrm{grd}}^{(\mathrm{pos})} = \mathcal{P}_{\mathrm{grd}}^{(\mathrm{pos})}(t_{\mathrm{fin}}) \times \left[\exp\left(-t_1/\tau_{\mathrm{grd}}^{(\mathrm{ann})}\right) + \exp\left(-t_2/\tau_{\mathrm{grd}}^{(\mathrm{ann})}\right) \right] \ ,$$
$$N_{\mathrm{meta}}^{(\mathrm{pos})} = \mathcal{P}_{\mathrm{meta}}^{(\mathrm{pos})}(t_{\mathrm{fin}}) \times \left[\exp\left(-t_1/\tau_{\mathrm{meta}}^{(\mathrm{ann})}\right) + \exp\left(-t_2/\tau_{\mathrm{meta}}^{(\mathrm{ann})}\right) \right] \ ,$$
$$N_{\mathrm{grd}}^{(\mathrm{neg})} = \mathcal{P}_{\mathrm{grd}}^{(\mathrm{neg})}(t_{\mathrm{fin}}) \times \left[\exp\left(-t_1/\tau_{\mathrm{grd}}^{(\mathrm{ann})}\right) + \exp\left(-t_2/\tau_{\mathrm{grd}}^{(\mathrm{ann})}\right) \right] \ ,$$
$$N_{\mathrm{meta}}^{(\mathrm{neg})} = \mathcal{P}_{\mathrm{meta}}^{(\mathrm{neg})}(t_{\mathrm{fin}}) \times \left[\exp\left(-t_1/\tau_{\mathrm{meta}}^{(\mathrm{ann})}\right) + \exp\left(-t_2/\tau_{\mathrm{meta}}^{(\mathrm{ann})}\right) \right] \ ,$$

where $\mathcal{P}_{\mathrm{grd}}(t_{\mathrm{fin}})$ and $\mathcal{P}_{\mathrm{meta}}(t_{\mathrm{fin}})$ denote the population in the ground and in the metastable state at the final simulation time $t_{\mathrm{fin}} = 50\,\mathrm{ns}$, respectively. As usual, the superscript "(pos)" or "(neg)" symbolises whether the respective parameter quantifies either a positive or negative background run. $\tau_{\mathrm{grd}}^{(\mathrm{ann})} = 140.8\,\mathrm{ns}$ stands for the ground state annihilation lifetime in a field of $B = 180\,\mathrm{G}$ and $\tau_{\mathrm{meta}}^{(\mathrm{ann})} = 1.11\,\mathrm{\mu s}$ for the annihilation lifetime of the metastable $2^3\mathrm{S}$ state, respectively. Finally, $t_1 = (450\,\mathrm{ns} - t_{\mathrm{fin}})$ is the left boundary of the time window used for the integration of the SSPALS curve, corrected for the offset time $t_{\mathrm{fin}} = 50\,\mathrm{ns}$ at which the population numbers $\mathcal{P}$ are taken. $t_2 = (600\,\mathrm{ns} - t_{\mathrm{fin}})$ applies equivalently for the right boundary. Each value N appearing in this definition thus represents the number of ground or metastable state atoms which annihilate in the time range used for the integration of the SSPALS curve in the experiment. It should be noted that due to the fact that the numerical data does not experience any long-term drifts, the value $y(t^{(\mathrm{pos})})$ of the negative trend line at the acquisition time of the positive run was directly replaced by the population $\mathcal{P}_{\mathrm{grd}}^{(\mathrm{neg})}$ of the corresponding background in definition (4.6) of the numerical $S\%$ signal.

4.4.4 Numerical results and comparison to the experimental measurements

To enable a direct comparison of the Monte-Carlo simulations with the experiment, the data obtained from the simulations were used to generate similar plots as for the experimentally acquired data, based on the definition above. As mentioned previously, to study the impact of quenching in an isolated way, each parameter configuration was simulated for two cases, once including all effects that also take place in the "real world", and once for the imaginary scenario in which no recoil effect exists. All plots were generated for both cases. The one taking recoil effects into account is labelled "Recoil ON" and the fictitious one, without recoil effect, accordingly "Recoil OFF". Because in the experiment only the data for the cooling laser detuning $\delta_{243} = +25\,\mathrm{pm}$ reasonably allows for quantitative analyses, the following discussion will also be completely devoted to this configuration.

As in the experiment, the first result of interest is the distribution of $S\%$ signals as a function of the probe detuning δ_{205} for the case including prior interaction with the 243 nm-cooling laser ("205+243_243") as well as for the reference case "205_OFF" showing the distribution of the freely expanding positronium cloud without 243 nm-laser interaction. Both distributions are shown in Fig. 4.34 with the "205+243_243" spectra again coloured red and the reference ones blue. The left panel shows the case with and the right panel that without recoil effect. To convey an impression of the quenching level, the orange points additionally specify the signals obtained from the comparison
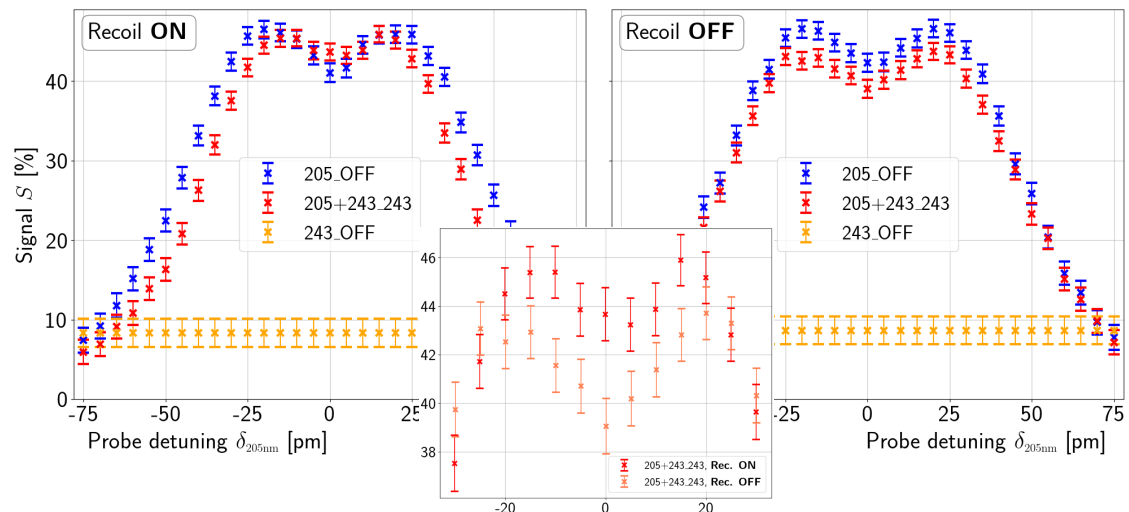
Figure 4.34: *Simulated Ps velocity distributions in laser cooling measurements within the* AEḡIS *experiment. The left plot shows the distribution of S% signals resulting from Monte Carlo simulations performed to numerically reproduce the experimentally measured velocity distribution presented in the middle panel of Fig. 4.29 (with $\delta_{243} = 25$ pm). All involved physical processes are included in the simulations. The data on the right represents the results of similar simulations with the same parameter configuration but deactivated recoil effect ("Recoil OFF"). The blue data points represent the distribution in the absence of the 243 nm-laser ("205_OFF") and the red points that with the 243 nm-laser involved ("205+243_243"). In both plots the orange points specify the signals produced by magnetic quenching (given by "243_OFF"). The inset figure contains a direct comparison of the central regions of the "205+243_243" distributions with activated (in dark red) and deactivated recoil (in light red). All error bars represent the ($\sqrt{\mathcal{P}_{grd}}$)-like Poisson noise in the ground state population $\mathcal{P}_{grd}$ on which the S% calculation is based. A total number of $N_0 = 10^4$ atoms were used. The external and internal evolution of the atoms was simulated for 50 ns, entirely covering the laser interaction that lasts up to ≈ 35 ns. All other parameter values are similar to the experiment.*

of the "243" to the laser OFF background. The amount of quenched $n = 2$ atoms is of course constant as a function of δ_{205} since it does not depend on the properties of the probe but rather the cooling laser, in particular the detuning and bandwidth that define the spectral coverage of the Ps velocity distribution. The level of quenching relative to the level of the photoionisation scans is similar to observations made in the experiment. This leads to the conclusion that the simulated cooling laser covers and saturates the velocity distribution in the same way as in the measurement.

The inset of Fig. 4.34 additionally shows a direct comparison of zooms into the central region of the two "205+243_243" distributions (recoil activated in red and deactivated in light red). The blue (uncooled) reference distributions were not included for reasons of clarity.

The most striking observation in the two plots is certainly the extremely high level of S% signals. Compared to the values obtained from the experimental measurements (cf. middle panel of Fig. 4.29) all numerically reproduced values are equally enhanced by a factor of 3.5 to 4. This observation is explained by the described deviation of the simulated grazing beam alignment, which results in premature laser interaction already before the atoms have reached the target surface and escape into free space.

To verify that this is the only reason for the enhanced signals, the number of ground state and photoionised atoms was numerically studied as a function of the offset x_{off} of the target with respect to the intersection point with the lasers. Even though this method should not be used to compensate the increase in the signal level, as pointed out earlier, it still allows to investigate the impact of a modification of the overlap between the laser and the Ps cloud. For this purpose, the
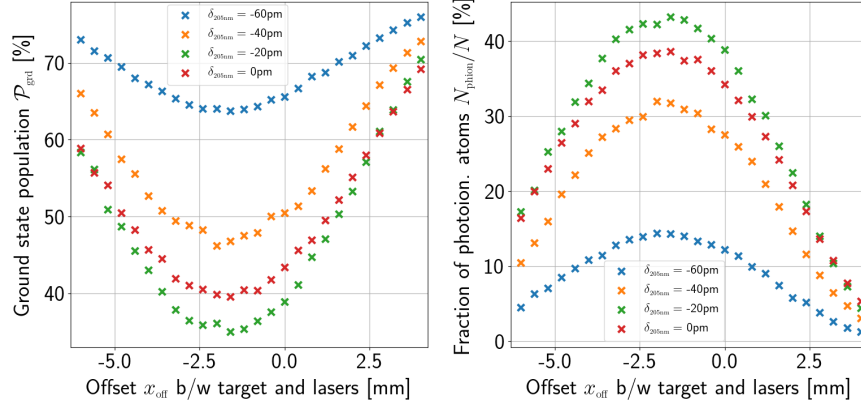
FIGURE 4.35: *Dependence of the signal level on the overlap between atomic cloud and cooling laser. Simulated evolution of the final ground state population $\mathcal{P}_{\mathrm{grd}}$ (left) and photoionised atoms N_{phion} (right), at $t_{\mathrm{fin}} = 50\,\mathrm{ns}$ (including both cooling and probing), as a function of the offset position x_{off} of the target with respect to the laser crossing point along the propagation direction of the effusive beam. The evolution was simulated for the four representative probe detunings $\delta_{205} = -60\,\mathrm{pm}$ (blue), $-40\,\mathrm{pm}$ (orange), $-20\,\mathrm{pm}$ (green), $0\,\mathrm{pm}$ (red). All atom numbers are specified as fractions of the total number of atoms, $N_0 = 8000$. The target offset was scanned over the range from $-6\,\mathrm{mm}$ to $+4\,\mathrm{mm}$ in steps of $0.4\,\mathrm{mm}$.*

laser cooling simulation was carried out for $\delta_{243} = 25\,\mathrm{pm}$ and four representative probe detunings ($\delta_{205} = -60\,\mathrm{pm}$, $-40\,\mathrm{pm}$, $-20\,\mathrm{pm}$ and $0\,\mathrm{pm}$) of the entire distribution shown in Fig. 4.34, while scanning x_{off} over a broad range from $-6\,\mathrm{mm}$ to $+4\,\mathrm{mm}$ in steps of $0.4\,\mathrm{mm}$ (the default value, used for the simulations of the experimental measurements, is $x_{\mathrm{off}} = 0\,\mathrm{mm}$). Negative values of x_{off} indicate that the Ps cloud crosses the laser beams with an equivalent delay, whereas with increasing positive offsets less and less atoms are subject to laser interaction at all. Fig. 4.35 presents the resulting evolution of the final fractions of ground state and photoionised atoms $\mathcal{P}_{\mathrm{grd}}/N_0$ and N_{phion}/N_0, respectively, as a function of x_{off} for the four studied probe detunings.

To understand the relation between the plotted populations and the final $S\%$ values it is worth recalling that $S\%$ is primarily determined by the ground state population (cf. the definition of the numerical S parameter given by Eq. (4.6)). For this reason, the fraction of ground state atoms was plotted in the figure. The number of photoionised atoms, with opposite evolution than the ground state atoms, is only shown because it represents a more direct indicator of the laser interaction efficiency.

As expected, the laser interaction is most efficient if the laser passes right in front of the target, i.e., for $x_{\mathrm{off}} \approx -2\,\mathrm{mm}$. Both the spatial and the temporal overlap between the expanding Ps cloud and the cooling pulses are maximised for this alignment, resulting in the longest possible interaction times. For the default alignment $x_{\mathrm{off}} = 0$, in which the central axis of the laser beam is closer to the target surface, the number of photoionised atoms (and thus the $S\%$ signals) is still very high. This explains the unexpectedly high values in the numerically simulated distributions shown in Fig. 4.34. The further the target is offset in negative x-direction, the later the atoms effectively start interacting and the lower the excitation efficiency at the time of probing becomes (all timings in this x_{off}-scan still agree with the cooling sequence of course). Naturally, the further the target is moved forward with respect to the laser axis, the less atoms interact, until, for values above $x_{\mathrm{off}} \gtrsim 4\,\mathrm{mm}$, the atoms no longer interact with the laser.

The experimental grazing alignment, in which a considerable fraction of the laser beam is cut off and the optical energy dumped on the target holder, is effectively equivalent to an offset of about $x_{\mathrm{off}} \approx (2-3)\,\mathrm{mm}$, for which only a part of the beam overlaps with the Ps cloud after generation. It is important to emphasise that this configuration does not represent the real spatial alignment of the target with respect to the laser beam, but only that which effectively yields signals similar

to those in the experiment. As the plot shows, the fraction of photoionised atoms has already decreased significantly at this offset position, compared to $x_{\mathrm{off}} = 0$, namely by a factor of about 2.5. This is exactly the scaling factor found in a comparison between experimentally measured and numerically simulated Ps population distributions (using $x_{\mathrm{off}} = 0$), which confirms that the degree of Ps-laser overlap is the reason for the high numerical $S\%$ signals. In this context, it should be emphasised once more that the offset was still not used as a tool to scale the numerically obtained values in order to adapt them to the experimentally observed ones, since this would make it necessary to use offset positions for which the alignment between target and laser would deviate substantially from the real configuration. Instead, an emphasis was put on replicating the experimental setup as closely as possible while accepting the discrepancy in the signal levels that results from the fact that beam clipping is not considered in the code. It is important to highlight that this shortcoming only affects the strengths, but not the detuning-dependence of the signals. This is validated by the fact that the populations, plotted in Fig. 4.35, show similar evolutions for all studied probe detunings. This is an important result as it confirms that the numerical results are suitable for studying the processes involved and observed in the experimental measurements. The high simulated signal levels are thereby to be regarded as tolerable.

To return to the simulated Ps distributions presented in Fig. 4.34, it can be clearly observed that the left plot (based on the data including all physical effects) shows the characteristic cooling effect that was already observed in the measurement results: While the population of the cooled distribution "205+243_243" is considerably reduced on the flanks, it is increased in the central region, effectively leading to a reduction in width. The behaviour on resonance furthermore confirms that, under the given experimental conditions, the recoil effect is indeed strong enough to outweigh the overall signal reduction produced by quenching, while not completely filling up the prominent Lamb dip around resonance, similarly to the measured distributions shown in Fig. 4.29. As expected, the described cooling effect does not occur in case of artificially deactivated recoil effects, as shown in the right panel in Fig. 4.34. All effects and modifications observed in this plot, and in particular the overall damping of the cooled ("205+243_243") with respect to the uncooled distribution ("205_OFF"), must therefore necessarily be due to the magnetic quenching of $n = 2$ states. Moreover, it can even be inferred that they must result from the secondary effect of quenching on the probe signal which was described in Sec. 4.4.2 by means of the schematic illustration in Fig. 4.33. This is simply due to the fact that the right plot of Fig. 4.34 is based on the data which is not only free of recoil effects but also of the primary effect of quenching (indicated by the orange areas A_{quench} in Fig. 4.33), which is eliminated by choosing the "243" runs for the quenching correction (i.e., as background data for the cooled distribution). The fact that the red and blue curves are not identical is solely owed to the previously described imperfection of this quenching correction. Especially on resonance, where the 205 nm- and 243 nm-spectra show maximum overlap, this imperfection actually has a considerable influence on the "205+243_243" distribution. It is important to point out that, although this effect could already be derived from the measured symmetrised signal differences $\Delta(S\%)$ plotted in Fig. 4.32, the simulations finally make it possible to reveal its real impact since only they allow to artificially deactivate recoil effects and consider quenching in isolation.

To analyse the quenching and recoil effects in more detail, the numerically acquired signal values of the cooled distribution were subtracted from the corresponding ones of the uncooled distribution to obtain the signal differences $\Delta(S\%)$, similar to the analysis of the measurement. The results of these numerical $\Delta(S\%)$ values are presented separately, for activated as well as deactivated recoil effects, in the upper row of Fig. 4.36. The subplots in the bottom row show a direct comparison of both cases, the original, unfolded version on the left and the folded one on the right. In all cases, the results of the simulations with all physical effects included are coloured in dark green whereas the light green points represent the numerical results of the (imaginary) scenario with deactivated recoil effects.

To focus first on the simulations of the real process in dark green, it can be concluded that there is an almost perfect qualitative agreement between the numerical and the experimental results
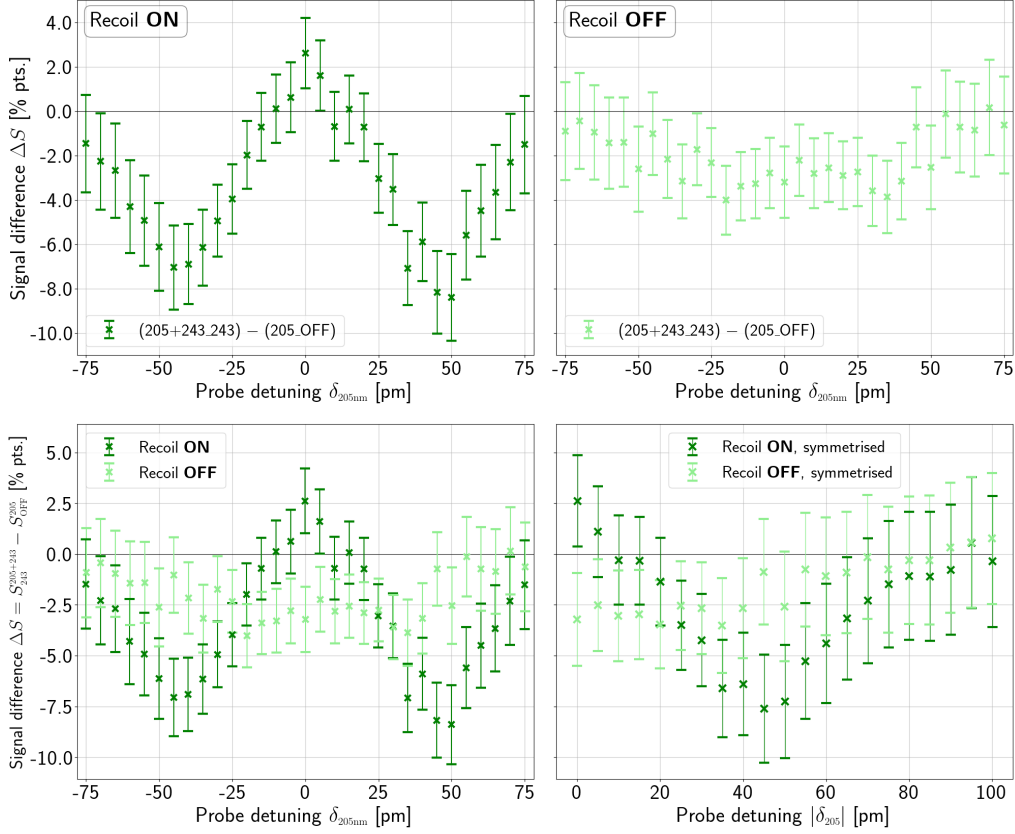
FIGURE 4.36: *Simulated signal differences* $\Delta(S\%)$ *for cooling at* $\delta_{243} = 25\,\mathrm{pm}$. *In analogy to the analysis of the experimental data, (Figs. 4.31 and 4.32) each data point* $\Delta(S\%)(\delta_{205})$ *represents the difference between the* $S\%$ *signals of the "205+243_243" distribution shown in Fig. 4.34 and the corresponding values of the reference distribution "205_OFF". The data in dark green (top left) is based on the simulation taking into account recoil effects (corresponding to the left plot of Fig. 4.34) whereas the plot in the top right panel presents the results for deactivated transfer of momentum (in light green, based on the data on the right of Fig. 4.34). The panel in the bottom left shows a direct comparison of both curves from the upper row and the one in the bottom right the symmetrised version of the latter. Since* ΔS *represents signal differences it is specified in units of percentage points.*

shown in Fig. 4.32. In other words, the measurements are fully consistent with the theoretical predictions and expectations made by the Monte Carlo simulations. Most importantly, in both cases the interaction with the cooling pulses generates a small, but statistically significant increase in $S\%$ signals in the narrow region around resonance, indicated by $\Delta(S\%){>}0$. This central maximum in $\Delta(S\%)$ is surrounded by a signal reduction that is roughly three times deeper than the peak is high and stretches over a much broader range of probe detunings. As already concluded from the measurement results, this imbalance can only be caused by the secondary effect of quenching since a transfer of momentum can produce signal differences $\Delta(S\%) \neq 0$ only by a displacement of atoms from their initial spectral position towards resonance, but not by a reduction in atom numbers which entails that recoil-induced $\Delta(S\%)$-depletion and -enhancement regions must be equal $(\sum(\Delta S)_{\mathrm{recoil}} = 0)$.

This conclusion can now finally be confirmed on the basis of the numerical simulations, more precisely by the light green data in the upper right panel in Fig. 4.36. This plots illustrates the secondary effect of quenching even more clearly than the direct comparison of the simulated recoil-free "205+243_243" and the "205_OFF" distributions discussed before. These signal differences $(\Delta S)_{\mathrm{quench}} < 0$ finally lead to an artificial reduction of the measurable effect

$\Delta S = (\Delta S)_{\text{recoil}} + (\Delta S)_{\text{quench}}$ of laser interaction and to the observed imbalance in the $\Delta(S\%)$ distribution. The term "artificial" is used here to emphasise that the effect does not have any physical origin, but is artificially induced by the data analysis procedure. If the signal differences induced by the recoil effect, i.e., the effect which is finally responsible for laser cooling, is offset by the described artificial reduction induced by quenching, the signal enhancement on resonance amounts to a remarkable value of $(\Delta S)_{\text{recoil}} = (\Delta S) - (\Delta S)_{\text{quench}} = (5.83 \pm 3.20)$ p.p. according to the simulation results (where ΔS is given by the data in dark green and $(\Delta S)_{\text{quench}}$ by that in light green, respectively).

With regard to the comparison between the numerically and experimentally obtained results, it must be concluded that the qualitative agreement cannot be fully substantiated quantitatively. Instead, the comparison reveals that the values are scaled both in vertical and horizontal direction. In general, characteristic effects seem to be stretched in both directions in the simulation results with respect to the experimental data. In the numerical $\Delta(S\%)$-curve, for example, the depletion zone reaches its lowest point at probe detunings $|\delta_{205}|$ between 45 pm and 50 pm, whereas in the measurement this point is already found at $|\delta_{205}| = 30$ pm. In contrast to the mismatch in signal strengths (vertical direction) which can directly be ascribed to the imperfect reproduction of the grazing beam alignment and laser interaction conditions, as explained above, it is much more difficult to clearly identify the reason for the stretching in horizontal direction.

As $\Delta(S\%)$ quantifies the difference between the cooled and uncooled distributions, "205+243_243" and "205_OFF" respectively, the shape of the depletion zone must be directly correlated with the interaction properties with the 243 nm-light and, thus, associated with the characteristics of the cooling laser. The width of the region in which $\Delta(S\%) \neq 0$ is a direct indicator for the spectral range of the laser for example. Consequently, the fact that the depletion zone in the simulation is broader than in the experimental results suggests that the numerically reproduced laser spectrum deviates from its real shape. Since the bandwidth defined in the simulation corresponds to the value precisely measured by means of the spectrometer, it can be concluded that the employed numerical model does not perfectly reproduce the real spectrum. The largest discrepancies can probably be found at the edges of the spectrum where the numerically employed Gaussian spectrum does not descend as quickly as the real one. Furthermore, a Gaussian function by nature never drops completely to zero but always approaches a finite residual value.

Furthermore, the minimum value of $\Delta(S\%)$, i.e., the maximum difference between the two distributions "205+243_243" and "205_OFF", is observed at much different probe detunings in the simulation compared to the measurement. This suggests that there is not only a mismatch in spectral coverage but also in the position of the region of strongest interaction. Intuitively, one might ascribe this effect directly to the 243 nm-detuning, since the position of the maximum population depletion induced by cooling is primarily defined by the spectral position of maximum cooling laser intensity that is defined by its detuning (as well illustrated for example in Fig. 3.5). On the other hand, there is probably no parameter whose value has been more precisely measured and which can be numerically reproduced more reliably than the detuning.

This means that there must be another parameter that plays a role as well. In fact, the spectral position of largest $|\Delta(S\%)|$ values is not only ruled by the detuning but also by the interaction time defined by the pulse length. The longer the pulses (the longer the interaction), the higher the number of photons absorbed by the atom and the stronger the optical force (pushing) of the atoms towards the centre of the distribution. The shift in the spectral position of the minimum $\Delta(S\%)$-value towards larger probe detunings might therefore also be an indicator of too short pulse lengths used in the simulation. In fact, this is the much more likely reason for the observed shift, since the pulse length cannot be measured as precisely as the laser detuning. Due to its fluctuations, it can furthermore be expected that it regularly exceeds the numerically chosen value of 24 ns, which can be regarded as the lowest limit. Finally, after rescaling by a factor of 0.67 in the horizontal and 2.4 in the vertical direction, the numerical result agrees almost perfectly with the measurement results as shown in Fig. 4.37. Discrepancies can only be observed at larger probe detunings where the measurement results are not as reliable as in the region around resonance.

This agreement between the Ps cooling measurements in a magnetic field and the corresponding
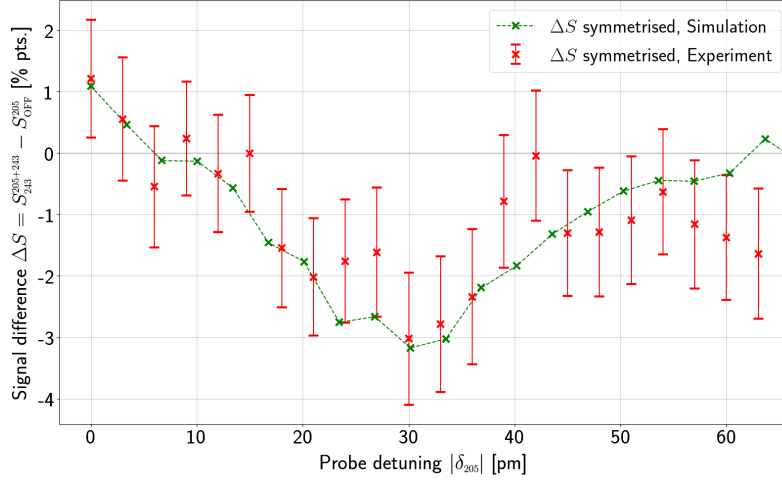
FIGURE 4.37: Comparison between experimental and numerical results. *Symmetrised signal differences ΔS as a function of the probe detuning $|\delta_{205}|$ for both the numerical (green points) and experimental results (red points). To enable the direct quantitative comparison, the original numerical data (c.f. dark green points in the bottom right panel of Fig. 4.36) was rescaled by a factor of 0.67 in horizontal and 2.4 in vertical direction, while the experimental results correspond exactly to the data presented in Fig. 4.32. As a guide to the eye, the numerical data was connected by a dashed green line. The labels $S_{243}^{205+243}$ and S_{OFF}^{205} on the y-axis are equivalent to $S^{(205+243\_243)}$ and $S^{(205\_OFF)}$, respectively.*

numerical predictions based on Monte Carlo simulations is remarkable. However, the most important result of the whole analysis and the comparison between experiment and simulation is the fact that the observation of positive $\Delta(S\%)$ values can only be explained by a successful transfer of momentum due to laser interaction. The results allow to draw the clear conclusion that the population enhancement in the centre of the distribution must necessarily result from a recoil effect, i.e., the exertion of an optical force on the Ps ensemble. Equally importantly, this is possible even in moderate magnetic fields, i.e., in the presence of magnetic quenching effects. Conversely, it can be concluded that the (statistically significant) enhancement of the signal on resonance, as observed in the present measurements, is an unambiguous indication of the successful exertion of an optical force on the atoms. It is important to emphasise once more that this unambiguous conclusion was made possible only by means of the additional numerical investigations and especially an isolated consideration of the impact of quenching. In this context, it is worth pointing out that the signal enhancement on resonance could be much more pronounced in the absence of quenching. According to the numerical results, it could reach $(\Delta S)_{\text{recoil}} = (2.43 \pm 1.33)\,\text{p.p.}$, taking into account the described scaling factor.

Whether the observed effect can be qualified as laser cooling strongly depends on the applied definition. If cooling is to describe a reduction in temperature or an increase in phase space density, respectively, the available results do not constitute an irrefutable proof due to the experimentally unknown (i.e., not precisely quantifiable) contribution of the magnetic quenching of $n = 2$ states. However, if cooling is defined as the exertion of a symmetrical optical force, accompanied by an enhancement in the population on resonance, it is possible to claim successful laser cooling based on the obtained results.

Chapter 5

Summary, conclusion and outlook

Not even a hundred years after the theoretical prediction of the existence of positronium by Stjepan Mohorovičić in 1934 [20], this exotic atom has sparked fascinating research in a wide variety of fields of physics, ranging from high energy physics and tests of fundamental symmetries to atomic physics and positronium chemistry. The work performed within the scope of this thesis was devoted to investigations of the interaction of the atom with light quanta, with the goal of laser cooling a thermal ensemble of Ps atoms in a magnetic field. Due to the complexity of the corresponding schemes, the studies included both theoretical and numerical considerations before finally culminating in the experimental attempt of Ps laser cooling in the framework of the AE$\bar{\text{g}}$IS experiment at CERN. Even if AE$\bar{\text{g}}$IS's motivation for positronium research is the primary goal of measuring gravity of antihydrogen [111], the generation of cold and dense Ps clouds also paves the way to several further independent Ps experiments, such as Ps spectroscopy or the creation of a Ps Bose-Einstein condensate.

Theoretical framework of Ps laser cooling in magnetic fields

The scheme of positronium laser cooling in a magnetic field is characterised by a high level of complexity as it involves a number of intertwined processes. What makes the whole scheme unique and sets it apart from standard laser cooling experiments, are the unique properties of the positronium atom. There are mainly two peculiarities which add complexity to the procedure, first its extraordinarily small mass $m_{\text{Ps}} = 2 \times m_{\text{e}}$ and, secondly, its antimatter properties, above all its limited lifetime of only 142 ns for ortho-Ps which imposes high requirements on the timing of Ps cooling experiments. The scheme is further complicated due to the presence of a magnetic field. The interaction between the Ps atoms with the magnetic field introduces two additional phenomena, namely the Zeeman effect and a motional Stark effect, which both have significant impact on the level structure. The field-induced effects lead to two different regions of level splitting, the standard Zeeman effect in weak fields and the Paschen-Back effect in strong fields. For the ground state the strong-field regime sets in at field strengths of about 5 T, while for the $n = 2$ level, the most relevant excited state manifold with regard to Ps cooling, it already starts to become effective for $B \gtrsim 1\,\text{T}$.

Due to the antimatter character of the Ps atom, in particular the large difference between the lifetimes of the singlet and triplet ground states, the presence of the magnetic field gives rise to another special phenomenon, the so-called magnetic quenching. Due to Zeeman-induced shifting and coupling of different spin states, certain ortho-Ps states acquire singlet character in magnetic fields which, depending on the field strength B, can lead to a substantial reduction in lifetime. Coupling takes place between all spin states with similar m quantum number. The presence of quenching requires minimising the involvement of quenched excited states in the laser cooling scheme. The situation only improves when the field strength exceeds the threshold to the Paschen-Back regime, where the coupling is broken.

As the name suggests, cooling of the atoms requires, the removal of momentum from the atomic ensemble. In the context of laser cooling this is achieved by taking advantage of the interaction between the atoms and laser fields that drive transitions between the internal atomic states via photon absorption and emission accompanied by momentum transfer. This light-induced recoil effect can be exploited for cooling by irradiating the Ps cloud with a coherent and directed beam of photons. The cooling efficiency is maximised by exciting and saturating the transition that has the shortest fluorescence lifetime, which, in the case of Ps, is the transition between the 1^3S and

2^3P states. Saturation ensures that a maximum fraction of up to 50% of the atoms is excited at all times.

The tiny mass of the Ps atom gives rise to another peculiarity of the Ps laser cooling scheme. While standard laser cooling generally takes place on broad-line transitions with linewidths Γ much larger than the recoil-equivalent frequency $\omega_{\mathrm{rec}} = \hbar k^2/(2m)$, the huge recoil of the Ps atoms has the consequence that, under certain conditions, the broad-line condition can no longer be fulfilled. This, in turn, requires an alternative mathematical treatment than the commonly applied Brownian motion approach. In case of narrow-line cooling it is instead necessary to describe the cooling process by means of a model based on momentum diffusion. In this framework the minimum temperature attainable by laser cooling, the recoil temperature T_{rec}, is determined by the recoil energy, whereas for broad-line cooling the minimum temperature is proportional to the natural transition linewidth Γ_{ge} and referred to as the Doppler temperature T_{Doppler}. In both cases, the dominant characteristic energy governs the limit.

The decisive condition for the classification as broad- and narrow-line processes is given by the ratio between the cooling transition linewidth Γ and the recoil-equivalent frequency ω_{rec}. For ordinary atoms that consist of at least one (anti-)proton it is in general greater than 1. Even within the same atomic system the linewidth Γ is not a constant of the respective atom-light interaction, but is subject to a number of broadening mechanisms. The most important process to be mentioned in this regard is the laser-induced power broadening, which represents a convenient tool to artificially enhance the linewidth significantly, thereby recovering the broad-line condition. In case of positronium this can be achieved by using high-intensity broadband laser radiation with bandwidths of the order of several tens of gigahertz and laser powers in the range of kilowatts – realistic requirements in experimental terms.

Even if photon transfer during absorption and emission is an intrinsically coherent process, the entire state dynamics during laser cooling does not necessarily have to be described coherently as well. Provided that the coherences of the system dephase much faster than the transition is driven, the dynamics effectively become an incoherent process that no longer needs to be treated within the complex framework of the optical Bloch equations. Instead, the transition events can then be regarded as stochastically occurring events, such that the individual state populations are adequately described by simple rate equations. This treatment is particularly valid for Ps laser cooling using broadband laser sources.

Numerical investigations of the Ps cooling scheme

Given the complexity of the Ps laser cooling scheme it becomes clear that any attempt of an experimental realisation of Ps laser cooling is challenging and requires control over a large number of parameters. To investigate this parameter space and identify the configuration which offers maximum cooling efficiency, the scheme was first investigated numerically based on the concept of incoherent rate equations solved by means of a kinetic Monte Carlo algorithm. To accurately account for all magnetic-field-induced interaction processes and allow for arbitrary field configurations, the eigenstates and -values were obtained from a diagonalisation of the full Hamiltonian at each simulation time step. The employed code is highly versatile and reliably simulates – within the scope of the rate equation formalism – the evolution of the Ps cloud by deterministically solving the trajectories of the Ps atoms in laser and external fields, while stochastically accounting for the internal level dynamics.

The simulations were first carried out in a one-dimensional configuration in which a cloud of 2000 atoms at a temperature of $T = 300\,\mathrm{K}$ in a magnetic field of $B = 1\,\mathrm{T}$ is cooled by means of a 75 GHz-broad laser at a wavelength of 243 nm and with a pulse length of 200 ns. The most important result of this study is that all main figures of merit for cooling can be improved over the entire 200 ns interaction window, demonstrating that the cooling laser allows to considerably increase the number of cold atoms compared to a situation without laser excitation. Within the first 50 ns of laser interaction the effective temperature T quickly drops from 300 K to almost 100 K, and over the remaining 150 ns more slowly to below 40 K. In addition, the gain in the number n_{r} of slow atoms (with velocities smaller than twice the recoil velocity) due to laser cooling can be

constantly enhanced from an initial ratio of 1 up to a final value of about 8. Cooling thereby occurs mainly on transitions that involve long-lived m states, despite the Zeeman and motional Stark mixing which lead to an increase in the final fraction of annihilated atoms from 70% in a field-free environment to roughly 85% in 1 T. This leads to the general recommendation to cycle the cooling transition preferably with $\sigma^{(+)}$ polarised light in order to avoid the population of short-lived states from the outset.

With regard to the magnetic field strengths there exists, however, a regime between about 0.1 T and 0.7 T where cooling becomes completely pointless due to the Zeeman- and motional Stark-induced coupling of laser-excited atoms to short-living states. In this range, the fast annihilation of cooled atoms causes a significant loss of slow atoms, resulting in the survival of only fast moving particles, as reflected by a dramatic increase in temperature T. In very weak, but also strong fields above 1 T, on the other hand, the benefits of laser cooling by far outweigh the potential negative side effects, in line with theoretical predictions, such as the transition to the Paschen-Back regime at $B \gtrsim 1$ T.

As far as the velocity distribution of the ensemble of Ps atoms is concerned, the interaction with the counter-propagating 243 nm-laser beams produces the characteristic features of laser cooling, namely two pronounced depletion zones around the spectral position of the beams and a corresponding strong enhancement in the centre. An important finding is that the cooling efficiency remains at a high level over a relatively broad parameter range, mitigating the requirement for optimal parameter configurations in the experiment.

The results of the 1D studies were confirmed by examinations of 3D-configurations. In general, all figures of merit for cooling significantly benefit from laser interaction, albeit not quite as strongly as in 1D. Still, cooling is highly efficient for all magnetic field strengths, except for the mentioned range that is to be excluded absolutely. By investigating two specific applications, namely the cooling of an effusive beam in two-dimensional transverse or 3D moving molasses configuration, it could be demonstrated that the experimental realisation of cooling, especially within the setup of the AEḡIS experiment, could also be successful with shorter laser pulses and offset target position. In both cases, the transverse temperature is reduced significantly by laser cooling, namely to 70 K in 2D and even to 10.5 K in 3D-molasses configuration.

Motivated by the highly promising results of the numerical studies, a design for an experimental realisation for Ps laser cooling was developed for the technical platform of the AEḡIS experiment. The crucial difference between the numerical and experimental approach lies in the observables for Ps-laser interaction as well as the choice of the figures of merit for evaluating the cooling efficiency. This is due to the fact that in the experiment the velocity distribution of the atomic ensemble is by far not as easy to access as in any numerical simulation, where the relevant velocities are immediately available as output data. In the experiment, on the other hand, this information can only be obtained by probing the Ps cloud. In the approach pursued for this thesis, this is achieved by means of an additional probe laser scheme, which must be completely independent of both the cooling sequence and the level dynamics of the cooling transition. The actual data recording process then relies on a special detection technique as an "information carrier", a component that is also not relevant in numerical studies.

In the present scheme, Ps detection was realised by means of the SSPALS technique, which is effectively based on the characteristics of positron annihilation either resulting from spontaneous annihilation of the Ps atoms or stimulated by laser-induced photoionisation, the tool employed for probing. In this technique, the effect of cooling is evaluated in terms of the $S\%$ parameter, which is defined as the laser-induced change of the temporal SSPALS spectrum within a specific time window. Changes in the $S\%$ signal directly correlate with modifications of the Ps population in the probed velocity class, such as those that result, for example, from a momentum transfer during cooling. The primary observable for cooling in the experiment is therefore the modification of the velocity distribution that consists of the $S\%$ values of each resolved velocity class.

To identify the pure recoil effect of the interaction with the cooling laser, the measurement scheme consists of a fourfold scheme that comprises all four possible combinations of probing and cooling lasers. The cooling pulses were generated in a multi-stage frequency doubling procedure that was set up in the course of this thesis. It ultimately provides pulses with tunable wavelength

around 243 nm, durations of 26 ns on average, powers of up to 1 mJ and bandwidths of 129 GHz FWHM for cycling the atoms on the standard cooling transition $1^3S \leftrightarrow 2^3P$. Probing was carried out subsequently to cooling via a two-photon transition scheme in which a strong 1064 nm laser selectively photoionises all atoms that were previously excited to the $n = 3$ level by means of a wavelength-tunable pulsed laser at 205 nm with a fixed bandwidth of $\sigma_{205} = 111$ GHz. At the same time, this value defines the resolution for probing the velocity distribution and thus limits the minimum spectral width of detectable cooling-induced modifications.

To address the high degree of complexity of the measurements a refined analysis method, the semi-detrending technique, was developed, which is capable of revealing the effect of laser interaction at 243 nm, while reliably accounting for all detrimental fluctuations in the system. Due to the presence of the magnetic field with a strength of 180 G all detected effects are inherently affected by magnetic quenching of the $n = 2$ states, which superimposes all recoil-induced effects. As the effects of quenching and momentum transfer are inextricably linked with laser excitation, even the most sophisticated measurement, detection and analysis techniques do not allow for a quantification of the quenching contribution. This represents one of the major limitations of the experimental measurements of Ps laser cooling in magnetic fields.

Cooling measurements were performed for three different detunings $\delta_{243} = 12$ pm, 25 pm and 42 pm. The quantitative analysis of the distributions acquired with 25 pm provides unambiguous evidence of a symmetrical optical force via the transfer of momentum by the cooling laser. Both a pronounced region of population depletion on the flanks of the Doppler distribution and a statistically significant enhancement in the centre were observed. Specified in terms of the difference $\Delta(S\%)$ in $S\%$ signals on resonance, the population increase in the cooled, with respect to the uncooled distribution, amounts to $\Delta S = (1.21 \pm 0.96)$ p.p. This laser-induced accumulation of atoms is a clear indication that the atoms have been pushed towards the centre as a result of the net recoil that is transferred via photon absorption and emission. Another important result of the analysis is that the enrichment $(\Delta S)_{\mathrm{recoil}}$, caused solely by the recoil effect, is roughly twice as large as the measured number suggests, due to the adverse effect of quenching.

Quenching was therefore studied in more detail by means of further dedicated simulations to reproduce the experimental measurements as precisely as possible. In contrast with the experiment, these calculations allowed to distinguish between recoil and quenching effects and to study both of them in isolation. The comparison between the numerical and experimental results confirms the outcome of the measurements as well as the qualitative and quantitative conclusions drawn from them. It furthermore reveals that the enhancement which solely results from momentum transfer amounts to $(\Delta S)_{\mathrm{recoil}} = (2.43 \pm 1.33)$ p.p.

Outlook and suggestions for future improvements

The performed measurements have exhausted the full potential of the current state of the experimental system. While exploring its entire range of capabilities a number of limitations were encountered that should be addressed with regard to future measurements. As far as the cooling process itself is concerned, the 243 nm-pulse length and -bandwidth are probably the most important parameters to be modified. The numerical studies presented in Sec. 3.1 clearly show that the cooling effect can be further enhanced by cycling the atoms for more than a few tens of nanoseconds. Even though the present bandwidth is already within the range of optimum values the cooling efficiency would furthermore benefit from an increase in spectral coverage of the Ps cloud. Bandwidth tunability would moreover allow for an exploration of its influence on the cooling performance. With regard to the spatial overlap, the excitation efficiency could be enhanced by modifying and expanding the beam shape while conserving its energy density.

As far as probing is concerned the cooling measurements are currently primarily limited by the bandwidth of the 205 nm-laser. Optimisation measures are necessary to ensure resolving the smallest possible cooling-induced alterations in the velocity distribution. In doing so, a reasonable compromise has to be found in order not to impair the signal strength too much. With constant monitoring, the bandwidth could additionally be included as a parameter in the data analysis.

Another bandwidth-related aspect to be studied further is the wavelength-dependence of the 205 nm-bandwidth that is induced by the non-linear optical generation process, but not yet fully understood. By far the most important technical limitations of Ps laser cooling is, however, the presence of the magnetic field required for efficient positron transport. In view of the high impact of magnetic quenching on the measurement outcome, it is clearly worth making every effort to mitigate or even eliminate this effect.

Due to the complexity of the experiment, the measurements are furthermore susceptible to a number of factors that cause random errors which should be minimised further or at least brought under control reliably. The most important factors to be mentioned are the various laser-induced fluctuations, such as the jitter of the pulse timing or the pulse length. Further sources of instability are the energy fluctuations of both UV-lasers. Especially for probing, the energy stability plays a crucial role as the energy can have an effect on the resolving power due to power broadening. Constant energy monitoring, including active feedback to the laser control, if feasible, is therefore indispensable.

For all these reasons, the AEḡIS Ps experiment will strongly benefit from several upgrades planned for the near future. The recently started refurbishment of the positron system, which is supposed to enable Ps generation in environments free of magnetic fields, is certainly a decisive step in the direction of measurements of the pure recoil effect. A second major improvement is the commissioning of an alexandrite laser for the production of pulsed 243 nm-laser beams by means of third-harmonic generation starting from a fundamental wavelength of 729 nm. Upon completion, this laser setup will provide laser pulses of up to 300 ns in length and significantly larger bandwidths, which could cover half the velocity distribution. Further promising experimental results, with unprecedented accuracy, can therefore be expected in the near future, once these upgrades have been successfully implemented.

As far as the numerical simulations are concerned, there are also some refinements conceivable that would allow for an even more precise replication of the experimental setup and a reproduction of the performed Ps laser cooling measurements. In addition to the implementation of the grazing beam alignments this applies in particular to an improved model of the real spectrum of the laser pulses. Another important aspect to address is the phase loss issue, which is currently the main limitation of the code as it has so far precluded the investigation of different polarisation schemes. Closer examination of this effect is required to develop improvements that would eventually increase the versatility of the code even further.

In conclusion, the results obtained in the context of this thesis have certainly brought the production of cold ensembles of Ps atoms, and hence a wide range of fascinating applications, within reach.

Appendix A

Annihilation and fluorescence lifetimes of the Ps atom up to $n=3$

State	Energy E $\left[\text{cm}^{-1}\right]$	$\Delta E^{(\text{QED})}$ [MHz]	Annihilation Lifetime $\tau^{(\text{ann})}$		Fluorescence Lifetime $\tau^{(\text{fl})}$	
1^1S_0	-6.81759	-111312	125 ps	[118]	N/A	
1^3S_1	0.00000	93074	142 ns	[118]	$\simeq 3 \cdot 10^7\,\text{s}$	[119]
2^1S_0	41147.81431	-17221	1.0 ns	[66]	$\simeq 243.1\,\text{ms}$	[85]
2^3P_0	41148.05779	-9921	99.75 µs	[66]	3.19 ns	[53]
2^3P_1	41148.24040	-4447	∞	[66]	3.19 ns	[53]
2^1P_1	41148.30127	-2622	3.63 ms	[67]	3.19 ns	[53]
2^3P_2	41148.38650	-67	374.06 µs	[66]	3.19 ns	[53]
2^3S_1	41148.66651	8327	1.11 µs	[67]	$\simeq 243.1\,\text{ms}$	[85]
3^1S_0	48768.85756	-5339	3.36 ns	[66]	312.5 ns	[9]
3^3P_0	48768.92970	-3176	284.05 µs	[66]	10.54 ns	[84]
3^3P_1	48768.98380	-1555	∞	[66]	10.54 ns	[84]
3^1P_1	48769.00185	-1013	9.75 ms	[67]	10.54 ns	[84]
3^3P_2	48769.02701	-259	1.065 ms	[66]	10.54 ns	[84]
3^3D_1	48769.01266	-689	$\geq 11\,\text{ms}$	[99]	30.92 ns	[84]
3^3D_2	48769.02712	-256	$\geq 11\,\text{ms}$	[99]	30.92 ns	[84]
3^1D_2	48769.03076	-148	$\geq 400\,\text{µs}$	[99]	30.92 ns	[84]
3^3D_3	48769.04105	162	$\geq 11\,\text{ms}$	[99]	30.92 ns	[84]
3^3S_1	48769.11007	2231	3.74 µs	[67]	312.5 ns	[9]

TABLE A.1: *Energy and lifetimes of all Ps states up to and including $n = 3$.*
The table shows the energy as well as lifetime values, separately for annihilation and fluorescence, of all states up to and including the $n = 3$ level. States are sorted by their energy in units of wavenumbers ($[cm^{-1}]$), i.e. $\tilde{\nu} = E/hc$, with the zero point chosen (arbitrarily) at the triplet ground state 1^3S_1 energy.
Additionally specified are the energy differences $\Delta E^{(\text{QED})}$ due to QED-corrections (in frequency units) with respect to the according Bohr level energy $E_0^{(n)}$ (the deviations of the values compared to Fig. A.1 are caused by different precision in the calculation of the QED-corrections). The specification "not applicable (N/A)" in the last column for the 1^1S_0 state means that this state does not show any fluorescence.
For the sake of visibility, term symbols are aligned according to the state's spin state, following the usual style singlets to the left and triplets to the right.
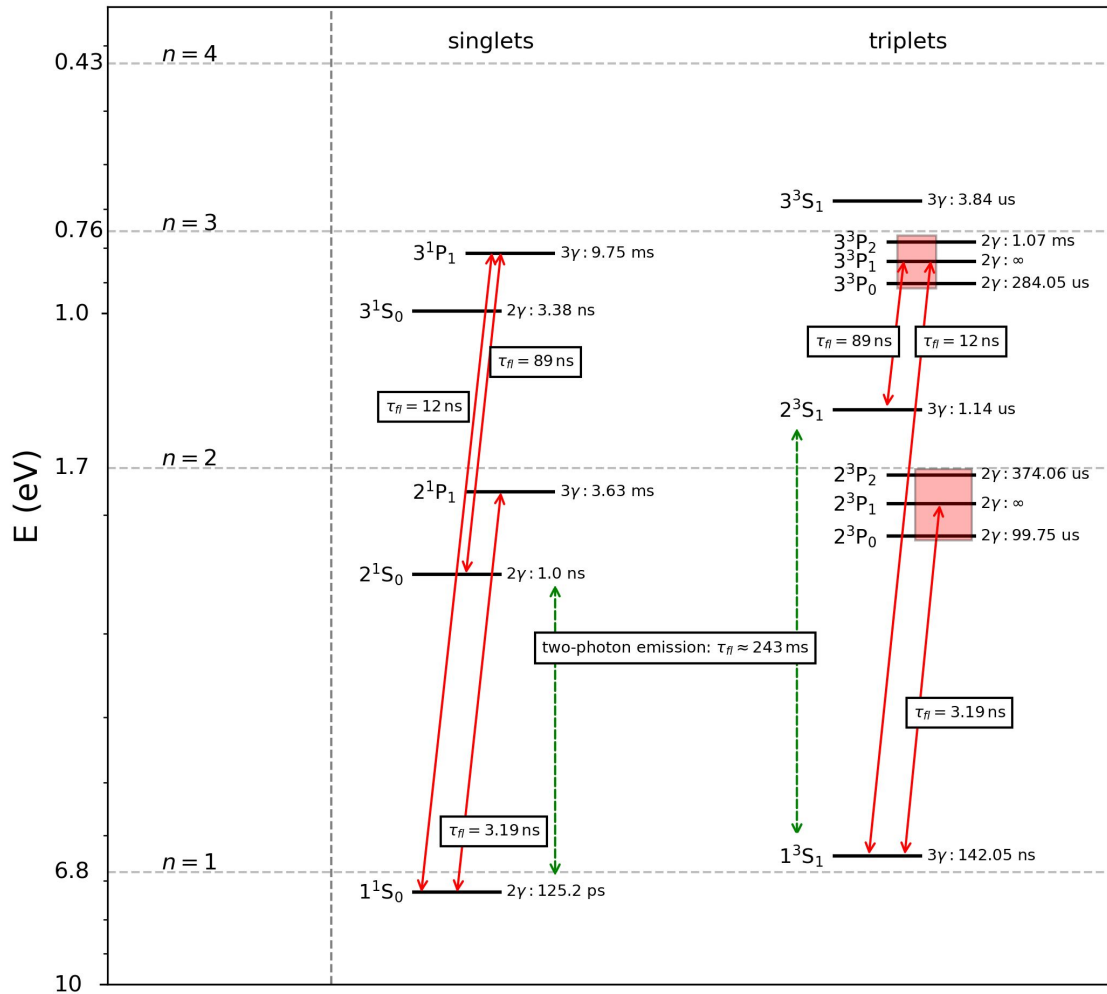
FIGURE A.1: *Ps level scheme including fluorescence and annihilation lifetimes for states up to and including $n = 3$ in absence of external fields.*

The energy level scheme shows the fluorescence and annihilation lifetimes of all states up to and including $n = 3$ (as listed in Tab. A.1) with the former as boxed numbers next to the red arrows indicating the respective transition and the latter specified next to each level together with the corresponding annihilation decay products. The green dashed arrows emphasise special feature of fluorescence decay through two-photon emission for the 2S-states. Figure taken from [28], 3D-states have not been added. All annihilation lifetimes in the figure result from expressions including relativistic corrections and can therefore slightly differ from the numbers listed in Tab. A.1.

Appendix B

The positronium atom in magnetic fields

In order to lay the foundation for investigations of Ps under realistic experimental conditions it is in the next step essential to add the interaction of the Ps atom with external magnetic fields. For this purpose the following section is first devoted to deriving such a notation of the Hamiltonian for two particles in magnetic fields which represents the most instructive structure for further analysis and discussion of involved processes. At the same time this exercise enables to reveal some peculiarities of a system composed of two particles with equal masses, such as the electron-positron pair in the Ps atom. Starting from the general notation of the Hamiltonian in Cartesian coordinates the most important step will consist in the transformation to the centre-of-mass frame. Prior to this though, a brief recap will be given on some relevant aspects with regard to the concept of momentum.

Since external electric fields (different than the Ps motion-induced Stark fields (more details later)) do not play a role in the context of this thesis, terms describing the interaction of charged particles with external electric fields will not be taken into account.

B.1 General Hamiltonian

In Cartesian coordinates the full Hamiltonian for two particles with masses m_i, charges q_i and spins $\boldsymbol{S}_i$ in a magnetic field $\boldsymbol{B}$ is given by

$$\hat{H} = \sum_i \left[\frac{1}{2m_i} \hat{p}_{\mathrm{kin},i}^2 - \hat{\boldsymbol{\mu}}_{s,i} \cdot \boldsymbol{B} + \frac{1}{2} q_i \Phi_j(\boldsymbol{r}_i) \right] \tag{B.1}$$

where $\hat{\boldsymbol{\mu}}_s = g_s q/(2m)\hat{s}$ denotes the particle's intrinsic magnetic dipole moment induced by their spin, with g_s indicating the spin gyromagnetic ratio, also known as spin g-factor. The term $1/2\, q_i \Phi_j(\boldsymbol{r}_i)$ represents the potential energy of charge i in the electrostatic potential of charge j at the position of particle i. In case of two point-like particles, as it is the case for one Ps atom, the two according terms sum up to the well-known Coulomb potential energy term given by

$$\hat{V}_{\mathrm{C}} = \frac{1}{2} q_1 \Phi_2(\boldsymbol{r}_1) + \frac{1}{2} q_2 \Phi_1(\boldsymbol{r}_2) = \frac{1}{4\pi\epsilon_0} \frac{q_1 q_2}{|\boldsymbol{r}_1 - \boldsymbol{r}_2|} \ .$$

B.2 Quantum field theory in a nutshell

Before proceeding with transforming this Hamiltonian to the more convenient center-of-mass (CM) frame where the further analysis and discussion becomes more instructive, a brief (experimentalist's) introduction of the terminology of coordinates will follow. The purpose of this short recap is first to point out why the transformation to the CM-frame is "valid" in quantum mechanical terms but also to justify and explain the reason for using different types of momentum, namely kinetic, conjugate, canonical and pseudomomenta. For more rigorous and profound interested readers are referred to abundant literature such as text books on Quantum Mechanics (e.g. [74, 120, 121]), Quantum Electrodynamics (e.g. [122]) or Quantum Field Theory (e.g. [123]).

Cartesian coordinates represent the most commonly used set of *generalised coordinates* q_i that means coordinates which can be used to specify the configuration of a given physical system in a unique way. In case of Cartesian coordinates the generalised coordinates are represented by the positions r_i. The dynamics of a given system is then described in terms of position $\boldsymbol{r}$ and its *canonically conjugate* momentum $\boldsymbol{p}$ which in EM-field is given by $\boldsymbol{p} = \boldsymbol{p}_{\mathrm{kin}} + q\boldsymbol{A}$ where

B| The positronium atom in magnetic fields

$\boldsymbol{p}_{\text{kin}} = m\boldsymbol{v}^2 = m\dot{\boldsymbol{r}}^2$ is the kinetic momentum and $\boldsymbol{A}$ the *vector potential* incorporating magnetic fields present. Let's now have a brief look what is meant by dynamics and the terms conjugate and canonical.

The momentum is called *conjugate* since it is related to the position according to the Fourier transform. In quantum mechanics variables are called conjugate if their according operators do not commute but are related to each other in terms of commutation relations. The pair $(\hat{\boldsymbol{r}}, \hat{\boldsymbol{p}})$, composed of position $\hat{\boldsymbol{r}}$ and conjugate momentum $\hat{\boldsymbol{p}}$, are for example related to each other by the well-known *canonical commutation relation* $[\hat{r}_i, \hat{p}_j] = i\hbar\delta_{ij}$ where $\hat{r}_i$ and $\hat{p}_i$ denote the components of the position and momentum respectively. Non-commutativity also implies that there always exists an *uncertainty principle* for conjugate variables, such as the well-known Heisenberg's uncertainty principle $\Delta\boldsymbol{r}\Delta\boldsymbol{p} \geq \hbar/2$ for position and momentum.

Among all commutation relations the canonical commutation relations play an outstanding and fundamental role in the formalism of quantum mechanics. This is due to the fact that historically quantum mechanics was deduced as extension of classical mechanics, called quantisation. One prominent example for this transition is the *canonical quantisation* which aims at preserving the formal structure of classical mechanics including symmetries for example.

In classical Hamiltonian mechanics a set of conjugate coordinates $\mathbf{r} = (\mathfrak{q}, \mathfrak{p})$ is called *canonical* if they satisfy the Poisson brackets and for which the time evolution of the system's state that means the equations of motion are given by Hamilton's equation

$$\dot{\mathfrak{q}}_i = \frac{\partial H}{\partial \mathfrak{p}_i} \qquad \text{and} \qquad \dot{\mathfrak{p}}_i = -\frac{\partial H}{\partial \mathfrak{q}_i} \tag{B.2}$$

which are called canonical due to their very simple and symmetric form [124]. $H(\mathfrak{q}_i, \mathfrak{p}_i, t)$ is the Hamiltonian which gives the system's energy at all times t in terms of the canonical variables $\mathfrak{q}_i$ and $\mathfrak{p}_i$ [125].

Preservation of the formal structure now implies to find quantum analogues for which quantum equations of motion take an equally symmetric form. This is achieved by choosing a set of conjugate variables $\mathbf{r} = (\mathfrak{q}, \mathfrak{p})$ for which the sometimes called *Quantum Hamilton equations* (that means Hamilton's equations applied to the quantum Hamiltonian $\hat{H}$) take the same canonical form [126, 127]. Then, the commutation relations which are satisfied by these canonical coordinates are called *canonical commutation relations*.

As an example for this analogy one might consider the equations of motion in the Heisenberg picture which, in agreement with the correspondence principle, reduce to the classical equations of motion [127] by exchanging the commutator relations with their classical counterparts the Poisson brackets [128] and vice versa. As a side note it is worthwhile to mention that the Heisenberg picture[28] is for example useful to understand whether a quantity is conserved that means is a *constant of motion*: According to the equation of motion in the Heisenberg picture the time evolution of an operator $\hat{X}$ (and thus also of operators), given by

$$\frac{d\hat{X}_H}{dt} = \frac{1}{i\hbar}\left[\hat{X}_H, \hat{H}\right] \tag{B.3}$$

is zero if it commutes with the Hamiltonian $\hat{H}$ (where the subscript H indicates the operator's Heisenberg representation).

Before returning to the initial problem of the Ps atom in magnetic fields, a last comment should be made on the canonical momentum in presence of an electromagnetic field which represents the environment the Ps atom is going to be analysed in: While for neutral free particles the canonically conjugate (with respect to the position $\boldsymbol{r}$) momentum $\boldsymbol{p}$ is equal to the kinetic momentum $\boldsymbol{p}_{kin} = m\dot{\boldsymbol{r}}$, in magnetostatics, i.e. environments with static homogeneous magnetic field, the

---

[28] The Heisenberg picture is that formulation of quantum mechanics where operators are time-dependent whereas states vectors are constant in time. This is in contrast to the Schrödinger picture where time dependence is incorporated in the opposite way: here states evolve in time while observables are constant. The Heisenberg and Schrödinger picture are the most important ways of formulating quantum mechanics.

canonical momentum is in *minimal coupling*[29] (in the non-relativistic case) given by $\boldsymbol{p} = \boldsymbol{p}_{kin} + q\boldsymbol{A}$ where q is the particle's charge and $\boldsymbol{A}$ the so called *vector potential* incorporating the magnetic field in the Hamiltonian $\hat{H}$ [130, 131].

Consequently, for a system of charged (q_α) (but still spin-less) particles of mass m_α in magnetic fields, the Hamiltonian which describes the energy of the system and is thus proportional to $\hat{\boldsymbol{p}}_{kin}^2$, then becomes

$$\hat{H} = \sum_\alpha \frac{1}{2m_\alpha} \left[\hat{\boldsymbol{p}}_\alpha - q_\alpha \boldsymbol{A}(\hat{\boldsymbol{r}}_\alpha) \right]^2 + \hat{V}_{\mathrm{C}} \tag{B.4}$$

(with $\hat{V}_{\mathrm{C}}$ the potential energy due to Coulomb interaction) which in position representation can be written as

$$\hat{H} = \sum_\alpha \frac{1}{2m_\alpha} \left[-i\hbar\nabla_\alpha - q_\alpha \boldsymbol{A}(\boldsymbol{r}_\alpha) \right]^2 + \hat{V}_{\mathrm{C}} \tag{B.5}$$

by using the well-known replacement $\boldsymbol{p} \to -i\hbar\nabla$ (as a direct consequence of the form Schrödinger's equation is postulated) [120], where ∇_α denotes the three-dimensional derivative with respect to the position of particle α.

As far as the canonical commutation relations are concerned though, it is (as their name already suggests) not the components of the kinetic momentum but rather of the canonical one p_i which, together with the position components x_i satisfy

$$[r_i, p_j] = i\hbar\delta_{ij} \ . \tag{B.6}$$

$\boldsymbol{p}$ is thus also the relevant momentum with regard to the equations of motion [122].

However, it should be mentioned that, in contrast to the kinetic momentum $\boldsymbol{p}_{\mathrm{kin}}$, the canonical momentum for particles in electromagnetic fields is not gauge invariant [132] which can easily be seen as follows: The vector potential is used to account for the magnetic field $\boldsymbol{B}$. Since the only constraint on $\boldsymbol{B}$ is to satisfy Maxwell's equation $\nabla\boldsymbol{B} = 0$ it can be written as the curl $\boldsymbol{B} = \nabla \times \boldsymbol{A}$ of the vector potential $\boldsymbol{A}$. Obviously, this definition of $\boldsymbol{A}$ leaves some degree of arbitrariness in choosing $\boldsymbol{A}$ as it is always possible to add an arbitrary scalar potential Ψ by $\boldsymbol{A}' \to \boldsymbol{A} + \nabla\Psi$ without changing $\boldsymbol{B}$ and contradicting Maxwell's equation [133]. This transformation is called gauge transformation and reflects the translation invariance of dynamics in constant magnetic fields [134]. Thus, the canonical momentum depends on the gauge and is thus not gauge invariant. This directly implies that the canonical momentum is also not physically measurable whereas the kinetic momentum can be observed [135]. In general, in presence of magnetic fields none of them, neither canonical nor kinetic momenta are conserved quantities.

In non-relativistic magnetostatics it is preferable to choose the gauge such that the vector potential fulfils the relation $\nabla \cdot \boldsymbol{A}(\boldsymbol{r},t) = 0$ which is the so called *Coulomb gauge*. The name Coulomb gauge is owing to the fact that in this gauge the vector potential is completely defined by the magnetic field while the charge density is completely absorbed by the scalar potential $\Phi(\boldsymbol{r},t)$ (in magnetostatics only required to account for the charge density $\rho(\boldsymbol{r},t)$) so that the latter potential then simply becomes the Coulomb potential [120, 133]. Vector and scalar potential can thus be considered as being decoupled in describing the fields in the sense that magnetic fields $\boldsymbol{B}(\boldsymbol{r},t)$ are purely generated by $\boldsymbol{A}(\boldsymbol{r},t)$ whereas the (external) electric field $\boldsymbol{E}(\boldsymbol{r},t)$ is determined by $\Phi(\boldsymbol{r},t)$. Consequently, if there are no charges $\Phi(\boldsymbol{r},t)$ vanishes. This decoupling transfers to and is reflected by the Hamiltonian (B.4) where the kinetic energy term is completely defined by the kinetic momentum since the scalar potential only enters the potential energy term $\hat{V}_{\mathrm{C}}$ [122, 136].

Many options exist for the choice of $\boldsymbol{A}$ which all satisfy the Coulomb gauge condition. Throughout this thesis the most commonly used expression

$$\boldsymbol{A}(\boldsymbol{r}) = \tfrac{1}{2}\boldsymbol{B} \times \boldsymbol{r} \tag{B.7}$$

is adopted which is also known as the *symmetric gauge*.

---

[29] In (quantum) field theory *minimal coupling* represents one possible way to account for electromagnetic interaction and introduce it in the Lagrangian and Hamiltonian. In contrast to the Pauli coupling it includes only the charge distribution itself whereas multipole moments are ignored [129].

B.3 Transformation to the centre-of-mass frame

To finally come back to the original path, the above derived equations shall be applied to the system of the Ps atom in a constant magnetic field. Since being composed of two particles with equal masses and opposite charge, bound due to reciprocally attracting Coulomb potentials, many symmetries exist. Thus, for describing, solving and analysing the result of the eigenvalue problem, it is clearly favourable and more instructive to introduce another set of generalised coordinates, than Cartesian ones, which benefit from physical constraints in the system and take advantage of the mentioned symmetries. For this purpose it is most convenient to transform the equation into the center-of-mass (CM) frame with the goal to separate the motion of the centre of mass $\boldsymbol{R}_{\mathrm{CM}}$ from the relative motion where $\boldsymbol{R}_{\mathrm{CM}}$ and the relative position r for a system of two particles with masses m_1 and m_2 located at positions $\boldsymbol{r}_1$ and $\boldsymbol{r}_2$ are respectively defined as

$$\boldsymbol{R}_{\mathrm{CM}} = \frac{m_1\boldsymbol{r}_1 + m_2\boldsymbol{r}_2}{m_1 + m_2} \qquad \text{and} \qquad \boldsymbol{r} = \boldsymbol{r}_1 - \boldsymbol{r}_2 \ . \tag{B.8}$$

In case of the Ps atom with $m_{\mathrm{e}^-} = m_{\mathrm{e}^+} = m_{\mathrm{e}}$ this simplifies to

$$\boldsymbol{R}_{\mathrm{CM}} = \frac{1}{2}(\boldsymbol{r}_{\mathrm{e}^-} + \boldsymbol{r}_{\mathrm{e}^+}) \qquad \text{and} \qquad \boldsymbol{r} = \boldsymbol{r}_{\mathrm{e}^-} - \boldsymbol{r}_{\mathrm{e}^+} \tag{B.9}$$

<div align="center">or</div>

$$\boldsymbol{r}_{\mathrm{e}^-} = \boldsymbol{R}_{\mathrm{CM}} + \frac{\boldsymbol{r}}{2} \qquad \text{and} \qquad \boldsymbol{r}_{\mathrm{e}^+} = \boldsymbol{R}_{\mathrm{CM}} - \frac{\boldsymbol{r}}{2} \ . \tag{B.10}$$

The center-of-mass-transformation is a so called *canonical transformation* [137]. In quantum mechanics, canonical transformations are invertible transformations that map one pair $\mathfrak{r} = (\mathfrak{q}, \mathfrak{p})$ of conjugate variables to a new one $\mathfrak{r}' = (\mathfrak{q}', \mathfrak{p}')$ while preserving the commutation relations, i.e. $[\hat{\mathfrak{q}}'_i, \hat{\mathfrak{p}}'_j] = i\hbar\delta_{ij}$ is still valid, and thus also the structure of the equations of motion [138]. Even though also non-canonical transformations can in principle be applied it is to some extent convenient to use only canonical ones since the transformation to another frame should preferably not modify the description of the dynamics in the system, expressed in terms of the equations of motion. The topic of canonical transformations is also related to the principle of covariance but since this can soon become quite complex, especially due to the quantum mechanical character, even for the "simple" center-of-mass transformation, it will not be discussed any further here but referred to literature such as [138–140]. Yet, in the context of the centre-of-mass frame, the fact that it is a canonical transformation implies that the Cartesian coordinates $\boldsymbol{r}_1$ and $\boldsymbol{r}_2$ and its canonical conjugate momentum can be transformed to new CM-position variables $(\boldsymbol{R}_{\mathrm{CM}}, \boldsymbol{r})$ for which there exist conjugate momenta, written as $(\boldsymbol{P}_{\mathrm{CM}}, \boldsymbol{p})$, such that their components still satisfy the canonical commutation relations $[R_{\mathrm{CM},i}, P_{\mathrm{CM},j}] = i\hbar\delta_{ij}$ and $[r_i, p_j] = i\hbar\delta_{ij}$. The Hamiltonian will then keep its original structure (B.1), as it will become evident below.

Based on these relations and using $[R_{\mathrm{CM},i}, p_j] = 0$ and $[r_i, P_{\mathrm{CM},j}] = 0$ it can easily be shown that the new canonical conjugate momenta $\boldsymbol{P}_{\mathrm{CM}}$ and $\boldsymbol{p}$ are given by

$$\boldsymbol{P}_{\mathrm{CM}} = \boldsymbol{p}_1 + \boldsymbol{p}_2 \qquad \text{and} \qquad \boldsymbol{p} = \frac{m_2\boldsymbol{p}_1 - m_1\boldsymbol{p}_2}{m_1 + m_2} \ . \tag{B.11}$$

In other words, the canonical conjugate momentum $\boldsymbol{P}_{\mathrm{CM}}$ to $\boldsymbol{R}_{\mathrm{CM}}$ is thus simply the total momentum as the sum over all individual particle momenta.

Finally, by expressing the momenta $\boldsymbol{p}_{\mathrm{e}^-}$ and $\boldsymbol{p}_{\mathrm{e}^+}$ in Eq. (B.1) in terms of the above relations, using Eq. (B.4) and writing

$$M = \sum_i m_i \qquad \overset{\text{(Ps atom)}}{=} \qquad m_{\mathrm{e}^-} + m_{\mathrm{e}^+} = 2m_{\mathrm{e}} \qquad \text{and} \tag{B.12}$$

$$\mu = \left[\sum_i \frac{1}{m_i}\right]^{-1} \qquad \overset{\text{(Ps atom)}}{=} \qquad \frac{1}{\frac{1}{m_{\mathrm{e}^-}} + \frac{1}{m_{\mathrm{e}^+}}} = \frac{m_{\mathrm{e}}}{2} \tag{B.13}$$

respectively for the total and reduced mass, it can easily be shown that the Hamiltonian of the Ps atom transforms to

$$\hat{H}' = \frac{\hat{\boldsymbol{P}}_{\mathrm{CM}}^2}{2M} + \frac{\hat{\boldsymbol{p}}^2}{2\mu} + \frac{e}{m_{\mathrm{e}}}\hat{\boldsymbol{p}} \cdot (\boldsymbol{B} \times \boldsymbol{R}_{\mathrm{CM}}) + \frac{e}{4m_{\mathrm{e}}}\hat{\boldsymbol{P}}_{\mathrm{CM}} \cdot (\boldsymbol{B} \times \boldsymbol{r})$$

$$+ \frac{e^2}{4m_{\mathrm{e}}}(\boldsymbol{B} \times \boldsymbol{R}_{\mathrm{CM}})^2 + \frac{e^2}{16m_{\mathrm{e}}}(\boldsymbol{B} \times \boldsymbol{r})^2 - \left(\hat{\boldsymbol{\mu}}_s^{(\mathrm{e}^-)} + \hat{\boldsymbol{\mu}}_s^{(\mathrm{e}^+)}\right) \cdot \boldsymbol{B} + \hat{V}_{\mathrm{C}} \qquad (\mathrm{B.14})$$

$$= \frac{1}{2M}\left[\hat{\boldsymbol{P}}_{\mathrm{CM}} + \frac{e}{2}(\boldsymbol{B} \times \boldsymbol{r})\right]^2 + \frac{1}{2\mu}\left[\hat{\boldsymbol{p}} + \frac{e}{2}(\boldsymbol{B} \times \boldsymbol{R}_{\mathrm{CM}})\right]^2 - \left(\hat{\boldsymbol{\mu}}_s^{(\mathrm{e}^-)} + \hat{\boldsymbol{\mu}}_s^{(\mathrm{e}^+)}\right) \cdot \boldsymbol{B} + \hat{V}_{\mathrm{C}} .$$

It should be noted that the more compact notation in the second row in fact does not contain the centre-of-mass and relative kinetic momenta $\boldsymbol{P}_{\mathrm{CM}} + \frac{e}{2}(\boldsymbol{B} \times \boldsymbol{R}_{\mathrm{CM}})$ and $\boldsymbol{p} + \frac{e}{2}(\boldsymbol{B} \times \boldsymbol{r})$ respectively, as one might intuitively be tempted to assume by simple deduction of (B.1) replacing the Cartesian kinetic momenta by their analogue centre-of-mass expressions. This difference reflects the coupling between the centre-of-mass and internal motion which in turn prohibits to separate the Hamiltonian, and thus also the wave functions, into those two contributions already here. Nevertheless, though, the first term still represents the total internal kinetic energy, but scaled by a factor of $1/4$:

$$\frac{1}{2M}\left[\hat{\boldsymbol{P}}_{\mathrm{CM}} + \frac{e}{2}(\boldsymbol{B} \times \boldsymbol{r})\right]^2 = \frac{1}{2M}\left[(\hat{\boldsymbol{p}}_{\mathrm{e}^-} + \hat{\boldsymbol{p}}_{\mathrm{e}^+}) + \frac{e}{2}\boldsymbol{B} \times (\hat{\boldsymbol{r}}_{\mathrm{e}^-} - \hat{\boldsymbol{r}}_{\mathrm{e}^+})\right]^2$$

$$= \frac{1}{2M}[\hat{\boldsymbol{p}}_{\mathrm{kin},\mathrm{e}^-} + \hat{\boldsymbol{p}}_{\mathrm{kin},\mathrm{e}^+}]^2 = \frac{1}{4}\frac{\hat{\boldsymbol{p}}_{\mathrm{kin}}^2}{2\mu} = \tfrac{1}{4}\hat{E}_{\mathrm{kin,internal}}$$

using Eqs. (B.9) and (B.11). Likewise, the second term can be identified as the total kinetic energy of the centre of mass, scaled though by four.

In the process of deriving (B.14), one of the peculiarities of the Ps atom becomes obvious and effective: The most general version of the Hamiltonian of two charges particles in magnetic fields contains several additional cross terms consisting of two of the variables $\boldsymbol{R}_{\mathrm{CM}}, \boldsymbol{r}, \boldsymbol{P}_{\mathrm{CM}}$ and $\boldsymbol{p}$. However, due to equal masses and opposite charges of the electron and positron most of them vanish in the case of the Ps atom and are thus not shown in (B.14). There are two among them though, namely

$$-\frac{q_1 + q_2}{2M}\hat{\boldsymbol{P}}_{\mathrm{CM}} \cdot (\boldsymbol{B} \times \boldsymbol{R}_{\mathrm{CM}}) \quad + \quad \left(\frac{q_1 m_2}{2m_1 M} + \frac{q_2 m_1}{2m_2 M}\right)\hat{\boldsymbol{p}} \cdot (\boldsymbol{B} \times \boldsymbol{r}) \qquad (\mathrm{B.15})$$

which are quite interesting and should be briefly discussed here since they give some additional insight into the physics of the Ps atom in such a way that they significantly impact the Zeeman effect of the Ps atom. By applying the relation $\boldsymbol{a} \cdot (\boldsymbol{b} \times \boldsymbol{c}) = -\boldsymbol{b} \cdot (\boldsymbol{a} \times \boldsymbol{c})$, it becomes obvious that both of these terms can be identified as interaction terms of an orbital angular momentum with the magnetic field, in the first case due to a total orbital angular momentum $\boldsymbol{L}_{\mathrm{CM}} = \boldsymbol{R}_{\mathrm{CM}} \times \boldsymbol{P}_{\mathrm{CM}}$ and the second based on a relative one $\boldsymbol{l} = \boldsymbol{r} \times \boldsymbol{p}$. While the first term though cancels already due to opposite charges ($q_1 = q_2$) (and thus for all neutral atoms), the second one vanishes only if additionally also the orbital angular momenta agree ($\boldsymbol{l}_1 = \boldsymbol{l}_2$) which is only rarely the case for single atoms. The positronium atoms indeed represents such an exceptional case. Consequently, in combination with the opposite charges this results in mutual elimination of the according orbital magnetic dipole moments $\boldsymbol{\mu}_l = -g_l q/(2m_{\mathrm{e}})\boldsymbol{l}$. The fact that both these terms vanish sets Ps clearly apart from the hydrogen atom since it leads to significantly different qualitative results, for example, with regard to the trajectories of the centre of mass.

Furthermore, it has substantial impact on the behaviour and physical properties of the Ps atom in magnetic fields, above all the missing linear Zeeman effect for the internal motion, which normally originates from the second term in Eq. (B.15).

Equation (B.14) still shows the blemish of being dependent on the centre-of-mass coordinate $\boldsymbol{R}_{\mathrm{CM}}$ including a coupling to the internal momentum $\boldsymbol{p}$, even though the behaviour of $\boldsymbol{R}_{\mathrm{CM}}$ is

expected to be rather irrelevant with respect to the dynamics of the internal degree of freedom. For analysing the internal dynamics it would thus be convenient to get rid of all terms containing the centre-of-mass coordinate $\boldsymbol{R}_{\mathrm{CM}}$. It can be shown (cf. for example [141, 142]) that this elimination (compensated by enhanced $(\boldsymbol{B} \times \boldsymbol{r})$ terms) can be realised by applying another unitary gauge transformation $\hat{H} = U\hat{H}'U^{\dagger}$, with transformation operator U, in momentum space implying

$$U\hat{\boldsymbol{P}}_{\mathrm{CM}}U^{\dagger} = \hat{\boldsymbol{P}}_{\mathrm{CM}} + \frac{e}{2}\left(\boldsymbol{B} \times \boldsymbol{r}\right) \tag{B.16}$$

$$U\hat{\boldsymbol{p}}U^{\dagger} = \hat{\boldsymbol{p}} - \frac{e}{2}\left(\boldsymbol{B} \times \boldsymbol{R}_{\mathrm{CM}}\right) \tag{B.17}$$

so that (B.14) simplifies to its final version

$$\hat{H} = \frac{1}{2M}\left[\hat{\boldsymbol{P}}_{\mathrm{CM}} + e(\boldsymbol{B} \times \boldsymbol{r})\right]^2 + \frac{\hat{\boldsymbol{p}}^2}{2\mu} - \left(\hat{\boldsymbol{\mu}}_s^{(\mathrm{e}^-)} + \hat{\boldsymbol{\mu}}_s^{(\mathrm{e}^+)}\right) \cdot \boldsymbol{B} + \hat{V}_{\mathrm{C}}$$

$$= \frac{\hat{\boldsymbol{P}}_{\mathrm{CM}}^2}{2M} + \frac{e}{M}\hat{\boldsymbol{P}}_{\mathrm{CM}} \cdot (\boldsymbol{B} \times \boldsymbol{r}) + \frac{e^2}{16m_{\mathrm{e}}}(\boldsymbol{B} \times \boldsymbol{r})^2 + \frac{\hat{\boldsymbol{p}}^2}{2\mu} - \left(\hat{\boldsymbol{\mu}}_s^{(\mathrm{e}^-)} + \hat{\boldsymbol{\mu}}_s^{(\mathrm{e}^+)}\right) \cdot \boldsymbol{B} + \hat{V}_{\mathrm{C}} . \tag{B.18}$$

It is worth mentioning that $U\hat{\boldsymbol{P}}_{\mathrm{CM}}U^{\dagger}$ is still a canonical conjugate momentum [143, 144] to the centre-of-mass coordinate $\boldsymbol{R}_{\mathrm{CM}}$ and the transformation is thus a canonical one, which can easily be verified by showing that they still obey the canonical commutation relations

$$\left[\boldsymbol{R}_{\mathrm{CM}} , U\boldsymbol{P}_{\mathrm{CM}}U^{\dagger}\right] = \left[\frac{1}{2}\left(\boldsymbol{r}_{\mathrm{e}^-} + \boldsymbol{r}_{\mathrm{e}^+}\right) , \left(\boldsymbol{p}_{\mathrm{e}^-} + \boldsymbol{p}_{\mathrm{e}^+}\right) + \frac{e}{2}\boldsymbol{B} \times \left(\boldsymbol{r}_{\mathrm{e}^-} - \boldsymbol{r}_{\mathrm{e}^+}\right)\right] = i\hbar .$$

The fact that this characteristic is preserved even though the canonical momentum is not gauge-invariant, is explicitly not prohibited here since the gauge transformation has been carried out only in momentum space while the non gauge-invariance of $\hat{\boldsymbol{P}}_{\mathrm{CM}}$ refers to gauge transformations of the vector potential. The same is true for $U\hat{\boldsymbol{p}}U^{\dagger}$.

Above result and the according equations of motion

$$\dot{\boldsymbol{R}}_{\mathrm{CM}} = \frac{1}{i\hbar}\left[\boldsymbol{R}_{\mathrm{CM}}, \hat{H}\right] = \frac{1}{M}\left(\boldsymbol{P}_{\mathrm{CM}} + e(\boldsymbol{B} \times \boldsymbol{r})\right) \tag{B.19}$$

$$\dot{\boldsymbol{P}}_{\mathrm{CM}} = \frac{1}{i\hbar}\left[\boldsymbol{P}_{\mathrm{CM}}, \hat{H}\right] = 0 \tag{B.20}$$

$$\dot{\boldsymbol{r}} = \frac{1}{i\hbar}\left[\boldsymbol{r}, \hat{H}\right] = \frac{1}{\mu}\boldsymbol{p} \tag{B.21}$$

$$\dot{\boldsymbol{p}} = \frac{1}{i\hbar}\left[\boldsymbol{p}, \hat{H}\right] = \frac{e}{M}\left(\boldsymbol{B} \times \boldsymbol{P}_{\mathrm{CM}}\right) + \frac{e^2}{4\mu}\boldsymbol{B} \times \left(\boldsymbol{B} \times \boldsymbol{r}\right) - \frac{e^2}{4\pi\epsilon_0}\frac{\boldsymbol{r}}{r^3} \tag{B.22}$$

allow drawing some interesting conclusions with partly high significance with respect to the physical properties of Ps which became evident only after transformation to the final Hamiltonian:

1. Since representing an important (intermediate) result of the derivation with important physical implications, the elimination of the Zeeman term of the internal motion linear in $\boldsymbol{B}$ be listed here as well. Due to the fact that in the centre-of-mass frame the orbital magnetic dipole moments of the electron and positron exactly cancel each other the linear Zeeman effect of Ps is thus completely based on the spin interaction with the magnetic field. The Zeeman effect be discussed in more detail in the following section.

2. The final gauge transformation turns the canonical momentum $\boldsymbol{p}$ of the internal motion into the kinetic momentum $\boldsymbol{p}_{\mathrm{kin}} = \mu\dot{\boldsymbol{r}}$ (cf. (B.21)) which at first glance seems to be consistent with the field-free case. In fact though this is deceptive as clearly shown by the dynamics of $\boldsymbol{p}$ (cf. (B.22)).

3. Expression (B.19) for the evolution of $\boldsymbol{R}_{\mathrm{CM}}$ once more demonstrates that the collective motion is not determined purely by external quantities but rather intimately coupled to the internal

degree of freedom. As a result the total kinetic momentum $\boldsymbol{P}_{\mathrm{kin,CM}} = M\dot{\boldsymbol{R}}_{\mathrm{CM}}$ is anything but conserved: $\dot{\boldsymbol{P}}_{\mathrm{kin,CM}} = M\ddot{\boldsymbol{R}}_{\mathrm{CM}} = e(\boldsymbol{B} \times \dot{\boldsymbol{r}}) \neq 0$.

Physically this can be interpreted as a consequence of the Lorentz force acting on both individual particles e$^-$ and e$^+$ giving rise to a kind of "motional electric field" $(\boldsymbol{B} \times \dot{\boldsymbol{r}})$ exerting a force on the particles.

4. By far one of the most interesting observation is the fact that $\boldsymbol{P}_{\mathrm{CM}}$ is a conserved quantity that means a constant of motion. This is due to the fact that $\hat{H}$ is finally independent of $\boldsymbol{R}_{\mathrm{CM}}$ and, thus, $\dot{\boldsymbol{P}}_{\mathrm{CM}} = \frac{1}{i\hbar}\left[\boldsymbol{P}_{\mathrm{CM}}, \hat{H}\right] = 0$.

   This is an important result with respect to the separation of the centre of mass from internal degrees of freedom as it entails that the wave functions, i.e. the eigenfunctions of (B.18) can be factorised into two parts, one of them depending only on $\boldsymbol{R}_{\mathrm{CM}}$ and another one only on $\boldsymbol{r}$: $\Psi(\boldsymbol{R}_{\mathrm{CM}}, \boldsymbol{r}) = \Phi(\boldsymbol{R}_{\mathrm{CM}})\Psi_K(\boldsymbol{r})$. Furthermore, it implies that $\Phi(\boldsymbol{R}_{\mathrm{CM}})$ is simultaneously an eigenfunction of $\hat{\boldsymbol{P}}_{\mathrm{CM}}$ with eigenvalue $\boldsymbol{K}$ so that Schrödinger's equation reduces to an effective equation depending only on the internal degrees of freedom and the parameter $\boldsymbol{K}$ which can be considered as a pseudoseparation of the centre of mass [141, 145]. Evidently, total separation is ruled out, though, by the remaining coupling term $^e/_M\hat{\boldsymbol{P}}_{\mathrm{CM}} \cdot (\boldsymbol{B} \times \boldsymbol{r})$.

   Due to these special properties, $\boldsymbol{P}_{\mathrm{CM}}$ is sometimes also called *pseudomomentum*. Finally, it should be noted that it is only the very last transformation (B.16) of the momentum which turns the momentum $\boldsymbol{P}_{\mathrm{CM}}$ into a pseudomomentum thereby making it a constant of motion. This transformation thus reduces the treatment effectively to a one-body problem by removing three degrees of freedom from Schrödinger's equation.

5. Eventually, the most interesting observation is the emergence of the only remaining coupling term $^e/_M\boldsymbol{P}_{\mathrm{CM}} \cdot (\boldsymbol{B} \times \boldsymbol{r}) = e \cdot \boldsymbol{r} \cdot (\boldsymbol{P}_{\mathrm{CM}}/M \times \boldsymbol{B})$ or, respectively, the included term $(\boldsymbol{P}_{\mathrm{CM}}/M \times \boldsymbol{B})$. The latter can easily be identified as a self-induced electric field, perpendicular to the magnetic field which arises from the individual action of the magnetic field on the moving electron-positron pair. Effectively acting as an electric field, this term thus induces a kind of Stark effect affecting the Ps energy even though no external static electric field is present. Due to the fact that it depends on the total velocity-like quantity $\boldsymbol{P}_{\mathrm{CM}}/M$ this effect is also referred to as *motional Stark effect* and, correspondingly, $\boldsymbol{E}_{\mathrm{MS}} = (\boldsymbol{P}_{\mathrm{CM}}/M \times \boldsymbol{B})$ as *motional Stark field*.

   In fact, the term $e\boldsymbol{r} \cdot \boldsymbol{E}_{\mathrm{MS}}$ that couples the collective and internal motion, is common to all neutral particle systems moving in magnetic fields [143]. However, it becomes significantly more pronounced for the Ps atom due to its extraordinarily small mass and accordingly high velocities. This once more illustrates the truly special case that the Ps atom represents.

   Finally, there is one last subtle detail to be made aware of: Despite showing the appearance of a velocity-like quantity, $\boldsymbol{P}_{\mathrm{CM}}/M$ should in general not be hastily misinterpreted as the velocity of the centre of mass of the Ps atom. Even though this might be obvious and intuitive it is not strictly correct simply due to the fact that $\boldsymbol{P}_{\mathrm{CM}}$ in general does not correspond to the eigenvalue of the (non-conserved) total kinetic momentum $M\dot{\boldsymbol{R}}_{\mathrm{CM}}$ (cf. Eq. (B.19)) but differs from the latter by another coupling to the internal coordinate.

   On average though for not too high fields it is justified to consider $\boldsymbol{P}_{\mathrm{CM}}$ as the kinetic momentum so that $\boldsymbol{v} = \boldsymbol{P}_{\mathrm{CM}}/M$ can be associated with the atom's velocity [145] representing an approach which will also be adopted in this thesis.

For more extensive discussions and profound details on theoretical aspects of the motion of charged particles and their bound states in electromagnetic fields, interested readers may be referred to several research articles [78, 134, 137, 143, 145–150].

Before taking the next step and adding the interaction of the Ps atoms with light fields the following subsection will briefly pick up once more the final Hamiltonian, Eq. (B.18), in order to discuss the problem of calculating the according energy levels and basis states in terms of the eigenvalues and -states of $\hat{H}$ which finally describe the physical properties of the Ps atom in magnetic fields and lay the foundation for the interaction with light fields.

In the following, the collective motion will be ignored (1st term in Eq. (B.18)) and only the much more important internal motion will be considered which corresponds to the treatment from the perspective of the rest frame of the Ps atom. Additionally, the term $\boldsymbol{P}_{\mathrm{CM}}/M$ will be considered as the velocity v of the atom and assumed to be constant.

B.4   Eigenvalues and -states

The full QED-corrected Hamiltonian for a Ps atom in magnetic fields is obtained by combining Equations (B.18) and (2.12) that means by replacing the kinetic and Coulomb terms in $\hat{H}$ (Eq. (B.18)) by the field-free QED-corrected Hamiltonian $\hat{H}_{\mathrm{QED}}$ (Eq. (2.12)) which yields

$$\hat{H} = \hat{H}_{\mathrm{QED}} + \hat{H}_{\mathrm{S}} + \hat{H}_{\mathrm{z}} + \hat{H}_{\mathrm{dia}} . \tag{B.23}$$

The individual contributions due to the motional Stark effect ($\hat{H}_{\mathrm{S}}$) originating from the self-induced motional Stark field $\boldsymbol{E}_{\mathrm{MS}} = (\boldsymbol{P}_{\mathrm{CM}}/M \times \boldsymbol{B})$, the (linear) Zeeman effect ($\hat{H}_{\mathrm{z}}$) and the quadratic Zeeman effect, also called diamagnetic term, ($\hat{H}_{\mathrm{dia}}$) are given by

$$\hat{H}_{\mathrm{S}} = e\boldsymbol{r} \cdot (\boldsymbol{v} \times \boldsymbol{B}) \tag{B.24}$$

$$\hat{H}_{\mathrm{z}} = -\left(\hat{\boldsymbol{\mu}}_s^{(\mathrm{e}^-)} + \hat{\boldsymbol{\mu}}_s^{(\mathrm{e}^+)}\right) \cdot \boldsymbol{B} \tag{B.25}$$

$$\hat{H}_{\mathrm{dia}} = \frac{e^2}{16m_{\mathrm{e}}} \left(\boldsymbol{B} \times \boldsymbol{r}\right)^2 \tag{B.26}$$

where $\boldsymbol{P}_{\mathrm{CM}}/M$ has already been replaced by the velocity $\boldsymbol{v}$ of the neutral atom. The spin magnetic dipole moment is given by $\hat{\boldsymbol{\mu}}_s = g_s q/(2m)\,\hat{\boldsymbol{s}}$ with the spin g-factor g_s which are equal for the electron and positron and indicated by $g_e = g_{\mathrm{e}^-} = g_{\mathrm{e}^+}$. Due to QED corrections g_e is not exactly 2 as predicted by the Dirac theory but $g_e \approx -2.002319$ [7].

As mentioned, in order to obtain the energy levels $E^{(i)}$ and good basis states $|\Psi^{(i)}\rangle$ describing the physics of the Ps atom in magnetic fields, one needs to solve Schrödinger's equation

$$\hat{H} |\Psi\rangle = E |\Psi\rangle \tag{B.27}$$

which is equivalent to finding the eigenvalues $E^{(i)}$ and -states $|\Psi^{(i)}\rangle$ of $\hat{H}$.

In weak fields $B \lesssim 0.1\,\mathrm{T}$ [71] or, equivalently, $E \lesssim 1000\,\mathrm{Vm}^{-1}$ (resulting from the motional Stark field) [72] it is still possible to realise this by means of a perturbation approach, where the effect of the vector potential is treated as the perturbation of the Coulomb potential. This approach, though, fails for Ps velocities typically found in experiments (of the order of 10^5 to $10^6\,\mathrm{m/s}$) which induce correspondingly high electric field strengths that rule out any perturbative treatment.In general, it is therefore recommendable or rather indispensable to diagonalise the full Hamiltonian $\hat{H}$. The Hamiltonian matrix can to this end be expressed in any arbitrary base composed of the countable set of orthonormal basis states which completely span the Hilbert space. The components of the eigenstate vector are then simply the projections onto these basis states, in terms of which the Hamiltonian matrix elements $H^{(ij)}$ read as

$$H^{(ij)} = \langle\Psi^{(i)}|\hat{H}|\Psi^{(j)}\rangle . \tag{B.28}$$

An essential preparatory task is thus to find the matrix elements of all four contributions $\hat{H}_{\mathrm{QED}}, \hat{H}_{\mathrm{S}}, \hat{H}_{\mathrm{z}}$ and $\hat{H}_{\mathrm{dia}}$. For this purpose and for weak perturbations (where spin-orbit interactions still dominate and it is thus adequate to apply the LS-coupling) it is convenient to use the relativistic eigenstates $|nlSJm\rangle$ (with n,l,J and S quantum numbers already introduced above and m denoting the projection of $\boldsymbol{J}$ on the quantisation axis established by the magnetic field $\boldsymbol{B}$) in terms of which $\hat{H}_{\mathrm{QED}}$ becomes diagonal and the matrix elements are known and given by the unperturbed QED-corrected energy levels $E_0^{(n)}$ (cf. equation (2.13)) with precision to the order of α^4. It is worth mentioning that the used order of quantum numbers in $|nlSJm\rangle$ corresponds to the

Russell-Saunders LS angular momentum coupling scheme $\boldsymbol{l} + \boldsymbol{S} = \boldsymbol{J}$ which is adopted throughout this thesis. The reversed SL-scheme, based on $\boldsymbol{S} + \boldsymbol{l} = \boldsymbol{J}$ and being entailed with a phase shift with respect to the LS-scheme, would explicitly be labelled as $|nSlJm\rangle$.

Since in almost all cases this non-perturbative approach exceeds analytical capabilities it is in general necessary to resort to numerical means to solve the eigenvalue problem of the Ps atom in crossed magnetic and electric fields. Depending on the number of levels n (while the $n = 1$-matrix is of size 4x4 the ones including $n = 2$ ($n = 3$) have already 20×20 (56×56) entries) and atoms N which need to be included even numerical methods can reach its limits necessitating the use of certain approximations and simplifications.

B.5   Zeeman interaction

The contribution due to the Zeeman effect to $\hat{H}$ consists of the linear term $\hat{H}_{\mathrm{z}}$ resulting from the interaction of the electron and positron spins with the magnetic field and the diamagnetic term $\hat{H}_{\mathrm{dia}}$ quadratic in B. The treatment of Ps is very similar to the hydrogen case with slight modifications. The major distinction between the positronium atom and the the general case of a two-body system is the exceptional feature of the missing term linear in the magnetic field for the internal motion.

B.5.1   Zeeman effect in moderate fields

The linear Zeeman effect is caused by the term $\hat{H}_{\mathrm{z}}$ which emerges purely from spin interaction with $\boldsymbol{B}$ owing to the vanishing orbital magnetic dipole moments. The according Zeeman-Hamiltonian can be written as

$$\hat{H}_{\mathrm{z}} = g_e \frac{e}{2m_{\mathrm{e}}} \left(\hat{\boldsymbol{s}}_{\mathrm{e}^-} - \hat{\boldsymbol{s}}_{\mathrm{e}^+} \right) \cdot \boldsymbol{B} = \frac{1}{2} g_e \mu_{\mathrm{B}} \left(\hat{\boldsymbol{\sigma}}_{e^-} - \hat{\boldsymbol{\sigma}}_{\mathrm{e}^+} \right) \cdot \boldsymbol{B} \qquad \text{(B.29)}$$

expressed in terms spin operator $\hat{\boldsymbol{s}}$ of the electron and positron or the corresponding Pauli matrices $\hat{\boldsymbol{\sigma}} = \hbar \hat{\boldsymbol{s}}/2$. As usual, μ_{B} denotes the Bohr magneton $e\hbar/(2m_{\mathrm{e}})$.

Applied on the individual electron and positron spin basis states $|m_{\mathrm{e}^-} m_{\mathrm{e}^+}\rangle$ (where $m_i = \pm\frac{1}{2}$, the projection of the spin angular momenta on the quantisation axis) is represented by arrows $\uparrow = 1/2$ and $\downarrow = -1/2$, $\hat{H}_{\mathrm{z}}$ becomes

$$\hat{H}_{\mathrm{z}} |m_{\mathrm{e}^-} m_{\mathrm{e}^+}\rangle = g_e \mu_{\mathrm{B}} B \left(m_{\mathrm{e}^-} - m_{\mathrm{e}^+} \right) |m_{\mathrm{e}^-} m_{\mathrm{e}^+}\rangle \qquad \text{(B.30)}$$

directly resulting in a diagonal matrix with non-zero elements only for the spin states $|\uparrow\downarrow\rangle$ and $|\downarrow\uparrow\rangle$. Since the wave functions $|nlSJm\rangle$ of the overall positronium atom are indicated by the total spin quantum number S though, it is necessary to switch the representation from the $|m_{\mathrm{e}^-} m_{\mathrm{e}^+}\rangle$-basis to the singlet ($S = 0$) / triplet ($S = 1$) basis states defined by

$$
\begin{aligned}
|S = 0, \ m_s = 0\rangle &= \frac{1}{\sqrt{2}} \Big(|\uparrow\downarrow\rangle - |\downarrow\uparrow\rangle \Big) \\
|S = 1, \ m_s = 1\rangle &= |\uparrow\uparrow\rangle \\
|S = 1, \ m_s = 0\rangle &= \frac{1}{\sqrt{2}} \Big(|\uparrow\downarrow\rangle + |\downarrow\uparrow\rangle \Big) \\
|S = 1, \ m_s = -1\rangle &= |\downarrow\downarrow\rangle \ .
\end{aligned}
$$

It can easily be derived that in this basis $\hat{H}_{\mathrm{z}}$ can be written as

$$\hat{H}_{\mathrm{z}} |S, m_s\rangle = g_e \mu_{\mathrm{B}} B \ \delta_{0m_s} |1 - S, 0\rangle \ . \qquad \text{(B.31)}$$

This compact notation clearly shows that, for $m_s = 0$, the operation of $\hat{H}_{\mathrm{z}}$ on these basis states does not only yield the according eigenvalues but also modifies the state itself in such a way that it

B| The positronium atom in magnetic fields

flips the total spin state. This immediately implies that the matrix is no longer diagonal. In fact the matrix elements $\langle S'm_s'|\hat{H}_z|Sm_s\rangle$ are non-zero only if $S \neq S'$ and $m_s = m_s' = 0$, and equal n and l [47] which shows that the Zeeman interaction couples states from the singlet manifold with compatible triplet ones one vice versa.

Consequently, in the $|nlSJm\rangle$ basis (with the usual LS-coupling) the complete matrix elements are given by Ref. [151]

$$\langle n'l'S'J'm'|\, \hat{H}_z\, |nlSJm\rangle \;=\; \tfrac{1}{2}g_e\mu_B B\; \delta_{n'n}\delta_{l'l}\delta_{m'm}(-1)^{l+m}\left[(-1)^{S+S'}-1\right]\times$$
$$\sqrt{3(2J'+1)(2J+1)} \times \begin{pmatrix} J' & 1 & J \\ -m' & 0 & m \end{pmatrix} \begin{Bmatrix} S' & l' & J' \\ J & 1 & S \end{Bmatrix} \qquad \text{(B.32)}$$

where the curved (curly) brackets stand for the Wigner 3J (6J) symbols and δ_{ij} denotes the Kronecker delta function of i and j.

Alternatively, in terms of the Clebsch-Gordan coefficients, defined as

$$C_{j_1m_1,j_2m_2}^{Jm} = \langle j_1m_1, j_2m_2|Jm\rangle$$

and applying the conditions $m_s = 0$ and $\Delta S = S' - S = \pm 1$ (for Ps), the matrix elements can be expressed as [47]

$$\langle n'l'S'J'm'|\, H_z\, |nlSJm\rangle \;=\; g_e\mu_B B\; \times\; \delta_{n'n}\delta_{l'l}\delta_{S,1-S'}\delta_{m'm}\; \times\; C_{lm,S0}^{Jm}\, C_{l'm',S'0}^{J'm'} \qquad \text{(B.33)}$$

using the Condon-Shortley phase convention [152].

Combining the Zeeman matrix with the diagonal zero-field matrix now allows to quantify the effects of the magnetic perturbation on the energy levels of an atom at rest (since H_s is not included yet): The perturbed energy levels E_i in magnetic field are obtained by diagonalisation which directly yields the new set of eigenvalues. The new basis states (eigenvectors $|EV\rangle_i$) are given as linear combinations of the initial ones $|EV_0\rangle_j = |nlSJm\rangle$ according to

$$|EV\rangle_i = \sum_j {}_j\langle EV_0|EV\rangle_i\; |EV_0\rangle_j = \sum_j \mathrm{EV}_{ji}\; |EV_0\rangle_j \qquad \text{(B.34)}$$

where $\mathrm{EV}_{ji} = {}_j\langle EV_0|EV\rangle_i$ represents the eigenvector matrix.

For the ground states $n = 1$ it is straightforward to diagonalise the according (4x4)-Hamiltonian matrix which yields the energies $E_{(S,m)}$ of the new (mixed) substates in magnetic field in terms of the unperturbed singlet and triplet levels E_s and E_t respectively, with

$$E_{0,0} = \frac{E_t + E_s}{2} - \frac{\Delta E_{grd}}{2}\sqrt{1 + \left(\frac{2g_e\mu_B}{\Delta E_{grd}}B\right)^2} \approx \frac{E_t + E_s}{2} - \frac{\Delta E_{grd}}{2}\sqrt{1 + (0.274\cdot B)^2}$$

$$E_{1,0} = \frac{E_t + E_s}{2} + \frac{\Delta E_{grd}}{2}\sqrt{1 + \left(\frac{2g_e\mu_B}{\Delta E_{grd}}B\right)^2} \approx \frac{E_t + E_s}{2} + \frac{\Delta E_{grd}}{2}\sqrt{1 + (0.274\cdot B)^2} \qquad \text{(B.35)}$$

$$E_{1,1} = E_{1,-1} = E_t$$

where $B = |\boldsymbol{B}|$ is the magnetic field strength in Tesla. The energy difference $\Delta E_{grd} = E(1^3S_1) - E(1^1S_0) = \frac{7}{12}\alpha^4 m_e c^2 = 0.845\,\text{meV} = 2\pi\hbar\,(204.39\,\text{GHz})$ specifies the field-free ground state singlet-triplet splitting [153]. This demonstrates clearly again that only the $(m = 0)$-states are shifted in energy as a consequence of the linear Zeeman effect whereas the $(m = \pm 1)$-states are completely unaffected by B (except for a tiny diamagnetic shift, of the order of $2\,\text{kHz}$ in $0.1\,\text{T}$ for example [144]).

The Zeeman-splitting ν_{trpl} between the triplet ground states, which is often made use of in precision experiment, due to easier accessibility, than the singlet-triplet transition, is thus well

described by the Breit-Rabi equation [154]

$$\nu_{\text{trpl}} = \frac{\Delta E_{\text{grd}}}{4\pi\hbar} \left[\sqrt{1 + \left(\frac{2g_e\mu_{\text{B}}}{\Delta E_{\text{grd}}} B\right)^2} - 1 \right] \tag{B.36}$$

$$\approx 3.835 \, \tfrac{\text{GHz}}{\text{T}^2} \times B^2 \qquad \text{(in weak fields)}.$$

The effect of the Zeeman interaction on the ground and first excited states ($n = 1$) is visualised in Fig. 2.2 (see p. 19) as a function of the magnetic field strength B. Obviously, the region of moderate Zeeman effects, manifesting in the quadratic dependence on B, is much broader for $n = 0$ than for $n = 1$, or, in other words, the excited states show much higher sensitivity to B than the ground states. This can simply be explained by the increasingly smaller energy spacings between the individual states of higher-n manifolds (resulting from the n^{-3}-scaling of the QED energy corrections, cf. Eq. (2.13)), which entails stronger Zeeman mixing the higher n.

B.5.2 Magnetic quenching

As already revealed by the Hamiltonian written in the total spin basis (cf. Eq. (B.31)) and, more tangibly, by the $n = 1$ energy eigenvalues given in Eq. (B.35), the linear (spin-based) Zeeman effect affects only the ($m = 0$)-substates, thereby inducing coupling of singlet and triplet states. Due to considerably different annihilation rates of ortho- (triplet) and para-Ps (singlet) states the resulting new mixed eigenstates in magnetic field can have significantly different annihilation lifetimes than their unperturbed analogues. This means especially that the triplet $m = 0$ ground states annihilates much faster in magnetic field environments which is also referred to as magnetic quenching.

The magnitude of lifetime reduction depends on the degree of singlet character, which allows for fast 2-photon decay, of the new ($S = 1, m = 0$) triplet state. Likewise, even though by far not to the same extent as triplets annihilate faster, the singlet lifetime is enhanced due to the magnetic perturbation. In general the magnetic field dependent annihilation rates $\tilde{\Gamma}_{S,m}^{(\text{ann})} = \Gamma_{S,m}^{(\text{ann})}(B) = (\tau_{S,m}^{(\text{ann})}(B))^{-1}$ can be calculated from the overlap of the perturbed mixed states[30] with the zero-field basis states according to [71]

$$\tilde{\Gamma}_j^{(\text{ann})} = \sum_j |\text{EV}_{ji}|^2 \, \Gamma_i^{(\text{ann})}. \tag{B.37}$$

Following Refs. [155] and [156] the rates of especially the new $m = 0$ ortho-like and para-like Ps ground states are given respectively by

$$\tilde{\Gamma}_{1,0}^{(\text{ann})} = \frac{\Gamma_{\text{trpl}}^{(\text{ann})} + y(B) \cdot \Gamma_{\text{sngl}}^{(\text{ann})}}{1 + y(B)} \qquad \text{and} \qquad \tilde{\Gamma}_{0,0}^{(\text{ann})} = \frac{\Gamma_{\text{sngl}}^{(\text{ann})} + y(B) \cdot \Gamma_{\text{trpl}}^{(\text{ann})}}{1 + y(B)} \tag{B.38}$$

where the unmarked $\Gamma_{\text{trpl}}^{(\text{ann})} = 0.0071\,\text{ns}^{-1}$ and $\Gamma_{\text{sngl}}^{(\text{ann})} = 8\,\text{ns}^{-1}$ denote the intrinsic ortho- and para-Ps decay rates at zero field and the field dependence is introduced by

$$y(B) = \left(\frac{\sqrt{1 + x(B)^2} - 1}{x(B)}\right)^2 \qquad \text{where} \quad x(B) = \frac{2g_e\mu_{\text{B}}B}{\Delta E_{\text{grd}}} \tag{B.39}$$

---

[30] In this context it should be mentioned that the use of the term "mixed state" for perturbed states, as resulting from interaction of Ps atoms with external magnetic fields, does not fully comply with the actual quantum mechanical definition of the term. As described in Section D.1.3, pursuant to the concept of coherence, it is necessary to distinguish between (coherent) superposition states and *real* mixed states describing (incoherent) statistical mixtures. This applies as well to the generally improper use of mixed states in the discussion of the motional Stark effect. Strictly speaking, all perturbed states resulting from interaction with external magnetic fields are in fact described by coherent superposition states.

For a more detailed explanation of the concept of coherence and the definition of superposition and mixed states, reference is made to Section D.1.3.
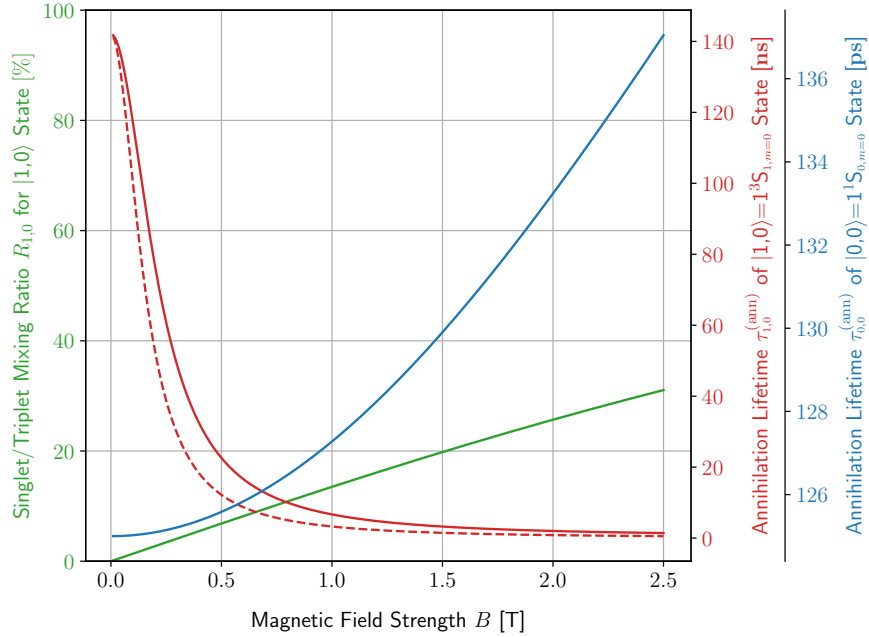
FIGURE B.1: *Change in ground state lifetime and spin state mixing ratio as a result of magnetic quenching.*
The figure shows the reduction in lifetime $\tilde{\tau}_{1,0}^{(\mathrm{ann})} = (\tilde{\Gamma}_{1,0}^{(\mathrm{ann})})^{-1}$ of the originally (i.e., in zero-field) triplet ground state $|1,0\rangle$ (red) and the concomitant enhancement in the zero-field singlet ground state lifetime $\tilde{\tau}_{0,0}^{(\mathrm{ann})} = (\tilde{\Gamma}_{0,0}^{(\mathrm{ann})})^{-1}$ (blue), due to magnetic quenching, as a function of the magnetic field strength B in the range from $0\,\mathrm{T}$ to $2.5\,\mathrm{T}$. The dashed red curve presents the evolution based on the approximation in Eq. (B.40). Additionally, the green line gives the mixing ratio $R_{1,0}$ of singlet and triplet character of the $|1,0\rangle$ state in this range of magnetic field, evaluated according to Eq. (B.41).
The lifetime curves are calculated based on Eq. (B.38) and are presented on different scales. While the reduction of the originally triplet lifetime ranges from the initial value of $142\,\mathrm{ns}$ down to the picosecond time scales, the initially singlet one varies only between the zero-field $125\,\mathrm{ps}$ and maximally $\approx 127\,\mathrm{ps}$. The evolution of the curves is based entirely on Zeeman interaction for atoms at rest, or, respectively, $(\boldsymbol{v} \times \boldsymbol{B}) = 0$ to exclude mixing due to motional Stark effects with potentially further impact on the lifetimes.

which for handiness can be approximated by

$$\tilde{\Gamma}_{1,0}^{(\mathrm{ann})} \approx \Gamma_{\mathrm{trpl}}^{(\mathrm{ann})} + \frac{x(B)^2}{2}\Gamma_{\mathrm{sngl}}^{(\mathrm{ann})} \tag{B.40}$$

which shows that in $1\,\mathrm{T}$ the annihilation rate is already enhanced by a factor of nearly 50 and the lifetime is then merely $3\,\mathrm{ns}$. Figure B.1 shows this reduction or, respectively, enhancement of lifetime for the $m = 0$ singlet and triplet ground states as a function of B.

Additionally plotted (green line) is the mixing ratio $R_{1,0}$ yielding the degree of singlet and triplet character for the $|1,0\rangle$ state which according to Ref. [157] is given by

$$R_{1,0} = \frac{1}{x}\sqrt{(2 + x^2) - 2\sqrt{1 + x^2}} \tag{B.41}$$

As a function of time the decay of Ps in those states then becomes

$$N_{1/0,0}(t) = N_{1/0,0}^{(0)} \cdot \exp\left(-\tilde{\Gamma}_{1/0,0}^{(\mathrm{ann})} \cdot t\right) \tag{B.42}$$

FIGURE B.2: *Illustration of magnetic quenching of the 2^3P excited states, based on partial level scheme.* *Even in absence of direct magnetic quenching of the 1^3S triplet ground states, a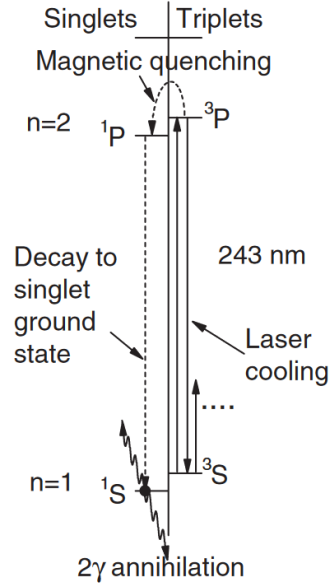toms can get quenched after excitation to 2^3P states due to magnetic field-induced mixing of excited states. The resulting fast annihilation can be highly detrimental to certain applications, such as laser cooling (cf. Sec. 2.4 et seq.). More details on the cascade of excitation, mixing and decay are given in the text. Figure taken from [159].*

Since the annihilation rate for the remaining ground states with $m = \pm 1$ is independent of B, the decay of Ps residing in these states is simply described by

$$N_{1,\pm 1}(t) = N_{1,\pm 1}^{(0)} \cdot \exp\left(-\Gamma_{\mathrm{trpl}}^{(\mathrm{ann})} \cdot t\right) \ . \tag{B.43}$$

Thus, the overall decay of a cloud of atoms populating all triplet ground states is a combination of the individual decay functions:

$$
\begin{aligned}
N_{\mathrm{trpl}}(t) &= N_{1,-1}(t) &&+ N_{1,0}(t) &&+ N_{1,+1}(t) \\
&= N_{1,-1}^{(0)} \cdot \exp\left(-\Gamma_{\mathrm{trpl}}^{(\mathrm{ann})} \cdot t\right) + N_{1,0}^{(0)} \cdot \exp\left(-\tilde{\Gamma}_{1,0}^{(\mathrm{ann})} \cdot t\right) + N_{1,+1}^{(0)} \cdot \exp\left(-\Gamma_{\mathrm{trpl}}^{(\mathrm{ann})} \cdot t\right) \ .
\end{aligned}
\tag{B.44}
$$

More extensive and profound theoretical investigations of magnetic quenching of the Ps decay, also in alternating fields, can be found in [158].

The phenomenon of magnetic quenching is not restricted only to the ground states. Rather, the same mechanism of mixing, accompanied by a corresponding reduction in triplet state annihilation lifetime, also takes place in excited states. However, quenching of higher-n states affects the Ps population of course only after excitation to the according state, as shown in Fig. B.2.

Here, the fast decay channel goes via (laser) excitation to the triplet 2^3P state which is quenched, that means mixed with the corresponding singlet 2^1P state accompanied by rapid decay to the singlet ground state where fast annihilation takes place. This channel is only opened, though, if the magnetic perturbation is still weaker than the energy width of the 2P manifold. In the reversed case in which the magnetic interaction starts dominating the 2P level scheme this quenching process can be eliminated, which has quite important implications with respect to laser experiments for example as they require longest possible annihilation lifetimes [159]. The following paragraph is dedicated to a more in-depth explanation of the underlying mechanism including the magnetic field values required to reach this regime.

B.5.3 Paschen-Back regime

The discussion of the Zeeman effect so far implicitly assumed that the magnetic perturbation $\mu_{\mathrm{B}}B$ is sufficiently weak compared to spin-orbit coupling. For historical reasons this weak field regime is also referred to as the *anomalous Zeeman effect*. Spin-orbit coupling can however soon be broken especially for excited states which are much more sensitive to magnetic perturbations

due to smaller energy level spacing, i.e. energetic width ΔE of the whole manifold, for higher n. Furthermore, spin-orbit coupling scales with n^{-3} and thus gets weaker with increasing n. As a result, for the first excited states in positronium, the $n = 2$ level, fields of $B > 1\,\mathrm{T}$ can already be sufficiently strong that $\mu_{\mathrm{B}} B$ becomes the dominant energy contribution and spin-orbit coupling is broken. For such strong fields the normal Zeeman effect turns into the so called *Paschen-Back effect* where the total angular momentum becomes undefined and J as a good quantum number loses its validity.

In this strong-field limit, where the external field exceeds any internal field of the atom, the individual electron and positron spins are decoupled and align autonomously with respect to the perturbing field. This necessitates the usage of the $|nlm_l\rangle \otimes |s_{\mathrm{e}^-} m_{\mathrm{e}^-} s_{\mathrm{e}^+} m_{\mathrm{e}^+}\rangle$ basis, instead of $|nlSJm\rangle$, with the spin wave functions being completely separated from each other as well as from the spatial, i.e. orbital, part of the wave function. In this factorised basis the Hamiltonian matrix is diagonal.

It is worth pointing out, though, that this change of basis states does not have any effect on the evaluation of the matrix elements. This is due to the fact that $\hat{H}_{\mathrm{z}}$ acts only on the spin wave functions and that the underlying physical effect is linear in S. The result of $\hat{H}_{\mathrm{z}}$ acting on the wave function is thus independent of the applied set of basis states as long as they can be written as linear combinations of each other. This is the case for $|nlSJm\rangle$ which can easily be expressed in terms of the $|nlm_l\rangle \otimes |Sm_s\rangle$ or $|nlm_l\rangle \otimes |s_{\mathrm{e}^-} m_{\mathrm{e}^-} s_{\mathrm{e}^+} m_{\mathrm{e}^+}\rangle$ basis states. It should be noted that the factorisation of $\boldsymbol{J}$ into $\boldsymbol{l}$ and $\boldsymbol{S}$ does as well not entail any complication of the description, since it is only $\hat{H}_{\mathrm{QED}}$ which acts on $\boldsymbol{J}$ and spin-orbit coupling terms can be neglected in the strong-field regime.

Consequently, in the Paschen-Back regime the matrix elements are as well given by equation (B.30).

The magnetic interaction now creates three branches depending only on the difference $m_{\mathrm{e}^-} - m_{\mathrm{e}^+} = +1, 0, -1$ [47]. Since the eight substates with $m_{\mathrm{e}^-} - m_{\mathrm{e}^+} = \pm 1$ do not show any net magnetic dipole moments ($\boldsymbol{\mu}_s^{(\mathrm{e}^-)}$ and $\boldsymbol{\mu}_s^{(\mathrm{e}^+)}$ exactly cancel each other) they are completely insensitive to the perturbation by the magnetic field and therefore stay flat in energy. Furthermore, they do not have any singlet component and thus completely retain their pure triplet character and corresponding properties such as longer lifetimes.

In contrast, the remaining eight $m_{\mathrm{e}^-} - m_{\mathrm{e}^+} = 0$ eigenstates are shifted in energy by $\pm 2\mu_{\mathrm{B}} B$ creating superpositions of singlet and triplet levels with, necessarily, 50% share each [47, 159] (as it is already the case in intermediate fields where they are superpositions of $|S = 0, m_s = 0\rangle$ and $|S = 1, m_s = 0\rangle$ in equal shares).

As far as dipole transitions between states are concerned, it should be kept in mind that the rearrangement of energy levels and change of eigenstates in the Paschen-Back, but also in the low-field regime, is accompanied by a change in initial and final states addressed by a similar laser pulse. While, for example, in zero field a certain transition might have ended up in a pure triplet state, in magnetic fields the very same laser stimulation (i.e. laser pulse with similar parameters) might lead to a final state which has transformed to a mixed state with considerable singlet character. This would of course have substantial implications with respect to the annihilation lifetime of the excited atom. Another aspect relevant for spectroscopic measurements is the fact that, especially in the Paschen-Back regime where the states are shifted equally in energy, transitions will as well become equal in energy which results in coinciding spectral lines.

In order to close the brackets left open in the discussion of Fig. B.2, it becomes clear now why and under which conditions the described succession of events, leading to fast decay, is broken. Clearly, the coupling to the excited singlet state $2^1\mathrm{P}$ becomes increasingly suppressed with level separation and completely eliminated when $\mu_{\mathrm{B}} B \gg \Delta E$. With regard to experiments such as laser cooling, requiring longest possible interaction times, it might thus, interestingly enough, be recommendable to work at rather high magnetic field strengths. This is confirmed by the results of the numerical studies presented in Sec. 3.2.1 on p. 55.

Finally, and well illustrated by Fig. 2.2, the magnetic field strengths required to reach the Paschen-Back regime are very different though for different n states. While for $n = 2$ fields of

about 1 T already seem to be strong enough to decouple the electron and positron spins, for $n = 1$ fields of 5 T are obviously not yet sufficiently strong to induce the transition to the Paschen-Back decoupling regime so that, except for the pure and flat triplet (with $m_s = \pm 1$) branch, the $m_s = 0$ singlet and triplet branches show increasing coupling. The upper $n = 1$ branch for example is still far away from being in a pure $m_{\mathrm{e}^-} - m_{\mathrm{e}^+} = 1$ state which would characterise the strong-field limit. According to Breit's estimation that the complete Paschen-Back regime is reached for $x > 3$ [153], this pure character will set in only for $B \gtrsim 11$ T.

Fig. 2.2 furthermore visualises that there is an intermediate range before finally the Paschen-Back regime is reached. Here it can be assumed that the field is already strong enough to break down spin-orbit coupling $\boldsymbol{L} \cdot \boldsymbol{S}$ but not yet the coupling of $\boldsymbol{s}_{\mathrm{e}^-}$ and $\boldsymbol{s}_{\mathrm{e}^+}$ into $\boldsymbol{S}$. It may then be justified to still use the total spin basis, in form of the factorised $|nlm_l\rangle \otimes |Sm_s\rangle$ basis, necessarily resulting in the non-diagonal matrix and spin state coupling.

B.5.4 Diamagnetic effect

Technically, the matrix elements of the diamagnetic Zeeman effect, arising from $\hat{H}_{\mathrm{dia}}$, can be obtained in a similar way as for the linear term, even though the calculation is far more complicated. Qualitatively, the main result is that they are non-zero only for $\Delta l = 0, \pm 2$ irrespective of n [53]. $\hat{H}_{\mathrm{dia}}$ can thus mix different l states, even from different levels n (provided that the spacing between different n states is sufficiently small, as it is the case for example for high n). However, its influence is negligible even in fields stronger than the ones usually found in experimental setups. Mixing starts having an appreciable effect only in extreme fields stronger than $B \approx 100$ T or quite high quantum numbers n. To convey an impression of its strength, it is worth mentioning that in fields of about 1 T the diamagnetic effect of the $n = 1$ leads to an energy shift of only $E/h \approx 0.2$ MHz [160], more than four orders of magnitude smaller than the Zeeman-splitting ν_{trpl} between the triplet ground states (cf. Eq. B.36). In weak fields the energy correction induced by $\hat{H}_{\mathrm{dia}}$ scales with n^4 and becomes thus important only for high-n levels. Furthermore, since this shift is equal for all four ground sublevel for example, it does not affect energy differences between those states [144, 160].

Since in the scope of this thesis the treatment is restricted to interaction of Positronium up to $n = 3$ with moderate magnetic field strengths, for which the transition structure is governed mainly be the Zeeman and Stark effects, the quadratic Zeeman effect is neglected in the following.

B.6 Stark effect and dipole transitions

As derived and partly discussed in Section B.3, the motional Stark effect is introduced during the transformation of the static magnetic field to the rest frame of the positronium atom and represents one of its few peculiar features. Its movement in a magnetic field gives rise to an electric field so that it is always required to take into account Stark effects in the rest frame of the atom even though no external fields might be present. This self-induced electric field, referred to as the motional Stark field $\boldsymbol{E}_{\mathrm{MS}} = (\boldsymbol{P}_{\mathrm{CM}} \times \boldsymbol{B})/M$, originates from the vectorial coupling of the collective motion of the electron-positron-pair with the magnetic field $\boldsymbol{B}$ and is therefore oriented perpendicularly to both the magnetic field as well as the trajectory of the atom, thereby destroying the axial symmetry of the atom-B field-system. The corresponding Stark energy term in the Hamiltonian in turn couples $\boldsymbol{E}_{\mathrm{MS}}$ to the internal electric dipole $e\boldsymbol{r}$ of the atom which creates the link between internal and collective coordinates.

It should further be recalled that the term $\boldsymbol{P}_{\mathrm{CM}}/M$ will be considered as the velocity $\boldsymbol{v}$ of the positronium atom even though, strictly speaking, it does not represent the kinetic momentum. Since neither the motional Stark field nor the magnetic field itself exert any force with components parallel to the trajectory of the atom, its velocity is assumed to be constant.

Due to the, under typical experimental conditions, high velocities of the very lightweight positronium atom the Stark energy can in fact become the dominant factor in the Hamiltonian and has thus considerable influence on the level scheme particularly for excited states. With regard to

experimental or numerical investigations of physical processes such as laser cooling positronium which this present thesis is devoted to, it is therefore essential to add also the Stark matrix to the Hamiltonian which is used for calculating the energies and states of a given system.

Starting from the Stark Hamiltonian defined in equation (B.23) and given by $\hat{H}_\mathrm{S} = e\boldsymbol{r} \cdot (\boldsymbol{v} \times \boldsymbol{B})$, the matrix elements can in principle be evaluated in a similar way as for the Zeeman matrix, which however is a bit more complex. For LS-coupling this results in [151]

$$\langle n'l'S'J'm'| \, e\boldsymbol{r}\boldsymbol{E} \, |nlSJm\rangle = \delta_{S'S}(-1)^{S+1+m'} e \times (n'l'|\boldsymbol{r}|nl) \begin{Bmatrix} S' & L' & J' \\ 1 & J & L \end{Bmatrix} \times$$

$$\sqrt{\max(l',l)(2J'+1)(2J+1)/2} \, \times \sum_q \tau_q \begin{pmatrix} J' & 1 & J \\ -m' & q & m \end{pmatrix} \quad \text{(B.45)}$$

where $(n'l'|\boldsymbol{r}|nl)$ is the radial matrix element[31]. τ denotes a vector with spherical components $\tau_{+1} = +E_\perp$, $\tau_{-1} = -E_\perp$ and $\tau_0 = -\sqrt{2} \, E_\parallel$ which depend on the projections $\boldsymbol{E}_\parallel$ and $\boldsymbol{E}_\perp$ of $\boldsymbol{E}$ onto the axis parallel to $\boldsymbol{B}$ or the perpendicular plane, respectively.

It should be noted that this expression describes the most general case for any, arbitrarily oriented electric field $\boldsymbol{E}$. The motional Stark field contribution can be obtained simply by decomposition of $\boldsymbol{E}$ into $\boldsymbol{E}_\parallel$ and $\boldsymbol{E}_\perp$.

Obviously, the Stark Hamiltonian only acts on the spatial part of the wave function with the result of leaving a radial overlap integral in the matrix element. The electric field perturbation mixes states from the same spin multiplicity whose orbital angular momenta differ by ±1. Hence, in contrast to the Zeeman Hamiltonian, it can even couple sublevels from different n manifolds. For low n states though these couplings are only of minor importance since the splitting between adjacent n is much bigger than the spacing between states from the same n level which makes transitions between the latter much more likely [151].

However, with increasing n the motional Stark field perturbation might become powerful enough to turn the situation around: The maximum energy width of the manifold of states belonging to the same n is given by

$$\Delta E_\mathrm{MS} = 3ea_\mathrm{Ps} \, n(n-1) \, |\boldsymbol{E}_\perp| = 3ea_\mathrm{Ps} \, n(n-1) \, Bv_\perp \quad \text{(B.46)}$$

where $a_\mathrm{Ps} = 2a_0$ is the Ps Bohr radius. $v_\perp$ denotes the velocity component perpendicular to $\boldsymbol{B}$ and can, for an atom at temperature T, be considered as the transverse component of the most probable thermal velocity $v_\perp = \sqrt{k_\mathrm{B}T/m_\mathrm{e}}$ of the centre of mass. For a temperature of $100\,\mathrm{K}$ for example this energy width is only $\Delta E_\mathrm{MS} = 12.6\,\mathrm{GHz}$ for $n = 3$ whereas for Ps Rydberg atoms with $n = 20$ it already amounts to $\Delta E_\mathrm{MS} = 800\,\mathrm{GHz}$. Thus, from $n = 17$ onwards, the motional Stark splitting exceeds the unperturbed energy difference of two adjacent n-manifolds so that they start to overlap [163]. This can have significant implications especially with respect to Ps Rydberg laser interaction experiments since for thermal Ps atoms the transition lines to high lying n states effectively turn into bands.

Another interesting consequence of the motional Stark perturbation, closely related to this energy splitting, is its potential capability to induce a kind of self-ionisation as soon as states are shifted in energy above the ionisation threshold. The minimum Stark field required to start triggering ionisation is given by

$$E_\mathrm{min} = \frac{e}{144\pi\epsilon_0 a_0^2} \, \frac{1}{n^4} \, . \quad \text{(B.47)}$$

For Ps at $100\,\mathrm{K}$ in $1\,\mathrm{T}$ fields this condition is already fulfilled for states above $n = 27$ [163].

B.7 Impact of magnetic field perturbation on lifetimes

Besides the energy shifts, the interaction with the magnetic field also has an influence on the lifetimes of all states affected by the perturbation, where the term "lifetime" is not restricted only

---

[31] The explicit version of its lengthy expression will not be given here and can for example be found in Ref. [161], in the appendix to Ref. [47] or, for $n' = n$, in Ref. [162].

to the annihilation lifetime but rather refers to the combination of annihilation and fluorescence decay times, given by $\tau^{-1} = (\tau^{(\mathrm{ann})})^{-1} + (\tau^{(\mathrm{fl})})^{-1}$. This lifetime modification becomes effective in all excited state manifolds, so especially also in $n = 2$, the most relevant level for the investigations presented in this thesis.

Figure B.3 shows two plots of the magnetic field-dependent lifetimes of the $n = 2$ states. It contains the combined contributions from the Zeeman as well as motional Stark effect, once for $v_\perp = 34\,\mathrm{km/s}$ in the left subplot and once for $v_\perp = 107\,\mathrm{km/s}$ on the right (figure taken from Ref. [71]).

The most distinctive feature is that for both velocities there are two states which show a very special behaviour, specifically in the region around $B = 0.4\,\mathrm{T}$ where the lifetime of the initial $^3\mathrm{S}$ state drops dramatically and the one of the P-state rises correspondingly. This is clearly the result of the combination of level crossing due to Zeeman energy shifts and mixing due to the Stark effect in the transition range from weak to strong fields. These mixtures consist of one of the unperturbed $^3\mathrm{S}_1(\pm 1)$-states and one P-state. This observation is in line with the fact that the motional Stark effect couples different l-states from the same spin multiplicity provided that they are sufficiently close in energy which, in this field region, is ensured by Zeeman energy shifts. Another interesting aspect in this context is the fact that the motional Stark effect obviously lifts the degeneracy of the initially equi-energetic $^3\mathrm{S}_1(m_s = \pm 1)$ states which does not immediately become evident from the general Stark matrix elements given by Eq. (B.45).

The figure furthermore shows that the impact of the magnetic perturbation on the lifetime becomes more pronounced with increasing velocity $v_\perp$ in the plane transverse to $\boldsymbol{B}$. This effect can be fully attributed to the motional Stark effect which, in contrast to the Zeeman effect, depends on the velocity.

Another prominent observation which can be made in both subplots is the overall reduction in the combined lifetime of all initial $^3\mathrm{S}_1$ states. For the two states which stem from the initial $m = \pm 1$ states this clearly results from (Stark-)coupling to the P-states. The evolution of the initial $^3\mathrm{S}_1(0)$ state, on the other hand, once more reflects the consequence of magnetic quenching, which is confirmed by the concomitant increase in lifetime of the $^1\mathrm{S}_0$. Due to coupling to the singlet state with equal m quantum number, the initially pure triplet ground state acquires more and more singlet character with increasing field strength which of course directly translates to a corresponding reduction in annihilation lifetime, as already visualised in Fig. B.1 showing the result of pure Zeeman interaction.

In order to get an impression of the strength of the effect, it is useful to consider the $n = 2$ manifold for instance: Ps atoms which populate the $2^3\mathrm{P}$ states decay (primarily radiatively) by two orders of magnitude faster (after $3.2\,\mathrm{ns}$) than those in the pure $^3\mathrm{S}_1$ which on average live for $1.14\,\mathrm{\mu s}$ before they annihilate (radiative decay of this state is prohibited according to the selection rules for electric dipole transitions). Mixing of these states could thus have implications on laser experiments relying on short radiative lifetimes of excited states to ensure high cycling rates, which is for example one of the most important figures of merit for an efficient laser cooling scheme. With regard to such experiments it is therefore important to take this mixing into account as it can result in population transfer to the metastable $^3\mathrm{S}_1$ state during excitation of the $1^3\mathrm{S} \leftrightarrow 2^3\mathrm{P}$ transition. Once populating metastable states, atoms drop out of the cooling cycle and are, thus, effectively lost for cooling.

A detailed discussion of the impact of the motional Stark effect on the internal state evolution as well as on the lifetime of the atom during laser cooling will follow, subsequent to the introduction of laser interaction (see Section 2.4.3, p. 34 onwards).

For a visualisation of the effect of the magnetic field perturbation on the energy states relevant for the laser cooling scheme (i.e. $n = 1$ and $n = 2$), reference shall be made to Fig. 3.1 on p. 45. The plots show the evolution of the energy states as a function of the magnetic field strengths for $v = 0\,\mathrm{m/s}$ (pure Zeeman effect) as well as $v = 10^5\,\mathrm{m/s}$ (combined Zeeman and motional Stark

(a) $v_\perp = 3.4 \cdot 10^4\,\mathrm{m/s}$ **(b)** $v_\perp = 10.7 \cdot 10^4\,\mathrm{m/s}$
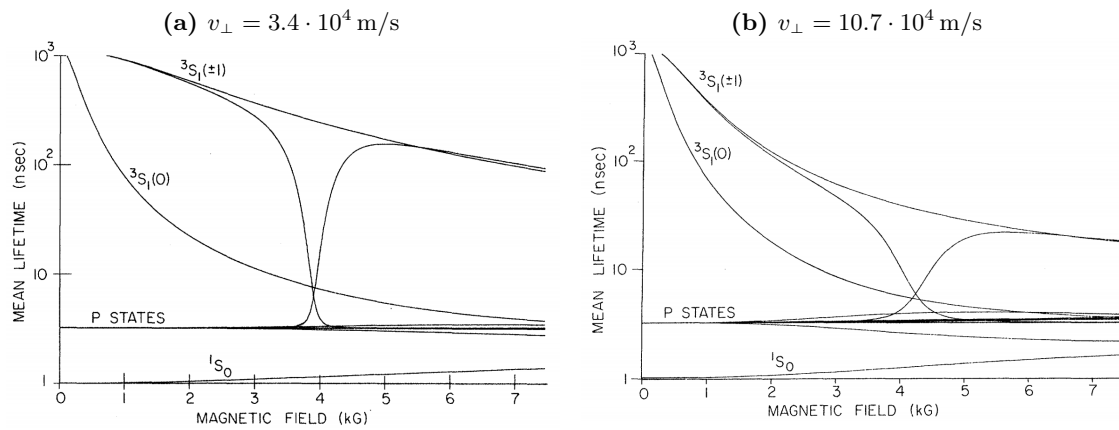
FIGURE B.3: *Modification of the decay lifetime of $n = 2$ states.*
*The two plots show the dependence of the combined annihilation and radiative decay lifetimes (on a logarithmic scale) on the magnetic field strength B (in units of 1 kG=0.1 T) for all $n = 2$ states and two Ps velocities $v_\perp$ transverse to **B**, $v_\perp = 3.4 \cdot 10^4$ m/s on the left and $v_\perp = 10.7 \cdot 10^4$ m/s on the right hand side. The figure includes the contributions from the Zeeman as well as motional Stark effect. Figure taken from Ref. [71].*

effects). A colour code furthermore indicates the evolution of the annihilation lifetime of each ground state. The information included in the whole figure thus nicely summarises the discussions of this chapter.

Appendix C

Atom-field interaction

So far, the discussion was restricted completely to the atomic spectra and their modification due to perturbation by static magnetic fields. This is however not yet the full picture to understand the mechanism of positronium laser cooling. The second type of interaction that plays a significant role is of course the interaction with lasers, or light fields in general, physically represented by electromagnetic (EM) waves. The importance of atom-light interaction for laser cooling results from the fact this is the mechanism responsible for driving transitions between the internal atomic states.

The fact that such transitions can occur at all, that means that atoms do not remain forever in one eigenstate (of $\hat{H}_\mathrm{A}$) can be explained by the interaction between the atomic degrees of freedom and the degrees of freedom of the electromagnetic field. To describe the full picture of the Ps atom, the Hamiltonian must thus be complemented by terms $\hat{H}_\mathrm{F}$ and $\hat{H}_\mathrm{int}$ that take into account the degrees of freedom of the field and the interaction with the atom, respectively, and is thus given by

$$\hat{H} = \hat{H}_\mathrm{A} + \hat{H}_\mathrm{B} + \hat{H}_\mathrm{int} + \hat{H}_\mathrm{F} \tag{C.1}$$

where $\hat{H}_\mathrm{B}$ summarises the interaction with a static magnetic field.

In general, eigenstates of the atomic Hamiltonian $\hat{H}_\mathrm{A}$ are not at the same time eigenstates of the full Hamiltonian. However, by considering the atom-field interaction as a perturbation of the non-interaction Hamiltonian, causing transitions between the unperturbed atomic eigenstates, it is possible to treat the interaction in the framework of time-dependent perturbation theory. It should be noted that these transitions are in general time-dependent even if the perturbation itself might be time-independent.

It is the objective of the following section to derive expressions for the probability of such transitions in the positronium atom which finally provides the theoretical framework for the discussion of the numerical as well as experimental laser cooling results, presented in Sec. 3.1 and Chap. 4, respectively. Unless otherwise stated this section is primarily based on the discussion given in Ref. [136].

C.1 Transitions in general

Before addressing the specific problem of atomic transitions induced by electromagnetic fields it is worth having a closer look first on the very general case since this yields, in the form of Fermi's famous Golden Rule, the basis for the subsequent treatment of the special case. The general approach considers any weakly perturbed physical system initially residing in an eigenstate of the unperturbed Hamiltonian $\hat{H}_0$ which can be described by $\hat{H} = \hat{H}_0 + \hat{W}$ with the small perturbation $\hat{W}$.

According to the concept of perturbation theory the orthonormalised eigenstates of the unperturbed Hamiltonian still form a complete basis of $\hat{H}$ in terms of which the exact time-dependent wave function $\Psi(t)$ can be expanded with time-dependent coefficients $c_n(t)$. The probability at time t to find the system, which initially resides in the eigenstate ϕ_i, in the state ϕ_f of $\hat{H}_0$ is then simply given by $w_{\mathrm{i} \to \mathrm{f}}(t) = |c_\mathrm{f}(t)|^2$.

To the first order in the matrix elements $W_{mn} = \langle \phi_m | \hat{W} | \phi_n \rangle$ of the perturbing operator $\hat{W}$, the coefficients can be written as

$$c_m(t) = c_m(0) + \frac{1}{i\hbar} \int_0^t dt' \sum_n W_{mn} \cdot \exp\left[\frac{i}{\hbar} (E_m - E_n) \, t' \right] \cdot c_n(0) \, . \tag{C.2}$$

Inserting in the next step the initial conditions $c_n(t = 0) = \delta_{n,i}$ already yields the *transition amplitude*

$$c_f(t) = \frac{1}{i\hbar} \int_0^t dt' \sum_n W_{fi} \cdot \exp\left[\frac{i}{\hbar}(E_f - E_i)\,t'\right] \tag{C.3}$$

which can directly be integrated, provided that $\hat{W}$ is time-independent, resulting in

$$|c_f(t)|^2 = w_{i\to f}(t) = |W_{fi}|^2 \cdot \frac{\sin^2\left[(E_f - E_i)t/(2\hbar)\right]}{\left[(E_f - E_i)t/2\right]^2} \xrightarrow{t\to\infty} \frac{2\pi}{\hbar}|W_{fi}|^2 t \cdot \delta(E_f - E_i)$$

so that the *transition probability per unit time* $P_{i\to f}$ becomes

$$P_{i\to f} = \frac{2\pi}{\hbar}|W_{fi}|^2 \cdot \delta(E_f - E_i)\ . \tag{C.4}$$

E_i and E_f are eigenvalues of $\hat{H}_0$ but, at the same time, expectation values of the the full Hamiltonian $\hat{H} = \hat{H}_0 + \hat{W}$.

The total probability per unit time comprising the transitions from the initial state ϕ_i to all possible final states ϕ_f is thus given by

$$P_{i\to f} = \lim_{\xi\to 0} \int_{E_i-\xi}^{E_i+\xi} \frac{2\pi}{\hbar}|W_{fi}|^2 \delta(E_f - E_i) \cdot \rho(E_f)\ dE_f$$

$$= \frac{2\pi}{\hbar}|\langle\phi_f|\hat{W}|\phi_i\rangle|^2 \cdot \rho(E_f = E_i) \tag{C.5}$$

with $\rho(E_f)$ denoting the *density of final states* ϕ_f. This last expression, giving (to first-order perturbation theory) the probability per unit time for transitions caused by a time-independent perturbation, is known as Fermi's **Golden Rule**. It is valid for a continuous energy spectrum of final states.

It should be mentioned that the Golden Rule represents the most general description of the probability for a transition from an energy eigenstate to a continuum of states, since it is completely independent of the actual type of perturbation inducing this transition. While there are plenty of possible mechanisms that can stimulate such transitions, the following treatment is restricted to the one relevant for this thesis, which is the perturbation by electromagnetic fields, in particular in the form of laser fields.

C.2 The electromagnetic field

According to Maxwell's equation which (in SI-units) are defined as

$$\boldsymbol{E} = -\nabla\Phi - \frac{\partial\boldsymbol{A}}{\partial t} \qquad \text{and} \qquad \boldsymbol{B} = \nabla \times \boldsymbol{A} \tag{C.6}$$

the electric fields $\boldsymbol{E}(\boldsymbol{r}, t)$ and magnetic fields $\boldsymbol{B}(\boldsymbol{r}, t)$ can classically be expressed in terms of the scalar potential $\Phi(\boldsymbol{r},t)$ and the vector potential $\boldsymbol{A}(\boldsymbol{r},t)$. In vacuum the speed of light is given by $c = 1/\sqrt{\epsilon_0\mu_0}$ with the vacuum permittivity ϵ_0 and the so called vacuum permeability μ_0.

While observable quantities such as the fields are gauge-invariant, the potentials in general still depend on the chosen gauge. Here it is again the Coulomb (or radiation or transverse) gauge which is used. Then

$$\nabla \cdot \boldsymbol{A} = 0 \qquad \text{and} \qquad \Delta\Phi = -4\pi\rho \tag{C.7}$$

where ρ stands for the electric charge density.

As seen above in the context of static magnetic field perturbations, $\boldsymbol{A}$ enters the Hamiltonian via the kinetic momenta $\hat{\boldsymbol{p}}_{kin} = \hat{\boldsymbol{p}} - q\boldsymbol{A}$ where q is the charge of the particle and Φ is taken into

account by adding the according potential energy terms. The Hamiltonian comprising the atomic degrees of freedom and the light-matter interaction then becomes

$$\hat{H}_{\mathrm{A}} + \hat{H}_{\mathrm{int}} = \sum_{i=\{e^-, e^+\}} \left(\frac{1}{2\mu} \left[\hat{\boldsymbol{p}}_i - q_i \boldsymbol{A}(\boldsymbol{r}_i, t) \right]^2 + q_i \Phi(\boldsymbol{r}_i, t) \right) + \hat{V} \ . \tag{C.8}$$

Obviously only the (observable) energy differences are gauge-invariant in contrast to the absolute energy eigenvalues which depend on the particular gauge.

Electromagnetic transitions can only be described consistently and completely (i.e. including all effects) by treating the field in a quantum mechanical way. Only then $\hat{H}$ contains an interaction between atom and field which induces transitions between the eigenstates of the non-interacting Hamiltonian, even if initially no field is present, such as in case of spontaneous emission.

The quantisation of the EM-field starts from the wave equation

$$\nabla^2 \boldsymbol{A}(\boldsymbol{r}, t) = \frac{1}{c^2} \frac{\partial^2}{\partial t^2} \boldsymbol{A}(\boldsymbol{r}, t) \tag{C.9}$$

for the (still classical) vector potential $\boldsymbol{A}(\boldsymbol{r}, t)$ which is derived from Maxwell's equations for a source-free field in vacuum. The general solution to this equation is given by a superposition of plane waves labelled by *mode* indices λ where each mode is characterised by a *wave vector* $\boldsymbol{k}_\lambda$, pointing along the propagation direction of the wave, by an angular frequency $\omega_\lambda = c|\boldsymbol{k}_\lambda|$ (as a direct result of the dispersion relation) and by a unit *polarisation vector* $\boldsymbol{\epsilon}_\lambda$, summarised by

$$\boldsymbol{A}_\lambda(\boldsymbol{r}) \, \mathrm{e}^{-i\omega_\lambda t} = \frac{1}{\sqrt{V}} \boldsymbol{\epsilon}_\lambda \, \mathrm{e}^{i(\boldsymbol{k}_\lambda \cdot \boldsymbol{r} - \omega_\lambda t)} \tag{C.10}$$

using the amplitude $\boldsymbol{A}_\lambda(\boldsymbol{r}) = \boldsymbol{\epsilon}_\lambda \mathrm{e}^{i\boldsymbol{k}_\lambda \cdot \boldsymbol{r}}/\sqrt{V}$. The normalisation factor $1/\sqrt{V}$ results from demanding

$$\int \mathrm{d}^3\boldsymbol{r} \, |\boldsymbol{A}_\lambda(\boldsymbol{r})|^2 = 1 \tag{C.11}$$

for all modes λ.

The choice of the Coulomb gauge directly entails the relation $\boldsymbol{\epsilon}_\lambda \cdot \boldsymbol{k}_\lambda = 0$ for each mode, which in other words means that in free space the electric field vector pointing along $\boldsymbol{\epsilon}$ is always aligned perpendicular to the propagation direction $\boldsymbol{k}$ of the wave.

All possible polarisation states can be expressed in terms of two basis vectors $\boldsymbol{\epsilon}_\lambda^{\prime(+)}$ and $\boldsymbol{\epsilon}_\lambda^{\prime(-)}$ with complex components (to account for phase differences) with the first one describing right-handed and the latter oppositely directed left-handed circular polarisation (with respect to the propagation direction). For a monochromatic wave travelling along the positive z-direction they are defined as

$$\boldsymbol{\epsilon}_\lambda^{\prime(+)} = \frac{1}{\sqrt{2}} \begin{pmatrix} -1 \\ -i \\ 0 \end{pmatrix} \qquad \text{and} \qquad \boldsymbol{\epsilon}_\lambda^{\prime(-)} = \frac{1}{\sqrt{2}} \begin{pmatrix} 1 \\ -i \\ 0 \end{pmatrix} \tag{C.12}$$

in terms of the Cartesian basis vectors $\mathbf{e}_x$, $\mathbf{e}_y$ and $\mathbf{e}_z$ of the coordinate system used for describing the light field. The use of primes will become clear later in the context of the relation between the polarisation state and type of electric dipole transition in Section C.5.1.

The general classical vector potential of an electromagnetic field in a source-free environment is finally given by the linear combination of all modes with mode amplitudes β_λ and β_λ^*

$$\boldsymbol{A}(\boldsymbol{r}, t) = \sum_\lambda \left(\beta_\lambda \boldsymbol{A}_\lambda(\boldsymbol{r}) \mathrm{e}^{-i\omega_\lambda t} + \beta_\lambda^* \boldsymbol{A}_\lambda^*(\boldsymbol{r}) \mathrm{e}^{+i\omega_\lambda t} \right) \ . \tag{C.13}$$

The requirement of physical measurability imposed on the fields derived from the vector potential requires that each mode is accompanied by its complex conjugate. Maxwell's Equation (C.13) then

yields the electric and magnetic field

$$\boldsymbol{E}(\boldsymbol{r},t) = -\frac{\partial}{\partial t}\boldsymbol{A}(\boldsymbol{r},t) = \sum_\lambda i\omega_\lambda \left[\beta_\lambda \boldsymbol{A}_\lambda(\boldsymbol{r}) \mathrm{e}^{-i\omega_\lambda t} - \beta_\lambda^* \boldsymbol{A}_\lambda^*(\boldsymbol{r}) \mathrm{e}^{+i\omega_\lambda t}\right]$$

$$\equiv \frac{1}{2}\sum_\lambda \left[\boldsymbol{E}_\lambda \mathrm{e}^{i(\boldsymbol{k}_\lambda \cdot \boldsymbol{r} - \varphi_\lambda(t))} + \boldsymbol{E}_\lambda^* \mathrm{e}^{-i(\boldsymbol{k}_\lambda \cdot \boldsymbol{r} - \varphi_\lambda(t))}\right] \tag{C.14}$$

$$\boldsymbol{B}(\boldsymbol{r},t) = \nabla \times \boldsymbol{A}(\boldsymbol{r},t) = i\sum_\lambda \boldsymbol{k}_\lambda \times \left[\beta_\lambda \boldsymbol{A}_\lambda(\boldsymbol{r}) \mathrm{e}^{-i\omega_\lambda t} - \beta_\lambda^* \boldsymbol{A}_\lambda^*(\boldsymbol{r}) \mathrm{e}^{+i\omega_\lambda t}\right] \ . \tag{C.15}$$

The electric field amplitude $\boldsymbol{E}_\lambda$ of mode λ which is related to the irradiance[32] I_λ by $I_\lambda = \epsilon_0 |\boldsymbol{E}_\lambda|^2 c/2$, can easily be identified as $2i\omega_\lambda\beta_\lambda \boldsymbol{\epsilon}_\lambda/\sqrt{V}$. Using the general phase $\varphi_\lambda(t)$ allows to take into account further effects such as the Doppler effect of the particle irradiated by the laser and moving with velocity $\boldsymbol{v}$ in which case $\varphi_\lambda(t) = (\omega_\lambda - \boldsymbol{k}_\lambda \cdot \boldsymbol{v})\,t$.

At this point it should be mentioned that the exact expression for the coefficients β_λ and β_λ^* shall still remain unspecified here since they are a direct consequence of a quantum mechanical postulation according to which the field operators $\hat{b}_\lambda$ and $\hat{b}_\lambda^\dagger$, which will only be introduced later as the quantum mechanical interpretation of β_λ and β_λ^*, are required to satisfy the fundamental commutation relations of quantum optics, which is $[\hat{b}_\lambda, \hat{b}_{\lambda'}^\dagger] = \delta_{\lambda,\lambda'}$ [164]. For methodological reasons it is thus more reasonable to construct them in the course of the second quantisation of the fields showing that only one definition exists which yields the required commutation relations. The next step in that direction is to consider the energy E_f of the EM-field which is given by the integral over the energy density $\epsilon_0/2(\boldsymbol{E}^2 + c^2\boldsymbol{B}^2)$, resulting in

$$E_\mathrm{F} = \frac{\epsilon_0}{2}\int \mathrm{d}^3\boldsymbol{r}\left(\boldsymbol{E}^2 + c^2\boldsymbol{B}^2\right) = 2\epsilon_0 \sum_\lambda \omega_\lambda^2 |\beta_\lambda|^2 \ . \tag{C.16}$$

In order to transform the last expression into the familiar structure

$$E_\mathrm{F} = \sum_\lambda \frac{\omega_\lambda}{2}(P_\lambda^2 + Q_\lambda^2) \tag{C.17}$$

it is convenient to define the (real) variables

$$Q_\lambda = \sqrt{\epsilon_0\omega_\lambda}\,(\beta_\lambda^* + \beta_\lambda) \qquad \text{and} \qquad P_\lambda = i\sqrt{\epsilon_0\omega_\lambda}\,(\beta_\lambda^* - \beta_\lambda) \qquad \text{or, respectively} \tag{C.18}$$

$$\beta_\lambda = \sqrt{\frac{1}{4\epsilon_0\omega_\lambda}}(Q_\lambda + iP_\lambda) \qquad \text{and} \qquad \beta_\lambda^* = \sqrt{\frac{1}{4\epsilon_0\omega_\lambda}}(Q_\lambda - iP_\lambda) \tag{C.19}$$

which can be interpreted as the canonically conjugate pair of momentum and displacement variables of mode λ.

In contrast to the description of the quantised atomic states, all fields and potentials have been treated classically so far. A fully quantised treatment (and Hamiltonian) is achieved by first identifying the variables $Q_\lambda(t) = Q_\lambda \mathrm{e}^{-i\omega_\lambda t}$ and $P_\lambda(t) = P_\lambda \mathrm{e}^{-i\omega_\lambda t}$ as time-independent Hermitian operators $\hat{Q}_\lambda$ and $\hat{P}_\lambda$ thereby imposing canonical commutation relations on each mode such that

$$\left[\hat{Q}_\lambda, \hat{P}_{\lambda'}\right] = i\hbar\delta_{\lambda,\lambda'} \ . \tag{C.20}$$

Subsequent interpretation of $\hat{Q}_\lambda$ and $\hat{P}_\lambda$ as quantum mechanical momentum and displacement operators respectively and the field Hamiltonian $\hat{H}_\mathrm{F}$ as the field energy operator (based on Eq. (C.17)) finally leads to

$$\hat{H}_\mathrm{F} = \sum_\lambda \frac{\omega_\lambda}{2}\left(\hat{P}_\lambda^2 + \hat{Q}_\lambda^2\right) \ . \tag{C.21}$$

---

[32] Throughout this thesis the quantity I always refers to the irradiance of the light (with units $\mathrm{Js^{-1}m^{-2}} = \mathrm{Wm^{-2}}$), even though it might sometimes be improperly called intensity (especially in the context of saturation of optical transitions discussed in Appendix D). Unfortunately its terminology is as well not always unambiguous throughout literature, nevertheless though the occurrence of I is generally understood as an optical energy flux.

The eigenstates of $\hat{H}_{\mathrm{F}}$, the so called *occupation number states* $|n_1, ..., n_\lambda, ...\rangle$ are indicated by the *occupation numbers* n_{λ_i} of the respective modes. Introducing those states is usually considered as the crucial step in the process of second quantisation.

To derive exact expressions of the eigenvalues (as well as -states) of $\hat{H}_{\mathrm{F}}$ it is next common to introduce operators $\hat{b}_\lambda$ and $\hat{b}_\lambda^\dagger$ defined as

$$\hat{b}_\lambda^\dagger = \frac{1}{\sqrt{2\hbar}} \left(\hat{Q}_\lambda - i\hat{P}_\lambda \right) \equiv \sqrt{\frac{2\epsilon_0\omega_\lambda}{\hbar}} \, \beta_\lambda^* \mathrm{e}^{i\omega_\lambda t}$$
$$\hat{b}_\lambda = \frac{1}{\sqrt{2\hbar}} \left(\hat{Q}_\lambda + i\hat{P}_\lambda \right) \equiv \sqrt{\frac{2\epsilon_0\omega_\lambda}{\hbar}} \, \beta_\lambda \mathrm{e}^{-i\omega_\lambda t}$$
(C.22)

or respectively

$$\hat{Q}_\lambda = \sqrt{\frac{\hbar}{2}} \left(\hat{b}_\lambda^\dagger + \hat{b}_\lambda \right) \qquad \text{and} \qquad \hat{P}_\lambda = i\sqrt{\frac{\hbar}{2}} \left(\hat{b}_\lambda^\dagger - \hat{b}_\lambda \right) \,. \tag{C.23}$$

Commutation relations for $\hat{b}_\lambda$ and $\hat{b}_\lambda^\dagger$ directly follow from $\left[\hat{Q}_\lambda, \hat{P}_{\lambda'} \right] = i\hbar\delta_{\lambda,\lambda'}$ and are given by the well-known quantum optical commutation relations

$$\left[\hat{b}_\lambda, \hat{b}_{\lambda'}^\dagger \right] = \delta_{\lambda,\lambda'} \,. \tag{C.24}$$

This result finally explains why both β_λ as well as $\hat{b}_\lambda$ have been defined in the way outlined above.

Applied on the occupation number states $|n_1, ..., n_\lambda, ...\rangle$ which are also known as *Fock states*, they respectively cause either an increase or reduction of the number of photons by one in the according mode λ

$$\hat{b}_\lambda^\dagger |..., n_\lambda, ...\rangle = \sqrt{n_\lambda + 1} \, |..., n_\lambda + 1, ...\rangle \tag{C.25}$$
$$\hat{b}_\lambda |..., n_\lambda, ...\rangle = \sqrt{n_\lambda} \, |..., n_\lambda - 1, ...\rangle \,. \tag{C.26}$$

For this reason they are called *creation* and *annihilation operators for photons*. It is thus possible to define an operator $\hat{N}_\lambda = \hat{b}_\lambda^\dagger \hat{b}_\lambda$ which acts on the eigenstates by counting the number of photons or quanta in mode λ

$$\hat{N}_\lambda |..., n_\lambda, ...\rangle = n_\lambda |..., n_\lambda, ...\rangle \tag{C.27}$$

which is the reason for $|..., n_\lambda, ...\rangle$ being called photon number state and the formalism as *occupation number representation* in terms of which usually also the actual state of the light field is expressed.

Using the creation and annihilation operators the EM-field Hamiltonian then simplifies to

$$\hat{H}_{\mathrm{F}} = \sum_\lambda \frac{\omega_\lambda}{2} \left(\hat{P}_\lambda^2 + \hat{Q}_\lambda^2 \right) = \sum_\lambda \frac{\hbar\omega_\lambda}{2} \left(\hat{b}_\lambda^\dagger \hat{b}_\lambda + \hat{b}_\lambda \hat{b}_\lambda^\dagger \right) = \sum_\lambda \hbar\omega_\lambda \left(\hat{b}_\lambda^\dagger \hat{b}_\lambda + \frac{1}{2} \right) \,. \tag{C.28}$$

Ultimately it is possible to define quantum mechanical operators associated to the classical vector potential and fields by simple quantisation of the expansion coefficients β_λ and β_λ^* according to the constructed prescription (C.22) given above, resulting in

$$\hat{\boldsymbol{A}}(\boldsymbol{r}) = \sum_\lambda \sqrt{\frac{\hbar}{2\epsilon_0\omega_\lambda}} \left(\boldsymbol{A}_\lambda(\boldsymbol{r})\hat{b}_\lambda + \boldsymbol{A}_\lambda^*(\boldsymbol{r})\hat{b}_\lambda^\dagger \right) \text{and} \tag{C.29}$$

$$\hat{\boldsymbol{E}}(\boldsymbol{r}) = i \sum_\lambda \sqrt{\frac{\hbar\omega_\lambda}{2\epsilon_0}} \left[\boldsymbol{A}_\lambda(\boldsymbol{r}) \, \hat{b}_\lambda - \boldsymbol{A}_\lambda^*(\boldsymbol{r}) \, \hat{b}_\lambda^\dagger \right]$$

$$= i \sum_\lambda \sqrt{\frac{\hbar\omega_\lambda}{2\epsilon_0 V}} \left[\boldsymbol{\epsilon}_\lambda \hat{b}_\lambda \mathrm{e}^{i\boldsymbol{k}_\lambda \cdot \boldsymbol{r}} - \boldsymbol{\epsilon}_\lambda^* \hat{b}_\lambda^\dagger \mathrm{e}^{-i\boldsymbol{k}_\lambda \cdot \boldsymbol{r}} \right] \,. \tag{C.30}$$

It is recalled here that $\boldsymbol{A}_\lambda(\boldsymbol{r}) = \boldsymbol{\epsilon}_\lambda \mathrm{e}^{i\boldsymbol{k}_\lambda \cdot \boldsymbol{r}}/\sqrt{V}$ summarises the spatial part of the plane wave solution of the homogeneous wave equation for the classical vector potential $\boldsymbol{A}(\boldsymbol{r}, t)$.

C.3   Atom-field interaction

The quantised vector potential serves now as the basic tool to describe the interaction of an atom with the field. Based on the interaction Hamiltonian and Fermi's Golden Rule is finally possible to derive the fundamental interaction processes of photon emission and absorption as expounded next.

C.3.1   Interaction Hamiltonian

The Hamiltonian treating the interaction in a fully quantum mechanical way can easily be obtained by complementing the atomic and interaction Hamiltonians $\hat{H}_\text{A}$ and $\hat{H}_\text{int}$, introduced above, by $\hat{H}_\text{f}$ describing the quantised degrees of freedom of the electromagnetic field.

By additionally replacing all potentials by the corresponding operators and setting $\Phi = 0$ for a source free field in Coulomb gauge leads to the full Hamiltonian

$$\hat{H} = \hat{H}_\text{A} + \hat{H}_\text{int} + \hat{H}_\text{F} \tag{C.31}$$

where $\hat{H}_\text{A}$ is given by the final QED-corrected atomic Hamiltonian given by Eq. (2.12), $\hat{H}_\text{F}$ by Eq. (C.28) and the interaction Hamiltonian by

$$\hat{H}_\text{int} = -\frac{1}{2\mu} \sum_{i=\{e^-,e^+\}} q_i \left[\hat{\boldsymbol{p}}_i \cdot \hat{\boldsymbol{A}}(\boldsymbol{r}_i) + \hat{\boldsymbol{A}}(\boldsymbol{r}_i) \cdot \hat{\boldsymbol{p}}_i \right]$$
$$+ \frac{1}{2\mu} \sum_{i=\{e^-,e^+\}} q_i^2 \hat{\boldsymbol{A}}(\boldsymbol{r}_i)^2 \ + \sum_{i=\{e^-,e^+\}} q_i \Phi(\boldsymbol{r}_i,t) \tag{C.32}$$

resulting from Eq. (C.8) with $\hat{\boldsymbol{A}}(\boldsymbol{r}_i)$ as defined above (cf. Eq. (C.29)).

The term quadratic in the vector potential does not act on the atomic states but only on the photon field, namely by adding a self energy which results from a sequence of photon creation and annihilation events. Since this contribution scales like the density of quanta that means photons it becomes relevant only in the case of extreme light fields. For this reason and in accordance with the concept of first-order perturbation this term will be neglected in the further course.

It is worth mentioning that, even though in this section again a vector potential $\boldsymbol{A}$ is involved, it here represents only the potential of the light field that means explicitly not as well the external magnetostatic potential which will be ignored for the moment. In the general case of positronium in magnetic fields it can easily be incorporated either in the respective term in $\hat{H}_\text{A}$ or as an additional Zeeman term.

In most cases of interest, the wavelength $2\pi/|\boldsymbol{k}_\lambda|$ of the photons created or absorbed in the process of light-matter interaction are much longer than the characteristic dimension of the atom. It is thus justified to assume that the vector potential is practically position independent on the atomic length scale so that $\hat{\boldsymbol{A}}(\boldsymbol{r})$ can well be approximated by $\hat{\boldsymbol{A}}$ by setting $\mathrm{e}^{i\boldsymbol{k}_\lambda \cdot \boldsymbol{r}_i} \approx 1$. In this so-called *dipole approximation* the interaction Hamiltonian simplifies to

$$\hat{H}_\text{int} = -\frac{1}{\sqrt{2\epsilon_0 V}} \sum_{i=\{e^-,e^+\}} \frac{q_i}{\mu} \sum_\lambda \sqrt{\frac{\hbar}{\omega_\lambda}} \ \hat{\boldsymbol{p}}_i \cdot \left[\boldsymbol{\epsilon}_\lambda \hat{b}_\lambda - \boldsymbol{\epsilon}_\lambda^* \hat{b}_\lambda^\dagger \right] \ . \tag{C.33}$$

C.4   Interaction processes – Emission and absorption of photons

Since the full Hamiltonian $\hat{H}$ encompasses the degrees of freedom of both the atom and the field, its eigenstates are given by states belonging to the joint Hilbert space. These states can be expressed in terms of linear combinations of the eigenstates of the non-interaction Hamiltonian, consisting

of $\hat{H}_\mathrm{A}$ and $\hat{H}_\mathrm{f}$ which are given by the tensor product of atomic and field eigenstates, $|\chi_j\rangle$ and $|...,n_\lambda,...\rangle$ respectively, that means

$$|\phi_j\rangle = |\chi_j\rangle \otimes |...,n_\lambda,...\rangle \ . \tag{C.34}$$

Applied on these joint states the interaction Hamiltonian induces transitions between certain atomic states which are accompanied by changes in the state of the field. This process in turn implies a change in the occupation number of the mode which $\hat{H}_\mathrm{int}$ acts on. In other words, the presence of the field induces atomic transitions in which the quanta of the field, the photons, serve as mediators of the interaction. Since the interaction Hamiltonian $\hat{H}_\mathrm{int}$ in the given form only contains terms linear in the operators, the treatment here shall be restricted to single-photon events.

In order to calculate the probability for the occurrence of such an event by means of perturbation theory, $\hat{H}_\mathrm{int}$ is interpreted as the perturbing operator $\hat{W}$. The according transition matrix elements are thereby given by

$$(\hat{H}_\mathrm{int})_\mathrm{fi} = \langle \phi_\mathrm{f} | \hat{H}_\mathrm{int} | \phi_\mathrm{i} \rangle \tag{C.35}$$

with the initial and final states, ϕ_i and ϕ_f, being eigenstates of the non-interaction Hamiltonian. The use of the tensor product notation introduced in Eq. (C.34) enables a separation of the field contributions F_λ so that the matrix elements reduce to the following expressions, involving only the atomic degrees of freedom

$$
\begin{aligned}
(\hat{H}_\mathrm{int})_\mathrm{fi} = \ & -\frac{1}{\sqrt{2\epsilon_0 V}} \frac{1}{\mu} \sqrt{\frac{\hbar}{\omega_\lambda}} \times \\
& \left[\langle \chi_\mathrm{f} | \sum_{j=\{e^-,e^+\}} q_j \hat{\boldsymbol{p}}_j \cdot \boldsymbol{\epsilon}_\lambda | \chi_\mathrm{i} \rangle F_\lambda^\mathrm{(abs)} + \langle \chi_\mathrm{f} | \sum_{j=\{e^-,e^+\}} q_j \hat{\boldsymbol{p}}_j \cdot \boldsymbol{\epsilon}_\lambda^* | \chi_\mathrm{i} \rangle F_\lambda^\mathrm{(em)} \right] \ .
\end{aligned} \tag{C.36}
$$

The field contributions F_λ are given by

$$
\begin{aligned}
F_\lambda^\mathrm{(abs)} &= \langle ...,n'_\lambda,... | \hat{b}_\lambda | ...,n_\lambda,... \rangle \\
F_\lambda^\mathrm{(em)} &= \langle ...,n'_\lambda,... | \hat{b}_\lambda^\dagger | ...,n_\lambda,... \rangle
\end{aligned}
$$

and can directly be evaluated for given occupation numbers n_λ. Needless to say that they take non-zero values only if $n'_\lambda = n_\lambda - 1$ and $n'_\lambda = n_\lambda + 1$ in case of photon absorption and emission, respectively.

The sum over λ vanishes since only single-photon events are considered here, implying that only one mode is involved. All other modes remain unchanged and are therefore also known as *spectator modes*. The energies

$$
\begin{aligned}
E_\mathrm{i} &= \varepsilon_\mathrm{i} + n_\lambda \hbar \omega_\lambda \\
E_\mathrm{f} &= \varepsilon_\mathrm{f} + n'_\lambda \hbar \omega_\lambda
\end{aligned}
$$

of the initial and final state, i.e. the eigenvalues to $|\phi_\mathrm{i}\rangle$ and $|\phi_\mathrm{f}\rangle$), can as well be separated into atomic ($\varepsilon_\mathrm{i/f}$) and photonic contributions which themselves are eigenvalues of $(\hat{H}_\mathrm{A} + \hat{H}_\mathrm{F})$, respectively. Due to the requirement of energy conservation $\varepsilon_\mathrm{f} - \varepsilon_\mathrm{i} = (n_\lambda - n'_\lambda)\hbar\omega_\lambda$ which merely means that the energy gained (or lost) by the atom is equal to the energy of the absorbed (or emitted) photon.

In order to further simplify the interaction matrix elements given in Eq. (C.36) it is convenient to express the momentum operators $\hat{\boldsymbol{p}}_j$ in terms of commutators between the displacement vectors $\boldsymbol{r}_j$ and the non-interaction Hamiltonian, according to

$$\hat{\boldsymbol{p}}_j = \mu \frac{i}{\hbar} \left[(\hat{H}_\mathrm{A} + \hat{H}_\mathrm{F}), \boldsymbol{r}_j \right] \ .$$

It should be noted that strictly speaking this is not entirely correct if the atomic Hamiltonian $\hat{H}_\mathrm{A}$ is assumed to represent the fully QED-corrected Hamiltonian $\hat{H}_\mathrm{QED}$ (cf. Eq. (2.12)) which contains

terms that do not commute in the same way with the Hamiltonian. This approximation is justified though that the interaction is treated in a perturbative, i.e. as well approximate, approach here.

Using this relation subsequently allows to convert the matter part of the interaction matrix elements $(\hat{H}_{\mathrm{int}})_{\mathrm{fi}}$ into matrix elements that depend on the *electric dipole moment operator* $\hat{\boldsymbol{d}} = \sum_j q_j \hat{\boldsymbol{r}}_j$ so that expression (C.36) simplifies to

$$(\hat{H}_{\mathrm{int}})_{\mathrm{fi}} = -i\frac{1}{\sqrt{2\epsilon_0 V}}\; \frac{\varepsilon_{\mathrm{f}} - \varepsilon_{\mathrm{i}}}{\sqrt{\hbar\omega_\lambda}}\; [\boldsymbol{\epsilon}_\lambda \cdot \boldsymbol{d}_{\mathrm{fi}}\; F_\lambda^{(\mathrm{abs})} + \boldsymbol{\epsilon}_\lambda^* \cdot \boldsymbol{d}_{\mathrm{fi}}\; F_\lambda^{(\mathrm{em})}] \tag{C.37}$$

with $\boldsymbol{d}_{\mathrm{fi}} = \langle\chi_{\mathrm{f}}|\hat{\boldsymbol{d}}|\chi_{\mathrm{i}}\rangle = \langle\chi_{\mathrm{f}}|\sum_j q_j \boldsymbol{r}_j|\chi_{\mathrm{i}}\rangle$ denoting the *transition dipole moment* that means the matrix elements of the electric dipole moment operator belonging to the transition between the initial and final state. The fact that this result in terms of the dipole moment could only be derived based on the assumption of position independence of $\hat{\boldsymbol{A}}$ also explains the use of the name *dipole approximation*.

Plugging the matrix elements given in Eq. (C.37) into Fermi's Golden Rule[33] (C.5) finally yields the total probability per unit time for the transition from the initial state ϕ_{i} to the continuum of final states ϕ_{f}

$$\begin{aligned} P_{\mathrm{i}\to\mathrm{f}} &= \frac{2\pi}{\hbar}|\langle\phi_{\mathrm{f}}|\hat{H}_{\mathrm{int}}|\phi_{\mathrm{i}}\rangle|^2 \cdot \rho(E_{\mathrm{f}}) \\ &= \frac{\pi}{\epsilon_0 V}\frac{(\varepsilon_{\mathrm{f}} - \varepsilon_{\mathrm{i}})^2}{\hbar^2\omega_\lambda}\;|\boldsymbol{\epsilon}_\lambda \cdot \boldsymbol{d}_{\mathrm{fi}}\; F_\lambda^{(\mathrm{abs})} + \boldsymbol{\epsilon}_\lambda^* \cdot \boldsymbol{d}_{\mathrm{fi}}\; F_\lambda^{(\mathrm{em})}|^2\, \rho(E_{\mathrm{f}})\; ; \end{aligned} \tag{C.38}$$

This expression clearly shows that different photon exchange processes are involved or, respectively, induced by the interaction of the atomic dipole with the electromagnetic field, both with equal probability. While the first term describes the removal of one photon from the light field by the atom, indicated by the matrix element $F_\lambda^{(\mathrm{abs})}$ which includes the annihilation operator, the second one represents the opposite process where the atom emits a photon which is reflected by the increase in the photon number n'_λ by one.

C.4.1 Spontaneous emission

If starting with an initial light field state containing no photon in any mode, the matrix element $\langle\phi_{\mathrm{f}}|\hat{H}_{\mathrm{int}}|\phi_{\mathrm{i}}\rangle$ gives a non-zero contribution only in the case that the final field state contains exactly one photon in one mode λ and $F_\lambda^{(\mathrm{abs})} = 0, F_\lambda^{(\mathrm{em})} = 1$. Due to energy conservation $\varepsilon_{\mathrm{f}} - \varepsilon_{\mathrm{i}} = \hbar\omega_\lambda$ the final atomic energy ε_{f} must thus be exactly equal to the one of the initial state ε_{i} reduced by the energy $\hbar\omega_\lambda$ of the emitted photon which implies deexcitation to a lower states in the atomic level scheme. The probability per unit time for such a transition, accompanied by the emission of a photon into the solid angle $\mathrm{d}\Omega$ is given by

$$P_{\mathrm{i}\to\mathrm{f}}^{(\mathrm{spont})}\; \mathrm{d}\Omega = \frac{\pi}{\epsilon_0 V}\omega_\lambda\,|\boldsymbol{\epsilon}_\lambda^* \cdot \boldsymbol{d}_{\mathrm{fi}}|^2\,\rho(E_{\mathrm{f}})\; \mathrm{d}\Omega\;. \tag{C.39}$$

The density of photon states $\rho(E)$ is obtained by assuming V to be the volume of an cube with side lengths L which, with periodic boundary conditions, represents the most appropriate model of free space. The density of possible plane wave vectors $\boldsymbol{k} = (n_x, n_y, n_z)2\pi/L$ (with $n_i \in \mathbb{Z}$) inside such a cube, that means the number $\mathrm{d}N/\mathrm{d}V$ of states per unit volume in k-space, is given by $(2\pi/L)^{-3}$ (where $\mathrm{d}V = k^2\mathrm{d}k\;\mathrm{d}\Omega$ in spherical coordinates).

---

[33] In this context, it is important to point out, that the general treatment of photon transfer events by means of Fermi's Golden Rule is only valid under certain conditions, in particular sufficiently long interaction times combined with the involvement of a mechanism inducing decoherence (cf. App. D for more details). This is due to the fact that the Golden Rule is applicable only for transitions from a discrete initial energy state to a *continuum* of final states. For this reason, only the special case of spontaneous emission, which is the transition from a single bound state (with discrete energy) to a continuum of final states allows unconditional application of Fermi's Golden Rule.

Thus, the number $\mathrm{d}N/\mathrm{d}k$ of photon states per unit wave number k (i.e. with $k \in [k,\, k+\mathrm{d}k]$ in the solid angle $\mathrm{d}\Omega$) can be written as

$$\frac{\mathrm{d}N}{\mathrm{d}k} = \frac{\mathrm{d}N}{\mathrm{d}V}k^2\mathrm{d}\Omega = (2\pi/L)^{-3}k^2\mathrm{d}\Omega = \rho(k)\mathrm{d}\Omega$$

and, similarly, the number of states per unit energy becomes

$$\frac{\mathrm{d}N}{\mathrm{d}E} = \frac{\mathrm{d}N}{\mathrm{d}k}\frac{\mathrm{d}k}{\mathrm{d}E} = \left(\frac{2\pi}{L}\right)^{-3}k^2\mathrm{d}\Omega\frac{\mathrm{d}k}{\mathrm{d}E} = \left(\frac{L}{2\pi}\right)^3\frac{k^2}{\hbar c}\mathrm{d}\Omega = \boxed{\left(\frac{L}{2\pi}\right)^3\frac{\omega^2}{\hbar c^3}\mathrm{d}\Omega = \rho(E)\mathrm{d}\Omega} \quad (\text{C.40})$$

using $E = \hbar\omega$ and the dispersion relation $\omega(k) = ck$.

Inserting Eq. (C.40) into Eq. (C.39) then yields the probability per unit time

$$P_{\mathrm{i}\to\mathrm{f}}^{(\mathrm{spont})}\,\mathrm{d}\Omega = \frac{1}{8\pi^2\epsilon_0}\frac{\omega_\lambda^3}{\hbar c^3}\left|\boldsymbol{\epsilon}_\lambda^* \cdot \boldsymbol{d}_{\mathrm{fi}}\right|^2\,\mathrm{d}\Omega \quad (\text{C.41})$$

for the transition from $|\phi_{\mathrm{i}}\rangle$ to $|\phi_{\mathrm{f}}\rangle$ with concomitant emission of one photon of distinct polarisation into the solid angle $\mathrm{d}\Omega$. Integration over all possible directions Ω and taking into account the two possible polarisation states $\boldsymbol{\epsilon}_\lambda^{(+)}$ and $\boldsymbol{\epsilon}_\lambda^{(-)}$ finally results in the total transition probability per unit time $\mathcal{P}$ for spontaneous emission of a photon with arbitrary polarisation

$$\mathcal{P}_{\mathrm{i}\to\mathrm{f}}^{(\mathrm{spont})} = \int\left[P_{\mathrm{i}\to\mathrm{f},\,\boldsymbol{\epsilon}_\lambda^{(+)}}^{(\mathrm{spont})} + P_{\mathrm{i}\to\mathrm{f},\,\boldsymbol{\epsilon}_\lambda^{(-)}}^{(\mathrm{spont})}\right]\mathrm{d}\Omega$$

$$= \frac{1}{3\pi\epsilon_0}\frac{\omega_\lambda^3}{\hbar c^3}\left|\boldsymbol{d}_{\mathrm{fi}}\right|^2 \stackrel{\mathrm{def}}{=} A_{\mathrm{fi}}\,. \quad (\text{C.42})$$

The resulting last term represents the well-known *Einstein A-coefficient* A_{fi} for spontaneous decay which is an intrinsic property of the atom. Summation over all possible decay channels yields the fluorescence lifetime (for spontaneous single-photon emission) of the atomic state $|\chi_{\mathrm{i}}\rangle$ given by

$$\tau = \left[\sum_{\varepsilon_{\mathrm{f}} < \varepsilon_{\mathrm{i}}}\mathcal{P}_{\mathrm{i}\to\mathrm{f}}^{(\mathrm{spont})}\right]^{-1}\,. \quad (\text{C.43})$$

Finally, it should be mentioned that the assumption of infinitely sharp atomic energy levels is only a very idealised model. In a more precise description the spectral lines of all excited states are subject to natural broadening which, roughly speaking, originates from the time-energy uncertainty principle leading to a natural line width Γ and thus resulting also in a broadening of the corresponding lifetime $\tau = \Gamma^{-1}$ (cf. Section C.7.2 for more details).

The spontaneous emission lifetimes of the Ps atom have already been listed in Tab. A.1 for all $n = 1,2$ and 3 levels, referred to as fluorescence lifetimes there.

C.4.2   Stimulated emission

If the field is not empty at the time of the photon emission event but contains already n_λ photons the probability $P_{\mathrm{i}\to\mathrm{f}}$ (cf. Eq. (C.38)) includes a field contribution $|F_\lambda^{(\mathrm{em})}|^2 = n_\lambda + 1$ bigger than one. The increase in emission probability added by n_λ then describes so called stimulated emission which depends on the field strength in terms of the number of available photons in this mode λ. The last connection between field strength and photon number becomes clear by considering an atom in a field whose modes are all occupied isotropically with spectral irradiance distribution $I_\omega(\omega)$, which is the irradiance I of a surface per unit frequency. It should be recalled here that the irradiance is a quantity indicating the radiative flux per unit area received by a surface, in other words and applied to the case here, the field energy per unit area and unit time which (literally) irradiates the cross-section surface of the atom. Alternatively, it represents the energy per unit volume at the position of the atom times the speed of light in the respective medium.

The quantity $I_\omega(\omega_\lambda)\mathrm{d}\omega_\lambda$ describing the irradiance contained in the infinitesimally small frequency interval $[\omega_\lambda, \omega_\lambda + \mathrm{d}\omega_\lambda]$ is then equal to the product of the (dimensionless) number of modes contained in $\mathrm{d}\omega_\lambda$ times the (mean) energy density per mode $n_\lambda \hbar \omega_\lambda / L^3$ (with units of energy per unit volume) multiplied by the speed of light c. Under the conditions specified, the number of modes is given by $2 \times 4\pi\rho(E)\hbar\,\mathrm{d}\omega_\lambda$ comprising all possible polarisation states (factor of two) and photon directions (factor of 4π) within $\mathrm{d}\omega_\lambda$. Since $\rho(E)$ has units of one over unit energy, the dimensionless number of modes is proportional to $\rho(E)$ times the infinitesimally small energy portion $\hbar\,\mathrm{d}\omega_\lambda$.

Combining this and making use of (C.40) the irradiance $I_\omega(\omega_\lambda)\mathrm{d}\omega_\lambda$ is finally given by the relation

$$I_\omega(\omega_\lambda)\mathrm{d}\omega_\lambda = 8\pi\rho(E)\hbar\mathrm{d}\omega_\lambda \cdot \mathrm{n}_\lambda \frac{\hbar\omega_\lambda}{\mathrm{L}^3} \mathrm{c} = \frac{\hbar\omega_\lambda^3}{\pi^2\mathrm{c}^2} \mathrm{n}_\lambda\mathrm{d}\omega_\lambda \ .$$

Rearrangement to

$$n_\lambda = \frac{\pi^2 c^2}{\hbar\omega_\lambda^3} I_\omega(\omega_\lambda)$$

and multiplication of Eq. (C.42) by n_λ yields the probability for stimulated emission

$$\mathcal{P}_{\mathrm{i}\to\mathrm{f}}^{(\mathrm{stim})} = \frac{\pi}{3\epsilon_0\hbar^2} |\boldsymbol{d}_{\mathrm{fi}}|^2 \frac{I_\omega(\omega_\lambda)}{c} \overset{\mathrm{def}}{=} B_{\mathrm{fi}}\frac{I_\omega(\omega_\lambda)}{c} \tag{C.44}$$

which introduces a second well-known probability, the *Einstein B-coefficient*

$$B_{\mathrm{fi}} = \frac{\pi}{3\epsilon_0\hbar^2} |\boldsymbol{d}_{\mathrm{fi}}|^2 = A_{\mathrm{fi}} \cdot \frac{\pi^2 c^3}{\hbar\omega_\lambda^3} \ . \tag{C.45}$$

The relation between both coefficients characterising spontaneous and stimulated emission respectively, directly implies that the larger the energy difference between the involved states the more does the number of spontaneous events dominate the number of stimulated ones. Interestingly, both Einstein coefficients B_{fi} and A_{fi} appear as well in a semi-classical treatment of light-matter interaction which reflects that the latter is just the classical limit of quantum mechanics.

C.4.3 Absorption

As announced initially the emission of photons is not the only process induced by atom-field interaction. In case that at least one mode λ initially contains already a certain number $n_\lambda > 0$ of photons, the atom can absorb one photon thereby reducing n_λ by one, i.e. $n_\lambda' = n_\lambda - 1$ and leading to a field contribution to the matrix elements of $F_\lambda^{(\mathrm{abs})} = n_\lambda$. Assuming that the final atomic state is still part of the discrete region of the spectrum, the probability for this extraction of one photon from the light field by the atom can be calculated according to Fermi's Golden Rule for the discrete case (cf. Eq. (C.4)), resulting in

$$P_{\mathrm{i}\to\mathrm{f}}^{(\mathrm{abs})} = \frac{\pi}{\epsilon_0 V}\omega_\lambda |\boldsymbol{\epsilon}_\lambda \cdot \boldsymbol{d}_{\mathrm{fi}}|^2 n_\lambda \cdot \delta(\varepsilon_{\mathrm{f}} - \varepsilon_{\mathrm{i}} - \hbar\omega_\lambda) \ . \tag{C.46}$$

Just like the probability for stimulated emission, the photon absorption probability from a uniform field is as well related to the spectral irradiance distribution $I_\omega(\omega_\lambda)$ so that in principle it is possible to write an expression $\mathcal{P}_{\mathrm{i}\to\mathrm{f}}^{(\mathrm{abs})}$ similar to Eq. (C.42) resulting in the B-coefficient B_{fi}, similar to the stimulated emission case. It is more common though to quantify the ability of the atom to absorb a photon by means of the so called *cross section* $\sigma^{(\mathrm{abs})}$. This experimentally more relevant (since directly measurable) quantity expresses the absorption probability per unit time from a uniform monochromatic beam in relation to the number of incident photons, that means the number of photons bombarding the particle. It is thus simply given by $P_{\mathrm{i}\to\mathrm{f}}^{(\mathrm{abs})}$ divided by the photon current density $(1/A)(\mathrm{d}n_\lambda/\mathrm{d}t) = (n_\lambda/V)(\mathrm{d}L/\mathrm{d}t) = cn_\lambda/V$ resulting in

$$\sigma^{(\mathrm{abs})} = \frac{\pi\omega_\lambda}{\epsilon_0 c} |\boldsymbol{\epsilon}_\lambda \cdot \boldsymbol{d}_{\mathrm{fi}}|^2 \cdot \delta(E_{\mathrm{f}} - E_{\mathrm{i}} - \hbar\omega_\lambda) \tag{C.47}$$

with units of m^2.

Illustratively, the cross section can be imagined as representing the size of the vertical surface which is passed by those photons which are absorbed by the atom per unit time. In other words, the number of absorbed photons is given by the number of photons (from a light field with uniformly distributed photon density) traversing an area $\sigma^{(\text{abs})}$ perpendicular to their direction of propagation.

It should be noted that $\sigma^{(\text{abs})}$ only quantifies the atom's ability to absorb photons, it does not have any relation though to the actual physical size of neither the atom nor the photons. As reflected by its frequency dependence, the scattering between atoms and photons experiences a large enhancement on resonance. For typical wavelengths in the VIS spectrum and for atomic diameters in the range of $d = 10^{-10}$ m the resonance cross section is much larger than the classical cross section πd^2 known from the kinetic theory of atom-atom collisions.

Finally, the three photon exchange processes can be summarised by expressing the corresponding probabilities for each transition between a pair of ground and excited states, $|\chi_{\text{g}}\rangle$ and $|\chi_{\text{e}}\rangle$, induced by interaction with a photon from mode λ in a structurally analogue way which results in the equations listed in Table C.1.

Spontaneous emission	$\lvert\chi_{\text{g}}\rangle \longleftarrow \lvert\chi_{\text{e}}\rangle$	$\mathcal{P}_{\text{g}\leftarrow\text{e}}^{(\text{spont})}$	$= \dfrac{1}{3\pi\epsilon_0}\dfrac{\omega_\lambda^3}{\hbar c^3}\,\lvert\boldsymbol{d}_{\text{ge}}\rvert^2$		$= A_{\text{ge}}$
Stimulated emission	$\lvert\chi_{\text{g}}\rangle \longleftarrow \lvert\chi_{\text{e}}\rangle$	$\mathcal{P}_{\text{g}\leftarrow\text{e}}^{(\text{stim})}$	$= \dfrac{\pi}{3\epsilon_0\hbar^2 c}\,\lvert\boldsymbol{d}_{\text{ge}}\rvert^2\,I_\omega(\omega_\lambda)$		$= B_{\text{ge}}\dfrac{I_\omega(\omega_\lambda)}{c}$
Absorption	$\lvert\chi_{\text{g}}\rangle \longrightarrow \lvert\chi_{\text{e}}\rangle$	$\mathcal{P}_{\text{g}\rightarrow\text{e}}^{(\text{abs})}$	$= \dfrac{\pi}{3\epsilon_0\hbar^2 c}\,\lvert\boldsymbol{d}_{\text{eg}}\rvert^2\,I_\omega(\omega_\lambda)$		$= B_{\text{eg}}\dfrac{I_\omega(\omega_\lambda)}{c}$

TABLE C.1: *Overview of transition probabilities for photon emission and absorption events including their relation to the according Einstein A- and B-coefficients respectively.*

By further taking into account the relation

$$B_{\text{ge}} = \frac{\pi}{3\epsilon_0\hbar^2}\,\lvert\boldsymbol{d}_{\text{ge}}\rvert^2 = A_{\text{ge}}\cdot\frac{\pi^2 c^3}{\hbar\omega_\lambda^3} \tag{C.48}$$

between the Einstein coefficients, this overview clearly demonstrates the similarity and interdependence of the three fundamental processes.

The transition probabilities given above are in fact those which are frequently referred to as transition or spontaneous decay rate $\Gamma_{\text{ge}} = 1/\tau$ which is the inverse (fluorescence) lifetime of the respective transition. For a single-channel decay this is equal to the total fluorescence lifetime of the excited state.

C.4.4 Photoionisation

The last remaining photon exchange process induced by atom-light interaction is the one where the atom is excited to a final which is not part of the discrete atomic spectrum but reaches into the continuum. Since the final state is then no longer a bound state and the absorption causes a separation of the atom into its constituents, it is also referred to as ionisation through photon absorption, in short *photoionisation*. The likelihood for this excitation process can, thanks to its great versatility, as well be calculated by means of Fermi's Golden Rule, this time again using the continuum version. This however is only possible after factorizing the overall Ps wave function into the single-particle ones, that means one describing the electron and a second the positron, which reflects the fragmentation of the atom. Using $\rho(E) = 1$ for unbound wave functions normalised in energy ($\langle\chi_{\text{f}}(E)|\chi_{\text{f}}(E')\rangle = \delta(E - E')$) the absorption probability is, except for the delta-function in energy, essentially equal to the probability for excitation to bound states, leading to the *photoionisation cross section*

$$\sigma^{(\text{phion})}(E) = \frac{\pi\omega_\lambda}{\epsilon_0 c}\,\lvert\boldsymbol{\epsilon}_\lambda\cdot\boldsymbol{d}_{\text{fi}}\rvert^2 \tag{C.49}$$

$$d^{(0)} = \sum_j q_j z_j$$

$$d^{(+)} = -\sum_j q_j \frac{x_j + iy_j}{\sqrt{2}}$$

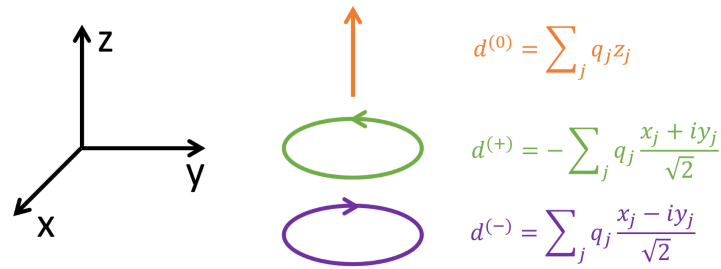$$d^{(-)} = \sum_j q_j \frac{x_j - iy_j}{\sqrt{2}}$$

FIGURE C.1: *Schematic visualisation of the spherical components of the electric dipole moment. In spherical coordinates any arbitrarily oriented electric dipole moment can clearly be defined by means of the three spherical components $\hat{d}^{(\pm)}$ and $\hat{d}^{(0)}$ as mathematically described in Eq.* (C.50).

with, by implication, similar physical meaning as the "standard" absorption cross section $\sigma^{(\mathrm{abs})}$.

It should finally be mentioned that, for any kind of absorption, a potential degeneracy of the initial and/or final atomic states can be taken into account by averaging over the probabilities for all degenerate initial states and/or summation over all degenerate final states of the respective manifold.

In the numerical simulation tool used for the investigations presented in Sec. 3.1, all four light-matter interactions are implemented based on the corresponding equations derived above. While photoionisation is taken into account by means of the applicable cross section, the rates for photon emission are calculated from the general Einstein coefficients. Details on specific technicalities of the code are given in App. F and can, to a limited extent, also be found in the appendix to Ref. [47].

C.5 Selection rules

So far, the transition dipole moments $\boldsymbol{d}_{\mathrm{fi}} = \langle \chi_{\mathrm{f}} | \hat{\boldsymbol{d}} | \chi_{\mathrm{i}} \rangle$ appeared only peripherally as certain unspecified quantities in the probability equations. However, since they are the decisive factors of the transition probabilities and, for symmetrical reasons vanish completely under certain conditions, they in fact deserve a closer examination in the following which shows that non-zero dipole moments are obtained only for specific combinations of involved atomic states. The transitions between those are then also referred to as allowed transitions. Describing the atomic states in terms of their quantum numbers which characterise their wave functions, allows to conveniently formulate those conditions by means of the so called *selection rules* specifying the combination of quantum numbers of the wave function pairs that produce non-zero dipole moments.

Note, that the term "allowed" is restricted to *electric dipole* transitions here, that means ignoring the possibility for higher-order transitions (such as quadrupole or octupole) and neglecting the magnetic dipole.

The simplest way to illustrate the dependence of $\boldsymbol{d}_{\mathrm{fi}}$ on the quantum numbers of the involved atomic states is to expand the dipole moment operator $\hat{\boldsymbol{d}}_{\mathrm{fi}}$ as a linear combination of its spherical components $\hat{d}_{\mathrm{fi}}^{(\nu)}$ (with $\nu = 0, \pm 1$) which can be written in terms of the spherical harmonics $Y_{1,\nu}(\theta,\varphi)$ multiplied by the radius r according to

$$\hat{d}^{(\pm)} = \mp \sum_j q_j \frac{x_j \pm iy_j}{\sqrt{2}} = \sqrt{\frac{4\pi}{3}} er Y_{1,\pm 1}(\theta,\varphi) \qquad \text{and} \qquad \hat{d}^{(0)} = \sum_j q_j z_j = \sqrt{\frac{4\pi}{3}} er Y_{1,0}(\theta) \ .$$

$$(\mathrm{C.50})$$

Figure C.1 illustrates schematically the geometrical appearance of these three spherical components $\hat{d}^{(\pm)}$ and $\hat{d}^{(0)}$ of the dipole moment.

Separation of the wave functions into radial and angular parts with the latter being described by spherical harmonics as well, converts the matrix elements of the components $d_{\mathrm{fi}}^{(\nu)}$ of $\boldsymbol{d}_{\mathrm{fi}}$ to integrals over the radial wave functions $R_{n,l}(r)$

$$
\begin{aligned}
d_{\mathrm{fi}}^{(\nu)} &= \langle \chi_{\mathrm{f}} | d_{\mathrm{fi}}^{(\nu)} | \chi_{\mathrm{i}} \rangle \\
&= \int_0^\infty R_{n,l_{\mathrm{f}}}^*(r)\, er\, R_{n,l_{\mathrm{i}}}(r)\, \mathrm{d}r\, \left(C_{1\nu,l_{\mathrm{i}}m_{\mathrm{i}}}^{l_{\mathrm{f}}m_{\mathrm{f}}} \right)^* \times
\begin{cases}
\sqrt{l_{\mathrm{f}}/(2l_{\mathrm{f}}+1)} & \text{for } l_{\mathrm{f}} = l_{\mathrm{i}}+1 \\
\sqrt{-l_{\mathrm{i}}/(2l_{\mathrm{f}}+1)} & \text{for } l_{\mathrm{f}} = l_{\mathrm{i}}-1
\end{cases}
\end{aligned}
\tag{C.51}
$$

The occurrence of the Clebsch-Gordan coefficients $(C_{1\nu,l_{\mathrm{i}}m_{\mathrm{i}}}^{l_{\mathrm{f}}m_{\mathrm{f}}})^* = \langle l_{\mathrm{f}}, m_{\mathrm{f}} | 1, \nu, l_{\mathrm{i}}, m_{\mathrm{i}} \rangle$ in the above expression for the matrix elements already imposes conditions on the set of involved l- as well as m-quantum numbers for allowed transitions. $C_{1\nu,l_{\mathrm{i}}m_{\mathrm{i}}}^{l_{\mathrm{f}}m_{\mathrm{f}}}$ gives only a non-zero contribution if and only if $m_{\mathrm{f}} = m_{\mathrm{i}} + \nu$ as well as the triangle condition $|l_{\mathrm{i}} - 1| \leq l_{\mathrm{f}} \leq l_{\mathrm{i}} + 1$ or are fulfilled. Furthermore, for reasons of parity of the integrand in Eq. (C.51), the sum $l_{\mathrm{f}} + 1 + l_{\mathrm{i}}$ must be even. In combination these conditions result in the more commonly known *selection rules for the angular momentum in electric dipole transitions*

$$
\Delta l = l_{\mathrm{f}} - l_{\mathrm{i}} = \pm 1 \qquad \text{and} \qquad \Delta m_l = m_{\mathrm{f}} - m_{\mathrm{i}} = 0, \pm 1
\tag{C.52}
$$

with m denoting the magnetic quantum numbers assigned to the orbital angular momentum $\boldsymbol{l}$ (instead of $\boldsymbol{J}$) quantifying the magnitude of its projection on the quantisation axis.

In order to derive similar rules for the spin quantum number S and the total angular momentum J the initial $|\chi_{\mathrm{i}}\rangle$ and final state $|\chi_{\mathrm{f}}\rangle$ are described by the coupled eigenstates $|nlSJm\rangle$ which are given by the generalised spherical harmonics (cf. Section 2.2.1). The Wigner-Eckart theorem states that the matrix elements $d_{\mathrm{fi}}^{(\nu)} = \langle \chi_{\mathrm{f}} | d_{\mathrm{fi}}^{(\nu)} | \chi_{\mathrm{i}} \rangle$ can then be written as a product of the *reduced matrix elements* $\langle J_{\mathrm{f}} || \hat{\boldsymbol{d}} || J_{\mathrm{i}} \rangle$ which only depend on the J-quantum numbers and the Clebsch-Gordan coefficients $(C_{1\nu,J_{\mathrm{i}}m_{\mathrm{i}}}^{J_{\mathrm{f}}m_{\mathrm{f}}})^*$. The exact derivation is beyond the scope of this thesis and shall therefore not be detailed any further here.

Analogous to the case above the occurrence of the Clebsch-Gordan coefficients results in the additional conditions

$$
\Delta J = J_{\mathrm{f}} - J_{\mathrm{i}} = 0, \pm 1 \qquad \text{and} \qquad \Delta m = m_{\mathrm{f}} - m_{\mathrm{i}} = 0, \pm 1
\tag{C.53}
$$

where m now explicitly relates to the total angular momentum $\boldsymbol{J}$.

Finally, due to the fact that the interaction Hamiltonian does not act on the spin part of the atomic states, the selection rules for the spin quantum number S are simply given by

$$
\Delta S = 0 \qquad \text{and} \qquad \Delta m_s = 0
\tag{C.54}
$$

which directly reflects that electric dipole transitions cannot be accompanied by any spin flip.

The selection rules can be illustrated very clearly by means of so called Grotrian diagrams showing the atomic level scheme including all allowed transitions indicated by arrows between the according initial and final states. Figure C.2 contains such a diagram showing all allowed transitions between ortho-positronium states with principal number up to $n = 2$.

It should once more be emphasised that the selection rules given here only govern the transitions induced by the electric dipole interaction. Transitions which are forbidden in this dipole approximation might however well be allowed in the context of higher order interactions. Such magnetic dipole and electric or magnetic quadrupole (or even octupole) transitions result from a treatment which includes also higher order of the series expansion of the position dependent terms $\mathrm{e}^{i\boldsymbol{k}\cdot\boldsymbol{r}}$ in the vector potential. Since all these higher order contributions are much weaker though than the constant leading term according transitions with concomitant few-photon absorption and emission processes are in general much less likely to occur. The treatment of these processes is of course also beyond the scope of first-order perturbation which is only an appropriate tool for transitions in the dipole approximation.
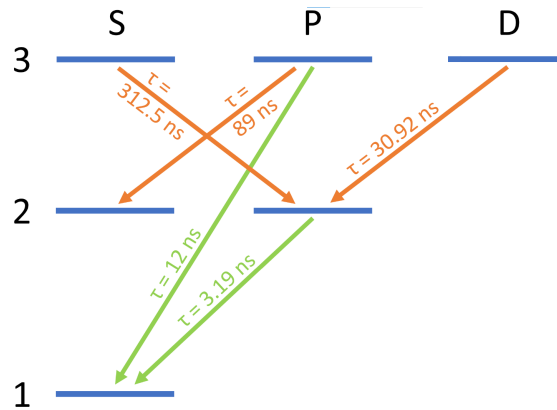
FIGURE C.2: *Grotrian diagram for the Ps atom for states up to and including* $n = 3$ *in absence of external fields.* *The Grotrian diagram illustrates all allowed transitions, that means obeying the selection rules in Eqs.* (C.52) *and* (C.53) *for electric dipole transitions, in the form of arrows between the according initial and final states. Shown are all transitions for ortho-positronium between states with principal quantum number up to and including* n = 3. *The numbers above each arrow specify the lifetime of the transition which is the inverse of the rate given by the according Einstein A-coefficient.*

C.5.1   Polarisation-dependence of Δm

As the derivation of the selection rules for the magnetic quantum numbers m shows, the absolute quantum number change accompanying a transition is primarily determined by the component of the dipole moment that contributes to the matrix element. More precisely, the value of Δm depends on the component $d_{\mathrm{fi}}^{(\nu)}$ of $\boldsymbol{d}_{\mathrm{fi}}$ which couples the initial and final atomic states. These components can be expressed in terms of the spherical harmonic $Y_{1,\nu}(\theta,\varphi)$ and clearly specified by the index ν of the expansion of $\boldsymbol{d}_{\mathrm{fi}}$. In general, transitions with concomitant quantum number change of $\Delta m = \pm 1$ are called $\sigma^{(\pm)}$-*transitions*, whereas those accompanied by $\Delta m = 0$ are referred to as π-*transitions*. This terminology originates from the connection between the matrix element and the polarisation state of the involved photon. Since this dependence of Δm on the photon polarisation is of quite significant importance with respect to experiments, such as for the realisation of so called *optical pumping*, it is worth having a closer look on it.

On the most fundamental level, the connection between the polarisation state and the induced quantum number change is established by the product of $\boldsymbol{\epsilon}_\lambda$ and the electric dipole $\boldsymbol{d}_{\mathrm{fi}} = \langle \chi_{\mathrm{f}} | \hat{\boldsymbol{d}} | \chi_{\mathrm{i}} \rangle = \langle \chi_{\mathrm{f}} | \sum_j q_j \boldsymbol{r}_j | \chi_{\mathrm{i}} \rangle$ in the general expression for the transition probability per unit time given in Eq. (C.38). This scalar product reflects that the actual direction of the electric field does not only depend on the polarisation states but also the propagation direction of the photon with respect to the orientation of the electric dipole moment $\boldsymbol{d}$ of the atom which is defined by the quantisation axis of the system. In absence of external fields the dipole moment does not show any preferential orientation but can be aligned arbitrarily in space. In field-free environments, it is common to define the Cartesian coordinate system such that the dipole agrees with the z-axis.

In case of an external magnetic field, on the other hand, $\boldsymbol{d}_{\mathrm{fi}}$, and thus also the quantisation axis, is usually defined by the orientation of the field. The alignment of the electric dipole thus constitutes the first coordinate system (with unit basis vectors $\mathbf{e}_x$, $\mathbf{e}_y$ and $\mathbf{e}_z$) involved in the light-matter interaction. It is this system which usually also serves as reference system for the interaction process.

The second coordinate system (with unit basis vectors $\mathbf{e}_x'$, $\mathbf{e}_y'$ and $\mathbf{e}_z'$) to be considered, is the one used for defining the polarisation state of the photon. For this purpose, it is expedient to choose the frame aligned along the propagation direction of the photon where it is again common practice to define the system such that the z'-axis represents the direction of travel. The basis vectors $\mathbf{e}_x'$, $\mathbf{e}_y'$ and $\mathbf{e}_z'$ are then the ones defining the two helicity basis states $\boldsymbol{\epsilon}_\lambda'^{(\pm)}$ for the laser
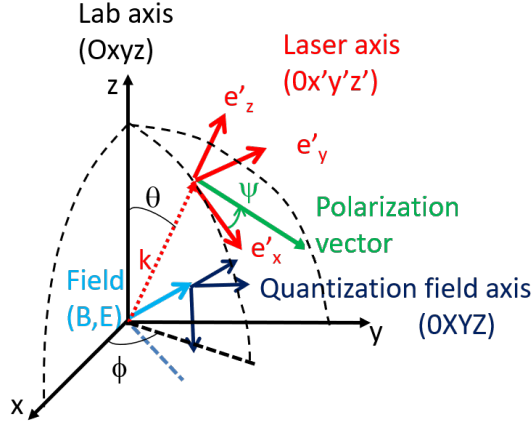
FIGURE C.3: *Definition of the different coordinate systems involved in atom-field interaction. All frames are defined with respect to the fixed lab frame spanned by the unit basis vectors $\boldsymbol{e}_x$, $\boldsymbol{e}_y$ and $\boldsymbol{e}_z$. The direction of the external fields $(\boldsymbol{B}, \boldsymbol{E})$, which defines the quantisation axis of the whole system, can in principle be chosen arbitrarily but typically coincides with $\boldsymbol{e}_z$. The laser frame which is generated by $\boldsymbol{e}'_x$, $\boldsymbol{e}'_y$ and $\boldsymbol{e}'_z$ is required for definition of the polarisation state of the light.*

To switch from the fixed lab frame to the laser axis, first a rotation by an angle ϕ around $\boldsymbol{e}_z$ is performed which is followed by a second rotation by θ around the new y-axis.

polarisation, which have already been introduced in Eq. (C.12) in the context of field quantisation. This finally explains the use of primes there.

Figure C.3 exemplarily illustrates one possible definition of the different involved frames where the external field is typically chosen along the z-axis of the lab frame, thereby fixing also the quantisation axis. This definition is also the one used in the numerical simulation tool presented later.

As soon as the atom starts to interact with the electromagnetic field, it is thus both the direction of the electric field component itself, described by the polarisation state $\boldsymbol{\epsilon}$, as well as its relative orientation, that determine which component $d_{\mathrm{fi}}^{(\nu)}$ contributes to the interaction matrix element $(\hat{H}_{\mathrm{int}})_{\mathrm{fi}}$. Mathematically, this is simply expressed by $\boldsymbol{\epsilon}_\lambda \cdot \boldsymbol{d}_{\mathrm{fi}}$ for light in mode λ.

If, in the simplest case in which the light propagates along the quantisation axis and the lab and laser frames coincide with each other, the laser has right-handed circular polarisation with $\boldsymbol{\epsilon}_\lambda = \boldsymbol{\epsilon}_\lambda^{\prime(+)} = \boldsymbol{\epsilon}_\lambda^{(+)} = (-\mathbf{e}_x - i\mathbf{e}_y)/\sqrt{2}$, the product $\boldsymbol{\epsilon}_\lambda \cdot \boldsymbol{d}_{\mathrm{fi}}$ reduces to $-\sum_j q_j(x_j + iy_j)/\sqrt{2}$ which is equivalent to the product of the spherical harmonic $Y_{1,\nu=+1}(\theta,\varphi)$ and the dipole $(\sqrt{4\pi/3} \; er)$ (cf. Eq. (C.50)). In this case right-handed circular polarisation thus induces transitions accompanied by $\Delta m = +1$, that means so called $\sigma^{(+)}$-transitions. The laser polarisation is then sometimes also referred to as $\sigma^{(+)}$-polarisation (and the polarisation basis vector $\boldsymbol{\epsilon}_\lambda^{\prime(+)}$ labelled with $^{(+)}$).

It is essential to note, though, that the designation of the laser polarisation state in terms of $\sigma^{(\pm)}$ or π obviously depends decisively on the actual configuration. For this reason, the indication $\sigma^{(\pm)}$- or π-polarisation for the polarisation state is only unambiguous if the orientation of the laser with respect to the quantisation axis is mentioned as well. Since the latter information is often not given, it is recommendable to avoid this designation of polarisation states and use the clearly defined handedness instead.

To make this more comprehensible, it is worth considering the opposite case to the one above. If the laser and quantisation axis are pointing into the opposite direction a $\sigma^{(+)}$-transition can only be induced by a photon with left-handed circular polarisation. Hence, while in the previous case it was right-handed circular polarisation, it is now the inverse left-handed one which represents $\sigma^{(+)}$-polarisation. This shows that the handedness is a much more consistent designation method.

π-transitions, on the other hand, can only be induced if the electric field of the electromagnetic
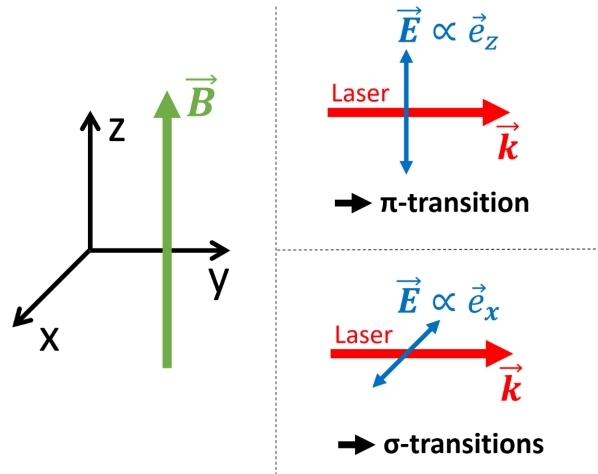
FIGURE C.4: *Schematic illustration of the relation between the transition type (σ or π) and the orientation of the linear polarisation of a laser beam propagating perpendicularly to the quantisation axis, defined by an external magnetic field B (**i.e., k $\perp$ B**).* In case the electric field vector **E** is aligned perfectly parallel to the quantisation axis (top) the radiation induces π-transitions, accompanied by a quantum number change of $\Delta m = 0$. In the case where **E** is rotated by $\pi/2$ and thus oriented perpendicularly to **B** (and **k**) the atom will be excited on a σ-transition with $\Delta m = \pm 1$ (bottom).

wave is aligned (anti-)parallel to the quantisation axis (or, at least, has components along this direction). This can only occur for photons with certain combinations of polarisation and propagation direction $\mathbf{k}$, namely if the propagation direction of the photons is tilted with respect to the quantisation axis and the electric field vector has non-zero component in the $\mathbf{k}$-$\mathbf{E}$-plane.

Fig. C.4 exemplarily illustrates two possible linear polarisation configurations for a laser beam propagating perpendicularly to the quantisation axis given by the external magnetic field $\mathbf{B}$. In the upper configuration the laser is polarised such that the electric field vector is directed parallel to the quantisation axis. The lower one represents exactly the same situation, but with the polarisation rotated by $\pi/2$ so that $\mathbf{E}$ is now pointing into the direction perpendicular to the quantisation axis. This comparison clearly demonstrates that, in the configuration with perpendicular laser beam, the transition type can be changed from σ to π (and vice versa) simply by rotating the polarisation by $\pi/2$.

C.6 Optical pumping

In experiments this relation between Δm and the polarisation state is often exploited for the purpose of so called *optical pumping* which is as well examined numerically in the third chapter. The underlying idea behind this method is to modify the population of a cloud of particles which are equally distributed over all m-substates of a certain state such that finally all atoms accumulate in one of the outermost substates $m = \pm J$. A transfer to $m = +J$ for example can easily be achieved by bombarding the cloud with a beam of $\sigma^{(+)}$-polarised photons (whose handedness needs to be chosen according to the orientation relative to the quantisation axis). This continually shifts the atoms from low-m substates to the highest by succession of excitation and spontaneous emission events. Even though spontaneous emission can of course take place via all allowed Δm changes, the change in quantum number of the whole cycling process is effectively greater than zero since the laser only induces $\sigma^{(+)}$-transitions. Since the time required for transferring all atoms is limited by the spontaneous emission time the atoms should ideally be pumped via the transition with shortest lifetime, if experimentally feasible.

In positronium experiments this method can for example be applied in order to prepare a cloud
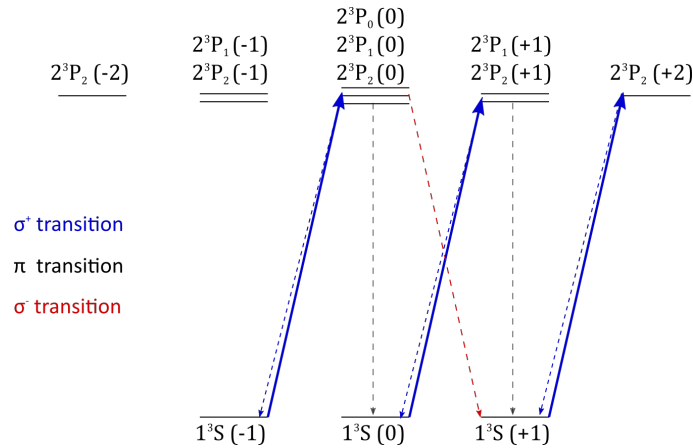
FIGURE C.5: *Schematic representation of the optical pumping scheme on the* $1^3S_1 \leftrightarrow 2^3P$ *transition in positronium.*

The procedure is visualised based on the detail of the Ps level scheme showing only the m-substates of the involved 1^3S_1 ground and 2^3P excited states. Layering of states symbolises the existence of several states with same m quantum number among the 2^3P level. The term symbol then indicates the corresponding J quantum number (as usual as subscript). The distance between the states is not intended to reflect the respective energy difference.

For the purpose of optical pumping the laser beam is polarised such that the atom is excited exclusively on $\sigma^{(+)}$ transitions, indicated by blue solid arrows. Stimulated emission (blue short-dashed arrows) is thus as well only possible via the same $\sigma^{(+)}$ transitions. Spontaneous emission on the other hand can still take place via all allowed decay paths (long- and short-dashed arrows) with either $\Delta m = 0$ or ± 1.

Arrows marked in blue represent $\sigma^{(+)}$ transitions, those in black π transitions and the red ones indicate $\sigma^{(-)}$ transitions.

of atoms in the $m = 1$ ground state prior to cooling. Only if all atoms initially populate this substate they will not decay to the $m = 0$ ground state during the cooling process where, in magnetic fields, they would directly be quenched and annihilate quickly. This fast population decline can thus simply be avoided by exciting the atoms on $\sigma^{(+)}$- transitions only. Such a quenching-free scheme is sometimes also called *pure cycling* and the according cooling transition referred to as a *pure transition*.

Fig. C.5 schematically illustrates the optical pumping procedure in the positronium atom on the basis of the level scheme focussing on the $1^3S_1 \leftrightarrow 2^3P$ transition at a wavelength of roughly $243\,\mathrm{nm}$ and with a lifetime of $3.2\,\mathrm{ns}$ which is the shortest fluorescence lifetime in Ps. For the purpose of optical pumping the laser beam is polarised such that the atom is excited exclusively on $\sigma^{(+)}$ transitions.

Consequently, even though spontaneous emission can still occur via all allowed decay channels, the atoms are successively pushed towards the 1^3S_1 or, respectively, 2^3P substates with highest m quantum number. Subsequent to the preparation of the atoms in those substates the excitation scheme will be restricted exclusively to the pure $(1^3S_1, m = +1) \leftrightarrow (2^3P, m = +2)$ transition. In this way population of the $1^3S_1(m = +1)$, which is quenched to the singlet $1^1S_1(m = 0)$ state, can be completely avoided.

Next to this application the tool of optical pumping is regularly applied as well in the Sisyphus cooling scheme.

C.7 Line shapes and transition rates

So far the whole treatment was restricted to single-mode light fields with irradiance $I(\omega_\lambda)$ and transition probabilities have only been discussed for this single mode λ. Under real conditions

though, that means especially in experiments, both the transition line as well as the intensity spectrum of the laser field are of course not restricted to single frequencies ω_λ but rather characterised by a spectral distribution function with specific width. Moreover, even on the most fundamental level each transition line is already subject to a naturally occurring broadening mechanism resulting in an intrinsic linewidth determined by the according Einstein A-coefficient. It is the purpose of this section to derive an expression for the spectral dependence of the transition rates on the frequency ω. This function is also the one implemented in the simulation tool which is used for the numerical studies of positronium laser cooling presented and discussed in the third chapter.

C.7.1 Width and shape of spectral lines

In general, the spectral distribution of the atomic transition line is described by a line shape function $g(\omega)$ which is a normalised distribution function, centred around resonance $\hbar\omega_0 = (E_f - E_i)$ in the rest frame of the particle. Its most important characteristic is its width, usually specified in terms of the full width at half maximum (FWHM), denoted by Γ.

Focussing for the moment only on spontaneous emission of photons, the transition rate is completely determined by the atomic properties without being affected by the spectral distribution of any initial light field, as in case stimulated emission.

Regarding the spectrum from the perspective of the fixed lab frame, such as in spectroscopy experiments measuring the emission spectrum of an ensemble of particles, several possible line broadening mechanisms exist. The most prominent ones are *natural* or *lifetime broadening*, *collisional broadening* and *Doppler broadening*. All broadening mechanisms can generally be classified as homogeneous and inhomogeneous. In the former case all individual atoms in the ensemble behave similarly, that means show identical spectra. Homogeneous broadening therefore generally refers to the single-particle spectrum. In case of inhomogeneous broadening, on the other hand, each atom behaves differently and thus contributes differently to the overall emission spectrum of the whole ensemble. Inhomogeneous broadening therefore generally refers to the shape of the spectrum emitted by the ensemble. The inhomogeneity can result for example from the fact that the atoms are either in different local environments or differ in certain individual properties such as their velocities. In other words, homogeneous broadening mechanisms appear already in the single-particle spontaneous emission spectrum whereas inhomogeneous ones become apparent only in the N-particle spectrum of the whole ensemble. An important consequence is that homogeneous processes in general produce Lorentzian line shapes, whereas inhomogeneous ones in most cases obey Gaussian line shapes [165].

C.7.2 Natural broadening

As already mentioned but not further elucidated before, all atomic transition lines feature a certain width determined by the respective lifetime which in turn is intrinsic to each transition. For this reason the resulting broadening mechanism is referred to as *natural* or *lifetime* broadening.

Natural broadening can descriptively be understood with the help of the energy-time uncertainty principle which connects the energy E emitted as a result of spontaneous emission to the corresponding fluorescence lifetime $\tau = \Delta t$ according to $\Delta E \cdot \Delta t \geq \hbar/2$. This directly implies that the width $\Delta\omega = E/\hbar$ of the spectral line shape function must be proportional to the inverse of the spontaneous emission lifetime τ.

The exact expression of the line shape function can be derived by modelling the relaxation process of the oscillating excited charge in the atom by means of a (classical) damped oscillator losing energy in form of radiation and subsequently performing a Fourier transformation finally resulting in the Lorentzian line shape function [165]

$$g_{\mathcal{L}}(\omega) = \frac{1}{\pi} \frac{\Gamma_{\mathcal{L}}/2}{(\omega - \omega_0)^2 + (\Gamma_{\mathcal{L}}/2)^2} \quad \text{or} \quad g_{\mathcal{L}}(\delta) = \frac{1}{\pi} \frac{\Gamma_{\mathcal{L}}/2}{\delta^2 + (\Gamma_{\mathcal{L}}/2)^2} \tag{C.55}$$

where $\delta = \omega - \omega_0$ specifies the so called *detuning* from the transition resonance frequency ω_0. $\Gamma_{\mathcal{L}}$ denotes the Lorentzian FWHM which in case of natural line broadening equals the inverse

spontaneous emission lifetime or respective Einstein A-coefficient respectively, i.e. $\Gamma_{\mathrm{fi}} = 1/\tau_{\mathrm{fi}} = A_{\mathrm{fi}}$ for the transition from $|\chi_{\mathrm{i}}\rangle$ to $|\chi_{\mathrm{f}}\rangle$.

Collisional broadening becomes only important if atoms in a gas experience collisions which are on average separated by a mean time τ_{coll} shorter than the spontaneous emission lifetime τ. This additional broadening mechanism is then simply accounted for by replacing the lifetime τ in the natural line shape function by τ_{coll} which results in a broader line. Since collisional broadening does not play a role in positronium experiments due to typically relatively low densities, it shall not be discussed any further here.

As far as line broadening and the motion of the atoms is concerned, it is furthermore important to make aware of another characteristic time to be taken into account, albeit only in the context of atom-light interaction. In case of a spatially restricted light field such as a laser beam, motion of the atoms gives rise to a time limitation defined by the travelling time τ_{int} of the atom through the light field. For typical thermal Ps velocities v of about $5 \cdot 10^4\,\mathrm{m/s}$ and laser beam diameters d of about $10\,\mathrm{mm}$, this interaction time limitation amounts to $\tau_{\mathrm{int}} = w/v = 200\,\mathrm{ns}$ which, in frequency domain, corresponds to a spectral width of $\Delta\omega = \tau_{\mathrm{int}}^{-1} = 5 \cdot 10^6\,\mathrm{s}^{-1} \approx 2\pi(0.8\,\mathrm{MHz})$ and thus much smaller than the spontaneous emission rate Γ_{fi} of about $2\pi(50\,\mathrm{MHz})$ for the $1^3\mathrm{S} \leftrightarrow 2^3\mathrm{P}$ transition in positronium.

A similar time restriction emerges from a finite laser pulse duration which, in standard laser cooling experiments with pulse lengths of few hundreds of nanoseconds (equivalent to a frequency of the order of a megahertz) is as well much smaller than the spontaneous emission rate.

C.7.3   Doppler broadening

Taking the perspective of an observer in the lab frame, the random uncoupled motion of the atoms in an ensemble gives rise to an inhomogeneous broadening of the received ensemble-spectrum of spontaneous emission. Mathematically this spectrum is given by the sum of the individual line shapes of all involved particles. Due to the superimposed relative motion of the particles with respect to the observer the received emission frequencies are subject to the Doppler effect which gives this broadening mechanism its name.

It is worth emphasising that Doppler broadening becomes effective only by considering the atomic cloud as a whole whereas natural broadening is a phenomenon which is inherent to each individual particle and therefore becomes already apparent in each single-particle spectrum.

Considering light emitted by an atom moving at speed $\pm v_x$ towards (away from) the observer (assuming that, without loss of generality, x defines the axis connecting the observer with the atom) the frequency ω' observed in the lab frame is Doppler shifted by $\delta\omega$ with respect to the rest frame transition frequency ω_0 emitted by the atom, whereby

$$\omega' = \omega_0 + \delta\omega = \frac{\omega_0}{1 \mp v_x/c} \approx \omega_0\left(1 \pm \frac{v_x}{c}\right)\,. \tag{C.56}$$

The last expression describes as well the reversed situation in which the source is stationary and the observer is moving. This is the case for instance when regarding the same situation from the perspective of the atom's rest frame but also in case of a moving atom receiving an electromagnetic wave emitted by a laser source which is stationary in the lab frame. This represents the typical Doppler laser cooling configuration.

In thermal equilibrium at temperature T the number of atoms $N(v_x)\mathrm{d}v_x$ with velocity components v_x in the infinitesimally small interval $[v_x, v_x + \mathrm{d}v_x]$ is determined by the Maxwell-Boltzmann probability distribution function $f(v_x)$ according to

$$N(v_x)\mathrm{d}v_x = N_0 f(v_x)\mathrm{d}v_x = N_0 \sqrt{\frac{2k_{\mathrm{B}}T}{\pi m_{\mathrm{Ps}}}}\,\exp\left(-\frac{m_{\mathrm{Ps}}v_x^2}{2k_{\mathrm{B}}T}\right)\mathrm{d}v_x \tag{C.57}$$

where N_0 specifies the total number of atoms in the ensemble [165].

Replacing v_x by the Doppler shifted frequency finally results in the normalised Gaussian N-particle line shape function

$$g_N^{(\text{spont})}(\omega) = \frac{c}{\omega_0}\sqrt{\frac{m_{\text{Ps}}}{2\pi k_B T}} \ \exp\left(-\frac{m_{\text{Ps}}c^2}{2k_B T}\left(\frac{\omega-\omega_0}{\omega_0}\right)^2\right) \tag{C.58}$$

with a FWHM of [165]

$$\Gamma_{\mathcal{G}} = 2\omega_0\sqrt{2\ln 2\,\frac{k_B T}{m_{\text{Ps}}c^2}} \ . \tag{C.59}$$

Strictly speaking, this description is not entirely correct because it is based on the assumption that Doppler broadening is much more pronounced than the natural linewidth so that the atomic line shapes can be approximated by delta-functions in frequency space. This however is no longer valid as soon as the widths of the two broadening mechanisms become comparable. In this case it is essential to take into account the finite natural linewidth Γ_{fi} (for the transition from $|\chi_\text{i}\rangle$ to $|\chi_\text{f}\rangle$) so that the spontaneous emission spectrum of the atomic ensemble is, more accurately, given by the expression

$$\begin{aligned} g_N^{(\text{spont})}(\omega) &\propto \int_{-\infty}^{\infty} g_1^{(\text{spont})}(\omega \pm k_x v_x)\ f(v_x)\ \mathrm{d}v_x \\ &= \frac{\Gamma_{\text{fi}}}{2\pi}\sqrt{\frac{2k_B T}{\pi m_{\text{Ps}}}}\int_{-\infty}^{\infty}\frac{\exp\left(-m_{\text{Ps}}v_x^2/(2k_B T)\right)}{(\omega \pm k_x v_x - \omega_0)^2 + (\Gamma_{\text{fi}}/2)^2}\ \mathrm{d}v_x \end{aligned} \tag{C.60}$$

which is merely the continuous sum of all individual Doppler-corrected single-particle spectra $g_1^{(\text{spont})}(\omega) = g_{\mathcal{L}}(\omega)$ with the parameter v_x distributed according to the Maxwell-Boltzmann velocity distribution function $f(v_x)$. $k_x = \omega/c$ denotes the angular wavenumber in x-direction. Obviously for $g_1(\omega) = \delta(\omega \pm k_x v_x - \omega_0)$ the integral would simply reduce to the expression given in Eq. (C.58).

In principle Eq. (C.60) represents nothing else than the convolution of the atomic line shape $g_{\mathcal{L}}(\omega)$ and the velocity distribution $f(v)$ of the atoms which is responsible for Doppler broadening. This examplarily confirms the general rule that a line shape which accrues from more than a single broadening mechanism is obtained from the convolution of the constituent spectra. Descriptively spoken, in case of two spectra for instance, the convolution quantifies their overlap as a function of the offset when shifting one spectrum over the other.

The physical argument employed in using the convolution is that the effects of Doppler and natural line broadening are completely uncorrelated and decoupled. Each point on a Doppler-broadened line shape is thus additionally subject to natural broadening.

The above treatment of Doppler broadening naturally requires to consider the ensemble of particles as a whole. However, in many cases, such as in numerical Monte-Carlo simulations which are based on single-particle probabilities, one is not interested in an overall spectrum but rather in the single-atom transition rates, denoted by $\gamma^{(j)}$ for atom j, that means the rates worked out above multiplied by the single-atom line shapes.

While the one-particle spontaneous emission spectra are simply given by the according natural line shape function (with Doppler-corrected detuning $\delta = \omega + \boldsymbol{kv} - \omega_0$ using the general Doppler shift $\boldsymbol{kv}$), evaluation of the absorption spectrum becomes a bit more complex since absorption also includes an additional light field. In the general case where the radiation is not simply monochromatic the laser spectrum induces an additional broadening of the transition line. Considering it consequently as a broadening mechanism the single-atom absorption line shape is thus given by the convolution of the natural line shape $g_{\mathcal{L}}(\omega + \boldsymbol{kv} - \omega_0)$ and the laser spectrum expediently given in terms of the spectral irradiance distribution $I_\omega(\omega)$. Thus

$$g_1^{(\text{abs})}(\omega + \boldsymbol{kv} - \omega_0) = (g_{\mathcal{L}} \otimes I_\omega/I)(\omega + \boldsymbol{kv} - \omega_0) \tag{C.61}$$

where $I = \int I_\omega(\omega)\mathrm{d}\omega$ denotes the total irradiance. The single-atom spectrum of the stimulated emission process can of course be obtained similarly.

Here, the physical argument for using the convolution is that in general any frequency in the laser spectrum can be responsible for the transition. If the laser is detuned from resonance then the transition is less probable. Since this fact applies to each spectral line of the natural line shape function the combined spectrum is given by the overlap and thus the convolution of the laser spectrum and the natural line shape function in frequency space.

This approach is also the one taken in the simulation code used for the numerical investigations on positronium where all particles in the ensemble are treated individually. For each of them all possible transition rates (both emission and absorption) are calculated, that means via all allowed channels. These single-particle rates subsequently enter the Monte-Carlo algorithm which predicts the probability for a transition to take place.

If desired, the absorption spectrum $g_N^{(\mathrm{abs})}(\omega + \boldsymbol{k}\boldsymbol{v} - \omega_0)$ produced by all atoms in the ensemble could finally be built from the convolution of $g_1^{(\mathrm{abs})}(\omega + \boldsymbol{k}\boldsymbol{v} - \omega_0)$ with the Maxwell-Boltzmann velocity distribution $f(\boldsymbol{v})$ in a similar way as above that means

$$
\begin{aligned}
g_N^{(\mathrm{abs})}(\omega) &= \left[g_1^{(\mathrm{abs})} \otimes f(\boldsymbol{v}) \right](\omega) \\
&= \left[\left[g_{\mathcal{L}}(\omega) \otimes I_\omega / I \right] \otimes f(\boldsymbol{v}) \right](\omega)
\end{aligned}
\tag{C.62}
$$

C.7.4 Laser spectrum

Before elaborating the final expression of the single-atom transition rates $\gamma^{(j)}$ used in the numerical simulation code few words should be said on the properties of the spectrum of the light field. In the following the term light or radiation generally refers to light generated by laser sources.

As mentioned, in general and especially for pulsed lasers used for Ps laser cooling, the radiation is not monochromatic but rather distributed over an oftentimes non-trivial spectrum described by a spectral irradiance distribution $I_\omega(\omega)$ and characterised by a certain FWHM Γ_{L}. The exact shape of the spectrum depends primarily on the type of laser generation and here specifically on the active laser medium. The emission spectrum of gas lasers for instance differs considerably compared to the one of solid-state or even dye lasers.

Furthermore, the laser spectrum as it is received by the atom in experiments significantly deviates from the one emitted by the laser itself due to spectral manipulation by interposed optical elements used for beam shaping and non-linear optical processes applied for the purpose of frequency conversion.

For this reason the exact shape of the laser spectrum is usually unknown so that it is in general not possible to give an accurate expression for the spectral distribution of laser radiation as it appears in the expressions for the absorption and emission probabilities (cf. Eqs. (C.44) and (C.46)). Furthermore, in case of numerical investigations consideration of the real shape can become difficult to model but, even more importantly, always goes at the expense of computation time. Instead of using the exact spectrum it is reasonable to approximate it by a certain simple distribution function such as a box shape, a Lorentzian or a Gaussian thereby hardly distorting the numerical result.

When using such approximations it should however be made sure that the transition rates resulting from the convolution of laser spectrum and atomic line shape drops sufficiently quickly to zero for large detunings. Transition lines which drop too slowly in frequency space might lead to physically wrong results. For this reason Gaussian distribution functions with quickly vanishing wings should in general be preferred over Cauchy distributions for modelling the laser spectrum. This could also be verified heuristically during the numerical investigations of Ps laser cooling.

Since laser emission spectra depend on many different laser properties and parameters a more detailed discussion is out of the scope of the present thesis and therefore omitted here.

Laser radiation is not only characterised by its spectral shape but also by the temporal signal (continuous wave versus pulsed generation) and the power distribution which, however, typically is already included in either the spectral or temporal distribution.

The type of laser is (apart from availability) always chosen on the basis of the laser parameters required for the respective application. First and foremost to be mentioned are the requirements concerning wavelength and line width (also called bandwidth), power and temporal characteristics (pulse lengths, shape and rate) but also features such as spectral tunability.

Positronium laser cooling on the $1^3\text{S} \leftrightarrow 2^3\text{P}$ transition for example requires using pulsed laser radiation at 243 nm with preferably large bandwidth in order to cover the largest possible fraction of the very broad Ps Doppler distribution. The shape of the laser spectrum thereby strongly depends on the laser generation procedure. For a dye laser, as it has been used in the scope of this thesis, the spectrum can be expected to be composed of a series of frequency peaks resulting from the fluorescence of the pump laser-excited dye molecules. These single-molecule spectra largely overlap each other, finally producing a broad frequency band around the fluorescence wavelength with a width determined by the velocity spectrum of the dye molecules in the solution.

To guarantee saturation of the transition line it is furthermore important to generate highest possible pulse energies.

It should finally be noted that transition lines can also be subject to so called power or radiative broadening caused by very intensive light fields. However, since this laser-induced broadening mechanism is best (and thematically more appropriately) described on the basis of transition line saturation and since it additionally does not relate to ex- or intrinsic atomic properties but exclusively on the laser intensity, it will be taken up again in the following section in the context of the population dynamics during atom-light interaction.

C.7.5 Absorption and stimulated emission rates

As introduced before, the spectral distribution of the single atom transition rates result, in the lab frame[34], from the convolution of the Lorentzian line shape function $g_{\mathcal{L}}(\omega + \boldsymbol{k v} - \omega_0)$ and the laser spectrum in terms of its (local) spectral irradiance $I_\omega(\omega)$ at the position of the atom.

Based on the expressions of the transition probabilities $\mathcal{P}_{\text{g} \leftarrow \text{e}}^{(\text{stim})}$ and $\mathcal{P}_{\text{g} \rightarrow \text{e}}^{(\text{abs})}$ specified in Tab. C.1, the most general expression for the frequency dependence of the stimulated emission and absorption rate $\gamma^{(j)}$ for the transition (i→f) in atom j induced by a laser beam characterised by the wave vector $\boldsymbol{k}$ is thus given by

$$\gamma_{\text{i} \rightarrow \text{f}}^{(j)}(\omega) = \frac{\pi}{3\epsilon_0 \hbar^2 c} |\boldsymbol{d}_{\text{fi}}|^2 \left[g_{\mathcal{L}} \otimes I_\omega\right] (\omega + \boldsymbol{k v} - \omega_0) \tag{C.63}$$

which depends on the detuning $\delta = \omega + \boldsymbol{k v} - \omega_0$ relative to the Doppler-shifted resonance frequency ω_0 [47].

In the simplest case where the laser spectrum were described by a Lorentzian function, the convolution appearing in Eq. C.63 could directly be evaluated analytically yielding the closed-form expression

$$\gamma_{\text{i} \rightarrow \text{f}}^{(j)}(\omega) = \frac{1}{3\epsilon_0 \hbar^2 c} |\boldsymbol{d}_{\text{fi}}|^2 I \frac{(\Gamma_{\text{fi}} + \Gamma_{\text{L}})/2}{(\omega + \boldsymbol{k v} - \omega_0)^2 + ((\Gamma_{\text{fi}} + \Gamma_{\text{L}})/2)^2} \tag{C.64}$$

which remains a Lorentzian function with a width given by the sum of the FWHM laser bandwidth Γ_{L} and the natural linewidth Γ_{fi} of the atom for the transition i→f. The quantity I denotes the full laser irradiance $\int I_\omega(\omega)\text{d}\omega$ which is related to the electric field amplitude $E = |\boldsymbol{E}|$ of the laser according to $I = \sqrt{2E/\epsilon_0 c}$. On resonance above expression drastically simplifies to the maximum transition rate

$$\gamma_{\text{i} \rightarrow \text{f}}^{(j)} = \gamma_{\text{i} \rightarrow \text{f}}^{(j)}(\omega_0) = \frac{8\pi}{3} \alpha \left(\frac{|\boldsymbol{d}_{\text{fi}}|}{e}\right)^2 \frac{I}{\hbar(\Gamma_{\text{fi}} + \Gamma_{\text{L}})} = \frac{2\pi c^2}{\hbar \omega_0^3} \frac{I}{1 + \Gamma_{\text{L}}\tau} \tag{C.65}$$

---

[34] The calculation can equally well be carried out in the rest frame of the atom. The Doppler effect is then taken into account by adding the Doppler shift $\boldsymbol{k v}$ to the phase of the electric field $\boldsymbol{E}(\boldsymbol{r},t)$ of the photon (instead of in the atomic line shape) which translates to the transition probabilities $\mathcal{P}_{\text{g} \leftarrow \text{e}}^{(\text{stim})}$ and $\mathcal{P}_{\text{g} \leftarrow \text{e}}^{(\text{abs})}$ via a simple modification of ω_λ to $\omega_\lambda + \boldsymbol{k v}$. Both derivations finally lead to the same expression for the spectral distribution of the single-particle transition rate containing the Doppler shift $\boldsymbol{k v}$ in the argument of the convolution.

where $\alpha = e^2/(4\pi\epsilon_0\hbar c)$ denotes the fine structure constant and $\tau = 1/\Gamma_{\mathrm{fi}}$ the excited state fluorescence lifetime.

In the more common case of inhomogeneously broadened laser radiation which is approximated by a Gaussian irradiance distribution $I_\omega(\omega)$ it is however no longer possible to write the transition rate $\gamma_{\mathrm{i}\to\mathrm{f}}^{(j)}(\omega)$ as a function of ω in an equally simple closed form. The convolution of the Lorentzian atomic line shape function and Gaussian laser spectrum is then given by a so called Voigt profile $V(\omega)$. In order to avoid its usually quite laborious numerical calculation, in most cases, such as the numerical code used here, the computation efficiency is optimised by approximating the Voigt profile by the so called pseudo-Voigt function $V_{\mathrm{p}}(\omega)$ which is a weighted sum of the deconvoluted Gaussian and Lorentzian functions.

As expounded by Thompson et al. in Ref. [166] and Ida et al. in Ref. [167] a good approximation is represented by the following expression

$$V_{\mathrm{p}}(\omega) = (1 - \eta) \cdot \mathcal{G}(\omega; \sigma_{\mathcal{G}}) + \eta \cdot \mathcal{L}(\omega; \Gamma_{\mathcal{L}}) \tag{C.66}$$

where $\mathcal{G}(\omega; \sigma_{\mathcal{G}}) = (\sqrt{2\pi}\sigma_{\mathcal{G}})^{-1} \exp(-\omega^2/(2\sigma_{\mathcal{G}})^2)$ and $\mathcal{L}(\omega; \Gamma_{\mathcal{L}}) = (\pi(\Gamma_{\mathcal{L}}/2))^{-1}(1 + \omega^2/(\Gamma_{\mathcal{L}}/2)^2)^{-1}$ denote the original normalised Gaussian and Lorentzian functions, respectively, with FWHM widths of $\Gamma_{\mathcal{G}} = 2\sqrt{2\ln 2}\,\sigma_{\mathcal{G}}$ and $\Gamma_{\mathcal{L}}$. The crucial parameter η which mixes the two constituent functions is given by the polynomial expansion

$$\eta = 1.36603\,(\Gamma_{\mathcal{L}}/\Gamma) - 0.47719\,(\Gamma_{\mathcal{L}}/\Gamma)^2 + 0.11116\,(\Gamma_{\mathcal{L}}/\Gamma)^3 \tag{C.67}$$

where the additional parameter Γ is in turn defined as

$$\Gamma = \left[\Gamma_{\mathcal{G}}^5 + 2.69269\,\Gamma_{\mathcal{G}}^4\Gamma_{\mathcal{L}} + 2.42843\,\Gamma_{\mathcal{G}}^3\Gamma_{\mathcal{L}}^2 + 4.47163\,\Gamma_{\mathcal{G}}^2\Gamma_{\mathcal{L}}^3 + 0.07842\,\Gamma_{\mathcal{G}}\Gamma_{\mathcal{L}}^4 + \Gamma_{\mathcal{L}}^5\right]^{1/5}. \tag{C.68}$$

The above definition of the Voigt profile is also adopted in the numerical simulations presented later where excitation and stimulated emission rates are evaluated according to

$$\begin{aligned}
\gamma_{\mathrm{i}\to\mathrm{f}}^{(j)}(\omega) &= \frac{\pi}{3\epsilon_0\hbar^2 c}\,|\boldsymbol{d}_{\mathrm{fi}}|^2\,I \cdot V_{\mathrm{p}}(\omega + \boldsymbol{k}\boldsymbol{v} - \omega_0) \\
&= \frac{\pi}{3\epsilon_0\hbar^2 c}\,|\boldsymbol{d}_{\mathrm{fi}}|^2\,I \cdot [\eta\,g_{\mathcal{L}}(\omega + \boldsymbol{k}\boldsymbol{v} - \omega_0; \Gamma_{\mathrm{fi}}) + (1 - \eta)I_{\mathrm{L}}(\omega + \boldsymbol{k}\boldsymbol{v} - \omega_0; \Gamma_{\mathrm{L}})]
\end{aligned} \tag{C.69}$$

with the normalised Gaussian laser spectrum $I_{\mathrm{L}}(\omega; \Gamma_{\mathrm{L}}) = \mathcal{G}(\omega; \Gamma_{\mathrm{L}}/(2\sqrt{2\ln 2}))$ and $g_{\mathcal{L}}$ as defined in Eq. (C.55).

It should once more be emphasised that this expression only gives the transition rate of the single atom j. It does explicitly not represent the transition spectrum of all particles in an ensemble of atoms.

Appendix D

Dynamics of atom-light interaction

Up to now the interaction between the atom(s) and light was only considered from the point of view of probabilities derived from Fermi's Golden Rule which finally lead to the transition rates predicting frequency for according transition events to take place. It is worth mentioning that these rates agree with those introduced in the rather heuristic approach directly starting with rate equations which are considered as balance equations. The relation between the rates can then be deduced from a purely thermodynamic perspective by assuming that the system reaches its steady state in the thermodynamic equilibrium. Since this was worked out and presented first by Einstein, it is also referred to as the *Einstein treatment*. Naturally though, this statistical treatment does not describe the complete picture as it does not address the dynamics of the interaction, that means does not for example answer the question on what happens to the irradiated atom *before* an absorption event is completed.

In order to accurately study the evolution of the involved quantum states it is therefore not sufficient to restrict the treatment only on statistical rates. This is due to fact that, due to their quantum nature, the states are linked to each other via clearly defined phase relations which are taken into account in the concept of coherences. In order to obtain the accurate time evolution of the quantum states it is necessary to solve the time-dependent Schrödinger equation for the interaction between the atom and light fields.

The objective of this chapter is to briefly introduce the basic concepts required to solve this problem and subsequently to work out the equations used for describing the coherent evolution of the quantum states for different configurations in terms of perturbation strength and spectral properties of the light field. Combined with the concept of damping, which induces decoherence to the system, this will directly yield the conditions for the validity of a rate equation approach to describe how the population of the states evolves in time. The concluding introduction of experimentally useful topics such as the saturation and power broadening of a transition completes the foundation required for the final discussion of Doppler laser cooling which this chapter will close with.

In the code used for simulating the atom-light interaction and laser cooling the calculation of the evolution of the state populations is as well based on the equations resulting from the following treatment with few exceptions discussed in the final section on Ps laser cooling.

D.1   Conceptual framework

To conveniently solve the problem of atom-light interaction as a solution of the time-dependent Schrödinger equation and to find analytical expressions which allow to elucidate mechanisms involved and processes resulting from the light-matter interaction it is necessary to make use of few approximations.

D.1.1   Semi-classical approach

While the above discussion of the processes involved in atom-light interaction and the derivation of according transition rates was based on a fully quantum mechanical approach since this is the only concept providing single quanta of light, i.e. photons, it turns out that the derivation of the dynamical equations presented next does not necessarily require a quantisation of the radiation field. Since in this theory only internal atomic properties are quantised and the field is treated in a classical way, in terms of electromagnetic waves, it is referred to as the *semi-classical approach*.

The answer to the question about the most appropriate approach is always based on the occurrence of phenomena which can only be explained after additional field quantisation. Since, from an empirical perspective, this is not the case in the following description of the quantum dynamics of the atomic states, it is common to simplify the treatment by taking the semi-classical approach.

Another crucial prerequisite for the validity of the semi-classical approach is that the atomic position is well defined on the shortest spatial scale of variation of the laser field parameters such as phase, polarisation or intensity [94]. Since the latter are generally characterised by the wavelength λ this definition is equivalent to ensuring that the atomic length scale, in terms of the dimension Δx of the atomic wave packet[35], is much smaller than λ, i.e., $\Delta x \ll \lambda$. Since this condition is clearly fulfilled in case of laser cooling positronium, but also any other atomic species, using light from the UV, VIS or IR section of the spectrum, it is entirely safe to treat the interaction in a semi-classical way.

It should be emphasised that the imperative requirement for quantisation of the atom only refers to its internal states. The description of the external states by means of the classical equations of motion does explicitly not contradict with the semi-classical theory even though changes of the motion are caused by (quantised) recoils $v_{\mathrm{rec}} = \hbar k/m$ (with the photon momentum $\hbar k = \hbar|\boldsymbol{k}|$) resulting from atom-light interaction. This directly implies though that care must be taken as the velocity of the atom approaches the same order of magnitude as the recoil velocity. From this point onwards the semi-classical concept using quantised internal states but classical equations of motion starts losing its validity so that it then becomes essential to modify the approach accordingly.

To evaluate whether this situation might arise it is convenient to introduce the recoil parameter $\epsilon_{\mathrm{rec}} = v_{\mathrm{rec}}/(2v_{\mathrm{D}}) = \hbar k^2/(2m\Gamma)$ of the system which relates the recoil velocity v_{rec} to a quantity denoted by v_{D} which represents the velocity associated with the temperature limit that can be achieved by means of Doppler laser cooling. With the photon wave number k, the atomic mass m and the natural line width Γ his criterion includes all characteristics of the system relevant for evaluation and represents a handy measure of the validity of the approach. A cooling limit that significantly exceeds the recoil velocity ($\epsilon_{\mathrm{rec}} \ll 1$) ensures that the semi-classical approach can be safely employed at all times. However, as soon as the spectral width equivalent to one recoils becomes comparable to the natural line width ($\epsilon_{\mathrm{rec}} \gtrsim 1$) the semi-classical condition no longer holds since the velocity evolution will then be highly affected by the quantum nature of the recoil that accompanies a single photon absorption or emission event [168].

More details on these two limiting cases and consequences with respect to the minimum temperature achievable are outlined in Sec. 2.4 with a special focus also on positronium laser cooling.

D.1.2 Approximation of 2-level System – Prerequisites, validity and extensions

In the standard Doppler laser cooling configuration, where the effects of atom-light interaction are exploited to slow down atoms by means of counter-propagating laser beams, the respective atomic transition is driven *resonantly* (albeit slightly red-detuned) by the Doppler-shifted laser frequency. Of course, atoms which spectrally surround the fraction of directly addressed atoms still interact with the radiation, especially in case of broadband laser sources. However, with increasing detuning $|\delta| = |\omega + \boldsymbol{k}\boldsymbol{v} - \omega_0|$, the resulting transition probabilities become more and more suppressed compared to the resonance case.

Hence, if the level dynamics of the two states belonging to the transition is not disturbed by any other state, the excitation scheme effectively reduces to a 2-level scheme consisting of only one ground and one excited state, $|\phi_{\mathrm{g}}\rangle$ and $|\phi_{\mathrm{e}}\rangle$, respectively.

The crucial criteria to evaluate the validity of this 2-level approach is thus the question whether

---

[35] In the density matrix formalism (see Section D.1.3) the size of the atomic wave packet is defined by the coherence length of the atomic density operator $\hat{\rho}$ [94].

the levels which lie energetically closest to the ones involved in the transition are sufficiently far separated from the latter as well as whether any additional state may be involved in the scheme. The latter might for instance be the case if the excited state $|\phi_\mathrm{e}\rangle$ does not only decay to $|\phi_\mathrm{g}\rangle$ but also to (an)other state(s). Depending on whether the latter subsequently decay(s) to $|\phi_\mathrm{g}\rangle$, thereby closing the cycle, or not, this additional decay channel can be taken into account either by means of a modified effective spontaneous emission rate Γ_eff or a superimposed exponential decay of the excited state population.

As already shown in Fig. A.1, in Ps only a single decay channel exists for the $2^3\mathrm{P}$ excited states, namely the direct path back to the according ground state (assuming zero magnetic field environments for the moment). The cooling transition $1^3\mathrm{S} \leftrightarrow 2^3\mathrm{P}$ thus represents an ideal closed 2-level system with the only blemish of the additional annihilation channel. However, the annihilation process does in fact not contradict with the concept of the 2-level system since this one-way process can again easily be incorporated by introducing an exponential decay of the ground state population with decay constant $\Gamma^{(\mathrm{ann})}$.

A further impediment of the 2-level approximation might accrue in the situation that, due to large Doppler broadening, the excitation of atoms with maximum velocities, or, more precisely, of those with velocities that differ most from the atoms in resonance, is, on the cooling transition, further detuned from resonance than for another transition. In other words, if, for any atom in the cloud, the detuning to the cooling transition is larger than to any other transition, implying that the probability for the latter transition becomes higher, the model of the cooling scheme can no longer be restricted to only one single 2-level system but has to be complemented by (an) additional system(s).

In case of an ideal cloud of thermalised positronium atoms at $T = 300\,\mathrm{K}$ for example, the HWHM of the Doppler distribution in terms of velocity amounts to $\Delta v_\mathrm{FWHM}/2 = \sqrt{2\ln(2)k_\mathrm{B}T/m_\mathrm{Ps}} = 56.1\,\mathrm{km/s}$ and the fastest travelling atoms can have velocities of up to $v_\mathrm{max} = 100\,\mathrm{km/s}$. This is equivalent to a maximum detuning of about $\delta_\mathrm{max} = kv_\mathrm{max} \approx 2\pi(400\,\mathrm{GHz})$ if the laser is resonant with the central fraction of the Doppler distribution. A comparison to the separation of excited states (cf. Fig. A.1 or Tab. A.1) directly reveals that, for Ps laser cooling on the $1^3\mathrm{S} \leftrightarrow 2^3\mathrm{P}$ transition, it is essential to include all states from the $n = 2$-manifold and thus introduce a corresponding number of 2-level systems into the calculation.

Obviously, though, the inclusion of additional 2-level systems besides the cooling transition does not only depend on the width of atom-related broadening mechanisms (Doppler or lifetime broadening) but in a similar way also on the laser bandwidth. If the radiation spectrum covers more than only one excited state, excitation takes place on several transitions in parallel. For typical laser bandwidth Γ_L of the order of $\Gamma_\mathrm{L} \approx 2\pi((10-100)\,\mathrm{GHz})$ this is in fact always the case, except for Ps in the Paschen-Back regime where the external magnetic field produces such strong energy splittings that only excited states from the $2^3\mathrm{P}$-manifold contribute and need to be taken into account (cf. Sec. B.5.3).

This list of shortcomings shows that the 2-level approximation does in fact not reflect the entire complexity of the excitation dynamics in real laser interaction schemes. Nevertheless, it represents a convenient approach for treating the process as it allows for resolving the mentioned defects by simply coupling several 2-level systems to form the entire complex system.

In the simulation code these issues are addressed, or rather prevented from arising at all, by simply calculating the transition rates via all allowed transitions, for each atom separately, and accounting for a corresponding number of transition schemes. Since laser spectra are, as mentioned above, approximated by Gaussian functions, the resulting Voigt-profile transition rates (cf. Eq. (C.69)) will, by definition, never reach exactly zero and a tiny residual rate will be left for all possible transitions. Therefore, in order to keep computational efforts within reasonable limits, transitions with too low rates can safely be neglected. The threshold for this to be the case is arbitrarily set to $\gamma = 1\,\mathrm{s}^{-1}$.

D.1.3 Concept of coherences and density matrix formalism

As mentioned previously, the treatment of resonant light-matter interaction includes the concept of coherences and must therefore be described by superposition states which sets the resulting evolution of the states clearly apart from classical or probabilistic dynamics. To clarify what makes these states different to statistical mixtures, it is worth to briefly outline the peculiarity of coherent superposition states and to introduce the density matrix formalism as a convenient and powerful tool for taking this subtle, but far reaching difference into account.

Based on the simplification of a 2-level system, a particle in a *superposition state* is described by

$$|\Psi\rangle = c_g |g\rangle + c_e |e\rangle \tag{D.1}$$

with complex coefficients c_g and c_e. The atom is thus simultaneously in both states $|g\rangle = |\phi_g\rangle$ and $|e\rangle = |\phi_e\rangle$ which implies the possibility for wave function interference. States described by such coherent superposition states are defined in a complete way, i.e. without leaving any uncertainty about the system. They are also known as *pure states*.

In contrast, a *statistical mixture* represents the description of a quantum system which is not completely defined that means not all information about it is given or known, leaving a residual uncertainty about it. This manifests itself in an unknown or arbitrary phase relation between the constituent states $|\Psi_j\rangle$ which means that interference is inhibited. Mixed states are probabilistic mixtures of pure states $|\Psi_j\rangle$. To describe the probability for each $|\Psi_j\rangle$ one usually imagines an ensemble of copies of the system which covers all possible configurations $|\Psi_j\rangle$ proportionate to their frequency of occurrence.

An example of such a statistical mixture would be a cloud of N_0 identical atoms, described by 2-level systems with wave function $|\Psi\rangle$ as given above, where each of them is *either* in state $|g\rangle$ or $|e\rangle$, an information which remains unspecified though. Consequently, $|\Psi\rangle = |g\rangle$ or $|e\rangle$.

To express the concept of coherence mathematically the coefficients c_j are usually written in terms of amplitudes $|c_j|$ and phase factors θ_j as $c_j = |c_j| e^{-i\theta_i}$.

Two states, such as $|g\rangle$ and $|e\rangle$ above, are called to be coherent if a distinct phase relationship exists between the states which is constant in time (i.e., $\theta_e - \theta_g = \text{const.}$) as it is obviously only the case in superposition states. On the other hand, in mixed states[36] such as the atomic cloud each individual atom is thus described by $|c_g|^2 = 1$ and $|c_e|^2 = 0$ or vice versa and the whole statistical mixtures finally in terms of the fractions $N_g/N_0 = |c_g|^2$ and $N_e/N_0 = |c_e|^2$ of atoms residing in either $|g\rangle$ or $|e\rangle$, respectively. The residual lack of information is thus reflected in the absence or random variation of phase relations between the individual states over time. Since the statistical mixture cannot be described by a single wave function, i.e., pure state, they are *incoherent* superpositions.

The reason for this subject to become relevant in the context of atom-light interaction is the fact that the interaction with the light pulse does not only cause the atom to jump between the states at rates predicted by the Einstein treatment, but rather does it additionally link the phases of the ground and excited states which directly implies that the treatment of this interaction must involve the concept of coherence [165].

At first glance the existence of coherence between $|g\rangle$ and $|e\rangle$ might surprise as it allows for the occurrence of phenomena which are not included in the Einstein analysis of the interaction which is based on discrete transitions and thus on statistical mixtures. As the description in the following chapter reveals this is however only seemingly in contradiction since the Einstein description of the state evolution solely represents a limiting case of the fully coherent treatment of the level dynamics which can be used only under certain conditions.

---

[36] In this context it is important to note that the use of the term "mixed state" for perturbed states, as resulting from interaction of Ps atoms with external magnetic fields, does not fully comply with the term's actual quantum mechanical definition described here. Specifically in the context of the Zeeman and motional Stark effect the term is often misused and perturbed states are improperly called mixed states even though they are in fact described by coherent superpositions.

A convenient mathematical tool to describe all quantum states of a system which incorporates the concept of coherences and directly allows to quantify the degree of coherence in the system is the density operator $\hat{\rho}$ or the density matrix ρ which is its representation in terms of a specific set of basis states, such as $|\mathrm{g}\rangle$ and $|\mathrm{e}\rangle$. The density matrix is defined as

$$\rho = \sum_j p_j |\Psi_j\rangle \langle \Psi_j| \tag{D.2}$$

with probabilities p_j which.

In the example of an ensemble of 2-level atoms with states $\Psi_i = c_{\mathrm{g}} |\mathrm{g}\rangle + c_{\mathrm{e}} |\mathrm{e}\rangle$ the matrix elements are simply given by $\rho_{ij} = \langle c_i c_j^* \rangle$ and the whole matrix can directly be written as

$$\rho = \sum_{i,j} |i\rangle \rho_{ij} \langle j| = \begin{pmatrix} \langle |c_{\mathrm{g}}|^2 \rangle & \langle c_{\mathrm{g}} c_{\mathrm{e}}^* \rangle \\ \langle c_{\mathrm{g}}^* c_{\mathrm{e}} \rangle & \langle |c_{\mathrm{e}}|^2 \rangle \end{pmatrix} \tag{D.3}$$

where the $\langle ... \rangle$ notation indicates the average over all atoms in the ensemble [165]. While the diagonal elements of the density matrix ρ, which only include amplitudes, simply represent the populations of the atomic states the off-diagonal elements also comprise the phase relation between them and are therefore called *coherences*.

The key difference between superposition and statistical mixtures, or coherent and incoherent systems, is the presence of off-diagonal elements in the density matrix. In case of a statistical mixture the off-diagonal terms are simply zero, either since they average to zero in case the phase relation is unknown or, as in the example with $|c_{\mathrm{g}}|^2 = 1 (=0)$ and $|c_{\mathrm{e}}|^2 = 0 (=1)$. The density matrix then reduces to

$$\rho = \begin{pmatrix} N_{\mathrm{g}}/N_0 & 0 \\ 0 & N_{\mathrm{e}}/N_0 \end{pmatrix} \tag{D.4}$$

In coherent superposition states, on the other hand, both $|c_{\mathrm{g}}|$ and $|c_{\mathrm{e}}|$ are non-zero which gives rise to off-diagonal elements and the density matrix takes the form (D.3). The presence of off-diagonal is thus an easily accessible criterion for a system to be in a mixed state or not.

General characteristics of the density operator or matrix respectively are

- It is Hermitian, i.e., $\rho = \rho^\dagger$.

- It is positive which means all eigenvalues are non-negative, i.e. $\rho \geq 0$.

- The statistical expectation value $\langle \hat{A} \rangle$ of an observable $\hat{A}$, that means the appropriately weighted average of the expectation values in each possible pure state, is given by

$$\langle \hat{A} \rangle = \sum_j p_j \langle \Psi_j | \hat{A} | \Psi_j \rangle = \sum_j p_j \, \mathrm{Tr}\left\{ |\Psi_j\rangle \langle \Psi_j| \hat{A} \right\} = \mathrm{Tr}\left\{ \sum_j p_j |\Psi_j\rangle \langle \Psi_j| \hat{A} \right\} = \mathrm{Tr}\left\{ \rho \hat{A} \right\}$$

where $\mathrm{Tr}(M) = \sum_j \langle j|M|j \rangle$ denotes the trace of a matrix M.

- The purity of a system described by ρ is defined as $\mathrm{Tr}(\rho^2)$. Hence, the purity is 1 if and only if the state is pure that means a coherent state. For mixed state one always finds $\mathrm{Tr}(\rho^2) \leq 1$.

- The density matrix of a pure state is idempotent that means $\rho^2 = \rho = 1$ which represents another means to identify whether ρ describes a pure state or not.

- In the Schrödinger picture, the time evolution of the density operator of a physical system described by the Hamiltonian $\hat{H}$ is given by the Von Neumann equation

$$i\hbar \frac{\partial \hat{\rho}(t)}{\partial t} = \left[\hat{H}, \hat{\rho}(t) \right] \tag{D.5}$$

To conclude, the fact that the concept of the density matrix allows to mathematically express both (incoherent) statistical mixtures of quantum states as well as (coherent) a systems described by superposition states makes the density matrix formalism obviously a very powerful tool.

Based on these concepts and approximations, the discussion will now proceed with the main business which is the description of the actual level dynamics during light-matter interaction which the Einstein treatment was not possible to provide.

The goal of the following discussion is to address the question about what happens to the irradiated atom *prior* (and *subsequent*) to a photon absorption event that means before and after the transition has taken place. This will lead to the dynamical equations describing the time evolution of the atomic states during interaction and finally, derived from that, to expressions which will allow to describe applications such as laser cooling and point out the connection to the solution by means of time-dependent perturbation theory culminating in the Golden Rule and resulting transition rates for the different interaction processes.

An essential component of the discussion will also be to work out the preconditions for the validity of the statistical rate equations approach. It turns out that this concept represents a limiting case of the fully coherent description and is of significant relevance with regard to the numerical algorithms as the one used for the investigations of Ps laser cooling in the following chapter. The treatment closely follows and adopts the notation of the exposition of the topic in [86, 89, 165].

After setting up the Schrödinger equation and outlining the problem the resulting coherent population evolution is described for different cases based on the 2-level approximation. This includes first the cases of weak perturbation either by mono-chromatic or incoherent broadband radiation followed by the solution for the more general case of a perturbation of arbitrary strength resulting in the well-known Rabi oscillations.

Based on the concept of coherence, the treatment will be generalised by complementing the solution for the dynamics of the population (= diagonal density matrix elements) with the behaviour of the off-diagonal elements. Integration of immanent damping mechanisms, which induce decoherence of the system, finally leads to the most general description in terms of the *optical Bloch equations* which allow to find expressions for the steady state and the saturation of a transition, both for monochromatic as well as incoherent broadband radiation.

D.2 Problem statement

To understand the coherent process of light-matter interaction and how it is connected to the probabilistic description provided by the Einstein treatment it is necessary, to start on the most fundamental level, the time-dependent Schrödinger equation. The derivation of the equations for the coherent description finally allows to identify under which conditions it is valid to simplify the description by using a set of rate equations and treat the population dynamics in an incoherent way. Rate equations are a crucial requirement for the practicability of numerical studies of Ps laser cooling experiments.

For light-matter interaction, the time-dependent Schrödinger equation is given by

$$i\hbar\frac{\partial \Psi}{\partial t} = \hat{H}\Psi \tag{D.6}$$

where the Hamiltonian $\hat{H} = \hat{H}_0 + \hat{H}_{\mathrm{int}}(t)$ is composed of the unperturbed $\hat{H}_0$ and the generally time-dependent interaction part $\hat{H}_{\mathrm{int}}(t)$. The unperturbed system is described by $\hat{H}_0$ with energies E_n of the corresponding wave functions $\Psi(\boldsymbol{r},t) = c_n(t)\phi_n(\boldsymbol{r})\exp(-iE_n t/\hbar)$ resulting from $\hat{H}_0\psi_n(\boldsymbol{r}) = E_n\psi_n(\boldsymbol{r})$.

Assuming a perturbation by light at frequencies close to resonance, i.e., $\omega = \omega_0 + \delta$ with $\delta \ll \omega_0$ and $\omega_0 = (E_{\mathrm{e}} - E_{\mathrm{g}})/\hbar$, the atom can be **approximated by a 2-level system**. The wave function

of the atomic state at any instant in time can then be written as

$$\Psi(\boldsymbol{r},t) \;=\; c_{\mathrm{g}}(t)\,\phi_{\mathrm{g}}(\boldsymbol{r})\exp\left(-i\frac{E_{\mathrm{g}}}{\hbar}t\right) \;+\; c_{\mathrm{e}}(t)\,\phi_{\mathrm{e}}(\boldsymbol{r})\exp\left(-i\frac{E_{\mathrm{e}}}{\hbar}t\right) \tag{D.7}$$

which is normalised by setting $|c_{\mathrm{g}}(t)|^2 + |c_{\mathrm{e}}(t)|^2 = 1$.

Based on the **semi-classical treatment** the Hamiltonian describing the interaction between the atom and the (real) oscillating field $\boldsymbol{E}(t) = \boldsymbol{E}_0\cos(\omega t)$ is given by $\hat{H}_{\mathrm{int}}(t) = e\boldsymbol{r}\boldsymbol{E}_0\cos(\omega t)$ which is the energy associated to the interaction of the electric dipole (based on precedent assumption of dipole approximation) with the electric field. This interaction causes mixing of the unperturbed states $|\mathrm{g}\rangle$ and $|\mathrm{e}\rangle$ which is described by the evolution of the two states (directly resulting from insertion into the Schrödinger equation) as

$$\begin{aligned} i\dot{c}_{\mathrm{g}} &= \Omega_{\mathrm{ge}}\cos(\omega t)\mathrm{e}^{-i\omega_0 t}c_{\mathrm{e}} \\ i\dot{c}_{\mathrm{e}} &= \Omega_{\mathrm{eg}}^*\cos(\omega t)\mathrm{e}^{i\omega_0 t}c_{\mathrm{g}} \;. \end{aligned} \tag{D.8}$$

The quantity Ω is an important parameter in the entire following treatment, denotes the so-called *Rabi frequency* and is defined as the frequency associated with the coupling energy of the transition dipole moment $\boldsymbol{d}$ and the electric field amplitude $\boldsymbol{E}_0$ and is thus given by

$$\Omega_{\mathrm{eg}} = \frac{1}{\hbar}\,\langle\mathrm{e}|\boldsymbol{d}\boldsymbol{E}_0|\mathrm{g}\rangle = \Omega_{\mathrm{ge}}^* \tag{D.9}$$

which, in position representation, becomes $\Omega_{\mathrm{eg}} = 1/\hbar\,\int\psi_{\mathrm{e}}^*(r)\boldsymbol{d}\boldsymbol{E}_0\psi_{\mathrm{g}}(r)\mathrm{d}^3 r$.

The solution of the system of coupled differential equations, given by Eq. (D.8), is facilitated by introducing a further approximation known as the **rotating-wave approximation**: Since in usual applications, such as laser cooling, the laser frequency is very close to the atomic resonance and the detuning is very small, $|\delta| \ll \omega_0$ it is reasonable to neglect all terms which include the factor $\mathrm{e}^{i(\omega_0+\omega)t}$ and keep only those evolving with $\mathrm{e}^{i(\omega_0-\omega)t}$. This approach is equivalent to ignoring all "fast rotating" terms (which lends the approximation its name) which anyway average to zero over any reasonable time scale of the atom-light interaction proportional to $t \approx 2\pi/(\omega_0 - \omega)$.

D.3 Undamped coherent population dynamics for different configurations

This basic framework already allows to derive exact solutions for few specific configurations. In all cases the level dynamics is still purely coherent that means the description does not yet incorporate any decoherence induced by damping due to (statistical) spontaneous decay, for example.

D.3.1 Weak monochromatic perturbation

In first-order approximation and assuming weak perturbation (which allows to approximate the cosine by a factor one) and applying the initial condition that all atoms populate the ground state, the probability to find the atom in the excited state at time t is given by the sinc-function

$$|c_{\mathrm{e}}(t)|^2 = \frac{1}{4}\,|\Omega_{\mathrm{eg}}|^2\,t^2\,\frac{\sin^2 x}{x^2} \tag{D.10}$$

with $x = (\omega_0 - \omega)t/2$. The width of the excited state population as a function of the frequency $(\omega_0 - \omega)$ is inversely proportional to the interaction time[37] t. Obviously, in the limit of very long interaction times $(t \to \infty)$ the excitation probability becomes a Dirac delta-function in frequency which means that in case of weak mono-chromatic radiation population transfer can only occur in case of precisely resonant interaction.

Note, that the assumption of weak perturbation implies that most of the atoms stay in the ground state so that even on resonance, no considerable population transfer takes place. Hence, Eq. (D.10) gives an accurate description only as long as $\Omega_{\mathrm{eg}}^2 t^2 \ll 1$.

---

[37] This relation between $\Delta\omega = \Delta E/\hbar$ and t is in fact simply a manifestation of Heisenberg's uncertainty relation.

D.3.2 Weak non-monochromatic perturbation and link to Einstein analysis

This finding can already be related to the result to Einstein's description of the population dynamics governed by statistical transition rates by extending the previously derived result to the case of non-monochromatic radiation characterised by a specific spectral distribution $E_0(\omega)$ which is defined in terms of the spectral energy density $\rho(\omega) = \epsilon_0 E_0^2(\omega)/2$, where $\boldsymbol{E}_0 = E_0\boldsymbol{\epsilon}_{\mathrm{L}}$ and $E_0 = |\boldsymbol{E}_0|$.

For broadband radiation the excitation probability can thus be obtained by expressing the Rabi frequency as

$$|\Omega_{\mathrm{eg}}|^2 = \frac{|\boldsymbol{d}_{\mathrm{eg}}\boldsymbol{\epsilon}_{\mathrm{L}}|^2}{\hbar^2} \frac{2\rho(\omega)\mathrm{d}\omega}{\epsilon_0} \tag{D.11}$$

and integrating $|c_{\mathrm{e}}(t)|^2$ over the whole spectrum. Assuming sufficiently long interaction times the sinc-function in Eq. (D.10) contributes only around resonance and the energy density becomes constant over this sharp interval ($\rho(\omega) \approx \rho(\omega_0) = \mathrm{const.}$). This assumption allows to derive the steady-state excitation rate $R_{\mathrm{eg}} = |c_{\mathrm{e}}(t)|^2/t$ from the integral which directly results in a transition rate

$$R_{\mathrm{eg}} = \frac{\pi}{3\epsilon_0\hbar^2} |\boldsymbol{d}_{\mathrm{eg}}|^2 \rho(\omega_0) = B_{\mathrm{eg}}\rho(\omega_0) \tag{D.12}$$

which miraculously yields the Einstein B-coefficient derived in previous sections (cf. Eq. (C.45)).

This result verifies that the Einstein treatment provides an accurate description of the interaction, but only under the described conditions. Only in the limit of long interaction times and under the assumption of broad-band radiation, the approach via the time-dependent perturbation theory yielding the coherent 2-level dynamics converges asymptotically to the result obtained from the probabilistic treatment. This represents a substantial result as it confirms that the rates are then completely defined by the corresponding Einstein coefficients.

It should be noted though, that this convergence of the two treatments does not yet apply to spontaneous emission which is so far not included in the system of differential equations given by Eq. (D.8).

D.3.3 General solution for monochromatic perturbation

In order to derive a more general solution for the interaction of the atom with radiation, without assuming a necessarily weak perturbation (but still applying the rotating-wave approximation), the coupled equations (D.8) can be transformed to a second-order differential equation. Note, that this description is restricted to monochromatic perturbation again in order to preserve the fully coherent character of the level dynamics.

Using similar initial conditions as above yields the probability

$$|c_{\mathrm{e}}(t)|^2 = \frac{\Omega_{\mathrm{eg}}^2}{\Omega_{\mathrm{eg}}^2 + \delta^2} \ \sin^2\left(\frac{t}{2}\sqrt{\Omega_{\mathrm{eg}}^2 + \delta^2}\right) \tag{D.13}$$

for atoms being located in the excited state. It should be kept in mind, that in general the detuning $\delta = \omega + \boldsymbol{k}\boldsymbol{v} - \omega_0$ includes the correction term $\boldsymbol{k}\boldsymbol{v}$ in order to account for a potential Doppler shift due to the movement of the atom with velocity $\boldsymbol{v}$.

This result reveals a completely new phenomenon compared to the treatment so far which described the effect of atom-light interaction in terms of statistically occurring complete jumps between the atomic states with probability determined by the intrinsic Einstein coefficients. In contrast, Eq. (D.13) indicates that the population between the states is in fact subject to oscillations (also referred to as *Rabi oscillations*) at a frequency $\sqrt{\Omega_{\mathrm{eg}}^2 + \delta^2}$ which is determined both by the coupling strength (in terms of Ω) as well as the detuning δ. The stronger the perturbing radiation the faster the oscillations, but also the less influential the detuning so that also off-resonant radiation can still cause considerable population transfer. However, full transfer to the excited state can only occur for perfectly resonant radiation, otherwise a small fraction of atoms will always remain in the ground state.

In case of resonant excitation, defined interaction times exist after which the interaction either results in a complete transfer of the whole population (for $\Omega t = \pi$, therefore also known as π-pulses) or generates a superposition of $|g\rangle$ and $|e\rangle$ with equal amplitudes ($\pi/2$-pulses due to $\Omega t = \pi/2$).

This oscillatory behaviour is in contrast to the result found above for weak, but broadband radiation (cf. Eq. (D.12)) which rather suggests that the rates and thus also the populations tend to equalise with increasing energy density $\rho(\omega)$. Population inversion from the ground to the excited state could then never occur. As shown above already for the case of weak perturbation, the comparison to the general result again demonstrates that spectrally broad radiation breaks up the phase relation between the states causing loss of coherence. This effect can easily be explained by imagining the interaction being induced stochastically by any frequency component of the laser spectrum. By averaging the process over the whole spectrum, the random phase relation between those spectral components thus destroys the coherence of the interacting atomic states. As a result, the coherent evolution in the monochromatic case is then transformed into a sequence of statistically occurring, discrete transition events. Non-monochromatic radiation can thus be interpreted as a damping mechanism with the simple rule that the broader the spectrum the faster the decoherence.

Finally, it should be noted that for electric dipole transitions in the ultraviolet (UV), visible (VIS) or infrared (IR) region, spontaneous emission (at a rate of $\Gamma_{\mathrm{ge}} = 1/\tau$) tends to wash out these Rabi oscillations on time scales of few nanoseconds, in case of Ps for example on average one event takes place every 3.19 ns. Coherent oscillations can thus only be observed on smaller time scales and only in case of intense laser radiation with high Rabi frequency, ensuring $\Omega_{\mathrm{eg}}\tau > 1$.

This is an important result with respect to the validity and justification for the use of a rate equation approach.

D.4   Bloch equation formalism

Obviously, the dynamics of the internal state of the atom during the interaction can only be described completely by taking into account all involved processes that means especially also mechanisms which might cause the coherent evolution to dephase. The treatment so far was completely restricted to the populations of the atomic states. However, as a matter of fact, decoherence can only be explained properly based on the coherences of the system[38] which represent the response of the atom at the transition frequency ω_0 to the driving field at ω.

This can conveniently be realised by making use of the density matrix formalism with the populations on the diagonal and the coherences on the off-diagonals. As described in Section D.1.3 the density matrix of a 2-level system is given by

$$\rho = |\Psi\rangle\langle\Psi| = \begin{pmatrix} c_{\mathrm{g}} \\ c_{\mathrm{e}} \end{pmatrix} \begin{pmatrix} c_{\mathrm{g}}^* & c_{\mathrm{e}}^* \end{pmatrix} = \begin{pmatrix} |c_{\mathrm{g}}|^2 & c_{\mathrm{g}}c_{\mathrm{e}}^* \\ c_{\mathrm{e}}c_{\mathrm{g}}^* & |c_{\mathrm{e}}|^2 \end{pmatrix} = \begin{pmatrix} \rho_{\mathrm{gg}} & \rho_{\mathrm{ge}} \\ \rho_{\mathrm{eg}} & \rho_{\mathrm{ee}} \end{pmatrix} \tag{D.14}$$

with $\rho_{\mathrm{ge}} = \rho_{\mathrm{eg}}^*$.

The derivation of the set of dynamical equations describing the (still fully coherent) evolution of the internal atomic states can be facilitated by transforming the coefficients $c_{\mathrm{g}}(t)$ and $c_{\mathrm{e}}(t)$ to the reference frame which rotates at frequency δ. This only affects the off-diagonal elements of the density matrix which are transformed to $\tilde{\rho}_{ij}$ while the populations $\rho_{jj} = \tilde{\rho}_{jj}$ remain unchanged. By additionally defining the variables

$$
\begin{aligned}
u &= \tilde{\rho}_{\mathrm{ge}} + \tilde{\rho}_{\mathrm{eg}} = \rho_{\mathrm{ge}}\mathrm{e}^{-i\delta t} + \rho_{\mathrm{eg}}\mathrm{e}^{i\delta t} = 2\,\mathrm{Re}(\rho_{\mathrm{ge}})\cos(\delta t) \\
v &= -i(\tilde{\rho}_{\mathrm{ge}} - \tilde{\rho}_{\mathrm{eg}}) = -i(\rho_{\mathrm{ge}}\mathrm{e}^{-i\delta t} - \rho_{\mathrm{eg}}\mathrm{e}^{i\delta t}) = -2\,\mathrm{Im}(\rho_{\mathrm{ge}})\sin(\delta t) \\
w &= \rho_{\mathrm{gg}} - \rho_{\mathrm{ee}}
\end{aligned}
\tag{D.15}
$$

where $u(t)$ and $v(t)$ represent the in-phase and quadrature components of the response of the system (i.e. real and imaginary parts of ρ_{ge}) respectively, it can easily be shown (after a lengthy

---

[38] It should be recalled that the populations only consist of the states' amplitudes $|c_i|^2 = c_i c_i^*$ whereas the coherences $c_i c_j^*$ also account for their phase relation.

procedure of simple calculation steps which are skipped here) that the coherent evolution of the atomic states reduces to the following set of coupled differential equations

$$\dot{u} = v\delta$$
$$\dot{v} = -u\delta + \Omega w \qquad\qquad (\text{D.16})$$
$$\dot{w} = -\Omega v$$

known as the *Bloch equations*.

Since the treatment shall for the moment be restricted to transitions between bound states, for which the Rabi frequency is a real quantity [86] (that means $\Omega_{\text{ge}} = \Omega_{\text{eg}}$), denoted by Ω in the above equations. The following expressions are simplified in the same way by only using Ω.

Obviously, the evolution of the population difference w and thus of the excited state population $\rho_{\text{ee}} = (1 - w)/2$ (with $\rho_{\text{gg}} + \rho_{\text{ee}} = 1$) is governed by the out-of-phase component of the system's response, and $\dot{\rho}_{\text{ee}} = \Omega v/2$.

It is common to summarise the atom-related variables u, v and w in the so called *Bloch vector* $\boldsymbol{R} = u\hat{\mathbf{e}}_1 + v\hat{\mathbf{e}}_2 + w\hat{\mathbf{e}}_3$ and the two interaction-related variables Rabi frequency Ω and detuning δ in the *generalised Rabi frequency* vector $\tilde{\boldsymbol{\Omega}} = \Omega\hat{\mathbf{e}}_1 + \delta\hat{\mathbf{e}}_3$ with magnitude $\tilde{\Omega} = \sqrt{\Omega^2 + \delta^2}$. $\boldsymbol{R}$ and $\tilde{\boldsymbol{\Omega}}$ allow to reduce the system of differential equations in Eq. (D.16) to

$$\dot{\boldsymbol{R}} = \boldsymbol{R} \times \tilde{\boldsymbol{\Omega}} \qquad\qquad (\text{D.17})$$

which is the compact version of the Bloch equations.

Obviously, $\dot{\boldsymbol{R}} \cdot \boldsymbol{R} = 0$ and thus $|\boldsymbol{R}|^2 = \text{const.}$, which suggests to interpret the Bloch vector $\boldsymbol{R}$ as a position vector living on the surface of a sphere, called *Bloch sphere*. The Bloch sphere has a constant radius which can be proven to be one [86]. The Bloch formalism thus shows that the response of a 2-level atom to radiation does not increase indefinitely with the intensity of the perturbing field.

It should be noted that this result is still based on the fully coherent evolution. Only if the evolution is purely coherent the Bloch vector can move over the whole sphere. As soon as it gets damped though, that means disturbed by incoherent processes which cause the evolution to dephase, the decoherence manifests itself in a restricted range of possible positions on the sphere. Once the coherences have completely vanished ($u = v = 0$) the Bloch vector will be fixed along $\hat{\mathbf{e}}_3$. The polar angle θ between $\boldsymbol{R}$ and $\hat{\mathbf{e}}_3$ can thus be interpreted as the degree of coherence which is still left in the evolution.

D.4.1 Phase-damped coherent dynamics

So far, the simple Bloch equations $\dot{\boldsymbol{R}} = \boldsymbol{R} \times \tilde{\boldsymbol{\Omega}}$ only involve the coherent interaction processes of absorption and stimulated emission. However, these processes are of course inherently competed by the incoherent process of spontaneous emission which causes decoherence of the system.

The concept of the Bloch equations highly facilitates the integration of any kind of damping mechanism characterised by a damping constant Γ. Another important example for an incoherent process, besides spontaneous emission, is excitation by incoherent non-monochromatic radiation[39]. The arbitrary fluctuation of the frequency of the electric field is commonly treated as stochastic phase noise at a rate Γ_{L}, which continuously disturbs the coherent phase relation between the complex state amplitudes finally leading to loss of coherence.

Even though processes which cause decoherence at a rate Γ also lead to broadening of the transition linewidth, it is difficult to establish a relation between the two resulting effects. They should rather be considered as two different manifestations of the same process, which is the

---

[39] In this context it should be pointed out that, even though potentially not explicitly mentioned, throughout this whole thesis but specifically in the following treatment of decoherence induced by excitation by means of broadband laser radiation the term "broadband" in general refers to ***spectrally incoherent*** broadband radiation. As far as the effect on the level dynamics is concerned, this must be clearly separated from excitation by coherent broadband radiation (such as ultra-short laser pulses) as will be discussed below.

existence of an incoherent process that interferes with the coherent state evolution. It is however important to emphasise that there is no causal relationship between line broadening and phase damping. For this reason, it is not possible to deduce the existence of phase damping from the mere presence of line broadening.

This can well be explained by means of the width Γ_{L} of the laser spectrum: In fact, in case of non-monochromatic excitation, the laser bandwidth enters the equation for the transition rate $\gamma_{\mathrm{i}\to\mathrm{f}}(\omega)$ (cf. Eq. (C.63)) via the convolution of the laser spectrum with the natural transition line, in all cases, regardless of whether the radiation is coherent or incoherent. This implies that it is not possible to make any statement on the rate of loss of coherence only based on the characteristics of the absorption line[40]. The only possible conclusion to draw in this respect is that all incoherent broadening mechanisms at the same time entail phase damping.

D.4.2 Optical Bloch equations for spontaneous emission

The most prominent and important example for damping is the process of emission taking place at a rate Γ_{ge} which even represents a very special mode of damping as it does not only affect the coherences ρ_{ge} and ρ_{eg} but in fact also the populations ρ_{gg} and ρ_{ee} simply due to the fact that it describes the decay of the atoms in the excited state $|e\rangle$.

As such, it therefore enters first of all the Bloch equations in the form of the decay term $-\Gamma\rho_{\mathrm{ee}}$ in the differential equation for ρ_{ee} which then becomes

$$\dot{\rho}_{\mathrm{ee}} = -\Gamma\rho_{\mathrm{ee}} + \frac{\Omega}{2}v \ . \tag{D.18}$$

Similarly, the equations for u and v have to be modified by adding decay terms[41] proportional to $\Gamma/2$ to the according Bloch equations. In case damping is caused entirely by spontaneous decay (also called *radiative damping*) the simple Bloch equations (D.16) from above transform to [90]

$$\dot{u} = v\delta - \frac{\Gamma_{\mathrm{ge}}}{2}u \tag{D.19}$$

$$\dot{v} = -u\delta + \Omega w - \frac{\Gamma_{\mathrm{ge}}}{2}v \tag{D.20}$$

$$\dot{w} = -\Omega v - \Gamma_{\mathrm{ge}}(w-1) \tag{D.21}$$

These equations describing the excitation of a 2-level atom by light at frequencies around resonance of a transition which decays by spontaneous emission are known as the ***optical Bloch equations***.

It should be emphasised that the way how spontaneous emission manifests itself in the Bloch equations is not the general one which can be transferred one-to-one to any other phase damping mechanism. In case the incoherent process does not affect the populations it only enters the equations for the coherences. A good example is again the excitation by an incoherent laser field with a bandwidth Γ_{L} which can thus be accounted for by replacing Γ_{ge} in the first and second equation by an effective decay constant $(\Gamma_{\mathrm{ge}}+\Gamma_{\mathrm{L}})$. Any additional phase damping such as collisional broadening can in principle be incorporated in the same way (cf. Ref. [89] or the appendix of Ref. [169]).

---

[40] In this context it is interesting to mention that even Doppler broadening effectively causes dephasing of coherent phenomena, such as the Rabi oscillations, where in this case the randomness of the phases originates from the distribution of atomic velocities (which enter the electric field via the Doppler phase factor $k\boldsymbol{v}$). This finally leads as well to dynamical equations similar to the ones found for non-monochromatic radiation [86]. However, since Doppler broadening is an effect which becomes visible only when regarding the spectrum of the whole atomic ensemble (whose derivation includes integration over the whole velocity distribution), it is not explicitly mentioned in the treatment here which, for the moment, shall be focussed on the single-particle interaction.

[41] The introduction of the damping terms is motivated here by the argument that the behaviour of the damped atomic dipole in the radiation field is similar to damping of a classical dipole. By analogy to the harmonic oscillator model the equations describing the coherences must thus, by comparison to the classical equations, contain damping terms proportional to half the damping constant. Such a heuristic approach is of course no rigorous derivation. This comparison is however justified a posteriori by the fact that the resulting equations describe the physics in an adequate way.

Steady state solution

Considering the final goal of this section to find an accurate description of the processes involved in laser cooling, one is in general only interested in solutions of the Bloch equations on time scales much longer than the lifetime of the excited state. On these time scales the system will settle down to a steady state. By simply setting the time derivatives to zero one obtains the solution

$$
\begin{pmatrix} u \\ v \\ w \end{pmatrix} = \frac{1}{\delta^2 + \Omega^2/2 + \Gamma_{\mathrm{ge}}^2/4} \begin{pmatrix} \Omega\delta \\ \Omega\Gamma_{\mathrm{ge}}/2 \\ \delta^2 + \Gamma_{\mathrm{ge}}^2/4 \end{pmatrix} \tag{D.22}
$$

which implies that the population of the excited state approaches an asymptotic value of

$$
\rho_{\mathrm{ee}} = \frac{1 - w}{2} = \frac{\Omega_{\mathrm{ge}}^2/4}{\delta^2 + \Omega_{\mathrm{ge}}^2/2 + \Gamma_{\mathrm{ge}}^2/4} \ . \tag{D.23}
$$

This expression is one of the most essential results with respect to the radiation force exerted by the laser on the irradiated atom which will be picked up several times again. At the same time it is the most accurate description for the population transfer to the excited state in the steady state since it includes all relevant interaction parameters, namely the Rabi frequency Ω as a measure for the coupling strength between the atom and light, the detuning δ and the spontaneous (or more generally phase damping) rate Γ_{ge}. It furthermore clearly demonstrates that very intense radiation (i.e., $\Omega \to \infty$) leads to equalisation of the populations.

D.4.3 General optical Bloch equations

It can be summarised that purely monochromatic resonant radiation causes the states to oscillate with a fully coherent evolution. Resulting coherent phenomena can however only be observed on time scales over which coherences are preserved and the atomic states still exhibit defined phase relations. On time scales much longer than the natural lifetime $\tau = 1/\Gamma_{\mathrm{ge}}$ of the excited state coherences will slowly fade away until they will finally have vanished completely and the dynamics enters into a regime of incoherent evolution.

Spontaneous emission is however not the only relaxation process than might disturb the coherent evolution of the system. It can for example also be exposed to random fields that modify their phase in an uncontrolled way. In an intuitive picture, these fields will not affect the population of the states, but provoke random dephasing of the coherence between $|e\rangle$ and $|g\rangle$ and finally damp these coherences [170].

It can furthermore be concluded that, as soon as coherences have vanished, the formerly coherent evolution of the quantum amplitudes reduces to a set of incoherent equations which is governed by transition rates describing the population dynamics. This state can be considered as a ***quasi-steady state*** of the Bloch equations. It is however important to note that in this state the population must not necessarily have reached a steady state as well. There is thus no relation between the use of rate equations and the steady state of the excited state population.

In general this subtlety is mathematically accounted for by distinguishing between so called *longitudinal* and *transverse relaxation* rates $\Gamma_{\parallel}$ and $\Gamma_{\perp}$, respectively, which are owing their names to the fact that the former describes decoherence that means damping of the transversal components u and v of the Bloch vector whereas the latter is responsible for the relaxation of the populations contained in the longitudinal component w.

In case the relaxation process is a pure phase damping process, that means exclusively affecting the evolution of the coherence, without any influence on the populations, its characterising rate Γ' only appears in the coherence equations and is consequently only included in the transverse rate $\Gamma_{\perp}$. An example for such a process is the excitation by incoherent non-monochromatic radiation where the incoherence reflects itself in fluctuating phases of the electric fields within a spectral bandwidth Γ_{L}. Mathematically, this randomness of phases is integrated in the treatment by considering the

statistical average of the excitation including random phase contributions over several repetitions [169].

On the other hand, if the process also induces incoherent de-excitation of the atoms in the excited states, such as spontaneous emission, its rate Γ'' appears in all three Bloch equations and therefore does not only enter $\Gamma_\perp$ but also the longitudinal rate $\Gamma_\parallel$. The extended or generalised version of the optical Bloch equations, accounting for the different nature of damping processes, thus becomes

$$\dot{u} = v\delta - \frac{\Gamma_\perp}{2}u \tag{D.24}$$

$$\dot{v} = -u\delta + \Omega w - \frac{\Gamma_\perp}{2}v \tag{D.25}$$

$$\dot{w} = -\Omega v - \Gamma_\parallel(w - 1) \tag{D.26}$$

with $\Gamma_\perp = \Gamma_{\mathrm{ge}} + \sum \Gamma'$ and $\Gamma_\parallel = \Gamma_{\mathrm{ge}} + \sum \Gamma''$ where the first sum goes over all rates Γ' of involved processes solely affecting the coherences and the second, respectively, over the rates Γ'' of processes with additional influence on the populations.

D.4.4   Quasi-steady state solution and rate equations

The differentiation between longitudinal and transverse damping, provided by the general optical Bloch equations, finally allows to discuss the consequence of the involvement of a process that only induces fast transverse relaxation, that means which only affects coherences, not though populations. In this case, it can be assumed that $\Gamma_\perp \approx \Gamma'$ exceeds all other rates and frequencies in the Bloch equations, but $\Gamma_\parallel$ stays unchanged which can for example occur in case of large incoherent laser bandwidths $\Gamma' = \Gamma_{\mathrm{L}}$. The evolutions of the coherences and the populations are then completely decoupled. While the former will assume a steady state with $\dot{u} = \dot{v} = 0$, the evolution of the populations is still far from having settled yet. By inserting the steady state solutions u_{st} and v_{st} into $\dot{w}$ and using $\rho_{\mathrm{ee}} = (1 - w)/2$ it is straightforward to show that then

$$\dot{\rho}_{\mathrm{ee}} = -\Gamma_\parallel \rho_{\mathrm{ee}} + \frac{\Omega^2}{2}\frac{\Gamma_\perp}{\delta^2 + \Gamma_\perp^2}(\rho_{\mathrm{gg}} - \rho_{\mathrm{ee}}) \ . \tag{D.27}$$

With $\rho_{\mathrm{ee}} = N_{\mathrm{e}}$ the population of the excited state, Eq. D.27 can easily be identified as a differential equation for the upper state with rate equations structure as it is well known from the statistical Einstein approach to light-matter interaction. It includes all three involved processes, absorption and stimulated emission with equal probabilities $(\Omega^2/2)\Gamma_\perp/(\delta^2 + \Gamma_\perp^2)$ as well as spontaneous decay with probability $\Gamma_\parallel$ which only goes from $|e\rangle$ to $|g\rangle$ as is reflected by the upper state population reduction by $-\Gamma_\parallel N_{\mathrm{e}}$.

Applied to the process of Ps laser cooling under the assumption that the only additional incoherent process involved besides spontaneous emission is excitation by incoherent non-monochromatic laser light, the transverse and longitudinal relaxation rates are simply given by $\Gamma_\perp = \Gamma_{\mathrm{ge}} + \Gamma_{\mathrm{L}}$ and $\Gamma_\parallel = \Gamma_{\mathrm{ge}}$, respectively. Insertion into the rate equation (D.27) yields

$$\dot{N}_{\mathrm{e}} = -\Gamma_{\mathrm{ge}}N_{\mathrm{e}} + \frac{\Omega^2}{2}\frac{\Gamma_{\mathrm{ge}} + \Gamma_{\mathrm{L}}}{\delta^2 + (\Gamma_{\mathrm{ge}} + \Gamma_{\mathrm{L}})^2}(N_{\mathrm{g}} - N_{\mathrm{e}}) \ . \tag{D.28}$$

This result recovers the transition rates derived in App. C, finally revealing the similarity of the incoherent solution of the Bloch equations with the result from the fully quantum mechanical treatment. The spontaneous rate can directly be spotted in the rate equation, but it is equally straightforward to also identify the absorption and stimulated emission rates $\gamma_{\mathrm{g}\leftrightarrow\mathrm{e}}(\omega)$ for a Lorentzian laser spectrum as given by Eq. (C.64). The rate equation for the excited state population of a single (closed) 2-level system can thus be written as

$$\dot{N}_{\mathrm{e}} = \gamma_{\mathrm{eg}}N_{\mathrm{g}} - (\gamma_{\mathrm{ge}} + \Gamma_{\mathrm{ge}})N_{\mathrm{e}} \tag{D.29}$$

with $\gamma_{eg} = \gamma_{g\to e}$ and $\gamma_{ge} = \gamma_{g\leftarrow e}$. Due to the implicit requirement of population balance the rate equation for the ground state population is accordingly given by

$$\dot{N}_g = -\gamma_{eg}N_g + (\gamma_{ge} + \Gamma_{ge})N_e \ . \tag{D.30}$$

Validity of the Rate Equation Approach

The applicability of a rate equation approach for the description of internal state dynamics can thus be put into the simple condition that decoherence must take place on shorter time scales than excitation of coherent oscillations between the internal states. In other words, the transverse relaxation rate $\Gamma_\perp$, responsible for phase damping, must exceed the Rabi frequency that characterises coherent effects, that means

$$\Gamma_\perp \gg \Omega \qquad \Longleftrightarrow \qquad \Gamma_\perp \gg \gamma_{ge} \ . \tag{D.31}$$

Rate equations can then be applied once the coherences have vanished. It can thus be concluded that rate equations represent an appropriate means to describe the quasi-steady state of the Bloch equations.

D.5 Saturation of an atomic transition

In the following, the attention shall be drawn to the application of the Bloch equation formalism to the case of strong radiation intensity leading to saturation of the atomic transition line. Several limiting cases of the level dynamics in the quasi- and full steady state shall be discussed and expressions, such as the saturation intensity, introduced which become useful in experimental respects. Furthermore, equations will be derived for describing saturation in the steady state, based on the set of equations (D.22).

A quantity often used in the context of the quasi-steady state of the Bloch equations and the incoherent rate equation formalism is the saturation of an atomic transition. It is usually quantified in terms of the irradiance $I_s(\omega)$ required to saturate the transition by means of light at an arbitrary frequency ω. It is thus defined as half the irradiance absorbed during transfer of photon energy $\hbar\omega$ at a rate A_{eg}. The relation between this (quantised) rate of energy transfer and the (classical macroscopic) laser irradiance is thereby simply given by the product $I\sigma$ of irradiance I and the atom's photon absorption affinity expressed in terms of the cross section[42] σ. Thus,

$$I_s(\omega) = \frac{\hbar\omega A_{eg}}{2\sigma(\omega)} \tag{D.32}$$

It can be shown (see e.g. Ref. [136]) that the cross section (Eq. (C.47)) for the absorption of arbitrarily polarised photons by an atom that can be modelled as a 2-level system, reduces to[43]

$$\sigma(\omega) \ = \ 3g_\epsilon \frac{\pi}{3\epsilon_0} \frac{\omega_0}{\hbar c} d_{eg}^2 g_1^{(abs)}(\omega) \ = \ 3g_\epsilon \frac{\pi^2 c^2}{\omega_0^2} A_{eg} g_1^{(abs)}(\omega) \ =: \ \sigma_0 g_1^{(abs)}(\omega) \tag{D.33}$$

where $g_1^{(abs)}(\omega)$ denotes the respective atomic line shape function as detailed in Section C.7. The pre-factor g_ϵ depends on the relative orientation between the electric dipole moment $\boldsymbol{d}_{eg}$ and the polarisation vector $\boldsymbol{\epsilon}$. The factor g_ϵ is obtained by averaging the term $|\boldsymbol{\epsilon}\cdot\boldsymbol{d}_{eg}|^2 = |\boldsymbol{d}_{eg}|^2\cos^2\theta$ which appears in Eq. (C.47) over all possible directions $d\Omega$ and can thus range from 0 to 1. Unpolarised

---

[42] For convenience only, and since it is solely the cross section for absorption which is relevant in the context here, in the following the superscript "(abs)" will be dropped and $\sigma^{(abs)}(\omega)$ simply be denoted by $\sigma(\omega)$

[43] It should be emphasised here that this expression is only valid for a 2-level atom. In general the cross section needs to be multiplied by the according degeneracy factors g_g and g_e of the manifolds involved in the transition.

light, that means with arbitrary direction θ, results in $g_\epsilon = 1/3$ whereas in case of optimally polarised light (optimally with respect to the orientation of $\boldsymbol{d}_{\mathrm{eg}}$) averaging simply yields a factor of 1. The latter case will be adopted here.

The minimum value I_{sat} of I_{s}, which obviously occurs on resonance $\omega = \omega_0$, is commonly referred to as *the* saturation intensity

$$I_{\mathrm{sat}} = I_{\mathrm{s}}(\omega_0) = \frac{\pi}{3} \frac{hc}{\lambda_0^3 \tau} \tag{D.34}$$

where $\tau = \Gamma_{\mathrm{ge}}^{-1} = A_{\mathrm{ge}}^{-1}$ is the lifetime of the according transition.

For the $1^3\mathrm{S}_0$ to $2^3\mathrm{P}_1$ transition in Ps the saturation intensity amounts to $I_{\mathrm{sat}} = 0.453\,\mathrm{W/cm}^2$ (see Tab. D.1 below for comparison to further parameters and values).

From the definitions of the saturation intensity, the Rabi frequency Ω and the intensity I it can easily be deduced that

$$\frac{I}{I_{\mathrm{sat}}} = \frac{2\Omega^2}{\Gamma_{\mathrm{ge}}^2} \tag{D.35}$$

which represents an identity which is oftentimes, especially in experimental respects, much more accessible than the rather theoretical Rabi frequency. Another quantity which is commonly used in the context of saturation of atomic transitions to simplify several equations is the *saturation parameter s* which is the generalised version of the above relation (D.35) and is defined as

$$s = \frac{2\Omega^2}{4\delta^2 + \Gamma_{\mathrm{ge}}^2} \ . \tag{D.36}$$

The comparison to the steady state solution of the Bloch equations, given by Eq. (D.22), shows that, in this steady state limit, the saturation parameter is equivalent to $s = (1/w) - 1$ where $w = \rho_{\mathrm{gg}} - \rho_{\mathrm{ee}}$ is the population difference (with $w \in (0,1]$, in the steady state). The latter relation between s and w well illustrates the physical meaning of the saturation parameter: If the transition is for example resonantly driven at highest possible intensity (and thus maximum Rabi frequency Ω), the saturation parameter takes huge numbers which means $w \to 0$ or, respectively, equalisation of the populations of the two states, as predicted by the Bloch equations. However, in case of simultaneously high detuning, s can even drop to zero which is reflected by $w \to 0$ in this case, that means negligible excited state population ρ_{ee}. In other words, far off-resonance even excessive radiation intensity does not yield any appreciable population transfer to the excited state.

A typical application example for the saturation parameter is the excited state population in the steady state which can be expressed in terms of s as

$$\rho_{\mathrm{ee}} = \frac{1}{2} \frac{s}{1+s} \ . \tag{D.37}$$

D.5.1 Power broadening

As already mentioned in the context of the discussion of line broadening in Section C.7, excessive laser intensity can cause additional line broadening[44]. This can most easily be understood on the basis of the steady state expression for the excited state population in Eq. (D.23) which can be transformed to

$$\rho_{\mathrm{ee}} = \frac{\Omega^2/4}{\delta^2 + \Omega^2/2 + \Gamma_{\mathrm{ge}}^2/4} = \frac{\Gamma_{\mathrm{ge}}^2/4 \cdot \frac{I}{I_{\mathrm{sat}}}}{\delta^2 + \Gamma_{\mathrm{ge}}^2/4 \left(1 + \frac{I}{I_{\mathrm{sat}}}\right)} = \frac{\Omega^2/4}{\delta^2 + \Gamma_{\mathrm{eff}}^2/4} \tag{D.38}$$

---

[44] It should be emphasised that this broadening mechanism must not be confused with broadening due to non-monochromatic radiation. Even though both mechanisms have the same origin, they are both induced by the incoming radiation, they in fact result from two distinctly different effects. Therefore they can also occur independently and depending on different conditions. Intense monochromatic radiation can for instance broaden the line just as much as weak radiation with a broad spectrum can.

where Γ_{eff}, the FWHM width of the Lorentzian function, can be identified as the effective steady state absorption linewidth

$$\Gamma_{\text{eff}} = \Gamma_{\text{ge}}\sqrt{1 + \frac{2\Omega^2}{\Gamma_{\text{ge}}^2}} = \Gamma_{\text{ge}}\sqrt{1 + \frac{I}{I_{\text{sat}}}} \ . \tag{D.39}$$

This phenomenon of the modification of the transition linewidth is generally referred to as *power broadening*. Obviously, in the limit of extreme light intensity the linewidth asymptotically approaches the value $\sqrt{2}\Omega$ which means that excitation then spreads over a spectral interval which by far exceeds the natural linewidth Γ_{ge}. It should once more be emphasised that the broadening of the line is not necessarily linked to the concept of coherence.

In line with the the existence of an upper limit for the excited state population in the steady state, it is found that intensive laser radiation only affects the width of the function for the excited state population, not though its amplitude (as one might hastily expect in case of (normalised) Lorentzian functions whose amplitude normally scales with its width Γ). In physical respects this makes perfect sense since otherwise one could imagine to enhance the excited state population beyond all measure by simple modification of the broadening, which is completely absurd.

What happens instead is quite different and can instructively be elucidated on the basis of the absorption coefficient[45] for example which is defined by the relation

$$\frac{\mathrm{d}I}{\mathrm{d}z} = -\kappa(\omega)I = N\sigma(\omega)I \tag{D.40}$$

which describes the attenuation of a beam travelling along z due to absorption of photons by the atom. It furthermore provides a connection between the observable macroscopic change $\mathrm{d}_z I$ and the microscopic descriptions to the right of the equal sign [86]. Insertion of Eq. (D.33) directly yields

$$\kappa(\omega) = N(\rho_{\text{gg}} - \rho_{\text{ee}})\sigma(\omega) = N\sigma_0 \ \frac{\Gamma_{\text{ge}}^2/4}{\delta^2 + \Gamma_{\text{ge}}^2/4\left(1 + \frac{I}{I_{\text{sat}}}\right)} \tag{D.41}$$

where $\sigma_0 = \sigma(\omega_0)$ denotes the resonance cross section and N the total number of atoms. Obviously, the absorption coefficient does not only take into account the cross section $\sigma(\omega)$ but also the population difference $w = \rho_{\text{gg}} - \rho_{\text{ee}}$. It thus quantifies the atom's ability to absorb a photon (quantified by the cross section $\sigma(\omega)$) in consideration of the fraction of atoms which already populates the excited state. In case of low excited state population the atom can absorb more energy from the beam than in case of saturation which leads to equalisation of the populations and thus $w \to 0$ and $\kappa \to 0$ which, in terms of the photon absorption affinity, means that the atom cannot absorb any more photons since the excited state is "fully occupied".

Instead of the atom-related parameters it is, with respect to saturation, however much more instructive to consider the counterpart of the interaction, the radiation where κ can be identified as a measure for the fraction of incoming energy that is absorbed by the atom. As intuitively expected, in case of low intensity the atom absorbs the whole radiation energy. For high intensities above saturation though, the fraction of absorbed energy κ scales with approximately I_{sat}/I and thus starts to decrease considerably until finally no more energy is absorbed than added to the light field. This is the state where the net energy transfer between the atom and the light field becomes zero. The absorption coefficient thus nicely demonstrates that even excessive light intensity cannot push the excited state population above its maximum value as predicted by the steady state solution of the optical Bloch equations, given by Eq. (D.23).

---

[45] It is important to note that the last transformation step in Eq. (D.41) is (still) based on the assumption of monochromatic laser radiation. In case of broadband radiation one needs to account for this additional line broadening by replacing the Lorentzian function in Eq. (D.41) by the appropriate line shape function $g_1^{(\text{abs})}(\omega)$ with a width including the laser bandwidth Γ_{L} (cf. Section C.7). This more realistic situation is analysed in the following subsection.
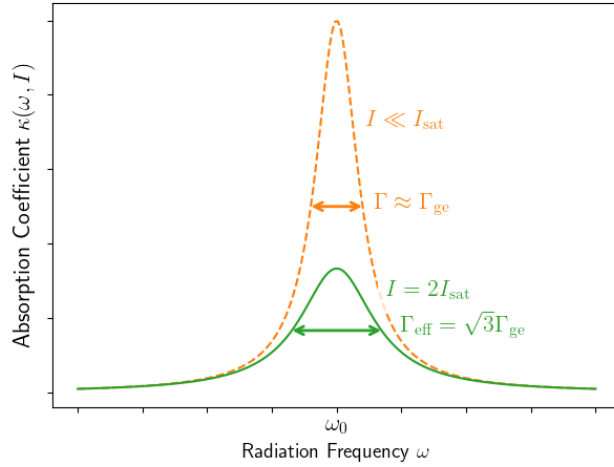
FIGURE D.1: *Illustration of power broadening by means of the Lorentzian absorption coefficient function.* Absorption coefficient $\kappa(\omega)$ as a function of frequency ω in case of weak light intensity $I \ll I_{\mathrm{sat}}$ (orange) and for $I = 2I_{\mathrm{sat}}$ (green). Intensities above saturation result in a broader Lorentzian line shape function (Γ_{eff}) with lower peak value, known as power broadening.

This gives rise to the question how intensities above saturation can then lead to a broadening of the line which can, however, be answered straightforwardly: As seen, with increasing light intensity the absorption coefficient will decrease since the ratio of absorbed intensity (= constant) and (increased) incoming intensity becomes smaller. This implies that the function of $\kappa(\omega)$ experiences an overall attenuation while keeping its original Lorentzian frequency dependence, as shown in Fig. D.1. Obviously, the increase in the width of $\kappa(\omega)$ due to high laser intensities is thus only an effective broadening that results from an overall reduction in amplitude.

While the fraction of absorbed radiation energy may be decreased above saturation (as reflected by an attenuation of $\kappa(\omega)$), this is not the case for its absolute value. Consequently, on resonance the excited state population $\rho_{\mathrm{ee}}(\omega_0)$ will not at all be affected by higher laser intensities. In contrast to $\kappa(\omega)$, the function of $\rho_{\mathrm{ee}}(\omega)$ therefore experiences a "real" broadening, which cannot be attributed to an amplitude reduction, as shown in Figure D.2. As it becomes clear from the functional dependence given in Eq. (D.38), for sufficiently high Rabi frequencies, that means intensities above the saturation threshold, the excited state population approaches its saturation value of $1/2$. The higher the intensity this more and more applies also to frequencies off-resonance since the intensity is then high enough to lead to appreciable population transfer also on frequencies adjacent to resonance.

Since power broadening is entirely unrelated to the laser spectrum it is not surprising that its derivation does not require to make any assumption with regard to the spectral distribution function of the laser intensity. This is in contrast to the derivation of the single-particle absorption spectrum $g_1^{(\mathrm{abs})}(\omega)$ which can only be written in a closed form in case of a Lorentzian spectrum (see Section C.7).

D.5.2   Saturation with broadband radiation

In the above treatment of saturation damping was restricted to the process of spontaneous emission. To include other influencing factors, such as the spectral characteristics of the irradiating light field, into the discussion, few modifications are required to accurately describe the saturation parameters. Since the definition of the saturation intensity primarily relies on the single-particle absorption
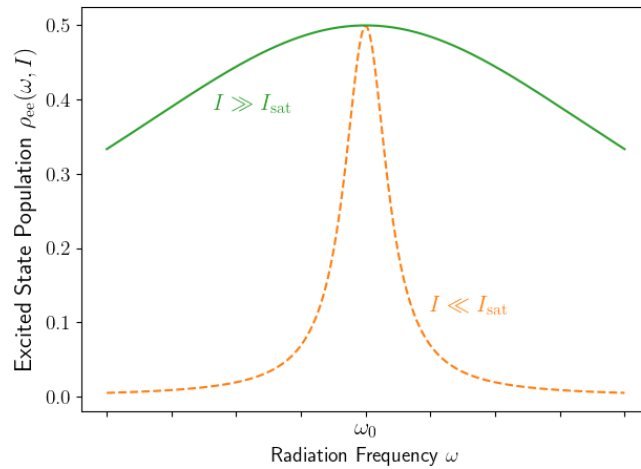
FIGURE D.2: *Illustration of power broadening by means of the Lorentzian function of the excited state population.* *Excited state population $\rho_{ee}(\omega)$ as a function of frequency ω in case of weak $I \ll I_{sat}$ (orange) and intense laser radiation $I \gg I_{sat}$ (green). In contrast to the function of the absorption coefficient $\kappa(\omega)$, in the case of ρ_{ee} intense light fields lead to a broadening of the Lorentzian function without affecting its amplitude. The population always saturates at a value of 1/2.*

linewidth $g_1^{(\mathrm{abs})}$ (cf. Eq. (C.61)) via the absorption cross section $\sigma(\omega)$ these modifications originate from an altered line shape. This linkage implies that any line broadening mechanism will have an effect on the saturation as well. Again, the most prominent example to mention in this respect is the bandwidth in case of excitation by broadband radiation.

At the same time this makes clear that saturation is an effect that is purely based on the transition line shape and is not at all related to the concept of coherence. As explained at the beginning of this section (cf. Sec. D.4.1 on p. 188) there is no causal link between line broadening and (de)coherence. Consequently, the radiation does not necessarily have to be incoherent to give rise to line broadening and thus difference in the saturation parameters. Rather, coherent broadband spectra will have the very same effect as incoherent ones of similar bandwidths.

Even though the following treatment of course applies to any mechanisms which affects the line shape in a similar way as broadband laser spectra do, below the focus shall lie especially on the inclusion of the laser bandwidth Γ_{L}.

As detailed in the context of the absorption rate $\gamma_{\mathrm{i}\to\mathrm{f}}(\omega)$ in Sec. C.7 the bandwidth Γ_{L} can easily be taken into account by replacing the natural width Γ_{ge} in the line shape function $g(\omega)$ by the effective width[46] $\Gamma_{\mathrm{ge}} + \Gamma_{\mathrm{L}}$. This modification of course translates to all expressions derived from the line shape function, especially including the saturation intensity $I_{\mathrm{s}} = \frac{\hbar\omega A_{\mathrm{eg}}}{2\sigma(\omega)}$ which depends on the line shape via the cross section $\sigma(\omega)$. It can easily be derived that appropriate adaptation of the linewidth finally yields the modified saturation intensity

$$I_{\mathrm{sat,L}} = \frac{\pi}{3}\frac{hc}{\lambda_0^3}(\Gamma_{\mathrm{ge}} + \Gamma_{\mathrm{L}}) = I_{\mathrm{sat}} \times \frac{\Gamma_{\mathrm{ge}} + \Gamma_{\mathrm{L}}}{\Gamma_{\mathrm{ge}}} \ . \tag{D.42}$$

In case the radiation does not only exhibit a broad spectrum but additionally an intensity comparable or bigger than this saturation intensity, the steady state absorption line becomes subject to even three broadening mechanisms. The line is then not only widened due to the intrinsic natural

---

[46] For the sake of presentability, this is again based on the assumption of a Lorentzian laser spectrum and only valid then.

broadening but also due to the two laser-induced effects of non-monochromatic excitation and power broadening.

In this situation the steady state absorption linewidth is described by the non-monochromatic power-broadened linewidth $\Gamma_{\text{eff,L}}$ which is the modified version of the effective linewidth Γ_{eff} (cf. Eq. (D.39)) valid for monochromatic excitation. A mathematical expression for $\Gamma_{\text{eff,L}}$ can be obtained in a similar way[47] as for Γ_{eff} in consideration of the linewidth adjustment $\Gamma_{\text{ge}} \to \Gamma_{\text{ge}} + \Gamma_{\text{L}}$. Exactly the same result can more straightforwardly, albeit less rigorously[48], be obtained by simply replacing all Γ_{ge} in the last (but explicitly not the first) expression for Γ_{eff} in Eq. (D.39) by $\Gamma_{\text{ge}} + \Gamma_{\text{L}}$ and I_{sat} by $I_{\text{sat,L}}$ which results in the non-monochromatic power-broadened linewidth

$$
\begin{aligned}
\Gamma_{\text{eff,L}} &= (\Gamma_{\text{ge}} + \Gamma_{\text{L}})\sqrt{1 + \frac{I}{I_{\text{sat,L}}}} \\
&= (\Gamma_{\text{ge}} + \Gamma_{\text{L}})\sqrt{1 + \frac{I}{I_{\text{sat}}}\frac{\Gamma_{\text{ge}}}{\Gamma_{\text{ge}} + \Gamma_{\text{L}}}} \quad = \quad (\Gamma_{\text{ge}} + \Gamma_{\text{L}})\sqrt{1 + \frac{2\Omega^2}{\Gamma_{\text{ge}}(\Gamma_{\text{ge}} + \Gamma_{\text{L}})}} \; .
\end{aligned}
\tag{D.43}
$$

D.5.3 Saturation of the Ps laser cooling transition

To convey an impression of the actual values for the application of Ps laser cooling, Tab. D.1 gives an overview of the excitation rate on resonance, the saturation intensity and power-broadened linewidths for monochromatic (upper table) as well as broadband excitation (middle table) with laser bandwidths of either $\Gamma_{\text{L}} = 2\pi(75\,\text{GHz})$ or $2\pi(150\,\text{GHz})$. For comparison, the last table additionally specifies the values of the natural linewidth Γ_{ge}, the Doppler-broadened width for a temperature of $300\,\text{K}$ and the angular frequency ω_{rec} associated with the energy of the recoil which accompanies the absorption or emission of a single photon. The latter is a quantity of great importance with regard to laser cooling as the following section will show. All values apply to the transition from 1^3S_0 to 2^3P_1 in the Ps atom at an energy of $E/(hc) = 41148.23871\,\text{cm}^{-1}$, used for laser cooling.

The Rabi frequency Ω is calculated from the laser power P based on the assumption of a Gaussian laser waist of $w_{\text{L}} = 5\,\text{mm}$. It results from the relation $\hbar\Omega = d_{\text{ge}}E_0$ where $d_{\text{ge}} = |\boldsymbol{d}_{\text{ge}}|$ is the absolute value of the transition dipole moment $q\boldsymbol{r}$ and $E_0 = |\boldsymbol{E}_0|$ the electric field amplitude of the irradiating light. Using the expression $I = \epsilon_0 c E_0^2/2$ for the irradiance and the relation $I = 2P/(\pi w_{\text{L}}^2)$ which links I and P and deducing d_{ge} from the Einstein coefficient $A_{\text{ge}} = 8\pi^2 d_{\text{ge}}^2/(3\epsilon_0 \hbar \lambda_0^3)$ finally yields

$$
\Omega = \sqrt{\frac{12c^2}{\hbar\omega_0^3\tau}\frac{P}{w_{\text{L}}^2}}
\tag{D.44}
$$

where $\tau = A_{\text{ge}}^{-1} = 3.19\,\text{ns}$ denotes the natural lifetime of the transition and $\omega_0 = 2\pi c/\lambda_0$ the resonance angular frequency.

The values specified in the middle table in Tab. D.1 are the ones which can be found in experimental environments aiming at Ps laser cooling. The laser parameters used represent the ones also applied in the numerical studies.

---

[47] This can be achieved by deriving the function of the absorption coefficient $\kappa_{\text{L}}(\omega)$ (or alternatively of the excited state population $\rho_{\text{ee,L}}(\omega)$) for the case of non-monochromatic excitation. The meticulous calculation is based on the single-particle absorption line shape $g_{1,\text{L}}^{(\text{abs})}(\omega)$ (with Γ_{ge} properly replaced by $\Gamma_{\text{ge}} + \Gamma_{\text{L}}$), the accordingly adjusted expression for the cross section (cf. Eq. (D.33)), the steady state condition $(N_{\text{g}} - N_{\text{e}})\sigma(\omega)I = N_{\text{e}}\Gamma_{\text{ge}}\hbar\omega$ (with the population N_i in state i and $\Gamma_{\text{ge}} = A_{\text{ge}}$) and the relation $I = (\hbar\omega^3/(6\pi c^2 A_{\text{ge}}))\Omega^2$, which links the laser irradiance I and Rabi frequency Ω (with the transition dipole d being determined by the definition of A_{ge}), finally yields $\kappa_{\text{L}}(\omega) = N\sigma_0/(2\pi)\,\Gamma_{\text{tot}}/(\delta^2 + \Gamma_{\text{tot}}^2/4[1 + 2\Omega^2/(\Gamma_{\text{ge}}\Gamma_{\text{tot}})])$ where $\Gamma_{\text{tot}} = \Gamma_{\text{ge}} + \Gamma_{\text{L}}$.
Alternatively (and strictly speaking only valid for incoherent spectra), the same result can be obtained by considering the broadband laser as a transverse relaxation process in which case $\Gamma_\perp = \Gamma_{\text{ge}} + \Gamma_{\text{L}}$. Solving the generalised optical Bloch equations for the excited state population $\rho_{\text{ee}} = (1 - w)/2$ finally yields a function featuring the very same effective width $\Gamma_{\text{eff,L}}$.

[48] Since this does not give insight in the physical cause and does not explain why the line has the width that it needs to have, it is recommended to refrain from this approach. Instead, it is certainly worth making the effort to take the much more instructive path outlined in the previous Footnote 47.

The resulting numbers presented in Tab. D.1, especially the values for the non-monochromatic power-broadened width $\Gamma_{\mathrm{eff,L}}$, might, at first glance, appear incredibly huge. However, here the same argument applies as already above for power broadening. As elucidated in the context of Γ_{eff} with the aid of the function of the absorption coefficient $\kappa(\omega)$, given by Eq. (D.41), line broadening in fact originates from an effective diminution of the amplitude of the function since (for large Γ) the absorption coefficient $\kappa(\omega)$ (or the excited state population $\rho_{\mathrm{ee}}(\omega)$, respectively) scales with the inverse of the applicable broadened rate Γ (cf. $\kappa_{\mathrm{L}}(\omega)$ in Footnote 47).

Apart from the influence on the populations and the line shape, the light field perturbation has an impact also on the absolute energy of the states. This effect is known as the *light shift* or sometimes also referred to as *AC Stark effect*, in analogy to the Stark effect caused by static electric fields. The energy shift is of the order of the Rabi frequency and thus becomes stronger with increasing radiation intensity. To convey an impression of its strength: If the atom is driven on the laser cooling transition from $1^3\mathrm{S}_0$ to $2^3\mathrm{P}_1$ (at an energy of $E/(hc) = 41148.23871\,\mathrm{cm}^{-1}$), the energy shift is of the order of few cm^{-1} for typical laser powers of about $10\,\mathrm{kW}$. However, since, in the case of Ps laser cooling, this phenomenon does not become apparent in the spectrum (which is based on energy differences), it shall not be expounded further here. It is worth mentioning, though, that the light shift is nevertheless implemented in the code used for simulating positronium laser cooling.

Finally, it shall be remarked that, even though the discussion above was restricted to transitions between bound states, this semiclassical approach can, with slight modifications, be extended and likewise be applied for example to photoionisation for transitions from a bound to an unbound state. The probability for such events to occur is given by the cross section $\sigma^{(\mathrm{phion})}$ specified in Section C.4.4. The main difference to transitions between bound states is the fact that photoionisation naturally represents a one-way process for which emission can of course not occur.

D.6 Summary

To draw conclusions with regard to the application of the above results to Ps laser cooling it is worth to briefly summarise the main message of the discussion.

Considering the solution of the central set of dynamical equations, the Bloch equations, one clearly observes two regimes of the dynamics. In the first case, the system evolves in a predominantly coherent way with defined phase relations between the atomic states which gives rise to certain coherent phenomena characterised by the Rabi frequency Ω, such as the Rabi oscillations.

However, as soon as the coherent evolution is damped, that means dephases as a result of the influence of any incoherent process such as inherent spontaneous emission or incoherent broadband radiation, the evolution passes over to the second regime in which the system enters into a quasi-steady incoherent state. Since here coherences no longer have to be considered, the treatment can be reduced to the evolution of the populations which are adequately described by rate equations with statistical transition probabilities related to the Einstein coefficients.

In case the system does not already start in the incoherent regime (due to incoherent broadband excitation from the outset, for example), the transition from the first to the second regime takes place rather smoothly and gradually. The time scale on which the second regime sets in is determined by the transverse relaxation rate $\Gamma_\perp$ of the system, i.e. the rate at which the coherent dynamics dephases due to incoherent perturbations (cf. Sec. D.4.3 on p. 190).

Depending on the impact of these incoherent processes, one has to distinguish between mainly three scenarios:

1. In case of fast dephasing, that means $\Gamma_\perp$ much bigger than the rate Ω which characterises the coherent evolution, coherences cannot even develop in the first place. In this case the system evolves in an incoherent way right from the beginning of the interaction since the dominance of incoherent processes forces it to directly assume the quasi-steady state. The distribution of the populations on the involved atomic states, that means the ratio $N_{\mathrm{e}}/N_{\mathrm{g}}$, is thereby determined by the light intensity and can be quantified by the saturation parameter

Monochromatic Radiation					
Laser Power P	Laser Bandwidth Γ_L	Rabi Frequency Ω (D.44)	Excitation Rate $\gamma_{if}(\omega_0)$ (C.65)	Saturation Intensity I_{sat} (D.34)	Power-broad. Linewidth Γ_{eff} (D.39)
5 kW	—	$37.102\,\mathrm{ns}^{-1} =$ $2\pi(\mathbf{5.90\,GHz})$	$1464.20\,\mathrm{ns}^{-1} =$ $2\pi(\mathbf{233.03\,GHz})$	$0.453\,\frac{\mathrm{W}}{\mathrm{cm}^2}$	$52.56\,\mathrm{ns}^{-1} =$ $2\pi(\mathbf{8.36\,GHz})$
10 kW	—	$52.471\,\mathrm{ns}^{-1} =$ $2\pi(\mathbf{8.35\,GHz})$	$2928.40\,\mathrm{ns}^{-1} =$ $2\pi(\mathbf{466.07\,GHz})$		$74.32\,\mathrm{ns}^{-1} =$ $2\pi(\mathbf{11.83\,GHz})$

Incoherent Broadband Radiation					
Laser Power P	Laser Bandwidth Γ_L	Rabi Frequency Ω (D.44)	Excitation Rate $\gamma_{if}(\omega_0)$ (C.65)	Saturation Intensity $I_{sat,L}$ (D.42)	Power-broad. Linewidth $\Gamma_{eff,L}$ (D.43)
5 kW	$471.24\,\mathrm{ns}^{-1}$ $= 2\pi(\mathbf{75\,GHz})$	$37.102\,\mathrm{ns}^{-1} =$ $2\pi(\mathbf{5.90\,GHz})$	$0.973\,\mathrm{ns}^{-1} =$ $2\pi(\mathbf{154.92\,MHz})$	$689.131\,\frac{\mathrm{W}}{\mathrm{cm}^2}$	$2092.17\,\mathrm{ns}^{-1} =$ $2\pi(\mathbf{332.98\,GHz})$
10 kW		$52.471\,\mathrm{ns}^{-1} =$ $2\pi(\mathbf{8.35\,GHz})$	$1.947\,\mathrm{ns}^{-1} =$ $2\pi(\mathbf{309.83\,MHz})$		$2920.96\,\mathrm{ns}^{-1} =$ $2\pi(\mathbf{464.88\,GHz})$
5 kW	$942.48\,\mathrm{ns}^{-1}$ $= 2\pi(\mathbf{150\,GHz})$	$37.102\,\mathrm{ns}^{-1} =$ $2\pi(\mathbf{5.90\,GHz})$	$0.487\,\mathrm{ns}^{-1} =$ $2\pi(\mathbf{77.48\,MHz})$	$1377.808\,\frac{\mathrm{W}}{\mathrm{cm}^2}$	$3032.44\,\mathrm{ns}^{-1} =$ $2\pi(\mathbf{482.63\,GHz})$
10 kW		$52.471\,\mathrm{ns}^{-1} =$ $2\pi(\mathbf{8.35\,GHz})$	$0.974\,\mathrm{ns}^{-1} =$ $2\pi(\mathbf{154.97\,MHz})$		$4183.61\,\mathrm{ns}^{-1} =$ $2\pi(\mathbf{665.84\,GHz})$

For Reference	
Natural Linewidth	$\Gamma_{ge} = 313.48\,\mu\mathrm{s}^{-1} = 2\pi(\mathbf{49.74\,MHz})$
Doppler-Broadened FWHM	$\Gamma_{Doppler} = 2902.35\,\mathrm{ns}^{-1} = 2\pi(\mathbf{461.92\,GHz})$
Recoil-Equivalent Frequency	$\omega_{rec} = E_{rec}/\hbar = 19.3\,\mathrm{ns}^{-1} = 2\pi(\mathbf{3.07\,GHz})$

TABLE D.1: *Overview of saturation parameters for the 1^3S_0 to 2^3P_1 transition in positronium.*
*The table in the **top** specifies the values for the Rabi frequency Ω, the excitation rate $\gamma_{if}(\omega_0)$ on resonance, the saturation intensity I_{sat} and the power-broadened linewidth Γ_{eff} for the excitation of the 1^3S_0 to 2^3P_1 transition by monochromatic radiation and laser powers of $P = 5\,\mathrm{kW}$ and $10\,\mathrm{kW}$. A Lorentzian laser spectrum has been assumed to enable easy calculation of the excitation rate by means of Eq. (C.65).*
*The table in the **middle** shows the values for the equivalent parameters $I_{sat,L}$ and $\Gamma_{eff,L}$ valid in case of non-monochromatic excitation by a laser with typical bandwidths of $\Gamma_L = 2\pi(75\,\mathrm{GHz})$ (upper row) or $2\pi(150\,\mathrm{GHz})$ (lower row) but similar laser powers.*
*For comparison the **bottom** table presents the values of the natural linewidth Γ_{ge}, the Doppler-broadening (in terms of the FWHM $\Delta\omega_{Doppler}$ in angular frequency space) for a temperature of $300\,\mathrm{K}$ and the angular frequency ω_{rec} associated with the energy of the recoil which accompanies the absorption or emission of one photon. All values apply for the transition from 1^3S_0 to 2^3P_1. Reference is made to the equations used to calculate the values. For reasons of clarity and comparability, the frequencies (in units of GHz) corresponding to quantities which typically represent angular frequencies are written in bold print.*

s. The excited state population in a 2-level atom saturates at $1/2$, intense perturbation thus results in equalisation of the populations.

2. In the second limiting case with negligible damping the Rabi frequency by far exceeds $\Gamma_\perp$ so that the atom can evolve in an almost entirely coherent way. This can only be achieved by means of monochromatic or coherent broadband laser light which preserves the phase relations between $|g\rangle$ and $|e\rangle$.

3. Finally, if neither coherent nor incoherent effects dominate the values of the Rabi frequency Ω and damping rate $\Gamma_\perp$ are of a comparable order of magnitude. If decoherence is then mainly induced by spontaneous emission the system starts to evolve in a coherent way which gradually dephases and passes over into the second regime, before eventually the steady state is reached. In case of incoherent excitation the stochastic phase fluctuations provokes additional phase damping. The system then first assumes a quasi-steady state before it fully enters into the steady state after interaction times much longer than the longitudinal relaxation time. The dynamics can however be described by incoherent rate equations already prior to the final steady state. The only requirement to this end is that coherences have vanished.

In all damping scenarios, additional decoherence arises from the incoherent processes leading to transition line broadening proportional to the corresponding rates Γ.

Thus, only in case of excitation by means of coherent or very narrow-band incoherent light fields it becomes mandatory to treat the level dynamics in the most general framework of the full optical Bloch equations. In all other cases it is, at least on time scales bigger than the longitudinal relaxation time $t_\parallel = \Gamma_\parallel^{-1}$, fully justified to make use of a rate equation approach to study the internal dynamics of the atom during interaction with the laser.

A review of the numbers given in Tab. D.1, which specify the values of all relevant parameters for Ps laser cooling, reveals that coherent effects are usually highly suppressed by fast relaxation, especially in case of incoherent laser radiation with bandwidths of the order of several tens of GHz. Consequently, under these conditions the coherent level dynamics dephases on such short time scales ($\Gamma_\perp^{-1} \lesssim \Gamma_\text{L}^{-1} = [2\pi(75\,\text{GHz})]^{-1} = 2.1\,\text{ps}$, much shorter than typical interaction times of several tens of nanoseconds) that the occurrence of coherent effects is prevented right from the start. A rate equation approach is thus valid in all cases.

In most cases, the absorption line is additionally subject to strong power-broadening since employed laser setups are intended to provide highest possible amounts of energy.

Appendix E

Differentiation between narrow- and broad-line cooling

If the orientation of the recoils resulting from spontaneous emission were not distributed isotropically but all along a preferential direction, one could imagine that the atom could almost be brought to a halt in the centre of three orthogonal pairs of counter-propagating laser beams. The spatial randomness, i.e. isotropy, of the process however gives rise to a diffusion of the particle velocities in momentum space which persists throughout the whole process. Since it counteracts the cooling process the resulting random walk can be considered as a process of heating which limits cooling to a certain value that depends on the fundamental velocity steps. As soon as the atom no longer has an appreciable velocity component pointing towards the laser source, cooling and heating enter into a mutual equilibrium and the temperature can no longer be reduced. It is then the fluctuations in the orientation of the spontaneous recoils which dominate the process. This is the state which is referred to as cooling limit. It is typically quantified in terms of the minimum temperature $T_{\min}$ which the atomic cloud can be cooled down to in the standard 1D cooling configuration through interaction with a pair of counter-propagating laser beams in the (1D) optical molasses configuration. To evaluate the minimum temperature value it is thus necessary to have a closer look on the sequence of spontaneous recoils.

The standard way of treating the cooling limit is based on the assumption that the fluctuations of the force (due to isotropy of spontaneous recoils) lead to a random walk of the atoms in momentum space which can be described by the concept of Brownian motion. Based on this model it is possible to assign a diffusion coefficient D to the process which is responsible for heating. This finally allows to treat the momentum fluctuations in a mathematical way and express the radiation force as well as the minimum temperature in terms of D (cf. for example Ref. [90] for a detailed derivation).

It is often concealed, though, that the atoms can only be considered as Brownian particles under the condition that momentum changes occur at a constant rate. Only a continuous sequence of sufficiently small steps produces a trajectory in momentum space which resembles a random walk over time. In case the sequence is occasionally interrupted for arbitrary periods of time this model can in fact though become highly problematic and invalid.

It should be noted that the very accurate description soon gets quite complex as it is related to theoretical concepts such as the fluctuation-dissipation theorem, whose introduction is out of the scope of this thesis. With regard to the special case of Ps laser cooling for which the standard treatment might become invalid, it is nevertheless important to scrutinise the derivation of the cooling limit. For this reason, the following sections will address the question in a rather heuristic way. A very thorough treatment of the topic can instead be found in Refs. [94], [90] but also [92] and [89].

E.1 The fundamental process

To understand under which conditions the path of the atom in momentum space consists of a continuous sequence of fundamental steps or is composed of irregular discrete jumps, and to show how the validity of the standard approach is linked to the laser interaction parameters, it is necessary to go back to the most basic level and recall the processes taking place at the cooling

limit. This will finally allow to define a decisive criterion on the basis of which the applicability of the Brownian motion approach can be assessed.

E.1.1 The interdependence of subsequent recoils

As far as the internal dynamics is concerned, the most basic process is of course the succession of photon absorption and emission events which is linked to the external motion via the transfer of momentum that accompanies each transition event. As explained earlier, due to the fact that the combination of absorption and stimulated emission do not contribute to the cooling process since their recoils cancel each other, it is especially the spontaneous emission events which are relevant for laser cooling. Since the heating process arises as well from spontaneous emission, due to the isotropy of the corresponding recoils that produces the randomness of the trajectory, it is sufficient to focus completely on these events[49].

To proceed with the heuristic treatment, it is important to point out that the link between external and internal motion is not only given by the fact that internal transitions are accompanied by transfer of momentum, but that the resulting recoils which govern the external motion of the atom in turn retroact on variables that influence the internal processes. This loop entails that each recoil might have an indirect impact on subsequent photon scattering events.

This link can best be illustrated by means of the effect of single events in frequency domain: Each spontaneous recoil will leave the atom behind with a modified velocity which, in frequency space, produces an additional Doppler shift $\boldsymbol{k}\boldsymbol{v}_{\mathrm{rec}}$. Consequently, all properties which depend on the detuning $\delta = \omega + \boldsymbol{k}\boldsymbol{v} - \omega_0$ will be affected as well. This concerns especially the absorption rate $\gamma_{\mathrm{g}\to\mathrm{e}}(\omega)$ but also the excited state population $\rho_{\mathrm{ee}}(\omega)$ and the saturation parameter s.

E.1.2 Impact and consequences of a single recoil

Obviously, each spontaneous recoil is thus capable of transferring the atom into a state that is described by potentially completely different characteristic parameters. The likelihood for considerable changes, however, largely depends on the width of the transition line. In case the atom is excited on a very broad line (in terms of ω_{rec}) a single recoil can naturally only have very little influence on the parameters $\gamma_{\mathrm{g}\to\mathrm{e}}(\omega)$, $\rho_{\mathrm{ee}}(\omega)$ or s since the corresponding functions spread over a large frequency interval, compared to which ω_{rec} appears rather small. In this case, these parameters evolve very "smoothly" over the course of a large number of absorption-emission cycles which especially means that the excitation probability is almost identical for consecutive absorption-emission cycles and that the transition rate stays on a constant (high) level, ensuring that the atom is immediately re-excited after decay to the ground state. This in turn implies that the rate at which random (spontaneous) recoils occur remains as well at a constantly high level, given (and limited) by its maximum value[50] Γ_{ge}.

In contrast, if the atom is excited on a very narrow transition, only a single recoil might already have severe implications on the interaction parameters, even though the size ω_{rec} of the recoil naturally remains unchanged. In the extreme case where the line is not broad enough to accommodate only a single recoil, the atom might even be kicked completely out of resonance so that interaction with the laser stops immediately.

But also in a less extreme scenario the interaction parameters and especially the transition rate γ can still be severely affected by a single cycle of absorption and spontaneous emission. A

---

[49] It should be noted that in reality it is, as usual, not as easy as this: Strictly speaking, the restriction to spontaneous emission events is not entirely correct as it ignores the fact that it might as well happen that an atom is excited by one beam but stimulated to decay by the counter-propagating one, thereby creating a net force on the atom. This contribution to the movement shall however be neglected here by assuming that it averages away. Its possibility should nevertheless be kept in mind as it demonstrated that the cycles of absorption and stimulated emission events play a subtle role as well, which at first glance might not directly become apparent.

[50] Note, that it was implicitly assumed here that the transition is saturated by the laser radiation which is normally the case in Doppler laser cooling. If this was not the case, the atom would remain for a certain period of time in the ground state before being re-excited which effectively reduces the average rate at which spontaneous emission eventss take place.

reduction in transition rates directly implies that the atom stays in the ground state for a longer time which in turn extends the average interval between spontaneous emission events. Consequently, in case of narrow transition lines, recoils occur by far not as regularly as in the case where the linewidth is much larger than ω_{rec}.

This shows how the properties of recoils are affected by preceding recoils and how this finally determines the appearance of the evolution in momentum space: If the transition line is sufficiently broad (with respect to ω_{rec}) interaction parameters barely change from one recoil event to the next. Consequently, spontaneous emissions occur at a constant rate, resulting in a continuous sequence of fundamental steps in momentum space which over time resembles a random walk. In contrast, in case of relatively narrow lines, the sudden modifications of the transition rate $\gamma_{\mathrm{g}\to\mathrm{e}}$ or the saturation parameter s randomly produces absence of spontaneous recoils which, in the course of time, makes the trajectory in momentum space rather look like a path consisting of irregular discrete jumps.

E.2 Broad- vs. narrow-line transitions

As the above discussion suggests, it is convenient to distinguish between mainly two cases, based on the width Γ of the transition line. This distinction is not only useful to decide on an applicable model for treating the fluctuations at the cooling limit but serves as well as a general classification criterion of the cooling configurations as will become clear later.

The following terminology has established for the two cases. A transition with a linewidth Γ much bigger than the frequency ω_{rec} associated with a single recoil is simply referred to as a *broad-line transition* and the corresponding condition $\Gamma \gg \omega_{\mathrm{rec}}$ as the *broad-line condition*. Since in such configurations the recoil energy ω_{rec} appears small compared to the linewidth, frequency-dependent variables such as the absorption probability $\gamma_{\mathrm{g}\leftrightarrow\mathrm{e}}$ evolve in a very smooth way over time. The opposite case of transitions with a linewidth Γ much smaller than ω_{rec} is logically called *narrow-line transition* and the corresponding inequality $\Gamma \ll \omega_{\mathrm{rec}}$ as the *narrow-line condition*.

In the context of these definitions, it should be mentioned that the conditions introduced above are in fact modified versions of the conditions that can generally be found in literature. There ω_{rec} is often compared to only the spontaneous rate Γ_{ge} instead of the full linewidth Γ (cf. for example in Ref. [94]). These descriptions are in general though focussed on cooling in the most usual broad-line configuration for which it does not matter whether the Γ or Γ_{ge} is used since the latter is anyway always smaller than Γ, i.e., $\Gamma_{\mathrm{ge}} < \Gamma$. With regard to the narrow-line case, though, it makes a huge difference which rate is applied.

Ps laser cooling represents a very good example in this regard: Obviously, due to the huge recoil energy of the Ps atom, all transitions exhibit spontaneous decay rates Γ_{ge} much smaller than ω_{rec} and would, according to the strict condition, based on Γ_{ge}, directly be classified as narrow lines. However, if $\Gamma > \omega_{\mathrm{rec}}$ can be satisfied and recoils occur continuously, at a constant rate Γ_{ge} the Brownian motion approach might still be applicable (even though only after thorough scrutiny).

Finally, the use of Γ instead of Γ_{ge} shows that it is, to a certain extent, possible to influence which case a given cooling configuration belongs to: While Γ_{ge} and ω_{rec} are unchangeable constants, the transition linewidth Γ is a quantity which can be modified by the type of laser radiation used. As seen before (cf. Tab. D.1), the use of high-intense broadband radiation allows to enhance the transition linewidth to such an extent, to $\Gamma_{\mathrm{eff,L}}$, that it by far exceeds the recoil-equivalent frequency ω_{rec}. By "artificially" modifying the transition line it is thus in principle possible to recover the broad-line condition for an initially narrow-line configuration [92].

To return to the initial question of the condition which decides upon the applicability of a Brownian motion approach, it can be concluded that the answer is by the competition of the energetic width of the transition and the recoil energy. If the line is broad enough to easily accommodate single recoils, the evolution takes place in a smooth way, variables can considered as continuous instead of discrete quantities and the motion can be treated in the Brownian motion

formalism based on a diffusion model. Cases with $\Gamma_{ge} \ll \omega_{rec}$ can only be treated in this way if the transition line can be broadened sufficiently.

E.3 Comparison of time scales

Switching the perspective and considering the process from the time instead of frequency domain conveys further interesting insights in the process. This helps to understand why the definition of the photon scattering force given above (cf. Eq. (2.37)) is only valid under certain conditions.

Based on the fact that the rate of spontaneous recoils is governed by the lifetime of the excited state, the condition for the classification into broad- or narrow-lines can be identified as a comparison of the time scales of the evolution of the variables which characterise the internal and external dynamics [171]:

In contrast to the internal motion, the time scale of the external dynamics is however not as obvious. According to the classical concept of speed and acceleration, the characteristic time t_{ext} of the movement of the atom can be interpreted as the time that it takes to observe an appreciable change in motional parameters. A useful definition is for instance given by the time which passes until the velocity v of a resonant atom has changed to such an extent that the atom becomes non-resonant. This applies if the Doppler shift kv becomes bigger than about twice the transition linewidth Γ, that means $kv = 2\Gamma$. Based on the characteristic acceleration of the sysem, given by the product Γv_{rec} of decay rate Γ and the elementary velocity steps of the process, v_{rec}, the velocity v of the atom can thus be written as $v = at_{ext} = \Gamma v_{rec} t_{ext}$. Hence, the time t_{ext} that passes until $kv = 2\Gamma$, is given by

$$t_{ext} = \frac{2}{kv_{rec}} = \frac{1}{\omega_{rec}} \ . \tag{E.1}$$

Obviously, the bigger the recoil energy $\hbar\omega_{rec}$, the faster do variables of the external motion change.

As discussed above, the validity of the Brownian motion approach relies on the continuity of spontaneous recoil events and is thus governed by the transition linewidth Γ. Additionally, the discussion of decoherence in coherent atom-light interaction revealed (cf. Secs. D.4.1 and D.4) that the linewidth is linked to the relaxation rate of the internal dynamics, even though only indirectly For this reason, the characteristic time scale of the internal motion can be defined as the time t_{int} that it takes until the level dynamics, described by the optical Bloch equations, reaches a steady state in which the evolution exhibits entirely incoherent character and the populations have adopted constant values. The time t_{int} of appreciable changes in internal variables is thus of the order of the relaxation time $\Gamma_\perp^{-1}$. The faster the relaxation, that means the faster the evolution dephases and the system settles into a steady state, the faster it reacts and adapts to sudden changes of interaction parameters.

The physical relevancy of these time scales becomes clear from the comparison of the two: In case of very slow external motion (i.e. long t_{ext} and small ω_{rec}) with respect to the internal response time, that means $t_{ext} \gg t_{int}$, the population equilibrium can well adapt to the new situation with modified interaction parameters. This implies that the internal state of the atom is at all times well described by steady state equations. Translated back to the frequency domain this is equivalent to the requirement $\omega_{rec} \ll \Gamma$, which can easily be identified as the broad-line condition.

It can be concluded that, under broad-line conditions, the atom can "adiabatically follow" the external evolution and is thus well described by expressions valid for the steady state. In the opposite case with very slow relaxation or too fast external motion, the system can however not react sufficiently fast to follow the evolution. This implies that the states still evolve coherently which requires to consider the full density operator instead of only the populations.

This shows that the differentiation between broad- and narrow-line transition is directly related to the evolution of the internal state dynamics. Obviously, the evolution at the cooling limit can only be considered as a random walk and treated by means of the concept of diffusion if the

level populations are able to adapt sufficiently fast to parameter changes induced by transfer of momentum in portions of $\hbar k$.

E.4 Scattering force revisited

In view of these results, it is necessary to revise the validity of the expression for the scattering force given by Eq. (2.37). By expressing the force in terms of the scattering rate $\Gamma_{ge}\rho_{ee}$ it was implicitly assumed that, on the time scale of the recoil-induced force, the internal dynamics has already reached a steady state, allowing for application of corresponding steady state equations. It was withheld though that this step becomes questionable in case of cooling on narrow-line transitions. The problem is that, as just explained, in the narrow-line case the internal dynamics does not react fast enough to adapt to the changes in external motion so that the use of steady state equations is simply not appropriate. Consequently, the given expression is not universally valid but only in case of relaxation rates of the order of at least the recoil frequency ω_{rec}.

Since the scattering force for narrow-line transitions is far more complex to derive and can furthermore only be written in an integral form [92], the broad-line scattering force was nevertheless introduced above as it conveys an impression of the mechanism and the force which the radiation exerts on the atoms. It is furthermore useful for assessing the spectral capture range of the radiation.

Appendix F

Simulation tool

The purpose of this appendix is to introduce the code used for the numerical investigations of Ps laser cooling performed in the scope of this thesis. Instead of describing very technical details it is the goal to outline the general approach and to present implemented numerical methods as well as the capabilities and versatility of the code with regard to the simulation of physical processes and effects.

F.1 The algorithm

The basis for the simulations performed for this thesis is a C++ code, originally developed by Daniel Comparat at the Université Paris-Saclay. Some details on its mathematical formalisms and concepts can also be found in the appendices to Refs. [169] and [47]. The code was developed under Code::Blocks (and Windows 64-bits) and is accessible under `https://github.com/dcompara/Laser-interaction-in-fields-rate-equations-forces`.

The algorithm is designed for the simulation of light-matter interaction by solving rate equations for absorption, spontaneous and stimulated emission of photons by atoms which move under external forces. Included are forces that are induced by scattering, dipolar interaction, external magnetic and/or electric fields and gravity. In case the particles are charged, the code takes into account N-body Coulombian interactions and Lorentz forces in addition to the types of interaction that also occur for neutral particles.

In the course of this thesis the simulation code has been refined further in order to allow for its use for general studies of positronium laser cooling in arbitrary magnetic fields as well as for investigations on the experimental scheme realised within the AEḡIS experiment.

F.1.1 General approach

It is important to emphasise that the implementation of particle-laser interactions in the code is not based on any approximation of the evolution by means of Brownian motion and the pressure force since these are only valid under certain conditions (cf. Section 2.4). Instead, to ensure highest versatility, the internal atomic dynamics is numerically simulated in the formalism of rate equations which are solved by means of a Kinetic Monte Carlo (KMC) algorithm that predicts the occurrence of single probabilistic transition events at a specified time step Δt. The KMC algorithm relies on pre-calculated rates for transitions between the eigenstates of the Hamiltonian of the given system which is defined by the input parameters (more details on those parameters will follow in Section F.4).

These eigenstates (and eigenvalues) result from diagonalisation of the full Hamiltonian in presence of magnetic and dynamical Stark fields. They are also used to derive external forces required for the calculation, such as the force exerted on the atom as a result of the transfer of momentum due to photon scattering, i.e., the recoil which accompanies photon absorption or emission events and which causes the atom to change its velocity. The evolution of the kinetic variables that describe the external motion of the atom in the fields is governed by Newton's equations of motion which is solved by means of a Verlet integrator.

A key assumption of the code is that the system evolves adiabatically in absence of photon transfer events that lead to changes of the internal state. This implies that the atom remains in the state $|nlsjm\rangle_{\boldsymbol{B}(t)}$ while moving under the field $\boldsymbol{B}$ at any time t. In this context, it is worth mentioning that the velocities of the atoms stay constant between consecutive transition events.

F.1.2 Calculation procedure

Schematically, in the code the basic procedure of the simulation of light-matter interaction in fields looks as follows:

1. Reading of input files and definition of parameters.

2. Initialisation of levels, transitions, external and internal states of the particles (i.e., initial positions $\boldsymbol{r}$, velocities $\boldsymbol{v}$ and level populations) as well as of the fields and laser beam(s).

3. Main time loop consisting of the following steps, repeated until $t > t_{\mathrm{final}}$.

    (a) (Re-)diagonalisation of Hamiltonian based on present fields and calculation of transition rates.

    (b) Prediction of transitions and according time of occurrence by KMC algorithm.

    (c) Evolution of dynamical variables $\boldsymbol{r}$ and $\boldsymbol{v}$ by Verlet and Boris algorithms under present forces and potentials based on analytically calculated Stark and Zeeman effects.

    (d) Evolution of internal states if applicable.

    (e) Output of defined parameters and variable values, such as particle velocities and positions or transition rates and internal states, to specified output files.

Each step includes numerous individual calculations which are executed by dedicated numerical functions. Those functions are thematically bundled and outsourced to separate code files, each designated for a specific task such as calculation of transition rates, diagonalisation or simply the (re-)initialisation of fields or particle positions. Further (technical) details about the individual files and functions as well as a more comprehensive explanation of the calculation procedure can be found in the user guide attached to the code files under the github link specified above.

F.2 Implementation of physical processes and applied numerical methods

Selected numerical methods shall briefly be considered in more details in the following. It is furthermore worth having a closer look on the incorporation of certain physical processes which are a bit more tricky to implement to ensure physically correct calculations.

F.2.1 Fundamental coordinate system

First of all, all vectors used in the course of the simulation such as for fields or lasers are defined according to the coordinate system shown in Fig. C.3. In order to ensure maximum applicability, fields and lasers are described in individual frames which are defined in polar coordinates relative to the lab frame, established by the unit basis vectors $\mathbf{e}_x$, $\mathbf{e}_y$ and $\mathbf{e}_z$.

All laser-related vectors are specified in the laser frame set up by the unit vectors $\mathbf{e}_x'$, $\mathbf{e}_y'$ and $\mathbf{e}_z'$ marked with primes. The laser frame is defined along the laser propagation direction $\boldsymbol{k}_{\mathrm{L}}$, with the $\mathbf{e}_z'$ vector corresponding to $\boldsymbol{k}_{\mathrm{L}}/\|\boldsymbol{k}_{\mathrm{L}}\|$. Its orientation with respect to the lab frame is fully defined by the polar angles θ for the $\mathbf{e}_z'$ axis and ϕ for the $\mathbf{e}_x'$ and $\mathbf{e}_y'$ axes. It is convenient to then describe the polarisation state of the lasers in the helicity basis $\mathbf{e}_0' = \mathbf{e}_z'$, $\mathbf{e}_{\pm 1}' = \mp(\mathbf{e}_x' \pm i\mathbf{e}_y')/\sqrt{2}$ relative to the laser frame. For each laser L the polarisation vector, defined as $\boldsymbol{E}_{\mathrm{L}}(\boldsymbol{r},t) = E_{\mathrm{L}}(\boldsymbol{r},t)\boldsymbol{\epsilon}_{\mathrm{L}}$, is thus given by $\boldsymbol{\epsilon}_{\mathrm{L}} = \sum_{p=-1,0,+1} \epsilon'^p \mathbf{e}_p'$ with $E_{\mathrm{L}} \geq 0$.

The magnetic and Stark fields (and thus also the quantisation axis of the system) in turn are described in yet another frame generated by the basis vectors $\mathbf{e}_X$, $\mathbf{e}_Y$ and $\mathbf{e}_Z$ that are labelled by capital letters.

F.2.2 Diagonalisation

Apart from the laser field, the key ingredients for the calculation of the atom-light interaction in the rate equation formalism are the individual transition dipole moments $\boldsymbol{d}$ for all considered transitions. It is not only the transition rates which, on the most fundamental level, rely on this quantity but also all derived interaction parameters such as the Rabi frequency, the saturation parameter and many more. The evaluation of the transition dipole moments is however not as straightforward as for the laser beams and spectra. While the latter can simply be defined by a set of parameters and values such as the intensity, the polarisation and the spectral bandwidth, the specified dipoles are only valid for zero fields. To properly account for arbitrary fields considering the fact that the Stark field can change during laser interaction, it is required to (re-)calculate the applicable dipoles after each transition event. With respect to the numerical simulation for which the evolution is discretised in time, this more precisely means to evaluate the transition dipole matrix elements $\boldsymbol{d}_{ij} = \langle i|\boldsymbol{d}|j\rangle$, in the quantisation frame, at each time step of the KMC algorithm.

The calculation of the transition dipole matrix elements itself becomes complicated by the fact that it is based on the eigenstates $|i\rangle$ and $|j\rangle$ that are applicable at the respective point of time that means under then present local fields. To obtain these perturbed eigenstates and -values, the code diagonalises the Hamiltonian in the presence of magnetic and dynamical Stark fields based on given zero-field Hamiltonian matrix elements that are calculated beforehand (separately by means of a MATHEMATICA code) and embedded into the code files. The unperturbed eigenstates required for diagonalisation are described in the zero-field $|nlsjm\rangle$ base defined with respect to the quantisation axis (which governs the momentum projection m). Due to adiabaticity, implying that the atom remains in its current state while moving under the field $\boldsymbol{B}$ at any time t, the quantisation axis can be associated with the magnetic field and the state can consequently be labelled by an index $B(t)$, i.e., $|nlsjm\rangle_{\boldsymbol{B}(t)}$.

Subsequent to the diagonalisation of the Hamiltonian $\hat{H} = \hat{H}_0 + \hat{V}$ with the local perturbation $\hat{V}(\boldsymbol{B}(\boldsymbol{r}), \boldsymbol{E}(\boldsymbol{r}))$, the new (perturbed) eigenvectors $|i\rangle$ can be expressed as superposition states

$$|i\rangle = \sum_{i_0} {}_0\langle i_0|i\rangle \, |i_0\rangle_0 = \sum_{i_0} \mathrm{EV}_{i_0 i} \, |i_0\rangle_0 \tag{F.1}$$

with the eigenvector matrix $\mathrm{EV}_{i_0 i} = {}_0\langle i_0|i\rangle$. This finally enables calculation of the applicable dipole matrix elements from the overlap integral $\langle i|\hat{\boldsymbol{d}}_q|j\rangle$.

F.2.3 Transition rates for rate equations

The most important parameters derived from the transition dipole moment are the transition rates which govern the rate equations for the level population evolution. All expression for the rates of absorption, stimulated and spontaneous emission have been elaborately deduced from atom-field interaction on the most fundamental, fully quantum mechanical level, in App. C. It shall briefly be recalled here that the spontaneous emission for a transition $j \to i$ between two (unperturbed) basis states $|j\rangle$ and $|i\rangle$ is characterised by the spontaneous emission rate

$$\Gamma_{i \leftarrow j} = \Gamma_{ij} = \frac{\omega_{ij}^3}{3\pi\epsilon_0 \hbar c^3}|\boldsymbol{d}_{ij}|^2 \tag{F.2}$$

It should be noted that spontaneous emission of course only occurs if the initial state $|j\rangle$ lies energetically higher than the final state $|i\rangle$, i.e. $E_j > E_i$. For this reason $\Gamma_{i \leftarrow j} = \Gamma_{ij}$ but $\Gamma_{i \to j} = 0$ if $E_j > E_i$.

In presence of magnetic fields the excited eigenstates are not given by a single basis state but consist of superpositions of unperturbed states. In this case the the spontaneous emission rate Γ_{ij} is obtained from Eq. (F.2) by evaluating the transition dipole moment $\boldsymbol{d}_{ij}$ from the *coherent* overlap integral, i.e., accounting for the coherent nature of the superposition. Since the transition dipole moment enters the equation for the spontaneous rate quadratically, the rate Γ_j is thus given

by the coherent sum

$$\Gamma_{ij} = \left[\sum_{j_0} \mathrm{EV}_{j_0 i} \Gamma_{ij_0}\right]^2 \tag{F.3}$$

instead of the incoherent sum

$$\Gamma_{ij} = \sum_{j_0} \left[\mathrm{EV}_{j_0 i}\right]^2 \Gamma_{ij_0} \tag{F.4}$$

where $\mathrm{EV}_{i_0 i}$ denotes the above introduced eigenvector matrix composed of the coefficients of the eigenvectors of the Hamiltonian. Even though this subtle difference might, at first glance, seem to be rather negligible, it in fact has quite important implications with respect to the resulting rates and thus to the state evolution as only the coherent sum properly accounts for the quantum character of the process. Only the inclusion of coherences between the states and potentially occurring interferences of involved decay channels finally ensures that the rate equations reproduce the real evolution in the correct way.

On the other hand, the rate γ characterising absorption and stimulated emission for the transition $i \leftrightarrow j$ using a laser with polarisation vector $\boldsymbol{\epsilon}$ results from the convolution

$$\gamma = \gamma_{ij} = \frac{\pi}{\epsilon_0 \hbar^2 c} \ (\boldsymbol{d}_{ij}\boldsymbol{\epsilon})^2 \ [g_{\mathcal{L}} \otimes I_\omega] \, (\omega + \boldsymbol{k}\boldsymbol{v} - \omega_0) \tag{F.5}$$

where $I_\omega(\omega)$ denotes the laser's spectral irradiance distribution defined by the full laser irradiance $I = \int I_\omega(\omega)\mathrm{d}\omega$ which in turn is linked to the electric field amplitude E of the laser according to $E = \sqrt{2I/(\epsilon_0 c)}$. The laser-induced transition rate γ indirectly depends on the spontaneous rate Γ_{ij} via the natural (Lorentzian) transition line shape function

$$g_{\mathcal{L}}(\delta) = \frac{\Gamma_{ij}}{2\pi} \frac{1}{\left(\delta^2 + \Gamma_{ij}/2\right)^2} \tag{F.6}$$

with the detuning $\delta = \omega - \omega_{ij} + \boldsymbol{k}\boldsymbol{v}$.

Due to the variety of different types and methods to generate laser light there does not exist a single universally applicable function to describe the laser spectrum. In most cases though, the laser spectrum is well approximated by a Gaussian function. In this case the transition rate γ is given by a Voigt profile, as derived step by step in Section C.7.5. Even though the calculation could be simplified considerably in case of Lorentzian laser spectra due to the fact that the convolution would then simply stay a Lorentzian function, the simulations presented here are all based on more realistic Gaussian spectra.

For a laser with a Lorentzian spectrum with FWHM Γ_L the rate simplifies to

$$\gamma = \ I \ \frac{(\boldsymbol{d}\boldsymbol{\epsilon})^2}{2\hbar^2 \epsilon_0 c} \ \frac{\Gamma_{ij} + \Gamma_L}{\left((\Gamma_{ij}+\Gamma_L)/2\right)^2 + \delta^2}$$

with the Doppler induced detuning $\delta = \omega + \boldsymbol{k}\boldsymbol{v} - \omega_{ij}$. This formula helps to understand how bound-bound and bound-free rates can be treated in a similar manner. While on resonance

$$\gamma = \ \frac{\Omega_{ij}^2}{\Gamma_{ij} + \Gamma_L} \ = \ 4\pi^2\alpha \ \frac{d_{ij}^2}{e^2} \ \frac{2I}{\hbar(\Gamma_{ij} + \Gamma_L)} \ .$$

Finally, the probability for the last remaining laser-induced process, photoionisation, can be derived from the corresponding cross section (cf. Eq. (C.49)) by means of the general relation between the cross section and the laser intensity, given by Eq. (D.32). It can be shown that the photoionisation rate can be written as

$$\gamma = 4\pi^2\alpha \ \frac{d_{ij}^2}{e^2} \ \frac{2I}{E_{\mathrm{h}}}$$

where α denotes the fine structure constant and $E_{\mathrm{h}} = m_{\mathrm{e}}c^2\alpha^2$ the Hartree energy (cf. introduction to Eq. (2.11)). Even though photoionisation in reality describes a transition from a bound state

to the continuum, the comparison to the (simplified) expression for the transition rate given by Eq. (C.65), valid for Lorentzian spectra, interestingly suggests that photoionisation can also be interpreted as a bound-bound transition with a "linewidth" proportional to the Rydberg constant E_h. The fact that photoionisation and bound-bound excitation are in fact processes similar in character (excitation of an atom due to interaction with a light field) thus also manifests in the mathematical description.

The above presented rates finally enter the set of rate equations for describing the temporal dynamics of the internal state populations during laser interaction. The applicable rate equations for the specific case of Ps laser cooling have been introduced and derived before (cf. Section 3.1.1 on p. 41), resulting in the two final equations

$$
\begin{aligned}
\frac{\mathrm{d}}{\mathrm{d}t}P_\mathrm{e} &= -(\Gamma_\mathrm{e}^{(\mathrm{ann})} + \Gamma_\mathrm{e}^{(\mathrm{phion})})P_\mathrm{e} + \sum_{|\mathrm{g}\rangle}\gamma_\mathrm{eg}P_\mathrm{g} - (\Gamma_\mathrm{ge} + \gamma_\mathrm{ge})P_\mathrm{e} \\
\frac{\mathrm{d}}{\mathrm{d}t}P_\mathrm{g} &= -(\Gamma_\mathrm{g}^{(\mathrm{ann})} + \Gamma_\mathrm{g}^{(\mathrm{phion})})P_\mathrm{g} + \sum_{|\mathrm{e}\rangle}(\Gamma_\mathrm{ge} + \gamma_\mathrm{ge})P_\mathrm{e} - \gamma_\mathrm{eg}P_\mathrm{g}
\end{aligned}
\tag{F.7}
$$

for the populations P_g and P_e of each pair of ground and excited states, $|\mathrm{g}\rangle$ and $|\mathrm{e}\rangle$ respectively, with $E_\mathrm{e} > E_\mathrm{g}$.

F.2.4   Kinetic Monte Carlo algorithm

For the simulation these rate equations are finally solved by means of a Kinetic Monte Carlo algorithm which predicts single transition events. The KMC scheme is based on the comparison of a random number with the pre-calculated transition rates which specify the relative strengths of all possible transitions in the considered atom, in the given state, at a certain point of time. The evolution of the system under the KMC algorithm is in principle indistinguishable from the one of a similar real system (which obeys incoherent rate equations) as it reproduces all processes taking place in a corresponding experiment, including statistical noise.

The implementation of of the KMC method in the code schematically consists of the following iteratively repeated sequence:

1. Initialisation of the system to its given internal state called k at the current time t.

2. Creation of the new transition rate list γ_{lk} for the system with integers $l = 1, \ldots, N$ where N denotes the number of possible, i.e., allowed transitions of the considered atom in state k.

3. Generation of a random number r from a unit-interval uniform random number distribution[51], $0 < r \leq 1$, and calculation of the first reaction time t' by solving

$$
\int_t^{t'} \sum_{l=1}^{N} \gamma_{lk}(\tau)\mathrm{d}\tau = -\ln r
$$

4. Generation of a second random number r' from a unit-interval uniform random number distribution, $0 < r' \leq 1$ required for determining the actually occurring transition by computing the integer (transition number) l for which

$$
R_{l-1} < r'R_N \leq R_l \qquad \text{where} \qquad R_j = \sum_{i=1,j} \gamma_{ik}(t') \quad \text{and} \quad R_0 = 0 \ .
$$

The calculation is carried out efficiently by means of a binary search algorithm.

5. Setting of the system to state l and evolving the time to t'. Finally, return to the first step.

---

[51] More precisely, the code makes use of the free implementations of the Mersenne twister unit-interval uniform random number generator of Matsumoto and Nishimura from GSL (GNU Scientific Library).

F.2.5 Equations of motion and Verlet algorithm

The evolution of the external dynamics in turn is simulated by means of the simple, but still efficient, algorithm, called *velocity leapfrog-Verlet-Störmer-Delambre algorithm*. For this method the equations of motion are transformed to

$$
\begin{aligned}
\boldsymbol{r}(t + \Delta t) &= \boldsymbol{r}(t) + \boldsymbol{v}(t) \cdot \Delta t + \frac{1}{2} \boldsymbol{a}(t) \cdot (\Delta t)^2 \\
\boldsymbol{v}(t + \Delta t) &= \boldsymbol{v}(t) + \frac{1}{2} \left[\boldsymbol{a}(t) + \boldsymbol{a}(t + \Delta t) \right] \cdot \Delta t .
\end{aligned}
\tag{F.8}
$$

The final solution has an accuracy of $\mathcal{O}((\Delta t)^3)$ for both the position $\boldsymbol{r}$ and velocity $\boldsymbol{v}$ for time steps of Δt. The crucial advantage of the used numerical algorithm over others often used for integrating Newton's equations of motion, such as the simple Euler or classical Runge–Kutta scheme, is the fact that its accuracy can be improved by applying higher order symplectic integrators. A symplectic integrator is the commonly used mathematical formalism for solving Hamiltonian systems. Another interesting feature of the Verlet integration scheme is time reversibility.

In the case of laser cooling each modification of the velocity directly results from recoils caused by photon transfer accompanying the transition of the atom between internal states. This makes it possible to evaluate the acceleration simply based on the gradient of the potential, which, for laser cooling, originates from the interaction of the atom with the light field or any possibly existing inhomogeneous external field.

The time scale of the process is thus characterised by the atom's motion in the laser interaction area or, if steeper, the inhomogeneous external fields. It is expedient to deduce an appropriate step size Δt of the integration scheme for example from the ratio of the laser waist w_{L} (or the characteristic size of the inhomogeneity) and the atom's thermal velocity v. Reliable (and physically meaningful) results can furthermore only be obtained in compliance with the principle of energy conservation at all times. It is therefore advisable to choose time steps not bigger than a small fraction of w_{L}/v. As a rule of thumb, a fraction of $10^{-3} w_{\mathrm{L}}/v$ has proven to be a suitable value to ensure this with an accuracy of about 10^{-3} while still ensuring efficient calculation.

F.2.6 Linkage between internal and external dynamics

In physical respects the link between the evolution of the internal state and modification of the atom's kinetic motion during laser interaction is simply governed by the transfer of momentum carried by photons absorbed or emitted. Once a transition takes place the atom experiences a corresponding recoil which effectively represents an acceleration that modifies its kinetic velocity (and energy).

In numerical respects, this cause-effect chain is established by combining the KMC algorithm responsible for evolving the internal state of the system and the N-body (Verlet) integrator which predicts the resultant evolution of the kinetic variables. Technically this is realised by comparing the predicted occurrence time for a transition with the external state evolution in the following way:

If at a time t the next transition is predicted (by the KMC algorithm) to take place at a time t' with $(t' - t) < \Delta t$, that means the reaction occurs prior to the full motion, the particles are evolved according to the equations of motion (Eq. (F.8)) up to t' (i.e., with a time step $(t' - t)$ instead of the usual one Δt) and the transition is numerically put into effect at t'.

If, on the other hand, $(t' - t) > \Delta t$ the system will dynamically evolve according to Eq. (F.8) at the usual time step Δt without any transition taking place. It is however important to note that it is, due to its probabilistic behaviour, internally still governed by the rate equations.

Finally, all interaction parameters, i.e., especially the laser fields and potentials as well as the transition rates, are recalculated and updated after each modification of kinetic variables or the internal state. In order to optimise computational efficiency, in case of $(t' - t) < \Delta t$, preponed

recalculation of relevant parameters is restricted to the atoms involved. The parameters of all other atoms are only updated at the end of the running dynamical time step Δt.

Besides the above mentioned stipulation of energy conservation it is advisable to choose the time step size Δt such that the transition rates stay almost constant from one time step to the next in order to ensure applicability of the KMC calculation rule

$$(t' - t) = -\frac{\ln r}{\sum_{l=1}^{N} \Gamma_{lk}(t)}$$

at all points in time (cf. third step of the KMC algorithm).

Obviously, the latter is again true in case the atom does not move too far with respect to the dimension of the laser interaction region. More precisely, the time step should be chosen such that it cannot move to a position with considerably different local laser intensity within one time step Δt as this would entail a correspondingly drastic change in transition rates which in turn would prohibit use of the calculation rule for the KMC algorithm.

These rules of thumb have been used in order to launch first simulations but eventually the time step Δt was successively reduced up to the point where convergence of the results was obtained which usually occurs for $\gamma \Delta t \lesssim 10^{-3}$.

F.3 Special remarks

This last subsection summarises few more physical processes which deserve special mention in order to either describe their concrete technical realisation, such as the construction of additional states for the implementation of annihilation and photoionisation, or to point out potential peculiarities in implementation which might have consequences with respect to the result of the simulation. The latter refers for example to the introduction of a subtle preventive measure to restrict the possibility of physically wrong diagonalisation results in case of state degeneracy (as elucidated in Section F.3.3).

F.3.1 Annihilation and photoionisation

As described before, the special processes of annihilation and photoionisation can easily be integrated in the concept of rate equations. Needless to say that is however only possible to treated as regular transitions between atomic states, in a similar way as the "standard" photon transfer processes of absorption and emission, if an appropriate pair of initial and final states exists. Since neither annihilation levels nor discrete state in the energy continuum are provided by nature, the simulated evolution resulting from the rate equation treatment can thus only be indistinguishable from the real dynamics upon prior creation of additional artificial levels.

In the first simulations which are restricted to the $n = 1$ and $n = 2$ levels, this is technically realised by adding five "dead" states (representing $n = 0$ with $m = -2, -1, 0, 1, 2$ and arbitrary energies $-10000\,\mathrm{cm}^{-1}$ below the $n = 1$ manifold) to the innate level scheme comprising twenty levels in total, four belonging to $n = 1$ and 16 to $n = 2$. This allows to treat annihilation as π-polarised spontaneous decay towards one of the "dead" states if, additionally, the dipole transition moments are defined such that the decay rate corresponds to the annihilation rate $\Gamma_{i_0}^{(\mathrm{ann})} = \Gamma_{j_0 \leftarrow i_0}$.

It is important to mention that, in contrast to fluorescence decay via spontaneous emission, the process of annihilation is inherently incoherent. For this reason the annihilation rate $\Gamma_i^{(\mathrm{ann})}$ of a given eigenstate $|i\rangle$ (which is potentially perturbed, i.e., resulting from diagonalisation) is obtained from the incoherent instead of coherent sum over the eigenvector components (cf. Eq. (F.4) vs. Eq. (F.3)) that means according to

$$\Gamma_i^{(\mathrm{ann})} = \sum_{i_0} |\mathrm{EV}_{i_0 i}|^2 \; \Gamma_{i_0}^{(\mathrm{ann})} \tag{F.9}$$

where the rates $\Gamma_{i_0}^{(\mathrm{ann})}$ for the unperturbed Ps eigenstates are given by the values listed in Tab. 2.5.

Next, seven additional "continuum" levels (representing $n = \infty$ with $m = -3, -2, -1, 0, 1, 2, 3$) are constructed at the ionisation threshold energy (of $E/(hc) = 54865.553\,\mathrm{cm}^{-1}$) to account for photoionisation by simply treating it as a polarisation dependent excitation towards those artificial levels with dipoles based on the photoionisation cross sections such that the rate, calculated as a stimulated rate, corresponds to the photoionisation rate $\Gamma^{(\mathrm{phion})}_{j_0 i_0} = \gamma_{j_0 i_0}$.

These two manual interventions finally allow to include all phenomena (spontaneous emission, absorption, stimulated emission, annihilation and photoionisation) only using dipolar transitions. The strength, i.e., probability of occurrence, of these processes is precisely known in zero field and the values in presence of fields can be obtained after diagonalisation of the Hamiltonian including Zeeman and dynamical Stark effects.

As far as photoionisation is concerned, the calculation of the according rates $\Gamma^{(\mathrm{phion})}$ of the perturbed eigenstates is however not as straightforward as in case of spontaneous emission or annihilation. Even though photoionisation is a coherent process the exact procedure in presence of magnetic and electric fields becomes highly complex due to involvement of various coherent phenomena such as quantisation of the cyclotron frequency, Landau resonance and more [47]. For this reason the most expedient approach is to simplify the treatment by downgrading the process to an incoherent phenomenon and tackling this loss channel in a similar way as annihilation. Based on this approximation the rate of a perturbed eigenstate $|i\rangle$ can be calculated from the incoherent sum over the unperturbed states according to

$$\Gamma^{(\mathrm{phion})}_{ji} = \sum_{i_0} |\mathrm{EV}_{i_0 i}|^2 \Gamma^{(\mathrm{phion})}_{ji_0} \ . \tag{F.10}$$

Since this treatment ignores quantum interference of all involved decay channels, it effectively averages over all possible configurations and thus underestimates the ones with constructive interference and overestimates those with destructive character.

In all laser cooling configurations considered and studied in this thesis, the impact of this simplification is however highly relativised by the fact that photoionisation is only very unlikely to occur. Furthermore, it is anyway only a one-way process, which a priori excludes secondary effects. The simplified treatment is thus not expected to entail major consequences.

Finally, it should be mentioned that in case the $n = 3$ manifold needs to be included in the considerations (such as for the simulations on the realisation of laser cooling in the AE$\bar{\mathrm{g}}$IS experiment) few more dead and continuum levels have to be added in order to properly account for all possible transitions, that means from all naturally occurring m-states. Seven dead and nine continuum states are required then, next to 56 states belonging to the manifolds $n = 1, 2$ and 3.

F.3.2 Diagonalisation and the possibility of level crossing

A chosen diagonalisation is always based on some kind of ordering of the basis states, which in the present case here is an energetic order. The results of the simulation will thereby only be useful if the order of the states remains unchanged at all times. If this cannot be ensured, in case of level crossing for example, the calculation method has to be modified at the respective point of time, where the order changes.

In case of laser cooling level crossing can, in rare cases, occur if the Stark effect becomes modified due to recoil-induced velocity changes, so that two states swap in energy as a result of this transition. It is important ot mention that the used simulation code assumes that such level crossings do not occur and that the possibility for changes in the order of the states can be ignored. This assumption is in general valid and appropriate if the magnetic field strength (and thus the Zeeman effect) stays constant in the course of the cooling process and if modifications of the Stark effect are small compared to the energy splitting of the states and can therefore not have consequences for the energetic ordering.

In case the states lie very close in energy, level crossings are of course possible though. In most cases, their impact will however still be negligible. Level crossings can furthermore only occur in

excited state manifolds. It has been verified that they do not occur in the $n = 1$ ground state manifold so that spontaneous emission can safely be treated using an ordered level scheme.

F.3.3   Diagonalisation and the problem of degeneracy

It should be pointed out that it is still possible that situations occur in which the rate equation approach delivers physically wrong results:

In order to account for the whole complexity of involved processes, it is in general necessary to diagonalise the full Hamiltonian including Zeeman as well as motional Stark effects in external magnetic fields. In a simulation of light-matter interaction, the Hamiltonian should in principle even be diagonalised after each transition event. This is due to the fact that laser interaction does not only affect the internal properties (population of internal states) of the atoms but also their external ones, especially the velocities, due to transfer of momentum during photon absorption or emission. This leads to modifications of the Stark interaction and thus as well of the Hamiltonian.

Under certain conditions, diagonalisation, even if carried out only once, can become problematic though. This is due to the fact that, technically, the diagonalisation procedure, and thus its outcome, are not unique. As a result, the eigenvectors are arbitrarily defined which results in uncontrolled coherent phases between the states. These coherences are however not taken into account in the rate equation formalism as it, by construction, relies on incoherent population dynamics.

This becomes especially important in case of degenerate energy states, as it implies that eigenstates are composed by different superpositions of the degenerate states, depending on the way the Hamiltonian has been diagonalised. As long as these superposition states are not populated and as long as the degenerate states do not show different behaviour or response to the light field, this does not pose a problem as it effectively yields similar population results. A problem might arise though, if the degenerate states become involved in the population dynamics and if show different properties, such as decay via different decay paths or different coupling to third states. If, in this case, coherences are not tracked, de-excitation or spontaneous emission might finally produce results which in reality never occurred. It is important to point out that this deficiency will not average out. Repetition of the same procedure will just accumulate the physically wrong results.

The issue gains further complexity due to the fact that the rate equation approach is not capable of handling superposition states. Thus, in case diagonalisation in the chosen basis produces a superposition eigenstate, the method used to solve the rate equations will select one of the states forming the actual superposition state. Only this will then become included in the calculation of the laser interaction. As this procedure does not consider the eigenstate as a whole, including coherences, it can again end up in physically meaningless results.

The whole problem can well be illustrated by means of the $\sigma^{(+)}$ transition $1^3\mathrm{S}_1(m = 1) \leftrightarrow 2^3\mathrm{P}_2(m = +2)$ in the Ps atom where (for vanishing Stark effects) the excited $2^3\mathrm{P}_2(m = +2)$ state is degenerate with the $2^3\mathrm{P}_2(m = -2)$ state. If initially only the $1^3\mathrm{S}_1(m = 1)$ is populated this interaction configuration is, in reality, not supposed to affect the population of the remaining ground states since atoms in $2^3\mathrm{P}_2(m = +2)$ can only decay back to the $m = +1$ ground state which in turn can only be excited back to $2^3\mathrm{P}_2(m = +2)$.

However, if, during the calculation, the according Hamiltonian is diagonalised eigenstates, such as $|\pm\rangle = (|m = +2\rangle \pm |m = -2\rangle)/\sqrt{2}$, might be produced which consist of a superposition of $2^3\mathrm{P}_2(m = +2)$ and $2^3\mathrm{P}_2(m = -2)$. The method employed to solve the rate equations will then choose (with a probability linked to the dipole transition strength, hence here with 50% chance each) to populate only one level after the excitation, for instance the $|+\rangle$ level. The $|+\rangle$ state in turn can decay by spontaneous emission to the $m = -1$ ground state. Obviously, an absorption-emission cycle would be created which in reality would never occur. This example illustrates how the rate equation formalism might produce wrong physical results. In the simulation, this mixing behaviour has indeed been observed for specific rotations and laser polarisation schemes.

One might argue that this deficiency can easily be solved by defining the coherent superposition states as additional states to be included in the ensemble of basis states.

This approach will fail though since the superposition states are in fact not completely independent from the basis states as its properties are linked to those of the basis states which they consist of. This becomes clear by considering for instance the calculation of the populations of any of the original basis states (such as $2^3P_2(m = +2)$ or $2^3P_2(m = -2)$): For this calculation it is not sufficient to only take into account the stand-alone basis state ($2^3P_2(m = +2)$ or $2^3P_2(m = -2)$) but also all superposition states which these basis state are part of, since the latter (at least partially) shares same properties of its constituents. Hence, the information about the considered basis state would obviously be incomplete if the superposition state was defined as an additional independent basis state.

Similarly, the superposition state shares the behaviour of its constituents in response to perturbing magnetic fields or interaction with radiation which means that a redefinition would become problematic in this respect as well.

As indicated, the described difficulty is again linked to the concept of coherences, this time not though to the mutual phase relation between ground and excited states of the 2-level system, but rather to the coherence of the superposition states that are composed of degenerate states. This can once more be illustrated by means of the above example. If the state evolution was subject to a fully coherent treatment, accounting for the full phase relation between $2^3P_2(m = -2)$ and $2^3P_2(m = +2)$, the contribution of the $2^3P_2(m = -2)$ would in all cases simply destructively interfere after consideration of all superposition states. Erroneous population of the $m = -1$ ground state does then simply not occur. The occurrence of faulty results can thus only be prevented by keeping track of all characteristics of the states or, respectively, carry the coherences through the whole calculation.

This demonstrates that the physically wrong results in fact originate from the incoherent nature of the rate equation concept which, by construction, reduces the level dynamics to changes in the incoherent populations as a result of statistically occurring transition events. This in turn implies nothing else than the necessity to treat the state evolution in the framework of the optical Bloch equations which however is highly impractical as it puts much higher demands on computational efforts, leading to a significant increase in time and memory consumption. Using Bloch equations it becomes almost impossible to carry out numerical simulations of laser interaction with a cloud of few thousands of atoms with complex level structure and on time scales of several tens of nanoseconds. The only feasible solution is thus to still make use of the concept of incoherent rate equations, but mitigate the problem as far as possible.

For this purpose, marginal energy shifts (of typically $E/(hc) = 10^{-5}\,\mathrm{cm}^{-1}$) have been introduced in the simulation code to artificially split those basis states which are normally degenerate in energy. This is however no viable strategy to prevent the same problem to occur in cases of field-induced level crossings of excited states for certain magnetic field strengths. In these cases diagonalisation might still produce superpositions that give rise to additional unreal transitions, different than the natural transition dynamics.

The effect can be mitigated further by using large enough atomic samples where a variety of possible initial atomic directions and, especially in 3D-cooling, various laser polarisations are involved. With regard to 1D-configuration though, it results in an artificial limitation of the efficiency of specific optical pumping schemes. However, tests conducted with different diagonalisation algorithms, producing different phases, yielded similar results. This confirms that the results presented here are not significantly affected by the effect, although special care has to be taken to draw conclusions from the analysis of certain polarisation schemes.

F.3.4   Light shift

It is finally worth mentioning that the light shift, which is also known as AC Stark effect and which has briefly been introduced at the very end of Section D.5 (cf. p. 198) in the context of saturation of atomic transition, is implemented in the simulation code.

F.4 Parameter configuration – In- and output data

Several parameters can be defined and modified for the numerical studies of Ps laser cooling by means of the described simulation code. Amongst the most important parameters are the initial temperature which defines the initial velocity distribution, the cloud size, the magnetic field strength and orientation and of course the laser parameters which are the power, the spectrum in terms of detuning and bandwidth, the wavelength and the polarisation. To get insight into the multivariate space of different cooling configurations, the numerical studies are first devoted to the 1D-cooling case before turning to the more complex 2D- and 3D-cooling configuration.

Two typical methods of Ps production are considered. First, Ps can be formed by charge exchange with a plasma of positrons [172, 173]. In this case, the ensemble of Ps atoms is well represented by a 3D expanding cloud with Gaussian velocity distribution and zero mean-velocity along each spatial direction. This is similar to a 3D molasses or magneto-optical trap simulation and has been used for all Ps numerical laser cooling studies before. This is the configuration considered for the very general 1D and 3D investigations in Section 3.2. However, as described in Section 2.1.1, positronium can and is often also created by implantation of positrons into a converter target. In this geometry, it is mostly emitted in the forward direction (orthogonal to the target) [7, 174] with a non-zero mean velocity which can well be modelled by an effusive beam. This case is investigated in the application-oriented studies in Sec. 3.2.

In order to convey an impression of the versatility of the simulation code it is worth to give few more (partly technical) details on the definable input parameters but also the output data of a simulation run.

Timing

One of the most crucial aspects of the initialisation procedure is certainly the timing. There are mainly two parameters available to define the timing configuration which is the time increment Δt for the N-body integrator and the duration of the simulation that means the period of time over which the evolution shall be calculated in time steps of Δt. A third parameter can be used to set the time step of data output, independently of the calculation steps step Δt. It is important to emphasise that the simulation duration is not determined by the time span of interaction between laser an atoms. Rather, the latter can be configured separately by means of a laser timing schedule so that the complete evolution can also contain an arbitrary number of interaction-free periods (i.e. temporal absence of a light field, as it is the case of pulsed laser sources).

In the standard configuration the simulation duration was nevertheless chosen to agree with the time span of a single laser pulse. As a compromise between the annihilation lifetime of 142 ns, the travelling time of the atoms through the laser waist and realistically achievable laser pulse duration, it was set to a value of 200 ns for the general studies of Ps laser cooling in magnetic fields.

Ps cloud configuration

Important parameters to characterise the Ps cloud are the temperature, the number of particles, the central position of the cloud and an optional offset velocity added to each particle's thermal velocity.

In case of laser cooling on a 3-dimensionally expanding cloud the initial particle position as well as initial velocity values are chosen randomly from a Gaussian distribution with a width defined by the thermal energy of the particle cloud. The initial temperature can thereby be specified along each spatial axis separately.

In case of equal temperature values T along all three directions, the values of the absolute velocity $v = \|\boldsymbol{v}\| = \sqrt{\sum_i v_i^2}$ resulting from the velocity vector components v_x, v_y and v_z thus obey

a Maxwell-Boltzmann distribution with probability density function (PDF) given by

$$f(v)\, \mathrm{d}v = \left(\frac{m_{\mathrm{Ps}}}{2\pi k_{\mathrm{B}} T} \right)^{3/2} 4\pi v^2 \exp\left(-\frac{m_{\mathrm{Ps}} v^2}{2 k_{\mathrm{B}} T} \right) \mathrm{d}v \ . \tag{F.11}$$

The algorithm for random number generation (a Mersenne-Twister generator, by default) can be initialised in different modes by means of an additional "seed" parameter which allows the user to choose between specific reproducible sets of randomly generated values, Gaussian distributed values. Hence, if the seed number is kept constant for different simulation runs, all Ps atoms in the cloud are for each run initialised in the same configuration that means at similar positions and with identical initial velocities while still obeying a random distribution.

The random number generator (RNG) seed thus allows to separate the effects of the statistical distribution from the ones of a modification of simulation parameters. In order to study the influence of certain laser properties on the cooling efficiency for example it is thus expedient to keep the seed at a fixed value in order to each time reproduce similar, but still random initial position and velocity distributions. This initialisation of the cloud in always the same dynamical state ensures highest degree of comparability of the simulation outcomes. On the other hand, the seed parameter is also a means to investigate to which extent the statistical error, resulting from the deviation of the randomly chosen values from an ideal Gaussian function, affects the simulation result. By keeping all parameters fixed, except for the seed, it is possible to examine the influence of statistics on the cooling effect. This strategy has for instance been pursued in order to investigate the statistical significance of certain cooling parameters which is presented in Section F.5.7.

In all 1D-simulations, the cloud is initialised instantaneously in time and with a Gaussian distribution of 0.1 mm waist along each of the three spatial directions. For the simulations of cooling on an effusive beam the initial cloud size is set to a volume of $(2 \times 2 \times 0.1)\,\mathrm{mm}^3$ (in terms of the width of the Gaussian distribution along the three spatial directions) which is supposed to represent the active area of a typical Ps converter target.

All 1D-cooling simulations have been carried out for a cloud of 2000 Ps atoms which is expanding isotropically in 3D with thermal velocities corresponding to a realistic experimental temperature of $T = 300\,\mathrm{K}$ [7]. At this temperature the most probable value of the velocity distribution becomes

$$v_{\mathrm{prob}} = \sqrt{\frac{2 k_{\mathrm{B}} T}{m_{\mathrm{Ps}}}} = 6.74\,\mathrm{km/s}$$

which can simply obtained by solving $\mathrm{d}_v f(v) = 0$ with the Maxwell-Boltzmann PDF given in Eq. (F.11). The mean velocity $v_{\mathrm{mean}} = \int v f(v) \mathrm{d}v = 2/\sqrt{\pi}\, v_{\mathrm{prob}}$ then amounts to 7.61 km/s and the rms-speed $v_{\mathrm{rms}} = (\int v^2 f(v) \mathrm{d}v)^{1/2} = \sqrt{3/2}\, v_{\mathrm{prob}}$ to 8.26 km/s.

The chosen number of 2000 atoms represents a compromise between computational time and sampling density of the velocity distribution. In all simulations, when the number of annihilated atoms is high, the results have lower statistical significance. However, this does not affect the conclusions of the studies presented in this thesis which are all based on statistically significant results.

Internal state configuration

In order to lay the foundation for Ps-laser interaction it is first and foremost required to specify, in two separate files, the internal atomic states as well as a list of allowed transitions. Each state is defined in terms of its energetic position and information on whether the level which it belongs to is a bound or dead level or part of the continuum. The states are furthermore numbered consecutively serving for identification throughout the whole evolution and required for example for the purpose of diagonalisation but also for defining the allowed transition in the second file. Besides the numbers each transition is characterised by means of the lower and upper state's m-quantum number, the information concerning the type of state (bound, dead or energy continuum), its energy and and finally the transition strength in terms of the unperturbed zero-field transition dipole moment.

As mentioned before, a total number of 32 states (including dead and continuum states) are taken into account for the general studies of Ps laser cooling in magnetic fields restricted to transitions between states from the $n = 1$ and $n = 2$ manifold. To incorporate the additional inclusion of the $n = 3$ manifold in the scheme of Ps cooling in the AE$\overline{\mathrm{g}}$IS experiment, for the purpose of probing the cloud, a total of 72 states are considered for these simulations.

The levels-file furthermore allows to specify whether a state is initially populated ("1") or not ("0"). During the initialisation procedure of a simulation run the total number of particles is then distributed only over the states assigned with "1". For all studies presented here the Ps atoms are initialised in the triplet ground state with equal distribution over all three m-states.

Finally, the matrix elements of the unperturbed zero-field Hamiltonian as well as those of the Zeeman and dynamical Stark interaction Hamiltonians are specified directly in one of the code files. The values are calculated beforehand by means of a MATHEMATICA code based on the very basic overlap of the corresponding wavefunctions.

Magnetic field

The homogeneous magnetic field is simply defined by means of the components of the field vector $\boldsymbol{B}$ which sets both the field orientation as well as its strength.

Laser configuration

In principle an arbitrary number of laser beams can be configured, where the parameters of each beam are defined separately. In case of 3D-cooling for example the laser setup comprises a total of six beams arranged in form of three orthogonal pairs of counter-propagating beams, in general all with similar parameters, except for the alignment. Only for certain applications of 3D-cooling the two beams, which constitute a pair of beams, differ in detuning. The results of an according experimental application will be presented in Section 3.2.2.

As far as the spectrum is concerned each beam is fully characterised in terms of the type of spectral function (Gaussian, Loretzian, etc.) and the parameters detuning and bandwidth. The spectral information is complemented by information on the wavelength, in terms of wavenumbers, and its power in units of watts. For pulsed lasers the pulse energy is as well specified in terms of a power value, in this case the equivalent power of a corresponding cw-laser, that means with the pulse energy equally distributed over the whole duty cycle. The definition of each beam is completed by the specification of its spatial alignment, in terms of the propagation direction ($\boldsymbol{k}$-vector) and an optional offset position (for example to spatially separate two beams or the beam from the Ps source), and finally its polarisation state.

The polarisation state is conveniently described in terms of the two helicity basis vectors $\boldsymbol{\epsilon}_\lambda'^{(+)}$ and $\boldsymbol{\epsilon}_\lambda'^{(-)}$ with complex components to account for relative phases (cf. Eq. (C.12)). The first mentioned state, $\boldsymbol{\epsilon}_\lambda'^{(+)}$, describes right-handed and the latter oppositely directed left-handed circular polarisation, in all cases with respect to the propagation direction. The linear polarisation vector can be rotated in the transverse plane either directly by means of the coefficients of $\boldsymbol{\epsilon}_\lambda'^{(+)}$ and $\boldsymbol{\epsilon}_\lambda'^{(-)}$ or an optional angle Ψ (cf. Fig. C.3).

The laser beam can thus possess either circular polarisation or transverse linear polarisation with any angle Ψ. Longitudinal polarisation, that means with electric field vector oscillating in longitudinal direction along the propagation axis is not possible as cooling is assumed to always be performed in free space in which the electric and magnetic field vectors are, pursuant to Maxwell's equations, exclusively lying in the transverse plane at all times.

Next to these mandatory specifications on the beam characteristics, for each beam, two additional files allow to optionally attenuate the spectral and/or temporal intensity distribution. In this way it is possible to shape the spectrum of each beam, for example to artificially cut the Gaussian spectrum, defined by detuning and bandwidth, at a certain frequency, or, respectively, to implement laser pulses of arbitrary shape, duration and repetition rate by means of the temporal attenuation.

The first simulations assume a laser spot size of the order of $1\,\mathrm{cm}$ diameter (i.e., a waist w of $5\,\mathrm{mm}$), for a pair of counter-propagating beams with a Gaussian spectral bandwidth Γ_{L} (FWHM) of $75\,\mathrm{GHz}$, a detuning δ of $-2.5\,\mathrm{cm}^{-1}$ (that is $-75\,\mathrm{GHz}$) from resonance $E_0 = \hbar\omega_0$. Cooling is then performed on the transition $1^3\mathrm{S}_1 \leftrightarrow 2^3\mathrm{P}_1$ at $41148.23871\,\mathrm{cm}^{-1}$ with a laser power of $2\,\mathrm{kW}$. This corresponds to an energy of $400\,\mu\mathrm{J}$ for a laser pulse lasting over the whole simulation time of $t = 200\,\mathrm{ns}$ (or, respectively, $240\,\mu\mathrm{J}$ for $120\,\mathrm{ns}$).

A discussion of the laser parameters and their influence on the cooling efficiency is presented in Section 3.2.1 for which the three most important parameters, the detuning, the power and the bandwidth are scanned over a certain range of values.

Output data

Even though in principle it is possible to output at any time the current values of each variable occurring in the calculation, there is only a handful of parameters which are relevant for calculating the cooling effect and rating its efficiency. This includes first and foremost the positions and velocities of each atom during the simulation. Together with a time stamp and the current internal states of all atoms they are written to a dedicated output file at a specifiable time interval. In order to analyse the internal dynamics during laser interaction it is sometimes useful to additionally output for each atom the values of all transition rates together with information on the corresponding transition (i.e., the initial and final states), written to a separate file with the elementary time increment Δt.

This compact dataset comprises all information required for studying the effect of cooling on the atom in terms of the above introduced figures of merit, namely the temperature, the number n_{r} of atoms around resonance and the S-parameter.

F.5   Preparatory work

Prior to the simulations of the full cooling scheme, including the entirety of effects, several checks have been performed in order to ensure that involved processes are reproduced in the way predicted by theory. This is particularly important in light of the fact that the used algorithm, as any other simulation code, relies on certain assumptions and models, described in detail above, whose applicability needs to be tested for the entire configuration space of interest. Special focus was therefore given to the verification of the suitability of the concept of (incoherent) rate equations, especially with regard to possible negative implications of an incoherent approach on the reliability of the simulation results. In this way it is possible to reveal potential limitations of the model for certain cooling configurations.

F.5.1   Simulation time steps

First of all, reliable simulation results can only be achieved for sufficiently small time steps Δt of the N-body (Verlet) integrator, which at the same time though should be long enough to allow for simulation of laser interaction over time spans of few hundred nanoseconds within a reasonable computation time. In order to determine the most expedient time step duration, a typical parameter configuration (with the values given in the previous Section F.4) was carried out for different values Δt while outputting the total energy given by the sum of all potential and kinetic energies of the particle evolution.

In compliance with the guidelines described in Sec. F.2.5 the step size Δt was successively increased starting from the rule of thumb based on laser waist w_{L} and thermal velocity v up to the value where energy could no longer be conserved. With additional consideration of the computation time, the step size Δt was finally set to a fix value of $500\,\mathrm{ps}$ used for both the general numerical investigations of Ps cooling in external fields and the simulations tailored to the realisation of cooling within the AEḡIS experiment.

Simulation	Runtime t_{comp}				
Duration t_{final} [ns]	$N = 10^1$	$N = 10^2$	$N = 10^3$	$N = 2 \times 10^3$	$N = 4 \times 10^3$
20	3.42 s	48.81 s	2501.91 s	9126.3 s	35530.10 s
50	5.35 s	79.42 s	3214.21 s	11241.1 s	44056.00 s
100	7.25 s	112.89 s	3849.81 s	13562.6 s	50690.60 s
200	9.69 s	149.53 s	4594.82 s	16144.7 s	57865.40 s

TABLE F.1: *Runtime study simulation code.* *The runtime values t_{comp} specify the time required to run a simulation for the standard set of 1D-cooling parameters (laser parameters $\Gamma_{\mathrm{L}} = 2\pi (75\,\mathrm{GHz})$, $\delta = -2\pi c\,(2.5\,\mathrm{cm}^{-1})$, $P = 2\,\mathrm{kW}$, a temperature $T = 300\,\mathrm{K}$, magnetic field strength $B = 1\,\mathrm{T}$ and calculation time steps of $\Delta t = 500\,\mathrm{ps}$) for different numbers of atoms N and simulation durations t_{final}.*
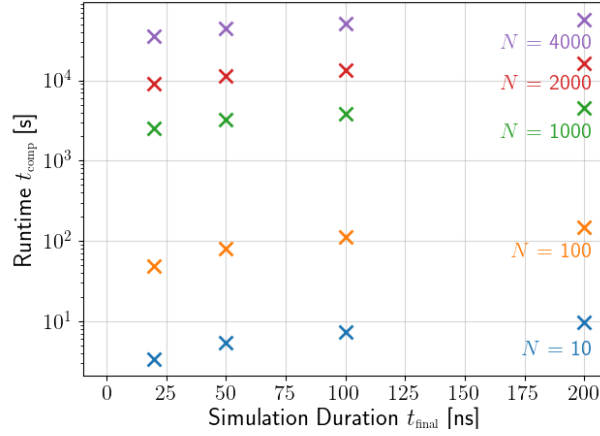
FIGURE F.1: *Runtime study of the simulation code.* *Plot of the values listed in Tab. F.1.*

F.5.2 Runtime study

In order to characterise the performance of the simulation code in terms of computation time, the simulation was configured with the standard set of parameters given above and run for different numbers of particles N and simulation durations t_{final}. Table F.1 shows an overview of the time required for a single simulation run for those configurations.

For illustration purposes, the values listed in Tab. F.1 have additionally been plotted in Fig. F.1 on a logarithmic scale. Obviously, the runtime scales linearly with the number of atoms N since the particles do not interact which implies that the calculation of their dynamics is completely decoupled. Furthermore, an extension of the simulation duration does not entail an equal increase in runtime. Instead, for durations $t_{\mathrm{final}} \gtrsim 100\,\mathrm{ns}$ the initially steep rise passes over to kind of a saturation regime where the runtime only barely increases with the length of the simulation. This is simply due to the fact that after sufficiently long simulation times the fraction of annihilated atoms has reached such a level that laser interaction is restricted to only few atoms and additional computation time is only needed to calculate the further evolution of the velocities of all atoms[52] no longer though to simulate laser interaction.

Even though not shown above, it is worth to mention that runtime scales approximately linearly with the calculation step size Δt in the range of the chosen value $\Delta t = 500\,\mathrm{ps}$.

---

[52] The Verlet integrator keeps solving the equations of motion for all atoms, regardless of their actual state, that means especially also for already annihilated one.

F.5.3 Annihilation

Before addressing the very basis of the simulation, the limitations of the rate equations, first checks were devoted to the most basic processes involved. A noteworthy test in this regard was addressing the process of annihilation which can be verified in a very simple way by simulating the evolution of a cloud of sufficiently many particles (to achieve high statistical significance) in a laser-free environment and tracking their internal states for an adequate time span. This was carried out separately for all states by appropriately configuring the initial population. To check for magnetic quenching the procedure was furthermore repeated for different magnetic field strengths. In all cases the resulting evolution showed perfect agreement with the theoretically predicted development, given by the equations in Section B.5.2.

F.5.4 Recoils

As far as atom-light interaction and laser cooling is concerned, it was first of all important to verify that recoils, the basis for cooling, appear in the expected way both in terms of orientation and size. For this purpose cooling was simulated in the most simple configuration conceivable which is resonant interaction of a single laser beam with defined parameters with a single atom resting in the centre of the frame (i.e., at $T = 0\,\mathrm{K}$ and with zero offset velocity). By analysing the particle velocities at each time step together with its current internal state, it could directly be confirmed that photon transfer (either absorption or emission) is accompanied by correctly sized recoils with, in case of laser-stimulated transfer (i.e. absorption and stimulated emission), well defined alignment along the laser propagation direction but random 3D-orientation in case of spontaneous emission.

F.5.5 Laser polarisation and induced transitions

As far as the internal dynamics of the atom during laser interaction is concerned there are mainly two aspects to be considered, namely the type of the transition induced by the laser and the corresponding strength. The transition type refers to the change Δm in the magnetic quantum number as a result of an excitation event. As explained in Sec. C.5.1 Δm primarily depends on the product of polarisation state $\boldsymbol{\epsilon}$ and the transition dipole moment $\boldsymbol{d}_{\mathrm{eg}}$ and thus on both the polarisation state itself as well as its relative orientation with respect to the quantisation axis which defines the orientation of $\boldsymbol{d}_{\mathrm{eg}}$.

Depending on the polarisation state, expressed in terms of the helicity basis vectors $\boldsymbol{\epsilon}'^{(\pm)}$, different components $d_{\mathrm{eg}}^{(\nu)}$ of the dipole moment vector $\boldsymbol{d}$ (with $\nu = 0, \pm 1$) are responsible for coupling the ground state to the excited states. It is these components which also decide on the resulting change in quantum number m caused by photon absorption and thus establish the link between the polarisation state and Δm. Finally, it is the polarisation of the absorbed photon that determines which transition are possible in the respective configuration.

In order to verify correct implementation of this relationship between $\boldsymbol{\epsilon}$ and Δm in the code and that proper execution of rotations, different polarisation schemes, i.e. different configurations of $\boldsymbol{\epsilon}$ and its orientation to $\boldsymbol{B}$, have been simulated. By analysing the evolution of the internal states during laser interaction it could be confirmed that

1. a circularly $\sigma^{(\pm)}$-polarised laser beam (i.e., $\boldsymbol{\epsilon} = \boldsymbol{\epsilon}^{(\pm)}$) parallel to $\boldsymbol{B}$ induces transitions with $\Delta m = \pm 1$,

2. a circularly $\sigma^{(\pm)}$-polarised laser beam antiparallel to $\boldsymbol{B}$ induces transitions with $\Delta m = \mp 1$,

3. excitation by means of a circularly $\sigma^{(\pm)}$-polarised laser beam (i.e., $\boldsymbol{\epsilon} = \boldsymbol{\epsilon}^{(\pm)}$) perpendicular to $\boldsymbol{B}$ leads to either $\Delta m = 0$ or ± 1 since in this configuration the projection of the polarisation vector on $\boldsymbol{d}$ involves all components $d_{\mathrm{eg}}^{(\nu)}$,

4. a linearly polarised laser beam (i.e., with $\boldsymbol{\epsilon} \propto (\boldsymbol{\epsilon}^{(+)} \pm \epsilon^{(-)})$) either parallel or antiparallel to $\boldsymbol{B}$ induces all kinds of transitions, for the same argument as in the previous case, namely contribution of all components $d_{\mathrm{eg}}^{(\nu)}$,
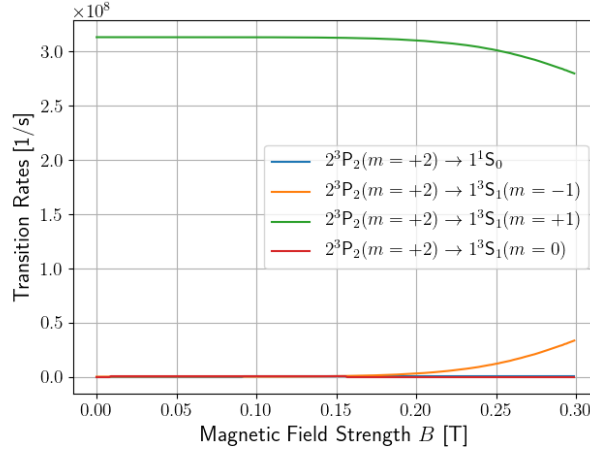
FIGURE F.2: *Simulated transition rates from $2^3\mathrm{P}_2(m = +2)$ to ground states.* *The plot shows the transition rates from $2^3\mathrm{P}_2(m = +2)$ to all ground states as a function of the magnetic field strength B. The values result from the incoherent calculation in the simulation code based on diagonalisation and subsequent dipole superposition.*

5. a laser beam with both alignment as well as linear polarisation perpendicular to $\boldsymbol{B}$ drives transitions with either $\Delta m = -1$ or $+1$ (contributions of $d_{\mathrm{eg}}^{(\pm)}$ but not $d_{\mathrm{eg}}^{(0)}$) and, finally, that

6. a laser beam with alignment perpendicular but linear polarisation parallel to $\boldsymbol{B}$ drives ($\Delta m = 0$)-transitions only (since then $\boldsymbol{\epsilon}' \cdot \boldsymbol{d}_{\mathrm{eg}} = d_{\mathrm{eg}}^{(0)}$).

F.5.6 Transition rates

For checking the strength of the transitions the simulation was performed in the same simple laser interaction configuration as above, this time though by additionally outputting the transition rates.

In zero field it could straightforwardly be confirmed that all rates are in perfect agreement with the theoretical predictions both relative to each other as well as in absolute values as a function of the laser detuning. An interesting observation was however made in higher magnetic fields for certain cooling configuration. The stronger the field the more do some calculated rates show unexpected behaviour that deviates significantly from theoretical predictions. This deviation becomes especially apparent for the stretched states, such as $2^3\mathrm{P}_2(m = +2)$ or $2^3\mathrm{P}_2(m = -2)$, the states which have been used for illustrating the limitations of incoherent approaches in Sec. F.3.3. Since these states are insusceptible to magnetic field perturbations, they are expected to stay entirely pure in magnetic fields, that means not coupled to any other states, regardless of the field strength. This implies in particular that the transition rates from $2^3\mathrm{P}_2(m = +2)$ to the ground states should as well stay constant and pure, that means unaffected by additional channels in magnetic fields.

This behaviour is however not entirely reproduced by the simulation code, as visualised in Fig. F.2. The plot shows the decay rates from state $2^3\mathrm{P}_2(m = +2)$ to all ground states $1^1\mathrm{S}_0(m = 0)$ and $1^3\mathrm{S}_1(m = 0, \pm 1)$ separately, as a function of the magnetic field strength B up to a value of $0.3\,\mathrm{T}$. In this range no level crossings are actually expected to occur (cf. Fig. 3.1). Obviously, the code produces rates which are not constant and thus deviate from expectations.

In order to understand this disagreement it is important to recall the implemented method of computing transition rates: As explained in detail in Section F.2 the values of the rates are calculated according to Equations (F.2) and (F.5) where the dipoles are based on the eigenstates provided by diagonalisation of the full Hamiltonian. Hence, deviations of calculated values from theoretical predictions do not necessarily have to be caused by the use of a wrong calculation rule. Instead, it can also result from a defectiveness of calculated transition dipole moments

$\boldsymbol{d}_{\text{ge}}$, originating from the fact that coherences are not taken into account. This explains that the verification of the transition rates is in fact also a means to examine whether and for which configurations the deficiency of an incoherent calculation approach, described in Sec. F.3.3, might have detrimental impact on the reliability of the simulation results.

In order to identify whether the deviation is caused by a wrong calculation rule or wrong dipoles, it is thus useful to plot the calculated transition rates of each state as a function of the magnetic field, as exemplarily done for $2^3\text{P}_2(m = +2)$ in Fig. F.2. By analytically evaluating the rates for this state in zero field according to Eq. (C.69) and comparing it to the ones involved in the simulated transition dynamics, it turns out that the zero-field values in the code are indeed correct. This in turn leads to the conclusion that faulty rates in higher fields are caused by partially incorrect dipoles and thus finally by disregard of coherences.

As explained in Sec. F.3, this does in general not pose a problem to the simulation of the cooling effect, especially in 3D where a maximum of transition schemes, that means beams with different polarisations from all spatial directions, are involved and contribute to the cooling process. Here, faulty rates do not have an impact on the simulation results, in terms of the cooling efficiency, since anyway a variety of transitions are excited and mixed. Special care has to be taken though as far as studies of certain polarisation schemes in 1D are concerned for which phase loss can in fact have quite severe implications. This can well be illustrated by means of the optical pumping scheme where the atom is excited by means of a perfectly circularly polarised laser beam. As explained in Sec. C.6, this scheme generally allows to cycle and cool the atom on a pure transition and thus makes it possible to avoid population of the $m = 0$ ground state, the only ground state that is quenched in magnetic fields. For this reason, the stronger the field, the more beneficial is optical pumping expected to be for cooling as it effectively reduces the overall annihilation rate which is one of the two decisive parameters of the cooling efficiency.

The condition sine qua non for this technique to work is the preservation of the pure character of the scheme. However, if the diagonalisation procedure produces superposition states whose coherences are not taken into account, the natural transition dynamics is superimposed by additional artificial transitions, that in reality do not exist and finally destroy the purity of the transition scheme and impair its efficiency.

This once more demonstrates that the study of polarisation schemes decisively relies on correct calculation of eigenstates, including phase relations where necessary. Since this cannot be ensured in the code and the impact of phase loss cannot easily be estimated, the occurrence of artificial transitions makes it impossible to draw reliable conclusions on the benefit of such cooling schemes in 1D.

At the same time it is however important to emphasise that disregard of coherences can at most lead to impairment of the efficiency, that means in reality cooling will only perform better instead of worse than simulated. In other words, the simulations will not raise unrealistic expectations and make predictions which in reality can never be achieved. This is an important conclusion to keep in mind when analysing the results of the simulation.

In this context, it is finally interesting to mention that this phase loss does not only prohibit investigation of polarisation schemes but also leads to different cooling results depending on the spatial configurations. This means for example that 1D-cooling by means of a circularly polarised laser beam propagating along z in a magnetic field along x might lead to another result than for the similar scheme, but with the field being aligned along y, although relative orientations are the same in both cases. This is due to the fact that rotations are nothing else than phase shifts which again get lost in case of uncontrolled phase relations. This is as well only relevant for 1D polarisation schemes and does not affect the efficiency in 3D-simulations.

F.5.7 Statistical significance

To be able to assess to which degree cooling effects in the simulation results can be attributed to physical processes or not, it is important to know the impact of statistics on the values of the figures of merit for cooling, defined in Sec. 3.1.2. The statistical effect in the simulation originates

from the random generation of initial positions and velocities of the atoms. The smaller the number of particles the more are the results affected by this randomness.

In the simulation there are two parameters which enable to exercise influence on the impact of statistics, namely either by modifying the number of particles contained in the cloud or by running the same cooling parameter configuration for different values of the random number generator seed and linearly combining the individual data sets.

The strategy to reach statistical significance is thus to increase the number of atoms or samples to such a value that the cooling efficiency will no longer significantly change if more atoms or samples are added. To determine the appropriate number of particles the evolution of the cloud was simulated in a given parameter configuration for either 500, 1000, 2000 and 4000 atoms, each for ten different RNG seed values. The average over the ten different random datasets serves as a measure for the statistical significance of the results for the respective number of particles.

Fig. F.3 shows an overview of the evolution of the most relevant characteristic parameters of the laser interaction simulation for four different numbers of atoms. Next to the above introduced cooling parameters, temperature T, number of atoms around resonance n_r and the signal S, the second row in each of the four varicoloured subfigures contains from left to right the fraction of atoms in ground states, in excited states and the fraction of annihilated atoms. Each subplot visualises the evolution of the statistical mean value in dark colour as well as, in faint colour, the corresponding standard deviation of the data at each point of time, derived from the ten samples with different RNG seeds.

The data shown in Fig. F.3 is based on simulations of 1D longitudinal cooling in a magnetic field of 1 T using the standard set of laser parameters as already used for the runtime study (cf. caption of Tab. F.1). A detailed physical analysis of the evolution of the shown parameters can be found in the fourth chapter.

This study for different numbers of particles allows to draw the following conclusions with respect to statistics: It can clearly be seen that the results of the evolution of atoms in ground state, excited state and annihilated atoms are much more reliable than the ones for the temperature, n_r and S parameters which is simply due to error propagation and the fact that the latter quantities do not concern all particles of the ensemble but only half in case of T or only those in a certain velocity range in case of n_r and S.

It can furthermore be observed that the statistical deviation progressively increases in the course of the simulation. This can be explained by the continuous decrease in still available atoms due to constant annihilation. Naturally, the influence of a single atom on the cooling efficiency thus grows with time leading to increasing fluctuations at the expense of statistical significance of derived parameters. This implies that the simulation duration over which the data can be considered as reliable is limited to a maximum value depending on the initially chosen total number of atoms N. The decreasing number of available atoms is also the reason for the decline of the n_r parameter in the second half of the simulation.

The statistical significance of the data can be evaluated by defining two separate (arbitrary) threshold levels: The data is considered as statistically significant if the evolution of the populations (three lower subplots of each subfigure) does not deviate by more than 1% and the cooling parameters T, n_r and S by not more than one tenth of the maximum range between the most extreme values. The data in Fig. F.3 is coloured according to this valuation standard, where green indicates "passed" and red "rejected" in terms of significance. This colour code shows that the results for 2000 atoms meet the criteria for reliability almost completely with the only exception represented by n_r which only partially meets the criterion. As far as this parameter is concerned it has to be taken into account though that it is calculated from a very restricted number of atoms (only those with $v < v_\mathrm{rec}$) which results in much higher fluctuations compared to all other parameters. For this reason higher deviations are acceptable for n_r. It can however be ensured that for $N = 2000$ more than half of the values meet the condition and that the maximum deviation exceeds the threshold by only 40%. Furthermore, the third subplots in the upper row of the subfigure in bottom left reveals that the signal S, which is derived from $n_\mathrm{r}^{(\mathrm{ON})}$ and $n_\mathrm{r}^{(\mathrm{OFF})}$, is statistically significant at almost all simulation times. Interestingly, even for $N = 4000$ not all values meet the significance criterion.
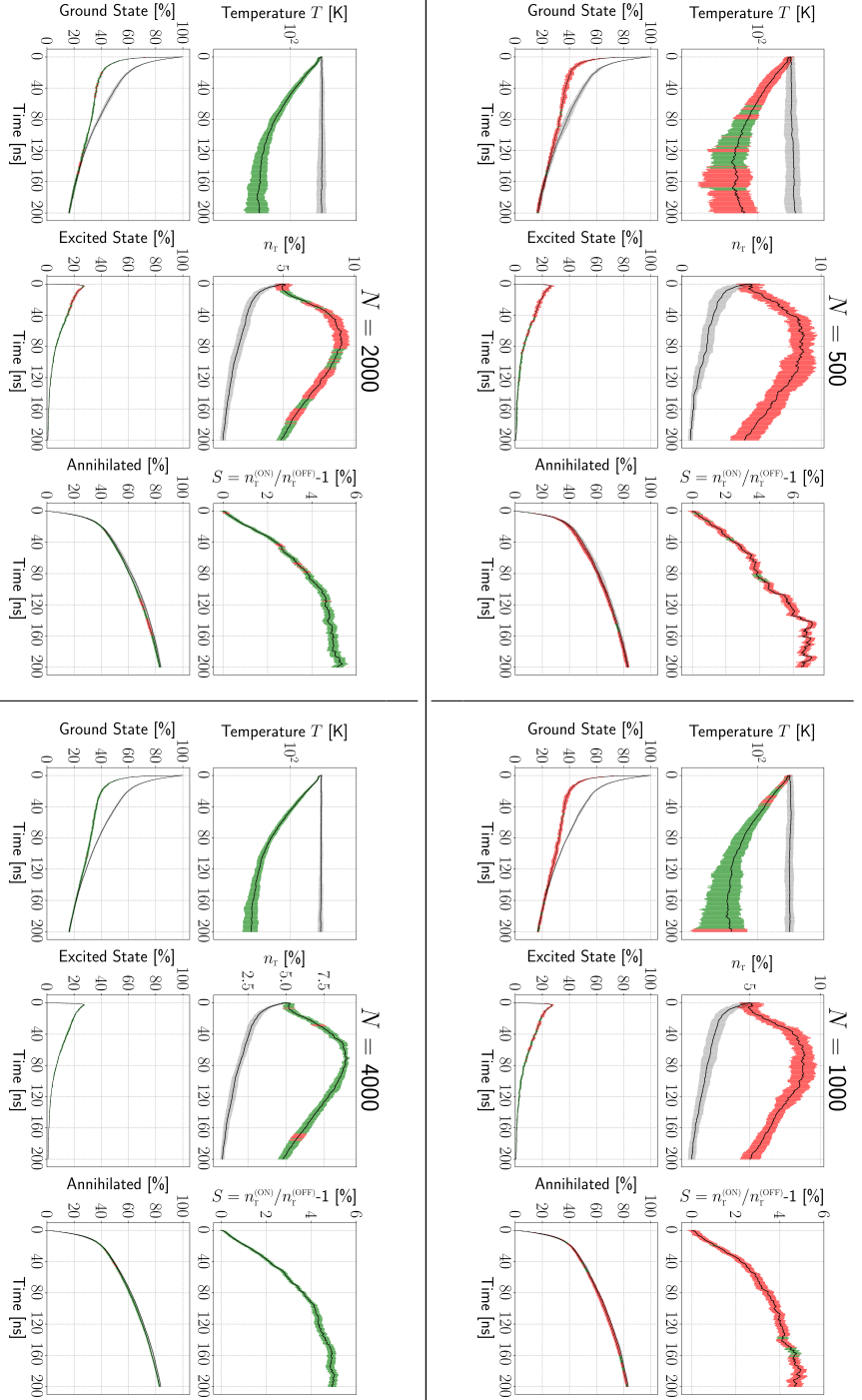
FIGURE F.3: Impact of statistics on simulation results.
The figure shows, for four different total numbers of atoms N, the mean and standard deviation of the most relevant characteristic parameters of the simulation based on a dataset obtained from varying the RNG seed over a range of ten values for 1D longitudinal Ps laser cooling in a magnetic field of 1 T. The laser parameters are set to their standard values. In each subfigure the subplots in the upper row visualise the evolution of the cooling parameters T, n_{r} and S and the ones in the bottom row the evolution of the ground and excited states population as well as of the number of annihilated atoms.
The colour code indicates the statistical significance of the values of the laser ON simulations, where green signifies "passed" and red "rejected" (explanations for valuation criteria are given in the text). The curve in grey represents the laser OFF simulation result for comparison.

The gain in precision can best be illustrated by comparing the deviation of each simulation parameter for different initial particle numbers N as a function of the number of annihilated atoms as shown in Fig. F.4. All curves present the data for the laser ON cases for the standard set of laser parameters (cf. caption of Fig. F.1).

Obviously and as expected, the doubling from $N = 500$ to $N = 1000$ yields a much higher gain in precision than the one from $N = 2000$ to $N = 4000$, especially for low numbers of annihilated atoms (i.e., short laser interaction times). For n_r (2nd subplot), the ground state population (4th subplot) and the number of annihilated atoms (6th subplot) the increase to $N = 4000$ does not even yield a significant improvement. This confirms the previous result that $N = 2000$ is already a solid number producing results with high statistical significance.

In order to decide on the appropriate number of atoms to be used, it is important to also account for the required computation time (cf. also Fig. F.1). In this regard it is interesting to note that it took almost 13 days of non-stop computing time to acquire the dataset for the subfigure of Fig. F.3 for 4000 particles while the same simulations for 2000 atoms took only 3.5 days. Obviously, the gain in precision from 2000 to 4000 atoms is thus not worth the huge increase in computation time. For this reason a number of 2000 atoms was chosen for all simulations as an expedient compromise between precision and efficiency.
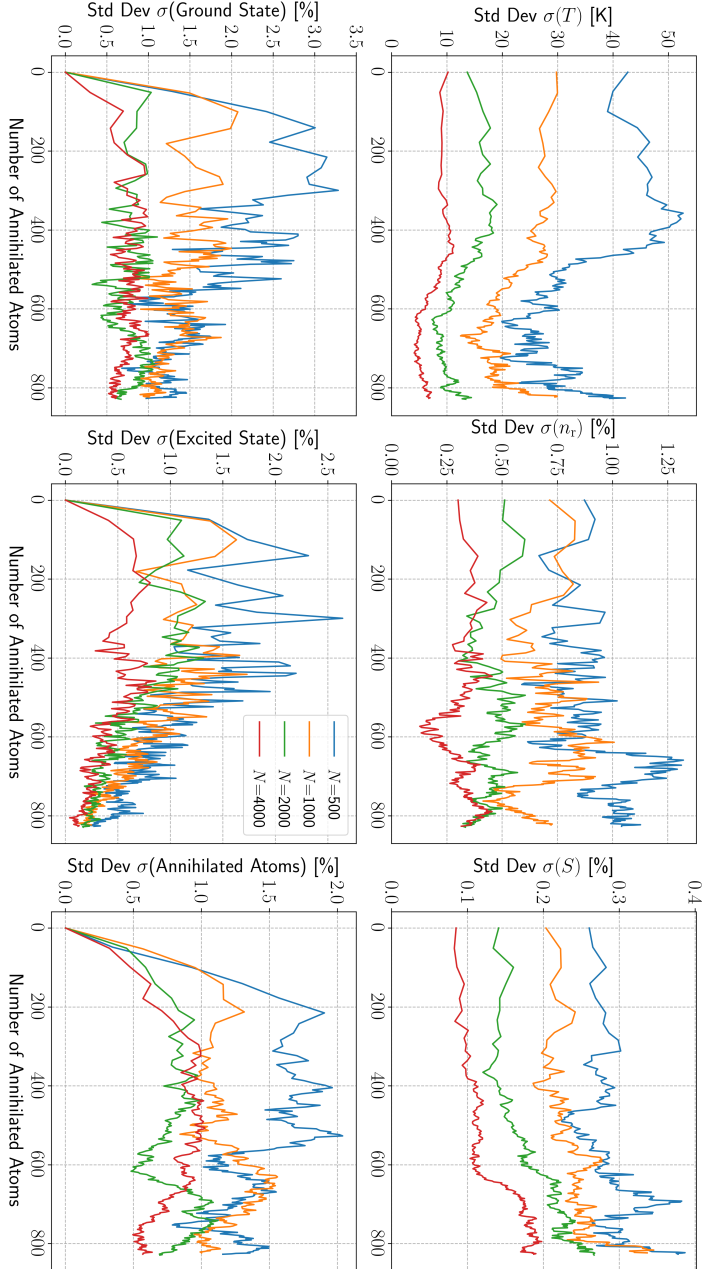
FIGURE F.4: Standard deviation of relevant cooling parameters as a function of the number of annihilated atoms for different initial numbers of particles.
The subplots provide a comparison of the standard deviation of all relevant cooling parameters (equal to the standard deviation for the laser ON cases in Fig. F.3) for the different numbers of initial particles, as indicated in the legend. The deviation is plotted as a function of the number of annihilated atoms with similar chronological progression, from left to right in the course of the simulation. The values for $n_{\rm r}$, the state population and the numbers of annihilated atoms have been normalised by the total number of atoms N.

Publications with significant own contribution

[49]   The following publication has been included in the present thesis:
        C. Zimmer *et al.*, "Positronium laser cooling in a magnetic field," *Phys. Rev. A*, vol. 104,
        p. 023 106, 2 2021. DOI: `10.1103/PhysRevA.104.023106`. [Online]. Available: `https://link.aps.org/doi/10.1103/PhysRevA.104.023106`.

[175]   S Mariazzi *et al.*, "High-yield thermalized positronium at room temperature emitted by
        morphologically tuned nanochanneled silicon targets," *Journal of Physics B: Atomic, Molecular and Optical Physics*, vol. 54, no. 8, p. 085 004, 2021. DOI: `10.1088/1361-6455/abf6b6`.
        [Online]. Available: `https://doi.org/10.1088/1361-6455/abf6b6`.

[176]   C. Amsler *et al.*, "Pulsed production of antihydrogen," *Communications Physics*, vol. 4,
        no. 1, p. 19, 2021, ISSN: 2399-3650. DOI: `10.1038/s42005-020-00494-z`. [Online]. Available:
        `https://doi.org/10.1038/s42005-020-00494-z`.

[177]   A. Hinterberger *et al.*, "Trapping of C2- in a digital ion trap," *Journal of Physics B: Atomic,
        Molecular and Optical Physics*, vol. 52, no. 22, p. 225 003, 2019. DOI: `10.1088/1361-6455/ab4940`. [Online]. Available: `https://doi.org/10.1088/1361-6455/ab4940`.

Bibliography

[1]   W. Isaacson, *Einstein: His Life and Universe*. Simon & Schuster, 2007, ISBN: 9781416539322.

[2]   G. Gabrielse *et al.*, "Background-free observation of cold antihydrogen with field-ionization
       analysis of its states," *Phys. Rev. Lett.*, vol. 89, p. 213 401, 21 2002. DOI: `10.1103/PhysRevLett.89.213401`. [Online]. Available: `https://link.aps.org/doi/10.1103/PhysRevLett.89.213401`.

[3]   M. Amoretti *et al.*, "Production and detection of cold antihydrogen atoms," *Nature*, vol. 419,
       no. 6906, pp. 456–459, 2002, ISSN: 1476-4687. DOI: `10.1038/nature01096`. [Online]. Available:
       `https://doi.org/10.1038/nature01096`.

[4]   G. B. Andresen *et al.*, "Trapped antihydrogen," *Nature*, vol. 468, no. 7324, pp. 673–676,
       2010, ISSN: 1476-4687. DOI: `10.1038/nature09610`. [Online]. Available: `https://doi.org/10.1038/nature09610`.

[5]   R. Pohl *et al.*, "Muonic hydrogen and the proton radius puzzle," *Annual Review of Nuclear
       and Particle Science*, vol. 63, no. 1, pp. 175–204, 2013. DOI: `10.1146/annurev-nucl-102212-170627`. [Online]. Available: `https://doi.org/10.1146/annurev-nucl-102212-170627`.

[6]   R. Pohl *et al.*, "The size of the proton," *Nature*, vol. 466, no. 7303, pp. 213–216, 2010, ISSN:
       1476-4687. DOI: `10.1038/nature09250`. [Online]. Available: `https://doi.org/10.1038/nature09250`.

[7]   D. B. Cassidy, "Experimental progress in positronium laser physics," *The European Physical
       Journal D*, vol. 72, no. 3, p. 53, 2018, ISSN: 1434-6079. DOI: `10.1140/epjd/e2018-80721-y`.
       [Online]. Available: `https://doi.org/10.1140/epjd/e2018-80721-y`.

[8]   S. G. Karshenboim, "Precision physics of simple atoms: {qed} tests, nuclear structure and fundamental constants," *Physics Reports*, vol. 422, no. 1 - 2, p. 1 63, 2005, ISSN: 0370-1573. DOI: `http://dx.doi.org/10.1016/j.physrep.2005.08.008`. [Online]. Available: `http://www.sciencedirect.com/science/article/pii/S0370157305003637`.

[9]   M. Oberthaler, "Anti-matter wave interferometry with positronium," *Nuclear Instruments and Methods in Physics Research Section B: Beam Interactions with Materials and Atoms*, vol. 192, no. 1, pp. 129–134, 2002, ISSN: 0168-583X. DOI: `https://doi.org/10.1016/S0168-583X(02)00793-0`. [Online]. Available: `https://www.sciencedirect.com/science/article/pii/S0168583X02007930`.

[10]   M. Dine *et al.*, "Origin of the matter-antimatter asymmetry," *Rev. Mod. Phys.*, vol. 76, pp. 1–30, 1 2003. DOI: `10.1103/RevModPhys.76.1`. [Online]. Available: `https://link.aps.org/doi/10.1103/RevModPhys.76.1`.

[11]   A. D. Sakharov, "Violation of CP Invariance, C asymmetry, and baryon asymmetry of the universe," *Pisma Zh. Eksp. Teor. Fiz.*, vol. 5, pp. 32–35, 1967. DOI: `10.1070/PU1991v034n05ABEH002497`.

[12]   W. Bernreuther *et al.*, "Cp violation andz boson decays," *Zeitschrift für Physik C Particles and Fields*, vol. 43, no. 1, pp. 117–132, 1989, ISSN: 1431-5858. DOI: `10.1007/BF02430617`. [Online]. Available: `https://doi.org/10.1007/BF02430617`.

[13]   A. Mills *et al.*, "Can we measure the gravitational free fall of cold Rydberg state positronium?" *Nuclear Instruments and Methods in Physics Research Section B: Beam Interactions with Materials and Atoms*, vol. 192, no. 1, pp. 102–106, 2002, ISSN: 0168-583X. DOI: `https://doi.org/10.1016/S0168-583X(02)00789-9`. [Online]. Available: `https://www.sciencedirect.com/science/article/pii/S0168583X02007899`.

[14]   D. Cassidy *et al.*, "Atom control and gravity measurements using Rydberg positronium," in *International Journal of Modern Physics: Conference Series*, World Scientific, vol. 30, 2014, p. 1 460 259.

[15]   M. Antonello *et al.*, "Efficient 2^3S positronium production by stimulated decay from the 3^3P level," *Phys. Rev. A*, vol. 100, p. 063 414, 6 2019. DOI: `10.1103/PhysRevA.100.063414`. [Online]. Available: `https://link.aps.org/doi/10.1103/PhysRevA.100.063414`.

[16]   C. Amole *et al.*, "Description and first application of a new technique to measure the gravitational mass of antihydrogen," *Nature Communications*, vol. 4, no. 1, p. 1785, 2013, ISSN: 2041-1723. DOI: `10.1038/ncomms2787`. [Online]. Available: `https://doi.org/10.1038/ncomms2787`.

[17]   S. Aghion *et al.*, "A moiré deflectometer for antimatter," *Nature Communications*, vol. 5, no. 1, p. 4538, 2014, ISSN: 2041-1723. DOI: `10.1038/ncomms5538`. [Online]. Available: `https://doi.org/10.1038/ncomms5538`.

[18]   P. Pérez *et al.*, "The gbar antimatter gravity experiment," *Hyperfine Interactions*, vol. 233, no. 1, pp. 21–27, 2015, ISSN: 1572-9540. DOI: `10.1007/s10751-015-1154-8`. [Online]. Available: `https://doi.org/10.1007/s10751-015-1154-8`.

[19]   A. Antognini *et al.*, "Studying antimatter gravity with muonium," *Atoms*, vol. 6, no. 2, 2018, ISSN: 2218-2004. DOI: `10.3390/atoms6020017`. [Online]. Available: `https://www.mdpi.com/2218-2004/6/2/17`.

[20]   S. Mohorovičić, "Möglichkeit neuer Elemente und ihre Bedeutung für die Astrophysik," *Astronomische Nachrichten*, vol. 253, no. 4, pp. 93–108, 1934. DOI: `https://doi.org/10.1002/asna.19342530402`. [Online]. Available: `https://onlinelibrary.wiley.com/doi/abs/10.1002/asna.19342530402`.

[21]   M. Deutsch, "Evidence for the formation of positronium in gases," *Phys. Rev.*, vol. 82, pp. 455–456, 3 1951. DOI: `10.1103/PhysRev.82.455`. [Online]. Available: `https://link.aps.org/doi/10.1103/PhysRev.82.455`.

[22] S Berko *et al.*, "Positronium," *Annual Review of Nuclear and Particle Science*, vol. 30, no. 1, pp. 543–581, 1980. DOI: `10.1146/annurev.ns.30.120180.002551`. [Online]. Available: `https://doi.org/10.1146/annurev.ns.30.120180.002551`.

[23] P. Platzman *et al.*, "Possibilities for Bose condensation of positronium," *Physical Review B*, vol. 49, no. 1, p. 454, 1994.

[24] S. K. Adhikari, "Positronium interaction and its Bose-Einstein condensation," *physica status solidi (c)*, vol. 6, no. 11, pp. 2272–2276, 2009.

[25] A. Mills Jr, "Positronium Bose-Einstein condensation in liquid He 4 bubbles," *Physical Review A*, vol. 100, no. 6, p. 063 615, 2019.

[26] N. N. Mondal, "Challenges and advances of positronium Bose-Einstein condensation," *AIP Advances*, vol. 9, no. 5, p. 055 310, 2019.

[27] Y. Zhang *et al.*, *Possibility of forming a stable bose-einstein condensate of 2^3S_1 positronium atoms*, 2019.

[28] B. Rienäcker, "Creation and manipulation of positronium for efficient antihydrogen production at aegis," PhD thesis, Technische Universität München, 2021.

[29] J. Dalibard *et al.*, "Foreword: Laser cooling and trapping of neutral atoms," in *Atomic and Molecular Beams: The State of the Art 2000*, R. Campargue, Ed. Berlin, Heidelberg: Springer Berlin Heidelberg, 2001, pp. 43–62, ISBN: 978-3-642-56800-8. DOI: `10.1007/978-3-642-56800-8_2`. [Online]. Available: `https://doi.org/10.1007/978-3-642-56800-8_2`.

[30] H. J. Metcalf *et al.*, "Laser cooling and trapping of atoms," *J. Opt. Soc. Am. B*, vol. 20, no. 5, pp. 887–908, 2003. DOI: `10.1364/JOSAB.20.000887`. [Online]. Available: `http://josab.osa.org/abstract.cfm?URI=josab-20-5-887`.

[31] H. J. Metcalf *et al.*, "Laser cooling and trapping of neutral atoms," in *The Optics Encyclopedia*. American Cancer Society, 2007, ISBN: 9783527600441. DOI: `https://doi.org/10.1002/9783527600441.oe005`. [Online]. Available: `https://onlinelibrary.wiley.com/doi/abs/10.1002/9783527600441.oe005`.

[32] W. D. Phillips, "Nobel lecture: Laser cooling and trapping of neutral atoms," *Rev. Mod. Phys.*, vol. 70, pp. 721–741, 3 1998. DOI: `10.1103/RevModPhys.70.721`. [Online]. Available: `https://link.aps.org/doi/10.1103/RevModPhys.70.721`.

[33] E. P. Liang *et al.*, "Laser cooling of positronium," *Optics Communications*, vol. 65, no. 6, pp. 419 –424, 1988, ISSN: 0030-4018. DOI: `http://dx.doi.org/10.1016/0030-4018(88)90116-2`. [Online]. Available: `http://www.sciencedirect.com/science/article/pii/0030401888901162`.

[34] D. Cassidy *et al.*, "Fundamental physics with cold positronium," in *AIP Conference Proceedings*, vol. 1037, American Institute of Physics, 2008, pp. 66–83. DOI: `10.1063/1.2977858`. [Online]. Available: `https://aip.scitation.org/doi/abs/10.1063/1.2977858`.

[35] C. Hugenschmidt, "Positron sources and positron beams," in *Proceedings of the International School of Physics "Enrico Fermi", Course CLXXIV: Physics with many positrons*, vol. 174, IOS Press, 2010, pp. 399–417. DOI: `10.3254/978-1-60750-647-8-399`. [Online]. Available: `http://doi.org/10.3254/978-1-60750-647-8-399`.

[36] P Crivelli *et al.*, "Experimental considerations for testing antimatter antigravity using positronium 1s-2s spectroscopy," in *International Journal of Modern Physics: Conference Series*, vol. 30, World Scientific, 2014, p. 1 460 257. DOI: `10.1142/S2010194514602579`. [Online]. Available: `https://doi.org/10.1142/S2010194514602579`.

[37] H Iijima *et al.*, "Laser cooling system of ortho-positronium," *Nucl. Instru. Meth. Phys. Res. A*, vol. 455, p. 104 108, 2000. DOI: `http://dx.doi.org/10.1016/S0168-9002(00)00714-2`. [Online]. Available: `http://www.sciencedirect.com/science/article/pii/S0168900200007142`.

BIBLIOGRAPHY

[38] N. N. Mondal, "Construction of a position-sensitive scintillation detectors system to view the laser cooled ortho-positronium," in *Nuclear Science Symposium Conference Record, 2001 IEEE*, vol. 1, IEEE, 2001, pp. 319–324. DOI: `10.1109/NSSMIC.2001.1008467`.

[39] T. Kumita *et al.*, "Study on laser cooling of ortho-positronium," *Nucl. Instru. Meth. Phys. Res. B*, vol. 192, p. 171 175, 2002. DOI: `http://dx.doi.org/10.1016/S0168-583X(02) 00863-7`. [Online]. Available: `http://www.sciencedirect.com/science/article/pii/ S0168583X02008637`.

[40] K Wada *et al.*, "Study of ortho-positronium laser cooling," in *Proc. 21st Beam Dynamics Workshop on Laser-Beam Interactions*. [Online]. Available: `https://www.stonybrook.edu/ icfa2001/Papers/tu4-9.pdf`.

[41] T Hirose *et al.*, "Laser cooling of ortho-Positronium: Toward realization of Bose-Einstein Condensation," in *Quantum Aspects Of Beam Physics*, World Scientific, 2002, pp. 279–289. DOI: `10.1142/9789812777447_0023`. [Online]. Available: `https://www.worldscientific. com/doi/abs/10.1142/9789812777447_0023`.

[42] K Shu *et al.*, "Study on cooling of positronium for Bose Einstein condensation," *J. Phys. B*, vol. 49, no. 10, p. 104 001, 2016. [Online]. Available: `http://stacks.iop.org/0953- 4075/49/i=10/a=104001`.

[43] A. Ishida *et al.*, "Study on positronium Bose–Einstein condensation," in *JJAP Conference Proceedings*, vol. 7, The Japan Society of Applied Physics, 2017. DOI: `10.7567/JJAPCP.7. 011001`. [Online]. Available: `https://journals.jsap.jp/jjapproceedings/online/7- 011001`.

[44] K Shu *et al.*, "Study on Bose-Einstein condensation of positronium," in *Journal of Physics: Conference Series*, vol. 791, IOP Publishing, 2017, p. 012 007. DOI: `10.1088/1742-6596/791/ 1/012007`. [Online]. Available: `https://doi.org/10.1088/1742-6596/791/1/012007`.

[45] P Yzombard *et al.*, "Overview of recent work on laser excitation of positronium for the formation of antihydrogen," in *Proceedings of the 12th International Conference on Low Energy Antiproton Physics (LEAP2016)*, 2017, p. 011 026.

[46] M. Charlton *et al.*, *Antihydrogen and Fundamental Physics*, ser. SpringerBriefs in Physics. Springer, Jul. 2020, ISBN: 978-3-030-51712-0, 978-3-030-51713-7. DOI: `10.1007/978-3-030- 51713-7`.

[47] C. Zimmer *et al.*, "Positronium laser cooling in a magnetic field," *Phys. Rev. A*, vol. 104, p. 023 106, 2 2021. DOI: `10.1103/PhysRevA.104.023106`. [Online]. Available: `https: //link.aps.org/doi/10.1103/PhysRevA.104.023106`.

[48] D. B. Cassidy, "Experimental progress in positronium laser physics," *The European Physical Journal D*, vol. 72, no. 3, p. 53, 2018.

[49] C. Zimmer *et al.*, "Positronium laser cooling in a magnetic field," *Phys. Rev. A*, vol. 104, p. 023 106, 2 2021. DOI: `10.1103/PhysRevA.104.023106`. [Online]. Available: `https: //link.aps.org/doi/10.1103/PhysRevA.104.023106`.

[50] S Mariazzi *et al.*, "High-yield thermalized positronium at room temperature emitted by morphologically tuned nanochanneled silicon targets," *Journal of Physics B: Atomic, Molecular and Optical Physics*, vol. 54, no. 8, p. 085 004, 2021. DOI: `10.1088/1361-6455/abf6b6`. [Online]. Available: `https://doi.org/10.1088/1361-6455/abf6b6`.

[51] A. Rubbia, "Positronium as a probe for new physics beyond the standard model," *International Journal of Modern Physics A*, vol. 19, no. 23, 3961–3985, 2004, ISSN: 1793-656X. DOI: `10.1142/s0217751x0402021x`. [Online]. Available: `http://dx.doi.org/10.1142/ S0217751X0402021X`.

[52] S. G. Karshenboim, "Precision study of positronium: Testing bound state QED theory," *International Journal of Modern Physics A*, vol. 19, no. 23, 3879–3896, 2004, ISSN: 1793-656X. DOI: `10.1142/s0217751x04020142`. [Online]. Available: `http://dx.doi.org/10.1142/ S0217751X04020142`.

[53] H. A. Bethe *et al.*, *Quantum Mechanics of One- and Two-Electron Atoms*. Springer US, 1977, ISBN: 9780306200229.

[54] B. A. Robson, "Cosmological consequences of a quantum theory of mass and gravity," in *Trends in Modern Cosmology*, A. J. C. de Souza, Ed., Rijeka: IntechOpen, 2017, ch. 8. DOI: `10.5772/intechopen.68410`. [Online]. Available: `https://doi.org/10.5772/intechopen.68410`.

[55] L. Michel, "Selection rules imposed by charge conjugation," *Il Nuovo Cimento (1943-1954)*, vol. 10, no. 3, p. 319, 2008, ISSN: 1827-6121. DOI: `10.1007/BF02786202`. [Online]. Available: `https://doi.org/10.1007/BF02786202`.

[56] P. Dirac, *The Principles of Quantum Mechanics*, ser. Comparative Pathobiology - Studies in the Postmodern Theory of Education. Clarendon Press, 1981, ISBN: 9780198520115.

[57] P Crivelli *et al.*, "Positronium portal into hidden sector: A new experiment to search for mirror dark matter," *Journal of Instrumentation*, vol. 5, no. 08, P08001–P08001, 2010. DOI: `10.1088/1748-0221/5/08/p08001`. [Online]. Available: `https://doi.org/10.1088/1748-0221/5/08/p08001`.

[58] A. Badertscher *et al.*, "Improved limit on invisible decays of positronium," *Phys. Rev. D*, vol. 75, p. 032 004, 3 2007. DOI: `10.1103/PhysRevD.75.032004`. [Online]. Available: `https://link.aps.org/doi/10.1103/PhysRevD.75.032004`.

[59] T. Mitsui *et al.*, "Search for invisible decay of orthopositronium," *Phys. Rev. Lett.*, vol. 70, pp. 2265–2268, 15 1993. DOI: `10.1103/PhysRevLett.70.2265`. [Online]. Available: `https://link.aps.org/doi/10.1103/PhysRevLett.70.2265`.

[60] B. Schwarzschild, "CERN Experiment Clarifies Origin of CP Symmetry Violation," *Physics Today*, vol. 41, no. 10, pp. 17–20, 1988. DOI: `10.1063/1.2811586`. [Online]. Available: `https://doi.org/10.1063/1.2811586`.

[61] ——, "B-Decay Experiments Show Clear Violation of CP Symmetry," *Physics Today*, vol. 54, no. 9, pp. 19–19, 2001. DOI: `10.1063/1.1420501`. [Online]. Available: `https://doi.org/10.1063/1.1420501`.

[62] M. Peskin, "The matter with antimatter," *Nature*, vol. 419, no. 6902, pp. 25–27, 2002, ISSN: 1476-4687. DOI: `10.1038/419024a`. [Online]. Available: `https://doi.org/10.1038/419024a`.

[63] R. Aaij *et al.*, "First observation of CP violation in the decays of B_s^0 mesons," *Phys. Rev. Lett.*, vol. 110, p. 221 601, 22 2013. DOI: `10.1103/PhysRevLett.110.221601`. [Online]. Available: `https://link.aps.org/doi/10.1103/PhysRevLett.110.221601`.

[64] R. Aaij *et al.*, "Observation of CP violation in charm decays," *Phys. Rev. Lett.*, vol. 122, p. 211 803, 21 2019. DOI: `10.1103/PhysRevLett.122.211803`. [Online]. Available: `https://link.aps.org/doi/10.1103/PhysRevLett.122.211803`.

[65] K. Abe *et al.*, "Constraint on the matter–antimatter symmetry-violating phase in neutrino oscillations," *Nature*, vol. 580, no. 7803, pp. 339–344, 2020, ISSN: 1476-4687. DOI: `10.1038/s41586-020-2177-0`. [Online]. Available: `https://doi.org/10.1038/s41586-020-2177-0`.

[66] A. Alekseev, "Two-photon annihilation of positronium in the P-state," *Sov. Phys. JETP*, vol. 34, pp. 826–830, 1958.

[67] ——, "Three-photon annihilation of positronium in the P-state," *Sov. Phys. JETP*, vol. 36, pp. 1312–1315, 1959.

[68] A. Sen *et al.*, "Two-photon decay of P-wave positronium: A tutorial," *Canadian Journal of Physics*, vol. 97, no. 7, pp. 693–700, 2019.

[69] G. S. Adkins *et al.*, "Two-loop correction to the orthopositronium decay rate," *Annals of Physics*, vol. 295, no. 2, pp. 136–193, 2002, ISSN: 0003-4916. DOI: `https://doi.org/10.1006/aphy.2001.6219`. [Online]. Available: `https://www.sciencedirect.com/science/article/pii/S0003491601962190`.

BIBLIOGRAPHY

[70] G. S. Adkins *et al.*, "Two-loop corrections to the decay rate of parapositronium," *Phys. Rev. A*, vol. 68, p. 032 512, 3 2003. DOI: `10.1103/PhysRevA.68.032512`. [Online]. Available: `https://link.aps.org/doi/10.1103/PhysRevA.68.032512`.

[71] S. M. Curry, "Combined Zeeman and Motional Stark Effects in the First Excited State of Positronium," *Phys. Rev. A*, vol. 7, pp. 447–450, 2 1973. DOI: `10.1103/PhysRevA.7.447`. [Online]. Available: `https://link.aps.org/doi/10.1103/PhysRevA.7.447`.

[72] R. Caravita, "Towards measuring gravity on neutral antimatter," PhD thesis, Università degli Studi di Genova, 2017.

[73] A. Messiah, *Quantum Mechanics*, ser. Quantum Mechanics Bd. 2. Elsevier Science, 1981, ISBN: 9780720400458.

[74] D. Griffiths, *Introduction to Quantum Mechanics*. Cambridge University Press, 2017, ISBN: 9781107179868.

[75] K. Pachucki *et al.*, "Complete results for positronium energy levels at order $m\alpha^6$," *Phys. Rev. Lett.*, vol. 80, pp. 2101–2104, 10 1998. DOI: `10.1103/PhysRevLett.80.2101`. [Online]. Available: `https://link.aps.org/doi/10.1103/PhysRevLett.80.2101`.

[76] A. Czarnecki *et al.*, "Positronium hyperfine splitting: Analytical value at $\mathcal{O}(m\alpha^6)$," *Phys. Rev. Lett.*, vol. 82, pp. 311–314, 2 1999. DOI: `10.1103/PhysRevLett.82.311`. [Online]. Available: `https://link.aps.org/doi/10.1103/PhysRevLett.82.311`.

[77] J. Zatorski, "$\mathcal{O}(m\alpha^6)$ corrections to energy levels of positronium with nonvanishing orbital angular momentum," *Phys. Rev. A*, vol. 78, p. 032 103, 3 2008. DOI: `10.1103/PhysRevA.78.032103`. [Online]. Available: `https://link.aps.org/doi/10.1103/PhysRevA.78.032103`.

[78] W. E. Lamb, "Fine structure of the hydrogen atom. iii," *Phys. Rev.*, vol. 85, pp. 259–276, 2 1952. DOI: `10.1103/PhysRev.85.259`. [Online]. Available: `https://link.aps.org/doi/10.1103/PhysRev.85.259`.

[79] J. Pirenne, PhD thesis, University of Paris, 1944.

[80] ——, "The proper field and the interaction of Dirac particles. I–III," *Arch. Sci. phys. nat*, vol. 28, pp. 233–272, 1946.

[81] V. Berestetskii, "On the spectrum of positronium," *Zhurnal Eksperimentalnoi i Teoreticheskoi Fiziki*, vol. 19, no. 12, pp. 1129–1135, 1949.

[82] R. A. Ferrell, "The positronium fine structure," *Phys. Rev.*, vol. 84, pp. 858–859, 4 1951. DOI: `10.1103/PhysRev.84.858`. [Online]. Available: `https://link.aps.org/doi/10.1103/PhysRev.84.858`.

[83] A. M. Alonso *et al.*, "Positronium decay from $n = 2$ states in electric and magnetic fields," *Phys. Rev. A*, vol. 93, p. 012 506, 1 2016. DOI: `10.1103/PhysRevA.93.012506`. [Online]. Available: `https://link.aps.org/doi/10.1103/PhysRevA.93.012506`.

[84] H. Marxer *et al.*, "Semiclassical estimation of the radiative mean lifetimes of hydrogenlike states," *Phys. Rev. A*, vol. 43, pp. 1268–1274, 3 1991. DOI: `10.1103/PhysRevA.43.1268`. [Online]. Available: `https://link.aps.org/doi/10.1103/PhysRevA.43.1268`.

[85] J. Shapiro *et al.*, "Metastability of 2s States of Hydrogenic Atoms," *Phys. Rev.*, vol. 113, pp. 179–181, 1 1959. DOI: `10.1103/PhysRev.113.179`. [Online]. Available: `https://link.aps.org/doi/10.1103/PhysRev.113.179`.

[86] C. J. Foot, *Atomic Physics*. Oxford University Press, 2005.

[87] C. Cohen-Tannoudji *et al.*, *Atom-Photon Interactions: Basic Processes and Applications*, ser. A Wiley-Interscience publication. Wiley, 1998, ISBN: 9780471293361.

[88] C. Muldoon, "Control and manipulation of cold atoms trapped in optical tweezers," PhD thesis, Oxford University, 2012.

[89] D. A. Steck, *Quantum and Atom Optics*, available online athttp://steck.us/teaching(revision 0.13.4,24 September 2020), 2020.

[90] C. Cohen-Tannoudji, "Atomic motion in laser light," in *Fundamental Systems in Quantum Optics*, J. Dalibard *et al.*, Eds., Elsevier Science Publishers B.V., 1992, pp. 1–164.

[91] E. P. Liang *et al.*, "Laser cooling of positronium," *Optics Communications*, vol. 65, no. 6, pp. 419–424, 1988, ISSN: 0030-4018. DOI: `https://doi.org/10.1016/0030-4018(88)90116-2`. [Online]. Available: `https://www.sciencedirect.com/science/article/pii/0030401888901162`.

[92] J. Dalibard, *Une brève histoire des atomes froids*, University Lecture, Cours 2014-15.

[93] Y. Castin *et al.*, "Limit of Doppler cooling," *J. Opt. Soc. Am. B*, vol. 6, no. 11, pp. 2046–2057, 1989. DOI: `10.1364/JOSAB.6.002046`. [Online]. Available: `http://josab.osa.org/abstract.cfm?URI=josab-6-11-2046`.

[94] J. Dalibard *et al.*, "Laser Cooling from the Semi-Classical to the Quantum Regime," in *Proceedings of the International School of Physics "Enrico Fermi"*, ser. Course CXX, Frontiers in Laser Spectroscopy, NorthHolland, 1994: edited by T.W. Hänsch and M. Inguscio, 1992, pp. 445–476.

[95] H. Wallis *et al.*, "Broadband laser cooling on narrow transitions," *J. Opt. Soc. Am. B*, vol. 6, no. 11, pp. 2211–2219, 1989. DOI: `10.1364/JOSAB.6.002211`. [Online]. Available: `http://josab.osa.org/abstract.cfm?URI=josab-6-11-2211`.

[96] S. Aghion *et al.*, "Producing long-lived 2^3S positronium via 3^3P laser excitation in magnetic and electric fields," *Phys. Rev. A*, vol. 98, p. 013 402, 1 2018. DOI: `10.1103/PhysRevA.98.013402`. [Online]. Available: `https://link.aps.org/doi/10.1103/PhysRevA.98.013402`.

[97] C. Amsler *et al.*, "Velocity-selected production of 2^3S metastable positronium," *Phys. Rev. A*, vol. 99, p. 033 405, 3 2019. DOI: `10.1103/PhysRevA.99.033405`. [Online]. Available: `https://link.aps.org/doi/10.1103/PhysRevA.99.033405`.

[98] S. K. Adhikari, "Positronium interaction and its bose-einstein condensation," *physica status solidi (c)*, vol. 6, no. 11, pp. 2272–2276, 2009.

[99] P. Yzombard, "Laser cooling and manipulation of antimatter in the aegis experiment," PhD thesis, Université Paris-Saclay, 2016.

[100] P Yzombard *et al.*, "Overview of recent work on laser excitation of positronium for the formation of antihydrogen," in *Proceedings of the 12th International Conference on Low Energy Antiproton Physics (LEAP2016)*, 2017, p. 011 026.

[101] G. Grynberg *et al.*, *Introduction aux lasers et à l'optique quantique*, ser. Cours de l'Ecole polytechnique. Ellipses, 2006, ISBN: 9782729857783.

[102] R. Caravita *et al.*, "Positronium Rydberg excitation diagnostic in a 1T cryogenic environment," *AIP Conference Proceedings*, vol. 2182, no. 1, p. 030 002, 2019. DOI: `10.1063/1.5135825`. [Online]. Available: `https://aip.scitation.org/doi/abs/10.1063/1.5135825`.

[103] S. Mariazzi *et al.*, "Toward inertial sensing with a 2^3S positronium beam," *The European Physical Journal D*, vol. 74, pp. 1–9, 2020.

[104] M. Rhee, "Refined definition of the beam brightness," *Physics of Fluids B: Plasma Physics*, vol. 4, no. 6, pp. 1674–1676, 1992.

[105] L. C. A. J, "Emittance and brightness: Definitions and measurements," English, *ADV. ELECTRON. ELECTRON PHYS., SUPPL.; USA; DA. 1980; VOL. 13A; PP. 159-259; BIBL. 5 P.*, 1980.

[106] C. A. Brau, "The physics and applications of high brightness electron beam," in, W. Scientific, Ed. Proceedings of the ICFA Workshop, Chia Laguna, Sardinia, 2002, ch. What Brightness means, p. 20.

[107] M. Reiser, *Theory and Design of Charged Particle Beams*. Weinheim: Wiley-VCH, 2008.

BIBLIOGRAPHY

[108] T. Chanelière *et al.*, "Phase-space-density limitation in laser cooling without spontaneous emission," *Phys. Rev. A*, vol. 98, p. 063 432, 6 2018. DOI: `10.1103/PhysRevA.98.063432`. [Online]. Available: `https://link.aps.org/doi/10.1103/PhysRevA.98.063432`.

[109] D. B. Cassidy *et al.*, "Single shot positron annihilation lifetime spectroscopy," *Applied Physics Letters*, vol. 88, no. 19, p. 194 105, 2006. DOI: `10.1063/1.2203336`. [Online]. Available: `https://doi.org/10.1063/1.2203336`.

[110] S. Aghion *et al.*, "Laser excitation of the $n = 3$ level of positronium for antihydrogen production," *Phys. Rev. A*, vol. 94, p. 012 507, 1 2016. DOI: `10.1103/PhysRevA.94.012507`. [Online]. Available: `https://link.aps.org/doi/10.1103/PhysRevA.94.012507`.

[111] C. Amsler *et al.*, "Pulsed production of antihydrogen," *Communications Physics*, vol. 4, no. 1, p. 19, 2021, ISSN: 2399-3650. DOI: `10.1038/s42005-020-00494-z`. [Online]. Available: `https://doi.org/10.1038/s42005-020-00494-z`.

[112] R. S. Brusa *et al.*, "The AEgIS experiment at CERN: Measuring antihydrogen free-fall in earth's gravitational field to test WEP with antimatter," *Journal of Physics: Conference Series*, vol. 791, p. 012 014, 2017. DOI: `10.1088/1742-6596/791/1/012014`. [Online]. Available: `https://doi.org/10.1088/1742-6596/791/1/012014`.

[113] B. Rienäcker, "Investigation of positron/positronium converter targets at aegis (cern)," Master's thesis, University of Applied Sciences Munich, 2015.

[114] S. Cialdi *et al.*, "Efficient two-step Positronium laser excitation to Rydberg levels," *Nuclear Instruments and Methods in Physics Research Section B: Beam Interactions with Materials and Atoms*, vol. 269, no. 13, pp. 1527–1533, 2011, ISSN: 0168-583X. [Online]. Available: `https://www.sciencedirect.com/science/article/pii/S0168583X11004599`.

[115] R. Caravita, "Laser apparatus for exciting Positronium in AEGIS Positronium spectroscopy experiment," Master's Thesis, Università degli Studi di Genova, 2011.

[116] P.-H. Cu-Nguyen, "Tunable hyperchromatic lenses," PhD thesis, University of Freiburg, Jan. 2015.

[117] F. Castelli *et al.*, "Efficient positronium laser excitation for antihydrogen production in a magnetic field," *Phys. Rev. A*, vol. 78, p. 052 512, 5 2008. DOI: `10.1103/PhysRevA.78.052512`. [Online]. Available: `https://link.aps.org/doi/10.1103/PhysRevA.78.052512`.

[118] A. Ore *et al.*, "Three-photon annihilation of an electron-positron pair," *Phys. Rev.*, vol. 75, pp. 1696–1699, 11 1949. DOI: `10.1103/PhysRev.75.1696`. [Online]. Available: `https://link.aps.org/doi/10.1103/PhysRev.75.1696`.

[119] P. Wallyn *et al.*, "The Positronium Radiative Combination Spectrum: Calculation in the Limit of Thermal Positrons and Low Densities," *APJ*, vol. 465, p. 473, Jul. 1996. DOI: `10.1086/177434`.

[120] R. Eisberg *et al.*, *Quantum Physics of Atoms, Molecules, Solids, Nuclei, and Particles*, ser. Quantum Physics of Atoms, Molecules, Solids, Nuclei and Particles. Wiley, 1985, ISBN: 9780471873730.

[121] R. Feynman *et al.*, *The Feynman Lectures on Physics, Vol. III: The New Millennium Edition: Quantum Mechanics*. Basic Books, 2015, ISBN: 9780465040834.

[122] *Atom—Photon Interactions: Basic Process and Appilcations*. John Wiley & Sons, Ltd, 1998, ISBN: 9783527617197. DOI: `https://doi.org/10.1002/9783527617197`. [Online]. Available: `https://onlinelibrary.wiley.com/doi/abs/10.1002/9783527617197`.

[123] S. Weinberg, *The Quantum Theory of Fields*. Cambridge University Press, 1995, vol. 1. DOI: `10.1017/CBO9781139644167`.

[124] L. Landau *et al.*, *Mechanics and Electrodynamics*. Elsevier Science, 2013, ISBN: 9781483285290.

[125] H. Goldstein *et al.*, *Classical Mechanics*. Addison Wesley, 2002, ISBN: 9780201657029.

[126] C.-D. Yang, "Quantum Hamilton mechanics: Hamilton equations of quantum motion, origin of quantum operators, and proof of quantization axiom," *Annals of Physics*, vol. 321, no. 12, pp. 2876–2926, 2006, ISSN: 0003-4916. DOI: `https://doi.org/10.1016/j.aop.2006.07.008`. [Online]. Available: `https://www.sciencedirect.com/science/article/pii/S0003491606001588`.

[127] W. Heisenberg, "Über quantentheoretische kinematik und mechanik," *Mathematische Annalen*, vol. 95, no. 1, pp. 683–705, 1926, ISSN: 1432-1807. DOI: `10.1007/BF01206633`. [Online]. Available: `https://doi.org/10.1007/BF01206633`.

[128] P. W. Atkins *et al.*, "The interaction of molecular multipoles with the electromagnetic field in the canonical formulation of non-covariant quantum electrodynamics," *Proceedings of the Royal Society of London. Series A, Mathematical and Physical Sciences*, vol. 319, no. 1539, pp. 549–563, 1970, ISSN: 00804630. [Online]. Available: `http://www.jstor.org/stable/77736`.

[129] E. A. Power *et al.*, "Coulomb gauge in non-relativistic quantum electro-dynamics and the shape of spectral lines," *Philosophical Transactions of the Royal Society of London. Series A, Mathematical and Physical Sciences*, vol. 251, no. 999, pp. 427–454, 1959, ISSN: 00804614. [Online]. Available: `http://www.jstor.org/stable/91664`.

[130] H Hoogland, "Minimal electromagnetic coupling in elementary quantum mechanics; a group theoretical derivation," *Journal of Physics A: Mathematical and General*, vol. 11, no. 5, pp. 797–804, 1978. DOI: `10.1088/0305-4470/11/5/009`. [Online]. Available: `https://doi.org/10.1088/0305-4470/11/5/009`.

[131] E. E. Jenkins *et al.*, "On gauge invariance and minimal coupling," *Journal of High Energy Physics*, vol. 2013, no. 9, p. 63, 2013, ISSN: 1029-8479. DOI: `10.1007/JHEP09(2013)063`. [Online]. Available: `https://doi.org/10.1007/JHEP09(2013)063`.

[132] B. Berche *et al.*, "Gauge transformations and conserved quantities in classical and quantum mechanics," *American Journal of Physics*, vol. 84, no. 8, pp. 616–625, 2016. DOI: `10.1119/1.4955153`. [Online]. Available: `https://doi.org/10.1119/1.4955153`.

[133] J. Jackson, *Classical Electrodynamics*. Wiley, 2012, ISBN: 9788126510948.

[134] J. Avron *et al.*, "Separation of center of mass in homogeneous magnetic fields," *Annals of Physics*, vol. 114, no. 1, pp. 431–451, 1978, ISSN: 0003-4916. DOI: `https://doi.org/10.1016/0003-4916(78)90276-2`. [Online]. Available: `https://www.sciencedirect.com/science/article/pii/0003491678902762`.

[135] T. Ozawa, "Feel the gauge," *Nature Physics*, vol. 11, no. 10, pp. 801–802, 2015, ISSN: 1745-2481. DOI: `10.1038/nphys3447`. [Online]. Available: `https://doi.org/10.1038/nphys3447`.

[136] H. Friedrich, *Theoretical Atomic Physics*. Springer Berlin Heidelberg, 2010, ISBN: 9783642065033.

[137] M Vincke *et al.*, "Centre-of-mass effects on the hydrogen atom in a magnetic field," *Journal of Physics B: Atomic, Molecular and Optical Physics*, vol. 21, no. 13, pp. 2407–2424, 1988. DOI: `10.1088/0953-4075/21/13/009`. [Online]. Available: `https://doi.org/10.1088/0953-4075/21/13/009`.

[138] F. Giacomini *et al.*, "Quantum mechanics and the covariance of physical laws in quantum reference frames," eng, *Nature communications*, vol. 10, no. 1, pp. 494–494, 2019, ISSN: 2041-1723. DOI: `10.1038/s41467-018-08155-0`. [Online]. Available: `https://pubmed.ncbi.nlm.nih.gov/30700718`.

[139] G. Lugarini *et al.*, "Center-of-mass operators and covariant decomposition of the total angular momentum," *Il Nuovo Cimento A (1965-1970)*, vol. 47, no. 2, pp. 299–318, 1967, ISSN: 1826-9869. DOI: `10.1007/BF02818351`. [Online]. Available: `https://doi.org/10.1007/BF02818351`.

[140] A. Anderson, "Canonical Transformations in Quantum Mechanics," *Annals Phys.*, vol. 232, pp. 292–331, 1994. DOI: `10.1006/aphy.1994.1055`.

BIBLIOGRAPHY

[141] W. F. Palmer *et al.*, "Separability of center of mass and relative motion of hydrogen in very strong magnetic fields," *American Journal of Physics*, vol. 49, no. 9, pp. 855–857, 1981. DOI: 10.1119/1.12382. [Online]. Available: https://doi.org/10.1119/1.12382.

[142] W. Schleich, *Quantum Optics in Phase Space*. Wiley, 2011, ISBN: 9783527635009.

[143] P Schmelcher, "Regularity and irregularity in the centre of mass motion of the positronium atom in a magnetic field," *Journal of Physics B: Atomic, Molecular and Optical Physics*, vol. 25, no. 11, pp. 2697–2708, 1992. DOI: 10.1088/0953-4075/25/11/023. [Online]. Available: https://doi.org/10.1088/0953-4075/25/11/023.

[144] G. Feinberg *et al.*, "Quadratic Zeeman effect in positronium," *Phys. Rev. A*, vol. 41, pp. 3478–3480, 7 1990. DOI: 10.1103/PhysRevA.41.3478. [Online]. Available: https://link.aps.org/doi/10.1103/PhysRevA.41.3478.

[145] B. R. Johnson *et al.*, "Interaction of atoms, molecules, and ions with constant electric and magnetic fields," *Rev. Mod. Phys.*, vol. 55, pp. 109–153, 1 1983. DOI: 10.1103/RevModPhys.55.109. [Online]. Available: https://link.aps.org/doi/10.1103/RevModPhys.55.109.

[146] P. Schmelcher *et al.*, "Electronic and nuclear motion and their couplings in the presence of a magnetic field," *Phys. Rev. A*, vol. 38, pp. 6066–6079, 12 1988. DOI: 10.1103/PhysRevA.38.6066. [Online]. Available: https://link.aps.org/doi/10.1103/PhysRevA.38.6066.

[147] M. H. Johnson *et al.*, "Motion in a constant magnetic field," *Phys. Rev.*, vol. 76, pp. 828–832, 6 1949. DOI: 10.1103/PhysRev.76.828. [Online]. Available: https://link.aps.org/doi/10.1103/PhysRev.76.828.

[148] H. Grotch *et al.*, "Hydrogenic atoms in a magnetic field," *Phys. Rev. A*, vol. 4, pp. 59–69, 1 1971. DOI: 10.1103/PhysRevA.4.59. [Online]. Available: https://link.aps.org/doi/10.1103/PhysRevA.4.59.

[149] H Herold *et al.*, "The two-body problem in the presence of a homogeneous magnetic field," *Journal of Physics B: Atomic and Molecular Physics*, vol. 14, no. 4, pp. 751–764, 1981. DOI: 10.1088/0022-3700/14/4/022. [Online]. Available: https://doi.org/10.1088/0022-3700/14/4/022.

[150] P. Droz-Vincent, "Pseudomomentum conservation for one-body and two-body relativistic dynamics in a constant electromagnetic field," *Phys. Rev. A*, vol. 52, pp. 1837–1844, 3 1995. DOI: 10.1103/PhysRevA.52.1837. [Online]. Available: https://link.aps.org/doi/10.1103/PhysRevA.52.1837.

[151] C. D. Dermer *et al.*, "Perturbative analysis of simultaneous Stark and Zeeman effects on n=1⇆n=2 radiative transitions in positronium," *Phys. Rev. A*, vol. 40, pp. 5526–5532, 10 1989. DOI: 10.1103/PhysRevA.40.5526. [Online]. Available: https://link.aps.org/doi/10.1103/PhysRevA.40.5526.

[152] D. Varshalovich *et al.*, *Quantum theory of angular momentum*. World Scientific, 1988.

[153] G. Breit *et al.*, "Measurement of nuclear spin," *Phys. Rev.*, vol. 38, pp. 2082–2083, 11 1931. DOI: 10.1103/PhysRev.38.2082.2. [Online]. Available: https://link.aps.org/doi/10.1103/PhysRev.38.2082.2.

[154] V. W. Hughes *et al.*, "Hyperfine structure of positronium in its ground state," *Phys. Rev.*, vol. 106, pp. 934–947, 5 1957. DOI: 10.1103/PhysRev.106.934. [Online]. Available: https://link.aps.org/doi/10.1103/PhysRev.106.934.

[155] G. Consolati, "Magnetic quenching of positronium," *Journal of Radioanalytical and Nuclear Chemistry*, vol. 210, no. 2, pp. 273–292, 1996, ISSN: 1588-2780. DOI: 10.1007/BF02056373. [Online]. Available: https://doi.org/10.1007/BF02056373.

[156] Y. Nagashima *et al.*, "Effects of positron spin polarization on orthopositronium and para-positronium formation in a magnetic field," *Phys. Rev. B*, vol. 41, pp. 3937–3942, 7 1990. DOI: 10.1103/PhysRevB.41.3937. [Online]. Available: https://link.aps.org/doi/10.1103/PhysRevB.41.3937.

[157] W. C. Sauder *et al.*, "Zeeman Effect in Positronium Annihilation at Low Temperatures," *Journal of research of the National Bureau of Standards. Section A, Physics and chemistry*, vol. 71A, no. 5, pp. 347–353, 1967, ISSN: 0022-4332. DOI: 10.6028/jres.071A.039. [Online]. Available: https://pubmed.ncbi.nlm.nih.gov/31824058.

[158] O. Halpern, "Magnetic quenching of the positronium decay," *Phys. Rev.*, vol. 94, pp. 904–907, 4 1954. DOI: 10.1103/PhysRev.94.904. [Online]. Available: https://link.aps.org/doi/10.1103/PhysRev.94.904.

[159] D. B. Cassidy *et al.*, "Laser excitation of positronium in the paschen-back regime," *Phys. Rev. Lett.*, vol. 106, p. 173 401, 17 2011. DOI: 10.1103/PhysRevLett.106.173401. [Online]. Available: https://link.aps.org/doi/10.1103/PhysRevLett.106.173401.

[160] R. H. Garstang, "Atoms in high magnetic fields (white dwarfs)," *Reports on Progress in Physics*, vol. 40, no. 2, pp. 105–154, 1977. DOI: 10.1088/0034-4885/40/2/001. [Online]. Available: https://doi.org/10.1088/0034-4885/40/2/001.

[161] M. Badawi *et al.*, "Closed-form hydrogenic radial r^k matrix elements and the factorization method," *Phys. Rev. A*, vol. 8, pp. 727–733, 2 1973. DOI: 10.1103/PhysRevA.8.727. [Online]. Available: https://link.aps.org/doi/10.1103/PhysRevA.8.727.

[162] M. Enciso-Aguilar *et al.*, "Radial matrix elements for the hydrogen atom," *El. J. Theor. Phys.*, vol. 3, pp. 117–120, 13 2006. [Online]. Available: http://www.ejtp.com/ejtpv3i13.html.

[163] F. Villa, "Laser system for positronium excitation to rydberg levels for aegis experiment," PhD thesis, Università degli Studi di Milano, 2011.

[164] F. Setzpfandt, *Lecture notes "Quantum optics"*, University Lecture, 2018.

[165] M. Fox, *Quantum Optics: An Introduction*, ser. Oxford Master Series in Physics. OUP Oxford, 2006, ISBN: 9780198566731.

[166] P. Thompson *et al.*, "Rietveld refinement of Debye–Scherrer synchrotron X-ray data from Al_2O_3," *Journal of Applied Crystallography*, vol. 20, no. 2, pp. 79–83, 1987. DOI: 10.1107/S0021889887087090. [Online]. Available: https://doi.org/10.1107/S0021889887087090.

[167] T. Ida *et al.*, "Extended pseudo-Voigt function for approximating the Voigt profile," *Journal of Applied Crystallography*, vol. 33, no. 6, pp. 1311–1316, 2000. DOI: 10.1107/S0021889800010219. [Online]. Available: https://doi.org/10.1107/S0021889800010219.

[168] B. Smeets *et al.*, "Laser-cooling simulation based on the semiclassical approach," *J. Opt. Soc. Am. B*, vol. 22, no. 11, pp. 2372–2377, 2005. DOI: 10.1364/JOSAB.22.002372. [Online]. Available: http://josab.osa.org/abstract.cfm?URI=josab-22-11-2372.

[169] D. Comparat, "Molecular cooling via sisyphus processes," *Phys. Rev. A*, vol. 89, p. 043 410, 4 2014. DOI: 10.1103/PhysRevA.89.043410. [Online]. Available: https://link.aps.org/doi/10.1103/PhysRevA.89.043410.

[170] J. Raimond, *Lecture notes "Atoms and photons"*, University Lecture, 2013.

[171] H. Perrin, *Les Houches lectures on laser cooling and trapping*, 2012.

[172] C. Storry *et al.*, "First laser-controlled antihydrogen production," *Physical review letters*, vol. 93, no. 26, p. 263 401, 2004.

[173] R McConnell *et al.*, "Large numbers of cold positronium atoms created in laser-selected Rydberg states using resonant charge exchange," *Journal of Physics B: Atomic, Molecular and Optical Physics*, vol. 49, no. 6, p. 064 002, 2016.

[174] S. Mariazzi *et al.*, "Positronium cooling and emission in vacuum from nanochannels at cryogenic temperature," *Physical review letters*, vol. 104, no. 24, p. 243 401, 2010.

[175] S Mariazzi *et al.*, "High-yield thermalized positronium at room temperature emitted by morphologically tuned nanochanneled silicon targets," *Journal of Physics B: Atomic, Molecular and Optical Physics*, vol. 54, no. 8, p. 085 004, 2021. DOI: 10.1088/1361-6455/abf6b6. [Online]. Available: https://doi.org/10.1088/1361-6455/abf6b6.

BIBLIOGRAPHY

[176] C. Amsler *et al.*, "Pulsed production of antihydrogen," *Communications Physics*, vol. 4, no. 1, p. 19, 2021, ISSN: 2399-3650. DOI: 10.1038/s42005-020-00494-z. [Online]. Available: https://doi.org/10.1038/s42005-020-00494-z.

[177] A. Hinterberger *et al.*, "Trapping of C2- in a digital ion trap," *Journal of Physics B: Atomic, Molecular and Optical Physics*, vol. 52, no. 22, p. 225 003, 2019. DOI: 10.1088/1361-6455/ab4940. [Online]. Available: https://doi.org/10.1088/1361-6455/ab4940.

Acknowledgements

Danksagung

Last but not least I would like to express my great thankfulness to all those who made this work possible in the first place. There are undoubtedly many who contributed and supported me over the past five years so that it would definitely not be possible to list, let alone remember, all of them. Therefore, my thanks goes to everyone who feels addressed. Nevertheless there are a number of people whom I owe my most sincere gratitude to:

First of all, I wish to thank Alban Kellerbauer for supervising me during my doctoral studies. Thank you, Alban, for taking your time for the many inspiring discussions and for giving me advice whenever necessary. Thanks as well for making me aware of and guiding me around numerous obstacles that I was sometimes blind to or simply did not want to see. During my visits at the Max-Planck-Institut in Heidelberg I could furthermore spend some great time with your team, Giovanni Cerchiari, Stefan Erlewein and Pauline Yzombard. Thanks Giovanni for the many valuable experimental advices that you gave me with regard to the Borealis experiment. And thanks Pauline for your support on our joint paper a few years later.

Among the many people at CERN I am especially grateful to Michael Doser for giving me the chance to join the AEḡIS experiment and your great team for my PhD studies in 2016. Thanks for your scientific advice and for giving me a lot of freedom in many respects. Only this made it possible for me to conduct such fascinating research over the whole five years.

With regard to my first two years at CERN it is first and foremost the whole Borealis team whom I wish to thank, in particular Sebastian Gerber for establishing the very first contact and for motivating me to join the AEḡIS experiment but also for several valuable discussions. Thanks a lot also to all other group members, Julian Fesel, Alexander Hinterberger, Stefan Erlewein and of course Emanuel Oswald. Furthermore, I would like to thank Lilian Nowak and Tim Wolz for the many encouraging words.

Next, I owe great gratitude of course to the whole AEḡIS team from whom I learned so much more than over all previous years of studies and with whom I spent a lot of great moments, not only in the control room but of course also directly at the experiment. Since the list of people which have been, or still are part of the AEḡIS collaboration is long and I cannot name all of them without missing anyone, I would hereby like to thank the whole collaboration for its support. Nevertheless, there are a few people whom I am particularly grateful to. First of all, Stefan Haider, thank you very much for sharing your great wealth of experience with me and of course for constantly filling the coffee supply without which life would sometimes have been so much harder. Benjamin Rienäcker, thank you for the many discussions that I had with you, be it about physics, the measurements and the experiment or about the many other things which sometimes move a physicist's life. Thanks as well for sharing some of your valuable python codes with me and for being available whenever there was urgent need for the positron expert. Ruggero Caravita, thank you so much for sharing your incomparable physical understanding and wealth of experience on the experiment with me. Thanks as well for the many encouraging words in less successful times. It was a great pleasure to work with all of you! Merci beaucoup, grazie mille, und vielen Dank!

There is good reason for not having mentioned Antoine Camper so far. This is owing to the fact that you, Antoine, played a very special role over the whole time that I spent in the AEḡIS collaboration. Triggered by my decision to work on laser cooling of positronium atoms I had the chance to develop a very special relationship with you. Starting from our mere cooperation to refurbish the cooling laser setup, for which we spent many hours together in the laser hut and during which I benefited a lot from your invaluable experience, you soon became a real mentor for me. Thank you so much for the numerous ways in which I experienced your great support, be it for revision of several manuscripts or applications, the remote advice on technical matters, the fruitful cooperation in writing our paper leading to considerable improvement or finally for granting

Acknowledgements